TUNNEL BEHAVIOR UNDER COMPLEX ANISOTROPIC CONDITIONS

by

Osvaldo Paiva Magalhães Vitali

A Dissertation

Submitted to the Faculty of Purdue University

In Partial Fulfillment of the Requirements for the degree of

Doctor of Philosophy

Lyles School of Civil Engineering

West Lafayette, Indiana

August 2020

THE PURDUE UNIVERSITY GRADUATE SCHOOL
STATEMENT OF COMMITTEE APPROVAL

Dr. Antonio Bobet, Co-Chair

Lyles School of Civil Engineering, Purdue University

Dr. Tarcisio B. Celestino, Co-Chair

Sao Carlos Engineering School, University of São Paulo

Dr. Thomas Siegmund

School of Mechanical Engineering, Purdue University

Dr. Ghadir Haikal

Southwest Research Institute

Approved by:

Dr. Dulcy M. Abraham

To my wife, Bruna, and my parents, Ângela e Osvaldo.

ACKNOWLEDGMENTS

I would like to express my sincere gratitude to:

My wife, Bruna Nunes, for the unwavering support.

My family in Brazil.

Professor Antonio Bobet, the advisor of the doctoral research, for accepting me as a Ph.D. student, for the guidance and great enthusiasm with the research and for developing the analytical solutions presented in this thesis. I was very fortunate to have Prof Bobet as academic advisor.

Professor Tarcisio Celestino, co-advisor of the doctoral research, for the orientation and deep interest in the conducted research and for suggesting this interesting topic for research.

Professor Maria Caterina Santagata, for inviting me to work as Teaching Assistant for Geotechnical Engineering I. It was a great experience.

The Brazilian National Council for Scientific and Technological Development - CNPq, Brazilian Government, for having granted a full scholarship for doctoral studies abroad.

Midas Co., which kindly provided a license of the FEM software Midas GTS NX, used on the numerical analyses conducted in this research.

Professor Thomas Siegmund and Professor Ghadir Haikal, members of the Doctoral Committee, for the suggestions that greatly improved the research.

TABLE OF CONTENTS

LIST OF TABLES

LIST OF FIGURES

ABSTRACT

Rock masses may present remarked geostatic stress anisotropy and anisotropic material properties; thus, the tunnel alignment with the geostatic principal stress directions and with the axes of material anisotropy is unlikely. Nevertheless, tunnel design often neglects those misalignments and; yet, the misalignment effects were unknown. In this doctoral research, tunnels under complex anisotropic conditions were modelled analytically and numerically with 3D nonlinear Finite Element Method (FEM). When the tunnel misaligns with the geostatic principal stress directions, anti-symmetric axial displacements and shear stresses are induced around the tunnel. Analytical solutions for misaligned shallow and deep tunnels in isotropic elastic ground are provided. The analytical solutions were validated with 3D FEM analyses. Near the face, the anti-symmetric axial displacements are partially constrained by the tunnel face, producing asymmetric radial displacements and stresses. The asymmetric radial displacements at the face can be divided into a rigid body displacement of the tunnel cross-section and anti-symmetric radial displacements. Those asymmetries may affect the rock-support interaction and the plastic zone developed around the tunnel. In anisotropic rock masses, the tunnel misalignment with the axes of material anisotropy also produces anti-symmetric axial displacements and stresses around the tunnel. It occurs because when the tunnel is not aligned with the principal material directions, the in-plane stresses are coupled with the axial displacements (i.e. the compliance matrix is fully populated). Thus, tunnels in anisotropic rock mass not aligned with the geostatic principal stresses and with the axes of material anisotropy are substantially more complex than tunnels not aligned with the principal stress directions in isotropic rock mass. An analytical solution for misaligned tunnels in anisotropic rock mass is provided. It was observed that the relative orientation of the geostatic principal stresses with respect to the axes of material anisotropy plays an important role. The axial displacements produced by far-field axial shear stresses and by the rock mass anisotropy may compensate each other; thus, axial and radial displacements around the tunnel are reduced. On the other hand, those anti-symmetric axial displacements may be amplified; thus, the ground deformations are increased. Asymmetric radial and axial deformations, and asymmetric spalling of the tunnel walls are commonly observed on tunnels in anisotropic rock masses. The tunnel misalignment with the geostatic principal stress directions and with the axes of material anisotropy could be associated with those phenomena that, so far, are not well comprehended.

1. INTRODUCTION

1.1 Importance of the Research

The literature shows that rock masses are likely to present remarked geostatic stress anisotropy and anisotropic mechanical properties. Those are consequences of the rock's complex formation processes. According to Brady & Brown (2006), the main factors affecting rock behavior and geostatic stresses are: topography (elevations and valleys); residual stresses (due to cooling, for instance); tectonic movements; fracturing and sets of joints; and inclusions. The interplay among those factors is complex; thus, geostatic stresses and mechanical properties are expected to be complex as well. In addition, it is anticipated that residual soils, since they inherit the fabric structure from the rock matrix, also present anisotropic behavior. Examples include the granite residual soils in Porto (Gomes & Fonseca, 2013) and the gneiss residual soils in Sao Paulo (Futai et al., 2013).

Brown & Hoek (1978) compiled the in-situ stresses of a large variety of rock masses at a large number of locations and depths. The authors observed that the vertical stress (σ_v) follows a scattered linear trend with depth (z), in which the line σ_v=0.027z (MPa) fits the data relatively well. However, the ratio of the average horizontal stress with the vertical stress ($K=\sigma_{h,average}/\sigma_v$) varies significantly with depth. Jaeger et al. (2007) observed that for depths shallower than 300 m, the scatter was large and ranged between 1 and 4. Below 2,000 m, the range was narrower and most of the data fell below or around one. There is consensus in the literature that the large scatter of K close to the surface is due to topographic effects (Brady & Brown, 2006; Goodman, 1989; Hoek, 2008) and tectonic activity (Haimson et al., 2003; Park et al., 2014). McGarr & Gay (1978) compiled the full in-situ stress tensor at 77 different sites. This compilation included the principal stress ratios (σ_1/σ_3, σ_2/σ_3 and σ_1/σ_2), with depth, and a variety of rock masses. The interval with 95% confidence for each principal stress ratio was: $\sigma_1/\sigma_2=1.45\pm0.80$; $\sigma_1/\sigma_3=2.42\pm2.28$; and $\sigma_2/\sigma_3=1.66\pm1.0$. These statistics showed that the expected stress anisotropy in rock masses was high and quite variable. Indeed, the literature is rich in measurements of in-situ stresses and shows that strong stress anisotropy should be expected in rock masses (Evans et al., 1989; Gysel, 1975; Haimson et al., 2003; Park et al., 2014; Read & Martin, 1992; Wileveau et al., 2007).

Rock masses may have a structure defined by bedding, stratifications, layering, foliations, joints and flow structures, to name a few; thus, anisotropic behavior should be anticipated. Anisotropic elastic and elastoplastic models are mostly used to represent such behavior. Amadei et al. (1987) compiled the stiffness ratio E_1/E_3 versus G_{12}/G_{13}, and the Poisson's ratios ν_{12} versus ν_{13} for a wide range of rocks and test procedures ("1" is the direction parallel to the fabric structure, "3" is the perpendicular direction and "2" is the longitudinal direction, i.e. normal to planes with directions 1 and 3). The compiled ratios E_1/E_3 were usually smaller than two. There was a large scatter on the measured Poisson's ratios, but most of the data fit within the range 0.1 to 0.3, which is typical of rocks. The majority of the tests showed E_1 larger than E_3, indicating that the stiffness parallel to the fabric structure is larger than the stiffness perpendicular to it. Worotnicki (1993) also compiled results of the stiffness ratio E_1/E_3. The author pointed out that granites, sandstones, gneisses and amphibolites showed small to moderate anisotropy (i.e. 70% of the tested rocks had $E_1/E_3 < 1.3$, 80% had $E_1/E_3 < 1.5$ and only 3% had $E_1/E_3 > 2$); mudstones, slates, phyllites and schists showed high anisotropy (50% had $E_1/E_3>2$ and 30% had $E_1/E_3<1.5$; also, the maximum measured ratio was 6); limestones, marbles and dolomites (carbonatic rocks) had low to moderate anisotropy (60% had $E_1/E_3 < 1.3$, 80% had $E_1/E_3 < 1.5$ and the largest E_1/E_3 was 1.7). More recently, Park & Min (2015) found a stiffness ratio E_1/E_3 of 1.4 for Asan Gneiss; 1.75 for Boryeong shale and 3.8 for Yeoncheon schist, which is consistent with the compiled data previously presented.

Tonon & Amadei (2003) conducted a 2D FEM parametric analysis to assess the influence of the stiffness anisotropy on tunnel behavior. The authors observed that, for a highly anisotropic ground ($E_1/E_3 = 3.25$), the stress field around an unsupported tunnel was not significantly affected; however, the ground deformations were very much dependent on the anisotropy ratios. A similar observation was made by Fortsakis et al. (2012), who also conducted a series of 2D FEM analyses. The authors concluded that the assumption of an equivalent isotropic ground could lead to an underestimation of the ground deformations.

The importance of the tunnel orientation with respect to the geostatic principal stress directions is recognized by the practical recommendation of aligning the tunnel with the geostatic major principal stress (σ_H) (Goodman, 1989). Tunnels were constructed in an Underground Research Laboratory (URL) in France to investigate their behavior by adopting different construction methods and supports. The URL was placed at 490m depth in an anisotropic Claystone rock mass. The principal stress ratios were, as average, $\sigma_h/\sigma_v=1$ and $\sigma_H/\sigma_v = 1.3$

(Wileveau et al., 2007). Because of the sedimentation process, the rock had an oriented structure (bedding), with E_1/E_3 varying from 1.2 to 2 (Armand et al., 2013). Tunnels were excavated parallel and perpendicular to σ_H. A supported circular tunnel of radius of 2.6m aligned with σ_H showed a horizontal convergence of 37 to 58mm and a vertical convergence of 24 to 30mm. A similar tunnel aligned with σ_h showed horizontal convergence of 19mm to 34mm and vertical convergence of 112mm to 158mm (Armand et al., 2013). The data illustrates the importance of the tunnel orientation with respect to the geostatic principal stresses.

As discussed, rock masses may present remarked stress and material anisotropy, which may strongly affect tunnel behavior. However, tunnel design often neglects the tunnel orientation with respect to the far-field stress or with the directions of material anisotropy; yet, there is lack of research on the effects of the tunnel misalignment with respect to the geostatic principal stresses and to the material anisotropy directions. When the tunnel is not aligned with the geostatic principal stresses, those stresses can be decomposed into stresses in the plane of the tunnel cross-section and perpendicular to the tunnel cross-section, i.e. axial shear and normal stresses. The far-field axial shear stresses cause anti-symmetric axial displacements and shear stresses along the axis of the tunnel. If the rock mass has anisotropic properties, the tunnel misalignment with the principal directions of material anisotropy also induces anti-symmetric axial displacements and axial shear stresses along the tunnel. The reason for this is that the tunnel response is fully coupled in the transverse and longitudinal directions (i.e. the compliance matrix of the system is fully populated) when the tunnel axis misaligns with the axes of material anisotropy. The consequences of the induced axial shear stresses and axial distortion on the behavior of tunnels has been unexplored in the literature. This doctoral research seeks to fill this gap. The objective of this research is to fully understand the behavior of tunnels under complex anisotropic conditions. To achieve this goal, an exhaustive numerical modeling campaign was conducted, investigating several scenarios of tunnels under complex anisotropic conditions. Numerical results were confronted with the actual behavior of tunnels in highly anisotropic rock masses. Analytical solutions for misaligned tunnels were also developed and validated with numerical results. The excellent agreement between analytical and numerical solutions essentially shows that both solutions are correct. The results presented in this Dissertation show that the misalignment of tunnels with principal directions of stress and material anisotropy can explain the asymmetric deformations and asymmetric failure commonly observed in tunnels in anisotropic rock masses.

1.2 Dissertation Organization

This Dissertation is a collection of articles that have been published or are in the review process for publication. Eleven papers were written (eight papers in peer-reviewed journals and three conference papers). The list of articles is shown below. The articles are organized as chapters of this Dissertation. The research can be divided into three parts: (1) Numerical modeling of tunnels, papers 1 to 3; (2) Tunnels misaligned with the geostatic principal stress directions in isotropic ground, papers 4 to 7; and (3) Tunnels misaligned with the geostatic principal stress directions in anisotropic ground, papers 8 to 11.

The first stage of the research focused on the numerical modeling of tunnels. Topics regarding three-dimensional numerical modeling of tunnels using a nonlinear Finite Element Method (FEM), such as mesh discretization, model dimensions, boundary conditions, ground-support interaction, 3D face effects, influence of the construction sequence and buoyancy effects, were investigated. Three papers were written on this topic: papers (1) to (3).

The second stage of the research focused on tunnels not aligned with the geostatic principal stress directions. When the tunnel is not aligned with the principal stresses, far-field axial shear stresses are present. Those stresses induce anti-symmetric axial displacements around the tunnel. These effects are often neglected in tunnel design; yet, their influence on tunnel behavior has not been fully explored. The influence of the far-field axial shear stresses was exhaustively investigated near and far-behind the face, for unsupported and supported tunnels in elastic and elastoplastic rock masses. Four papers were written on this topic: papers (4) to (7).

The third research stage concentrated on tunnels in anisotropic rock masses not aligned with principal stress directions and with the principal axes of material anisotropy. Supported and unsupported tunnels were investigated, considering different orientations of the principal stress directions with respect to the axes of material anisotropy. Four papers were written on this topic: papers (8) to (11).

(1) VITALI, O. P. M.; CELESTINO, & BOBET, A. (2017). 3D finite element modelling optimization for deep tunnels with material nonlinearity. Underground Space, 3(2), 125–139. https://doi.org/10.1016/j.undsp.2017.11.002

(2) VITALI, O. P. M.; CELESTINO, & BOBET, A. (2019). Buoyancy effect on shallow tunnels. International Journal of Rock Mechanics and Mining Sciences. 114(2), 1–6. https://doi.org/10.1016/j.ijrmms.2018.12.012

(3) VITALI, O. P. M.; CELESTINO, & BOBET, A. (2020). Construction strategies for a NATM tunnel in Sao Paulo, Brazil, in residual soil. Manuscript under review for publication in a peer-reviewed journal.

(4) VITALI, O. P. M.; CELESTINO, & BOBET, A. (2018). Analytical solution for tunnels not aligned with geostatic principal stress directions. Tunnelling and Underground Space Technology, 82: 394–405. https://doi.org/10.1016/j.tust.2018.08.046

(5) VITALI, O. P. M.; CELESTINO, & BOBET, A. (2019). Shallow tunnel not aligned with the geostatic principal stress directions. In: Proceedings of Geo-Congress2019, GSP 313:214-222. https://ascelibrary.org/doi/10.1061/9780784482155.023

(6) VITALI, O. P. M.; CELESTINO, & BOBET, A. (2019). Shallow tunnels misaligned with geostatic principal stress directions: analytical solution and 3D face effects. Tunnelling and Underground Space Technology.89: 268-283. https://doi.org/10.1016/j.tust.2019.04.006

(7) VITALI, O. P. M.; CELESTINO, & BOBET, A. (2019). Progressive failure due to tunnel misalignment with geostatic principal stresses. In: Proceedings of ISRM 14th International Congress on Rock Mechanics: 2292-2299.

(8) VITALI, O. P. M.; CELESTINO, & BOBET, A. (2020). Analytical solution for a deep circular tunnel in anisotropic ground and anisotropic geostatic stresses. Manuscript under review for publication in a peer-reviewed journal.

(9) VITALI, O. P. M.; CELESTINO, & BOBET, A. (2020). 3D face effects of tunnels misaligned with the principal directions of material and stress anisotropy. Manuscript under review for publication in a peer-reviewed journal.

(10) VITALI, O. P. M.; CELESTINO, & BOBET, A. (2020). Tunnel misalignment with geostatic principal stress directions in anisotropic rock masses. Soils and Rocks. Accepted for publication on Feb/13/2020.

(11) VITALI, O. P. M.; CELESTINO, & BOBET, A. (2020). Deformation patterns and 3D face effects of tunnels misaligned with the geostatic principal stresses in isotropic and anisotropic rock masses. 54th US Rock Mechanics /Geomechanics Symposium (ARMA 2020).

1.3 References

Amadei, B., Savage, W. Z., & Swolfs, H. S. (1987). Gravitational stresses in anisotropic rock masses. International Journal of Rock Mechanics and Mining Sciences, 24(1), 5–14.

Armand, G., Noiret, A., Zghondi, J., & Seyedi, D. M. (2013). Short- and long-term behaviors of drifts in the Callovo-Oxfordian claystone at the Meuse/Haute-Marne Underground Research Laboratory. Journal of Rock Mechanics and Geotechnical Engineering, 5(3), 221–230. https://doi.org/10.1016/j.jrmge.2013.05.005

Bobet, A. (2003). Effect of pore water pressure on tunnel support during static and seismic loading. Tunnelling and Underground Space Technology, 18(4), 377–393. https://doi.org/10.1016/S0886-7798(03)00008-7

Brady, B. H. G., & Brown, E. T. (2006). Rock Mechanics for underground mining: Third edition. Rock Mechanics for underground mining: Third edition. https://doi.org/10.1007/978-1-4020-2116-9

Brown, E. T., & Hoek, E. (1978). Trends in relationships between measured in-situ stresses and depth. International Journal of Rock Mechanics and Mining Sciences And, 15(4), 211–215. https://doi.org/10.1016/0148-9062(78)91227-5

Do, N. A., Dias, D., Oreste, P., & Djeran-Maigre, I. (2014). Three-dimensional numerical simulation of a mechanized twin tunnels in soft ground. Tunnelling and Underground Space Technology, 42, 40–51. https://doi.org/10.1016/j.tust.2014.02.001

Evans, K. F., Engelder, T., & Plumb, R. A. (1989). Appalachian Stress Study .1. a Detailed Description of Insitu Stress Variations in Devonian Shales of the Appalachian Plateau. Journal of Geophysical Research-Solid Earth and Planets, 94, 7129–7154.

Fortsakis, P., Nikas, K., Marinos, V., & Marinos, P. (2012). Anisotropic behaviour of stratified rock masses in tunnelling. Engineering Geology, 141–142, 74–83. https://doi.org/10.1016/j.enggeo.2012.05.001

Futai, M., Cecilio, M., & Abramento, M. (2013). Shear Strength and Deformability of Residual Soils from the Sao Paulo Metropolitan Area. Twin Cities: Solos Da Regiao Metropolitana de Sao Paulo e Curituba, Chapter 7.

Gomes, A. . T., & Fonseca, A. . V. da. (2013). Aspects influencing stiffness on a granite residual soil. Geotechnical and Geophysical Site Characterization 4, 851–857.

Goodman, R. E. (1989). Introduction to rock mechanics. https://doi.org/10.1016/0148-9062(81)90521-0

Gysel, M. (1975). In-Situ stress measurements of the primary stress state in the Sonnenberg tunnel in Lucerne, Switzerland. Developments in Geotectonics, 9(C), 301–314. https://doi.org/10.1016/B978-0-444-41420-5.50036-8

Haimson, B. C., Lee, M. Y., & Song, I. (2003). Shallow hydraulic fracturing measurements in Korea support tectonic and seismic indicators of regional stress. International Journal of Rock Mechanics and Mining Sciences, 40(7–8), 1243–1256. https://doi.org/10.1016/S1365-1609(03)00119-9

Hoek, E. (2008). Practical Rock Engineering. https://doi.org/10.2113/gseegeosci.14.1.55

Jaeger, J. C., Cook, N. G. W., & Zimmerman, R. W. (2007). Fundamentals of Rock Mechanics Fourth Edition. Rock Mechanics. https://doi.org/10.1016/0040-1951(77)90223-2

McGarr, a, & Gay, N. C. (1978). State of Stress in the Earth's Crust. Ann. Rev. Earth Planet. Sci., 6, 405–436.

MIDAS Information Technology Co. (2014). Benchmarks & Verification GTS NX manual.

Park, B., & Min, K.-B. (2015). Bonded-particle discrete element modeling of mechanical behavior of transversely isotropic rock. International Journal of Rock Mechanics and Mining Sciences, 76, 243–255. https://doi.org/10.1016/j.ijrmms.2015.03.014

Park, E. S., Choi, B. H., Bae, S. H., & Jeon, S. (2014). Horizontal stresses at shallow depths in Seoul (Korea) gneissic region. Rock Engineering and Rock Mechanics: Structures in and on Rock Masses - Proceedings of EUROCK 2014, ISRM European Regional Symposium, 399–404.

Read, R., & Martin, C. D. (1992). Monitoring the excavation-induced response of granite. The 33th U.S. Symposium on Rock Mechanics (USRMS), 10. Retrieved from https://www.onepetro.org/conference-paper/ARMA-92-0201

Tonon, F., & Amadei, B. (2003). Stresses in anisotropic rock masses: An engineering perspective building on geological knowledge. International Journal of Rock Mechanics and Mining Sciences, 40(7–8), 1099–1120. https://doi.org/10.1016/j.ijrmms.2003.07.009

Verruijt, A., & Booker, J. R. (2000). Complex variable analysis of Mindlin' s tunnel problem, (January 2000), 1–20.

Wileveau, Y., Cornet, F. H., Desroches, J., & Blumling, P. (2007). Complete in situ stress determination in an argillite sedimentary formation. Physics and Chemistry of the Earth, 32(8–14), 866–878. https://doi.org/10.1016/j.pce.2006.03.018

Worotnicki, G. (1993). 13 – CSIRO Triaxial Stress Measurement Cell. Rock Testing and Site Characterization. Pergamon Press Ltd. https://doi.org/10.1016/B978-0-08-042066-0.50020-3

2. 3D FINITE ELEMENT MODELLING OPTIMIZATION FOR DEEP TUNNELS WITH MATERIAL NONLINEARITY

VITALI, O. P. M.; CELESTINO, & BOBET, A. (2017). 3D finite element modelling optimization for deep tunnels with material nonlinearity. *Underground Space*, 3(2), 125–139. https://doi.org/10.1016/j.undsp.2017.11.002

Abstract

3D modeling of tunnels using a nonlinear ground model is still a time-consuming task because it usually requires a large number of incremental phases with iterative processes, to ensure accuracy while minimizing computational effort. Optimization of the finite element mesh is of utmost importance. Despite the current tendency towards 3D modeling of tunnels, few publications are concerned with mesh optimization considering model size, grid refinement and order of elements. This paper improves the understanding of key issues that affect 3D modeling of tunnels. Our results shown that: (1) 2nd order elements are more efficient when material nonlinearity is present and should be preferred; (2) the plastic zone size has a strong influence on the model dimensions and may require discretizations much larger than those currently accepted. The paper provides recommendations for mesh refinement and model dimensions (width and length) as a function of the plastic zone size, for accurate 3D models with reduced computational cost.

2.1 Introduction

Tunnel design currently relies on numerical models thanks to the increase of computer capabilities, together with the development of sophisticated and user-friendly finite element codes and ground models. The 3D modeling of tunnels is becoming more attractive due to recognized limitations of the 2D modeling (Janin et al., 2015; Möller, 2006), and because 3D modelling is able to capture better the response of tunnel excavations (Janin et al., 2015; Mašín, 2009; Möller, 2006; Svoboda & Masin, 2011; Yeo et al., 2009).

Despite the improvements in hardware and software, 3D modelling of tunnels is still a time-consuming task because it involves incremental phases to simulate the excavation and, most often, incorporates material nonlinearity (i.e. plasticity). The step-by-step excavation procedure

consists of a sequence of phases where the elements inside the opening (excavation rounds) are deactivated while the elements that represent the liner are activated.

The potentially large number of incremental phases, complemented with material nonlinearity (i.e. several iterations to converge), makes the 3D modelling of tunnels expensive. For instance, Franzius & Potts, 2005 mentioned calculation times of 291.3h to run a 45,947 nodes finite element model with 40 incremental phases and 194.9h to run a 38,083 nodes model with 32 incremental phases on a Sun SF 880 server at Cambridge University. They also suggested that the excavation round length used in the model should be linked to the computational capabilities, given that this parameter strongly influences the time for processing.

More recently, Do et al., 2014, performed a 3D numerical study of mechanized twin tunnels simulating details of the excavation, such as face pressure, shield weight and gap filled with grouting. Their models had 1,100,000 nodes and required 340h (approx. 2 weeks) to run using a 2.67 GHz core i7 CPU RAM 24G computer. Despite improvements of hardware, tunnel models are increasing in complexity and, therefore, requiring more computational effort to run. Such effort may make 3D modelling unfeasible for some applications. An optimum finite element mesh that leads to accurate results in reasonable time is necessary to make 3D modelling feasible, for both industry and research. Surprisingly, few publications on numerical modelling of tunnels are dedicated to mesh optimization.

The literature presents a wide range of model sizes (length and width) and finite element grids (Do et al., 2014; Eberhardt, 2001; Gomes & Celestino, 2009; Janin et al., 2015; Möller, 2006; Nam & Bobet, 2007; C. W. W. Ng, Lee, Ng, & Lee, 2005; Svoboda & Masin, 2011; Yeo et al., 2009), that seem to indicate that there is no well-stablished procedure to define model dimensions and grid refinement. For instance, Franzius & Potts, 2005, summarized the model dimensions carried out by other authors. From the summary, one can observe that the model width has an average of $17.8R_{tunnel}$ and a standard deviation of $10R_{tunnel}$ (R_{tunnel} is the radius of the tunnel); and the model length has an average of $27.2R_{tunnel}$ and a standard deviation of $15.2R_{tunnel}$. These statistics illustrate the large scatter of the models sizes found in the literature.

Most of the recommendations for model size consider stresses, strains and displacements at the boundaries. Meisnerr, 1996, cited by Möller, 2006, states that a $8R_{tunnel}$ to $10R_{tunnel}$ model width would be enough to minimize errors; this is in agreement with the rule of thumb that the boundaries should be at least $10R_{tunnel}$ far from the opening. However, such recommendation

suggests that the boundaries are only affected by the size of the tunnel and not by other variables such as the initial stresses, plastic size and/or geological features.

Möller, 2006, proposed expressions to establish the model dimensions for shallow tunnels as a function of the tunnel diameter and the overburden ratio (ratio between tunnel depth and tunnel radius), by using an advanced constitutive model for the ground (a hardening soil model), while considering surface settlements and shear stress mobilization at the boundaries. The criteria were that the settlement at a lateral boundary should not exceed 1% of the maximum settlement along the surface and that the principal stress directions should not rotate more than 2.5° with respect to their initial directions at the boundaries. Such limits are uncertain and do not provide information on the accuracy achieved by the numerical model around the opening; also, the conclusions did not explicitly consider the size of the plastic zone. Interestingly, Möller, 2006, found that the necessary mesh width was the same for 2D and 3D models.

Vlachopoulos & Diederichs, 2014, recommended that the boundaries should be placed at least 12 tunnel radius (R_{tunnel}) from the opening and at least $3R_{yield}$ (yield radii) from the plastic zone around the opening. However, no relation was provided between the size of the model and the accuracy achieved around the opening, nor the criteria for the recommendation.

This paper seeks to improve our understanding on how the finite element mesh and the sequential excavation modelling affect the numerical results, considering material nonlinearity; thus, providing guidelines and information for practitioners and academicians to build more efficient and reliable 3D models.

2.2 Grid refinement and type of element

3D models of tunnels are usually built by extruding a 2D grid along the tunnel axis. All references consulted (except Janin et al., 2015, which adopted a 3D mesh with tetrahedron elements) used extrusion. Figure 2.1 illustrates the most common type of 3D models found in the literature. The aim of this section is to investigate the transversal grid refinement and the order of the elements (i.e. interpolation function) for 3D simulations.

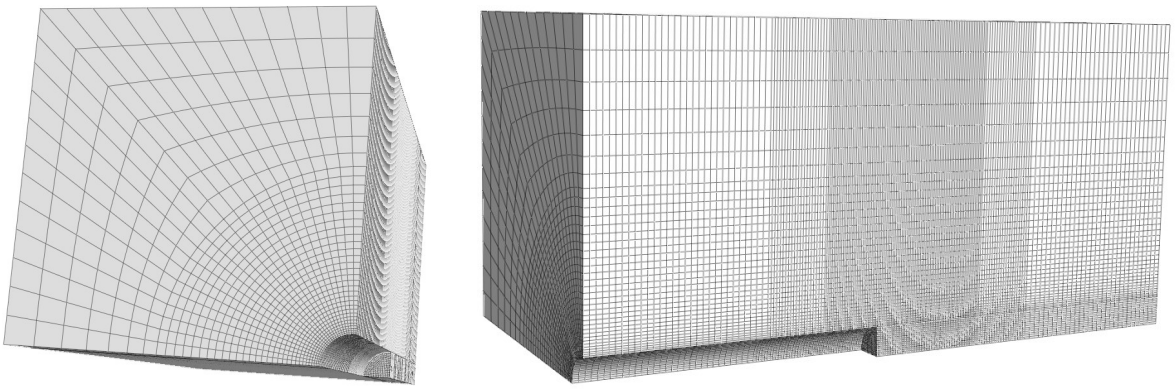

Figure 2.1 Typical 3D tunnel model found in the literature, typically built by extrusion of a 2D grid.

Grid refinement and order of elements were evaluated such that nonlinear behavior was accurately captured; that is, the goal was to find whether there is an advantage of using quadratic interpolation elements (serendipity 2nd order elements – 20 node hexahedron elements) instead of linear interpolation elements (1st order elements – 8-node hexahedron elements) and how refined the grid should be to obtain accurate results.

Numerical accuracy, defined as how close a result is from its true value, was assessed using the results obtained with a very refined grid. Figure 2.2 shows a cross section perpendicular to the tunnel axis, far from the face such that uniform results are obtained. The numerical output is consistent with the analytical solution developed for plane strain hollow plates loaded at the boundaries, for elastic perfectly plastic Mohr-Coulomb material (Salesçon, 1969). Such analytical solution has been used to validate the elastic perfectly plastic Mohr-Coulomb model in FEM codes, such as Midas NX GTS (MIDAS, 2014)More specifically, comparisons are made with the radial displacements at the perimeter of the opening.

Accuracy is calculated using the following equation, which measures the error between the true (reference) solution and the value obtained from a given realization. $Accuracy(\%) = \frac{\left|u - u_{reference}\right|}{\left|u_{reference}\right|}$. Where $u_{reference}$ is taken from the reference mesh. Note that the accuracy is expressed as a percentage.

A deep unsupported circular tunnel is assumed, with a radius of 5 m (R_{tunnel}=5m), subjected to far-field geostatic pressures of 100 kPa and coefficient of earth pressure at rest, K_o, equal to 1, i.e. hydrostatic loading. Note that under these conditions, the problem has axial symmetry. It is

common practice to adopt a uniform stress field with depth for deep tunnel analysis. This is a valid assumption because the changes in stress with depth are negligible for a deep tunnel (Bobet, 2003). For the models, the lateral boundaries are placed at 250m ($50R_{tunnel}$) from the center of the tunnel, a distance large enough such that errors due to the boundaries are avoided, and the axial boundaries are also far enough such that plane strain conditions are achieved at the cross section of interest.

The ground models were either linear elastic ($R_{yield}=R_{tunnel}$) or elastic perfectly plastic with a Mohr-Coulomb failure with associated flow rule ($\Psi=\varphi=19.6°$), that results in $R_{yield}=3R_{tunnel}$ (the soil properties are presented in Table 2.1). Note that a yield radius greater than three times the tunnel radius is unlikely in practice because it would lead to unacceptable ground movements and even collapse of the opening. In weak ground conditions, the support would prevent such large plastic deformations around the opening. Therefore, $R_{yield}=3R_{tunnel}$ is representative of the worst case scenario. Further, an associated flow rule was assumed, which carries relatively high volumetric plastic strains ($\Psi=\varphi=19.6°$), making the material nonlinearity more noticeable.

Figure 2.2 shows the refined mesh with 2nd order elements, used as reference. Figure 2.2 also shows the yield radius obtained using the parameters presented in Table 2.1 for $R_{yield}=3R_{tunnel}=15$m. The size of the yield radius matches the analytical solution.

The strength parameters shown in Table 2.1 (cohesion and friction angle) were determined given the yield radius (R_{yield}) for 100kPa hydrostatic pressure, using Salesçon's solution. The size of the plastic zone is representative of the level of nonlinearity of the numerical model. Therefore, the recommendations throughout the paper may be applicable to other ground conditions, far-field stresses and to supported tunnels, based on the size of the plastic zone developed around the tunnel.

Table 2.1 Soil properties for R_{yield}/R_{tunnel} ratios. Tunnel with R_{tunnel} = 5m and 100kPa far-field hydrostatic pressure.

R_{yield} / R_{tunnel}	c (kPa)	ϕ (°)	E (MPa)	ν
1	-	-	100	0.3
1.5	28.1	19.6	100	0.3
2	17.5	19.6	100	0.3
2.5	12.7	19.6	100	0.3
3	10.0	19.6	100	0.3

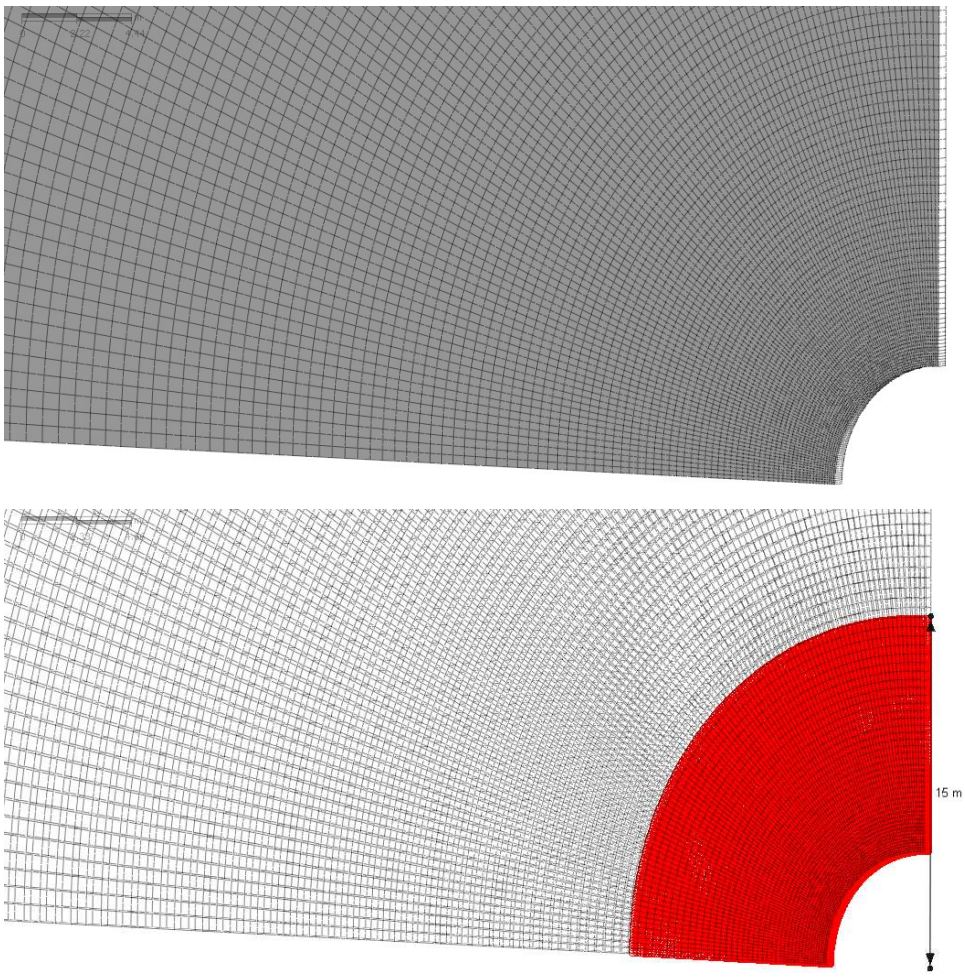

Figure 2.2 Refined mesh using 2nd order hexahedra, used as reference, and yield ground.

Both structured and unstructured grids are investigated. Structured grids have a regular pattern, and are common in the literature (Eberhardt, 2001; Gomes & Celestino, 2009; Nam & Bobet, 2007; Nicholas Vlachopoulos & Diederichs, 2014). Unstructured grids have an irregular pattern. Unstructured grids provide more flexibility to discretize the domain compared to structured grids, given that they allow complex nodal connectivity and different element types (i.e. rectangular and triangular elements). Therefore, initially, unstructured grids could be preferable because they allow a more efficient distribution of nodes and quadrature points; that is, a more refined grid in the region near the opening and a coarser grid far from the opening.

First, structured grids are analyzed. A total of 6 different grids are assessed. The grids are made by dividing the opening perimeter and the boundaries equally, adopting a refined grid close to the opening that gradually coarsens towards the boundaries.

Figure 2.3 plots the normalized radial displacement at the perimeter of the opening, as a function of the number of nodes of the different grids. The radial displacements are normalized by those of the reference model (Figure 2.2) using the same ground properties. The computational effort is directly related to the number of nodes, which determines the size of the system of equations to be solved, while the efficiency of a model relates the accuracy achieved with the number of nodes in the model; that is, the higher the accuracy and the smaller the number of nodes, the more efficient the mesh is. Thus, the efficiency of the finite element mesh can be assessed by comparing the number of nodes with the accuracy achieved.

Figure 2.3 shows that, for all cases analyzed, the difference in normalized displacements from the case considered "correct" decreases as the number of nodes (i.e. as the number of elements) increases. It is interesting to note that irrespective of the type of element, either first order or second order, the errors are small if the ground model is elastic. This is not the case however when plasticity is considered. Indeed, when the material yields ($R_{yield}=3R_{tunnel}$ and associated flow rule, $\Psi=\varphi=19.6°$), the most refined mesh with 1st order elements achieves a 12.8% accuracy using 918 nodes, while the coarser mesh with 2nd order elements achieves a 4.9% accuracy using only 287 nodes. The grid with 2nd order elements considered optimum (coarsest grid with errors smaller than 1% for nonlinear material) is presented in Figure 2.4. In this case, the errors are 0.6% with 836 nodes.

The data in Figure 2.3 show that 2nd order elements are more efficient than 1st order elements, when material nonlinearity is present. This observation can be explained because of the quadratic interpolation of the 2nd order elements that can capture the nonlinear material behavior more accurately than the linear interpolation of 1st order elements. This conclusion is strengthened by the fact that, for linear material ($R_{yield}=R_{tunnel}$), there is no advantage in using 2nd order elements over 1st order elements.

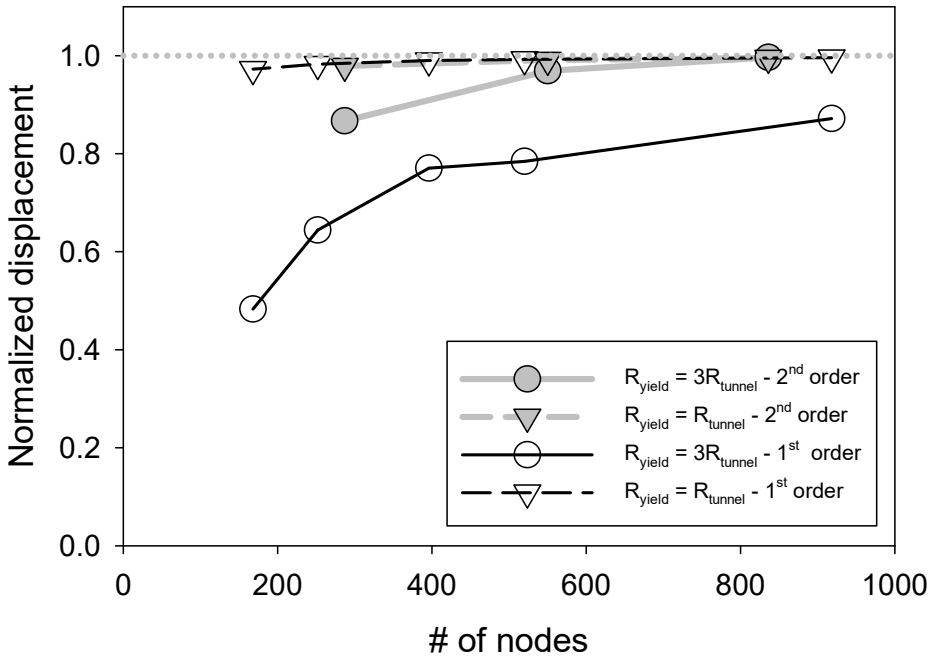

Figure 2.3 Convergence towards reference radial displacement for structured grid with 1st order and 2nd order elements (8-nodes and 20-nodes hexahedral elements).

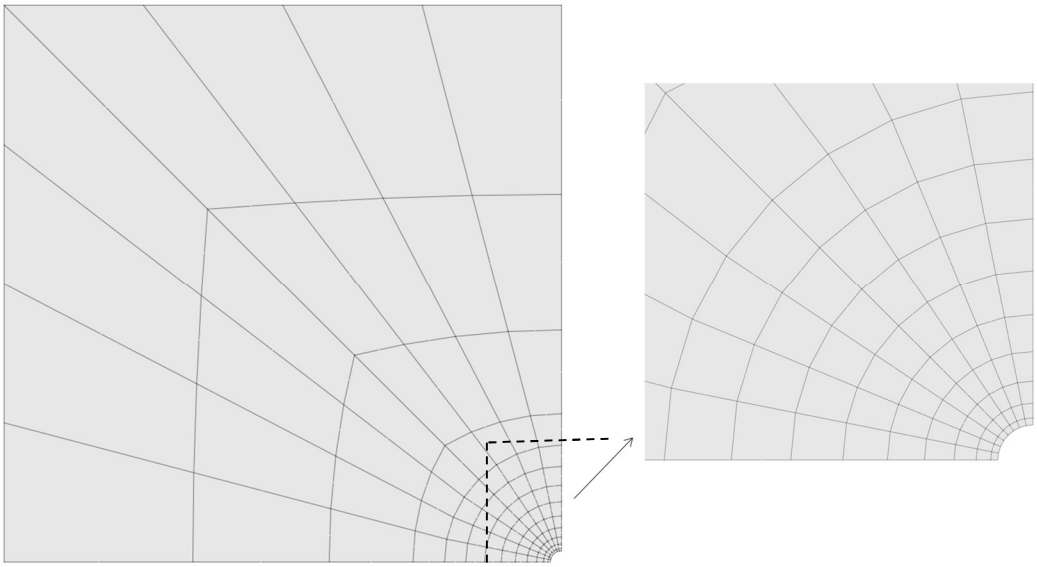

Figure 2.4 Front view of the optimum structured grid with 2nd order elements.

To assess the influence of the grid pattern, three types of grids using 2nd order elements with approximately the same number of nodes are compared: 1) structured grid using hexahedron elements; 2) unstructured grid using only pentahedron elements (grid A); and 3) unstructured grid using hexahedron and pentahedron elements (grid B). The grids are developed using a mesh

generator with Delaunay algorithm with a refined mesh close to the opening that gradually coarsens toward the boundary.

Similar to Figure 2.3, Figure 2.5 compares the radial displacements at the perimeter of the opening, normalized with respect to the reference model displacements (Figure 2.2), for different types of grid and number of nodes. Results are obtained for nonlinear material ($R_{yield}=3R_{tunnel}$ and associated flow rule, see Table 2.1). As expected, as the number of nodes in the discretization increases, e.g. as the number of elements increase, the errors decrease and the solution converges towards the correct solution. The three types of grids provide similar accuracy for the same number of nodes. Therefore, the type of the grid structure is not as important as the type of element. Figure 2.6 andFigure 2.7 show the optimum unstructured grids. Grid A, with pentahedron elements only, has 724 nodes and achieves 0.8% accuracy, while grid B, with hexahedron and pentahedron elements, has 589 nodes and 1% accuracy.

Despite the advantage of using 2nd order elements (i.e. quadratic interpolation), with respect to 1st order elements, models are found in the literature that use 1st order elements (i.e. linear interpolation). For instance, Ng & Lee, 2005, used 1st order elements due to limitations of computational resources; however, it is arguable that a faster mesh resulting in equally or better results is possible using a coarser grid with 2nd order elements, based on the results presented in this paper.

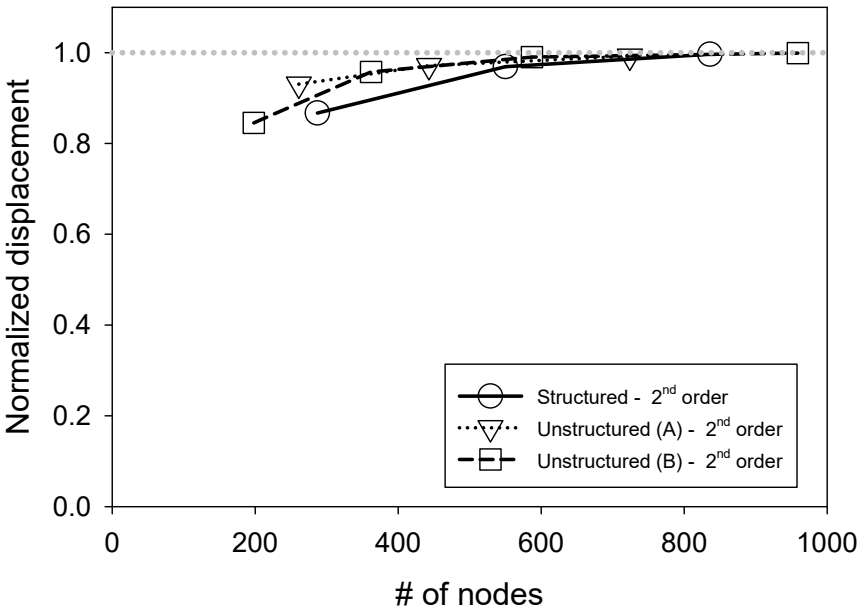

Figure 2.5 Convergence towards reference radial displacement for different types of grid with 2nd order elements.

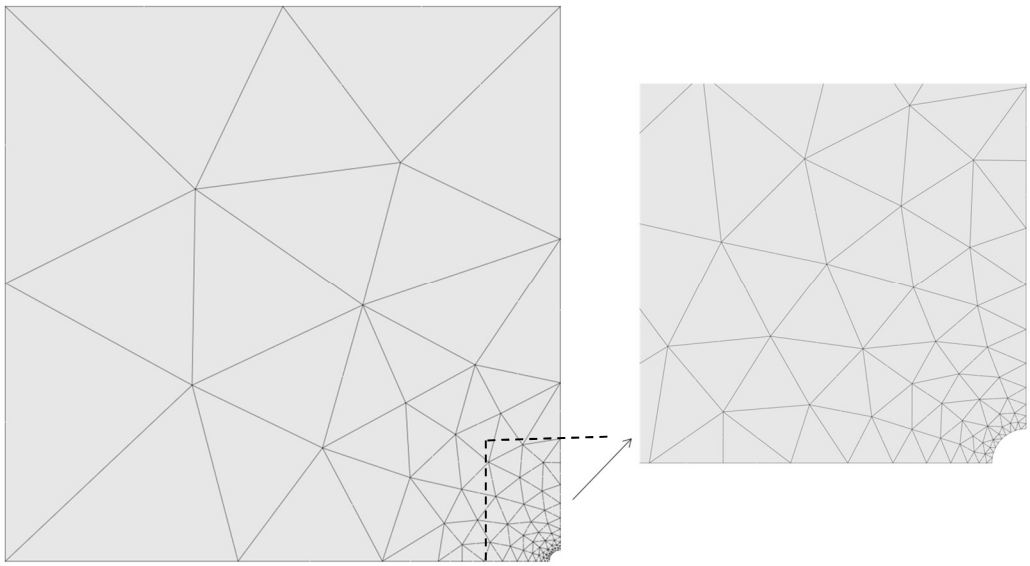

Figure 2.6 Front view of the optimum unstructured grid A with 2nd order elements.

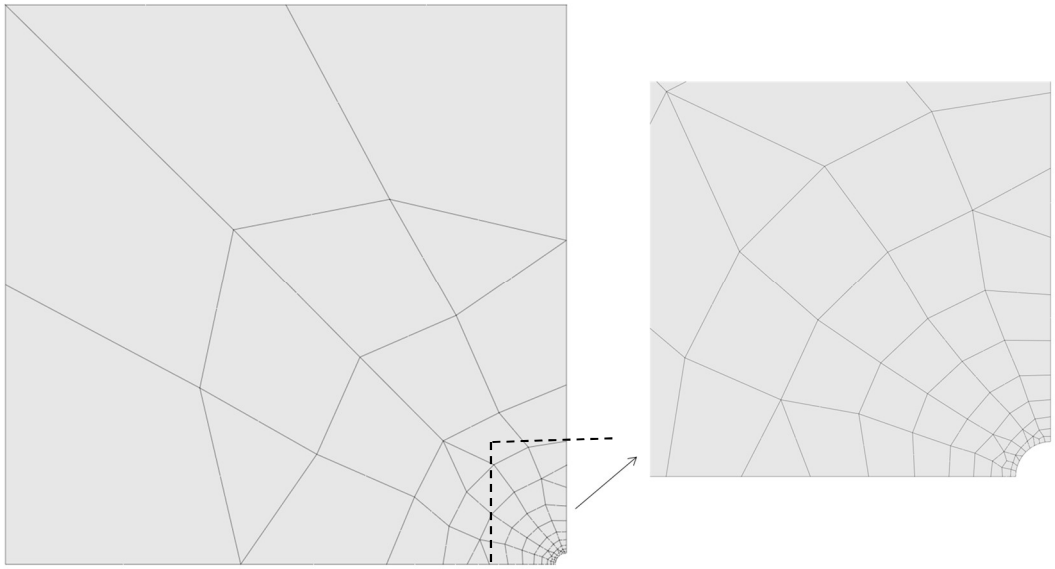

Figure 2.7 Front view of the optimum unstructured grid B with 2nd order elements.

2.3 Mesh width

The influence of the model width on the accuracy of the results was assessed by a set of analyses varying the model width (L_{width}) and the degree of material nonlinearity (yield radius ranging from 1 to 3 times the tunnel radius; see soil properties in Table 2.1). Examples of the meshes investigated are presented in Figure 2.8 (only the front face is shown, for clarity). Similar

to previous examples, the tunnel radius is 5m and the stress state is hydrostatic (i.e. $K_0 = 1$), with far field stress 100kPa.

As discussed, the range of model widths found in the literature is high, from $48.2R_{tunnel}$ to $8R_{tunnel}$ (Franzius & Potts, 2005). Also, there is no well-established procedure to determine the model width. Further, most of the suggestions found often do not account for important aspects such as the size of the plastic zone and there are no recommendations relating mesh size and accuracy.

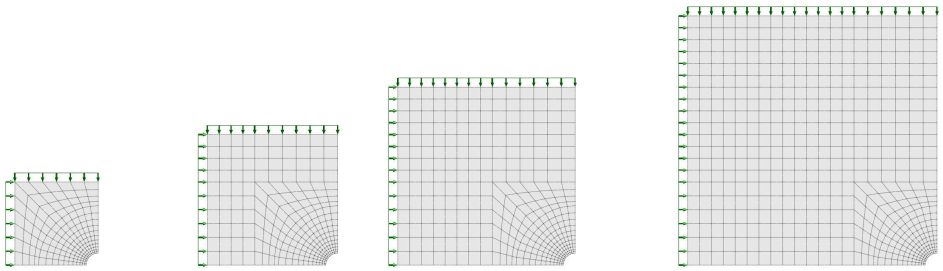

Figure 2.8 Examples of the front view of finite element meshes with 2nd order elements (20-node hexahedra) to assess the influence of model width. Note that the grid refinement is kept constant regardless of the mesh size.

Figure 2.9 plots the error of the radial displacements at the perimeter of the opening with respect to the reference value, which is the displacement obtained numerically with a model extremely wide ($200R_{tunnel}$), using the grid structure shown in Figure 2.8. The figure shows that the errors quickly decrease as the width of the mesh increases. The figure also shows that, as the size of the plastic zone around the tunnel increases, the errors increase.

It is interesting to see that the errors are smaller than 5% for mesh widths larger than about 15 times the tunnel radius and become negligible for widths larger than 40-45 tunnel radius. It is worth noting that, for a model width equal to $10R_{tunnel}$, which is a common reference in the literature (Möller, 2006), the error is acceptable for linear elasticity (1.3%), but may be unacceptable for $R_{yield}=3R_{tunnel}$ (13%). Also, the Vlachopoulos & Diederichs, 2014, recommendation to adopt a model size of $3R_{yield}$ beyond the plastic zone may lead to inaccurate results. For instance, for $R_{yield}=3R_{tunnel}$, the criterion requires a model size of $12R_{tunnel,}$ which would result in an error of 8.5%, according to Figure 2.9.

Figure 2.10 shows the required model width (L_{width}), as a function of the yield radius, to obtain errors below 2%, 1% and 0.5%. For a given accuracy, the width of the mesh needed

increases with the size of the plastic zone. These observations, however, apply for the case of isotropic stress field, which results in a yield zone that has axial symmetry. In general, the far-field stresses are anisotropic, and so the plastic zone around the tunnel will not be cylindrical. In this case, the recommendation is to adopt the largest plastic zone size, measured from the center of the opening. This is discussed in more detail in Section 6, where a case with anisotropic stress field is analyzed.

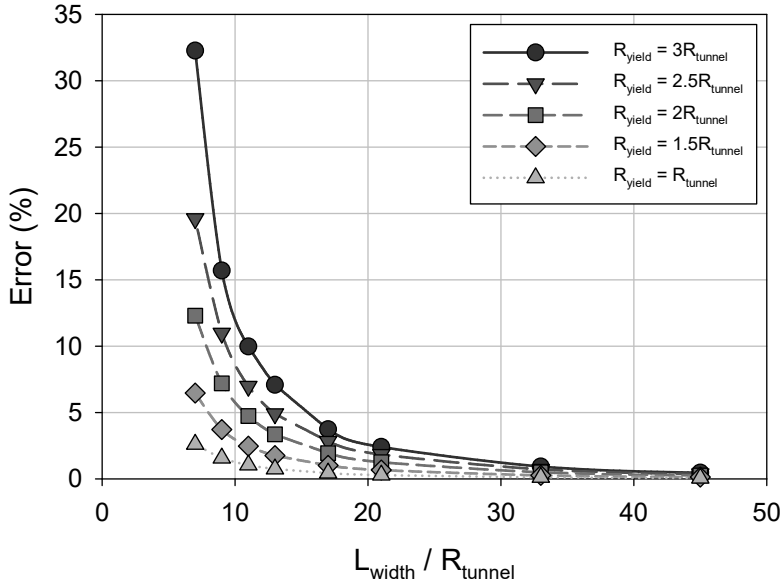

Figure 2.9 Relation between accuracy, model width (L_{width}) and plastic radius (R_{yield}).

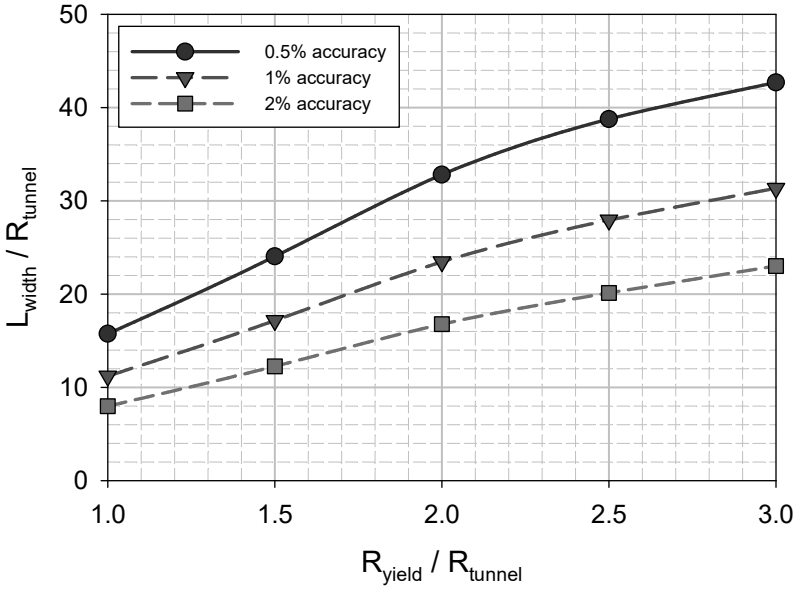

Figure 2.10 Model width and accuracy with plastic radius.

2.4 Mesh length

The model must be long enough to capture the changes of stresses and displacements ahead and behind the excavation face of the tunnel, without any undesirable effects due to the boundaries. To do this, it is necessary to determine the influence length of the tunnel face; that is, the distance ahead and behind the tunnel face affected by the excavation. Also, it is necessary to assess the influence of the front and back boundaries on the results, such that the solution is free from boundary effects. The goal is to find the minimum model length that accurately captures the 3D tunnel excavation.

As mentioned before, there is no well-established procedure in the literature to estimate the model length. In fact, most of the recommendations disregard the influence of material nonlinearity and do not relate model length with accuracy.

2.4.1 Tunnel face effects

The tunnel excavation changes the stresses in the ground, mobilizing shear stresses (longitudinal and transversal arching) to achieve a new stress state. This process is gradual, starts with the initial stresses in the ground and ends up with a steady-state response at some distance behind the face of the tunnel.

It is informative to determine the location where the stresses in the ground start to be affected by the tunnel excavation and where the displacements stop changing behind the tunnel face; in other words, to determine the length of influence of the tunnel face, which can be done by assessing the displacements and stresses evolution along the tunnel.

A model with $80R_{tunnel}$ length and $50R_{tunnel}$ width using a suitable grid with 2^{nd} order elements is built for the analyses (Figure 2.11). The length of $80R_{tunnel}$ is large enough to capture the evolution of stresses and displacements along the excavation and avoid boundary effects. Also, the $50R_{tunnel}$ width minimizes boundary effects (see Section 3.1). The grid refinement and the order of the elements have been discussed in Section 2. In the analyses, the tunnel radius is 5m and the initial stress state is hydrostatic (i.e. $K_0 = 1$), with a far field stress of 100kPa. The model has been run for different degrees of material nonlinearity (yield radius ranging from 1 to 3 times the tunnel radius with associated flow rule; see parameters in Table 2.1).

Möller, 2006, found that the mesh length is almost independent of the excavation round length using a hardening elastoplastic model; therefore, the stress path history due to a step-by-step simulation of the excavation should have a small influence on the model length. Such finding is confirmed by comparing the radial displacement profile obtained with a step by step excavation with a round length of $0.2R_{tunnel}$ and with a single step until the center of the model ($40R_{tunnel}$ long), as will be shown and discussed later in Figure 2.12. Therefore, to assess the influence length of the tunnel face, the excavation is simulated in a single step $40R_{tunnel}$ long until the center of the model; this is convenient because of faster computation and simple analysis of the data, given that the single step does not produce the "saw-tooth" shaped results associated with the step by step excavation.

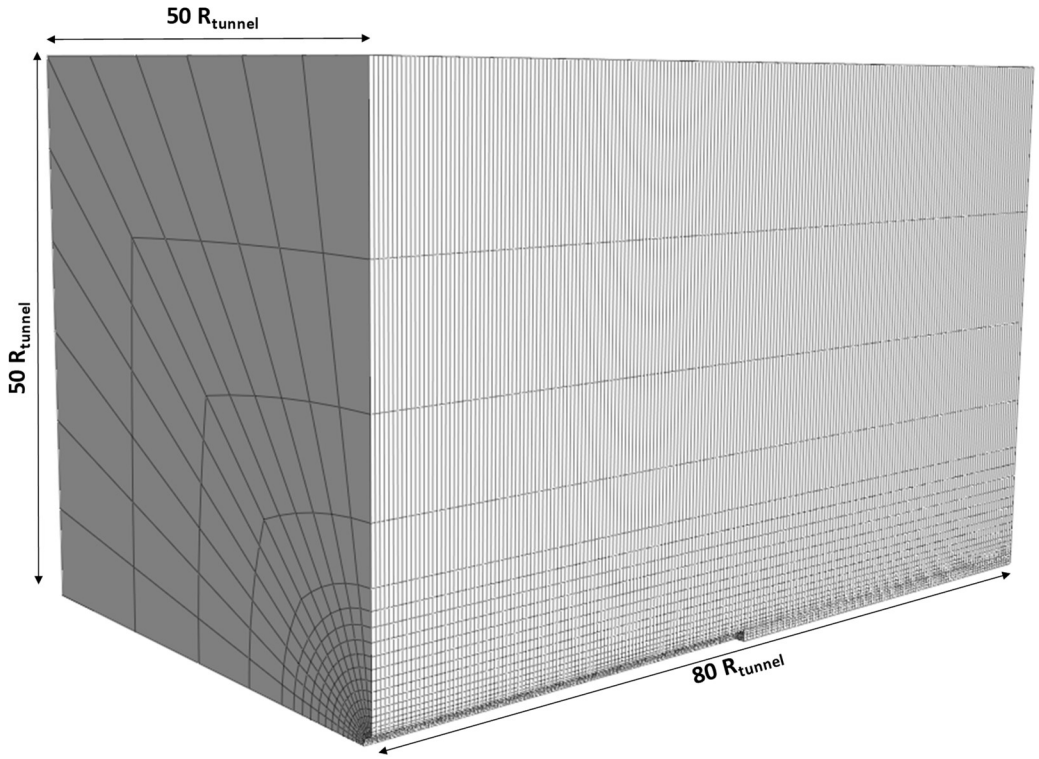

Figure 2.11 3D model using 2nd order elements to assess the length of influence of the tunnel face.

Figure 2.12 shows the total radial displacements at the perimeter of the opening and those radial displacements normalized with respect to the displacements far from the tunnel face (note also that the figure includes results from a step-by-step excavation with a round length of $0.2R_{tunnel}$). The results are plotted as a function of the distance from the tunnel face (D_{face}) normalized by the

tunnel radius (R_{tunnel}). Note that $D_{face}/R_{tunnel}=0$ is the tunnel face, $D_{face}/R_{tunnel}>0$ represents a distance ahead of the tunnel face and $D_{face}/R_{tunnel}<0$ behind the tunnel face.

The displacements start to be mobilized relatively close to the face (at around $4R_{tunnel}$ ahead of the face), with the largest changes occurring near the face. At the face ($D_{face}=0$), the normalized radial displacement is 0.16 for $R_{yield}=3R_{tunnel}$ and 0.29 for $R_{yield}=R_{tunnel}$, which is consistent with the literature (Vlachopoulos & Diederichs, 2009). The radial displacement shows an abrupt increase just behind the face and a continued increase towards a steady displacement with distance behind the face. This happens at around $15R_{tunnel}$. The shape of the curves, as one can see in the figure, strongly depends on the size of the plastic zone around the tunnel.

Despite the influence of the step-by-step excavation on the total displacements (note that the radial displacement far behind the face increases by 20% with the step by step excavation for $R_{yield}=3R_{tunnel}$ and associated flow rule, compared with the single step), for the normalized displacements, after a distance of around $4R_{tunnel}$ behind the face, the normalized radial displacements for $R_{yield}=3R_{tunnel}$ for the step by step and single step match, denoting that both methods give the same results.

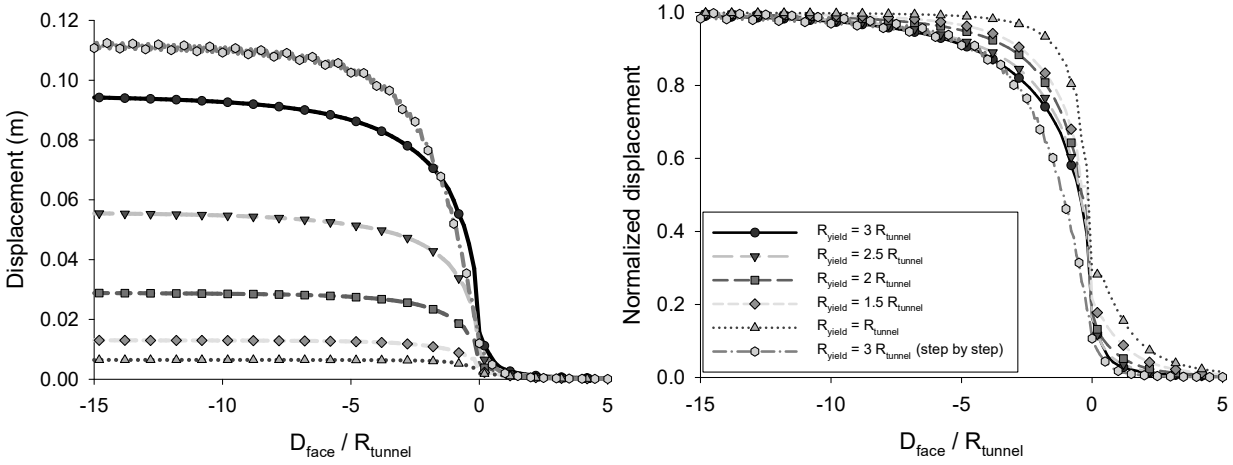

Figure 2.12 Radial displacement with distance from the face.

Figure 2.13 shows the tangential stresses ($\sigma_{\theta\theta}$) near the perimeter of the opening, normalized with respect to the initial stresses, with the distance from the face, normalized by the tunnel radius. For a hydrostatic far-field stress ($\sigma_{11}=\sigma_{22}=\sigma_{33}=p$), the normalized stress is $\sigma_{\theta\theta}/p$. Far ahead from the excavation face, the stress field is isotropic and of magnitude 100kPa. As the excavation face approaches, the shear stresses are mobilized (longitudinal and transversal arching)

and the tangential stresses start to increase. For a linear elastic material (R_{yield}=R_{tunnel}), the tangential stresses monotonically increase until they reach a constant value behind the excavation face. For an elasto-plastic material, yielding limits the increase of the tangential stresses. Once the material yields, the tangential stresses start to decrease until they reach a constant magnitude behind the face, at a distance of around $2R_{tunnel}$. Note that the distance ahead of the face where the shear stresses are mobilized increases with the size of the plastic zone. The stresses shown in Figure 2.13 Tangential stresses near the opening perimeter, with distance from the face. Figure 2.13 are consistent with Cantieni & Anagnostou, 2009, results for an unsupported tunnel. Note that if a support is installed, an increase in the stresses behind the tunnel face is expected after the support installation, as shown by Cantieni & Anagnostou, 2009.

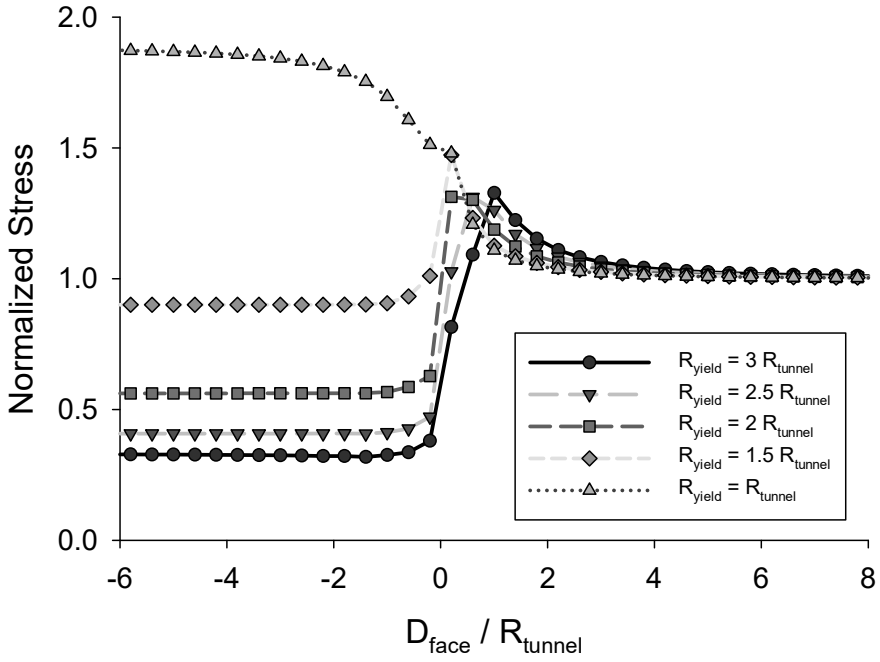

Figure 2.13 Tangential stresses near the opening perimeter, with distance from the face.

The length of the model must, at least, extend from the location where stresses or displacements start to be mobilized ahead of the face to where stresses and displacements reach a constant value behind the excavation face; that is, the length must be inclusive of the largest influence of the excavation face.

Figure 2.14 shows the distance from the tunnel face (D_{face} as multiples of the tunnel radius R_{tunnel}) required to reach an accuracy of 2%, 1% and 0.5%, for tangential stresses and radial

displacements, for different sizes of the plastic zone. The plots can be used to estimate the model length, even for models with anisotropic far-field stress, by using the largest size of the yield zone, as it will be shown later in the verification section. Also, the model must include the length affected by the front and back boundaries, as discussed in the next section.

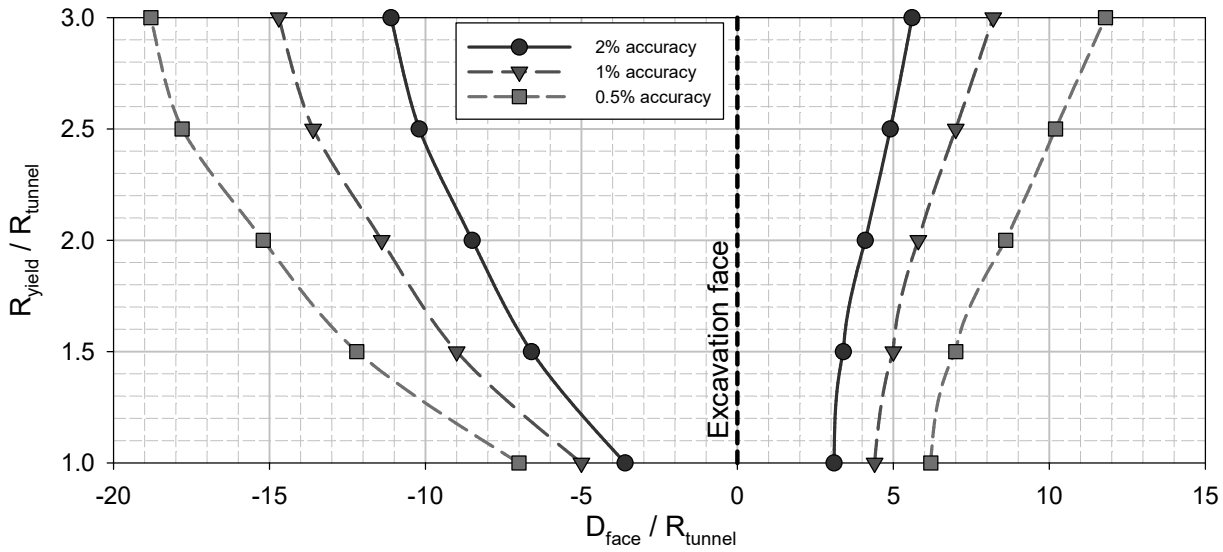

Figure 2.14 Minimum distance ahead and behind the tunnel face required to reach a target accuracy, as a function of the plastic zone size.

2.4.2 Front and back boundaries

The aim of the section is to determine how results are affected by the front and back boundaries of the model. A model with $20R_{tunnel}$ length and $50R_{tunnel}$ width, with a suitable refined grid, using 2nd order elements is built for the analyses. Figure 2.15 shows the model. A step-by-step excavation is implemented throughout the entire model to assess the length of influence of the front and back boundaries. As it will be shown, the $20R_{tunnel}$ model length is enough to obtain displacements free from boundary effects.

The model is run for different plastic zone sizes (R_{yield} from 1.5 to 3 R_{tunnel} with associated flow rule, $\psi=\phi=19.6°$; see input parameters in Table 2.1), and with an excavation round length of $0.2R_{tunnel}$. Similar to previous discussions, the tunnel radius is 5m and the stress state hydrostatic (i.e. $K_0 = 1$), with a far field stress of 100kPa.

Figure 2.16 shows the radial displacements at the perimeter of the tunnel normalized by the radial displacements far from the influence of the face. The results are plotted as a function of

the distance from the center of the model (D_{center}), normalized by the tunnel radius. That is, $D_{center}/R_{tunnel}=0$ represents the middle of the model; $D_{center}/R_{tunnel}=10$ represents the back boundary, and $D_{center}/R_{tunnel}=-10$, the front boundary.

As Figure 2.16 shows, the front boundary has an influence over a length of $2R_{tunnel}$ and the back boundary, over $6R_{tunnel}$. It is interesting to note that the length of influence of the front and back boundaries does not vary significantly with the plastic zone size. Thus, in general, results over a length of $2R_{tunnel}$ ahead of the front boundary and $6R_{tunnel}$ behind the back boundary should be disregarded. In other words, any mesh discretization should include an additional $2R_{tunnel}$ length beyond the front boundary and $6R_{tunnel}$ behind the back boundary, to achieve acceptable results.

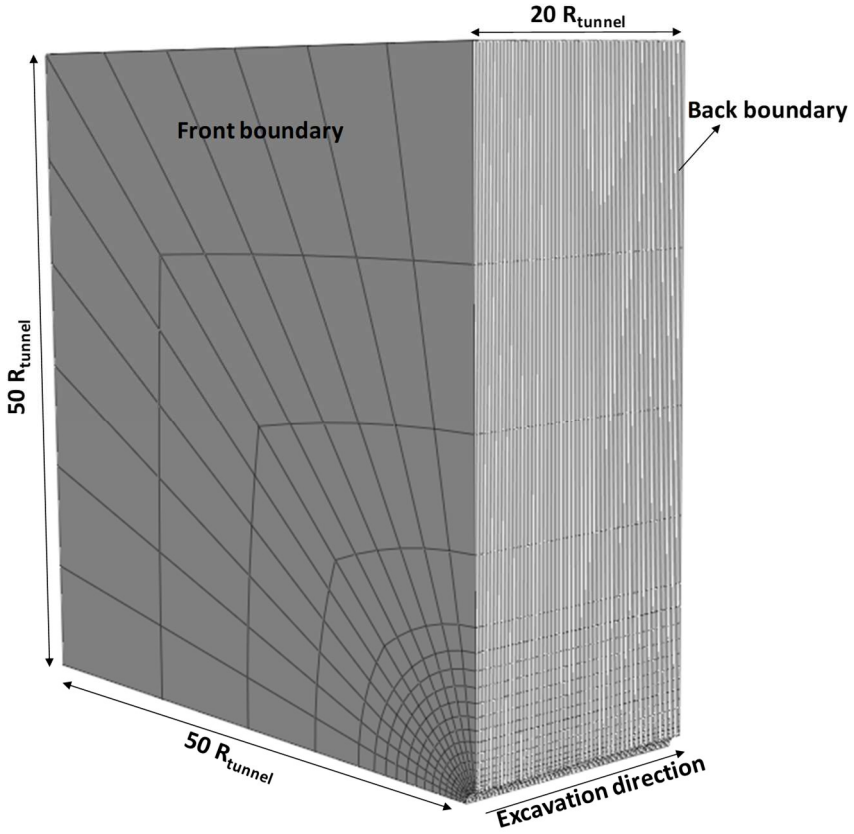

Figure 2.15 3D model to assess the influence of the front and back boundaries.

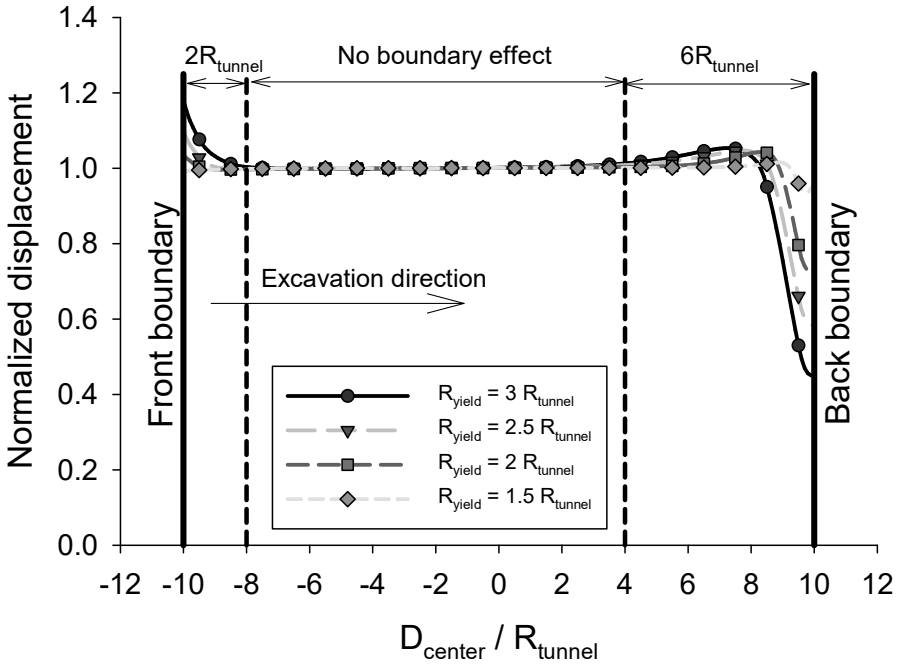

Figure 2.16 Normalized radial displacements at the perimeter of the opening, along the tunnel length.

2.5 Axial grid refinement

A 3D tunnel model is usually built by extruding a 2D grid along the tunnel axis. Despite the strong influence that the axial grid refinement has on accuracy and computational effort, as highlighted by Franzius & Potts, 2005, and Möller, 2006, there is limited research on the axial grid refinement. In this section, this issue is discussed.

The models used for this study are similar to those presented in section 3.2.2 (same dimensions and boundary conditions), but with an excavation round length (L) of $1R_{tunnel}$, $0.4R_{tunnel}$ and $0.2R_{tunnel}$. These values encompass a wide range of excavation round lengths used in practice. The goal is to evaluate the radial displacement profile obtained with the different excavation round lengths, to determine which element length ensures accurate results regardless of the excavation round length. Note that the excavation round length affects the stress path of the ground around the opening; therefore, the radial displacements profile varies with different excavation round lengths, as mentioned by Vlachopoulos & Diederichs, 2009.

Each model is run using different element lengths ($L_{element}$) (i.e. different axial grid refinements). Also, the models are run with $R_{yield}=3R_{tunnel}$ (see soil properties in Table 2.1) and

associated flow rule ($\psi=\phi=19.6°$). Figure 2.17 shows the models using $L_{element}=0.1R_{tunnel}$ and $L_{element}=1R_{tunnel}$.

Figure 2.18 toFigure 2.20 show the radial displacements at the perimeter of the tunnel after excavation throughout the entire model (similar to what was done in previous section), shown in Figure 2.16, with distance from the center of the model (D_{center}) normalized by the tunnel radius, for excavation round lengths (L) of $1R_{tunnel}$, $0.4R_{tunnel}$ and of $0.2R_{tunnel}$. As before, $D_{center}/R_{tunnel}=0$ represents the center of the model; $D_{center}/R_{tunnel}=10$ the back boundary, and $D_{center}/R_{tunnel}=-10$, the front boundary. Those graphs illustrate the influence of the step by step excavation in the displacements, for $R_{yield}=3R_{tunnel}$ using an elastic perfectly plastic Mohr Coulomb model with associated flow rule. Note that the displacements increase as the excavation round length decreases. For a round length of $0.2R_{tunnel}$, the step by step excavation causes 18% increase of the radial displacements with respect to a single step excavation.

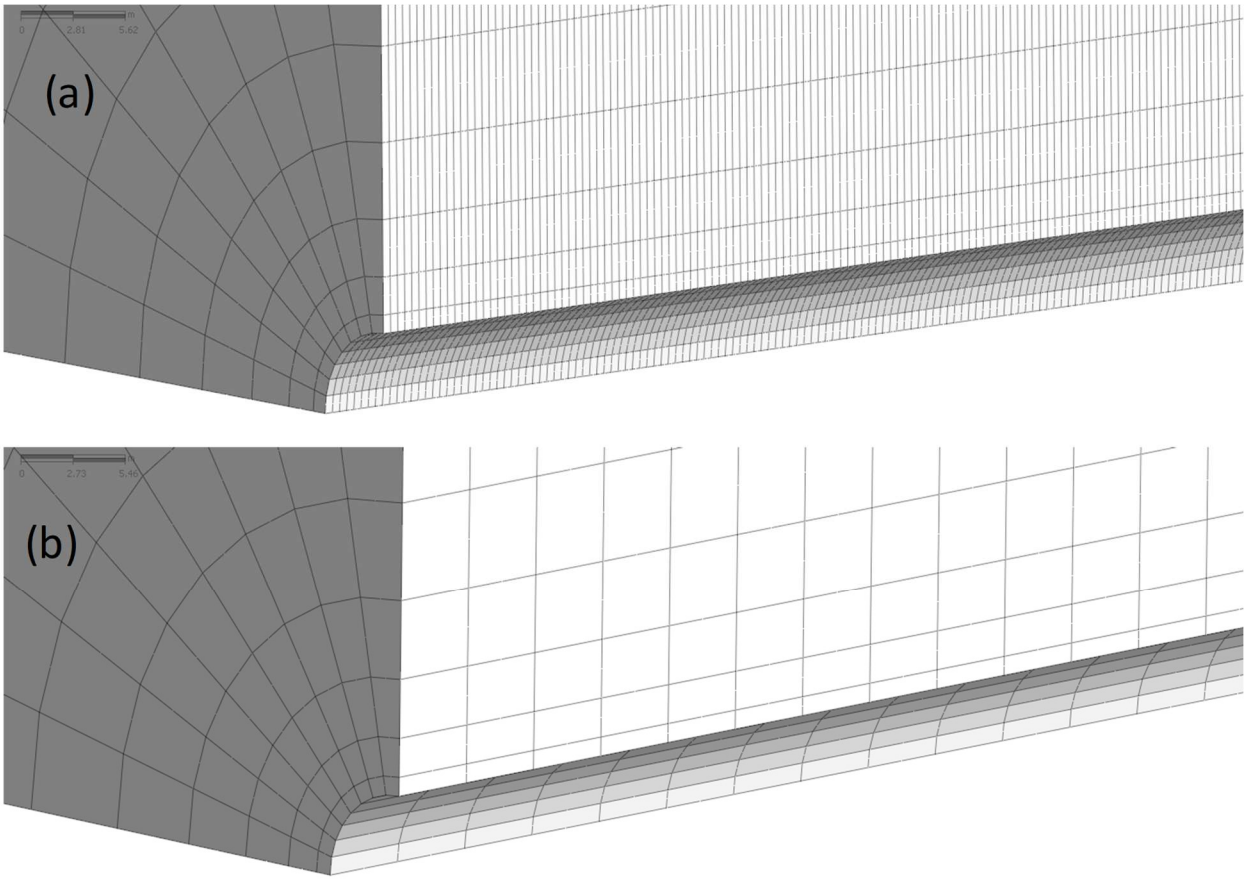

Figure 2.17 Models with different axial grid refinement. (a) $L_{element}=0.1R_{tunnel}$ and (b) $L_{element}=1R_{tunnel}$.

The displacements have the characteristic saw-tooth shape with a periodicity equal to the excavation round. This is a result that has been observed by others (e.g. Möller, 2006). Note also that the amplitude of the saw-tooth, that is the difference between the maximum and minimum displacements, decreases as the round length is reduced; however, the overall magnitude of the displacements increases by decreasing the round length.

For the largest round length, $L=1R_{tunnel}$, (Figure 2.18), the radial displacement profiles obtained for $L_{element}=R_{tunnel}$ (1 element per round) and for $L_{element}=0.5R_{tunnel}$ (2 elements per round) are inconsistent with the profile obtained using the most refined axial grid ($L_{element}=0.1R_{tunnel}$). In contrast, the difference between the radial displacements between $L_{element}=0.2R_{tunnel}$ (5 elements per round) and $L_{element}=0.1R_{tunnel}$ (10 elements per round) is negligible.

Similarly, for $L=0.4R_{tunnel}$ (Figure 2.19), the radial displacement profiles for $L_{element}=0.1R_{tunnel}$ and $L_{element}=0.2R_{tunnel}$ are comparable, but different than $L_{element}=0.4R_{tunnel}$. Similar observations can be made for $L=0.2R_{tunnel}$ (Figure 2.20). In short, discretization using $L_{element}=0.2R_{tunnel}$ leads to satisfactory results for all round lengths assessed regardless of the number of elements per round length. Thus, element lengths of $0.2R_{tunnel}$ or shorter seem appropriate for the axial grid, regardless of the excavation round length.

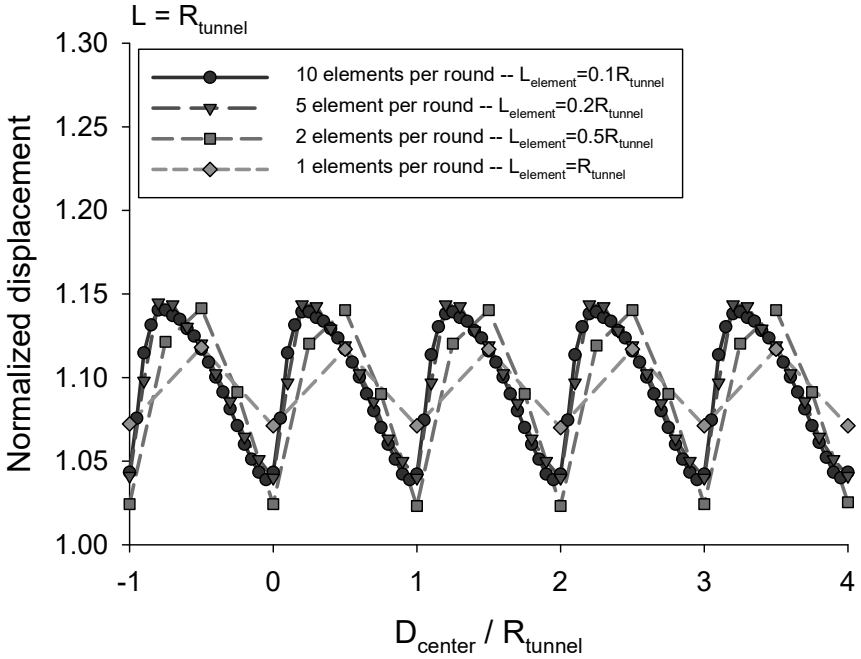

Figure 2.18 Radial displacements at the perimeter of the opening along the tunnel length for round lengths (L) of 1 tunnel radius (R_{tunnel}), for different axial grid refinements.

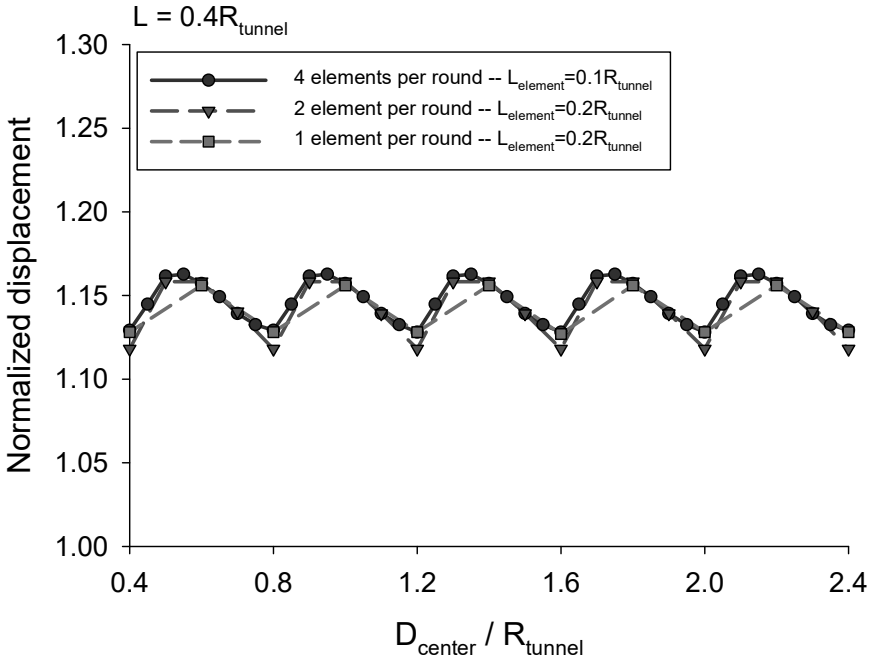

Figure 2.19 Radial displacements at the perimeter of the opening along the tunnel length for round lengths (L) of 0.4 tunnel radius (R_{tunnel}), for different axial grid refinements.

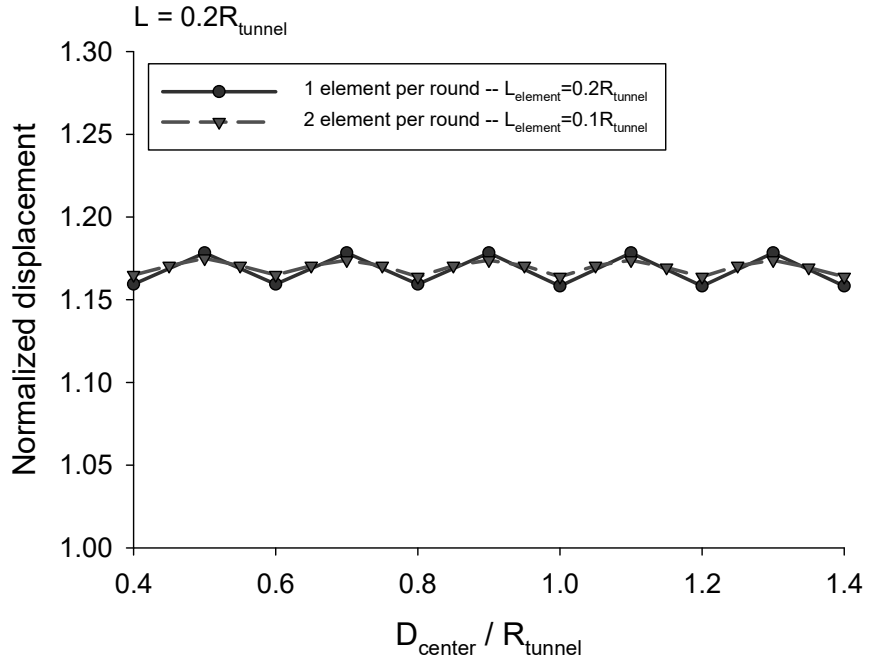

Figure 2.20 Radial displacements at the perimeter of the opening along the tunnel length for round lengths (L) of 0.2 tunnel radius (R_{tunnel}), for different axial grid refinement.

2.6 Verification

The previous analyses have been conducted assuming a hydrostatic far-field stress. While the assumption has been useful to identify the critical issues and reach simple conclusions, in reality, the geostatic stresses are anisotropic. It is thus imperative to determine to what extent the observations made can be generalized. To do this, additional analyses are made: a 3D model with large dimensions and refined mesh (reference model) is compared with a 3D model with dimensions and mesh refinement following the recommendations made based on the previous simulations. An excavation round length of 5m (i.e. one tunnel radius), tunnel radius of 5m, anisotropic stress field (i.e. σ_1 = 100kPa, $\sigma_2 = \sigma_3$ =50kPa) and an elastic, perfectly plastic Mohr-Coulomb material with parameters for $R_{yield}=2R_{tunnel}$ and non-associated flow rule ($\Psi=0°$) (see Table 1) is adopted. Under such conditions, the shape of the plastic zone around the opening is not circular and the maximum distance from the center of the opening to the limit of the plastic zone is approximately $2R_{tunnel}$.

Figure 2.21 shows the reference 3D model, which uses 2nd order elements and has $80R_{tunnel}$ length and $50R_{tunnel}$ width. Such dimensions are sufficient to capture the displacements and stresses in the tunnel without boundary effects. The model uses an element length of $0.2R_{tunnel}$ within the volume comprised between $30R_{tunnel}$ behind the excavation face and $20R_{tunnel}$ ahead of the excavation face. The axial grid is coarsened close to the front and back boundaries to save processing time.

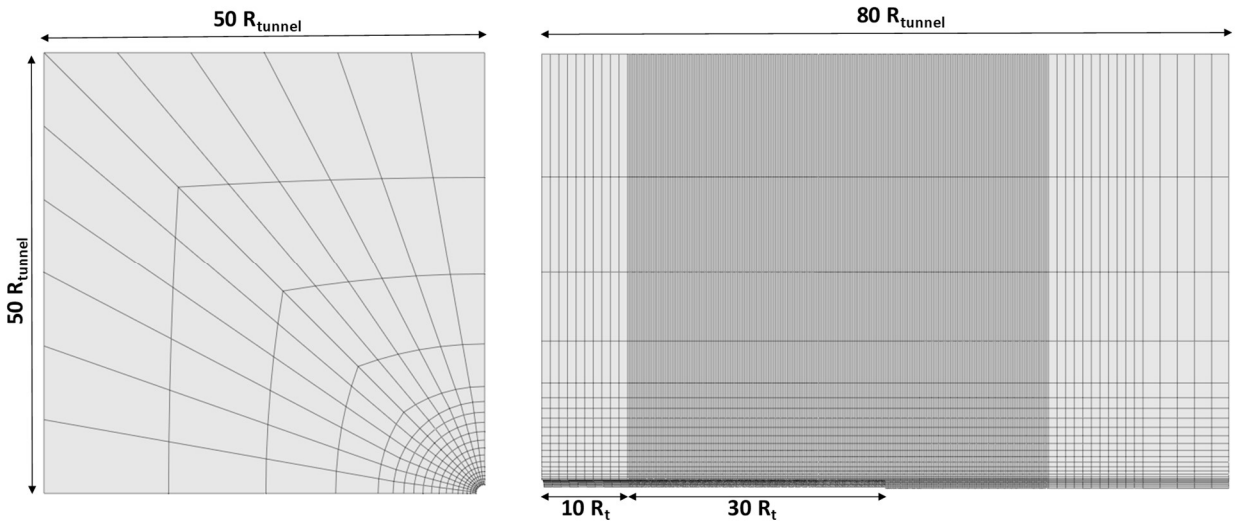

Figure 2.21 Front and side view of the reference 3D model.

Figure 2.22 shows the grid built following previous recommendations. That is, the model uses 2nd order elements and mesh following Figure 2.4; the model width is $25R_{tunnel}$, based on Figure 2.10 (assuming a 1% accuracy and $R_{yield}=2R_{tunnel}$); the model length is $26R_{tunnel}$, based on Figure 2.14 and Figure 2.16 (assuming 1% accuracy and $R_{yield}=2R_{tunnel}$; $12R_{tunnel}$ behind the face and $6R_{tunnel}$ ahead of the face); and the element length is $0.2R_{tunnel}$, as discussed in section 4.

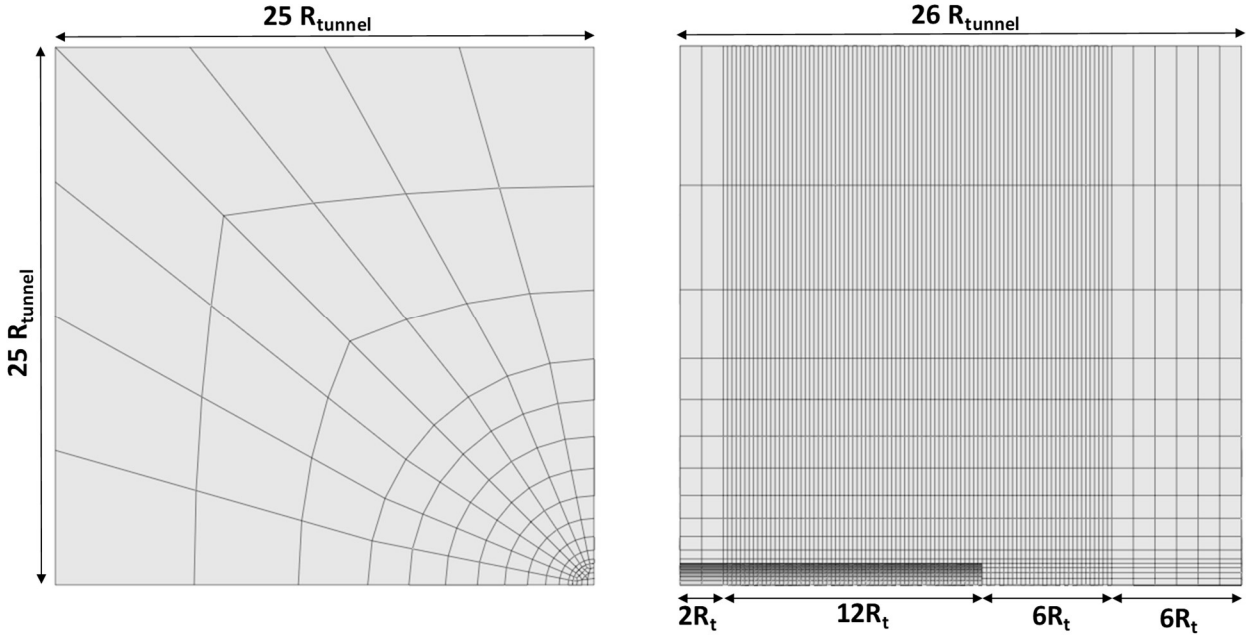

Figure 2.22 Front and side view of the recommended 3D model, which dimensions and grid were determined based on the recommendations provided.

Figure 2.23 shows the radial displacements obtained from both models along the axis of the tunnel (represented by the distance from the face normalized by the tunnel radius; $D_{face}/R_{tunnel}=0$ is the tunnel face, $D_{face}/R_{tunnel}>0$ is ahead of the tunnel face and $D_{face}/R_{tunnel}<0$ is behind the tunnel face). The displacements profiles are similar to each other, showing that the recommendations reached with a hydrostatic far-field stresses can be used for anisotropic geostatic stresses. This observation is supported by the results shown in Figure 2.24, which is a plot of the principal stresses obtained from both models. As one can see, the results are similar.

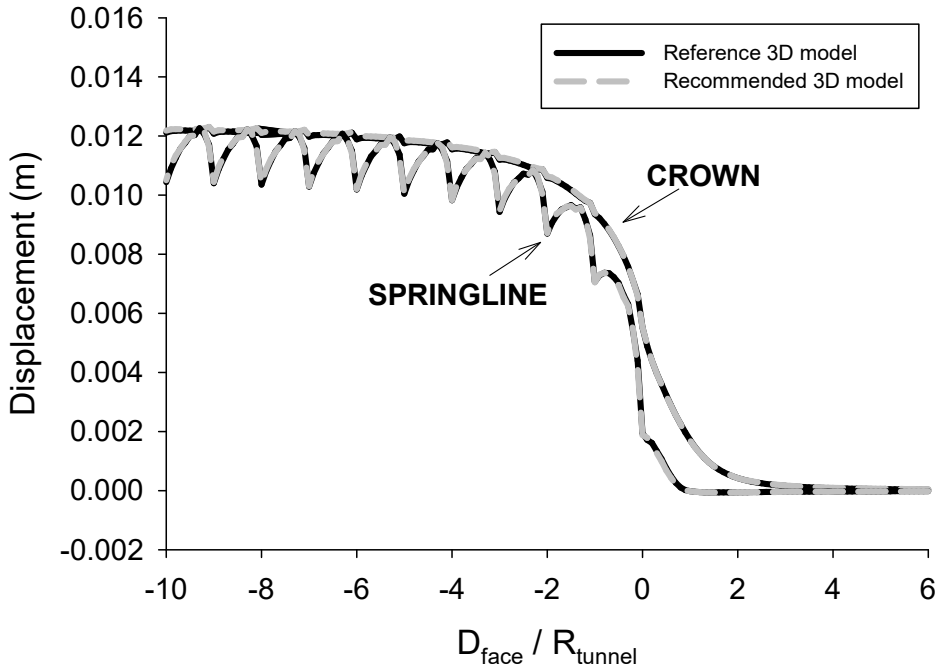

Figure 2.23 Radial displacements at the wall and crown of the opening obtained with the reference and the recommended 3D models.

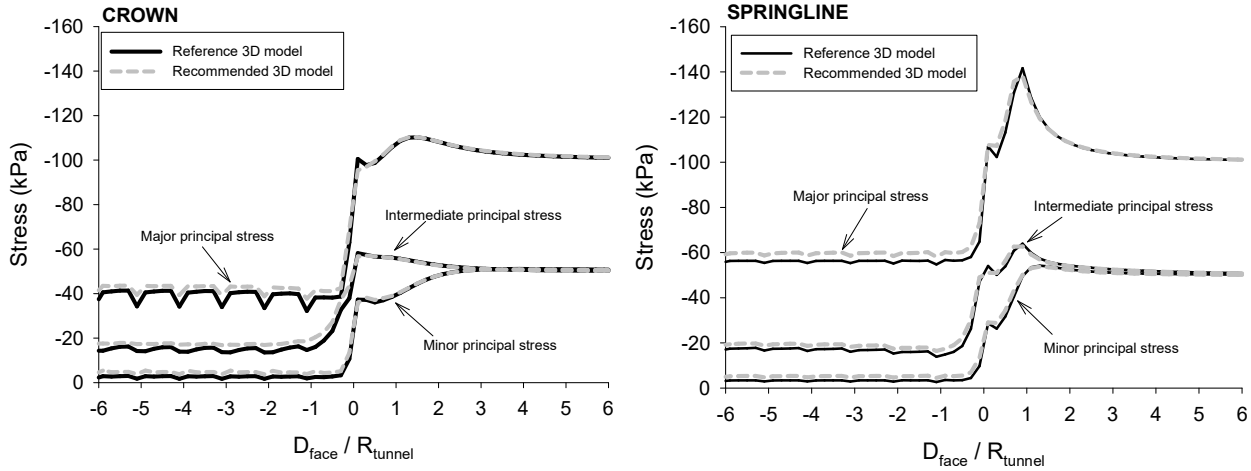

Figure 2.24 Principal stresses at near the wall and crown of the opening obtained with the reference and the recommended 3D models.

It is worth mentioning that the reference 3D model has 326,906 nodes and requires 40 excavation steps, taking 13.46 hours to run, while the recommended model has 51,246 nodes and 14 excavation steps, taking only 0.29 hours to complete. That is, the recommended model runs almost 50 times faster than the reference model and provides equivalent results. Both models were run on the same computer (32Gb RAM and Xeon E5-1660 v4, with 3.2GHz processor).

2.7 Conclusions

In this paper, aspects that affect the 3D modelling of tunnels such as model size (width and length), grid refinement (transversal and longitudinal), grid type (structured and unstructured) and order of elements (i.e. interpolation functions) are investigated, to provide recommendations for 3D meshing of FEM simulations of deep tunnels.

Finite element grids with 2nd order elements (i.e. quadratic interpolation) show better performance than finite element grids using 1st order elements (i.e. linear interpolation) when material nonlinearity is involved. Therefore, 2nd order elements should be preferred. Also, the structure of the grid (structured or unstructured grid) has a secondary importance compared with the order of the elements.

The size of the plastic zone has a major influence on the model dimensions. Requirements for model widths have been determined for yield radii (R_{yield}) varying from 1 (linear material) to 3 (worst case scenario). To achieve a 1% accuracy, for $R_{yield}=3R_{tunnel}$ and associated flow rule, a model width of $32R_{tunnel}$ is required, while for $R_{yield}=1R_{tunnel}$ (linear material), a width of 11 R_{tunnel} is needed. This is in contrast with the common reference found in the literature of $10R_{tunnel}$, which may be suitable for a linear material but may not be acceptable for a nonlinear material.

Minimum model lengths have been also determined as a function of the yield radius. To obtain stresses and displacements with 1% accuracy, for $R_{yield}=3R_{tunnel}$ and associated flow rule, the influence length of the excavation face is $23R_{tunnel}$ ($15R_{tunnel}$ behind the face and $8R_{tunnel}$ ahead), while for $R_{yield}=1R_{tunnel}$ (linear material), the influence length is $9R_{tunnel}$ ($5R_{tunnel}$ behind and $4R_{tunnel}$ ahead). Common references found in the literature suggesting influence length of $4R_{tunnel}$ behind the face and $4R_{tunnel}$ ahead the face (e.g. Eberhardt, 2001, and Shahin, et al, 2004) may be appropriate for linear materials, but can lead to unacceptable errors when a nonlinear material is involved. Further, the length affected by the front and back boundaries should be added to the model length. It is recommended to add $8R_{tunnel}$ to the length of influence of the excavation, $2R_{tunnel}$ from the front boundary and $6R_{tunnel}$ from the back boundary, to avoid boundary effects.

The paper also examines the minimum element length to be used when step-by-step excavation is attempted. This is necessary when an elastoplastic model is used, as the solution is stress-path dependent. Results from a number of simulations that explore the errors associated with different element sizes and excavation round lengths show that using 2nd order elements, with a maximum length of $0.2R_{tunnel}$, provides acceptable values for stresses and displacements.

While the recommendations provided have been found with the assumption of hydrostatic far-field initial stresses, additional cases using the suggested mesh dimensions with far-field anisotropic stresses indicate that the recommendations are also applicable to those cases with anisotropic far-field stresses.

The recommendations and conclusions reached with the work presented are not intended to cover all possible cases, as they have been obtained from a finite number of numerical experiments that, while covering a widespread of possibilities, are necessarily limited (e.g. they may not be applicable to shallow tunnels since they have not been included in the investigation). What is suggested should be taken as a first approximation for mesh optimization, while future work will, no doubt, refine and add to the recommendations.

Acknowledgments

The research is being supported by the research funding agency of Brazilian government CNPq ("Conselho Nacional de Desenvolvimento Cientifico"). The authors acknowledge the support from CNPq and also Midas company, which kindly provided the license of Midas GTX NX software, used in the present work.

2.8 References

Bobet, A. (2003). Effect of pore water pressure on tunnel support during static and seismic loading. *Tunnelling and Underground Space Technology*, *18*(4), 377–393. https://doi.org/10.1016/S0886-7798(03)00008-7

Cantieni, L., & Anagnostou, G. (2009). The effect of the stress path on squeezing behavior in tunneling. *Rock Mechanics and Rock Engineering*, *42*(2), 289–318. https://doi.org/10.1007/s00603-008-0018-9

Do, N. A., Dias, D., Oreste, P., & Djeran-Maigre, I. (2014). Three-dimensional numerical simulation of a mechanized twin tunnels in soft ground. *Tunnelling and Underground Space Technology*, *42*, 40–51. https://doi.org/10.1016/j.tust.2014.02.001

Eberhardt, E. (2001). Numerical modelling of three-dimension stress rotation ahead of an advancing tunnel face. *International Journal of Rock Mechanics and Mining Sciences*, *38*(4), 499–518. https://doi.org/10.1016/S1365-1609(01)00017-X

Franzius, J. N., & Potts, D. M. (2005). Influence of Mesh Geometry on Three-Dimensional Finite-Element Analysis of Tunnel Excavation. *International Journal of Geomechanics*, *5*(3), 256–266. https://doi.org/10.1061/(ASCE)1532-3641(2005)5:3(256)

Gomes, R. a. M. P., & Celestino, T. B. (2009). Influence of physical and geometrical parameters on three-dimensional load transfer mechanism at tunnel face. *Canadian Geotechnical Journal*, *46*(7), 855–868. https://doi.org/10.1139/T09-016

Janin, J. P., Dias, D., Emeriault, F., Kastner, R., Le Bissonnais, H., & Guilloux, A. (2015). Numerical back-analysis of the southern Toulon tunnel measurements: A comparison of 3D and 2D approaches. *Engineering Geology*, *195*, 42–52. https://doi.org/10.1016/j.enggeo.2015.04.028

Mašín, D. (2009). {3D} modelling of a {NATM} tunnel in high {K_0} clay using two different constitutive models. *Journal of Geotechnical and Geoenvironmental Engineering ASCE*, *135*(9), 1326–1335.

Meisnerr, H. (1996). Tunnelbau unter tage - Empfelunghen des Arbeitskreises. *Geotechnik*, *19(2)*, 99–108.

MIDAS Information Technology Co. (2014). Benchmarks & Verification GTS NX manual.

Möller, S. (2006). *Tunnel induced settlements and structural forces in linings*. PhD Thesis, Institute of Geotechnical Engineering, Universitat of Stuttgart, Stuttgart.

Nam, S. W., & Bobet, A. (2007). Radial deformations induced by groundwater flow on deep circular tunnels. *Rock Mechanics and Rock Engineering*, *40*(1), 23–39. https://doi.org/10.1007/s00603-006-0097-4

Ng, C. W., & Lee, G. T. (2005). Three-dimensional ground settlements and stress-transfer mechanisms due to open-face tunnelling. *Canadian Geotechnical Journal*, *42*(4), 1015–1029. https://doi.org/10.1139/t05-025

Salesçon, J. (1969). Contraction Quasi-Statique D'une Cavite a Symetrie Spherique Ou Cylindrique Dans Un Milieu Elasto-Plastique. In *Annales Des Ports Et Chaussees* (Vol. 4, pp. 231–236).

Shahin, H. M., Nakai, T., Hinokio, M., & Yamaguchi, D. (2004). 3D Effects on Earth Pressure and Displacements during Tunnel Excavations. *Soils and Foundations*, *44*(5), 37–49.

Svoboda, T., & Masin, D. (2011). Comparison of displacement field predicted by 2D and 3D finite element modelling of shallow NATM tunnels in clays. *Geotechnik*, *34*(2), 115–126. https://doi.org/10.1002/gete.201000009

Vlachopoulos, N., & Diederichs, M. S. (2009). Improved longitudinal displacement profiles for convergence confinement analysis of deep tunnels. *Rock Mechanics and Rock Engineering*, *42*(2), 131–146. https://doi.org/10.1007/s00603-009-0176-4

Vlachopoulos, N., & Diederichs, M. S. (2014). Appropriate Uses and Practical Limitations of 2D Numerical Analysis of Tunnels and Tunnel Support Response. *Geotechnical and Geological Engineering*, *32*(2), 469–488. https://doi.org/10.1007/s10706-014-9727-x

Yeo, C. H., Lee, F. H., Tan, S. C., Hasegawa, O., Suzuki, H., & Shinji, M. (2009). Three dimensional numerical modelling of a NATM tunnel. *Japanese Committee for Rock Mechanics*, *5*(1), 33–38.

3. BUOYANCY EFFECT ON SHALLOW TUNNELS

VITALI, O. P. M.; CELESTINO, & BOBET, A. (2019). Buoyancy effect on shallow tunnels. *International Journal of Rock Mechanics and Mining Sciences*. 114(2), 1–6. https://doi.org/10.1016/j.ijrmms.2018.12.012

Abstract

When a shallow tunnel is excavated, an overall upward movement appears as a result of the weight removal from the excavation. This movement is analogous to buoyancy. When numerical simulation of shallow tunnels is used, the magnitude of the upward movement increases with the depth of the lower boundary, defined as the distance from the tunnel center to the bottom of the mesh. This seems counterintuitive, and yet it is mathematically correct. This paper investigates the influence of the assumptions made to model the buoyancy phenomenon numerically, and specifically the (typical) 2D plane strain and elasticity assumptions. 3D and 2D plane strain numerical models are carried out using a linear elastic model, where the influence of the ground stiffness increasing with depth is assessed. The results show that the buoyancy effect, i.e. increasing upwards movements with depth of the lower boundary, decreases when the ground stiffness increases with depth.

3.1 Introduction

The design of shallow tunnels is more challenging than that of deep tunnels because of the presence of the ground surface. The mathematical treatment of the problem becomes more complex because the ground surface must be treated as a free boundary and ground stresses increase with depth (gravity loading), while for deep tunnels, it is acceptable to consider the boundaries as infinite and the ground initial stresses as uniform and equal to the stresses at the center of the tunnel (Bobet, 2003). Despite the complexity of shallow tunnel analysis, analytical solutions have been developed by several authors (Sagaseta, 1987; Bobet, 2001; Park, 2005; Pinto & Whittle, 2014; Strack & Verruijt, 2002; Verruijt, 1997; Verruijt & Booker, 1996; Verruijt & Booker, 2000). Such solutions are useful for fast assessment of tunnel behavior and are alternatives to empirical methods, such as the well-known Peck (1969) empirical approach to surface settlements, later improved by e.g. Celestino et al. (2000); Marshall et al. (2012). The applicability

of the analytical solutions to actual tunnel cases was assessed by Chou & Bobet, (2002), Park (2005) and Pinto et al. (2014). The three publications concluded that analytical solutions can be used to predict the ground deformations around tunnels for different construction methods and geotechnical profiles. Despite the non-linear behavior of soils, linear-elasticity may be reasonable if the ground movements are small. For instance, Ledesma & Alonso (2017), obtained accurate ground movement predictions for tunnels excavated in soft ground near sensitive structures using analytical solutions.

Together with the ground deformations due to the redistribution of stresses around the opening, i.e. ground loss and distortion of the tunnel cross section (Verruijt & Booker, 1996, Verruijt, 1997, and Pinto & Whittle, 2014), an upward rigid body motion occurs as a consequence of the ground weight removal due to the excavation (Strack & Verruijt, 2002, Verruijt & Booker, 2000, Bobet, 2001). This upward rigid body motion is called "buoyancy displacement" throughout the paper. The weight removal can be represented as an upward force with magnitude $\gamma\pi r^2$ (unit weight of the ground times the area of the excavation, per unit length of the tunnel) applied at the center of the tunnel (Verruijt & Booker, 2000). To balance this upward force, at least one point on the half space domain must have the vertical displacement constrained. For instance, Strack & Verruijt (2002) constrained the displacements of two points at the ground surface at a horizontal distance of five times the tunnel depth, while Verruijt & Booker (2000) and Bobet (2001) opted to zero the vertical displacements of a point below the center of the tunnel. Both assumptions have provided reasonable results. The first one, by imposing the displacements at the tunnel perimeter as a boundary condition, as shown by Strack and Verruijt (2008) and Strack (2002). The second one, because one would expect that the vertical displacements at some distance below the tunnel should be negligible.

Analytical solutions for shallow tunnels that consider gravity loading (and therefore the buoyancy effect) show an unbalanced term *log(r)* in the expressions for the vertical displacement, where *r* is the radial distance from the tunnel center (Bobet, 2001, Verruijt & Booker, 2000 and Strack & Verruijt, 2002). According to Verruijt & Booker (2000): "*This is in agreement with the well-known singular behavior of the displacements of an elastic half plane loaded by a stress distribution having a non-zero resultant force (Timoshenko & Goodier, 1951)*". In other words, the vertical displacements increase with the logarithm of the radial distance from the tunnel, which arguably makes no physical sense, but it is mathematically correct. The consequence for any

numerical discretization attempted is that the vertical displacements, in particular on the surface, increase with the depth of the lower boundary, defined as the distance from the tunnel centerline to the lower boundary of the numerical model. This is supported by Chou & Bobet (2002), who showed that the magnitude of the buoyancy displacement depends on the depth of the lower boundary: the deeper the mesh, the larger the buoyancy displacement. It is worth mentioning that buoyancy displacements are not considered neglected in those analytical solutions where the ground deformations along the tunnel perimeter are used as input, such as Verruijt (1997), Verruijt & Booker (1996) and Pinto & Whittle (2014).

The effects of the buoyancy on the vertical displacements at the surface were addressed by Chou & Bobet (2002) using the analytical solution developed by Bobet (2001). The authors obtained a good agreement between field data and analytical results by imposing zero displacement at a distance of two diameters (2D) below the tunnel centerline. Such distance minimizes the buoyancy displacements and so the authors recommended using a finite element mesh no deeper than 2D from the tunnel centerline. This recommendation is consistent with Möller (2006), who recommended a mesh depth (d) of 1.3 to 2.2D below the tunnel center for 2D models and 1.1 to 1.45D below the tunnel center for 3D models. The range proposed by the author was associated with the tunnel diameter, which varied from 4 to 12m. According to Verruijt and Strack (2008), the buoyancy effect is more relevant in soft soils, where the relative stiffness ($G/\gamma h$) is small and the buoyancy phenomenon may dominate deformations. Strack (2002) suggested to use a constitutive model that considers the unloading-reloading modulus of the ground, which is stiffer than the loading modulus, to achieve more realistic results. However, those factors do not affect the buoyancy displacement dependency on the depth of the lower boundary.

So far, the buoyancy effect has been investigated assuming a homogeneous linear elastic ground; that is, with constant stiffness with depth. It is well known that the stiffness of the ground increases with the confinement stress, thus, the ground stiffness is expected to increase with depth (Gibson, 1967; Gibson, 1974; Schanz & Vermeer, 1998). In this paper, the causes of the buoyancy dependency on the depth of the lower boundary are investigated. The assumptions found in the literature, i.e. 2D plane strain and homogeneous linear elasticity, are assessed using numerical modelling. The goal of the simulations is to evaluate how those assumptions link buoyancy with depth of the lower boundary, and to investigate the effect of the ground stiffness increasing with depth on buoyancy.

3.2 Numerical model validation with Verruijt & Booker (2000) analytical solution

In this section, numerical results are compared to the analytical solution proposed by Verruijt & Booker (2000). The reason is to show that the discretization used for all the analyses is essentially correct. Verruijt & Booker (2000) re-addressed the Mindlin's problem (Mindlin, 1940) using complex variable analysis and conformal mapping techniques, which allowed them to obtain the displacement, stress and strain fields. The problem, first addressed by Mindlin (1940), consists of a circular opening in an elastic half space loaded by the unit weight of the material (γ). Mindlin (1940) found an analytical solution using bi-polar coordinates and assuming that the ground surface and the tunnel perimeter were stress boundaries. Verruijt & Booker (2000) incorporated the buoyancy effect by superimposing on the Mindlin's problem the results of an upward vertical force applied at the center of the tunnel cross section and equivalent to the weight of the removed ground.

Figure 3.1 illustrates the geometry of the shallow tunnel problem with the boundary conditions used in the numerical models, where one can see that the displacements at the lateral and bottom boundaries are restricted. In this simulation, the tunnel diameter (D) is 10m, the tunnel depth (h) is 25m and the model size (L and d) are both equal to 1,000D, which is intentionally very large such that boundary effects are negligible. The numerical model was built to reproduce the analytical solution, i.e. linear elastic ground and 2D plane strain analysis. The ground properties are E= 50MPa, ν= 0.3, K_0= 1 and γ= 20kN/m^3. The numerical model has two phases: the first phase generates the gravitational stress field, where the displacements due to the gravitational load are zeroed; in the second phase, the elements inside the tunnel are deactivated, simulating the tunnel excavation. The FEM code Midas GTS was used to conduct the numerical simulations. Details about the incrementally phased analysis and about the elements deactivation can be found on the software manual (Midas GTS, 2018). Note that the buoyancy effect does not depend on the support installation or if the ground is elastoplastic and yielding occurs. The buoyancy effect depends only on the ground weight being removed from the interior of the tunnel. Given that the weight of the liner is usually negligible compared to the weight of the excavated ground, its effects on buoyancy are generally small. It is worth to mention that the longitudinal bending stiffness of the tunnel liner may affect the buoyancy displacements near the face, which is not considered in the 3D FEM models.

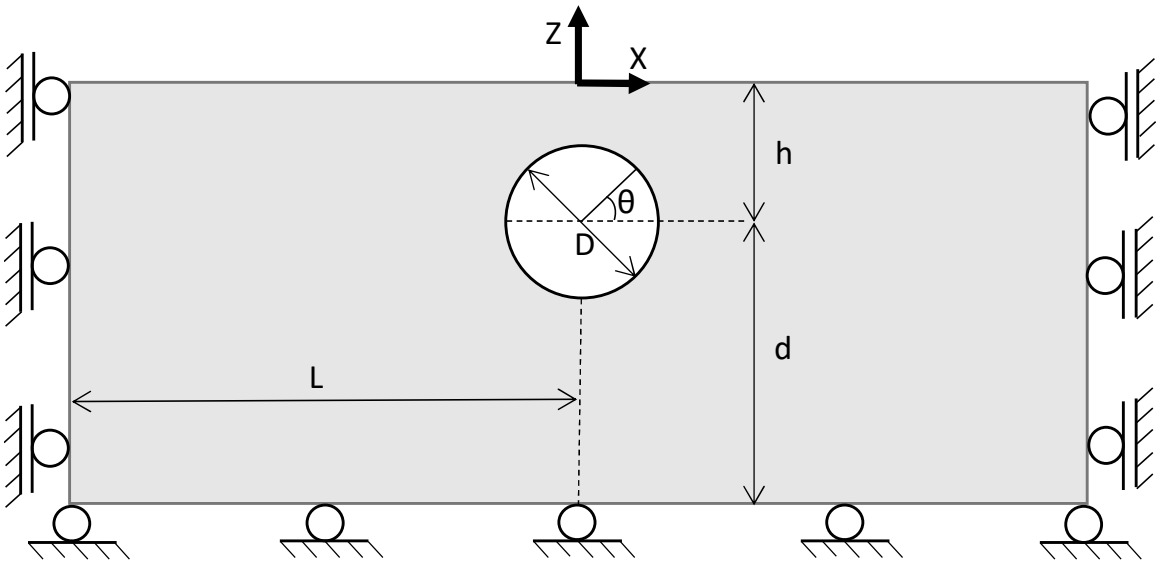

Figure 3.1 Boundary conditions for the FEM models, i.e. rollers at the lateral boundaries and pins at the bottom boundary.

Figure 3.2 shows the vertical displacement field with the deformed mesh after the tunnel excavation. As one can see, there is an upward movement, causing heave at the surface. The comparison between numerical and analytical solutions is shown in Figure 3.3 and 3.4. Figure 3.3 compares the normalized displacements (i.e. rigid body, radial and tangential displacements) at the tunnel perimeter and Figure 3.4, the normalized vertical displacement at the ground surface (u_s). The displacements at the tunnel perimeter obtained with the numerical and with the analytical solution are consistent with each other. The differences between numerical and analytical results are smaller than 1% for the radial displacements (i.e. u_r). There is an upward rigid body motion of the tunnel cross section due to the buoyancy effect (i.e. the buoyancy displacement). There is a small different, about 2% between the analytical and numerical buoyancy displacements. The tangential displacements (u_θ) are almost zero. The vertical displacement at the ground surface obtained numerically and analytically are also consistent. Both numerical and analytical vertical displacements at the ground surface follow the same trend, with differences of around 3%. Those differences are considered sufficiently small.

The good agreement between the analytical and the numerical solutions shows that both methods provide similar results if the mesh is sufficiently large. Such large upward ground movement is unexpected in practice, but it is mathematically correct and is associated with the large depth of the lower boundary (d=1,000D). Note that the depth of the lower boundary used is

unrealistically large, but it is adopted to show that numerical and analytical results are essentially the same if the model is large enough.

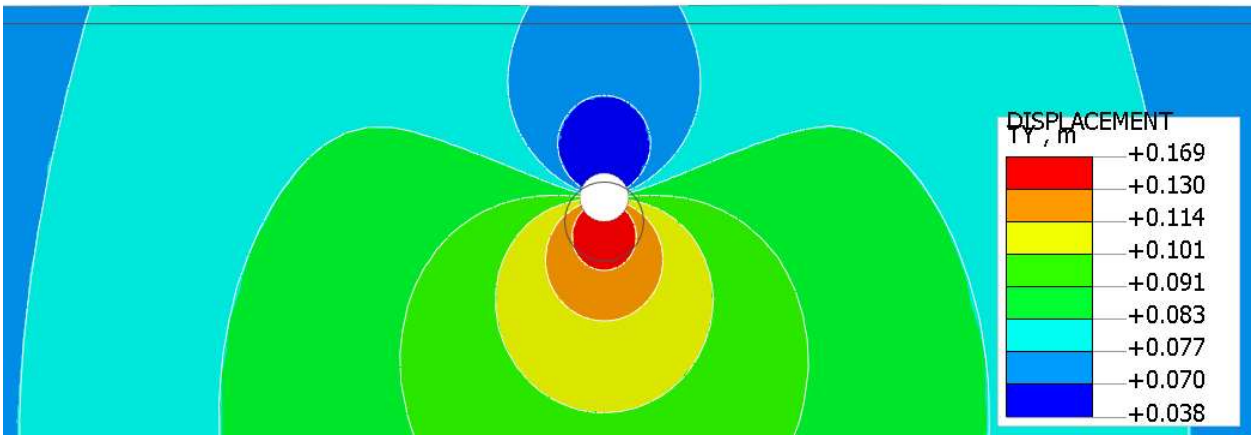

Figure 3.2 Vertical displacement field with deformed mesh near the tunnel. Positive values indicate upward movement.

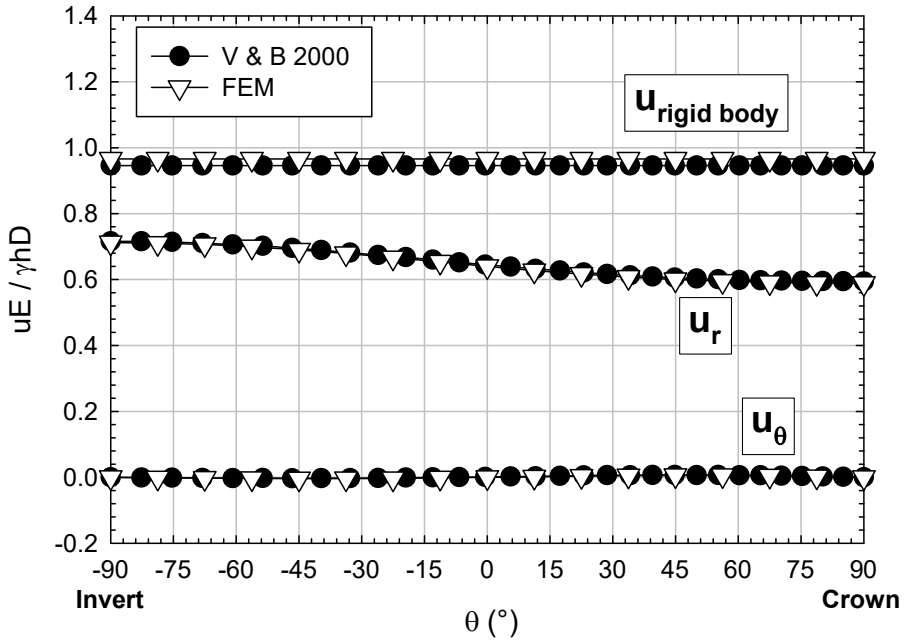

Figure 3.3 Normalized rigid body, radial and tangential displacements ($u_{rigid\ body}$, u_r and u_θ) along the tunnel perimeter for h=2.5D and d=1000D. Positive radial displacements are inwards. Positive rigid body displacement is upwards.

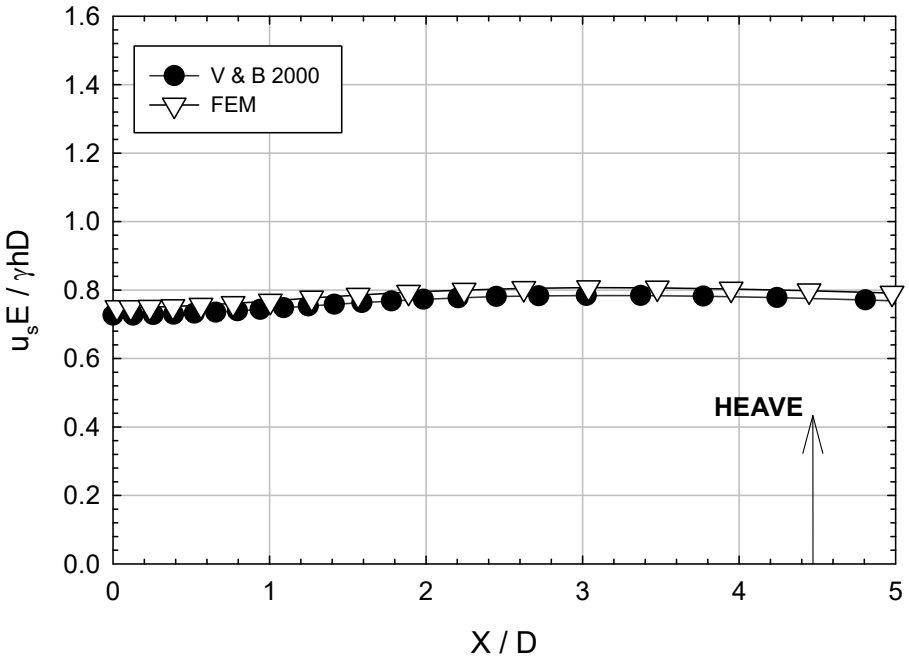

Figure 3.4 Normalized vertical displacements at the ground surface with horizontal distance from the tunnel center (X) normalized with the tunnel diameter (D), for h=2.5D and d=1000D. Positive values denote upward vertical displacement (heave).

3.3 Influence of depth of lower boundary on displacements.

The influence of the depth of the lower boundary on displacements is evaluated numerically through 2D plane strain and 3D FEM models. The 2D plane strain model is included to evaluate the assumption of "very long tunnel" on the magnitude of the buoyancy. 3D models with different depths of the lower boundary (d) are built. Figure 3.5 shows the 3D mesh with d= 4D. This discretization is representative of the other models. As before, D=10m and h=25m. The ground properties are also the same. In all the models, the gravity load is imposed in the first phase, while in the second phase, the elements that represent the tunnel are deactivated to simulate the excavation; see Figure 3.5. The model is built using 2nd order elements, as recommended by Vitali et al.(2017). The settlements from the 3D models are taken at a distance of 20D behind the tunnel face, which is large enough to make them comparable to the 2D simulations (Vitali et al., 2017). The results are shown in Figure 3.6, which is a plot of the vertical displacements of the ground surface (u_s) above the tunnel crown with the depth of the lower boundary (d), normalized with respect to the tunnel diameter (D). It includes the Verruijt & Booker (2000) analytical solution, and the 2D plane strain and 3D FEM models. As one can see in Figure 3.6, the settlements increase

with the logarithm of the depth of the lower boundary (d), for both 2D and 3D models, as well as for the analytical solution. All three models provide similar results and thus show that 3D modeling does not eliminate the phenomenon. The differences observed between analytical and numerical results for values of d/D smaller than 4 (i.e. lower boundary near the tunnel) are due boundary effect. It happens because the boundary conditions at the lower boundary are different on the analytical solution and on the numerical model.

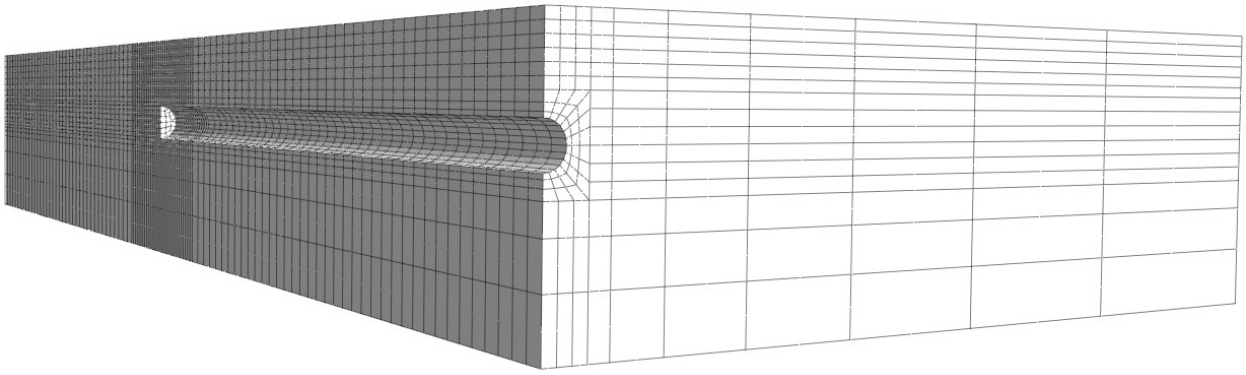

Figure 3.5 3D mesh with d= 4D, D= 10m, h= 25m, L= 20D and length 40D and excavation length of 20D. All other models with different depths (d) are similar.

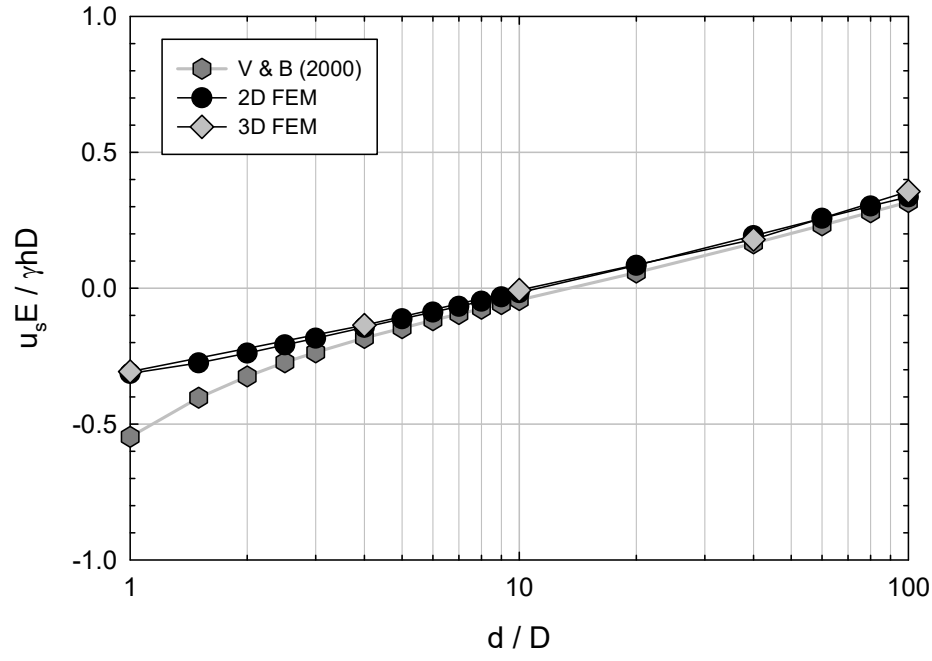

Figure 3.6 Normalized vertical displacements at the ground surface above the crown (u_s) with depth of the lower boundary (d), normalized by the tunnel diameter (D). Positive values represent upward vertical displacements (heave).

3.4 Buoyancy effect with increasing stiffness of the ground with depth

In this section, the influence of the assumption of homogenous ground, i.e. uniform stiffness, on buoyancy is assessed. It is well known that the ground stiffness is dependent on confinement stress, i.e. the higher the confinement, the higher the ground stiffness. Then, it is expected that the ground stiffness increases with depth. Three scenarios are considered for the analysis: Young's modulus of the ground constant with depth ($E=E_0$); increasing linearly with depth ($E=E_0+\alpha Z$ and $E=\alpha Z$); and increasing with the square root of depth (Rostovtsev, 1964; Gibson, 1967; Gibson, 1974; Schanz & Vermeer, 1998). Figure 3.7 illustrates those stiffness profiles. Note that the profiles were taken such that E is 50MPa at the depth of the tunnel center. The stiffness profiles with negligible stiffness at the surface (i.e. $E=\alpha Z$ and $E = E_{ref}\sqrt{K_0\gamma Z/p_{ref}}$) may represent non-cohesive soils, such as sands and normally consolidated clays. These soils have both strength and stiffness dependent on effective confinement stress, which is zero at the ground surface. The stiffness profiles with larger stiffness at the surface (i.e. $E=E_0+\alpha Z$ and $E=E_0$) are representative of cohesive soils such as overconsolidated clays and cemented sands.

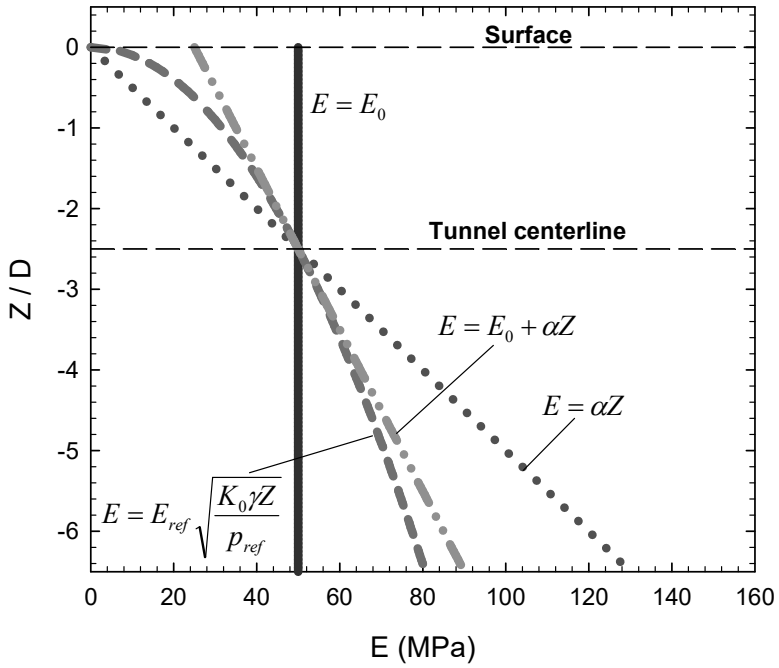

Figure 3.7 Stiffness profiles assessed: Ground stiffness (E) with depth (Z) normalized with respect to the tunnel diameter (D).

Figure 3.8 shows the vertical displacements of a point on the surface, above the crown, normalized with the tunnel diameter, as a function of depth of the lower boundary (d). It is obtained from 2D plane strain models. The figure shows that when the ground stiffness increases with depth, the buoyancy effect reduces substantially. The increase of stiffness with depth appears to compensate the stress/strain increase also with depth due to the weight loss associated with the excavation, thus reducing the displacements with distance below the tunnel. Buoyancy however is not fully eliminated. For instance, from d/D= 4 to d/D= 100, the settlement decreases its magnitude from -31.5mm to -25.1mm (6.4mm difference) for the scenario of linear increase of the Young's modulus with depth, given by $E = \alpha Z = 2Z$ (E is given in *MPa* and Z in *m, Z=0 at ground surface*); from -22.7mm to -11.7mm (difference of 11mm) for the scenario of linear increase of the Young's modulus with depth given by $E = E_0 + \alpha Z = 25 + Z$; and from -24.1mm to -7.4mm (16.7mm difference) for E increasing with the square root of depth ($E = E_{ref}\sqrt{K_0 \gamma Z / p_{ref}} = 50\sqrt{0.02Z / 0.5}$); all this compared with the change from -14.4mm to 33.6mm (heave) (48mm difference), for E constant with depth ($E=50MPa$). Note that the ratio of stiffness increment with depth affects the buoyancy dependency on the depth of the lower boundary: the larger the stiffness increment with depth, the smaller the buoyancy effect is.

Situations where the deformable ground layer is thick and a rigid layer, i.e. bedrock, is found far below the tunnel are common in practice. The discretization of the entire soft ground layer adopting a constant stiffness with depth might lead to an unrealistic prediction of the vertical displacements at the ground surface because of the buoyancy. It is arguable that considering the stiffness increase with depth may yield more realistic results in terms of surface settlements compared to those obtained with the assumption of uniform, e.g. average, stiffness.

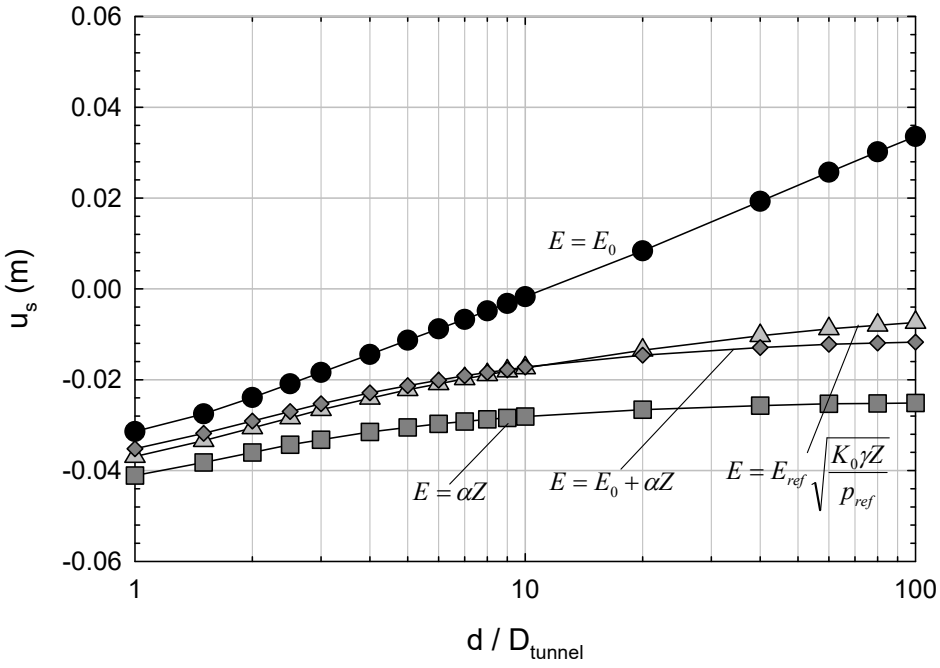

Figure 3.8 Vertical displacements at a point on the surface above the crown, with depth of the lower boundary (d), normalized with the tunnel diameter. Results taken from 2D FEM models.

Figure 3.9 shows convergence of the tunnel, between the crown and invert, with depth of the lower boundary, normalized with the tunnel diameter. As one can see, buoyancy does not affect the results. The changes in convergence observed at smaller depths are due to boundary effects; that is, the bottom boundary is not far enough from the tunnel such that the stress field is affected by the proximity of the boundary (the influence of the lower boundary is negligible when d is larger than 4D). As mentioned in the Introduction, buoyancy is compensated in Verruijt & Booker's (2000) analytical solution by choosing a point below the tunnel where the vertical displacement is zero. In other words, buoyancy can be addressed with a vertical rigid body motion. Since convergence is the difference of radial displacements between two points in the tunnel diametrically opposed, the rigid body motion needed to compensate for buoyancy cancels out. Note that the vertical convergence of the analytical solution does not depend on the depth of the lower boundary; for $E=E_0$, the vertical convergence is 0.642 for d=4D and is 0.649 for d=100D, thus, the difference is negligible (1%).

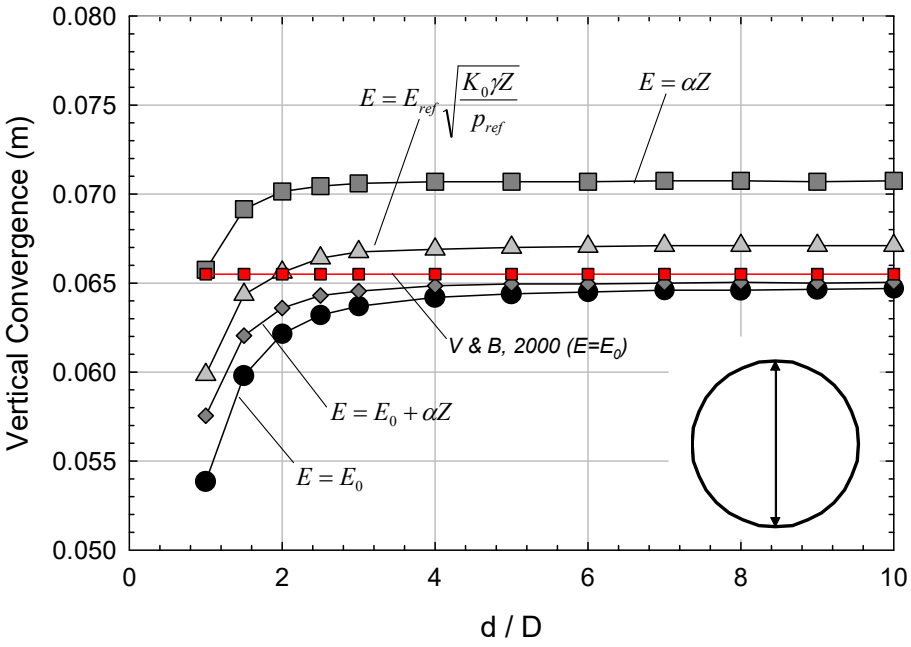

Figure 3.9 Vertical convergence at the crown and invert normalized with tunnel diameter, with depth of the lower boundary (d). Results taken from 2D FEM models.

Figure 3.10 is a plot of the normalized vertical displacements of a point on the ground surface above the crown, with the distance from the tunnel face, for E constant with depth and for E increasing linearly with depth. Those results are taken from the 3D models shown in Figure 3.5. For $E=E_0$, the displacements profiles changed significantly with d. Note that for $E= E_0$ and d= 10D, the shape of the displacement profile is unrealistic because of the large buoyancy displacements near the face. For the case of the ground stiffness increasing linearly with depth ($E=\alpha Z$, Figure 3.7), the displacement profiles, for different depths of the lower boundary, have the same shape. Also, the displacement profiles for d= 4D and d= 10D are similar, since the buoyancy effect is minimized when the stiffness increases with depth. Those results show that the assumption of the ground stiffness increasing with depth may lead to more realistic deformation predictions.

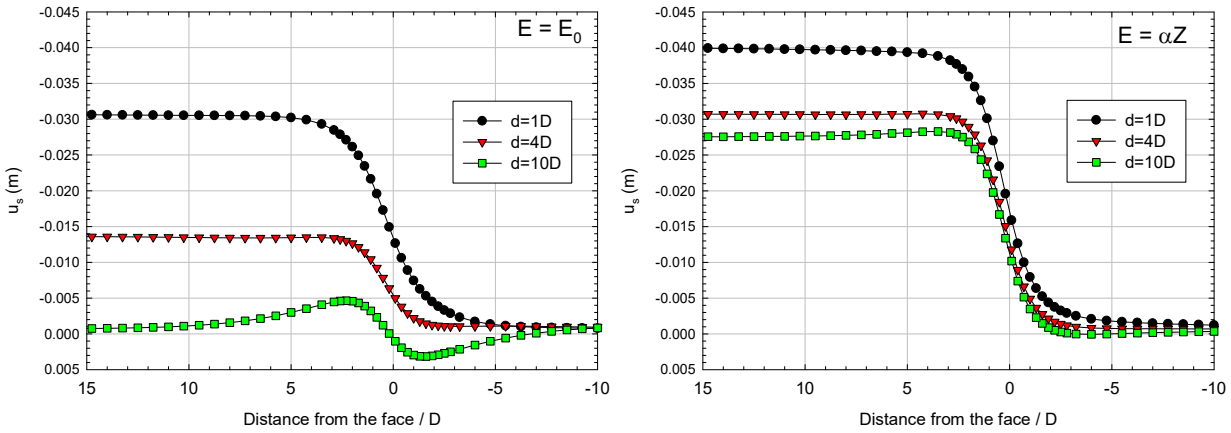

Figure 3.10 Vertical displacements at the ground surface above the crown (u_s) with distance from the tunnel face, for E constant with depth ($E= E_0$) and E increasing linearly with depth ($E= \alpha Z$).

3.5 Conclusion

The effects of tunnel buoyancy and depth of the lower boundary on the magnitude of the ground displacements are assessed in the paper. It is shown that the vertical displacement of a point above the tunnel crown on the ground surface increases with the logarithm of the depth of the lower boundary, when a homogeneous linear-elastic ground is considered. This is explained, mathematically, as an upwards line force at the center of the tunnel representing the weight removal due to the tunnel excavation. Displacements due to such line force include a *log(r)* term, and so ground deformations follow the counterintuitive trend of increasing as the distance from the tunnel increases. A direct consequence of this phenomenon is that vertical displacements at the ground surface increase with the depth of the lower boundary. It is important to note that strains and stresses both in the ground and the tunnel support are not affected by the buoyancy effect. It is shown in the paper that this is not an issue due to a 2D modeling, as 3D models show the same results. Note that the longitudinal bending stiffness of the liner may affect the buoyancy displacement near the face, which was not considered in this paper.

Buoyancy effects, which are not supported by field observations, decrease substantially when appropriate consideration of the stiffness of the ground is given. That is, geomaterials show an increase of stiffness with confinement; thus, the stiffness of the ground increases with depth. When such dependency is included in the numerical models, settlements on the surface become less sensitive to the depth of the lower boundary, albeit such dependency does not disappear completely. Given that buoyancy can be accounted for in numerical and analytical simulations by

including in the results a rigid body motion (i.e. by determining the point below the tunnel of no vertical displacements), convergence displacements are not affected in the analytical solutions, nor in numerical models when the lower boundary is far enough from the tunnel (i.e. distance between tunnel center and lower boundary larger than about 4 times the tunnel diameter).

The work presented suggests that, when surface settlements need to be accurately determined, a proper representation of the increase of stiffness of the ground is needed in numerical and analytical models. Uniform (i.e. average) assumptions for the ground stiffness require the location of the point of zero vertical displacement below the tunnel, which can be estimated from e.g. semi-empirical recommendations such as those from Chou and Bobet (2002). If the focus of the analyses is on stresses and strains of the ground and/or tunnel support, buoyancy does not affect the results, and so the location of the bottom boundary is not relevant, as long as it is far enough from the tunnel to avoid boundary effects.

Acknowledgments

The research is being partially supported by the research funding agency of Brazilian government CNPq ("Conselho Nacional de Desenvolvimento Cientifico"). The authors acknowledge the support from CNPq and also Midas company, which kindly provided the license of Midas GTX NX software, used in the present work.

3.6 References

Bobet A. Effect of pore water pressure on tunnel support during static and seismic loading. *Tunn. Undergr. Sp. Technol.* 2003; 18(4): 377–393.

Bobet A. Analytical Solutions for Shallow Tunnels in Saturated Ground. *Journal of Engineering Mechanics*. 2001; 127(12): 1258–1266.

Celestino TB, Gomes RAMP, Bortolucci AA. Errors in ground distortions due to settlement trough adjustment. *Tunn. Undergr. Sp. Technol.* 2000; 15(1): 97–100.

Chou WI, Bobet A. Predictions of ground deformations in shallow tunnels in clay. *Tunn. Undergr. Sp. Technol.* 2002; 17(1): 3–19.

Gibson RE. Some results concerning displacements and stresses in a non-homogeneous elastic half-space. *Geotechnique*. 1967; 17(1):58–67.

Gibson R. The analytical method in soil mechanics. *Geotechnique*. 1974; 24(2): 115–140.

Ledesma A, Alonso EE. Protecting sensitive constructions from tunnelling: the case of World Heritage buildings in Barcelona. *Géotechnique*. 2017; 67(10), 914-925.

Marshall AM, Farrell R, Klar A, Mair A. Tunnels in sands: the effect of size, depth and volume loss on greenfield displacements. *Géotechnique*. 2012; 62(5) 385–399.

MIDAS Information Technology Co. *Analysis Reference Manual*. 2018.

Mindlin RD. Stress distribution around a tunnel. *Transactions of the American Society of Civil Engineers*; 1940, 195(1): 1117-1140.

Möller S. *Tunnel induced settlements and structural forces in linings*. PhD Thesis, Institute of Geotechnical Engineering, Universitat of Stuttgart, Stuttgart, 2006.

Park KH. Analytical solution for tunnelling-induced ground movement in clays. *Tunn. Undergr. Sp. Technol.* 2005; 20(3): 249–261.

Peck RB. Deep Excavations and Tunneling in Soft Ground. In *Proceedings of 7th International Conference on Soil Mechanics and Foundation Engineering*. Mexico City; 1969; 7(3): 225–290.

Pinto F, Whittle AJ. Ground Movements due to Shallow Tunnels in Soft Ground. I: Analytical Solutions. *J. Geotech. Geoenvironmental Eng.* 2013; 140(4): 04013040.

Pinto F, Zymnis DM, Whittle AJ. Ground Movements due to Shallow Tunnels in Soft Ground. II: Analytical Interpretation and Prediction. *J. Geotech. Geoenvironmental Eng.*, 2014; 140(4): 04013041.

Rostovtsev N. On the theory of elasticity of a nonhomogeneous medium. *J. Appl. Math. Mech.* 1964, 28(4): 745–757.

Sagaseta C. Analysis of undrained soil deformation due to ground loss. *Géotechnique*. 1987; 37:301–320.

Schanz T, Vermeer PA. On the Stiffness of Sands. In: *Pre-failure Deform. Behav. geomaterials*, RJ Jardine, editor. ICE publishing; 1998: 383–387.

Strack OE. *Analytic Solutions of Elastic Tunneling*. PhD thesis. Delft University of Technology, Delft, 2002.

Strack OE, Verruijt A. A complex variable solution for a deforming buoyant tunnel in a heavy elastic half-plane. *Int. J. Numer. Anal. Methods Geomech.* 2002; 26 (12); 1235–1252.

Timoshenko S, Goodier JN. *Theory of Elasticity*, vol. 49. McGraw-Hill, 1951.

Verruijt A. A complex variable solution for a deforming circular tunnel in an elastic half-plane. *Int. J. Numer. Anal. Methods Geomech.* 1997; 21(2): 77–89.

Verruijt A, Booker JR. Surface settlements due to deformation of a tunnel in an elastic half plane. *Géotechnique*. 1996; 46(4): 753–756.

Verruijt A, Booker JR. Complex variable analysis of Mindlin' s tunnel problem. In: *Proceedings of Developments in Theoretical Geomechanics - The John Booker Memorial Symposium*. Rotterdam; Jannuary 2000.

Vitali OPM, Celestino TB, Bobet A. *3D finite element modelling optimization for deep tunnels with material nonlinearity*. *Undergr. Sp.* 2017; 3(2): 125–139.

4. CONSTRUCTIONS STRATEGIES FOR A NATM TUNNEL IN SAO PAULO, BRAZIL, IN RESIDUAL SOIL

VITALI, O. P. M.; CELESTINO, & BOBET, A. (2020). Construction strategies for a NATM tunnel in Sao Paulo, Brazil, in residual soil. Manuscript under review for publication in a peer-reviewed journal.

Abstract

Due to the fast growth of urban areas worldwide, the demand for tunnels in developed areas is increasing. The design and construction of those tunnels is complex because of their shallow depths and their interaction with existing aboveground and buried structures, which results in rather limited allowable ground deformations induced by the tunnel excavation and support. In tropical regions, residual porous soils near the surface are common. Those soils are highly deformable; thus, tunneling may induce large ground deformations that may damage nearby structures. The NATM method is being widely employed in several big cities in tropical regions, but little research has been conducted to assess the induced ground deformations in residual soils, common in tropical areas. This paper provides insight into this issue. A well-documented metro tunnel in Sao Paulo, Brazil, in a residual red porous clay, was analyzed using 3D FEM. The behavior of the residual red porous clay was approximated by an advanced constitutive soil model calibrated with triaxial tests on intact samples extracted at the site. Predictions of the tunnel deformations during construction matched the field data. The calibrated model was then used to explore tunnel performance under different construction strategies. The influence of partial-face excavation, unsupported span length, support stiffness and pipe roof umbrella were assessed. The numerical results showed that partial-face excavation was effective to reduce ground deformations ahead of the face of the tunnel and to improve face stability; however, the settlements behind the face increased because of the delay in closing the primary lining. The installation of a stiffer liner closer to the face reduced the ground deformations significantly. The pipe roof umbrella was the most effective technique to reduce the ground deformations around the tunnel; however, the numerical results did not consider deformations that could be induced by the drilling and grouting operations. The results shown in this paper provide both qualitative and quantitative information about the ground deformations induced by NATM tunneling in residual porous soils, that could

help designers and contractors choose the optimum support and construction methods to minimize ground deformations.

4.1 Introduction

The increasing urbanization worldwide is creating a large demand for reliable underground infrastructure, as pointed out by Broere (2016). Tunnels in urban environments are usually excavated at shallow depths, in soft ground, and underneath aboveground and other buried structures. This normally requires rather limited ground deformations due to the tunnel excavation. For these reasons, the design and construction of those tunnels are challenging. The NATM principles (Rabcewicz, 1964), have been widely and successfully applied to excavate shallow tunnels in urban areas under challenging conditions. The NATM key characteristics include relatively simple execution, high flexibility during construction and reduced cost. The construction process of NATM tunnels may have a significant impact on induced ground deformations (Farias et al., 2004). NATM tunnels usually rely on partial excavation of the tunnel cross-section to reduce ground deformations (New and Bowers, 1994; Deane and Bassett, 1995). Typically, the excavation starts at the crown, then bench and invert in sequence (HSE, 1996). The tunnel support is typically shotcrete reinforced with steel ribs and steel fibers or wire mesh. In urban areas, tunnels may advance with small excavation steps and the support is installed close to the face. During tunnel construction, ground and support deformations are monitored, and those measurements are compared with the ground deformations predicted during design. Thus, tunnel excavation and support may be optimized during construction as new information becomes available. In urban areas, however, support optimization should never compromise deformations.

Lateritic or mature residual soils are common in tropical regions. The residual soil may be highly weathered and heavily leached, so the void ratio may be large and the soil structure unstable and weakly bonded (Leroueil and Vaughan, 1990). Tunnels in those soils may induce large ground deformations that may affect aboveground and nearby buried structures. Ortigao et al. (1996) and Marques (2006) reported large ground deformations during the excavation of several kilometers of NATM tunnels in residual porous soils, for the metro system in Brasilia, Brazil. Surface settlements up to 500mm were reported. Those authors pointed out an unusual behavior in those soils: the vertical displacements decreased with depth (settlements at the ground surface were larger than at the tunnel crown), which is the opposite of expected behavior, e.g. Mair et al. (1993).

The ratio of the settlement at the surface and at the tunnel crown ranged between 1.2 and 1.3. Ortigao and Macedo (1993) associated this unusual behavior with the collapsible nature of the residual porous soil.

Large ground deformations were observed during the construction of the "Paraiso tunnel" in Sao Paulo, Brazil, excavated in residual porous soil. This tunnel is well-described by Parreira (1991). Azevedo et al. (2002) conducted 2D FEM analysis of the Paraiso tunnel using an advanced constitute model (i.e. the Lade's model) to represent the residual porous soil. The model parameters were calibrated with the laboratory test results conducted by Parreira (1991) on intact samples. The authors observed that the ground deformations around the tunnel were better predicted with the advanced soil model rather than with an elastic perfectly plastic model. The Paraiso tunnel was later investigated by Almeida e Souza et al. (2011). The authors observed that the settlement trough was not well captured by the empirical Gaussian curve (Schmidt, 1969; Peck, 1968), but the Yield density curve, proposed by Celestino and Ruiz (1998) and Celestino et al. (2000), fit quite well the field data. Almeida e Souza et al. (2011) conducted 3D FEM analysis of the Paraiso tunnel using the Lade's constitutive model with the parameters calibrated by Parreira (1991) and Azevedo et al. (2002). The authors obtained an excellent match between numerical results and field data. They showed that a nonlinear constitutive model should be adopted to properly reproduce the deformations around the tunnel. Almeida e Souza et al. (2011) also showed that the 2D analysis was not able to capture the complex stress paths near the face of the tunnel. According to Cantieni and Anagnostou (2009), the radial stresses at the tunnel perimeter increase ahead of the face, reduce to zero at the unsupported span and increase behind the tunnel support. Also, axial shear stresses are mobilized near the face and those shear stresses may remain mobilized (i.e. not reduce to zero) far-behind the face (Ng and Lee, 2005). The mobilization of the axial shear stresses near the face causes the rotation of the principal stress directions, as shown by Eberhardt (2001). Attempts to correlate 2D analysis techniques, such as the stress relief method (Panet and Guenot, 1982), with 3D analysis has shown that the "stress relief factor" changes substantially depending on the target (i.e. settlements at the surface or at depth, or internal forces in the support) and with the tunnel construction sequence, as pointed out by Moller (2002).

Despite the large demand for shallow tunnels in highly deformable residual porous soils, insufficient research has been dedicated to investigate the ground deformations induced by tunneling in those soils. This paper seeks to provide insight into this issue. The Paraiso tunnel was

analyzed using a 3D FEM with an advanced soil constitutive model to represent the residual porous soil at the site (Schanz et al., 1999). An excellent match between numerical results and field data was obtained. The model was then used to investigate the effects of different construction strategies and assess their impact on ground deformations and on face stability.

4.2 Project overview

The Paraiso tunnel was completed in 1991. Detailed information about this tunnel is provided by Parreira (1991). Figure 4.1 illustrates the tunnel cross section and the excavation sequence. The tunnel cross section has an ellipsoidal shape, with 11.6m width and 8.5m height. The excavation was performed in three stages: crown (1), bench (2) and invert (3). The crown (1) was excavated in rounds of 1.6m. A bench (2) was kept to improve face stability. Immediately after excavation of the crown, two sets of steel ribs spaced 0.8m were installed and a layer of 0.2m of shotcrete was placed at the tunnel wall. The invert (3) was excavated 4.8m from the face, in advances of 1.6m. A 0.2m concrete layer reinforced with wire mesh was sprayed on the tunnel invert. A secondary liner of reinforced concrete with 0.15m thickness was installed later.

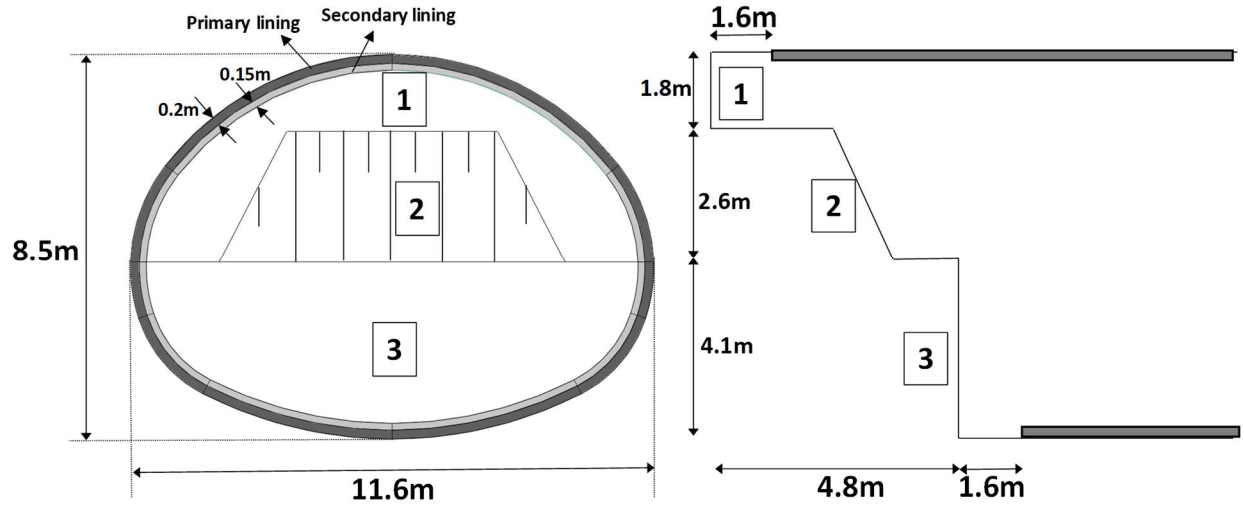

Figure 4.1 Transversal and longitudinal cross section of the Paraiso tunnel.

The geotechnical investigation in the region revealed a thin layer of landfill, a layer of residual red porous clay, a layer of stiff residual variegated clay and a layer of very dense clayey

sand. The water level was found at the transition between the residual red porous clay and the residual variegated clay. Figure 4.2 includes the geotechnical profile and the position of the tunnel instrumentation. In the instrumented cross-section analyzed, the residual red porous clay was 12m thick and the residual variegated clay, 10.6m thick. The soil profile described is the same as that adopted by Azevedo et al. (2002) and Almeida e Souza et al. (2011) for their analyses. The crown was located 7.6m below the surface and was excavated in the residual red porous clay, while the invert was excavated in the stiff variegated clay. Ground and support deformations were monitored during the excavation. Surface settlements were measured by bench marks; the vertical displacements above the crown were measured with vertical extensometers and the horizontal displacements near the springline were measured with an inclinometer. The deformations in the shotcrete support were measured at the crown and at the perimeter of the tunnel. Figure 4.2 provides a sketch of the instrumentation used.

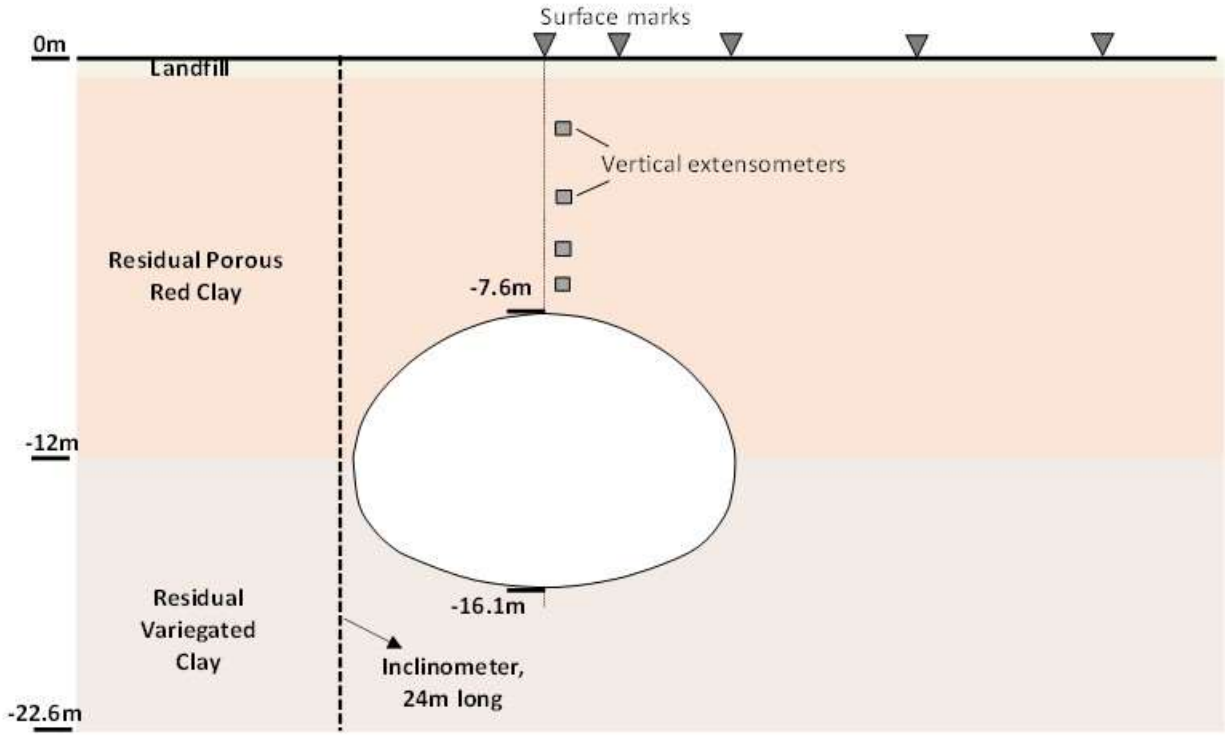

Figure 4.2 Geotechnical profile and tunnel instrumentation.

4.3 Soil model calibration of the Sao Paulo residual red porous clay

The geotechnical properties of the Sao Paulo residual red porous clay have been extensively studied. This soil is classified as lateritic or mature residual soil. It is highly weathered

and heavily leached, with large void ratio and unstable soil structure. Indeed, Leroueil and Vaughan (1990) found that the behavior of these soils was dependent on their structure. Parreira (1991) conducted an exhaustive laboratory test campaign on samples of residual red porous clay collected from the excavation site. Undisturbed blocks of soil were excavated at depths of 3.5m and 6.5m. Table 4.1 shows the properties of the soil obtained from the block samples, as well as the values compiled by Massad et al. (1992) for the Sao Paulo residual porous clay. The properties of the soil samples at 3.5m and 6.5m depth are similar and are within the range of expected values for the Sao Paulo residual red porous clay. Note also that the soils are unsaturated. As pointed out by Parreira (1990), if the water content increases, the soil structure collapses, producing large volumetric deformations.

Table 4.1 Properties of the Sao Paulo residual red porous clay from data compiled by Massad et al. (1992) and from the intact block samples from the Paraiso tunnel site.

	Massad et al. (1992)		**Undeformed block samples (Parreira, 1991)**			
			3.5m depth		**6.5m depth**	
	Range	**Average**	**Range**	**Average**	**Range**	**Average**
e	1.38-1.85	1.54	1.49-1.77	1.62	1.47-1.57	1.52
w (%)	33-47	41	40-44	41.5	40-43	41
γ_n (kN/m^3)	13.5-16.5	15.2	13.6-15.1	14.4	14.1-15.1	14.7
S_r (%)	62-88	74	64-75	70	68-77	72.4

Drained triaxial compression loading tests and triaxial compression unloading tests were conducted by Parreira (1991) on intact specimens. The results from the triaxial tests, under confinement of 25 and 49kPa, of samples collected at 3.5m depth, and under 25, 49 and 98kPa confinement, for samples extracted at 6.5m depth, were selected to calibrate the constitutive model. Those confinement stresses were similar to the in-situ stress from where the samples were collected, so the soil structure was not altered by the confinement stress.

The Hardening Soil Model (Schanz et al., 1999) was selected to represent the residual porous soil. This model is available in the material models library of Midas GTS NX, the FEM code used in this paper. It is a sophisticated elastoplastic model with Coulomb failure criterion and nonlinear elastic formulation. The model was developed considering the classical theory of Plasticity and captures the most relevant aspects of soil behavior such as: stiffness-stress-strain

dependence; hardening behavior; overconsolidation effects and critical state after large deformations. The input parameters for the Hardening Soil Model can be easily determined from conventional laboratory tests. The hardening soil model is, perhaps, the most popular constitutive model for soils, extensively used in both Industry and Academia. The model however may not capture the strain-softening behavior typically observed in dense sands and highly overconsolidated clays under small confinement stresses.

Figure 4.3 plots the maximum shear stress $(\sigma_1-\sigma_3) / 2$ with the mean stress $(\sigma_1+\sigma_3) / 2$ at failure for selected triaxial tests, as well as the failure envelope. One can see that the failure envelope, with a friction angle (φ) of 30° and a cohesion intercept of 30kPa, fit well the results of the triaxial tests. Large suction stresses were measured in the laboratory (between 125 and 140kPa), as reported by Parreira (1991). Thus, the cohesion intercept is probably affected by the suction. For the Sao Paulo residual red porous clay, Massad et al. (1992) reported cohesion values of 10 to 70kPa (average 32kPa), and 23 to 33° (average of 27°) for the friction angle; the strength parameters obtained from the triaxial tests fall within those ranges.

Figure 4.4 presents the deviatoric stresses $(\sigma_1-\sigma_3) / 2$ and the volumetric deformations with axial deformation, obtained from the triaxial compression loading tests (Figure 4.4 a) and from the triaxial compression unloading tests (Figure 4.4 b). Figure 4.4 also presents the results from the calibrated constitutive model (Hardening Soil Model, Schanz et al., 1999). As one can see in Figure 4.4, the calibrated constitutive model fits well the experimental data. For the triaxial compression tests (Figure 4.4a), the soil deforms following a hyperbolic stress-strain curve with failure at, approximately, 20% of axial deformation. Interestingly, Parreira (1991) observed that the initial stiffness of the residual red porous clay decreased as the confinement stress increased from 25 to 98kPa. Such behavior is unexpected in conventional soils, but in this case, it was thought to be associated with the soil structure. The hardening soil model could capture well volumetric deformations, because they were weakly dependent on confinement. As one can see in Figure 4.4 a, the volumetric strains in the triaxial tests were large, up to 12%, which is expected for residual porous soils because of the large in-situ void ratio and unstable structure. The constitutive model could reproduce well the magnitude of the volumetric deformations up to an axial deformation of about 10%; afterwards, the model slightly underpredicted volumetric deformations. For the triaxial compression unloading tests (Figure 4.4 b), the experimental results showed an initial quasi-linear increase of the deviatoric stress with axial deformations, up to about 0.2%; afterwards, the

deviatoric stresses slightly increased with axial deformations. As one can see in Figure 4.4 b, the hardening soil model was able to reproduce this behavior. Regarding volumetric deformations, the model predicted a very small increase with axial deformations, much smaller than that observed in the experiments.

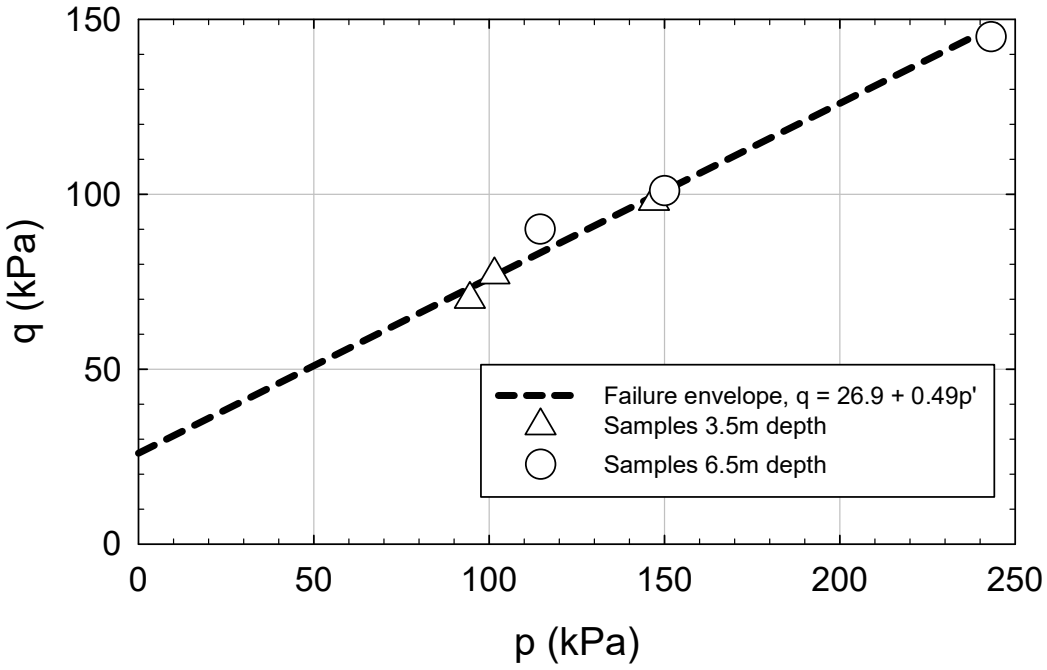

Figure 4.3 Failure envelope from triaxial compression loading tests with confinement stress (25kPa, 49kPa and 98kPa). The Coulomb strength properties are φ=30° and cohesion=30kPa.

Vaughan and Kwan (1984) showed that the in-situ horizontal stress decreased as the original rock mass decomposed due to weathering and leaching. The authors observed that when the stiffness of the residual soil decreased to 1% of its original value, the in-situ horizontal stress approached the limit: $\frac{\sigma'_h}{\sigma'_v} = K_0 = \frac{\upsilon}{1-\upsilon}$. This is also the case for the residual porous soil. According to Vaughan and Kwan (1984), conventional laboratory tests, to determine K_0, destroy the soil structure, and so K_0 values tend to be overestimated. Ortigao et al. (1995) conducted in-situ measurements of K_0 using the Menard pressuremeter. The authors obtained K_0 values around 0.5.

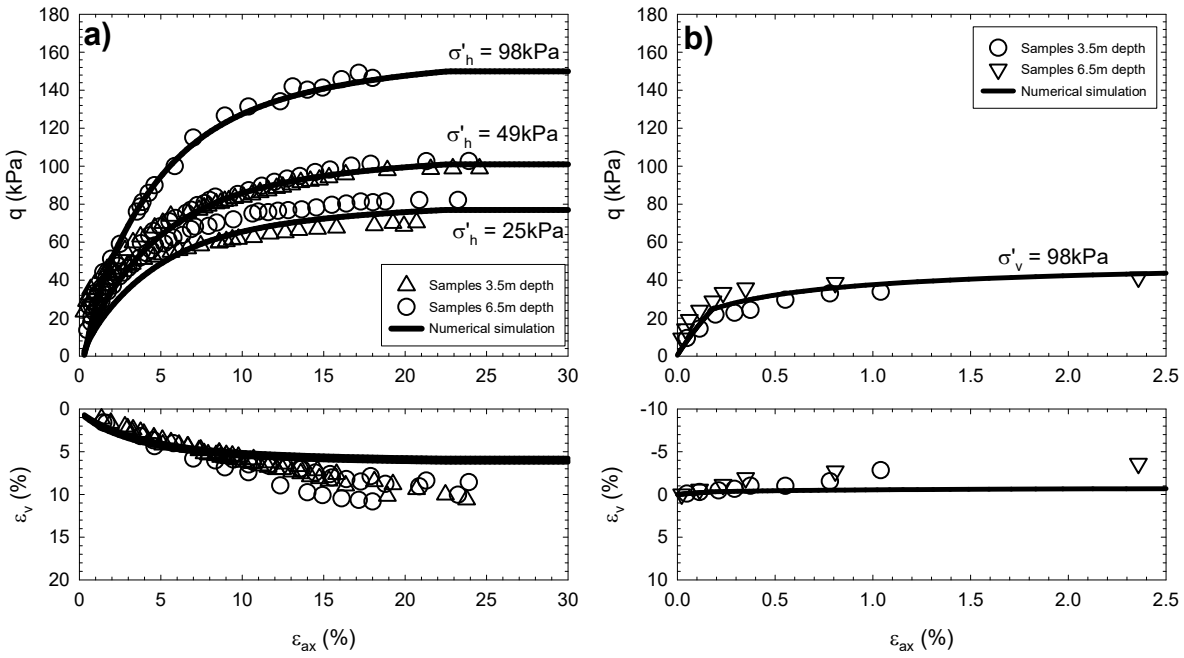

Figure 4.4 Experimental data and numerical simulation of the triaxial tests. (a) Triaxial compression loading 25kPa, 49kPa and 98kPa confinement; and (b) Triaxial compression unloading for 98kPa vertical stress.

Table 4.2 shows the calibrated parameters for the hardening soil model. The numerical results from the 3D FEM model of the Paraiso tunnel, shown in the following sections, were also considered in determining the best-fit values for the parameters. In other words, the parameters in Table 4.1 provided the best predictions for the selected laboratory triaxial tests and for the field data.

For the residual variegated clay underneath the residual red porous clay (Figure 4.2), an elastic, perfectly plastic model with a Coulomb failure envelope was adopted. The geotechnical properties were: Young modulus (E), 120 MPa; Poisson's ratio (ν), 0.17; cohesion (c), 66kPa; friction angle (φ), 25°; specific unit weight (γ) 18kN/m^3; and K_0 0.84. Those are the same properties used by Almeida e Souza (2011).

Table 4.2 Calibrated hardening soil model parameters to simulate the Sao Paulo residual red porous clay.

$E_{50,ref}$ (kPa)	6000
$E_{oed,ref}$ (kPa)	2000
$E_{ur,ref}$ (kPa)	12000
R_f	0.9
p_{ref} (kPa)	50
n	1
ϕ (°)	30
$K_{0,NC}$	0.5
Ψ (°)	0
c (kPa)	30
γ_n (kN/m^3)	15
ν	0.27
OCR	1

4.4 Numerical modelling of the Paraiso Tunnel

3D FEM modeling was conducted to analyze the Paraiso tunnel. Figure 4.5 shows the FEM model. The mesh was built using 2nd order hexahedron elements and was refined enough to ensure the accuracy of the numerical results (Vitali et al., 2017). The model dimensions were selected to avoid the interference of the boundaries with the results. Because the tunnel excavation was symmetric with respect to the tunnel vertical axis, only half of the tunnel was discretized. The bottom of the model was located at the transition between the residual variegated clay and the very dense clayey sand layer located 6.5m below the invert. Thus, buoyancy effects (Vitali et al., 2018) were negligible because the bottom of the mesh was located near the tunnel. The lateral boundaries were pinned and the bottom boundary was fixed. At the ground surface, the horizontal displacements were constrained to consider the effects of the pavement, as recommended by Azevedo (2002) and Almeida e Souza (2011).

A front view of the mesh near the tunnel is presented in Figure 4.6. The mesh was refined near and above the tunnel crown, where the ground deformations were larger. The thickness of the residual red porous clay and of the residual variegated clay are given in Figure 4.2. The tunnel crown was 7.6m below the ground surface. As shown in the figure, the crown was located in residual red porous clay, while the invert, in residual variegated clay. The construction sequence

described previously was included in the 3D FEM analysis, as illustrated in Figure 4.7. The length of the excavation rounds was 1.6 m (note that the length of the 2nd order hexahedron elements was 0.8 m; thus, the longitudinal mesh refinement was sufficient to obtain accurate results, according to Vitali et al., 2017). The model was run in 37 stages. In the first stage, the geostatic stress field was generated, with K_0 equal 0.5 for the residual red porous clay and 0.84 for the residual variegated clay. The following stages simulated the excavation and support processes, by deactivating elements corresponding to a particular excavation sequence and activating elements representing the support. The tunnel support with shotcrete and steel sets was represented by shell elements with linear-elastic behavior and thickness of 0.2m (Figure 4.1). No slip between ground and support was allowed. The support had the following material properties: Young modulus (E), 5GPa, and Poisson's ratio (ν), 0.2. The stiffness taken for the support was somewhat small compared to typical values. This was done to simulate the early-age shotcrete and the reduced final stiffness caused by the loading of the shotcrete at early-age (Golser, 2001). Ideally, the time-dependent behavior of the shotcrete should be considered in 3D FEM tunnel analysis, but since this information is unknown, it was assumed a constant Young modulus with time.

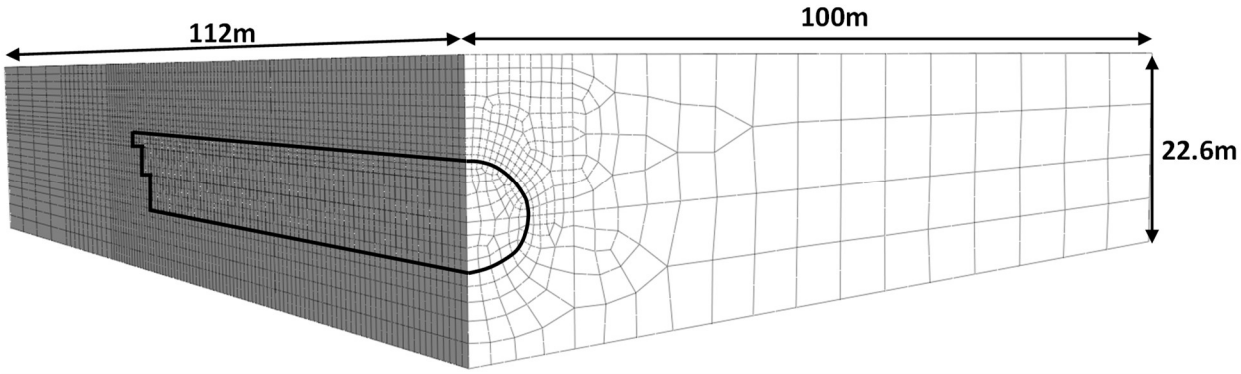

Figure 4.5 Finite element mesh and model dimensions.

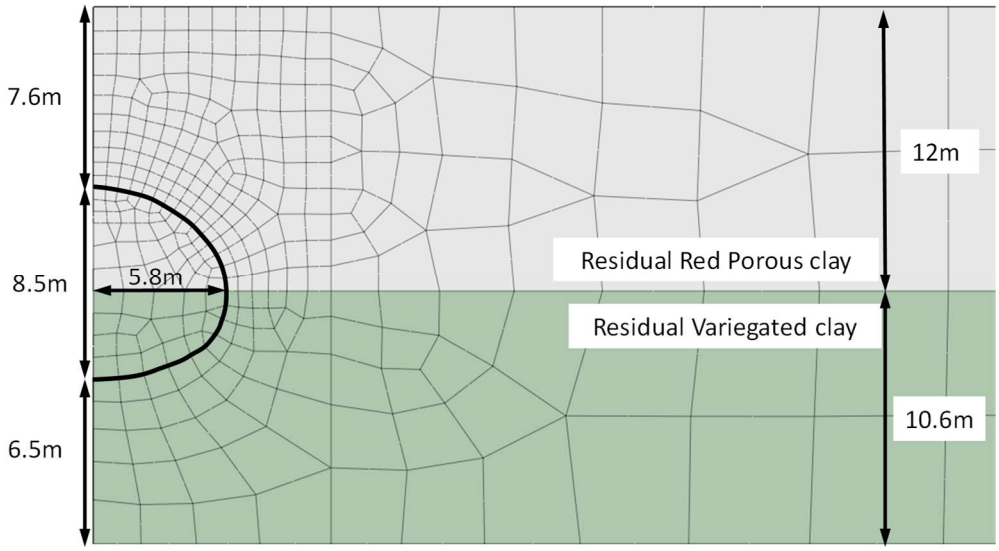

Figure 4.6 Front view of the mesh near the tunnel, with dimensions and geotechnical profile.

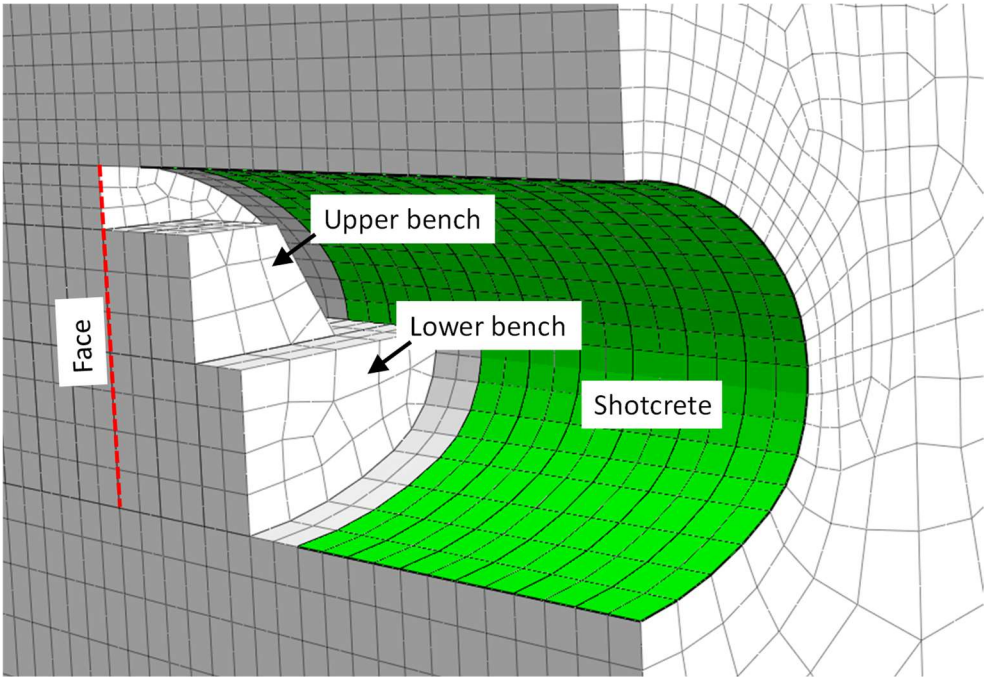

Figure 4.7 Numerical simulation of the excavation sequence.

Figure 4.8 shows the surface settlements, calculated with the model, as a function of the axial distance from the tunnel face (Figure 4.8 a, i.e. longitudinal settlement profile), and with the horizontal distance from the vertical axis of the tunnel (Figure 4.8 b, i.e. settlement trough). An excellent match between the actual ground deformations and numerical results was obtained. The

longitudinal settlement profile has a sigmoidal shape, with settlements starting to increase at around 20m ahead of the face of the tunnel, i.e. approximately at two tunnel diameters, and reaching a steady-state at around 20 m behind the face. Above the face of the tunnel, the measured settlement was 41mm, while the numerical model gave 45mm; far-behind the face, the measured settlement above the crown was 85mm, and the calculated settlement, 89mm. As one can see in Figure 4.8 b, the settlement trough calculated by the numerical model was close to the field data, except at about 10m from the tunnel axis, where the measured settlement was 20mm while the obtained settlement was 39mm.

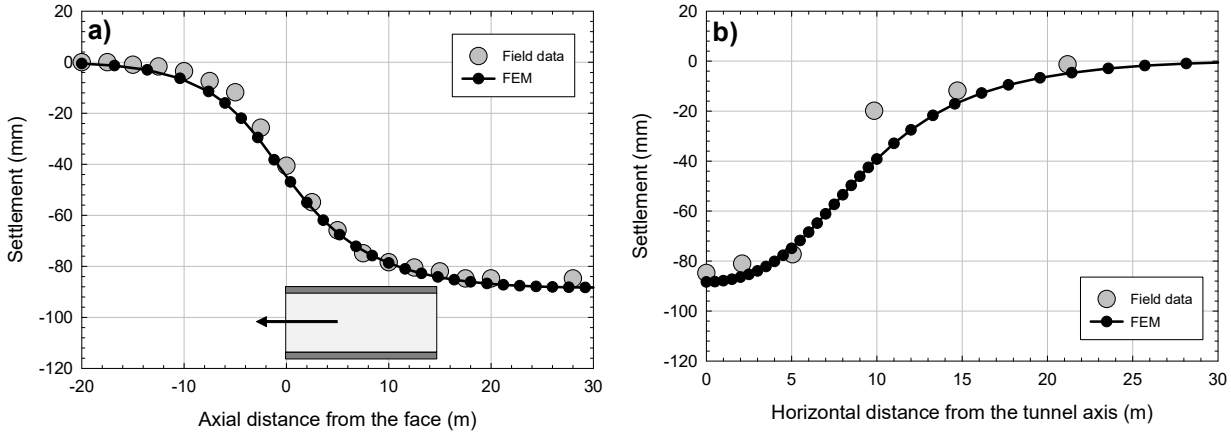

Figure 4.8 Surface settlements with: (a) axial distance from the face; and (b) horizontal distance from the vertical tunnel axis.

Figure 4.9 shows the vertical displacements above the crown, at different depths and at different distances from the tunnel face (i.e. at 5.5m ahead of the face, at the face, and far-behind the face). The location of the vertical extensometer is shown in Figure 4.2. Numerical results and field data are in an excellent agreement. As one can see, the vertical displacements were almost constant with depth. Note that, far-behind the face, the numerical model gave a sharp reduction of the vertical displacements near the crown. This reduction is associated with the 3D face effects. It is interesting to note that this behavior is different from what is expected (Mair et al., 1993), where vertical displacements above the crown increase with depth. This seems to be the result of the large volume strains due to the collapsible behavior of the residual porous soils, as pointed out by Ortigao and Macedo (1993). Further, tunnels excavated in the Brasilia residual porous clay present similar behavior, as reported by Ortigao et al. (1996) and Marques (2006).

Figure 4.10 plots the horizontal displacements near the tunnel springline, with depth. The location of the inclinometer is illustrated in Figure 4.2. The horizontal displacement at the surface was zero because the pavement constrained the horizontal ground movements. The horizontal displacements increased with depth until about 6m below the surface (1.6m above the crown), and then they decreased to zero at 10m depth. The horizontal displacements increased again, with a peak at the transition between the residual red porous clay and the residual variegated clay. Below the transition, the horizontal displacements, in the variegated residual clay, were small. The numerical results showed an increase of the horizontal displacements until 5m depth, similar to the field data. Below that, the calculated horizontal displacements decreased, similar to the field data, but they were larger than those measured. In the residual variegated clay, the numerical horizontal displacements were small, in agreement with the field data.

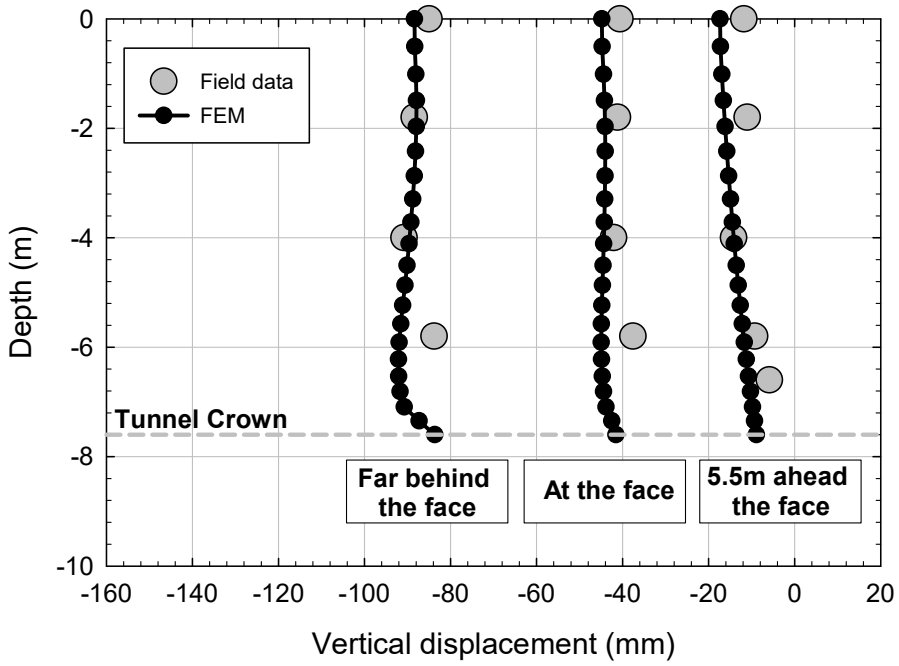

Figure 4.9 Vertical displacements with depth above the tunnel crown, at different distances from the face of the tunnel.

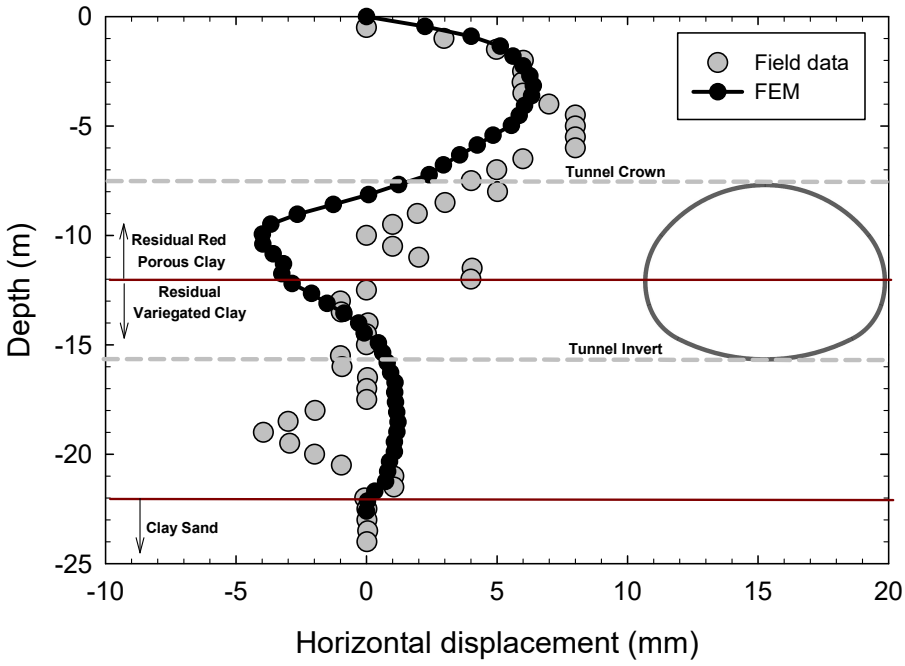

Figure 4.10 Horizontal displacements near the tunnel.

Figure 4.11 shows the support deformation with axial distance from the face of the tunnel. The deformations of the primary support (shotcrete with steel sets) were assessed through the vertical displacements at the crown and the relative horizontal displacements at the tunnel walls, as indicated in Figure 4.11. The deformations increased with the distance from the face until about 10m behind the face (at about 1 tunnel diameter), where the support deformations became constant. Large deformations were observed at the tunnel crown (up to 46mm), while at the invert, they were negligible. The displacements calculated by the numerical model at the two locations on the tunnel perimeter matched well the actual support deformations, as one can see in Figure 4.11. The vertical displacements at the crown were somewhat smaller than the actual measurements, and displayed a saw-tooth shape that oscillated between 43mm maximum to 33mm minimum. The average displacement was 38mm, 8mm lower than the actual displacements. The saw-tooth shape appears in numerical models of tunnels (Moller, 2002, Vitali et al., 2017) and is associated with the sharp stiffness contrast between the support and the ground, at the edge of the support near the face, and has a period that matches the length of the excavation/support rounds in the numerical model.

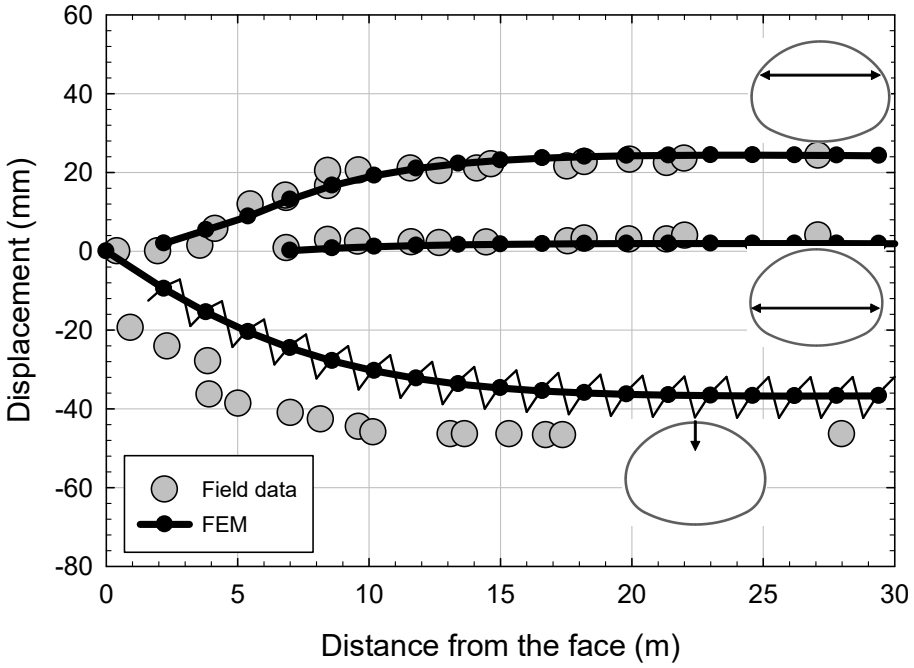

Figure 4.11 Displacements of the shotcrete.

The stress paths of points in the ground at the tunnel perimeter are shown in Figure 4.12. "q" is the maximum shear stress $((\sigma_1-\sigma_3)/2)$ and "p" is the mean stress $((\sigma_1+\sigma_3)/2)$. The stresses were taken at 0.25m from the tunnel perimeter to avoid the singularity at the (sharp) corner of the face of the tunnel (i.e. where the face intersects the perimeter). Three points were investigated: the crown; springline, and a point between the crown and the springline (crown/springline), as illustrated in Figure 4.12. All those points are in the residual red porous clay, where most of the ground deformations occur. Ahead of the face, both mean stress and maximum shear stress increase towards the excavation. At the unsupported span, unloading occurs (i.e. both shear and mean stresses decrease), and behind the support, the stresses increase until they are constant far-behind the face.

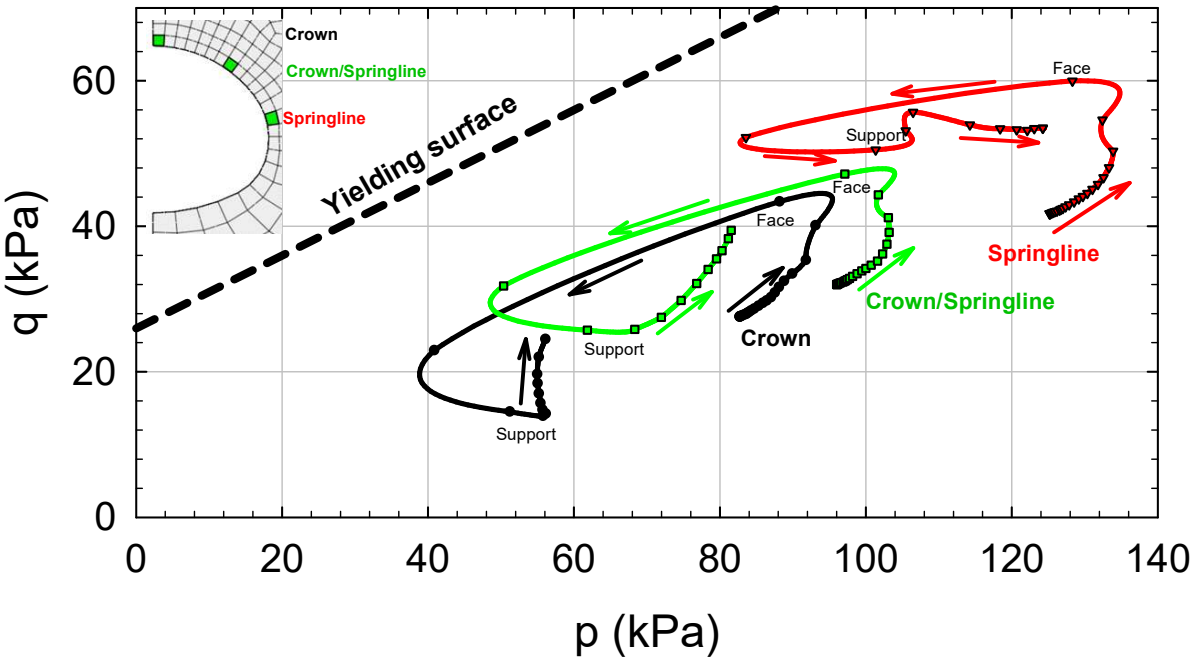

Figure 4.12 Stress paths at points around the tunnel. q= (σ_1- σ_3)/2 and p= (σ_1+ σ_3)/2.

The stresses of the ground at the tunnel crown are shown in Figure 4.13. The stresses were taken at the tunnel perimeter. The stresses started to change at about 10m ahead of the face. The radial stress (σ_{rr}) increased ahead of the face, decreased to zero at the unsupported span and increased behind the support until reaching a constant value. The tangential ($\sigma_{\theta\theta}$) and the axial stresses (σ_{zz}) slightly increased ahead of the face, decreased at the unsupported span and increased behind the support. The axial shear stress (τ_{rz}) was zero far-ahead of the tunnel face and increased as the distance from the face decreased. At the face, the axial shear stress was maximum and then decreased τ_{rz} until reaching a constant value far behind the face.

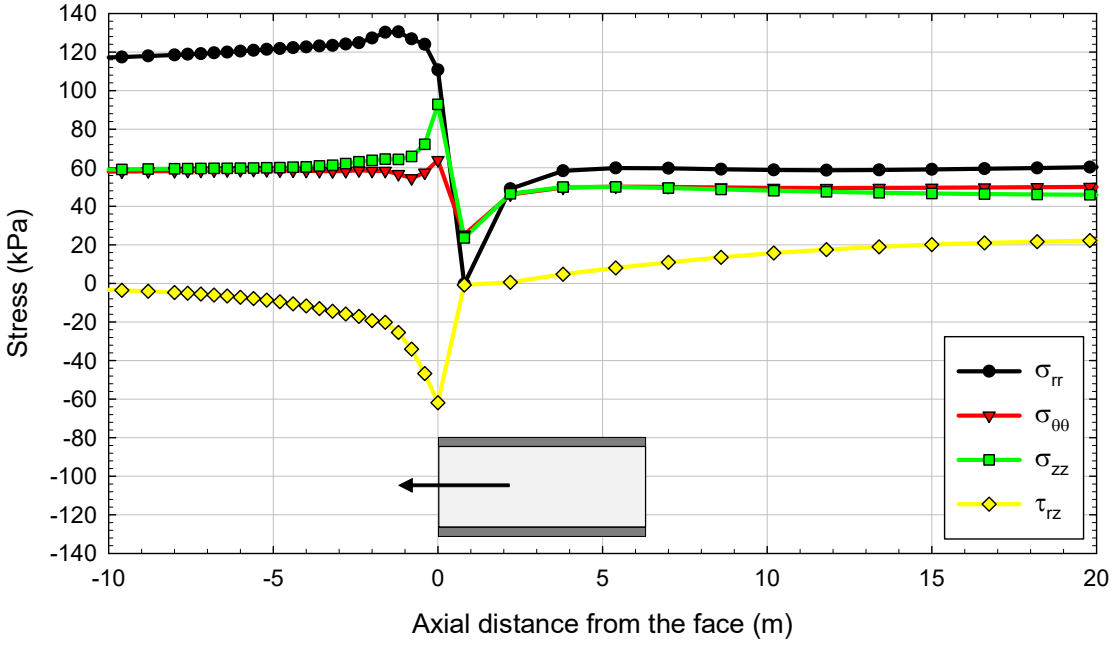

Figure 4.13 Stresses at the tunnel crown, with axial distance from the face.

4.5 Discussion

In this section, the influence of different construction schemes on ground deformations and face stability are evaluated, for the Paraiso tunnel. Different construction schemes were simulated numerically and compared with the observations and numerical results from the actual tunnel. Face stability was evaluated using the "Strength Reduction Factor" (Midas, 2019). This technique consists of the gradual reduction of the strength properties of the ground until failure occurs and is similar to limit equilibrium analysis. It is done numerically after the last phase of the 3D FEM analysis, considering that the residual red porous clay could be represented by an elastic perfectly plastic model with Coulomb failure criteria, with the strength properties already discussed (i.e., φ=30° and c=30kPa).

NATM tunnels usually keep benches at the face to reduce ground deformations and improve face stability. The Paraiso tunnel had two benches, as shown in Figure 4.1 and Figure 4.7. Also, a common decision to reduce ground deformations is to reduce the unsupported span and increase the stiffness of the support. Those measures are widely applied in practice. In addition, ground improvement techniques may be used to reduce ground deformations induced by tunneling, such as the ADECO-RS method (Lunardi, 2008), that relies on extensive ground treatment and

full-face excavation, or the pipe roof umbrella system (Volkmann and Schubert, 2007). These three strategies, namely: (1) partial face excavation and support using benches; (2) length of unsupported span and support stiffness; and (3) ground treatment through umbrella support are explored in the following Sections.

4.5.1 Partial face excavation

The excavation of the Paraiso tunnel included two benches, as shown in Figure 4.1 and Figure 4.7: the upper bench (#2 in Figure 4.1), and the lower bench (#3 in Figure 4.1) that supports the upper bench. The contribution of the benches to support the face of the tunnel and limit ground displacements was investigated through three different scenarios, in addition to the actual case already discussed (the base case; see Figure 4.7): excavation without the upper bench; without benches (i.e. full face excavation); and partial face or full-face excavation preventing axial displacements of the ground at the face of the tunnel, to investigate the effectiveness of the benches. Figure 4.14 illustrates the 3D FEM models used for the simulations; Figure 4.14a shows the tunnel without the upper bench, and Figure 4.14b the full-face excavation. Note that the full-face excavation allows an earlier closure of the primary support.

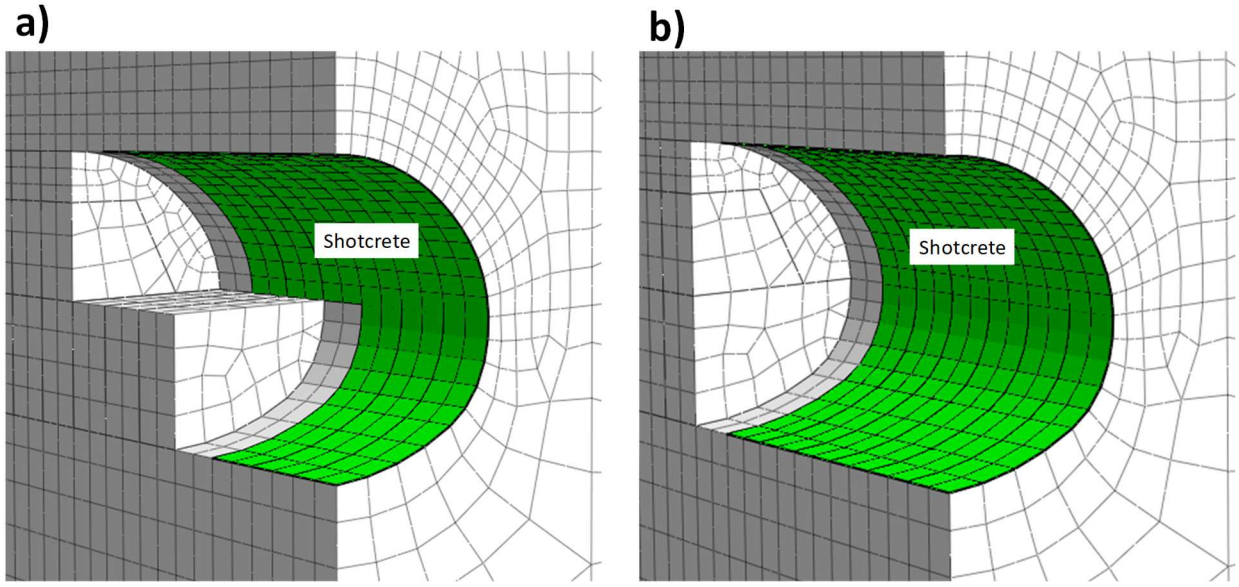

Figure 4.14 3D FEM models to investigate the influence of benches. (a) No upper bench; (b) full face excavation.

Figure 4.15 shows the surface settlements with the axial distance from the face (i.e. longitudinal settlement profile, Figure 4.15 a) and with the horizontal distance from the vertical tunnel axis (i.e. settlement trough, Figure 4.15 b). All scenarios present similar deformation patterns: no significant deformations far from the tunnel, and an increase as the distance to the tunnel decreases. What is interesting is to observe the effect of the face support on the settlements provided by all different scenarios. Two scenarios: the base case, no upper bench with face constrained, resulted in similar longitudinal and transverse deformations. The full-face scenario caused large longitudinal settlements ahead of the tunnel, similar to those obtained when the tunnel was excavated with no upper bench. The smallest deformations were obtained with the full-face scenario with constrained axial displacements. These observations highlight the importance of constraining the deformations at the face of the tunnel, and in particular those corresponding to the residual porous soil (encountered on the top half of the tunnel), rather than those of the residual variegated clay, which is a much stiffer deposit. It is interesting to note that the full-face scenario resulted in settlements similar to those of the no-upper-bench scenario ahead of the tunnel, and smaller behind the face of the tunnel. This is counterintuitive, as one would expect that the support provided by the lower bench, albeit on the stiffer soil, would result in smaller settlements. Indeed, this is the case, but the benefits of the support in the second scenario are counterbalanced by the benefits of providing an early closure of the support to the tunnel, which is the case with the full-face excavation scenario.

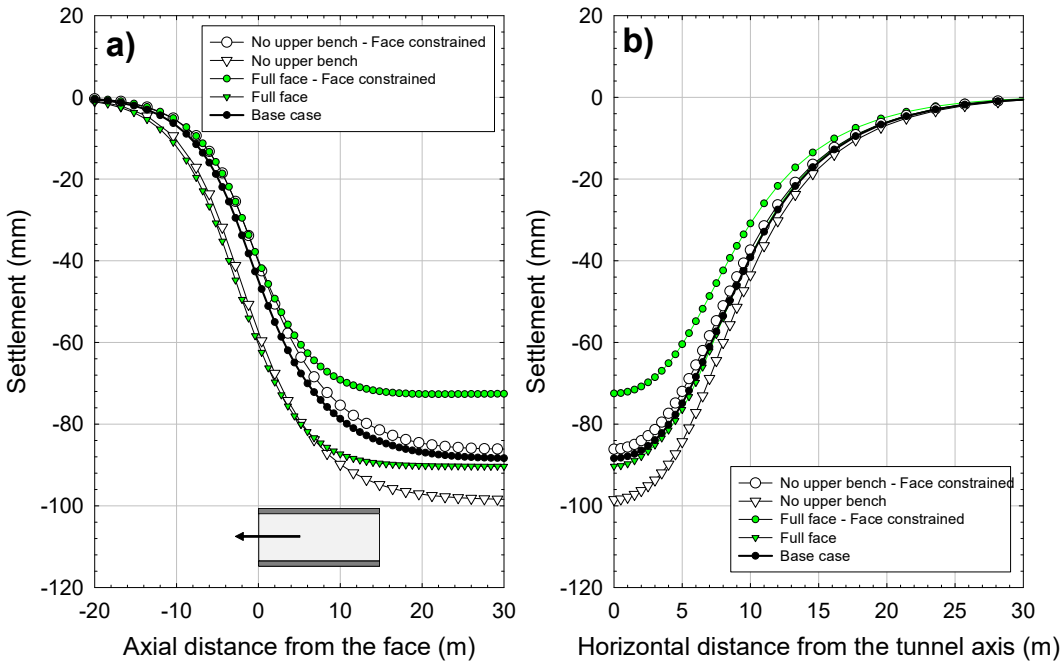

Figure 4.15 Surface settlements. (a) longitudinal vertical cross section; (b) settlement trough far behind the face of the tunnel.

Figure 4.16 shows the stress paths ahead of the face for the base case, no upper bench case and full-face case. The stresses were taken at the mid-height of the crown excavation. Far-ahead the face, the stress paths are the geostatic stresses. Closer to the tunnel, both mean and maximum shear stresses increase (i.e. loading stress path). Near the face, the mean stress decreases substantially while the maximum shear stress does so slightly. The stress paths for the cases without benches are similar. For the base case, the stress state at the face is farther from the yield surface than the stress state for the cases without bench. It is interesting to note that the mean stress at the face, for the base case, is substantially larger than the mean stresses for the cases without benches, while the maximum shear stresses are close to each other. Thus, one benefit of installing benches is that they increase the confinement stresses at the tunnel face, thus improving the face stability of the tunnel.

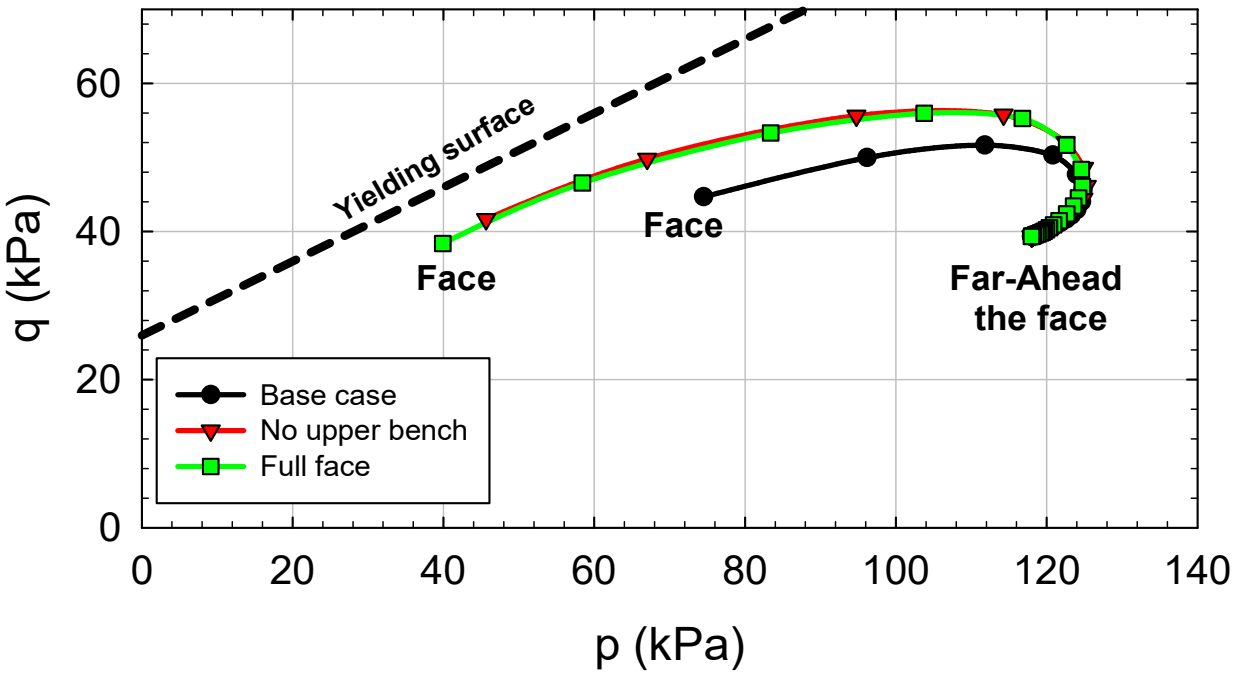

Figure 4.16 Stress paths ahead of the face for the base case, no upper bench case and full-face case.

Figure 4.17 shows the normalized settlement with the strength reduction factor (n) for the base case (Figure 4.7), no upper bench (Figure 4.14a) and full face (Figure 4.14b). The settlements are normalized with respect to the settlement when n=1 (i.e. no reduction in the strength properties). The settlement is taken at the point where the slip surface reaches the ground surface, as indicated in Figure 4.17. As one can see, the settlements slightly increase with the increase of the strength reduction factor; that is, as the strength of the soil decreases. The modest increase is the result of limited yielding of the ground. The numerical simulations showed that when the slip surface reached the ground surface, the rate of the settlements increased (i.e. settlements became more sensitive to the reduction of the strength). In each scenario, the settlement had a sharp increase (orders of magnitude) at a given strength reduction factor, which indicated failure. Thus, the strength reduction factor can be associated with the factor of safety against failure. The largest factor of safety was found for the base case, while the smallest for the full face excavation scenario. The results in Figure 4.17 show that the benches were efficient in increasing the face stability of the tunnel. Figure 4.18 shows the plastic deformations around the tunnel, at failure, for the base case (Figure 4.18a), for the no-upper-bench scenario (Figure 4.18b) and for the full-face

excavation scenario (Figure 4.18c). The figures illustrate the failure mechanism at the face of the tunnel. It is interesting to note that the slip surface for the base case extended to the invert of the tunnel, while for the no upper bench scenario, failure was concentrated at the tunnel crown, and for the full-face excavation scenario, the slip surface included the entire face. The effect of the benches was to send the critical failure surface deeper into the ground, inside the stiffer lower soil layer, thus increasing the face stability of the tunnel.

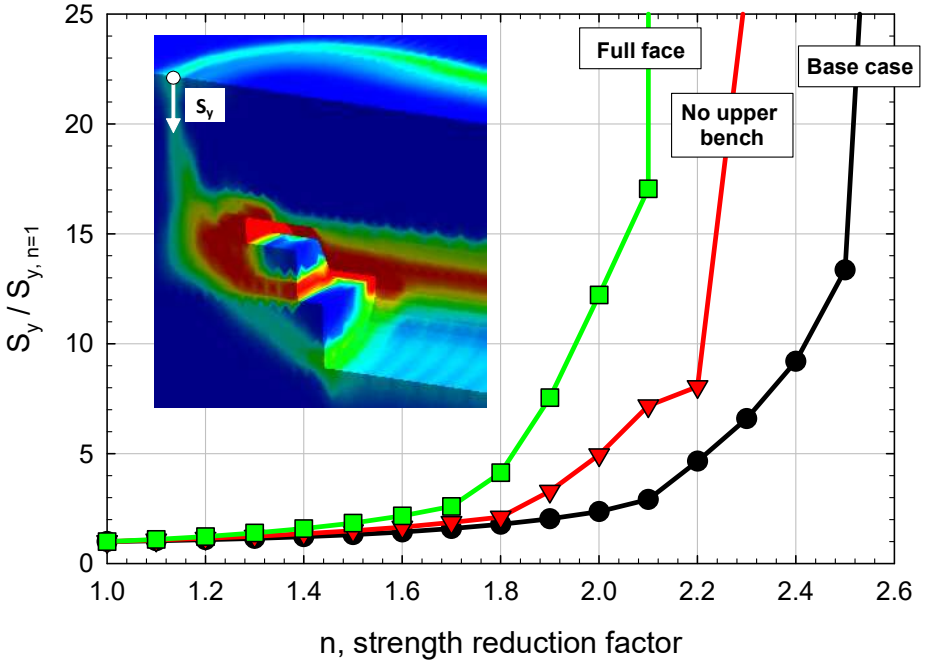

Figure 4.17 Normalized settlement (S_y) with the strength reduction factor (n) for the base case, no upper bench case, and full face excavation case. Settlements are normalized with respect to the case when n=1 ($S_{y,n=1}$).

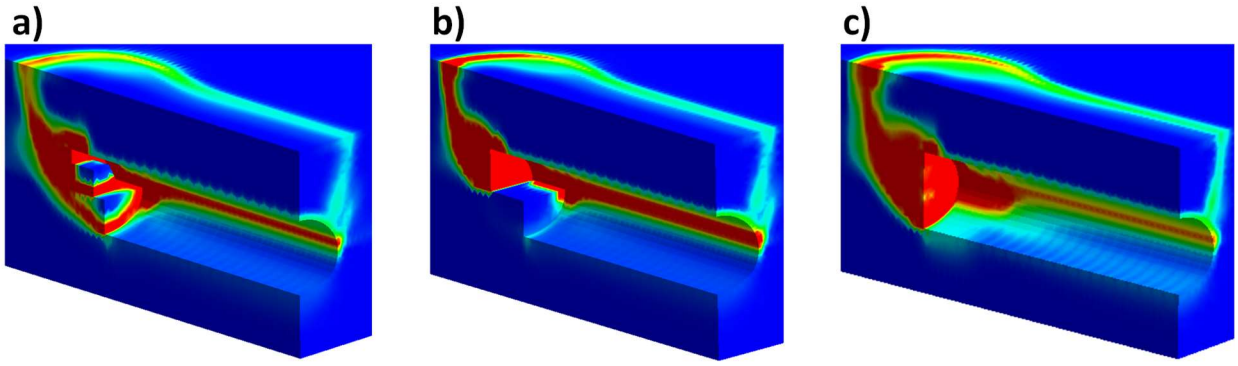

Figure 4.18 Equivalent plastic deformation around the tunnel, at failure. (a) base case (b) no upper bench; (c) full face excavation. The red color represents equivalent plastic deformations equal or larger than 2%. The blue color represents no plastic deformation. Colors between red and blue represent equivalent plastic deformations between zero and 2%.

4.6 Unsupported span and liner stiffness

The importance of the unsupported span length and of the stiffness of the primary lining support on ground deformations was investigated through 3D FEM models of the Paraiso tunnel. The following parameters were considered: unsupported span length (L) of 0.8 m and 1.6 m (these are common in NATM tunnels with 10m diameter in soft ground; 1.6 m is the base case), and primary support thickness (t) 0.2 m to 0.6 m; additional cases with undeformable support with L=0.8m and L=1.6m were also included for comparison purposes.

The surface settlements for all cases are presented in Figure 4.19. Figure 4.19a plots the settlements along a vertical axial cross section of the tunnel, and Figure 4.19b plots the settlement trough through a vertical cross section located far behind the face of the tunnel. As one can see, the surface settlements decrease as the support stiffness increases and as the unsupported span length decreases. For the base case (i.e. L=1.6m and t=0.2m), the settlement far-behind the face is 89mm above the crown. If the lining thickness increased to 0.4m, the settlement is 73mm, 18% smaller than the base case. For t = 0.4m and L = 0.8m, the surface settlements are further reduced to 58mm far-behind the face (35% smaller than the base case). Thus, the numerical results showed, as expected, that the ground deformations can be significantly reduced by simply installing a thicker liner closer to the face. Note that the settlements would be heavily reduced if an undeformable liner was installed, which highlights the importance of the liner stiffness in the results. For L = 0.8m and undeformable liner, the surface settlement decreased to 30mm (67% smaller than the base case). These findings are in contrast to those from Azevedo et al. (2002), who found a negligible influence of the tunnel support stiffness on ground deformations. Given that those authors used a 2D FEM for the calculations, the difference in the results illustrates the importance of the longitudinal arching of the support, as well as the loading path in the soil, which is not captured by 2D analyses.

The influence of the liner stiffness on the ground stresses is illustrated in Figure 4.20. The figure is a longitudinal plot of the ground stresses at the tunnel crown with the distance from the face. Two cases are investigated: the base case (i.e. L=1.6m and t=0.2m) and the case with L= 0.8 m and undeformable liner. Those were the cases with maximum and minimum ground deformations; thus, the other cases are in between. The figure shows that, far from the face, the stresses are the in-situ stresses. Close to the face of the tunnel, the radial stresses decreased, while the shear stresses increased. Both radial and axial shear stresses were zero along the unsupported

span length. Far-behind the face, the radial stresses increased and were much larger for the case of undeformable liner than for the base case. This is expected because a stiffer liner closer to the face attracts more load from the ground through 3D face effects (i.e. longitudinal arching), which reliefs the stresses in the ground and reduces ground deformations. Interestingly, no axial shear stresses occurred behind the face of the tunnel for the case of undeformable liner. Since the liner was undeformable, no axial deformation occurred at the tunnel perimeter.

Figure 4.21 shows the normalized settlement with the strength reduction factor for the base case and for the case with L=0.8m and undeformable liner. Those two cases show the influence of the unsupported span and of the support stiffness on face stability. As one can see, the collapse of the tunnel face required a further reduction of the strength of the ground when the support was placed closer to the face (note that failure of the support was neglected in all cases). The results show that reducing the unsupported span length and increasing the liner stiffness improves the safety of the tunnel face against failure. The reason for this is that a stiff liner closer to the face of the tunnel attracts more load and so there is a transfer of load from the ground to the liner. This is done, in part, through longitudinal arching (i.e. 3D face effects), which reliefs the stresses in the ground ahead of the face.

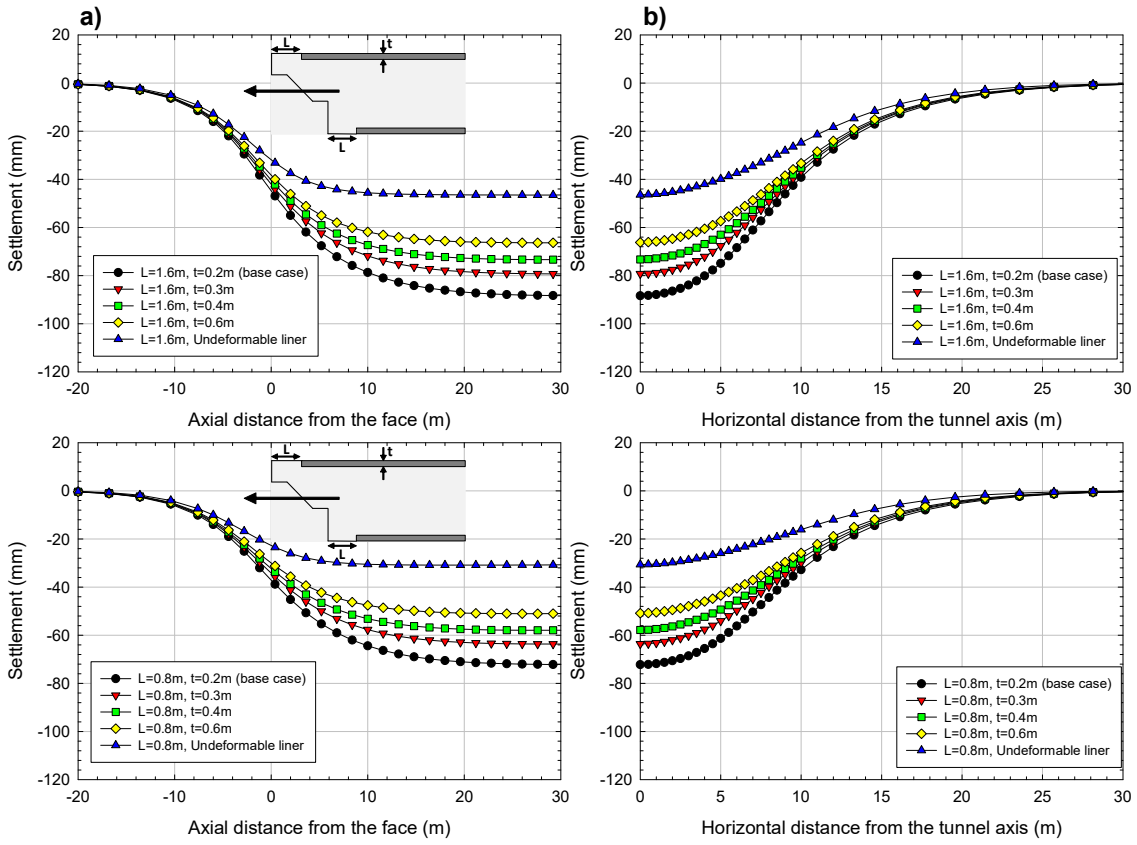

Figure 4.19 Surface settlements with axial distance from the tunnel face: (a) longitudinal vertical cross section; and (b) settlement trough far behind the face of the tunnel. Unsupported span length (L) 0.8 m and 1.6 m, lining thickness (t) 0.2 m to 0.6 m, and undeformable liner.

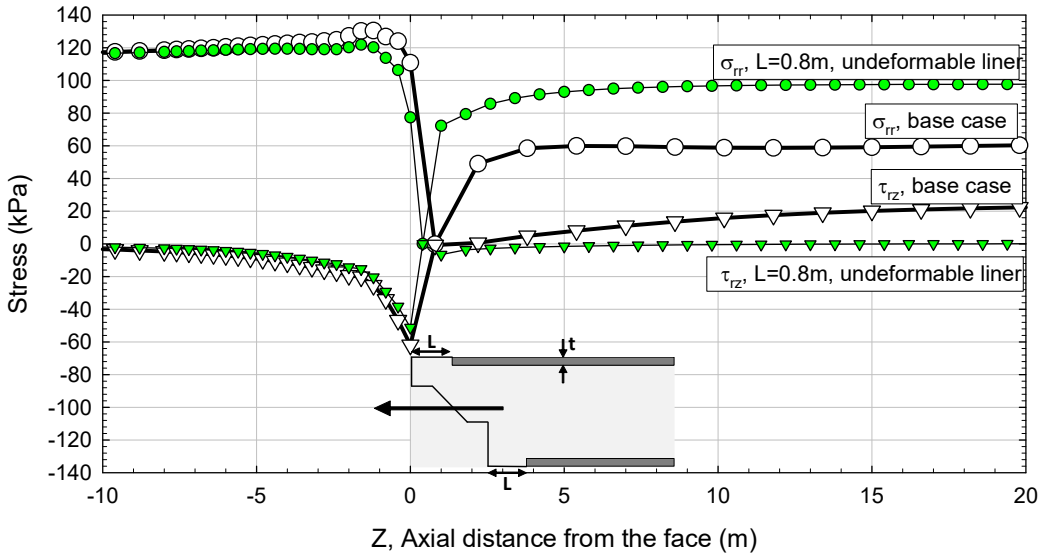

Figure 4.20 Stresses at a point of the ground, located at the crown, with axial distance from the face of the tunnel. Base case and for undeformable liner with unsupported span of 0.8 m.

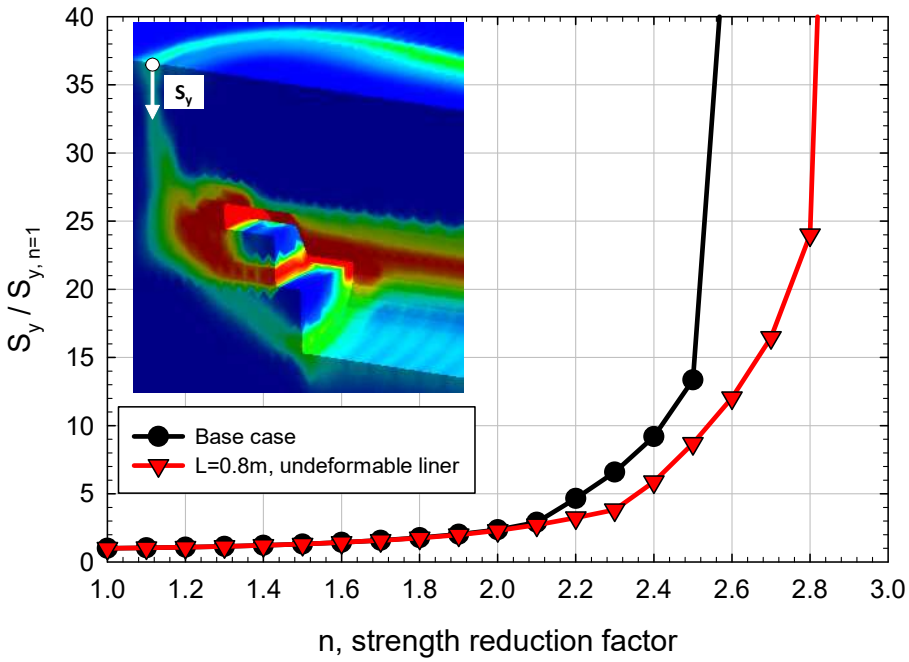

Figure 4.21 Normalized settlement (S_y), respect to the case n=1 ($S_{y,n=1}$), with the strength reduction factor (n), for the base case (L=1.6m and t=0.2m), and L=0.8 with underformable liner.

4.6.1 Reinforcement with pipe roof umbrella system

The pipe roof umbrella system (Volkmann and Schubert, 2007) is a common method to reduce ground deformations due to tunneling. The umbrella may consist of horizontal jet-grouting columns reinforced with steel pipes placed along the tunnel perimeter. The idea is to create an umbrella for the tunnel excavation, so the unsupported span (L) is protected. The efficiency of this technique in reducing ground deformations is assessed through 3D FEM models of the Paraiso tunnel. Figure 4.22 shows the excavation sequence with the umbrella. The umbrella was 0.5m thick, reached 8m ahead of the face of the tunnel, and was placed around the crown of the tunnel, where most of the ground deformation occurred. An elastic perfectly plastic model with Tresca failure was selected to represent the umbrella. The umbrella was modeled using hexahedron elements with properties equivalent to those of horizontal jet-grouting columns reinforced with steel pipes; namely, Young's modulus (E) 1GPa, Poisson's ratio (v) 0.2, and cohesion (c) 700kPa. Those properties were estimated based on a continuous reinforcement along the perimeter of the tunnel using steel tubes with outer diameter 113mm and thickness 6.3mm, grouted. The full-face excavation with umbrella (Figure 4.22a) and the base case with umbrella (Figure 4.22b) were used

for the analyses. Note that the use of umbrella and benches may not be realistic because of constructability issues, but it was included for comparison purposes with the base case.

Figure 4.23 shows the surface settlements with the axial distance from the face (i.e. longitudinal settlement profile, Figure 4.23a) and with the horizontal distance from the vertical tunnel axis (settlement trough, Figure 4.23b) for the base case and for the cases with umbrella shown in Figure 4.22. As one can see, the surface settlements were substantially reduced when the umbrella was included, with maximum surface settlement about 29% of that calculated in the base case. The settlements started to increase at about 20m (two tunnel diameters) ahead of the face. Note that the settlements with full-face excavation with umbrella started earlier than for the other two cases, were larger than those with the base case with umbrella, and yet they ended up far behind the face with a magnitude similar to those of the base case with umbrella. This seems counterintuitive as the base case provides support to the face with the benches, which does not occur for the full-face case. As discussed before, the reason for this behavior is that the closure of the liner occurs earlier with the full-face case than with the base case. The settlement trough far-behind the face for the base case with umbrella and for the full face with umbrella is almost the same.

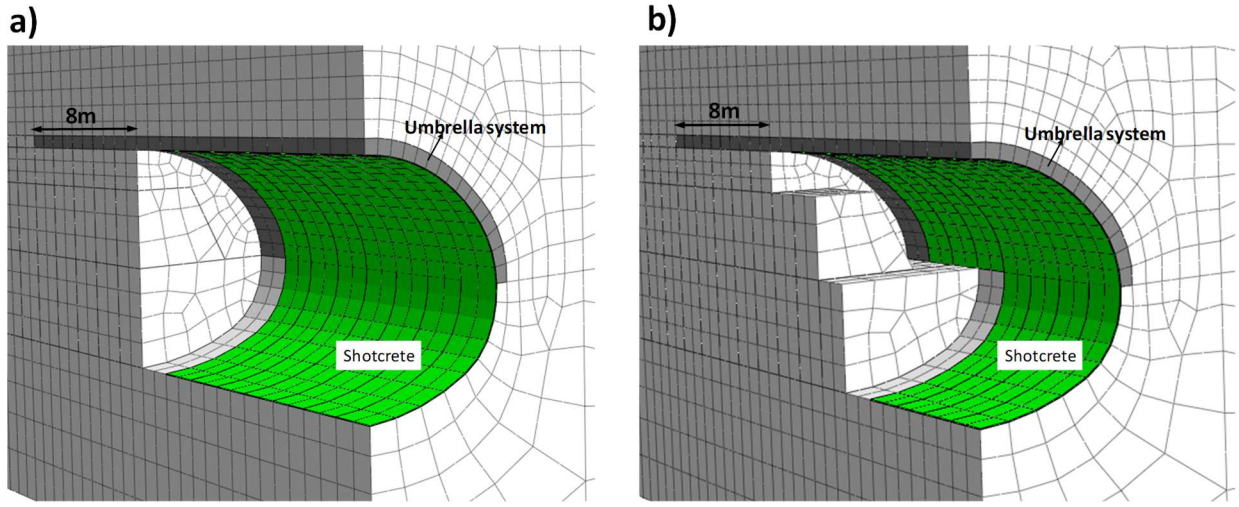

Figure 4.22 Construction sequence with umbrella. (a) full face excavation with umbrella; (b) base case with umbrella.

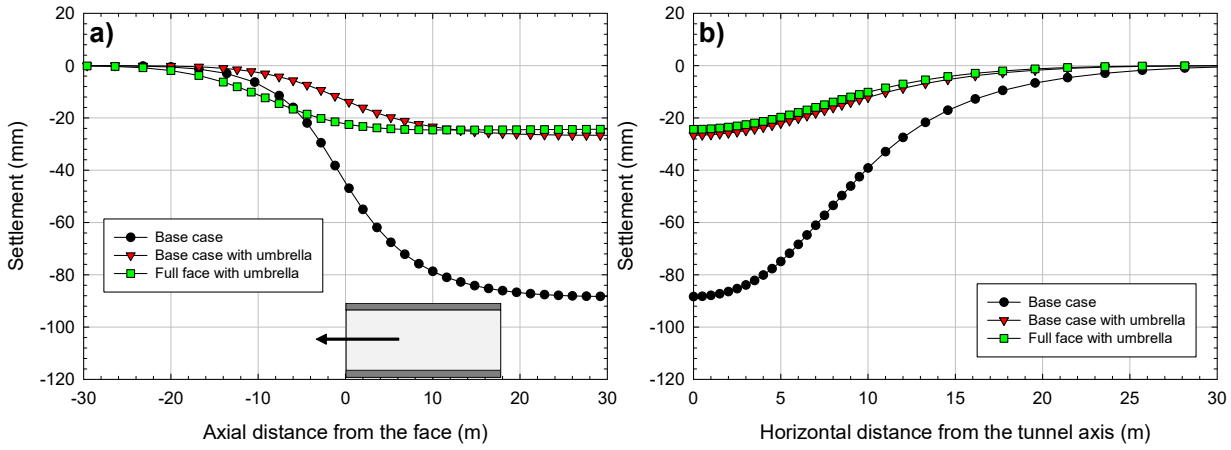

Figure 4.23 Surface settlements for the base case, the base case with umbrella and for full face with umbrella, (a) with axial distance from the face, and (b) with horizontal distance from the vertical tunnel axis.

The normalized settlements, as a function of the strength reduction factor (n), are shown in Figure 4.24, for the base case, the base case with umbrella, and the full face with umbrella. As before, the settlement was taken at the point where the failure slip first reached the surface, as indicated in the figure. When the umbrella was included in the base case, a larger reduction of the strength properties was required for failure (n at failure for the base case with the umbrella was around 3.2, and for the base case, 2.5). For the case of full face excavation with umbrella, the failure occurred when n=2.5, which is larger than the strength reduction required for failure of the full-face excavation case (n=2.1, Figure 4.17). For the base case, there are two well-identified regimes in the figure: the first, at n=2.1, when the failure slip reaches the ground surface; and the second, at n=2.5, when the tunnel collapses. Those points are not clearly identified on the other cases. This suggests that the umbrella provides ductility to the failure mechanism. Figure 4.25 shows the plastic deformations around the tunnel, at failure, for all the cases. It is interesting to note that failure, and so large plastic deformations, are confined in a volume of ground ahead of the face of the tunnel.

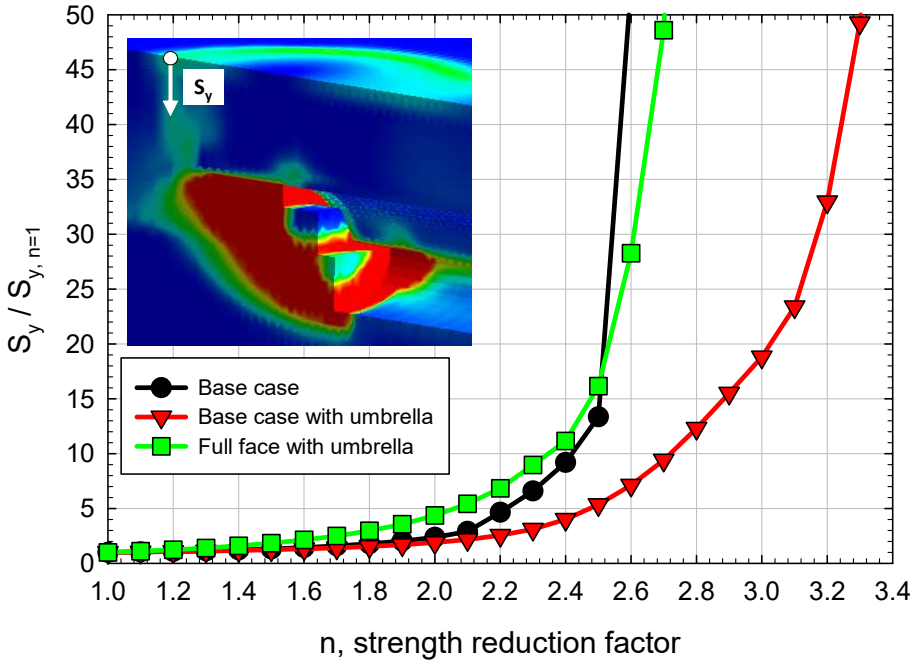

Figure 4.24 Normalized settlement (S_y) with respect to n=1 ($S_{y,n=1}$), with the strength reduction factor (n), for the base case , the base case with umbrella and the full face with umbrella.

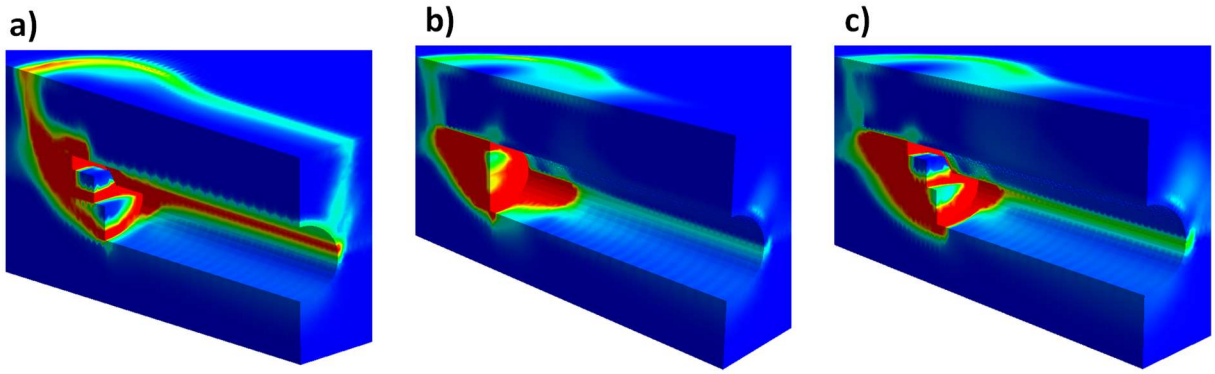

Figure 4.25 Plastic deformation around the tunnel at failure. (a) base case, n=2.5; (b) Full face excavation with umbrella, n=2.5; (c) base case with umbrella, n=3.2. The red color represents equivalent plastic deformations equal or larger than 2%. The blue color represents no plastic deformation. Colors between red and blue represent equivalent plastic deformations between zero and 2%.

The numerical simulations show that the use of an umbrella is highly effective in reducing ground deformations and increasing safety against failure. It is implicit, in the numerical analyses, that the umbrella is perfectly executed, so no ground deformations are induced due to the drilling and grouting operations. It is important to mention that large settlements have been reported during

the execution of the umbrella in some tunnels. Farrell et al. (2014) reported large settlements caused when using an umbrella near sensitive buildings. The authors showed that approximately 25mm occurred due to the execution of the horizontal jet-grouting columns and an additional 10mm, due to the tunnel excavation. In other words, 70% of the surface settlements occurred during the execution of the horizontal jet grouting columns. Thus, the efficiency of the umbrella is highly dependent on the quality of the execution.

4.7 Conclusion

The impact of different construction strategies of NATM tunnels on ground deformations and face stability are assessed in this paper. The Paraiso tunnel, a metro tunnel in Sao Paulo, Brazil, was used for the analysis. The tunnel was excavated in a residual porous soil and induced large surface settlements. A 3D FEM numerical model with an advanced soil constitutive model, calibrated with the properties of the soil encountered at the site, was used to simulate the tunnel construction and predict ground deformations. The results from the model were in close agreement with the field data. The face stability of the tunnel was assessed using the strength reduction method.

The Paraiso tunnel was built with partial-face excavation with two benches to improve face stability. The influence of those benches was investigated, as well as the impact of changing the support scheme, either by reducing the unsupported span or increasing the stiffness of the liner. In addition, the benefits of installing an umbrella to the face of the tunnel were also analyzed. The results of the simulations showed that the benches reduced the ground deformations ahead of the face. With no benches, i.e. with full-face excavation, the settlements ahead the face increased by 36%, and the factor of safety of the face of the tunnel decreased by about 20%. Interestingly, the settlement through far-behind the face for the base case (actual tunnel construction process) and for the case with full face excavation were very similar, although the longitudinal settlement profiles were rather different. For the full face excavation case, the settlements ahead the face were larger than the base case, but behind the face, the settlements for the full face case were smaller than the base case. It occurred because the entire tunnel liner was completed near the face for the excavation with full face while, for the base case, the tunnel liner could not be closed near the face because of the benches. It was observed that the base case collapsed with a strength reduction factor (n) of 2.5 and the full-face case, with n=2.1.

The numerical results also showed that, as expected, a stiffer support closer to the face, reduced the ground deformations induced by the tunnel. The Paraiso tunnel was excavated with an unsupported span length of 1.6m and supported with shotcrete with thickness of 0.2m. By reducing the unsupported span length to 0.8m, the surface settlement above the crown far-behind the face decreased by 19%. For an unsupported span length of 0.8m and support thickness of 0.4m, the surface settlement far-behind the face above the crown was 35% smaller than the settlement of the base case. When an undeformable liner was considered, and installed 0.8m behind the face, the surface settlements were 67% smaller than those of the base case. In addition, the installation of a stiffer support close to the tunnel face improved face stability. The strength reduction required for failure of the tunnel with an unsupported span length of 0.8m was 2.8, while for the base case, with 1.6m unsupported span, was 2.5. Note that adopting a thicker shotcrete liner would increase substantially the cost of the project, while reducing the unsupported span length would be less costly. The drawback of reducing the unsupported span length is to slow down the tunnel advance.

The pipe roof umbrella system considered in the numerical analysis consisted of jet-grouted columns reinforced with steel pipes, along the tunnel perimeter. The numerical results showed that the umbrella was highly effective in reducing ground deformations and in improving the face stability. The surface settlements above the crown far-behind the face was 71% smaller than the base case. It was also observed that, at failure, the failure surface developed ahead of the umbrella; thus, a larger mass of soil was mobilized before failure, resulting in a factor of safety larger than the base case. Note that the numerical results assumed no ground deformations due to the execution of the umbrella (cases where large settlements due to the execution of the umbrella have been reported). Thus, the pipe roof umbrella system may not be a good option if an excellent execution quality is not ensured.

The ground deformations caused by the Paraiso tunnel were large and could potentially damage nearby structures. Based on the numerical analyses conducted, the settlements could have been reduced if a shorter excavation step and a stiffer support were adopted. Thus, for future NATM tunnels in porous soils near sensitive structures, a small excavation step and a thick primary support should be considered. It would also be advantageous to use early strength shotcrete that can reach large stiffness soon after installation, given that the numerical results revealed that the stiffness of the tunnel support was effective in reducing ground deformations. The numerical results showed that the earlier closure of the liner ring was highly effective in reducing ground

deformations. They also showed that the lower bench had negligible influence on the ground deformations, since it was located in a very competent soil layer. Thus, the construction process could be optimized by reducing the length of the lower bench, or even eliminating it, so the lining could be closed earlier. The numerical results showed that the upper bench was highly effective in reducing the ground deformations ahead of the face and in improving the face stability. Optimization of the upper bench length would be desirable, so that the primary support could be closed as early as possible. Although the numerical results indicated that an umbrella system would be highly effective to limit ground deformations, the drilling and grouting operations could cause large ground deformations, especially in unstable soils (i.e. residual porous clays). Thus, the umbrella system should be used only when ground deformations due to its execution are negligible.

Acknowledgments

The research is being partially supported by the research funding agency of the Brazilian government CNPq ("Conselho Nacional de Desenvolvimento Cientifico"). The authors acknowledge the support from CNPq and from Midas company, which kindly provided the license of Midas GTX NX software, used in the present work. We are thankful to Professor Alexandre Parreira, who kindly sent us a digital copy of his Ph.D. dissertation, from where we extracted essential information for this research work.

4.8 References

Almeida e Sousa J., Negro A., Matos Fernandes M., Cardoso, A.S., 2001. Three-Dimensional Nonlinear Analyses of a Metro Tunnel in São Paulo Porous Clay, Brazil. J. Geotech. Geoenviron. Eng., 137(4): 376-384.

Azevedo, R. F., Parreira, A., and Zornberg, J. G., 2002. Numerical analysis of a tunnel in residual soils. J. Geotech. Geoenviron. Eng., 128(3): 227–236.

Broere, W., 2016. Urban underground space: Solving the problems of today's cities. Tunnelling and Underground Space Technology, 55: 245–248

Cantieni, L., Anagnostou, G., 2009. The effect of the stress path on squeezing behavior in tunneling. Rock Mechanics and Rock Engineering, 42(2), 289−318.

Celestino, T. B.; Ruiz, A. P. T., 1998. Shape of settlement throughs due to tunneling through different types of soft ground. *Felsbau*, 16: 118-121.

Celestino, T. B.; Gomes, R. A. M.; Bortuluci, A. A., 2000. Errors in ground distortions due to settlement trough adjustment. *Tunnelling and Underground Space Technology*, 15(1): 97-100.

Deane, A. P., Bassett, R.H., 1995. The Heathrow Express trial tunnel. Proc. Instn. Civ. Engrs. Geotech Engrs, 113:144-156

Eberhardt, E., 2001. Numerical modelling of three-dimension stress rotation ahead of an advancing tunnel face. International Journal of Rock Mechanics and Mining Sciences, 38(4), 499–518.

Farrell R, Mair R, Sciottic A, Pigorinic A, 2014. Building response to tunneling. Soils and Foundation; 54(3):269–279.

Farias MM, Moraes Junior AH, Assis AP, 2004. Displacement control in tunnels excavated by the NATM: 3-D numerical simulations. Tunnelling and Underground Space Technology, 19:283–293.

Golser, J, 2001. Behavior of early-age shotcrete. In: Proc. Of Shotcrete for Underground Support VIII: 83-93.

Health and Safety Executive, 1996. *Safety of New Austrian Tunneling Method (NATM) Tunnels - A review of sprayed concrete lined tunnels with particular reference to London clay*. Technical report. ISBN 978 0 7176 1068

Leroueil, S., Vaughan, P. R., 1990. The general and congruent effects of structure in natural soils and weak rocks. Geotechnique, 40(3): 467-488.

Lunardi P., 2008. Design and construction of tunnels - Analysis of controlled deformation in rocks and soils(ADECO-RS).Springer-Verlag Berlin Heidelberg.

Mair, R. J., Taylor, R. N., and Bracegirdle, A., 1993. Subsurface settlement profiles above tunnels in clays. Géotechnique, 43(2), 315–320.

Massad F, Sousa Pinto C de, Nader JJ, 1992. Strength and Deformability. Brazilian Society of Soil Mechanics Conference on Soils of the Sao Paulo city: 141-179, (in Portuguese).

MIDAS Information Technology Co., 2019. Midas GTS NX manual.

Marques, F.E.R., 2006. Behavior of shallow tunnels in porous soils – the Brazilia metro case (in Portuguese). Ph.D. dissertation. University of Coimbra.

Moller, S., 2006. Tunnel induced settlements and structural forces in linings. PhD dissertation. Institute of Geotechnical Engineering, Universitat of Stuttgart.

New B. M., Bowers K. H., 1994. Ground movement model validation at the Heathrow Express trial tunnel. *Tunneling'94*: 301-329

Ng, C. W., Lee, G. T., 2005. Three-dimensional ground settlements and stress-transfer mechanisms due to open-face tunnelling. Canadian Geotechnical Journal. 42(4): 1015−1029.

Peck, R. B., 1969. Deep excavation and tunnelling in soft ground. in Proc. *7th Int. Conf. on Soil Mechanics and Foundation Engineering*, Mexico City, State of the Art Volume: 225-290.

Ortigao J.A.R., Macedo P., 1993. Large settlements due to tunneling in porous clay. In: Proceedings of International Conference on Underground Transportation Infrastructure, AFTES, 119, Sept-Oct 93: 245-250.

Ortigao J.A.R., Cunha R.P., Alves L.S., 1995. In-situ tests in Brasília porous clay. Canadian Geotechnical Journal, 33: 189-198.

Ortigao JAR, Kochen R, Farias MM, Assis AP, 1996. Tunnelling in Brasília porous clay. Canadian Geotechnical Journal, 33(4): 565-573.

Parreira, A. B., 1991. Analysis of shallow tunnels in soil. The NATM Paraíso Tunnel at Paulista Avenue in São Paulo City. Ph.D. thesis, Catholic Univ. of Rio de Janeiro, Rio de Janeiro, Brazil (in Portuguese).

Panet, M., Guenot, A., 1982. Analysis of convergence behind the face of a tunnel. In: Proc., Tunnelling 82, Institute of Mining and Metallurgy, London, 197–204.

Rabcewicz L.V., 1964/1965. The new Austrian tunnelling method. Water Power, Part 1: November 1964, 571-515, Part 2: January 1965, 19-24.

Schanz T, Vermeer PA, Bonnier PG, 1999. The hardening soil model: Formulation and verification. In book: Beyond 2000 in Computational Geotechnics, pp.281-296.

Schmidt B., 1969. Settlements and ground movements associated with tunneling in soil, Ph.D. Dissertation, University of Illinois.

Vaughan P.R., Kwan C.W., 1984. Weathering, structure and in situ stress in residual soils. Geotechnique 34(1): 43-59.

Vitali, O. P. M.; Celestino, Bobet, A., 2019. Buoyancy effect on shallow tunnels. International Journal of Rock Mechanics and Mining Sciences. 114(2), 1–6. https://doi.org/10.1016/j.ijrmms.2018.12.012

Vitali, O. P. M.; Celestino, Bobet, A., 2017. 3D finite element modelling optimization for deep tunnels with material nonlinearity. Underground Space, 3(2), 125–139. https://doi.org/10.1016/j.undsp.2017.11.002

Volkmann, G.M., W. Schubert, 2007. Geotechnical Model for Pipe Roof Supports in Tunneling. In Proc. of the 33rd ITA-AITES World Tunneling Congress: 755-760

5. ANALYTICAL SOLUTION FOR TUNNELS NOT ALIGNED WITH GEOSTATIC PRINCIPAL STRESS DIRECTIONS

VITALI, O. P. M.; CELESTINO, & BOBET, A. (2018). Analytical solution for tunnels not aligned with geostatic principal stress directions. *Tunnelling and Underground Space Technology*, 82: 394–405. https://doi.org/10.1016/j.tust.2018.08.046

Abstract

It is well-known that rock masses may present marked stress anisotropy. However, most of the tunnel analyses (numerical and analytical) assume the tunnel axis aligned with one of the principal stress directions. When this is not the case, axial shear stresses appear, which then are neglected, as it is done in all analytical solutions available for tunnel analysis. Existing solutions may consider advanced nonlinear ground behavior (i.e. elastic-brittle-plastic with e.g. Hoek and Brown failure criteria), linear-elastic ground with transversely anisotropic properties, seismic loading, groundwater and support, etc., but all consider that the axis of the tunnel aligns with one of the principal far-field stresses. This is also what is generally assumed when conducting more sophisticated, three dimensional numerical analyses. In this paper, an analytical solution to calculate the stresses and displacements induced by far-field axial shear stresses is presented. Solutions for supported and unsupported tunnels are provided. The proposed analytical solution can be combined with the classical Kirsch and Einstein-Schwartz solutions to determine the complete stress and displacement fields around the tunnel. Further, the effects of stress anisotropy are discussed.

5.1 Introduction

Analytical solutions have been extensively developed for tunnels. Some of them are regularly used in practice, such as the Kirsch and Einstein-Schwartz solutions (Kirsch, 1898; Einstein & Schwartz, 1979). Despite improvements on numerical modeling, analytical solutions are still used because they allow fast and robust tunnel analysis. For instance, Ledesma & Alonso, 2017, obtained accurate ground deformation predictions caused by tunnels under the World Heritage Structures “Sagrada Familia Basilica” and “Casa Mila”, in Barcelona, Spain, using analytical solutions. For reliability problems, which may require a large number of calculations,

analytical solutions are widely used because numerical methods may be unmanageable or even unfeasible. Analytical solutions are attractive because they incorporate the most significant variables in a closed-form formulation and are benchmarks to sophisticated numerical analysis and code validation. However, the mathematical treatment of analytical solutions may be cumbersome and simplifications must be assumed. The analytical solutions for tunnels normally rely on 2D plane strain conditions and circular tunnel cross-sections.

New analytical solutions for tunnels are being developed. For example, the solutions proposed by Kirsch and Einstein Schwartz were expanded by Bobet (2003) to incorporate the effects of groundwater flow and seismic loading for lined and unlined deep tunnels in linear elastic ground. Further expansions, to include transversely anisotropic elastic ground, were carried out by Hefny & Lo (1999), Bobet (2011), Zhang & Sun, (2011), Bobet & Yu (2016), Bobet (2016a) and Bobet (2016b). Analytical solutions for viscoelastic ground are also available. Those solutions were proposed by Wang et al. (2013), Wang, et al. (2015) and Wang et al. (2017) for deep tunnels with elliptical cross-section and also for circular twin tunnels. The analytical solutions mentioned so far are applicable to deep tunnels. Analytical solutions for shallow tunnels in linear-elastic ground were presented by Bobet (2001), Park, (2005), Pinto & Whittle, (2014), Strack & Verruijt (2002), Verruijt & Booker (1996) and Verruijt (1997). The applicability of analytical solutions for shallow tunnels was assessed by Chou & Bobet (2002) and Pinto et al. (2014). Both papers found good agreement between field data and predictions using analytical methods.

The closed-form solutions found so far assume elasticity and, thus, are valid only if minor or no yielding is present around the opening. Including plasticity in the solutions increases the complexity of the problem, and results are currently limited to unsupported tunnels, static loading, dry ground and isotropic far-field stresses. Salençon (1969) developed an analytical solution for a loaded hollow plate in elastic perfectly plastic ground with Mohr-Coulomb failure. Such solution applies to deep tunnels. The solution considers associated and non-associated flow rules. Other solutions, for other failure criteria are currently available, for example the solution from Carranza-Torres (2004) with the Hoek and Brown failure criteria. Sharan (2003, 2005) incorporated elastic-brittle-plastic behavior with Hoek and Brown failure in an analytical solution. Massina & Sakellariou (2009) found an analytical solution for shallow tunnels considering elastic perfectly plastic material with Coulomb failure.

In all the formulations discussed, the tunnel axis is aligned with one of the principal directions because all solutions assume plane strain conditions on any cross-section perpendicular to the axis of the tunnel. Therefore, the far-field axial shear stress that appears due to the misalignment of the tunnel with the horizontal principal stresses is neglected.

It is well-known that rock masses may have pronounced anisotropic far-field stresses (Brady & Brown, 2006; Jaeger & Cook, 2007; McGarr & Gay, 1978). Under these conditions, the plane strain assumption may be incorrect and may lead to erroneous conclusions (Hoek, 2008). The importance of the orientation of the underground excavation with respect to the far-field stress tensor is well-recognized in choosing the orientation of caverns and their shape. It is generally recommended to orient them parallel to the major principal stress direction, and with a shape such that stress concentrations are minimized (Goodman, 1989). However, for most applications in Civil engineering, the tunnel alignment is pre-determined and must be designed regardless of its orientation with respect to the far-field stress tensor.

McGarr & Gay (1978) determined the complete geostatic stress tensor from 77 different sites. From their compilation, it is possible to estimate the level of stress anisotropy expected in rock masses. Figure 5.1 shows the scatter of the principal stress ratios compiled by McGarr & Gay (1978) (σ_1/σ_2, σ_1/σ_3, σ_2/σ_3) with depth. The average, plus or minus one standard deviation, for each principal stress ratio is: $\sigma_1/\sigma_2=1.45\pm0.40$; $\sigma_1/\sigma_3=2.42\pm1.14$; and $\sigma_2/\sigma_3=1.66\pm0.5$. Those ratios may be even higher for shallow depths (smaller than 100m) because of the topography influence (Jaeger and Cook, 2007). These statistics show that the expected anisotropy is indeed high and quite variable. Most of the data for σ_1/σ_2 and σ_2/σ_3 are in the range between 1 and 2. Figure 5.1 also shows that the geostatic stress tensor most often shows anisotropy in the 3 directions (i.e. $\sigma_1\neq\sigma_2\neq\sigma_3$).

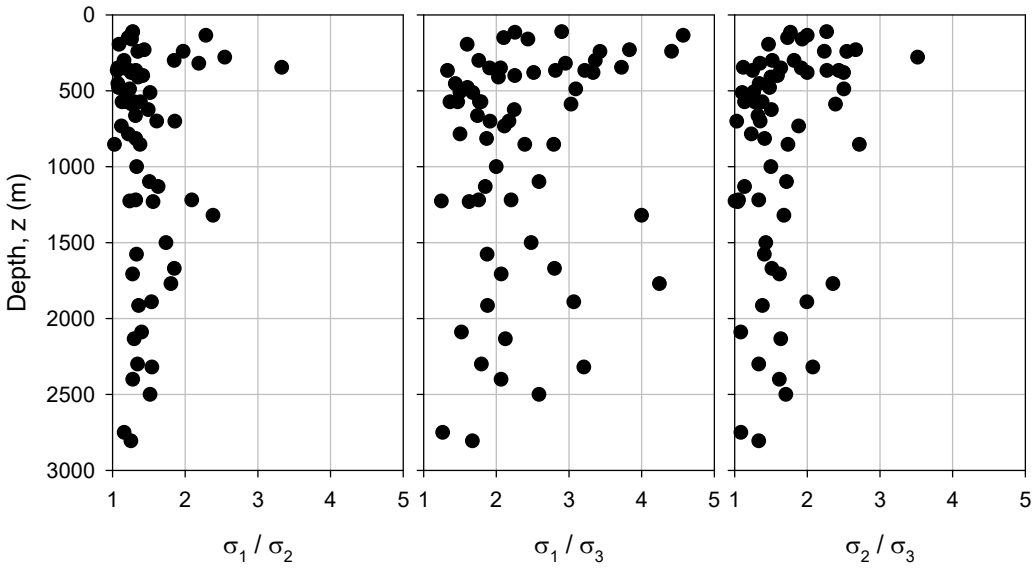

Figure 5.1 Ratio of principal stresses with depth, from McGarr & Gay (1978) data compilation.

Gysel (1975) presents the geostatic stress tensors with respect to the tunnel alignment for two sections of the Sonnerberg tunnel, built in the Alps, in Lucerne, Switzerland. The sections are 1km apart approximately and excavated in different types of sandstone. Table 5.1 shows the geostatic stress tensors normalized with respect to the vertical stress in the two sections. The results illustrate the stress anisotropy with respect to the tunnel axis and spatial variability. In section 2, the axial shear stresses are relatively large (43% and 17% of the vertical stress). Clearly, neglecting those stresses may be unsafe.

Table 5.1 Geostatic stress tensors normalized with respect to the vertical stress, where z is the tunnel axis, y the vertical to the tunnel and x the horizontal. (modified from Gysel, 1975).

	$\sigma_{xx} / \sigma_{yy}$	$\sigma_{zz} / \sigma_{yy}$	τ_{xy} / σ_{yy}	τ_{zy} / σ_{yy}	τ_{zx} / σ_{yy}
Section 1	2.17	0.98	-0.07	0.05	0.05
Section 2	2.73	1.36	-0.32	-0.43	-0.17

This paper presents an analytical solution to calculate the stresses and displacements of unsupported and supported tunnels when the axis of the tunnel is not aligned with the direction of the horizontal principal stresses. The new analytical solution assumes: 1) linear elastic, homogeneous and isotropic ground; 2) one of the principal stresses is the vertical stress (this is done for convenience, but it is not a limitation of the solution); 3) circular cross section; 4)

infinitely long; and 5) deep tunnel. The analytical solution includes the calculation of the axial shear forces in the liner, which may be relevant for the support design. In addition to the closed-form solution, the paper explores, numerically, the influence of the tunnel misalignment on the size of the yield zone around the tunnel, when plasticity is introduced.

5.2 Analytical solution for out of plane shear stresses

Given that far-field anisotropic stresses may be expected in rock masses, as discussed in the Introduction, it may be unlikely that the tunnel axis is aligned with one of the principal directions, as it is often assumed for tunnel design. Figure 5.2 shows the plan view (i.e. normal to the vertical, y-axis) of a tunnel not aligned with the horizontal principal stresses. In the figure, the tunnel makes an angle, α, with the direction of the major horizontal stress (σ_H). So that $\alpha=0°$ means that the tunnel is aligned with the major horizontal stress (σ_H). The geostatic stress tensor can be rotated such that one of the rotated axes is parallel to the axis of the tunnel and the other perpendicular (recall that, for convenience, the vertical axis is taken as a principal stress axis). This is convenient for the analysis, as it will be shown later. Figure 5.3 shows the plan view of the tunnel aligned with the geostatic stress tensor, where the far-field stresses are decomposed into an axial stress ($\sigma_{zz,ff}$), horizontal stress ($\sigma_{xx,ff}$), vertical stress ($\sigma_{yy,ff}$) and shear stress ($\tau_{xz,ff}$). The convention presented in Figure 5.3 is adopted throughout the paper.

Because of the superposition principle, valid for linear-elastic materials, the problem shown in Figure 5.3 can be divided in two problems: 1) a circular tunnel in an infinite elastic medium under far-field horizontal and vertical stresses ($\sigma_{xx,ff}$ and $\sigma_{yy,ff}$; Figure 5.4a) and 2) a circular tunnel in an infinite elastic medium under far-field shear stress ($\tau_{xz,ff}$; Figure 5.4b). Note that problem (1), shown in Figure 5.4a, can be solved using Kirsch or Einstein-Schwartz solutions for unlined and lined tunnels, respectively.

A new analytical solution, to calculate the stress and displacement fields for the 2nd problem (illustrated in Figure 5.4b), is provided for lined and unlined tunnels. The stress and displacement fields from the proposed analytical solution can be added to the Kirsch or Einstein-Schwartz solutions to obtain the full 3D stresses and displacements. This is possible because the far-field axial normal stress ($\sigma_{zz,ff}$) does not affect the radial and the tangential stresses and displacements on an infinitely long tunnel, for a linear elastic ground. The Kirsch and Einstein-Schwartz solutions are included in the Appendix, for completeness.

The calculation procedure consists of: 1) identify the in situ principal stress directions and their magnitudes (Figure 5.2); 2) align the tunnel axis with the stress tensor by rotating the principal stress tensor (Figure 5.3); 3) use the horizontal and vertical far-field stresses ($\sigma_{xx,ff}$ and $\sigma_{yy,ff}$) as input to the Kirsch or Einstein-Schwartz solutions (Figure 5.4a); and (4) use the far-field axial shear stress ($\tau_{xz,ff}$) as input to the presented analytical solution (Figure 5.4b). The solution is the result of the addition of stresses and displacements obtained in steps (3) and (4).

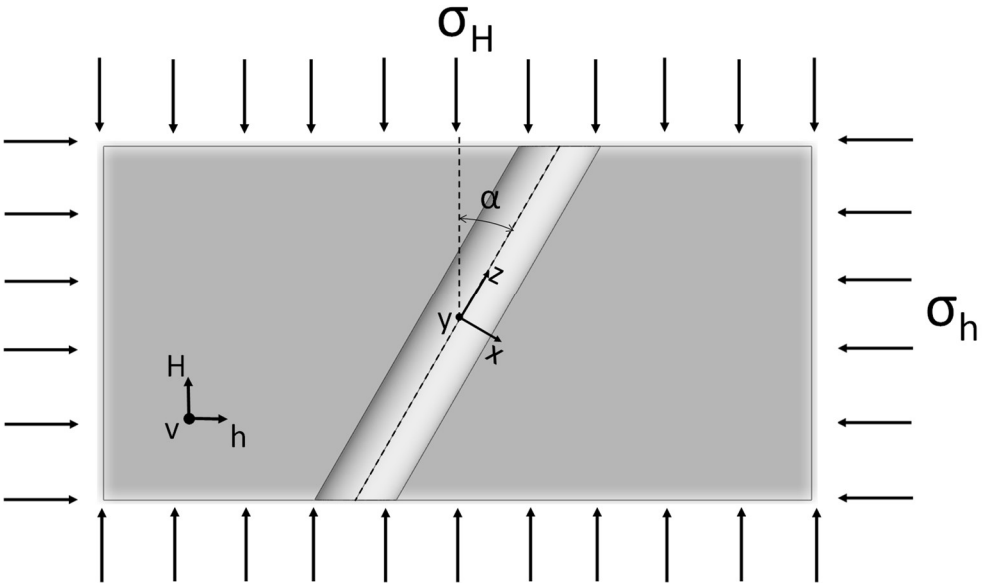

Figure 5.2 Plan view of a circular tunnel not aligned with one of the principal horizontal stress directions.

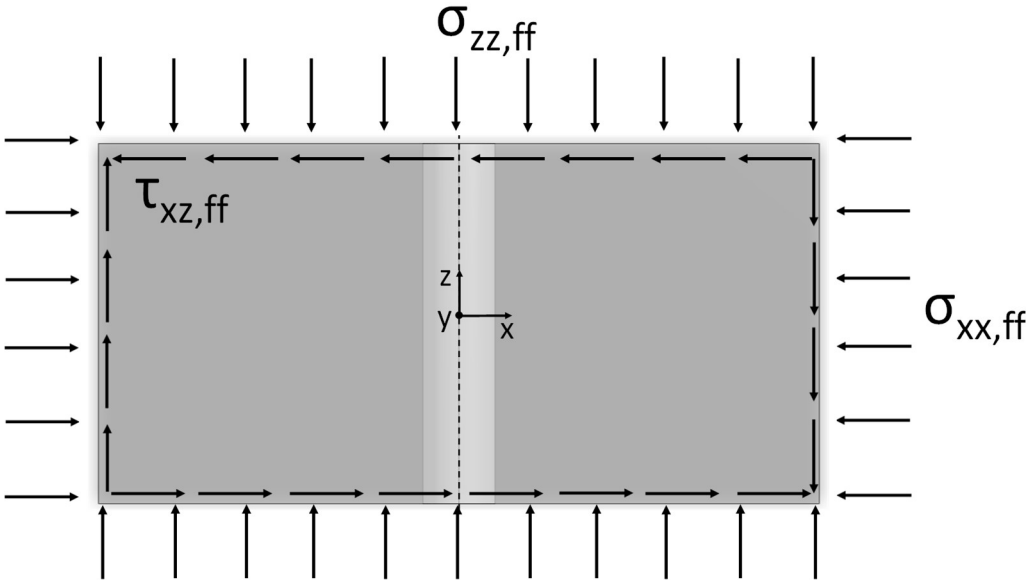

Figure 5.3 Plan view of a circular tunnel and far-field stresses.

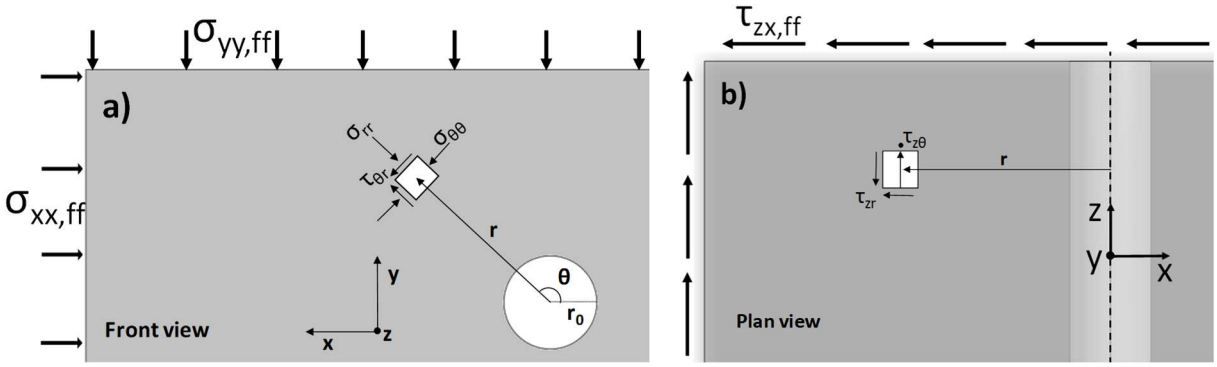

Figure 5.4 Decomposition of the far-field horizontal and vertical stresses ($\sigma_{xx,ff}$ and $\sigma_{yy,ff}$) and far-field axial shear stress ($\tau_{xz,ff}$) into two problems.

Given that the tunnel is long, $\partial/\partial z = 0$ applies and thus, equilibrium, in cylindrical coordinates, simplifies into:

$$\frac{\partial \tau_{rz}}{\partial r} + \frac{1}{r}\frac{\partial \tau_{z\theta}}{\partial \theta} + \frac{\tau_{rz}}{r} = 0 \tag{1}$$

Note that, given the problem in Figure 5.3, the axial stresses, σ_{zz}, are equal to $\sigma_{zz,ff}$.

The strains are:

$$\begin{cases} \gamma_{rz} = \dfrac{\partial w}{\partial r} \\ \gamma_{z\theta} = \dfrac{1}{r}\dfrac{\partial w}{\partial \theta} \end{cases} \tag{2}$$

where w is the axial displacement (i.e. displacements parallel to the z-axis). Stresses and strains, given the assumption of linear-elasticity, are:

$$\begin{cases} \tau_{rz} = G\gamma_{rz} \\ \tau_{z\theta} = G\gamma_{z\theta} \end{cases} \tag{3}$$

where G is the ground shear modulus.

Substituting (3) and (2) in (1):

$$\frac{\partial^2 w}{\partial r^2} + \frac{1}{r}\frac{\partial w}{\partial r} + \frac{1}{r^2}\frac{\partial^2 w}{\partial \theta^2} = 0 \tag{4}$$

Equation (4) can be solved assuming that the displacements w can be decomposed into a function of the radial coordinate r, f(r), and a function of θ, g(θ). That is, w= f(r) g(θ). Substitution in (4) and integration, results in the expression:

$$w = \sum_{n=1}^{\infty} \left(A_n \sin(n\theta) + B_n \cos(n\theta) \right) r^n + \sum_{n=1}^{\infty} \left(C_n \sin(n\theta) + D_n \cos(n\theta) \right) r^{-n} \tag{5}$$

Therefore, strains and stresses are given as:

$$\begin{aligned} \gamma_{rz} &= \frac{\partial w}{\partial r} = \sum_{n=1}^{\infty} n\left(A_n \sin(n\theta) + B_n \cos(n\theta) \right) r^{n-1} - \sum_{n=1}^{\infty} n\left(C_n \sin(n\theta) + D_n \cos(n\theta) \right) r^{-n-1} \\ \gamma_{z\theta} &= \frac{1}{r}\frac{\partial w}{\partial \theta} = \frac{1}{r}\left(\sum_{n=1}^{\infty} n\left(A_n \cos(n\theta) - B_n \sin(n\theta) \right) r^{n} + \sum_{n=1}^{\infty} n\left(C_n \cos(n\theta) - D_n \sin(n\theta) \right) r^{-n} \right) \end{aligned} \tag{6}$$

$$\begin{aligned} \tau_{rz} &= G\left(\sum_{n=1}^{\infty} n\left(A_n \sin(n\theta) + B_n \cos(n\theta) \right) r^{n-1} - \sum_{n=1}^{\infty} n\left(C_n \sin(n\theta) + D_n \cos(n\theta) \right) r^{-n-1} \right) \\ \tau_{z\theta} &= G\left(\sum_{n=1}^{\infty} n\left(A_n \cos(n\theta) - B_n \sin(n\theta) \right) r^{n-1} + \sum_{n=1}^{\infty} n\left(C_n \cos(n\theta) - D_n \sin(n\theta) \right) r^{-n-1} \right) \end{aligned} \tag{7}$$

where A_n, B_n, C_n *and* D_n are constants that can be found imposing the boundary conditions, which depend on the tunnel being unsupported or supported, as discussed in the following.

5.3 Unsupported tunnel

The boundary conditions for the unsupported tunnel are:

$$r = r_0 \rightarrow \tau_{zr} = 0 \tag{8}$$

$$r = \infty \rightarrow \begin{matrix} \tau_{zr} = \tau_{ff} \cos\theta \\ \tau_{z\theta} = -\tau_{ff} \sin\theta \end{matrix} \tag{9}$$

The solution is:

$$\begin{aligned} \tau_{zr} &= \left(1 - \frac{r_0^2}{r^2} \right) \tau_{ff} \cos\theta \\ \tau_{z\theta} &= -\left(1 + \frac{r_0^2}{r^2} \right) \tau_{ff} \sin\theta \\ w &= \frac{1}{G}\left(1 + \frac{r_0^2}{r^2} \right) \tau_{ff} r \cos\theta \end{aligned} \tag{10}$$

The expression for the axial displacements, w, shown in (8) includes the (initial) displacements due to the geostatic stresses. The "net" displacements, that is those that occur due to the tunnel excavation, are:

$$w^{net} = \frac{1}{G}\frac{r_0^2}{r} \tau_{ff} \cos\theta \tag{11}$$

5.4 Supported tunnel

The solution assumes no-slip (i.e. no relative displacement between ground and liner). Note that if a full slip condition is intended, the ground does not transfer shear stress to the liner. Equations (5-7) apply to both the ground and the liner (in the following the superscript g denotes the ground, and s, the liner). Figure 5.5 illustrates the geometry of the liner.

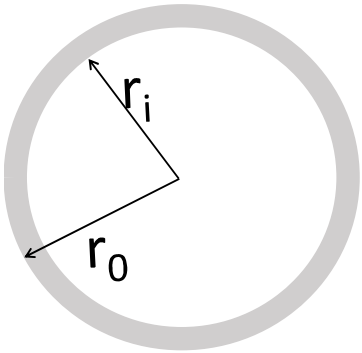

Figure 5.5 Geometry of the liner.

The axial liner displacements are:

$$w^s = \sum_{n=1}^{\infty}\left(A_n{}^s \sin(n\theta) + B_n{}^s \cos(n\theta)\right)r^n + \sum_{n=1}^{\infty}\left(C_n{}^s \sin(n\theta) + D_n{}^s \cos(n\theta)\right)r^{-n} \tag{12}$$

The boundary conditions are:

$$r = \infty \rightarrow \begin{cases} \tau^g{}_{zr} = \tau_{ff} \cos\theta \\ \tau^g{}_{z\theta} = -\tau_{ff} \sin\theta \end{cases} \tag{13}$$

$$r = r_i \rightarrow \tau^s{}_{zr} = 0$$

$$r = r_0 \rightarrow \begin{cases} \tau^s{}_{zr} = \tau^g{}_{zr} \\ w^s = w^g \end{cases} \tag{14}$$

The complete solution is:

For $r > r_0$

$$\tau^{g}{}_{zr} = \left(1 - \frac{r_0^2}{r^2} + \left(1 - \frac{r_i^2}{r_0^2}\right)\frac{G_s}{G_g} A \frac{r_0^2}{r^2}\right)\tau_{ff} \cos\theta$$

$$\tau^{g}{}_{z\theta} = -\left(1 + \frac{r_0^2}{r^2} - \left(1 - \frac{r_i^2}{r_0^2}\right)\frac{G_s}{G_g} A \frac{r_0^2}{r^2}\right)\tau_{ff} \sin\theta\,, \tag{15}$$

$$w^{g} = \frac{1}{G}\left(\frac{r_0^2}{r^2} - \left(1 - \frac{r_i^2}{r_0^2}\right)\frac{G_s}{G_g} A \frac{r_0^2}{r^2}\right)\tau_{ff} r \cos\theta$$

For $r_i < r < r_0$

$$\tau^{s}{}_{zr} = \left(1 - \frac{r_i^2}{r^2}\right)\frac{G_s}{G_g} A\,\tau_{ff} \cos\theta$$

$$\tau^{s}{}_{z\theta} = -\left(1 + \frac{r_i^2}{r^2}\right)\frac{G_s}{G_g} A\,\tau_{ff} \sin\theta\,, \tag{16}$$

$$w^{s} = \frac{1}{G_g}\left(1 + \frac{r_i^2}{r^2}\right) A\,\tau_{ff} r \cos\theta$$

Where A is given by:

$$A = \frac{1}{1 + \frac{G_s}{G_g} + \left(\frac{r_i}{r_0}\right)^2\left(1 - \frac{G_s}{G_g}\right)} \tag{17}$$

For a thin liner, with thickness t, i.e. $t = r_o - r_i << r_0$,

$$\tau^{g}{}_{zr} = \left(1 - \frac{r_0^2}{r^2} + \frac{t}{r_0}\frac{G_s}{G_g} B \frac{r_0^2}{r^2}\right)\tau_{ff} \cos\theta$$

$$\tau^{g}{}_{z\theta} = -\left(1 + \frac{r_0^2}{r^2} - \frac{t}{r_0}\frac{G_s}{G_g} B \frac{r_0^2}{r^2}\right)\tau_{ff} \sin\theta \tag{18}$$

$$w^{g} = \frac{1}{G_g}\left(\frac{r_0^2}{r^2} - \frac{t}{r_0}\frac{G_s}{G_g} B \frac{r_0^2}{r^2}\right)\tau_{ff} r \cos\theta$$

$$\tau^{s}{}_{zr} = \frac{1}{2}\frac{G_s}{G_g} B\left(1 - \frac{r_0^2}{r^2}\right)\tau_{ff} \cos\theta$$

$$\tau^{s}{}_{z\theta} = -\frac{1}{2}\frac{G_s}{G_g} B\left(1 + \frac{r_0^2}{r^2}\right)\tau_{ff} \sin\theta \tag{19}$$

$$w^{s} = \frac{1}{2}\frac{1}{G_g} B\left(1 + \frac{r_0^2}{r^2}\right)\tau_{ff} r \cos\theta$$

Where B is given by:

$$B = \frac{1}{1 + \frac{G_s}{G_g}\frac{t}{r_0}} \tag{20}$$

5.5 Verification

The analytical solution is validated through comparisons with 3D finite element models, where the tunnel axis is inclined at an angle α with the principal horizontal stress, and the vertical stress is a principal stress. Four cases are considered, with α= 90°, 75°, 60° and 45° (see Figure 5.2). The radius of the tunnel for all the cases is r_0=5 m.

Figure 5.6 to 8 show the finite element model, for the case with α=45°, and the boundary conditions and dimensions of the model, which is representative of the other discretizations. The mesh combines unstructured and structured grids, uses 2nd order elements (i.e. quadratic interpolation elements) and the model dimensions are large enough to avoid boundary effects. The numerical results around the opening are taken from a structured grid at the center (core) of the model (Figure 5.8). Such mesh provides accurate results even for highly nonlinear materials (Vitali et al., 2017). The liner is represented with shell elements with $0.1r_0$ (0.5m) thickness. Linear-elastic models are adopted for both ground and liner. The input properties are: E=100MPa, ν=0.3 for the ground, and E=25GPa, ν=0.2 for the liner. The models are solved in two steps. The first step generates the geostatic stress field by applying normal stresses and restricting the normal displacements at the boundaries, as illustrated in Figure 5.6 and Figure 5.7. In the second step, the solid elements inside the tunnel are deactivated and the shell elements are activated (for the lined tunnel), so that the liner is installed with no delay. The displacements from the 1st stage are zeroed. Those two steps are intended to duplicate the analytical solution. The following coordinate systems are used: (1) coordinate system x-y-z; it is aligned with the tunnel, where the z-axis is the axial direction, the x-axis is the horizontal direction perpendicular to the tunnel axis and the y-axis, the vertical direction; and (2) coordinate system v-h-H that represents the principal stress directions, i.e. vertical and horizontal directions σ_h and σ_H, respectively. Note that the vertical, i.e. the y-axis, is a principal stress axis.

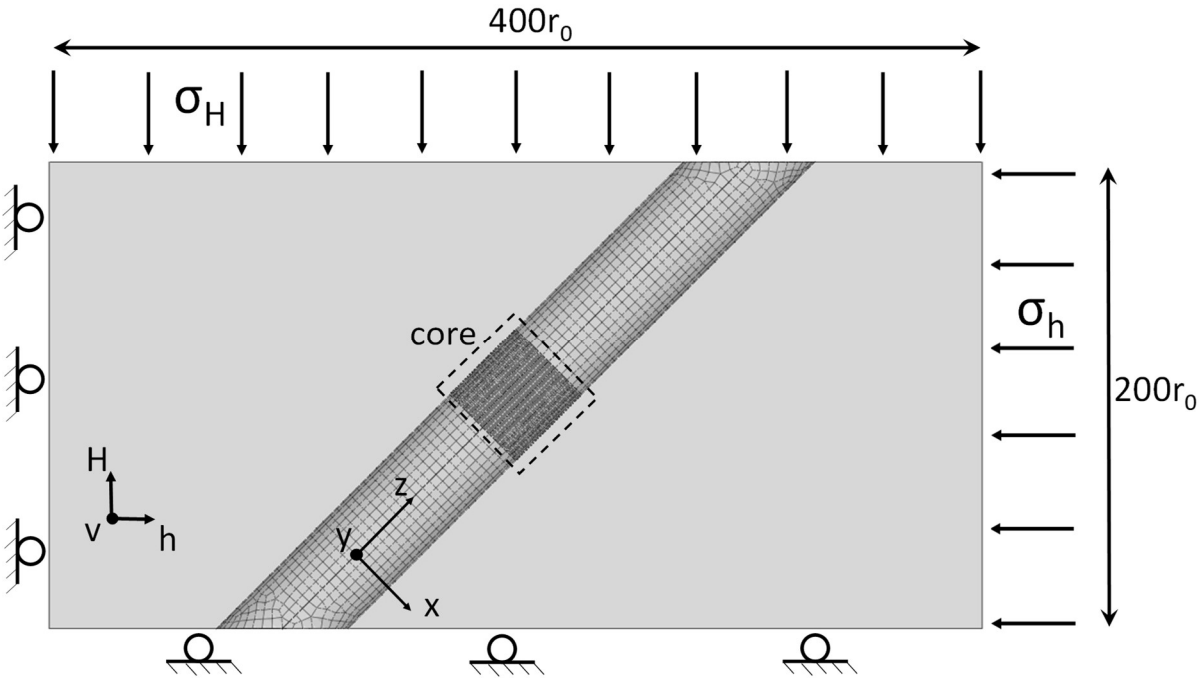

Figure 5.6 Plan view of the finite element model with dimensions and boundary conditions.

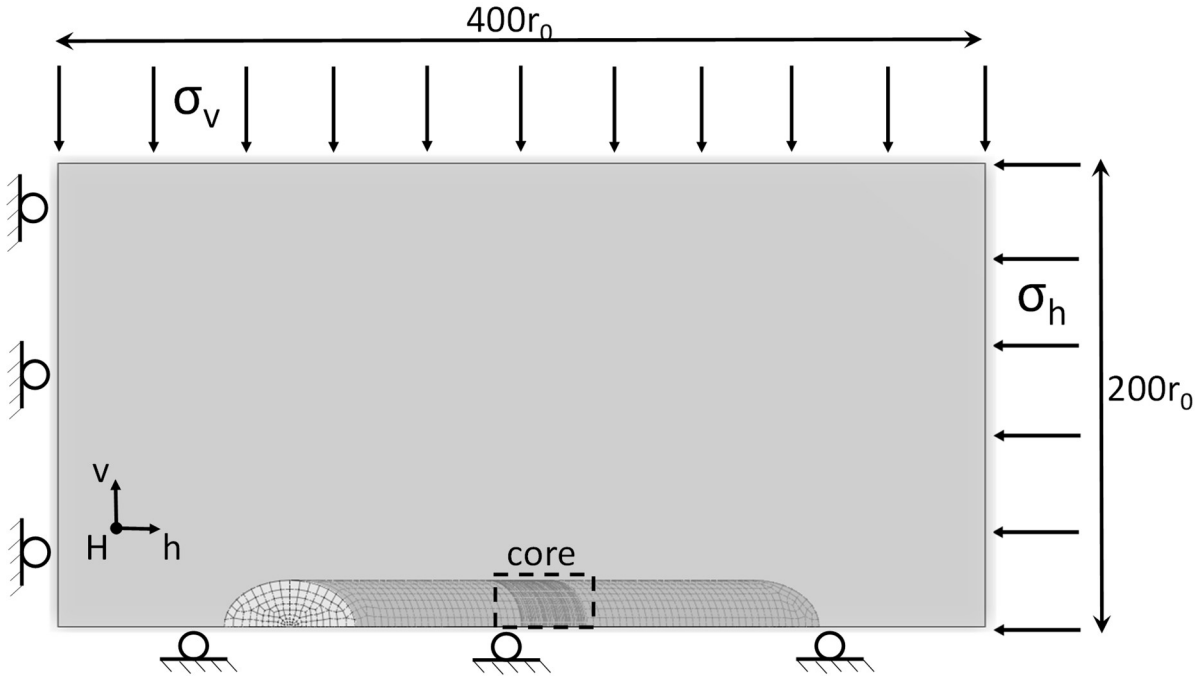

Figure 5.7 Front view of the finite element model with dimensions and boundary conditions.

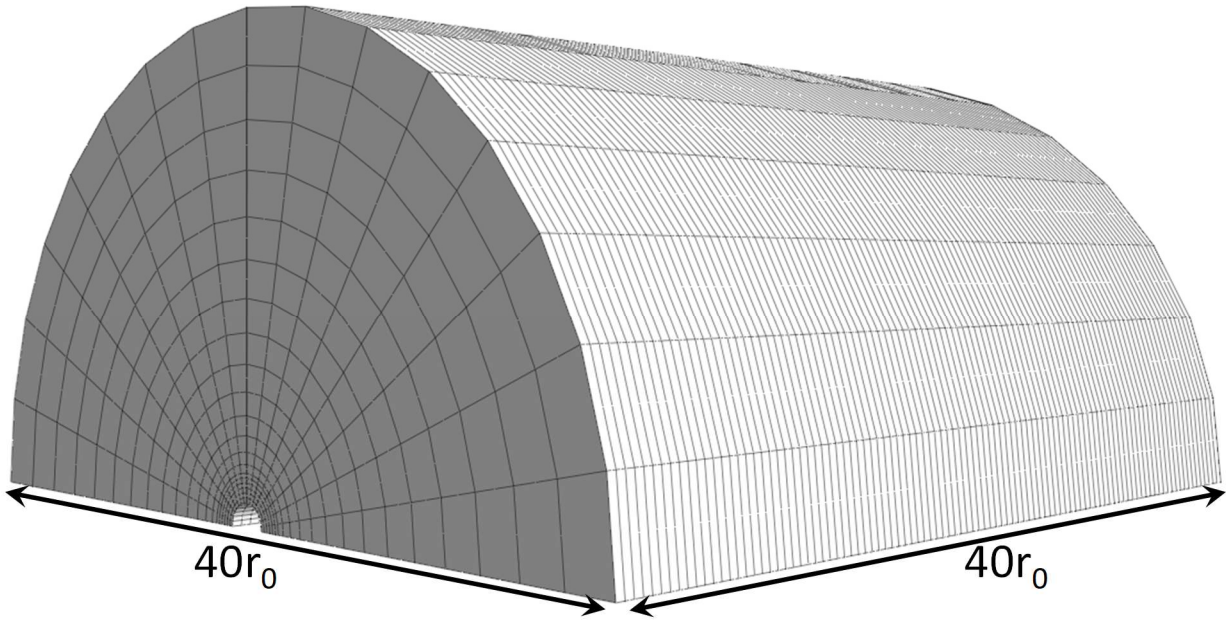

Figure 5.8 Finite element mesh of the core of the model, where the results are taken.

The geostatic stresses used for the simulations are shown in Table 5.2; note that they are referenced with respect to the coordinate system *x,y,z* shown in Figure 5.2 (the axis *z* is parallel to the axis of the tunnel and *y* is vertical). For α=90°, the tunnel axis is aligned with the minor horizontal stress (σ_h) and, as a consequence, no far-field shear stress is present. As the tunnel axis rotates (see Figure 5.2), the far-field shear stress ($\tau_{xz,ff}$) increases, the horizontal stress ($\sigma_{xx,ff}$) increases, while the vertical stress remains constant. The selected scenario encompasses a range of K_{xy} (defined as the ratio between horizontal and vertical stress, i.e. $\sigma_{xx,ff}/\sigma_{yy,ff}$) from 0.5 to 1 and $\tau_{xz,ff}/\sigma_{yy,ff}$ from 0 to 0.5.

Table 5.2 Far-field stresses in the coordinate system, x-y-z, attached to the tunnel.

α (°)	**$\sigma_{xx,ff}$ (MPa)**	**$\sigma_{yy,ff}$ (MPa)**	**$\sigma_{zz,ff}$ (MPa)**	**$\tau_{xz,ff}$ (MPa)**
90	1	2	3	0
75	1.13	2	2.87	0.5
60	1.5	2	2.5	0.87
45	2	2	2	1

Figure 5.9 and Figure 5.10 compare the analytical and numerical results for the unsupported tunnel. The results are presented in cylindrical coordinates for convenience, where

θ=0° and 180° correspond to the springlines and θ=90° to the crown of the tunnel. The values plotted from the numerical solution are those provided by the simulations, while those from the analytical solution are obtained from the superposition of the Kirsch solution, using as input the far-field horizontal and vertical stresses ($\sigma_{xx,ff}$ and $\sigma_{yy,ff}$; the equations are shown in the Appendix), and the predictions from the analytical solution, using as input the far-field shear stresses ($\tau_{xz,ff}$) (equations (10)). As one can see in the figures, the analytical and numerical results provide consistent values, with differences smaller than 1%, as average.

Note that the largest displacements and stresses occur at the springline and at the crown. As expected, when K_{xy}=1 (α=45°), the radial displacements and the tangential stresses are constant along the tunnel perimeter. Also, as expected, the differences between radial and tangential stresses at the springline and at the crown increase as K_{xy} decreases. The far-field axial shear stress ($\tau_{xz,ff}$) causes anti-symmetric axial displacements at the springline and no axial displacements at the crown. Note that the tunnel cross-section remains planar. Also, the shear stresses are zero at the springline and reach a maximum value at the crown.

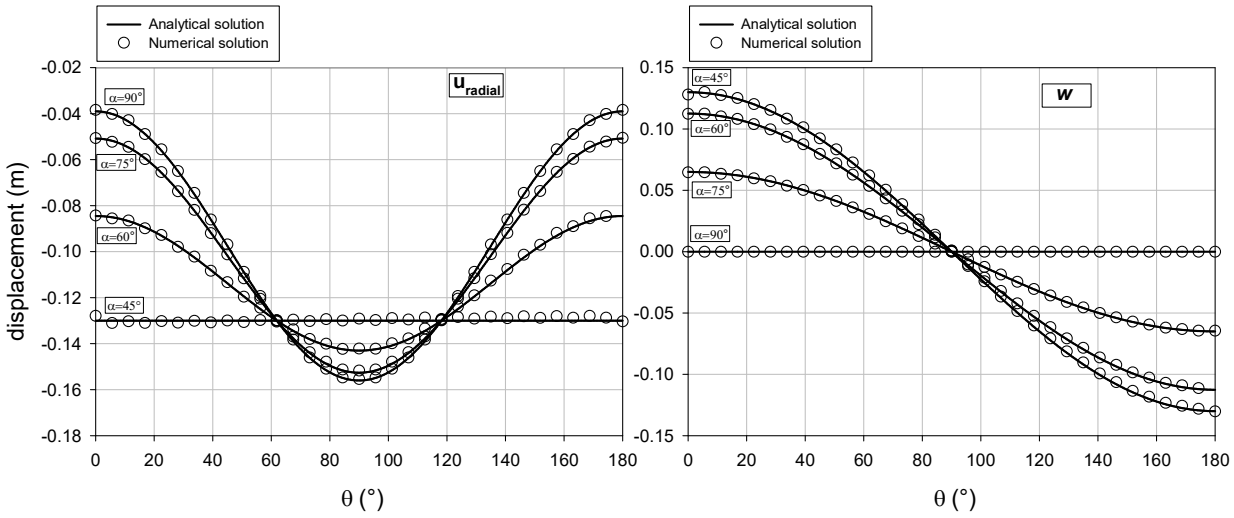

Figure 5.9 Unsupported tunnel. Radial and axial displacements of the ground at the tunnel perimeter.

Figure 5.11 and Figure 5.12 compare the analytical and numerical results for the supported tunnels. As with the unsupported tunnel, the results for the analytical solution are obtained from superposition using the Einstein and Schwartz solution (the equations are presented in the Appendix), using as input the far-field stresses normal to the cross section of the tunnel ($\sigma_{xx,ff}$ and $\sigma_{yy,ff}$), and the new solution (equations for thin liner), using the far-field shear stress ($\tau_{xz,ff}$). The

figures show that the analytical solution compares well with the numerical solution, with errors of the order of 1%. As one can see, for K_{xy}=1 (α=45°), the radial stresses at the ground-liner interface are constant along the tunnel perimeter and, therefore, the bending moment is zero and the thrust force is constant. As K_{xy} decreases from 1 to 0.5, i.e. as the angle α decreases, the radial stresses become less compressive, but non-uniform, so the liner is subjected to bending moments and thrust forces. The shear stress ($\tau_{\theta z}$) is zero at the springline and increases towards the crown, where it reaches a maximum. The in-plane shear stress ($\tau_{\theta r}$) is zero at the crown and springline, and has a maximum at θ=45° and θ=135°.

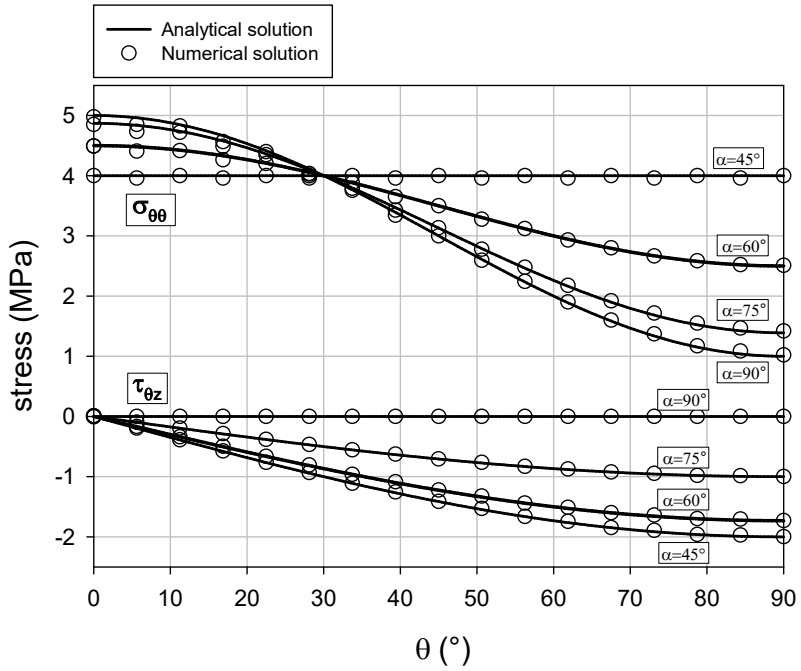

Figure 5.10 Unsupported tunnel. Tangential and shear stresses of the ground at the tunnel perimeter.

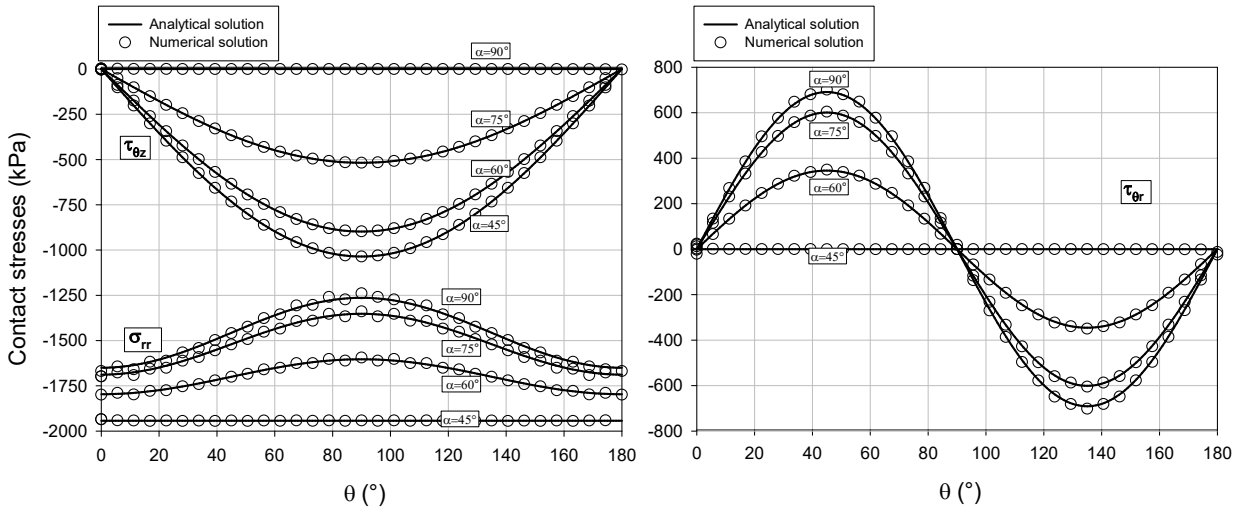

Figure 5.11 Supported tunnel. Radial and shear stresses at the liner-ground contact.

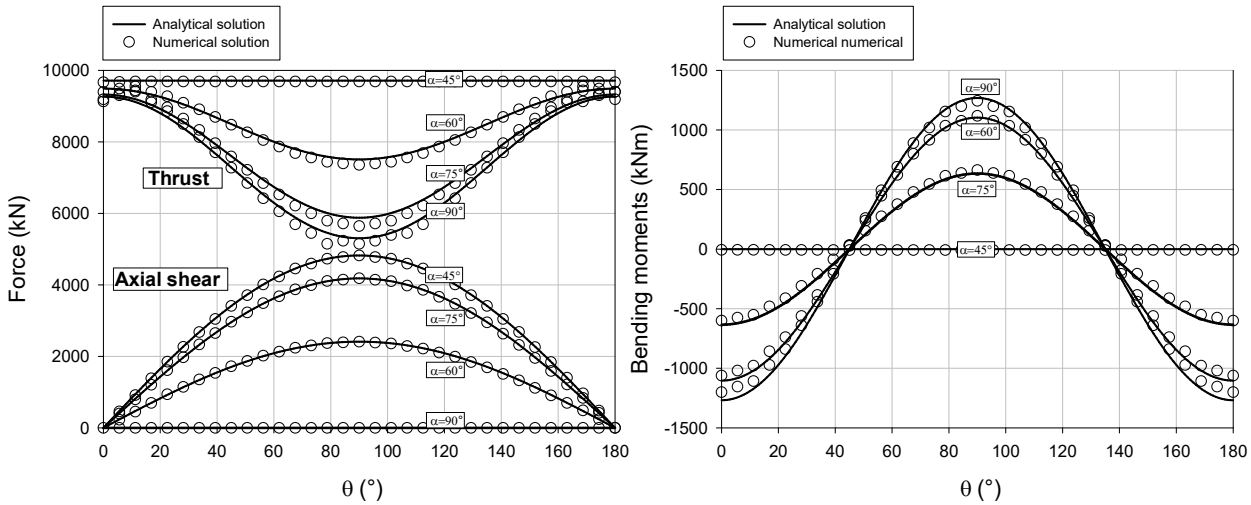

Figure 5.12 Supported tunnel. Forces and bending moments in the liner.

5.6 Discussion

The interplay that exists between ground, liner and far-field stresses on the plane of the tunnel cross section is now well understood (e.g. Einstein and Schwartz, 1979). However, the effects of tunnel misalignment with the far-field stresses, i.e. due to the presence of far-field shear stresses, is not well known. To discuss this issue, the anisotropic geostatic stress field obtained by Gysel (1975), for section 1 of the Sonnerberg tunnel, is taken as reference. The stress tensor has principal stress ratios $\sigma_1/\sigma_3 = 2.33$ and $\sigma_2/\sigma_3 = 1.11$, which are within the range of expected stress anisotropy, according to McGarr & Gay (1978). The same numerical model used for the

verification is employed for the analysis in elastoplastic ground, i.e. same mesh, dimensions, boundary conditions and steps, except for the values of the far-field stresses. The ground and liner properties are E_{ground}=1GPa; E_{liner}=25GPa; t=0.1r_0 (0.5m); ν_{ground}=0.3; ν_{liner}=0.2, which are typical values for deep tunnels in soft rock. No slip between liner and ground is considered.

It is assumed that the vertical stress is a principal stress, i.e. $\sigma_{yy,ff}$= σ_v =1MPa. For α=0° (Figure 5.2), the tunnel is aligned with the major principal horizontal stress, i.e. $\sigma_{zz,ff}$ = σ_H =2.33MPa and $\sigma_{xx,ff}$ = σ_h =1.11MPa. For the analyses, the tunnel axis is rotated clockwise by an angle α with respect to the vertical, *y* axis, from the major principal horizontal stress (σ_H) towards the minor principal horizontal stress (σ_h); that is, when α=90°, the tunnel axis is aligned with the minor principal horizontal stress (σ_h), i.e. $\sigma_{zz,ff}$ = σ_h =1.11MPa and $\sigma_{xx,ff}$ = σ_H =2.33MPa. The expressions for the far-field stresses $\sigma_{xx,ff}$, $\sigma_{zz,ff}$ and $\tau_{xz,ff}$ are:

$$\sigma_{xx,ff} = \sin^2(\alpha)\sigma_H + \cos^2(\alpha)\sigma_h$$

$$\sigma_{yy,ff} = \sigma_v$$

$$\sigma_{zz,ff} = \cos^2(\alpha)\sigma_H + \sin^2(\alpha)\sigma_h;$$

$$\tau_{xz,ff} = \frac{(\sigma_H - \sigma_h)}{2}\sin(2\alpha);$$

The far-field horizontal stress ($\sigma_{xx,ff}$) increases and the far-field axial stress ($\sigma_{zz,ff}$) decreases as the tunnel axis rotates from 0° to 90°. The far-field shear stress ($\tau_{xz,ff}$) is zero when the tunnel axis is aligned with one of the principal stresses (i.e., α=0° and 90°) and it is maximum at α=45°. Figure 5.13 shows the stress ratio K_{xy} ($\sigma_{xx,ff}/\sigma_{yy,ff}$) and the far-field axial shear stress normalized with respect to the far-field vertical stress ($\tau_{xz,ff}/\sigma_{yy,ff}$) with the rotation angle (α). For α=0°, K_{xy} is 1.1 and there is no far-field shear stress. The stress ratio K_{xy} increases with α and is maximum (i.e. K_{xy} of 2.33) when α=90°. The far-field shear stress ($\tau_{xz,ff}$) increases until α=45° and then decreases ($\tau_{xz,ff}$ at α=45° is 0.61$\sigma_{yy,ff}$).

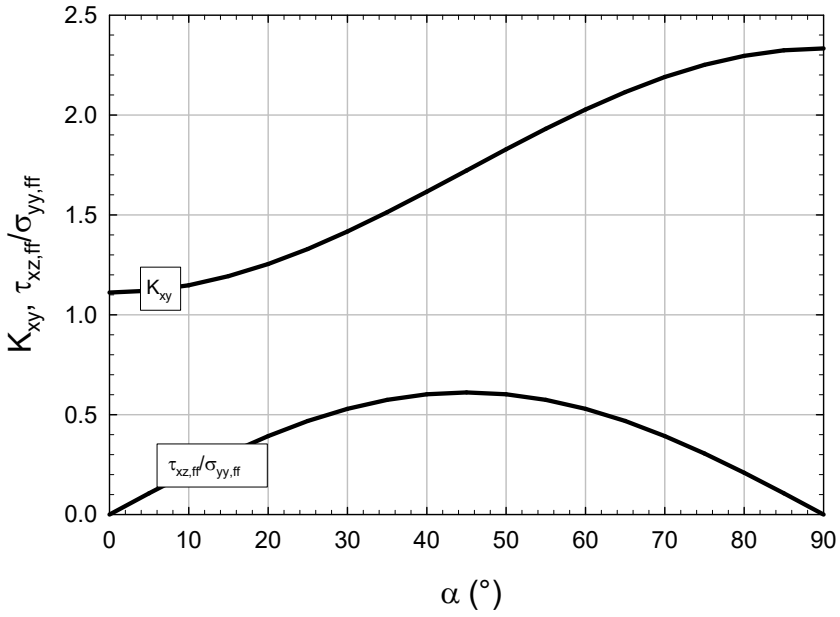

Figure 5.13 Stress ratio (K_{xy}) and normalized far-field shear stress with respect to the vertical stress, with the tunnel rotation angle (α).

Figure 5.14 shows the normalized tangential and shear stresses with respect to the far-field vertical stress and the normalized radial displacements with respect to the tunnel radius with the rotation angle (α). The results are computed at the perimeter ($r=r_0$) of an unsupported tunnel, at the springline and crown. The tangential stress ($\sigma_{\theta\theta}$) decreases at the springline and increases at the crown as the horizontal stress ($\sigma_{xx,ff}$) increases (as the rotation angle α increases). At the same time, the radial displacement increases at the springline while it decreases at the crown. The shear stress ($\tau_{\theta z}$) at the crown and the axial displacement (w) at the springline are maximum at α=45° and zero when the tunnel is aligned with a principal stress (α=0° and 90°). Note that $\tau_{\theta z}$ is 1.22 times the vertical stress for α=45°.

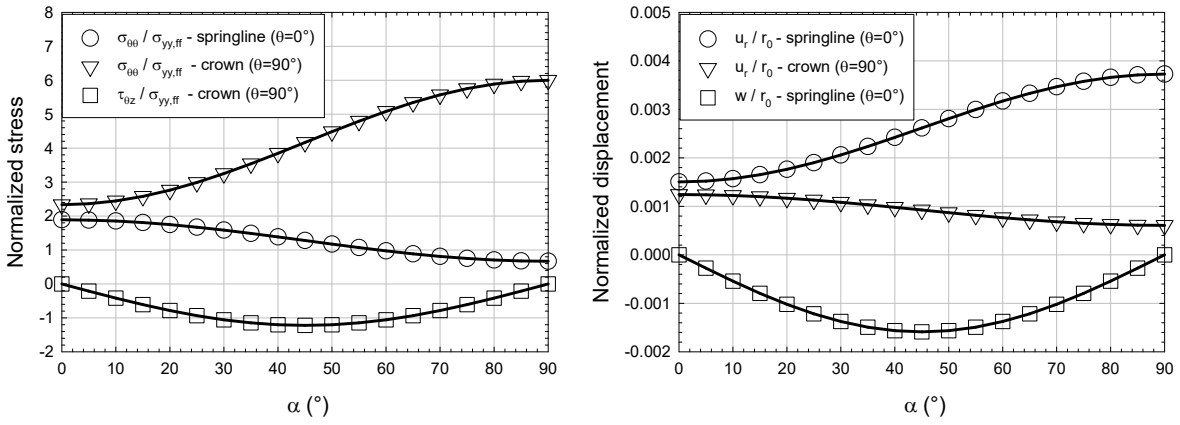

Figure 5.14 Unsupported tunnel in elastic ground. Normalized stresses with respect to the far-field vertical stress and normalized displacements with respect to the tunnel radius with tunnel rotation.

The tunnel axis orientation may strongly affect the internal forces in the liner, when the tunnel is supported. Figure 5.15 shows the radial stresses (σ_{rr}) and the shear stress ($\tau_{\theta z}$) at the ground-liner contact, with the tunnel axis rotation (α). The contact stresses are normalized with respect to the far-field vertical stress ($\sigma_{yy,ff}$). As the tunnel rotates, the radial stress over the crown increases while at the springline it remains almost constant. The shear stress ($\tau_{\theta z}$) at the crown is maximum for α=45° and zero for α=0° and α=90°, when the tunnel is aligned with the principal stresses. Figure 5.16 shows the normalized internal forces with respect to the tunnel radius (r_0) and the far-field vertical stress ($\sigma_{yy,ff}$), with the rotation angle (α). As the tunnel axis rotates from 0° to 90°, the bending moments, M, increase at both the crown and springline while the thrust, T, increases, prominently at the crown. At the same time, the shear force, V, in the liner first increases up to α =45° and then decreases.

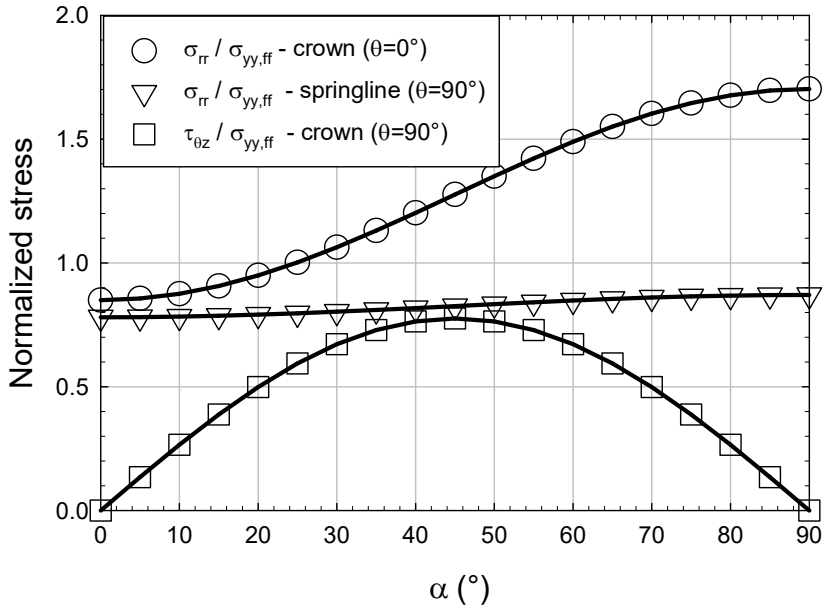

Figure 5.15 Supported tunnel in elastic ground. Stresses at the ground-liner contact, normalized with respect to the far-field vertical stress, with tunnel axis rotation.

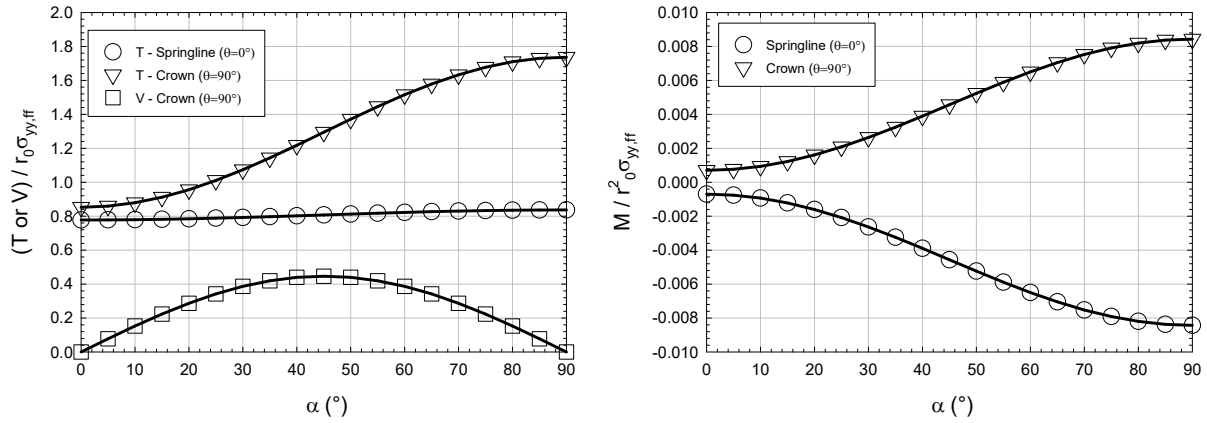

Figure 5.16 Supported tunnel in elastic ground. Thrust (T), shear force (V) and bending moment (M) normalized with respect to the tunnel radius and far-field vertical stress, with tunnel axis rotation.

Figure 5.17 shows the thrust-moment interaction diagram for the tunnel support for α=0°, 45° and 90°. The demand along the structure is compared with yielding envelope (forces taken from θ = 0° to 90°). The envelope is calculated neglecting the steel reinforcement and the tensile strength of the concrete. The adopted unconfined compression strength for the concrete is 20MPa.

No safety factors to reduce strength or to increase the load were applied to calculate the envelope. The failure envelope is calculated using the structural software "response 2000" (Bentz, 2000). It considers the non-linear stress distribution along the liner cross section and the cracked region. The yielding envelope shown in Figure 5.17 represents the crushing of the most compressed face. Examples of the tunnel liner verification can be found in Hoek et al. (2008).

When the tunnel is aligned with the major horizontal principal stress, σ_H, (α=0°), the stress ratio is K_{xy}=1.11, which results in relatively small bending moments and large factor of safety against failure. However, when the tunnel is aligned with the minor horizontal principal stress, σ_h, (α=90°), the stress ratio is K_{xy}=2.33 and the demand on the liner is larger than its strength. An eventual failure would be reached first at the crown.

It is important to note, as shown in Figure 5.16, that the far-field shear stress ($\tau_{xz,ff}$) produces an axial shear force (V) and axial displacements in the liner, as illustrated in Figure 5.18. The shear force (V) is maximum when the tunnel axis is oriented at 45° with the intermediate principal direction (α=45°), and is zero when the tunnel is parallel to one of the principal directions (α=0° or 90°). As a side note, for full slip between ground and support, the ground is not able to transfer shear stresses to the liner, the liner does not take load from the far-field shear and the stresses and displacements in the ground, due only to the far-field shear stresses, can be obtained using the expressions given in (11) for the unlined tunnel.

For α=45°, the stress ratio K_{xy} is 1.72 and the shear force is maximum. Note that in this case the combination of thrust and moment (Figure 5.17) does not induce failure. However, the large shear force, V, which is not considered in the force-moment diagram, can potentially damage the support and should be examined using e.g. suitable concrete codes. Note that the results presented are specific to the case discussed and may not be generalized.

Figure 5.19 shows the radial displacements, normalized with the tunnel radius, obtained from the numerical models, with the rotation angle (α). As one can see, the radial displacements from the 3D models with shear stresses are consistently larger than the other models, i.e. 2D plane strain and 3D with no shear stresses. The largest difference is for α=30°, where the radial displacements are 81.8%, at the crown, and 49.4%, at the springline, larger than those from the 2D model. The results seem to indicate that neglecting the far-field shear stress in tunnel analysis may underpredict ground deformations and, therefore, may lead to unsafe tunnel design. Note also that

the 3D models do not consider the step-by-step excavation, which could lead to even higher ground deformations, as shown in Vitali et al. (2017).

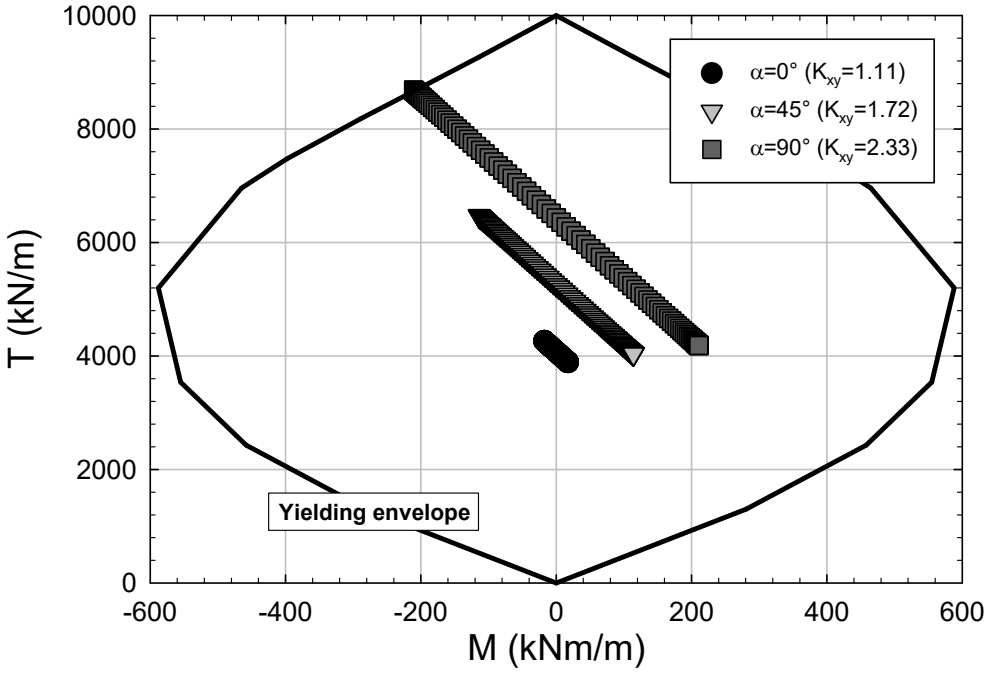

Figure 5.17 Supported tunnel. Thrust-moment Interaction diagram.

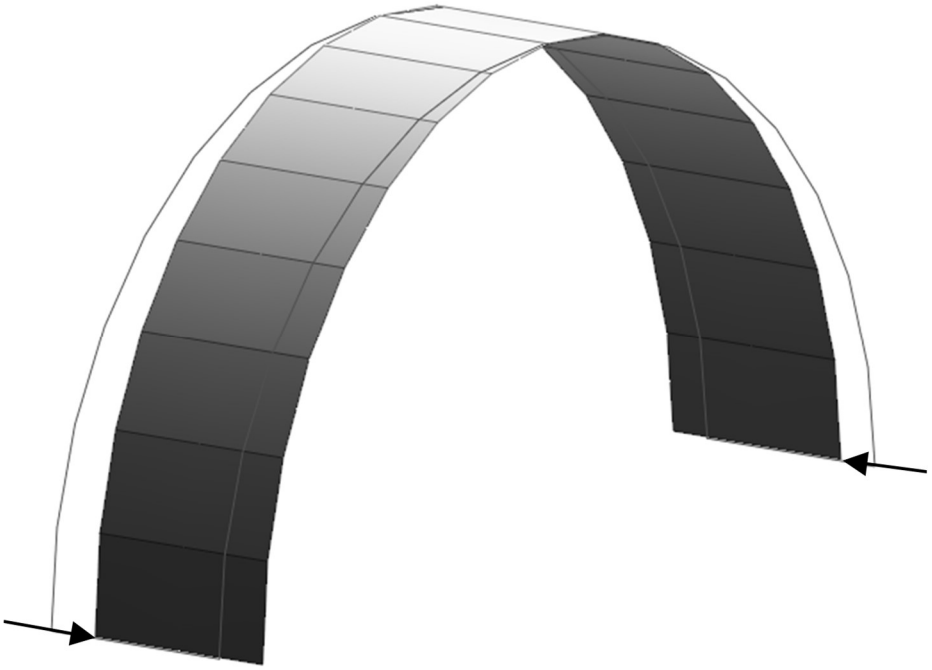

Figure 5.18 Distortion on the tunnel liner due to far-field shear stress ($\tau_{xz,ff}$).

In Figure 5.19, between α=0°, where the tunnel is aligned with the major principal stress, and α=45°, where the axial and horizontal stresses ($\sigma_{zz,ff}$ and $\sigma_{xx,ff}$) have the same magnitude, the radial displacements in the 3D models with no shear stresses are larger than those from the 2D plane strain models (the differences are 53.7% and 41.9% at the springline and crown, respectively, for α=0°). This is because when the axial stress is larger than the horizontal stress, the maximum shear stress ($(\sigma_1-\sigma_3)/2$) happens in the axial-vertical plane. That is, for elastoplastic ground, the axial normal stress may be relevant because it may affect the plastic zone size and the ground deformations. The differences between the 3D with no shear and 2D plane strain models are small compared to the differences obtained when using the 3D model with shear stress. For α between 45° and 90°, when the horizontal stress is larger than the axial stress, the 2D plane strain and 3D model with no shear predict the same ground deformations.

The deformations at the crown are always larger than at the springline. This is the result of the horizontal stresses increasing as the tunnel rotates, while the vertical stress remains constant. Therefore, there is an increasing stress concentration over the tunnel crown with the stress rotation, which in turn induces a larger plastic zone and larger deformations over the crown. It is interesting to note that this is the opposite for linear-elastic ground, where the displacements at the springline are larger (see Figure 5.14). The 3D models with shear stress show larger differences between displacements at the crown and springline than the 2D plane strain models and the 3D model with no shear stress. This is due to the effect of the tangential shear stress ($\tau_{\theta z}$), which is maximum at the crown and zero at the springline (as shown in Figure 5.10).

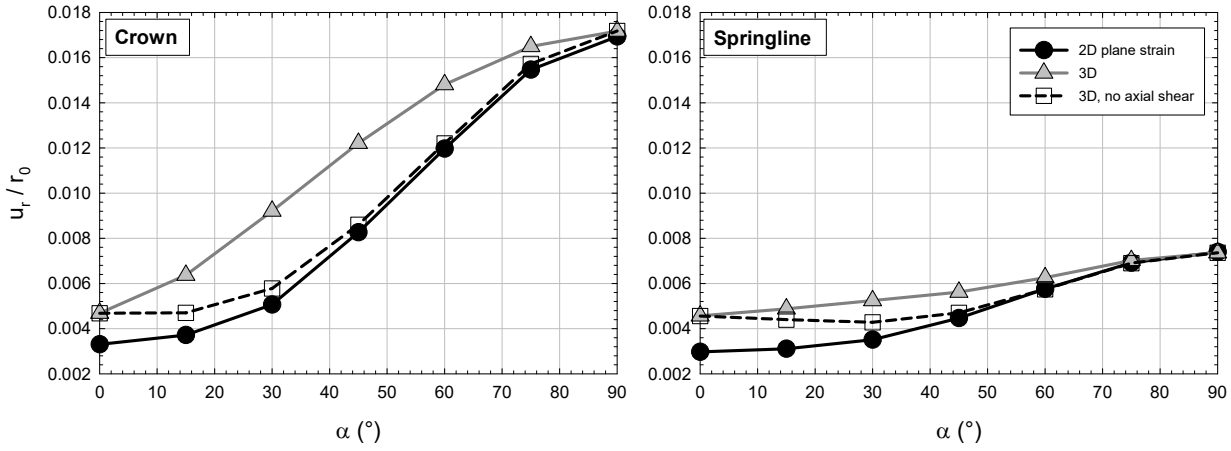

Figure 5.19 Normalized radial displacements at the crown and at the springline with respect to the tunnel radius with the rotation angle (α).

5.7 Conclusions

The paper presents an analytical solution to calculate stresses and displacements of the liner, if present, and the ground, for a deep circular tunnel, when its axis is not aligned with the principal directions of the far-field stresses. The solution assumes that both the ground and the liner remain elastic and accounts only for the far-field shear stress generated due to the tunnel misalignment with the principal stress directions. Since the proposed analytical solution assumes linear-elasticity, it can be combined with the Kirsch solution (for unsupported tunnel) and with the Einstein-Schwartz solution (for supported tunnel). The combined analysis has been validated by comparing the results from the new analytical solutions with those from a Finite Element Method. The differences are smaller than about 1%.

The tunnel misalignment with the principal stresses induces shear stresses around the opening. Those stresses distort the tunnel cross-section in the axial direction by inducing axial displacements in the ground. If the tunnel is lined and the liner is bonded to the ground, the shear stress induces axial shear forces in the liner, which may be relevant and should be considered for the support design. Further, the shear stress increases the deviatoric stresses in the ground and may increase the size and change the shape of the plastic zone around the opening, which may lead to ground deformations higher that those predicted when the effects of the tunnel misalignment are neglected.

The stress field in the ground, in general, and in rock masses in particular, may be highly anisotropic, and so alignment of the tunnel with the principal stresses may not generally occur. The paper shows that the tunnel response in terms of stresses and deformations of both ground and support strongly depend on the tunnel orientation with respect to the principal geostatic stresses. The numerical and analytical results show that the worst scenario is when the tunnel is aligned with the smallest horizontal principal stress, and the best, when the tunnel is aligned with the largest horizontal principal stress. This observation is consistent with the recommendation of aligning the axis of underground structures with the major principal stress direction (Goodman, 1989). Finally, the proposed analytical solution is valid for elastic ground (i.e. no yielding) or when there is localized, minor, yielding around the opening.

List of Variables

α = angle between tunnel axis and horizontal principal stress;

$\sigma_{xx,ff}$ = far-field horizontal stress normal to the tunnel axis;

$\sigma_{yy,ff}$ = far-field vertical stress, assumed normal to the tunnel axis;

$\sigma_{zz,ff}$ = far-field stress parallel to the tunnel axis;

$\tau_{zx,ff}$ = far-field axial shear stress;

K_{xy} = stress ratio ($\sigma_{xx,ff}$ / $\sigma_{yy,ff}$);

w = axial displacement;

u_r = radial displacement;

G=G_g = shear modulus of the ground;

G_s = shear modulus of the structure;

E = Young's modulus;

v = Poisson's ratio;

r_0 = tunnel radius;

t = support thickness;

r_i = tunnel internal radius (r_0+t);

T = thrust force of the liner;

M = bending moment of the liner;

V = axial shear force of the liner;

φ = friction angle of the ground;

c = cohesion of the ground;

Ψ = dilatancy angle of the ground;

x, y, z= coordinate system attached to the tunnel, with z-axis parallel to tunnel axis;

σ_v = vertical stress;

σ_h = minor principal horizontal stress;

σ_H = major principal horizontal stress;

r ,θ, z= cylindrical coordinate system, with z-axis parallel to tunnel axis;

$\sigma_{\theta\theta}$ = tangential stress in cylindrical coordinates;

σ_{rr} = radial stress in cylindrical coordinates;

$\tau_{r\theta}$ = in-plane shear stress in cylindrical coordinates;

τ_{rz} = axial shear stress in cylindrical coordinates;

$\tau_{\theta z}$ = axial shear stress in cylindrical coordinates;

5.8 Appendix

Stresses and displacements for a deep unsupported tunnel, with a circular cross section, excavated in elastic ground, assuming plane strain conditions are (Kirsch solution, Kirsch, 1898):

$$\sigma_{rr} = \frac{\sigma_{yy,ff}}{2}\left[\left(1+K_{xy}\right)\left(1-\left(\frac{r_0}{r}\right)^2\right)-\left(1-K_{xy}\right)\left(1-4\left(\frac{r_0}{r}\right)^2+3\left(\frac{r_0}{r}\right)^4\right)\cos 2\theta\right];$$

$$\sigma_{\theta\theta} = \frac{\sigma_{yy,ff}}{2}\left[\left(1+K_{xy}\right)\left(1+\left(\frac{r_0}{r}\right)^2\right)+\left(1-K_{xy}\right)\left(1+3\left(\frac{r_0}{r}\right)^4\right)\cos 2\theta\right];$$

$$\sigma_{r\theta} = -\frac{\sigma_{yy,ff}}{2}\left[\left(1-K_{xy}\right)\left(1+2\left(\frac{r_0}{r}\right)^2-3\left(\frac{r_0}{r}\right)^4\right)\sin 2\theta\right];$$

$$u_r = -\frac{\sigma_{yy,ff}}{2}\frac{(1+\nu)}{E}r\left[\left(1+K_{xy}\right)\left(\frac{r_0}{r}\right)^2-\left(1-K_{xy}\right)\left(4(1-\nu)\left(\frac{r_0}{r}\right)^2-\left(\frac{r_0}{r}\right)^4\right)\cos 2\theta\right]$$

$$u_\theta = -\frac{\sigma_{yy,ff}}{2}\frac{(1+\nu)}{E}r\left(1-K_{xy}\right)\left(2(1-2\nu)\left(\frac{r_0}{r}\right)^2+\left(\frac{r_0}{r}\right)^4\right)\sin 2\theta$$

Stresses and displacements for a supported deep circular tunnel, for elastic ground and liner, assuming plane strain conditions and no slip between ground and liner are (Einstein-Schwartz solution, Einstein & Schwartz, 1979):

At the ground-liner contact, i.e. r=r_0:

$$\sigma_{rr} = \frac{1}{2}\sigma_{yy,ff}\left(1+K_{xy}\right)(1-a_0^*)-\frac{1}{2}\sigma_{yy,ff}\left(1-K_{xy}\right)(1-6a_2^*+4b_2^*)\cos 2\theta$$

$$\tau_{r\theta} = \frac{1}{2}\sigma_{yy,ff}\left(1-K_{xy}\right)(1+6a_2^*-2b_2^*)\sin 2\theta$$

$$\frac{u_r E}{\sigma_{yy,ff} r_0 (1+\nu)} = -\frac{1}{2}\left(1+K_{xy}\right)a_0^*-\frac{1}{2}\left(1-K_{xy}\right)(4(1-\nu)b_2^*-2a_2^*)\cos 2\theta$$

$$\frac{u_\theta E}{\sigma_{yy,ff} r_0 (1+\nu)} = \left(1-K_{xy}\right)(a_2^*+(1-2\nu)b_2^*)\sin 2\theta$$

where:

$$a_0^* = \frac{CF(1-\nu)}{C+F+CF(1-\nu)};$$

$$\beta = \frac{(6+F)C(1-\nu)+2F\nu}{3F+3C+2CF(1-\nu)}$$

$$b_2^* = \frac{C(1-\nu)}{2[C(1-\nu)+4\nu-6\beta-3\beta C(1-\nu)]}$$

$$a_2^* = \beta b_2^*$$

And

$$C = \frac{E_{ground} r_0 \left(1-\nu_{liner}{}^2\right)}{E_{liner} t \left(1-\nu_{ground}{}^2\right)} \quad ; \quad F = \frac{E_{ground} r_0{}^3 \left(1-\nu_{liner}{}^2\right)}{E_{liner}\left(\frac{t^3}{12}\right)\left(1-\nu_{ground}{}^2\right)}$$

For the liner:

$$\frac{T}{\sigma_{yy,ff} r_0} = \frac{1}{2}(1+K_{xy})(1-a_0^*)+\frac{1}{2}(1-K_{xy})(1+2a_2^*)\cos 2\theta$$

$$\frac{M}{\sigma_{yy,ff} r_0{}^2} = \frac{1}{4}(1-K_{xy})(1-2a_2^*+2b_2^*)\cos 2\theta$$

Acknowledgments

The research is being partially supported by the research funding agency of Brazilian government CNPq ("Conselho Nacional de Desenvolvimento Cientifico"). The authors acknowledge the support from CNPq and also Midas company, which kindly provided the license of Midas GTX NX software, used in the present work.

5.9 References

Bentz, E. C. (2000). *Sectional analysis of reinforced concrete members*. PhD thesis, Department of Civil Engineering,University of Toronto, Toronto, CA.

Bobet, A. (2001). Analytical Solutions for Shallow Tunnels in Saturated Ground. *Journal of Engineering Mechanics*. https://doi.org/10.1061/(ASCE)0733-9399(2001)127:12(1258)

Bobet, A. (2003). Effect of pore water pressure on tunnel support during static and seismic loading. *Tunnelling and Underground Space Technology*, *18*(4), 377–393. https://doi.org/10.1016/S0886-7798(03)00008-7

Bobet, A. (2011). Lined circular tunnels in elastic transversely anisotropic rock at depth. *Rock Mechanics and Rock Engineering*, *44*(2), 149–167. https://doi.org/10.1007/s00603-010-0118-1

Bobet, A. (2016a). Deep Tunnel in Transversely Anisotropic Rock: Complementary Solutions. *Rock Mechanics and Rock Engineering*, *49*(12), 3817–3822. https://doi.org/DOI 10.1007/s00603-016-0942-z

Bobet, A. (2016b). Deep Tunnel in Transversely Anisotropic Rock with Groundwater Flow. *Rock Mechanics and Rock Engineering*, *49*(12), 4817–4832. https://doi.org/10.1007/s00603-016-1118-6

Bobet, A., & Yu, H. (2016). Full stress and displacement fields for steel-lined deep pressure tunnels in transversely anisotropic rock. *Tunnelling and Underground Space Technology*, *56*, 125–135. https://doi.org/10.1016/j.tust.2016.03.005

Brady, B. H. G., & Brown, E. T. (2006). *Rock Mechanics for underground mining: Third edition*. *Rock Mechanics for underground mining: Third edition*. https://doi.org/10.1007/978-1-4020-2116-9

Carranza-Torres, C. (2004). Elasto-plastic solution of tunnel problems using the generalized form of the Hoek-Brown failure criterion. *International Journal of Rock Mechanics and Mining Sciences*, *41*(SUPPL. 1), 1–11. https://doi.org/10.1016/j.ijrmms.2004.03.111

Chou, W. I., & Bobet, A. (2002). Predictions of ground deformations in shallow tunnels in clay. *Tunnelling and Underground Space Technology*, *17*(1), 3–19. https://doi.org/10.1016/S0886-7798(01)00068-2

Einstein, H., & Schwartz, C. (1979). Simplified analysis for tunnel supports. *ASCE J Geotech Eng Div*, *105*(GT4), 499–518.

Goodman, R. E. (1989). *Introduction to rock mechanics*. https://doi.org/10.1016/0148-9062(81)90521-0

Gysel, M. (1975). In-Situ stress measurements of the primary stress state in the Sonnenberg tunnel in Lucerne, Switzerland. *Developments in Geotectonics*, *9*(C), 301–314. https://doi.org/10.1016/B978-0-444-41420-5.50036-8

Hefny, A. M., & Lo, K. Y. (1999). Analytical solutions for stresses and displacements around tunnels driven in cross-anisotropic rocks. *International Journal for Numerical and Analytical Methods in Geomechanics*, *23*(2), 161–177. https://doi.org/10.1002/(SICI)1096-9853(199902)23:2<161::AID-NAG963>3.0.CO;2-B

Hoek, E. (2008). *Practical Rock Engineering*. https://doi.org/10.2113/gseegeosci.14.1.55

Hoek, E., Carranza-Torres, C., Diederichs, M., & Corkum, B. (2008). Integration of geotechnical and structural design in tunneling. In *The 2008 Kersten Lecture, Proceedings University of Minnesota 56th Annual Geotechnical Engineering Conference* (pp. 1–53).

Jaeger, J. C., Cook, N. G. W., & Zimmerman, R. W. (2007). *Fundamentals of Rock Mechanics Fourth Edition*. *Rock Mechanics*. https://doi.org/10.1016/0040-1951(77)90223-2

Kirsch, G. (1898). Die theorie der elastizitat und die bedurfnisse der festigkeitslehre. *Veit. Ver. Deut. Ing.*, *42*, 497–807.

Ledesma, A., & Alonso, E. E. (2017). Protecting sensitive constructions from tunnelling: the case of World Heritage buildings in Barcelona. *Géotechnique*, (10), 1–12. https://doi.org/10.1680/jgeot.SiP17.P.155

Massinas, S. A., & Sakellariou, M. G. (2009). Closed-form solution for plastic zone formation around a circular tunnel in half-space obeying Mohr–Coulomb criterion. *Géotechnique*, *59*(8), 691–701. https://doi.org/10.1680/geot.8.069

McGarr, a, & Gay, N. C. (1978). State of Stress in the Earth's Crust. *Ann. Rev. Earth Planet. Sci.*, *6*, 405–436.

Park, K. H. (2005). Analytical solution for tunnelling-induced ground movement in clays. *Tunnelling and Underground Space Technology*, *20*(3), 249–261. https://doi.org/10.1016/j.tust.2004.08.009

Pinto, F., & Whittle, A. J. (2014). Ground Movements due to Shallow Tunnels in Soft Ground. I: Analytical Solutions. *Journal of Geotechnical and Geoenvironmental Engineering*, *140*(4), 4013040. https://doi.org/10.1061/(ASCE)GT.1943-5606.0000948

Pinto, F., Zymnis, D. M., & Whittle, A. J. (2014). Ground Movements due to Shallow Tunnels in Soft Ground. II: Analytical Interpretation and Prediction. *Journal of Geotechnical and Geoenvironmental Engineering*, *140*(4), 4013041. https://doi.org/10.1061/(ASCE)GT.1943-5606.0000947

Salesçon, J. (1969). Contraction Quasi-Statique D'une Cavite a Symetrie Spherique Ou Cylindrique Dans Un Milieu Elasto-Plastique. In *Annales Des Ports Et Chaussees* (Vol. 4, pp. 231–236).

Sharan, S. K. (2003). Elastic-brittle-plastic analysis of circular openings in Hoek-Brown media. *International Journal of Rock Mechanics and Mining Sciences*, *40*(6), 817–824. https://doi.org/10.1016/S1365-1609(03)00040-6

Sharan, S. K. (2005). Exact and approximate solutions for displacements around circular openings in elastic-brittle-plastic Hoek-Brown rock. *International Journal of Rock Mechanics and Mining Sciences*, *42*(4), 542–549. https://doi.org/10.1016/j.ijrmms.2005.03.019

Strack, O. E., & Verruijt, A. (2002). A complex variable solution for a deforming buoyant tunnel in a heavy elastic half-plane. *International Journal for Numerical and Analytical Methods in Geomechanics*, *26*(12), 1235–1252. https://doi.org/10.1002/nag.246

Verruijt, A., & Booker, J. R. (1996). Surface settlements due to deformation of a tunnel in an elastic half plane. *Géotechnique*, *46*(4), 753–756. https://doi.org/10.1680/geot.1998.48.5.709

Verruijt, a. (1997). A complex variable solution for a deforming circular tunnel in an elastic half-plane. *International Journal for Numerical and Analytical Methods in Geomechanics*, *21*(2), 77–89. https://doi.org/10.1002/(SICI)1096-9853(199702)21:2<77::AID-NAG857>3.0.CO;2-M

Vitali, O. P. M., Celestino, T., & Bobet, A. (2017). 3D finite element modelling optimization for deep tunnels with material nonlinearity. *Underground Space*. https://doi.org/10.1016/j.undsp.2017.11.002

Wang, H. N., Li, Y., Ni, Q., Utili, S., Jiang, M. J., & Liu, F. (2013). Analytical solutions for the construction of deeply buried circular tunnels with two liners in rheological rock. *Rock Mechanics and Rock Engineering*, *46*(6), 1481–1498. https://doi.org/10.1007/s00603-012-0362-7

Wang, H. N., Utili, S., Jiang, M. J., & He, P. (2015). Analytical Solutions for Tunnels of Elliptical Cross-Section in Rheological Rock Accounting for Sequential Excavation. *Rock Mechanics and Rock Engineering*, *48*(5), 1997–2029. https://doi.org/10.1007/s00603-014-0685-7

Wang, H. N., Zeng, G. S., Utili, S., Jiang, M. J., & Wu, L. (2017). Analytical solutions of stresses and displacements for deeply buried twin tunnels in viscoelastic rock. *International Journal of Rock Mechanics and Mining Sciences*, *93*, 13–29. https://doi.org/10.1016/j.ijrmms.2017.01.002

Zhang, Z., & Sun, Y. (2011). Analytical solution for a deep tunnel with arbitrary cross section in a transversely isotropic rock mass. *International Journal of Rock Mechanics and Mining Sciences*, *48*(8), 1359–1363. https://doi.org/10.1016/j.ijrmms.2011.10.001

6. SHALLOW TUNNEL NOT ALIGNED WITH THE GEOSTATIC PRINCIPAL STRESS DIRECTIONS

VITALI, O. P. M.; CELESTINO, & BOBET, A. (2019). Shallow tunnel not aligned with the geostatic principal stress directions. In: Proceedings of *Geo-Congress2019*, GSP 313:214-222. https://ascelibrary.org/doi/10.1061/9780784482155.023

Abstract

Despite the well-known stress anisotropy that may be present in rock masses, tunnel design is often done with the assumption that the tunnel is aligned with one of the geostatic principal stress directions. However, this alignment is improbable and so axial shear stresses may be unintentionally neglected. These shear stresses distort the tunnel cross-section in the axial direction, which is not accounted for in 2D analyses. In this paper, the effects of axial shear stresses on shallow tunnels misaligned with the principal in-situ stress directions are assessed. 3D FEM models are conducted for that purpose and the results are compared with 2D plane strain models, often used in practice. Two scenarios are studied: competent rock mass, which behaves as a linear-elastic material, and soft ground, which undergoes plastic deformations. For soft ground, the axial stresses increase the size and change the shape of the plastic zone around the tunnel, thus inducing larger ground deformations.

6.1 Introduction

Tunnel design usually disregards the tunnel orientation with the geostatic principal stress directions despite the well-known fact that stress anisotropy often occurs in rock masses. For instance, the convergence-confinement method and 2D plane strain analysis, which are commonly used in tunnel design, assume that the tunnel is aligned with one of the geostatic principal stress directions.

The importance of tunnel orientation with respect to the existing stress field is well-recognized in the literature for cavern design. For instance, it is common practice, as recommended by Goodman (1989), to align the cavern with the major principal stress direction and choose the shape of the cavity cross-section such that stress concentrations are minimized. However, in civil engineering, the tunnel direction is normally pre-determined due to other considerations and so

design should consider the tunnel misalignment with respect to the principal directions of the geostatic stresses.

The literature shows that a highly anisotropic stress field may be present in rock masses. Brown & Hoek (1978) compiled a large amount of data across the world and showed that the vertical stresses (σ_v) follow a quasi-linear trend with depth (z), in which the line σ_v (MPa) = 0.027z (m) fits relatively well the data and recommended to use this relation to estimate the vertical stress. They also found that the stress ratio K ($\sigma_{h,average}/\ \sigma_v$) varied significantly with depth, with values larger than one. That is, the horizontal stresses were larger than the vertical stresses. Jaeger et al. (2007) observed that for depths shallower than 300m, the scatter of the K value was large and ranged between 1 to 4, but below 2,000 m, the range was narrow, with values often smaller than one. The large scatter of K observed close to the surface was associated with topography (Brady & Brown, 2006; Goodman, 1989; Hoek, 2008; Jaeger et al., 2007). However, large horizontal stresses can also be caused by tectonic movements. Haimson et al. (2003) and Park et al. (2014) conducted hydraulic tests at shallow depths on granitic and gneissic rock masses in South Korea, near Seoul, in an active seismic area. The measured horizontal stresses were consistently larger than the vertical stresses at shallow depths. The data also showed a remarked horizontal stress anisotropy. This horizontal stress anisotropy is consistent with observations by other authors. According to Brady & Brown (2006), the major horizontal stress (σ_H) and the minor horizontal stress (σ_h) rarely have the same magnitude. McGarr & Gay (1978) compiled data of the in-situ stresses for 77 different sites and found average values: σ_1/σ_2=1.45±0.80; σ_1/σ_3=2.42±2.28; and σ_2/σ_3=1.66±1.0. Read & Martin (1992) also reported a highly anisotropic stress field in a massive granitic rock mass in Canada. The average stresses were: σ_1/σ_2=1.15±0.1; σ_1/σ_3=3.93±0.5; and σ_2/σ_3=3.43±0.5. Because of the complexity and variability of the in-situ stresses in rock, Hoek (2008) recommended to measure the in-situ stress field for the design of underground structures in rock masses.

Clearly, given the large stress anisotropy that may be present in the ground, its effects on the tunnel should be considered. Deep tunnels not aligned with the principal stress directions have been investigated by Vitali et al. (2018). The authors observed that, if the ground has linear-elastic behavior, the 3D stress and displacement fields can be calculated analytically by adding the solutions for stresses acting normal and parallel to the tunnel axis. The authors suggested the use of the traditional Kirsch solution for unsupported tunnels and the Einstein-Schwartz solution

(Einstein & Schwartz, 1979) for supported tunnels to account for the stresses normal to the tunnel, i.e. vertical and horizontal stresses. To account for the tunnel misalignment with the principal directions of the geostatic stresses; that is, to include the axial shear stresses (τ_{xz}), the authors proposed an analytical solution for both supported and unsupported tunnels.

For shallow tunnels, given that stress anisotropy may be present and that it is unlikely that the tunnel aligns with one of the principal stress directions, consideration must be given to the potential effects on tunnel behavior that arise due to the presence of axial shear stresses. This paper investigates the influence of shallow tunnel misalignment with the principal stress directions. 3D FEM models have been conducted and the results compared with those from 2D plane strain models that neglect the influence of the axial shear stresses.

6.2 Effect of misalignment

FEM models of a shallow tunnel not aligned with the principal stress directions have been completed. See Figure 6.1Figure 6.1. The tunnel makes an angle α with the major horizontal stress, σ_H, as indicated in Figure 6.1. The angles α assessed are 0°, 15°, 30°, 45°, 60° 75° and 90°, where α= 0° represents a tunnel parallel to the major horizontal stress, σ_H, and α=90°, parallel to the minor horizontal stress, σ_h. In the figure, the y-axis is vertical, the z-axis is aligned with the axis of the tunnel and the x-axis is perpendicular to the tunnel cross section. Thus, σ_{xx} is the horizontal stress perpendicular to the tunnel axis, σ_{zz} is the axial stress and τ_{xz} is the axial shear stress. It is assumed that the vertical stress is a principal stress $\sigma_v=\sigma_{yy}$.

The models have a transitional mesh from the boundaries to a structured mesh refined at the center of the model. The mesh at the center of the model uses 2nd order hexahedron elements. This mesh ensures the accuracy of the numerical results even for high material nonlinearity (Vitali et al., 2017). The tunnel is circular with 5m radius (r_0). The tunnel centerline is 25m below the surface (2 tunnel diameters of overburden) and 40m above the bottom boundary. The simulations consist of three phases: the first phase generates the in-situ stresses based on the *K_0-procedure* (Midas, 2014); the second phase is a null stage, to balance the in-situ stresses generated during the first phase; and the third phase simulates the full excavation of the tunnel.

The anisotropic in-situ stress adopted for the numerical analyses is based on Park et al. (2014) measurements of horizontal stresses. The in-situ stresses are presented in Figure 6.2. The data are bound by the minor horizontal stress equal to the vertical stress, σ_v (MPa)=0.027z (m),

and the major horizontal stress, four times larger than the vertical stress. Figure 6.3 shows the in-situ stress ratios for each angle α. As the tunnel rotates from 0° to 90°, the in-situ horizontal stresses (σ_{xx}) increase and the axial stresses (σ_{zz}) decrease. The in-situ axial shear stress (τ_{xz}) is maximum for α=45° and is zero when the tunnel is aligned with one of the principal stresses.

The analyses are carried out considering credible strength parameters for gneissic rock. The first series of the simulations is done assuming that the rock is linear elastic and obeys the Mohr Coulomb failure criterion, with a non-associated flow rule (ψ=0°). They are: E= 10GPa, v= 0.2, c= 10MPa and ϕ= 50°. The results from 3D models are compared with 2D plane strain models. Figure 6.4 shows the tunnel convergence at the springline (horizontal) and at the crown/invert (vertical), obtained with the 3D and 2D models. The convergence from both models is identical. Since the ground has large strength, there is no yield around the opening and the ground behaves within its elastic regime. The axial stresses do not affect tunnel convergence, as observed also by Vitali et al. (2018) for deep tunnels.

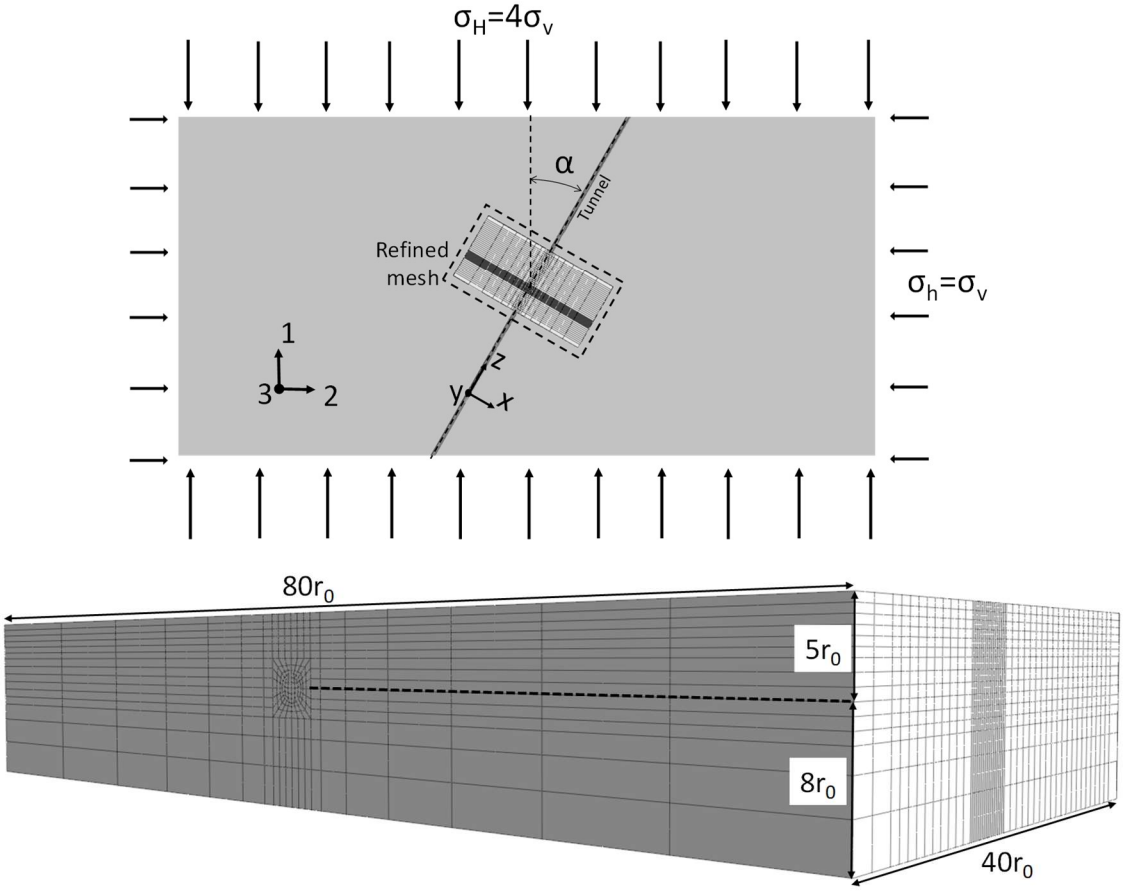

Figure 6.1 FEM model of a tunnel not aligned with the principal stress directions. Plan view and refined mesh at the center of the model. r_0 is the tunnel radius, 5m.

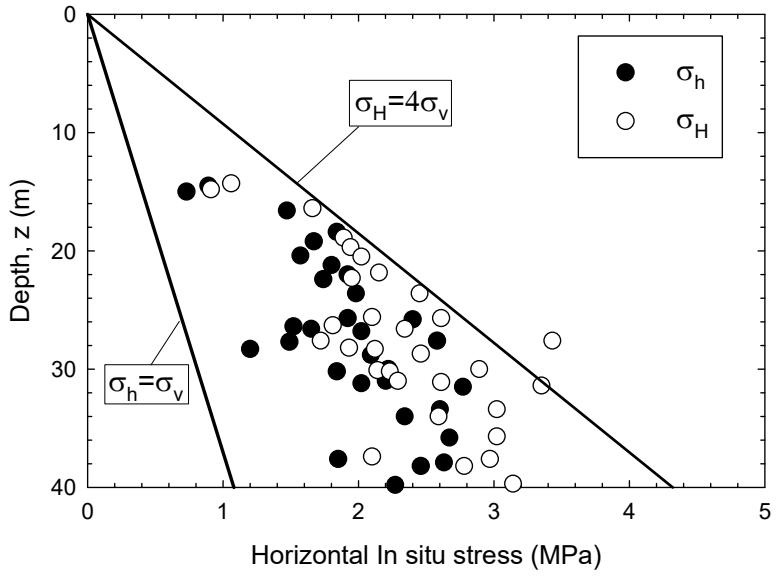

Figure 6.2 Horizontal stresses near the surface (data from Park et al. 2014).

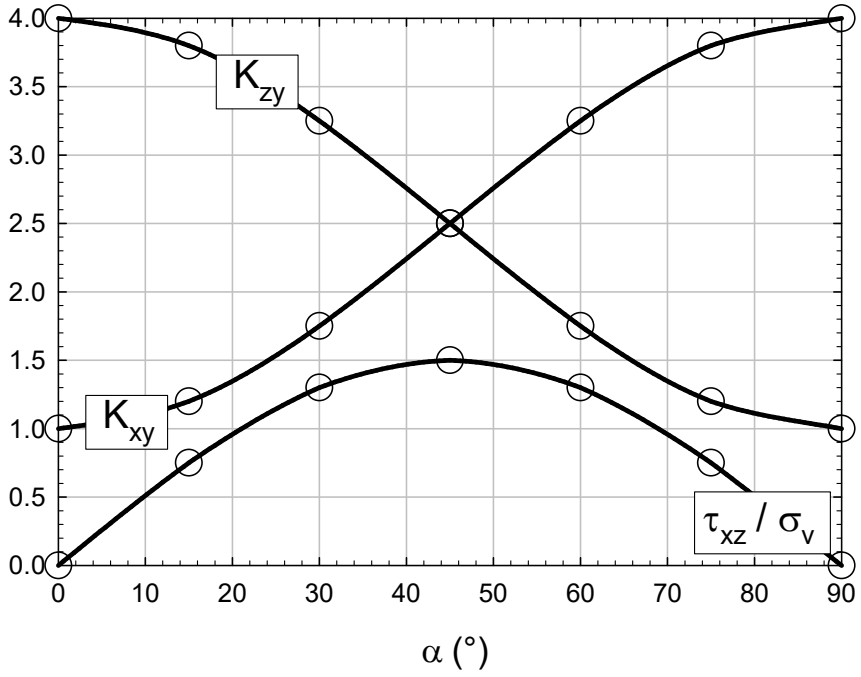

Figure 6.3 In-situ stress ratios normal and parallel to the tunnel. $K_{xy}=\sigma_{xx}/\sigma_v$; $K_{zy}=\sigma_{zz}/\sigma_v$.

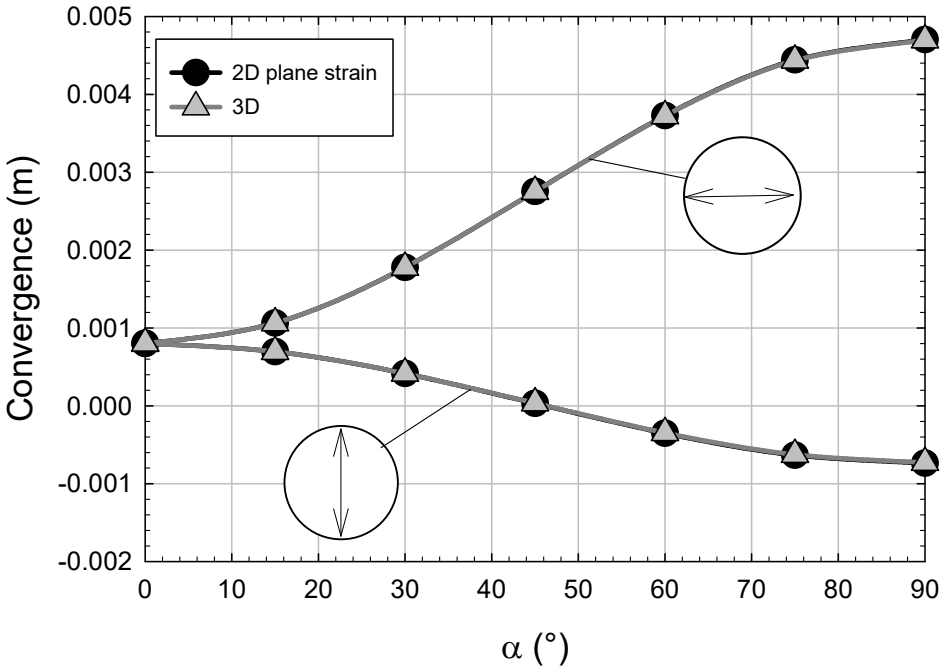

Figure 6.4 Tunnel convergence from 3D and 2D plane strain models, for linear-elastic ground. Positive convergence is inwards.

However, the 2D plane strain models do not provide the axial displacements or the axial shear stresses. Figure 6.5 shows the axial displacements and the axial shear stresses for α=45°. Note that the axial shear stresses are maximum over the crown and below the invert and zero at the springline (because of the unsupported opening). The axial displacements are anti-symmetric with respect to the tunnel vertical axis. They are maximum at the springline and zero at the crown and invert.

To investigate the influence of the tunnel alignment in soft ground, a second series of analyses is carried out considering: E= 1GPa, v= 0.2, c= 100kPa and ϕ= 45°. Figure 6.6 shows the tunnel convergence obtained from 3D and 2D plane strain models. Two types of 3D simulations are run: (1) full geostatic stress field (3D); and (2) no axial shear stress (3D, no axial shear). This is done to investigate the relative importance of the in-situ axial normal stress (σ_{zz}) and of the in-situ axial shear stresses (τ_{xz}). Note that a plane strain condition assumes zero axial strains. The magnitude of the tunnel convergence predicted by the 3D models is consistently larger than that predicted by the 2D plane strain model. This is due to a combination of effects not properly addressed (the effect of the axial stress) or not addressed at all (the effect of the axial shear stress) by the 2D model. Figure 6.7 shows the plastic zone around the tunnel for α=0°. The volume of

yielded rock extends up to a radial distance of about 11.3m for the 3D model and 5.5m for the 2D model. Figure 6.8 shows the plastic zone around the tunnel for α=45°. The yield zone extends to 14.2m for the 3D model and 9.3m for the 2D plane strain model. The plastic zone is consistently larger on the 3D models than on the 2D models (except for the α=90° case). As a consequence of the larger plastic deformations, the ground movements from the 3D models are larger than the 2D model.

The horizontal convergence (at the springline) increases as the tunnel rotates from being aligned with σ_H, (α=0°) to σ_h (α=90°). It is interesting to note that the differences between 3D and 2D decrease as the rotation, i.e. as the angle α, increases. The largest difference between the 3D and 2D horizontal convergence occurs at α=0°, where that of the 3D model is 2.7 times larger than of the 2D model. The differences are negligible at α=90°. The discrepancies are due to the axial stress (τ_{xz}=0 for α=0° and 90°); for α=0°, the in-situ axial stress is maximum ($\sigma_{zz}=4\sigma_v$ or K_{zy}=4) and for α=90°, it is minimum ($\sigma_{zz}=4\sigma_v$ or K_{zy}= 1). Thus, the maximum shear, as a difference between the vertical and horizontal stress, acts in the axial plane for α=0° and in the plane perpendicular to the tunnel axis for α=90°. The effects of the axial shear stress are noticeable when the tunnel is not aligned with one of the geostatic principal stresses (compare 3D and 3D with no axial shear), and are the largest at about α=45°. This is the result of the axial stresses having an impact on the yielding of the rock around the opening. Figure 6.8 provides a comparison of the size of the plastic zone around the tunnel between the 2D and the 3D simulations, for α=45°. As one can see, the effect of the axial shear on the size of the rock yielded is quite important. As a result, the plastic deformations in the 3D model are larger, and thus the tunnel convergence is also larger.

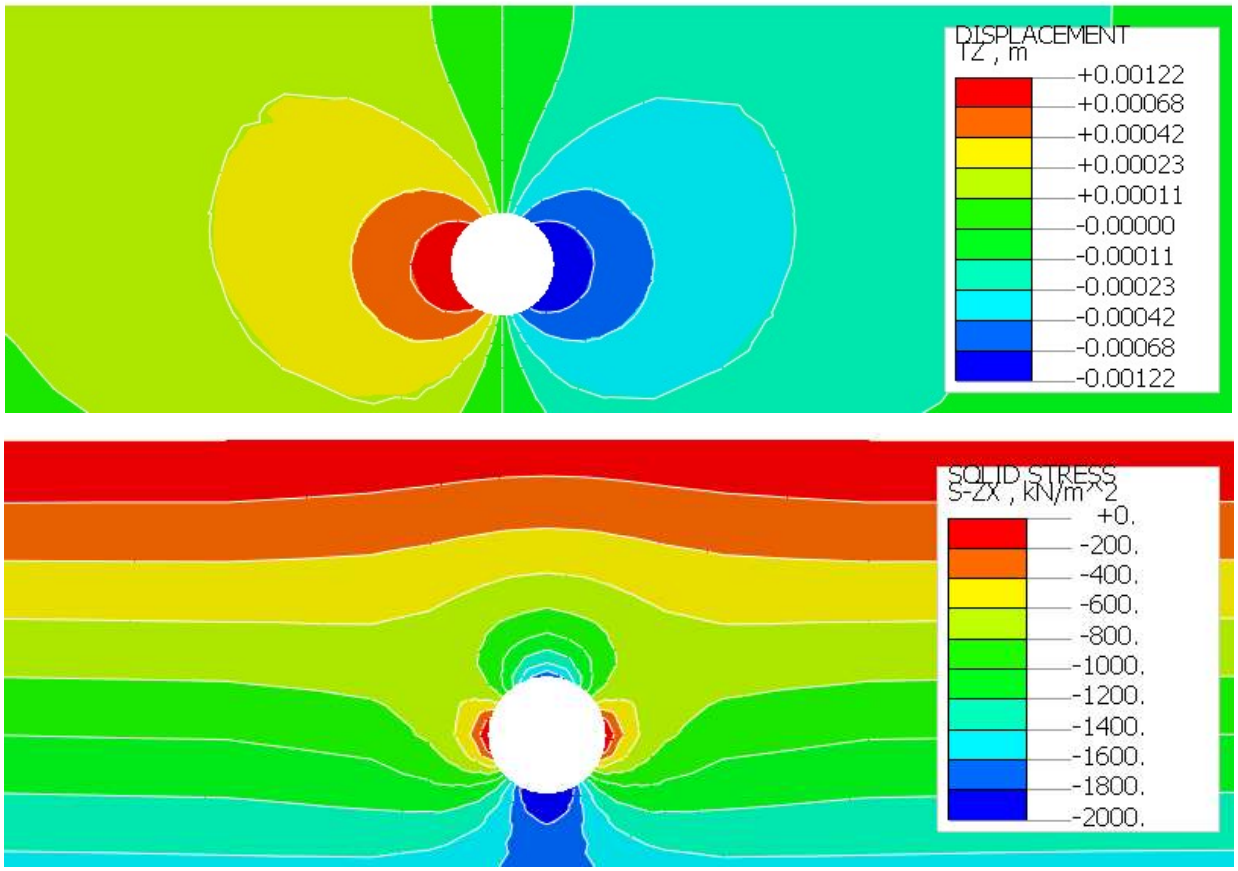

Figure 6.5 Axial displacements and axial shear stresses for α=45° for linear elastic ground.

The convergence between the crown and invert displays a complex evolution with α. However, the trends discussed, namely: (1) larger convergence for the 3D than the 2D models; (2) larger differences at α<45° and smallest at α=90°; (3) effects of the axial shear stress increasing with α, still apply. It is interesting to note that the vertical convergence is not the largest when the tunnel is aligned with the minor horizontal stress (α=90°), as one could expect. The plastic zone for α=90° is shown in Figure 6.9. The plastic zone over the crown and below the invert is larger for α=45° (Figure 6.8b) and for α=0° (Figure 6.7b) than for α=90° (Figure 6.9), which may explain the trend of the vertical convergence shown in Figure 6.6b.

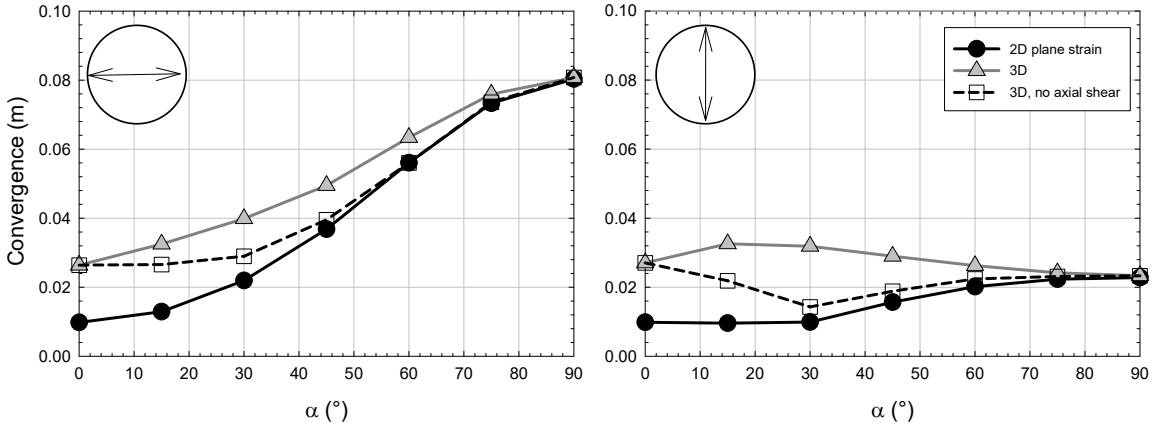

Figure 6.6 Tunnel convergence from 3D and 2D plane strain models, for soft ground. Positive convergence is inwards.

Figure 6.7 Plastic zone for α=0° from: (a) 2D plane strain; and (b) 3D models.

Figure 6.8 Plastic zone for α=45° from: (a) 2D plane strain; and (b) 3D models.

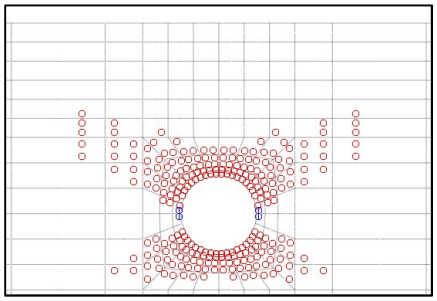

Figure 6.9 Plastic zone for α=90°.

The size of the plastic zone around the tunnel also affects the axial displacements. Figure 6.10 shows the axial displacements with α for the linear-elastic and for the soft ground. When the ground is elastic (Figure 6.10a), the axial displacements are proportional to the in-situ axial shear stress (τ_{xz}). When the ground is soft (Figure 6.10b), the plot of the axial displacements is not symmetric. In fact, axial displacements are comparatively larger when α>45° than the corresponding values of α when α<45°. This is due to the development of the plastic zone around the tunnel, which changes with the tunnel alignment, due to the changes of the axial and horizontal stresses.

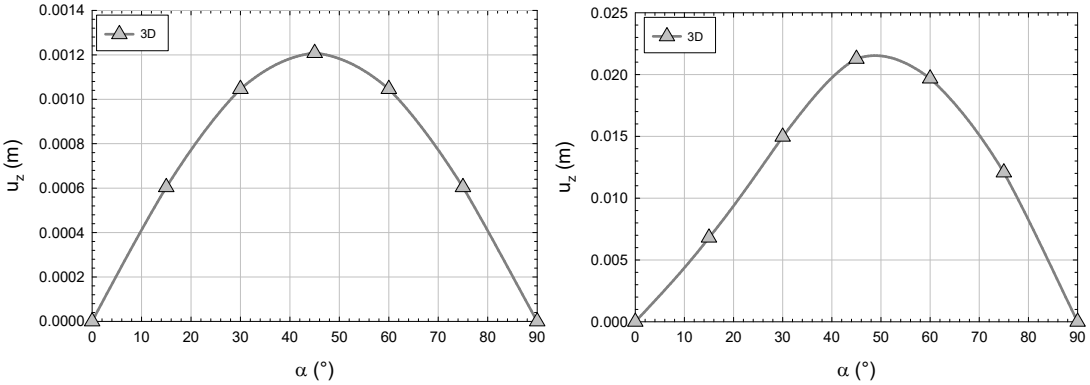

Figure 6.10 Axial displacements at the springline with α for: (a) linear elastic; and (b) soft ground.

6.3 Conclusion

Significant geostatic stress anisotropy may be expected in rock masses, especially close to the surface. Thus, alignment of a tunnel with one of the geostatic principal stresses is unlikely. The effects on shallow tunnels of the misalignment of the tunnel axis with respect to the in-situ principal stress directions are investigated in this paper. The in-situ stress field determined by Park et al. (2014) in a gneissic rock is taken as reference for the study. Two scenarios are explored. The first scenario assumes the properties of competent gneiss, while the second considers the properties of soft ground. In the first scenario, no yielding occurs around the tunnel. As a consequence, the axial stresses do not affect tunnel convergence and results from 2D, plane strain models, are comparable to those from 3D models, except for the axial deformations of the tunnel cross section. Those are the result of the presence of axial shear stresses that appear when the tunnel is not aligned with the principal geostatic stresses.

When the tunnel is excavated in soft ground, the tunnel convergence obtained with 3D models is consistently larger than that obtained with 2D plane strain models. The reason for this is that the 2D models do not capture the actual axial and axial shear stresses. Those contribute to increase the size of the yield zone around the tunnel with respect to that from 2D analyses. Therefore, 2D plane strain analysis may underpredict ground movements. The largest mismatch in terms of axial stresses occurs when the tunnel is aligned with the maximum or minimum horizontal geostatic stresses, and the largest mismatch in terms of axial shear stresses is when the tunnel is at 45° with one of the horizontal principal geostatic stresses.

The results shown highlight the importance of considering the actual alignment of the tunnel with the geostatic stress field. It also underscores the necessity of performing 3D modeling of tunnels, in particular when yielding of the ground may occur.

Acknowledgements

The research is being partially supported by the research funding agency of Brazilian government CNPq ("Conselho Nacional de Desenvolvimento Cientifico"). The authors acknowledge the support from CNPq and also Midas company, which kindly provided the license of Midas GTX NX software, used in the present work.

6.4 References

Brady, B. H. G., & Brown, E. T. (2006). *Rock Mechanics for underground mining*: Third edition. https://doi.org/10.1007/978-1-4020-2116-9

Brown, E. T., & Hoek, E. (1978). Trends in relationships between measured in-situ stresses and depth. *International Journal of Rock Mechanics and Mining Sciences* And, 15(4), 211–215. https://doi.org/10.1016/0148-9062(78)91227-5

Einstein, H., & Schwartz, C. (1979). Simplified analysis for tunnel supports. *ASCE J Geotech Eng Div*, 105(GT4), 499–518.

Goodman, R. E. (1989). *Introduction to rock mechanics*. https://doi.org/10.1016/0148-9062(81)90521-0

Haimson, B. C., Lee, M. Y., & Song, I. (2003). Shallow hydraulic fracturing measurements in Korea support tectonic and seismic indicators of regional stress. *International Journal of Rock Mechanics and Mining Sciences*, 40(7–8), 1243–1256. https://doi.org/10.1016/S1365-1609(03)00119-9

Hoek, E. (2008). *Practical Rock Engineering*. https://doi.org/10.2113/gseegeosci.14.1.55

Jaeger, J. C., Cook, N. G. W., & Zimmerman, R. W. (2007). *Fundamentals of Rock Mechanics* Fourth Edition. https://doi.org/10.1016/0040-1951(77)90223-2

McGarr, A, & Gay, N. C. (1978). State of Stress in the Earth's Crust. *Ann. Rev. Earth Planet. Sci*., 6, 405–436.

Midas Information Technology Co. (2014). *Benchmarks & Verification GTS NX manual*.

Park, E. S., Choi, B. H., Bae, S. H., & Jeon, S. (2014). Horizontal stresses at shallow depths in Seoul (Korea) gneissic region. Rock Engineering and Rock Mechanics: Structures in and on Rock Masses - *Proceedings of EUROCK 2014, ISRM European Regional Symposium*, 399–404.

Read, R., & Martin, C. D. (1992). Monitoring the excavation-induced response of granite. *The 33th U.S. Symposium on Rock Mechanics (USRMS)*, 10.

Vitali, O. P. M., Celestino, T. B., & Bobet, A. (2018). Analytical solution for tunnels not aligned with geostatic principal stress directions. *Tunnelling and Underground Space Technology*, 82(May), 394–405. https://doi.org/10.1016/j.tust.2018.08.046

Vitali, O. P. M., Celestino, T. B., Bobet, A., (2017). 3D finite element modelling optimization for deep tunnels with material nonlinearity. *Underground Space* 3 (2), 125–139. https://doi.org/10.1016/j.undsp.2017.11.002

7. SHALLOW TUNNEL MISALIGNED WITH GEOSTATIC PRINCIPAL STRESS DIRECTIONS: ANALYTICAL SOLUTION AND 3D FACE EFFECTS

VITALI, O. P. M.; CELESTINO, & BOBET, A. (2019). Shallow tunnels misaligned with geostatic principal stress directions: analytical solution and 3D face effects. *Tunnelling and Underground Space Technology*.89: 268-283. https://doi.org/10.1016/j.tust.2019.04.006

Abstract

Rock masses often present strong stress anisotropy, especially at shallow depths; thus, the alignment of a tunnel with one of the principal stress directions is unlikely. As a result, far-field out-of-plane shear stresses are present and, yet, their effects are often neglected in tunnel design because it is commonly assumed that the tunnel is aligned with one of the principal stress directions. The paper presents an analytical solution to determine the axial displacements and the axial shear stresses around shallow tunnels not aligned with the principal stresses in elastic ground, when subjected to a far-field shear stress. The analytical solution is developed using complex variable analysis and conformal mapping techniques to consider the presence of the ground surface. The analytical solution can be added to the Verruijt and Booker (2000) solution to determine the full 3D stress and displacement fields far-behind the face of unsupported shallow tunnels subjected to a general state of stress. In addition, 3D FEM models are conducted to investigate the effects of the far-field shear stress near the face of the tunnel. The far-field shear stress induces asymmetric ground deformations near the face, which remain far-behind the face when the tunnel is supported, and when the ground is elastoplastic.

7.1 Introduction

Tunnel design often neglects the effects of tunnel alignment with respect to the directions of the principal far-field stresses or the directions of material mechanical properties. However, rocks and soils may present strong in-situ stress and material anisotropy. There is lack of research on the effects of the tunnel's misalignment with far-field stresses, in spite the recognized importance of those effects. For instance, it is a well-known practical recommendation to align the direction of a cavern with the major horizontal principal stress to minimize stress concentrations

(Goodman, 1989). Also, Armand et al. (2013) present convergence measurements of tunnels constructed parallel and perpendicular to the major horizontal stress (σ_H), in an anisotropic claystone, that show that the ground deformation and the damage zone developed around the tunnel are heavily affected by tunnel orientation.

The literature is rich in examples of rock masses with remarked geostatic stress anisotropy, especially near the surface (Brown & Hoek, 1978; Evans et al., 1989; Martin & Kaiser, 1996; McGarr & Gay, 1978; Wileveau et al., 2007). The in-situ stresses compilation presented by Brown & Hoek (1978) clearly shows that such stress anisotropy is larger near the surface, most likely due to topographic effects (Brady & Brown, 2006; Goodman, 1989; Hoek, 2008) and tectonic activity (Haimson et al., 2003; Park et al., 2014). Residual soils inherit the rock matrix features and, therefore, may present stress anisotropy as well. In urban areas, buildings and excavations affect the stress field near the surface; thus, even isotropic ground may present stress anisotropy due to anthropogenic activities. Haimson et al. (2003) and Park et al. (2014) conducted hydraulic tests near the surface in Granitic and Gneissic rock masses in an active seismic area in South Korea. Figure 7.1 shows the principal stress ratios $K_{Hv}=\frac{\sigma_H}{\sigma_v}$ and $K_{hv}=\frac{\sigma_h}{\sigma_v}$ with depth. The horizontal stresses are consistently larger than the vertical stress at shallow depths and the major horizontal stress is larger than the minor horizontal stress; thus, it is probable that tunnels may not be aligned with one of the in-situ principal stress directions.

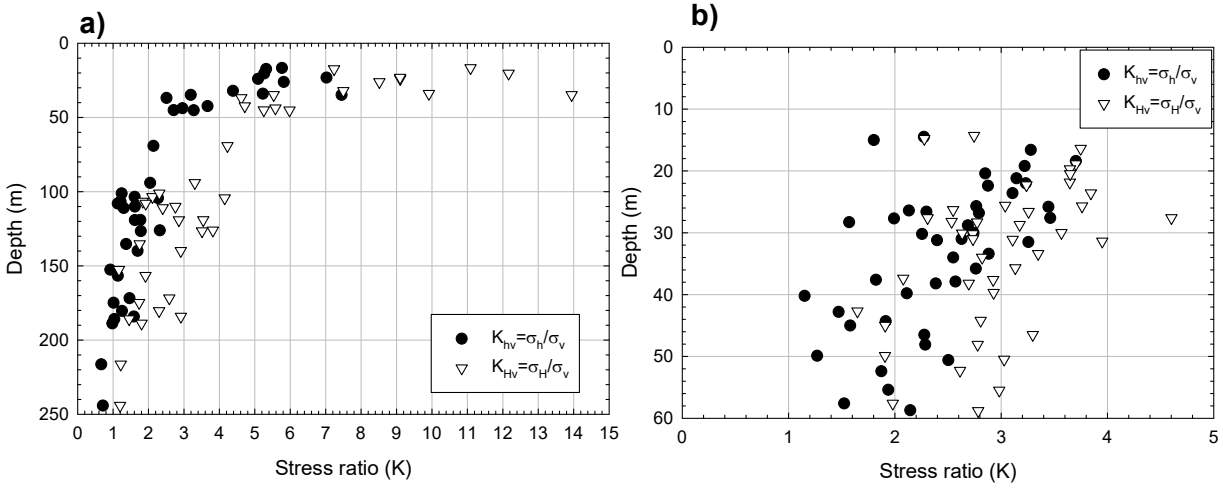

Figure 7.1 Stress ratios with depth reported by: (a) Haimson et al. (2003) in granitic rock mass; and (b) by Park et al. (2014) in gneissic rock mass.

Figure 7.2 illustrates a tunnel not aligned with the principal horizontal stresses (i.e. assuming that the vertical is one of the principal stress directions). The stress tensor can be rotated such that one of the axes of the coordinate system is parallel to the tunnel axis, as shown in Figure 7.3. As one can see, there is a far-field axial shear stress ($\tau_{xz,ff}$) that appears when the tunnel is not aligned with one of the horizontal principal stresses. The problem of an infinite opening in a general triaxial stress field was first addressed by Brady and Bray (1978). The authors extended the 2D plane strain stress problem to any orientation of the opening with respect to the triaxial stress field.

Deep tunnels, with their axis not parallel with one of the principal geostatic stresses, were studied by Vitali et al. (2018) and by Vitali et al. (2019b). The authors observed that, in elastic ground, $\tau_{xz,ff}$ causes axial displacements and stresses, but it does not affect stresses and displacements on the plane of the cross-section of the tunnel. In other words, the far-field stresses can be decomposed such that stresses and displacements in a plane perpendicular to the tunnel axis can be calculated without considering the axial stresses; thus, existing plane-strain analytical solutions can be used (Einstein & Schwartz, 1979; Kirsch, 1898). The axial shear stress and axial displacement fields for supported and unsupported deep tunnels were provided by Vitali et al. (2018). Thus, the 3D stress and displacement fields in the ground and in the liner, if present, can be determined analytically by adding the (existing) in-plane and (new) out-of-plane analytical solutions. This is possible because of the principle of superposition, valid for linear-elastic materials. In elastoplastic ground, such decomposition is not possible and Vitali et al. (2018) showed that $\tau_{xz,ff}$ strongly affected the ground deformations and the size and shape of the plastic zone around the tunnel.

Deep tunnels are simpler to analyze than shallow tunnels because one can assume that the boundaries are far from the tunnel and the far-field geostatic stresses are uniform (i.e. gravity loading may be neglected; Bobet, 2003). However, in shallow tunnels, the presence of the ground surface, as a stress boundary, and the increase of gravity loading with depth cannot be neglected. Thus, complex variable analysis and conformal mapping techniques may be needed to modify the geometry of the problem such that boundary conditions can be conveniently imposed (Strack & Verruijt, 2002; Verruijt, 1997; Verruijt & Booker, 2000). Verruijt & Booker (2000) re-addressed the Mindlin's tunnel problem using complex variable analysis and conformal mapping and provided an exact solution for stresses and displacements for an unsupported shallow tunnel in

isotropic elastic ground subjected to gravity and far-field horizontal stresses (defined by the ratio K between the horizontal and the vertical stress). An approximate solution for shallow supported tunnels subjected to water seepage was provided by Bobet (2001), which accounts for the mechanical effects induced by seepage forces.

Despite the simplified assumptions made for the analytical solutions, and more specifically the assumption of elasticity, ground deformations predicted are reliable if ground deformations are small, as shown in the work by Chou & Bobet (2002), Pinto et al. (2014) and Park et al. (2005), who provided comparisons between field data and settlement predictions from analytical solutions. Ledesma & Alonso (2017) also used analytical solutions to estimate ground deformations near sensitive historical structures in Barcelona and found that predictions were reasonably close to field measurements. Further, analytical solutions provide a fast assessment of tunnel behavior, and are very convenient for inexpensive parametric analysis. They can also be used to validate FEM models and can provide a first-order assessment of the problem, which can then be further investigated with sophisticated numerical models such as 3D FEM models.

In this paper, an analytical solution is presented to determine the axial shear stress and axial displacement fields for shallow tunnels not aligned with respect to the geostatic principal stresses. The solution, within the realm of elasticity, can be added to existing solutions that consider gravity loading and stresses on the plane perpendicular to the tunnel axis, e.g. Verruijt & Booker (2000), to obtain the full stress and displacement fields. The paper also investigates the near-face effects of the far-field axial shear ($\tau_{xz,ff}$) using 3D FEM models.

7.2 Analytical solution for shallow tunnels subjected to axial shear stresses

For the analysis, a circular shallow tunnel with depth h (distance between ground surface and tunnel centerline) and radius r_0 in a linear-elastic isotropic ground is considered. It is assumed that the vertical axis (y-direction) is a principal stress direction, that the principal horizontal stresses are σ_h (minor) and σ_H (major), and that the major horizontal stress (σ_H) makes an angle Ψ with the tunnel axis (z-direction), as illustrated in Figure 7.2. The principal stress tensor is rotated by an angle Ψ to have the stresses in the coordinate system (xyz), such that the axis z is parallel to the direction of the tunnel and the axis, x, perpendicular; note that the axis y remains unchanged and is vertical; see Figure 7.3. Equations (1) to (4) provide the rotated stresses.

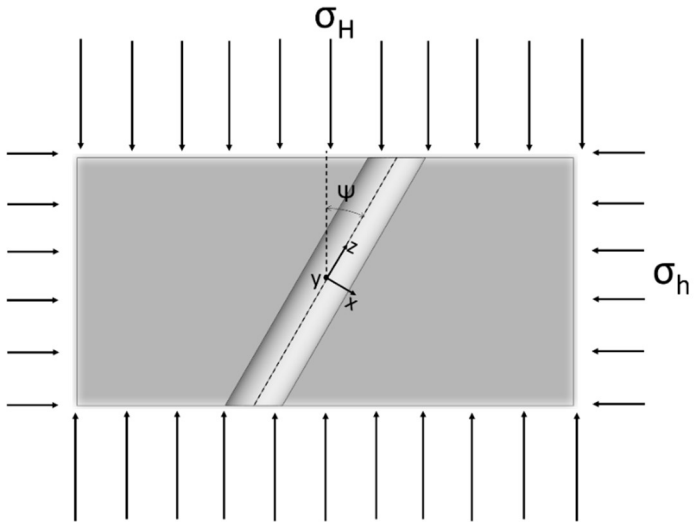

Figure 7.2 Tunnel axis direction with respect to the principal horizontal stresses.

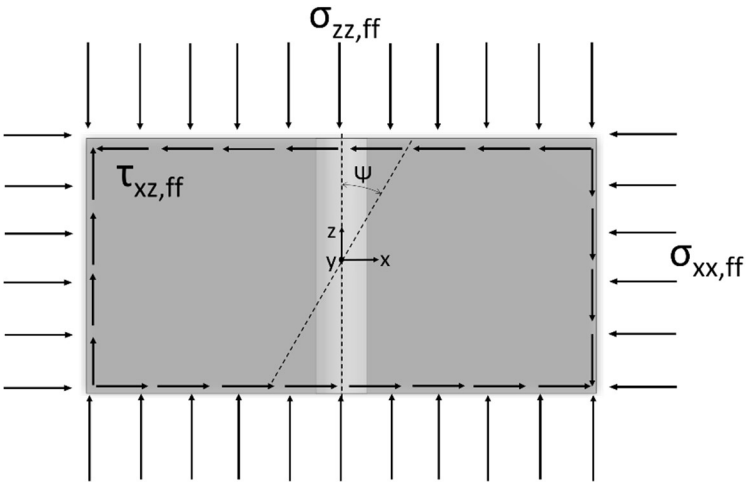

Figure 7.3 Tunnel axis aligned with the rotated stress tensor.

$$\sigma_{xx,ff} = \sin^2(\psi)\sigma_H + \cos^2(\psi)\sigma_h ; \quad (1)$$

$$\sigma_{yy,ff} = \sigma_v ; \quad (2)$$

$$\sigma_{zz,ff} = \cos^2(\psi)\sigma_H + \sin^2(\psi)\sigma_h ; \quad (3)$$

$$\tau_{xz,ff} = \frac{\sigma_H - \sigma_h}{2}\sin(2\psi) ; \quad (4)$$

Where $\sigma_{xx,ff}$ is the far-field horizontal stress; $\sigma_{zz,ff}$ is the far-field axial stress; $\sigma_{yy,ff}$ is the far-field vertical stress and; $\tau_{xz,ff}$ is the far-field axial shear stress. For a long tunnel (i.e. no face effects), the derivatives ($\partial/\partial z$) are zero, thus, the equilibrium equations ($\nabla \cdot \sigma + \vec{b} = 0$) are:

$$\frac{\partial \sigma_{xx}}{\partial x} + \frac{\partial \tau_{yx}}{\partial y} = 0 \tag{5}$$

$$\frac{\partial \tau_{xy}}{\partial x} + \frac{\partial \sigma_{yy}}{\partial y} = \gamma \tag{6}$$

$$\frac{\partial \tau_{xz}}{\partial x} + \frac{\partial \tau_{yz}}{\partial y} = 0 \tag{7}$$

Where γ is the unit weight of the ground. The shear stresses τ_{xz} and τ_{yz} only depend on the axial displacement w, given that $\partial w/\partial z = 0$, and can be expressed as:

$$\tau_{xz} = G \frac{\partial w}{\partial x} \tag{8}$$

$$\tau_{yz} = G \frac{\partial w}{\partial y} \tag{9}$$

Equations (5) and (6) describe equilibrium in the xy plane and are decoupled from equation (7). Also, equations (8) and (9) show that the axial shear stresses only produce axial displacements. Therefore, for long tunnels in linear elastic ground, the stresses σ_{xx}, σ_{yy} and τ_{xy}, on a plane perpendicular to the tunnel axis, and the axial shear stresses τ_{yz} and τ_{xz} can be analyzed independently. Further, the axial normal stress, σ_{zz}, is not present in the equilibrium equations (5) to (7) or in the strain-compatibility equations (given that $\partial w/\partial z = 0$); thus, σ_{zz} has no effect on long tunnels, given the problem described in Figure 7.2.

The problem illustrated in Figure 7.3 can be decoupled into two problems, as shown in Figure 7.4. Problem I represents the 2D plane strain scenario that includes gravity and the far-field stresses $\sigma_{xx,ff}$ and $\sigma_{yy,ff}$ (Figure 7.4a). Problem II includes the far-field axial shear stresses ($\tau_{xz,ff}$) (Figure 7.4 b). Note that the shear stresses increase with depth, as determined by equation (4). An exact solution for Problem I was provided by Verruijt & Booker (2000). The solution for problem II is presented in the following.

Equilibrium and compatibility for Problem II can be simultaneously satisfied by combining equations (8), (9) with (7); that is:

$$\frac{\partial^2 w}{\partial x^2} + \frac{\partial^2 w}{\partial y^2} = 0 \tag{10}$$

Problem II is divided in two problems, IIa and IIb (Figure 7.5). Problem IIa includes the geostatic stress field, but with no opening. Problem IIb includes the opening by imposing stresses

at the perimeter of the tunnel that are exactly the same, with opposite sign, as the stresses of Problem IIa, and zero stresses at all the boundaries. Thus, the addition of Problems IIa and IIb results in Problem II, as it should.

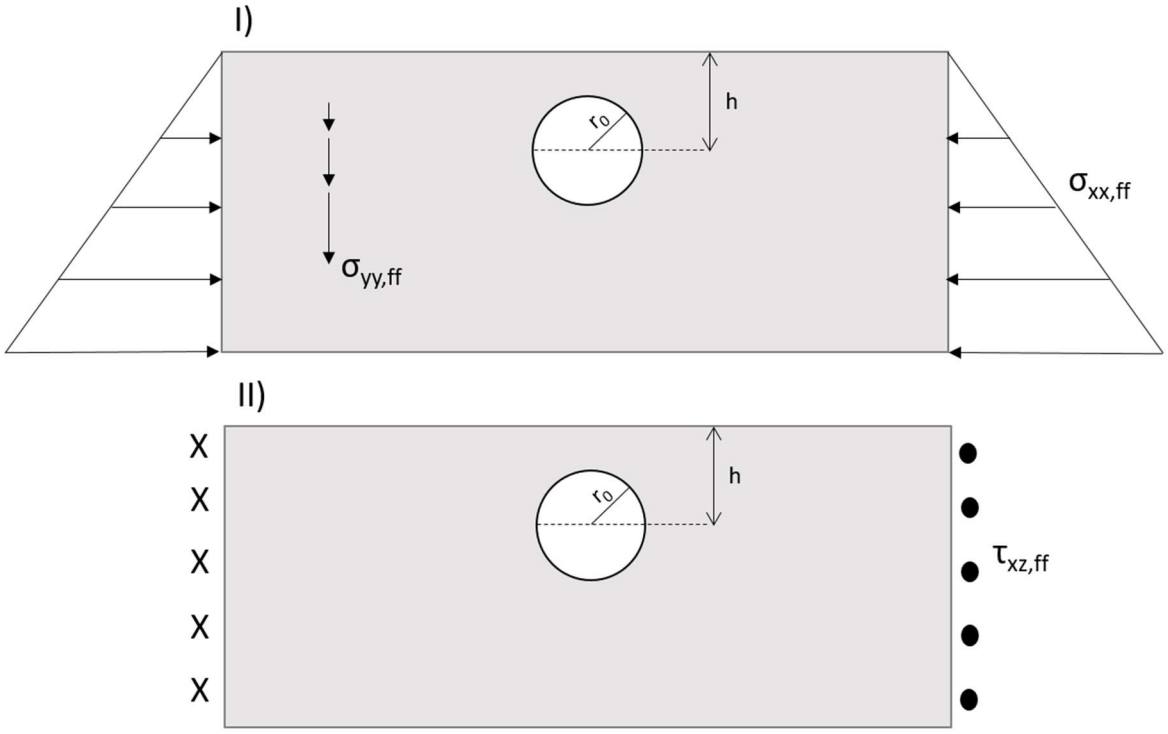

Figure 7.4 Decomposition of the 3D problem into: (I) Problem I and (II) Problem II.

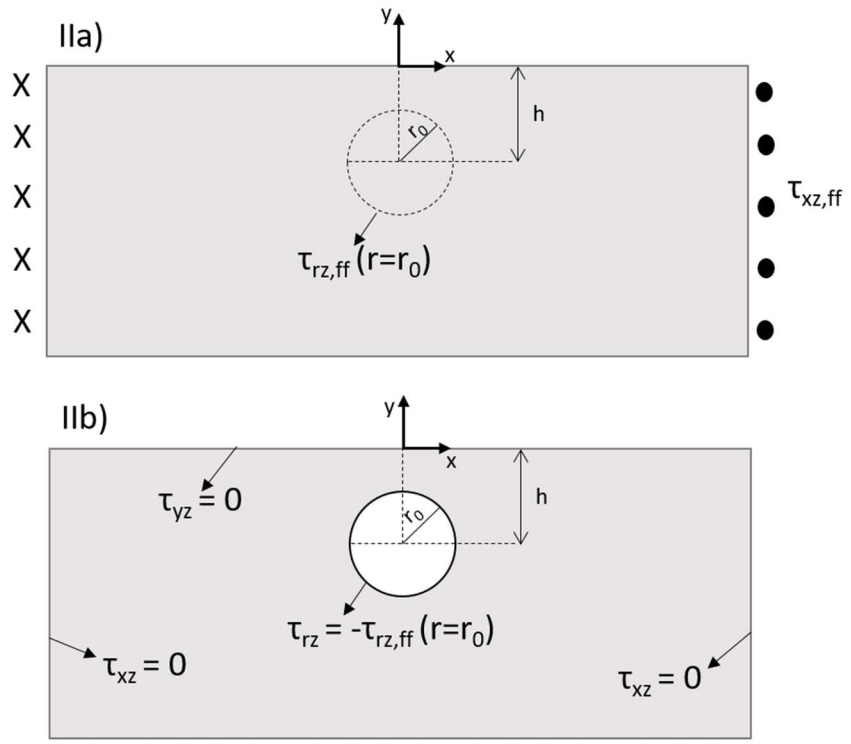

Figure 7.5 Decomposition of Problem II: (a) Problem IIa, far-field axial shear with no opening; and (b) Problem IIb, axial shear stresses at the perimeter of the tunnel only.

The solution of problem (IIa) is trivial: The axial shear stresses are given by $\tau_{xz}= \tau_{xz,\,ff}$. The solution of problem IIb requires satisfying equation (10) and the boundary conditions. All boundaries are free of stresses, except at the perimeter of the tunnel. Using polar coordinates with origin at the tunnel center (Figure 7.6),introducing the stress ratios $K_{Hv}=\frac{\sigma_H}{\sigma_v}$ and $K_{hv}=\frac{\sigma_h}{\sigma_v}$, and given that $\sigma_v=\gamma(-y)$; $\sigma_H=\sigma_{H0}+K_{Hv}\gamma(-y)$; $\sigma_h=\sigma_{h0}+K_{hv}\gamma(-y)$, the shear stress ($\tau_{rz}$) at the perimeter of the opening ($r=r_0$):

$$\tau_{rz} = p_1 \cos\theta + p_2 \sin\theta \tag{11}$$

where;

$$p_1 = -\frac{1}{2}\left[\sigma_H - \sigma_h + \gamma\left(K_{Hv} - K_{hv}\right)h\right]\sin\left(2\psi\right) \tag{12}$$

$$p_2 = \frac{1}{4}\gamma\left(K_{Hv} - K_{hv}\right)r_0 \sin\left(2\psi\right) \tag{13}$$

Equation (4) for the far-field axial shear stress ($\tau_{xz,ff}$) can be rewritten as:

$$\tau_{xz,ff} = \left(\frac{\gamma(-y)\left(K_{Hv} - K_{hv}\right)}{2} + \frac{\sigma_{H0} - \sigma_{h0}}{2} \right) \sin(2\psi) \tag{14}$$

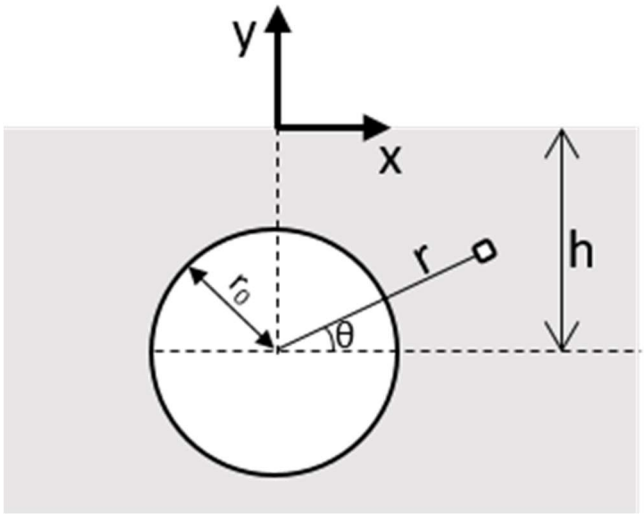

Figure 7.6 Coordinate systems. Polar coordinates with origin at the tunnel center, and Cartesian coordinates with origin at the ground surface above the tunnel.

Problem IIb is solved using complex analysis, in which the stress function is an analytic complex function. The boundary conditions are:

1) $x = \pm\infty \rightarrow \tau_{xz} = 0$ (15)

2) $y = 0 \rightarrow \tau_{yz} = 0$ (16)

3) $r = r_0 \rightarrow \tau_{rz} = -\left(p_1 \cos\theta + p_2 \sin\theta\right)$ (17)

A conformal mapping technique transforms the problem geometry to impose boundary conditions. Here, we follow the conformal mapping transformation used by Verruijt & Booker (2000). Given that $\Omega = x + iy$ and $\zeta = \xi + i\eta$, the conformal mapping function is:

$$\Omega = \omega(\zeta) = -ih \frac{1-\alpha^2}{1+\alpha^2} \frac{1+\zeta}{1-\zeta} \tag{18}$$

Where:

$$\alpha = \frac{h}{r_0} - \sqrt{\left(\frac{h}{r_0}\right)^2 - 1} \tag{19}$$

The inverse mapping is given by:

$$\zeta = \omega^{-1}(\Omega) = \frac{\left(1+\alpha^2\right)i\Omega - \left(1-\alpha^2\right)h}{\left(1+\alpha^2\right)i\Omega + \left(1-\alpha^2\right)h} \quad = \quad \rho\, cos\varphi + i\,\rho\, sin\varphi \tag{20}$$

Where ρ and φ are the modulus and polar coordinate of the complex variable ζ in the ξ-η plane. Thus, ξ and η can be expressed in terms of x and y as:

$$\xi = \frac{\left(1+\alpha^2\right)^2\left(x^2+y^2\right) - \left(1-\alpha^2\right)^2 h^2}{\left[\left(1-\alpha^2\right)h - \left(1+\alpha^2\right)y\right]^2 + \left(1+\alpha^2\right)^2 x^2} \tag{21}$$

$$\eta = \frac{2xh\left(1+\alpha^2\right)\left(1-\alpha^2\right)}{\left[\left(1-\alpha^2\right)h - \left(1+\alpha^2\right)y\right]^2 + \left(1+\alpha^2\right)^2 x^2} \tag{22}$$

Also, x and y can be written in terms of ρ and φ as:

$$x = h\frac{1-\alpha^2}{1+\alpha^2}\frac{2\rho\sin\varphi}{1+\rho^2-2\rho\cos\varphi} \tag{23}$$

$$y = -h\frac{1-\alpha^2}{1+\alpha^2}\frac{1-\rho^2}{1+\rho^2-2\rho\cos\varphi} \tag{24}$$

The mapping is shown in Figure 7.7. The shallow tunnel in the z-plane is transformed into a concentric annular region in the ζ-plane. The outer circle with radius 1 in the ζ-plane ($|\zeta| = 1$) corresponds to the ground surface in the z-plane (y=0), and the inner circle in the ζ-plane ($|\zeta| = \alpha$) corresponds to the tunnel perimeter in the z-plane ($r=r_0$).

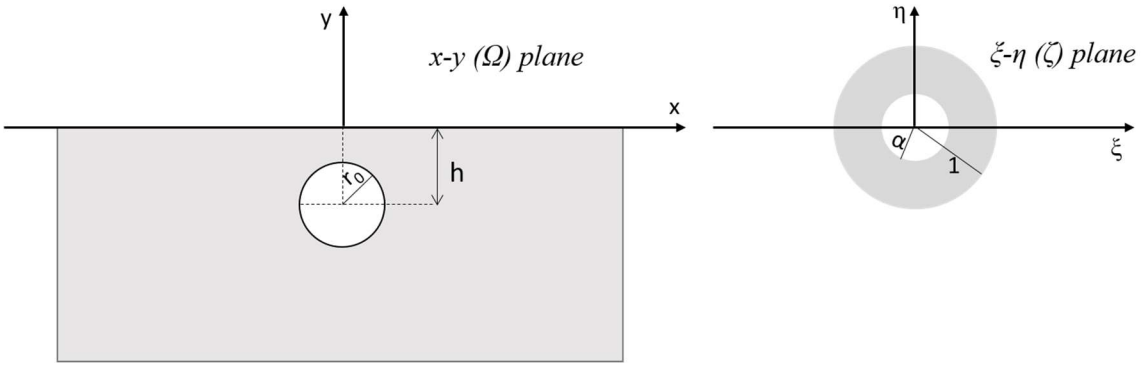

Figure 7.7 Mapping of the shallow tunnel region in the z-plane to a concentric annular region in the ζ-plane.

A solution for the axial displacement *w* can be found in the form of a Laurent Series. Since there is no rigid body motion in the axial direction ($a_0=0$), w is expressed as:

$$w = \mathrm{Re}\left(\sum_{n=1}^{\infty} a_n \zeta^{-n} + \sum_{n=1}^{\infty} b_n \zeta^{n} \right); \tag{25}$$

Where a_n and b_n are complex constants that are obtained from the boundary conditions in equations (15) to (17).

Imposing the boundary condition at y=0, i.e. equation (16), we obtain the following expression:

$$\tau_{yz}(y=0) = \mathrm{Re}\left(iG\left(\sum_{n=1}^{\infty} -n a_n \zeta^{-n-1} + \sum_{n=1}^{\infty} n b_n \zeta^{n-1} \right)\left(\frac{1}{2h} \frac{\left(1+\alpha^2\right)}{\left(1-\alpha^2\right)} i\left(1-\zeta\right)^2 \right) \right) = 0 \tag{26}$$

Given equation (26) and considering the symmetry of the problem, w(x=0) =0, we have:

$$w = \mathrm{Re}\left(i \sum_{n=1}^{\infty} a_n \left(\zeta^{-n} - \zeta^{n} \right) \right) \tag{27}$$

Where a_n are now real numbers. The shear stresses are, thus:

$$\tau_{xz} = \mathrm{Re}\left(\frac{\alpha}{1-\alpha^2} \frac{G}{r_0} \sum_{n=1}^{\infty} n a_n \left(\frac{1}{\zeta^{n+1}} - \frac{2}{\zeta^{n}} + \frac{1}{\zeta^{n-1}} + \zeta^{n-1} - 2\zeta^{n} + \zeta^{n+1} \right) \right) \tag{28}$$

$$\tau_{yz} = \mathrm{Re}\left(\frac{\alpha}{1-\alpha^2} \frac{G}{r_0} i \sum_{n=1}^{\infty} n a_n \left(\frac{1}{\zeta^{n+1}} - \frac{2}{\zeta^{n}} + \frac{1}{\zeta^{n-1}} + \zeta^{n-1} - 2\zeta^{n} + \zeta^{n+1} \right) \right) \tag{29}$$

Finally, the stress boundary condition, given in Equation 17, takes the form:

$$\tau_{rz} = \tau_{xz} \cos\theta + \tau_{yz} \sin\theta = -\left(p_1 \cos\theta + p_2 \sin\theta \right) \tag{30}$$

Note that the angles θ, in the x-y plane, and φ, in the ξ-η plane, are not the same. The constants a_n in Equation (27) are obtained by expressing the trigonometric functions in θ in terms of φ, i.e. cos θ= x/r_o and sin θ= y/r_o where x and y are taken from (23) and (24), and expanding the right-hand side of equation (30) as a Fourier series in terms of the angle φ, given equations (21) and (22), and equating term by term the right and left sides of the equation. This produces the series of linear equations (31) to (33), that are used to obtain the a_n constants.

$$\left(\alpha^4 + 2\alpha^2 - 2 - \frac{1}{\alpha^2} \right) a_1 - 4\left(\alpha^4 + 2\alpha^2 - 1 - \frac{1}{\alpha^2} \right) a_2 + 3\left(\alpha^4 - \frac{1}{\alpha^2} \right) a_3 = \frac{r_0}{G} \frac{\left(1-\alpha^2\right)^2}{\alpha} \left[p_1 + \left(\frac{2h}{r_0} - \frac{\left(1-\alpha^2\right)^2}{\alpha} \right) p_2 \right] \tag{31}$$

$$-2\left(\alpha^3 - \frac{1}{\alpha} \right) a_1 + 2\left(\alpha^5 + 4\alpha^3 + \frac{4}{\alpha} - \frac{1}{\alpha^3} \right) a_2 - 6\left(\alpha^5 + \alpha^3 - \frac{1}{\alpha} - \frac{1}{\alpha^3} \right) a_3 + 4\left(\alpha^5 - \frac{1}{\alpha^3} \right) a_4 = -\frac{r_0}{G} \frac{\left(1-\alpha^2\right)^4}{\alpha} p_2 \tag{32}$$

$$\begin{aligned} & n a_n \left(\alpha^{n+1} - \alpha^{-n+1} \right) - 2(n+1) a_{n+1} \left(\alpha^{n+3} + \alpha^{n+1} - \alpha^{-n+1} - \alpha^{-n-1} \right) + (n+2) a_{n+2} (\alpha^{n+5} + 4\alpha^{n+3} + \alpha^{n+1} - \alpha^{-n+1} - 4\alpha^{-n-1} \\ & - \alpha^{-n-3}) - 2(n+3) a_{n+3} \left(\alpha^{n+5} + \alpha^{n+3} - \alpha^{-n-1} - \alpha^{-n-3} \right) + (n+4) a_{n+4} \left(\alpha^{n+5} - \alpha^{-n-4} \right) = -\frac{r_0}{G} \frac{\left(1-\alpha^2\right)^4}{\alpha} p_2 \alpha^n, n = 1,2,3,\ldots,\infty \end{aligned} \tag{33}$$

Once the constants a_n are known (only several of those are needed for accurate results, and thus only several equations need to be considered), the complete solution in terms of axial displacements and shear stresses is obtained from (27) to (29), noting that the shear stresses from problem (IIa) must be added to those from equation (28).

In summary, stresses and displacements for a shallow tunnel can be obtained through the following steps: 1) select the ground properties (E, ν and γ), tunnel depth and geometry (h, r_0) and far-field shear stress ($\tau_{xz,ff}$); compute the value of α from (19); 2) obtain constants a_n from the linear system of equations 31 to 33 (10 to 15 equations are generally sufficient); 3) determine the axial shear stresses and the axial displacements using equations 27 to 29, given (20), at any coordinate x, y ($\Omega = x + iy$).

There is no particular difficulty, given the previous discussion, in extending the approach to the problem of a supported tunnel. Following the method used by Bobet (2011) for a similar scenario, Problem (II) in Figure 7.4, now with a liner, is decomposed into four problems: IIa, IIb, IIc and IId. Problems IIa and IIb are shown in Figure 7.5 and the solutions are presented in equations (26) to (33). They provide the stresses and displacements due to the opening. The interaction between the ground and the liner is described by Problems IIc and IId, which are illustrated in Figure 7.8. Such interaction is given by the unknown stresses $\Delta\tau_{rz}$ at the contact between the ground and the liner. Compatibility of stresses at the interface is automatically satisfied by imposing the same stresses, $\Delta\tau_{rz}$, at the perimeter of the opening and at the liner. Therefore, coefficients of equations (27) to (29) should be determined with the new boundary condition ($\Delta\tau_{rz}$ at the tunnel perimeter) together with the coefficients of equation (35) to (37) to determine $\Delta\tau_{rz}$. Then, the solutions of problems IIc and IIb are combined to determine problem IId. Compatibility of displacements requires that, at $r=r_0$:

$$w^{IId} = w^{IIb} + w^{IIc} \tag{34}$$

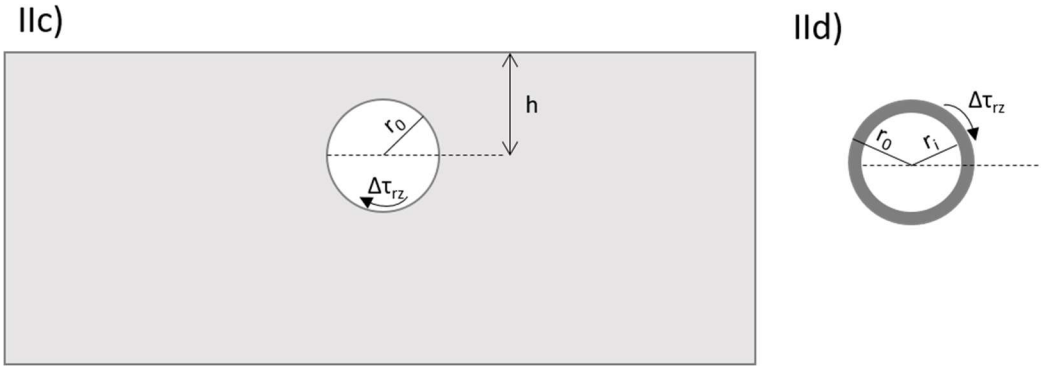

Figure 7.8 Problems IIc and IId. In combination with problems IIa and IIb, provide the solution for problem II of a supported shallow tunnel.

The solution for problem IIc is given by equations (27) to (29). The solution for problem IId is given by:

$$w^s = \sum_{n=2,4,6...}^{\infty} A_n r_i^n \left[\left(\frac{r}{r_i}\right)^n + \left(\frac{r}{r_i}\right)^{-n} \right] \sin(n\theta) + \sum_{n=1,3,5...}^{\infty} B_n r_i^n \left[\left(\frac{r}{r_i}\right)^n + \left(\frac{r}{r_i}\right)^{-n} \right] \cos(n\theta) \tag{35}$$

$$\tau_{rz}^s = \frac{1}{r} G_s \left\{ \sum_{n=2,4,6...}^{\infty} n A_n r_i^n \left[\left(\frac{r}{r_i}\right)^n - \left(\frac{r}{r_i}\right)^{-n} \right] \sin(n\theta) + \sum_{n=1,3,5...}^{\infty} n B_n r_i^n \left[\left(\frac{r}{r_i}\right)^n - \left(\frac{r}{r_i}\right)^{-n} \right] \cos(n\theta) \right\} \tag{36}$$

$$\tau_{z\theta}^s = \frac{1}{r} G_s \left\{ \sum_{n=2,4,6...}^{\infty} n A_n r_i^n \left[\left(\frac{r}{r_i}\right)^n + \left(\frac{r}{r_i}\right)^{-n} \right] \cos(n\theta) - \sum_{n=1,3,5...}^{\infty} n B_n r_i^n \left[\left(\frac{r}{r_i}\right)^n - \left(\frac{r}{r_i}\right)^{-n} \right] \sin(n\theta) \right\} \tag{37}$$

The solution of equation (34), given equations (35) to (37) requires a numerical method, again because the polar coordinate angle θ in the x-y plane is not the same as the angle φ in the ξ-η plane. The results however may have limited interest because, as it will be shown later, the presence of the face of the tunnel (not considered in the derivation) brings into question the problem decomposition postulated in equations (5) to (7). This is because stresses normal to the tunnel (Problem I in Figure 7.4) induce axial deformations in the ground near the face of the tunnel. This is discussed in more detail in section 4. So, unless the liner is placed far from the face, or simultaneously with the full excavation of the tunnel, which is not realistic, the close-form solution obtained may not represent the interplay that exists between the ground and the support.

7.3 Verification of the analytical solution

The analytical solution is verified using numerical methods. 3D FEM models are conducted considering angles Ψ= 0°, 15°, 30°, 45°, 60°, 75° and 90° (Figure 7.2). The results of the model are extracted from a structured refined mesh with boundaries far from the tunnel, as illustrated in Figure 7.9., to avoid boundary effects and ensure accuracy of the numerical results (Vitali et al., 2017). The refined mesh is located and the center of the model and a transitional mesh connects the refined mesh to the boundaries. Second order elements are used, as recommended by Vitali et al. (2017). The refined mesh at the center of the discretization is illustrated in Figure 7.9. The mesh has elements with $0.2r_0$ length behind the face. Such longitudinal refinement ensures accuracy even for high material non-linearity, as shown by Vitali et al. (2017). Two cases are run for the verification: one with overburden h= 10m and the other with h=25m; all simulations are done for a tunnel with diameter 10m (or radius r_0=5m). The case with h=25m represents a common shallow tunnel, and h=10m a tunnel very close to the surface and is used as an extreme case to further verify the analytical solution. The distance from the tunnel centerline to the bottom of the model is d= 40m, or $8r_0$, that ensures that the bottom boundary does not affect the results (Vitali et al., 2019a). The ground properties are: E=1GPa, ν=0.2 and γ=27kN/m^3, which are typical of soft rocks. The stress ratios are K_{hv}=1 (i.e. $\sigma_v=\sigma_h$) and K_{Hv}=4 (i.e. $\sigma_H=4\sigma_v$), which are within the range of the stress ratios reported by Park et al. (2014) in Gneiss (Figure 7.1) and are consistent with data compiled by McGarr & Gay (1978). The numerical models comprise two phases: in the 1st phase, the geostatic stress field is imposed and the ground displacements are zeroed; in the 2nd phase, the elements inside the tunnel are deactivated. Those two phases are intended to reproduce the analytical solution.

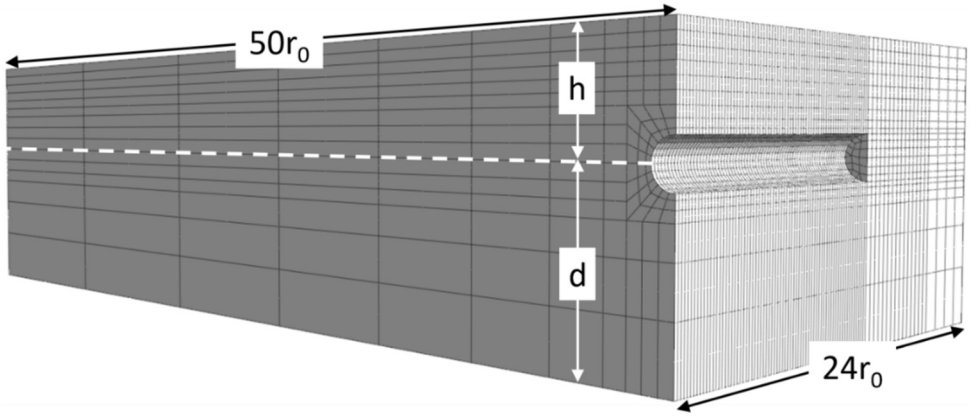

Figure 7.9 Mesh used for the simulations; h=5r_0, r_0 is the tunnel radius, r_0= 5m.

Figures 7.10 to 7.15 compare results from the analytical solution with the FEM results for different tunnel alignment angles Ψ and different tunnel depths. Stresses and displacements are taken at the tunnel perimeter. The in-plane tangential stresses, $\sigma_{\theta\theta}$, and displacements, u_x and u_y, are obtained analytically using Verruijt and Booker solution (Verruijt and Booker, 2000). The axial tangential stresses, $\tau_{\theta z}$, and displacements, *w*, are calculated using the proposed analytical solution. The comparison between FEM and analytical solutions shows that the equations derived are correct. The axial shear stress and tangential stresses at the tunnel perimeter are presented in Figure 7.10, for $h=2r_0$, and in Figure 7.11, for $h=5r_0$. As the tunnel rotates from Ψ=0° to 90°, the horizontal stress, $\sigma_{xx,ff}$, increases; it is minimum for Ψ=0° ($\sigma_{xx,ff}= \sigma_h= \sigma_v$) and maximum for Ψ=90° ($\sigma_{xx,ff}= \sigma_H= 4\sigma_v$). The axial shear, $\tau_{xz,ff}$, increases with Ψ and is maximum when Ψ=45° ($\tau_{xz,ff}= 1.5\sigma_v$). $\tau_{xz,ff}$ decreases as Ψ rotates from 45° to 90°. When the tunnel is aligned with one of the principal stresses (Ψ=0° and Ψ=90°), $\tau_{xz,ff}$ is zero. The magnitude of both tangential and axial shear stresses is larger for $h=5r_0$ than for $h=2r_0$. This is because the deeper the tunnel, the larger the geostatic stresses near the tunnel. The stresses along the tunnel perimeter show the same trend for both tunnel depths; that is, stresses are larger at the invert than at the crown and, because of gravity, the results are asymmetric with respect to the polar coordinate θ. The figure shows that as the misalignment of the tunnel with the major principal geostatic stress increases, i.e. as Ψ increases, both the tangential and axial shear stresses increase. Note that the axial shear stresses, $\tau_{\theta z}$, along the tunnel perimeter are the largest at Ψ=45°, i.e. when $\tau_{xz,ff}$ is maximum.

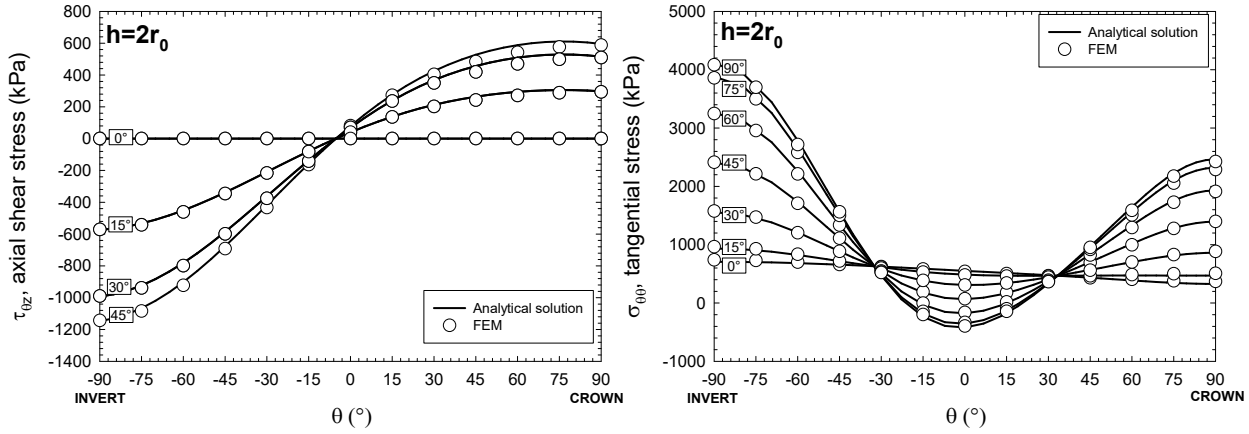

Figure 7.10 Axial shear and tangential stresses along the tunnel perimeter for h=10m.

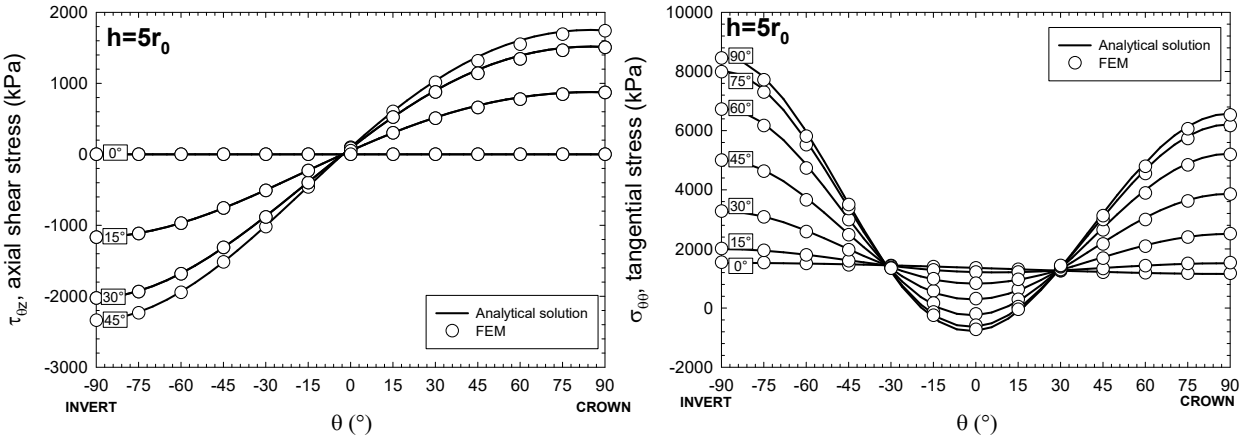

Figure 7.11 Axial shear and tangential stresses along the tunnel perimeter for h=25m.

The horizontal and the axial displacements along the tunnel perimeter are shown in Figure 7.12, for $h=2r_0$, and in Figure 7.13, for $h=5r_0$. The magnitude of the displacements is larger for $h=5r_0$ than for $h=2r_0$, because of the larger stresses for the deeper tunnel. Both horizontal and axial displacements, u_x and w, are maximum at the springline and zero at the crown and at the invert because of the symmetry of the problem with respect to the vertical axis; u_x is symmetric and w anti-symmetric with respect to the vertical axis (note that this is not the case for the horizontal axis); Figure 7.14 shows a view of the deformed mesh near the tunnel for $\Psi=45°$ that illustrates the axial deformations induced by the axial shear. Also note, again because of gravity, that the results are not symmetric with respect to the horizontal axis through the center of the tunnel. The plots in Figures 7.12 and 13 indicate that the results from the numerical simulations and from the analytical solution are essentially the same. The figures also show that as the tunnel misalignment increases, i.e. as Ψ increases up to 45^o, the horizontal and axial displacements increase. As the misalignment further increases, the axial displacements continue to increase, while the axial displacements decrease after their peak at $\Psi=45^o$.

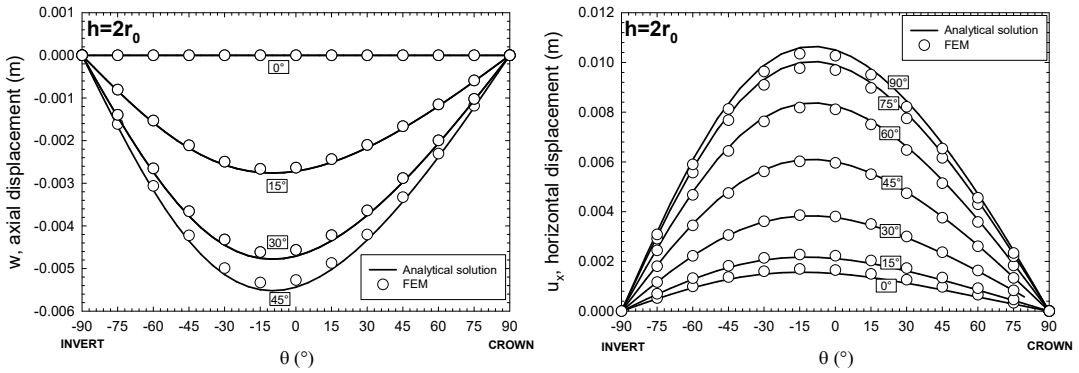

Figure 7.12 Horizontal and axial displacements along the tunnel perimeter for h=10m.

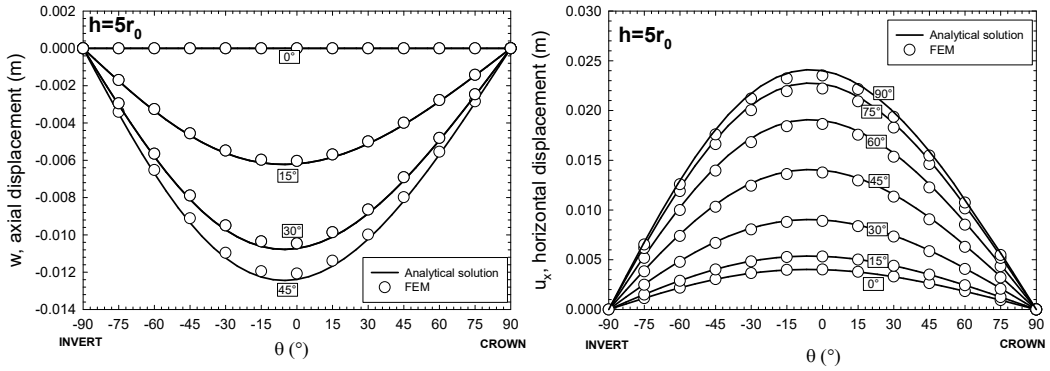

Figure 7.13 Horizontal and axial displacements along the tunnel perimeter for h=25m.

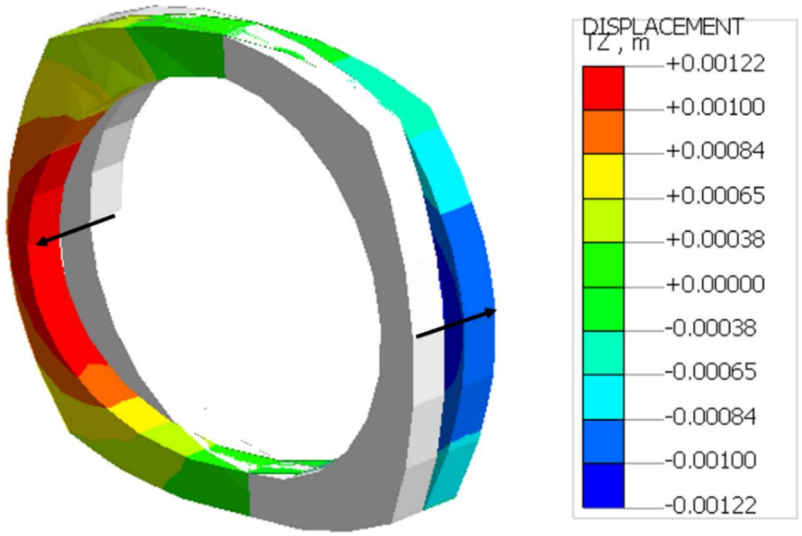

Figure 7.14 Axial displacements and deformed mesh near the tunnel, for Ψ=45°.

Figure 7.15 plots the tunnel convergence, taken as the difference in radial displacements between the crown and invert, obtained from both methods: analytical and numerical. Positive

convergence is in the inward direction and negative, outward. Again, the results are comparable, which provides confidence in the analytical solution. The figure shows a monotonic decrease of tunnel convergence with the rotation angle Ψ such that when the axis of the tunnel is parallel to the σ_H stress, Ψ=0°, the convergence is the largest positive (inwards deformation) and when the axis of the tunnel is parallel to σ_h, Ψ=90°, convergence is the largest negative (outwards deformation).

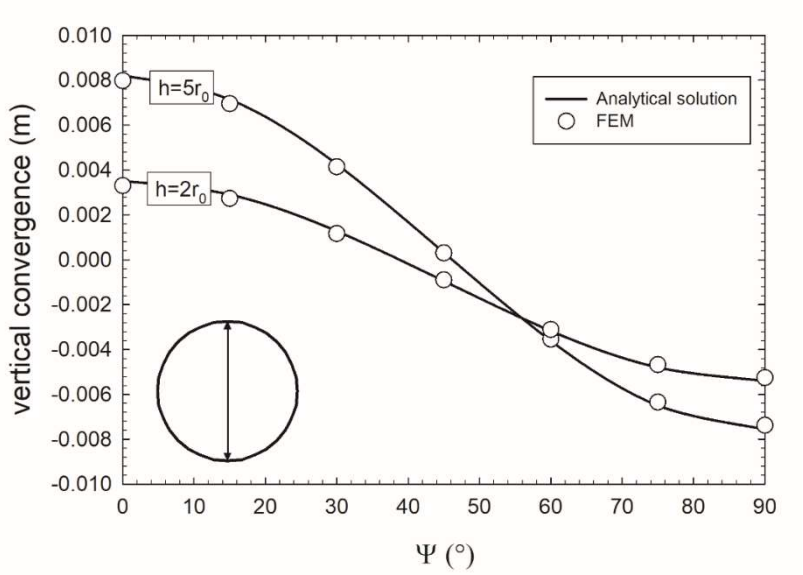

Figure 7.15 Vertical convergence with tunnel misalignment, Ψ, for h=10m; and h=25m.

7.4 Face effects

Past research has been conducted to investigate the stress paths and ground deformations near the tunnel face (Almeida e Sousa et al., 2011; Cantieni & Anagnostou, 2009; Eberhardt, 2001; Gomes & Celestino, 2009; Ng & Lee, 2005), but the work was done assuming that the tunnel was aligned with one of the principal stresses. Thus, the influence of the far-field axial shear stress ($\tau_{xz,ff}$) near the tunnel face has not been considered. In the following, the influence of $\tau_{xz,ff}$ near the tunnel face is assessed numerically, for unsupported and supported tunnels in elastic and elastoplastic ground. The FEM models and the boundary conditions presented in section 3 are used, with Ψ=45° (i.e. $\sigma_{xx,ff}/\sigma_v=\sigma_{zz,ff}/\sigma_v$ =2.5 and $\tau_{xz,ff}/\sigma_v$=1.5) and h=5r_0. The ground properties are E=1GPa, ν=0.3 and γ=27kN/m^3, the same as before. Results from the full 3D simulations (i.e. considering the presence of $\tau_{xz,ff}$, referred as *3D*) are then compared with those obtained without the presence of $\tau_{xz,ff}$, i.e. for $\sigma_{xx,ff}/\sigma_v=\sigma_{zz,ff}/\sigma_v$=2.5 and $\tau_{xz,ff}$=0 (referred as 3D no shear) to assess

the effect of $\tau_{xz,ff}$ on stresses and displacements near the face. Note that the good match between analytical and FEM results shown in previous section validates the FEM model built (i.e. mesh, model size and boundary conditions).

7.4.1 Tunnel in elastic ground

Figure 7.16 shows the mesh with the position of three reference sections, namely: Position (3) far-behind the face, where there are no face effects; Position (2) at the face; and Position (1), far-ahead the face, where the ground is under the geostatic stress field. Figure 7.17 shows the stress paths of points in the ground as the tunnel is excavated, i.e. the stress changes from position (1) to position (3). The stresses are taken at 2m distance (i.e. 0.2 tunnel diameter) from the tunnel perimeter to avoid the singularity effect on the stresses at the tunnel perimeter due to the corner at the face. The stress paths are assessed at three points: two at the springline, on the left and on the right, and one at the crown. The stress paths are obtained for the two scenarios: *3D* and *3D, no shear*. In the figure, $\sigma_{mean}=(\sigma_1+\sigma_2+\sigma_3)/3$ and $\tau_{max}=(\sigma_1-\sigma_3)/2$.

Figure 7.17 (a) shows the stress paths of points located at the springline, on the right and on the left side (the results differ due to the far-field axial shear). As one can see, the stress paths for the *3D* scenario are asymmetric. That is, the point on the right loads from (1) to (2) and unloads from (2) to (3) while on the left, it unloads from (1) to (2) and loads from (2) to (3). The different stress paths are the result of the effects of stresses normal to the axis of the tunnel (Figure 7.4, Problem I) that produce symmetric results and of the shear stresses (Figure 7.4, Problem II) that produce antisymmetric results. At position (3), far-behind the face, the stress state of the points on the left and on the right is the same. For the *3D, no shear* scenario, the stress paths of the two points at the springline are the same. Thus, the presence of $\tau_{xz,ff}$ causes asymmetry on the stresses near the face. Note that the point on the right experiences larger deviatoric stresses than the point on the left. This is because $\tau_{xz,ff}$ tends to distort the tunnel cross-section, as shown in Figure 7.14, and those axial displacements are partially constrained by the face. The stress paths of points on the crown are shown in Figure 7.17 (b) for the *3D* and *3D, no shear* scenarios. The results show loading from position (1) to (3) in both cases, with the two loading paths showing similar characteristics, except that the 3D scenario, which includes $\tau_{xz,ff}$, results in higher shear stresses than the *3D, no shear* scenario, which does not include $\tau_{xz,ff}$.

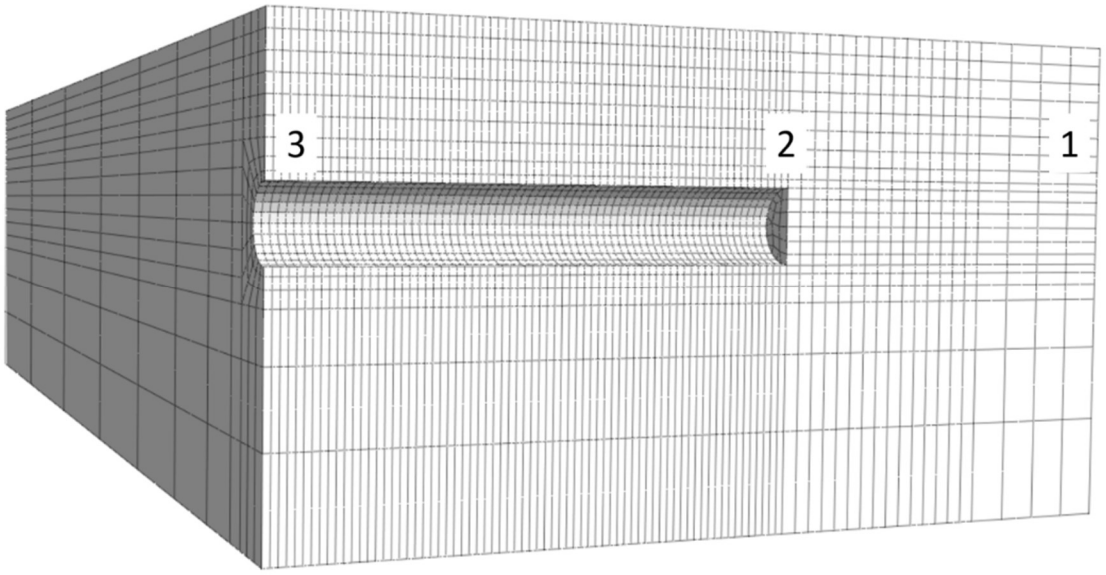

Figure 7.16 Position with respect to the tunnel face: position (3) far-behind the face; (2) at the face and; (1) far-ahead the face.

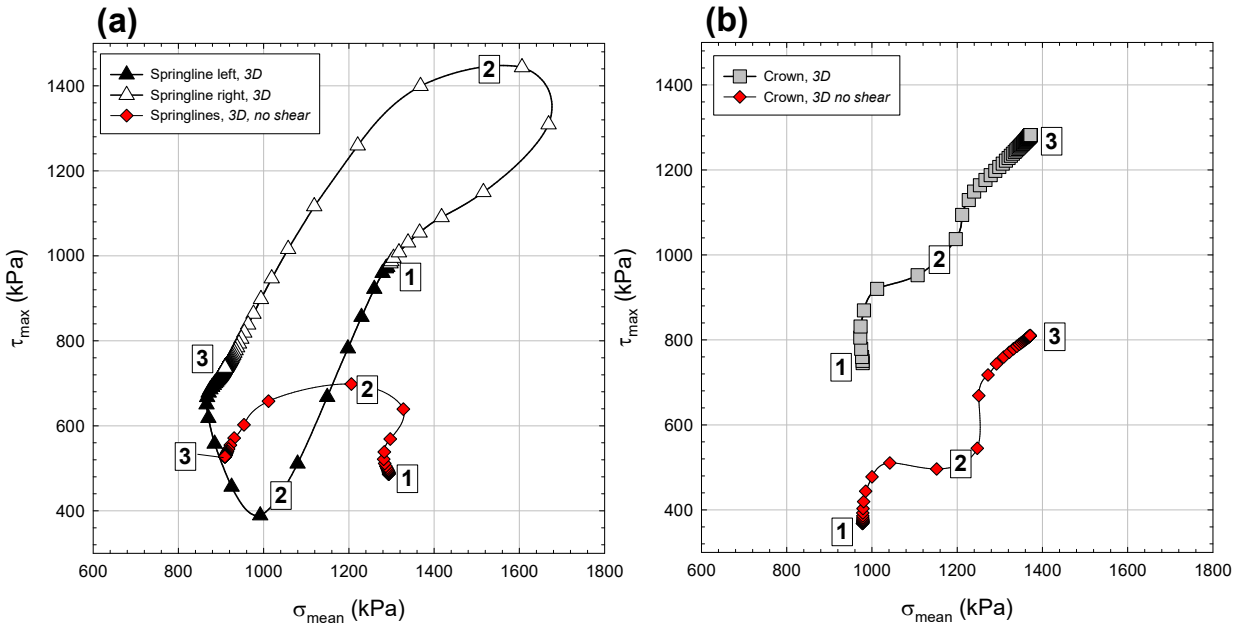

Figure 7.17 Stress paths near the tunnel face.

Figure 7.18 (a) shows the radial displacements at the springline for the *3D* scenario, with the distance from the face normalized with respect to the tunnel radius (Z/r_0); positive distance refers to locations ahead of the face and negative, behind the face. The figure also includes the horizontal displacements at the crown and invert. It is interesting to note that they are the same,

and thus they indicate a rigid body motion of the tunnel cross-section towards the right springline. This rigid body motion only occurs in the full 3D scenario and thus it is caused by $\tau_{xz,ff}$. The rigid body motion of the tunnel cross-section has been subtracted from the radial displacements in Figure 7.18 (a) to compare the displacements on both sides of the springline; as one can see, the displacements of the two points at the springline, right and left, are not the same near the face. A similar plot for the *3D no shear* scenario is presented in Figure 7.18 (b) and shows that the two points at the springline have the same displacement, i.e. there are no rigid body motions near the face. For both scenarios, the radial displacements are small at about four times the tunnel radius ahead of the face, and quickly increase close to the face. At a distance of about 4 to 6 radii behind the face, the displacements on both sides of the springline become equal. The horizontal displacements at the crown and invert, for the *3D* scenario, are small at about four radii ahead of the face, increase close to the face and then quickly decrease behind the face until they become zero far behind the face. Because of symmetry, the horizontal displacements at the crown and invert for the *3D no shear* scenario are zero.

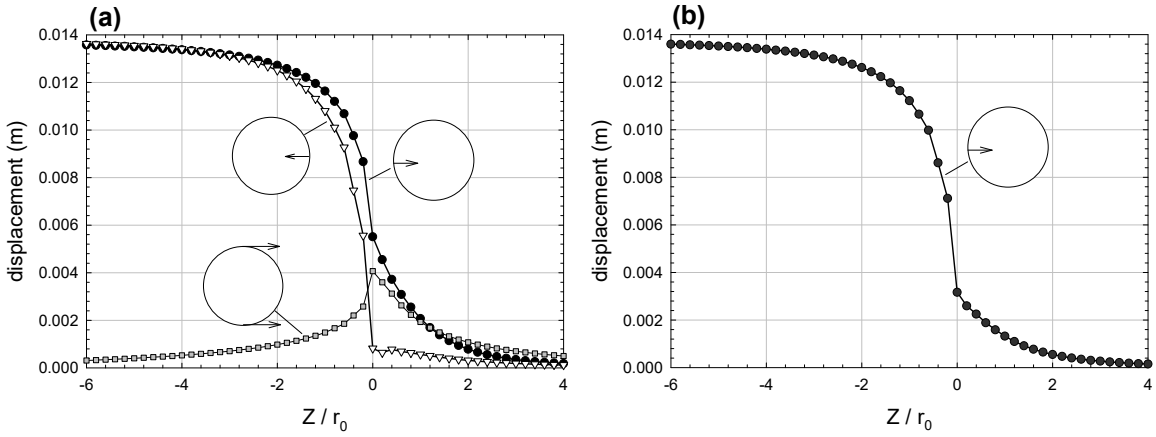

Figure 7.18 Displacements of points around the tunnel perimeter with normalized distance from the face, for unsupported tunnel in elastic ground. (a) *3D*; (b) *3D, no shear*.

Figure 7.19 shows the horizontal and vertical convergence with Z/r_0 for the *3D* and *3D*, *no shear* scenarios. Interestingly, the results of the two scenarios are exactly the same. For the vertical convergence, this is somewhat expected because the axial shear stress that appears due to the tunnel misalignment does not affect the crown due to the symmetry. It is also interesting to observe that the horizontal convergence takes a sigmoidal shape, similar to that observed in tunnels aligned with one of the geostatic principal stress directions. As one can see, the ground does not experience

deformations about four radii ahead of the face; the larger convergence rate occurs at the face, and the rate of convergence increases slowly behind the face, until a distance of about four tunnel radii where results do not change significantly with distance.

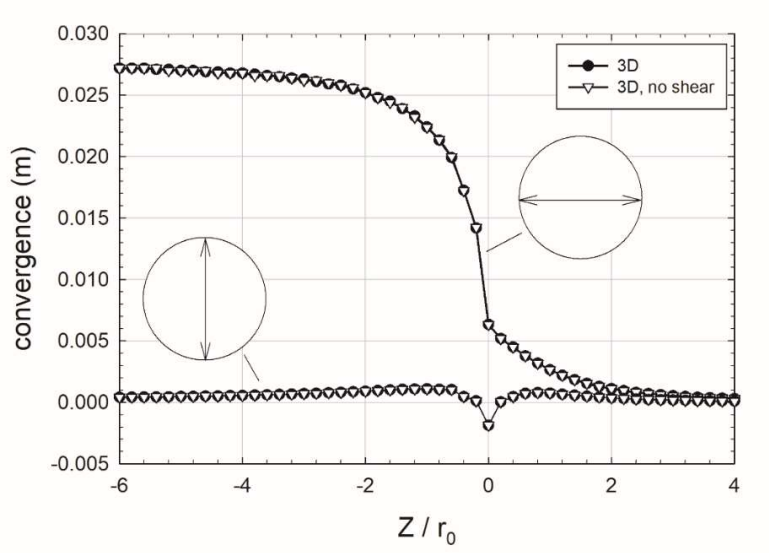

Figure 7.19 Horizontal and vertical convergence with distance from the tunnel face normalized with respect to the tunnel radius, for unsupported tunnel in elastic ground.

Figure 7.20 shows the displacements along the tunnel perimeter at the face (Z=0) for *3D* and *3D no shear* scenarios. As one can see, the radial and the axial displacements for the *3D no shear* scenario are symmetric while they are asymmetric for the *3D* scenario. The radial displacements plotted do not include the rigid body motions (i.e. the horizontal displacements at the crown and invert shown Figure 7.18). At the springline, the radial displacements are inwards (positive) and decrease towards the crown. At the crown, the radial displacement is outwards, i.e. the tunnel elongates in the vertical direction. The axial displacements, Figure 7.20 (b), are somewhat constant with θ for the *3D no shear* scenario, while, for the *3D* scenario, this is not the case (see also Figure 7.14). The tangential displacements are about the same on both scenarios, as shown in Figure 7.20 (c). They are the largest for θ of 45° and 135° and are zero at the springline and at the crown. The differences between the displacements at the face from *3D* and *3D no shear* scenarios are due to the far-field axial shear, $\tau_{xz,ff}$. The differences (u_{3D}–$u_{3D\ no\ shear}$) are shown in Figure 7.21. At the face, $\tau_{xz,ff}$ does not induce tangential displacements, but causes anti-symmetric radial and axial displacements and a horizontal rigid body displacement towards the right, given the far-field load used in the simulations.

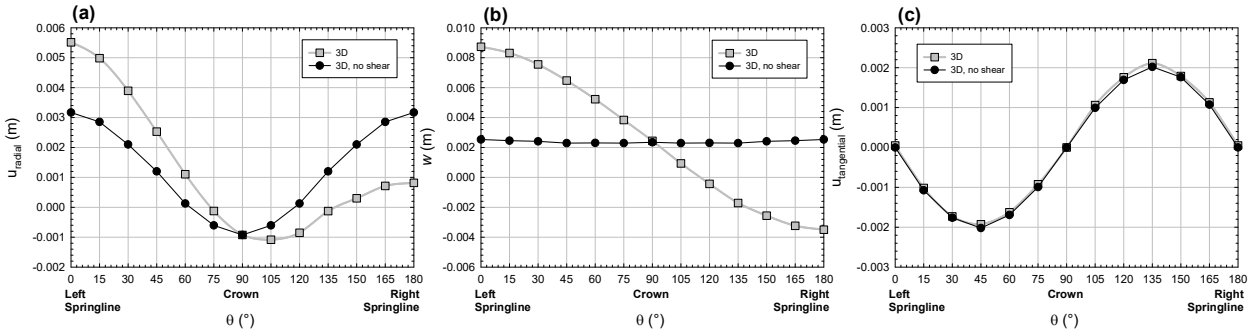

Figure 7.20 Displacements along the tunnel perimeter at the tunnel face for *3D* and *3D no shear* scenarios (i.e. $Z/r_0=0$): (a) radial displacements; (b) axial displacement and; (c) tangential displacements.

The axial displacements (w) with Z/r_0 for the *3D* and *3D, no shear* scenarios are shown in Figure 7.22. The *3D no shear* scenario, Figure 7.22(a), shows similar axial displacements at the crown and springline. The axial displacements are the largest near the face and quickly reduce behind the face. The *3D* scenario results in different axial displacements at the crown and at each side of the springline due to the combined effect of the tunnel distortion in the axial direction and the ground movements toward the excavation near the face. Due to the orientation of the tunnel, the axial displacements at the springline, left, are larger than at the point on the right. Far-behind the face, as it should, the axial displacements have the same magnitude, but opposite directions, and they are zero at the crown.

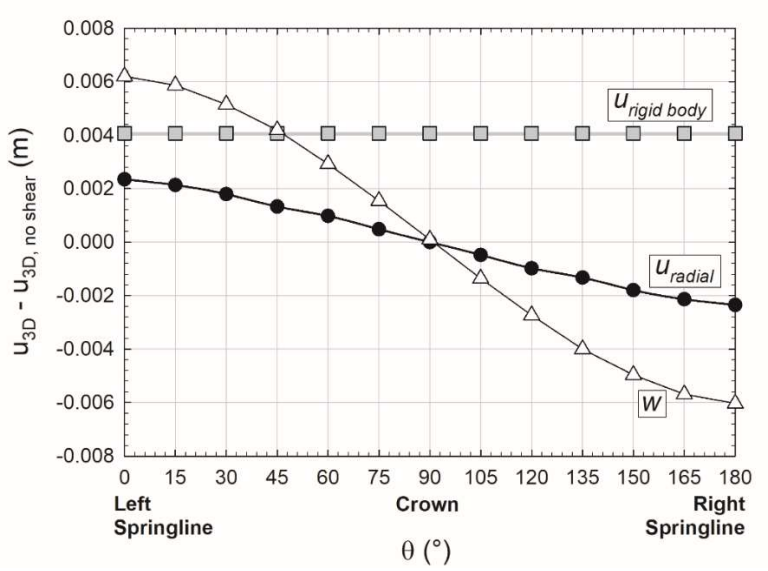

Figure 7.21 Difference between displacements from *3D* and *3D no shear* scenarios along the tunnel perimeter at the tunnel face (i.e. Z=0).

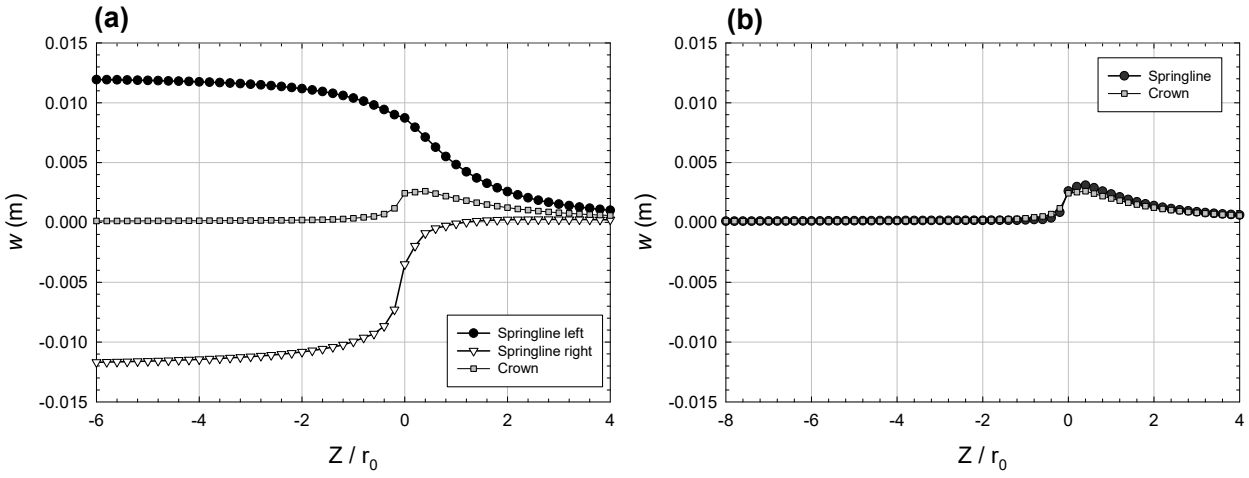

Figure 7.22 Axial displacements at points around the tunnel perimeter with normalized distance from the tunnel face with respect to the tunnel radius for unsupported tunnel in elastic ground. (a) *3D*; (b) *3D no shear*.

7.4.2 Supported tunnel

The models are run considering the construction sequence (i.e. step-by-step excavation and liner installation; see Möller, 2006) with the liner placed immediately after the excavation (i.e. no unsupported span length and excavation round length of $0.2r_0$). The liner is represented by shell elements with linear-elastic behavior. No-slip at the ground-liner contact is assumed. The liner properties are: E=20GPa, ν=0.2 and 0.5m thickness. These conditions are typical of reinforced concrete liners installed near the face to minimize the ground deformations Two scenarios are analyzed: full *3D* and *3D, no shear*.

Figure 7.23 shows the displacements with the normalized distance Z/r_0 at points at the tunnel perimeter. Similar to what happens with the unsupported tunnel (Figure 7.18), the horizontal displacements of points located at the right and left sides of the springline are different near the face for the *3D* scenario, but they are the same for the *3D, no shear* scenario. Note the slightly saw-tooth like plot of displacements behind the face. This is caused by the excavation-support sequence used in the simulations. An important difference between the results from the unsupported tunnel (Figure 7.18) and the supported tunnel (Figure 7.23) is that, far-behind the face, the radial displacements on the right and left of the springline are not the same, and the horizontal displacements are not zero at the crown and invert. In other words, the 2D plane strain conditions that could be assumed for an analytical (or numerical) solution are not met. Note that this is the

reason why the analytical solution for supported shallow tunnels discussed earlier may not represent well what actually happens. The reason for this behavior is that the $\tau_{xz,ff}$, at the face, induces radial and axial deformations, which the liner must accommodate.

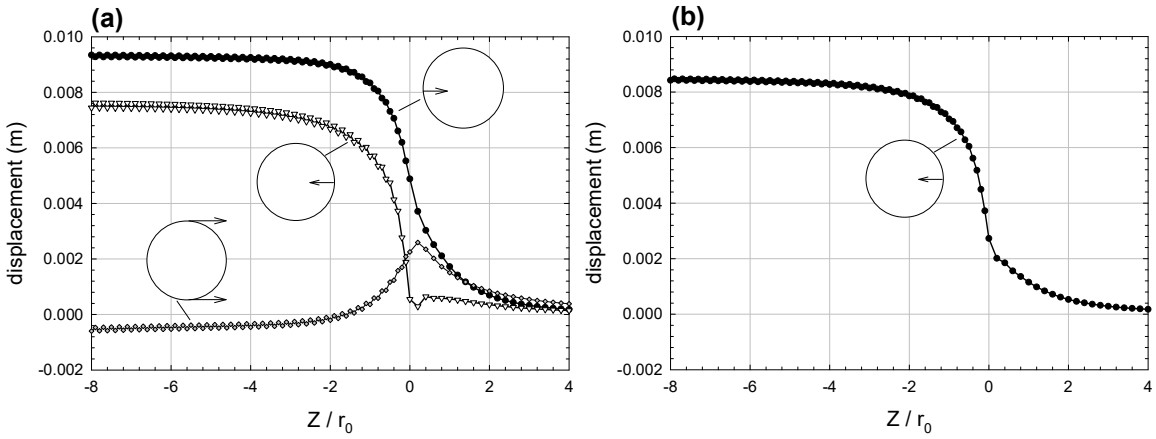

Figure 7.23 Displacements at points around the tunnel perimeter with normalized distance from the face, for supported tunnel in elastic ground. (a) *3D*; (b) *3D no shear*.

This observation is further supported by the results shown in Figure 7.24 that plots the radial stresses (σ_{radial}) of the ground with normalized distance Z/r_0 at the two points on the springline, one at the right and the other at the left. Note that the radial stresses at the tunnel perimeter are zero for the unsupported tunnel; however, for the supported tunnel, the radial stresses are not zero because of the load applied from the ground to the liner. The *3D, no shear* scenario (Figure 7.24a) results in a symmetric response, as it should, due to the absence of the $\tau_{xz,ff}$. The *3D* scenario (Figure 7.24b) gives an asymmetric response. As expected, far ahead of the face, the horizontal stresses are those of the free-field. As the ground approaches the face of the tunnel, the radial stresses show a very different behavior at the springline, depending on location, i.e. due to the $\tau_{xz,ff}$. The point on the right sees the radial stresses increase up to the face and then abruptly decrease behind the face. This is the opposite of what occurs at the point on the left, where the radial stresses monotonically decrease, from far ahead from the face to far behind the face. Far-behind the face, the two radial stress are different.

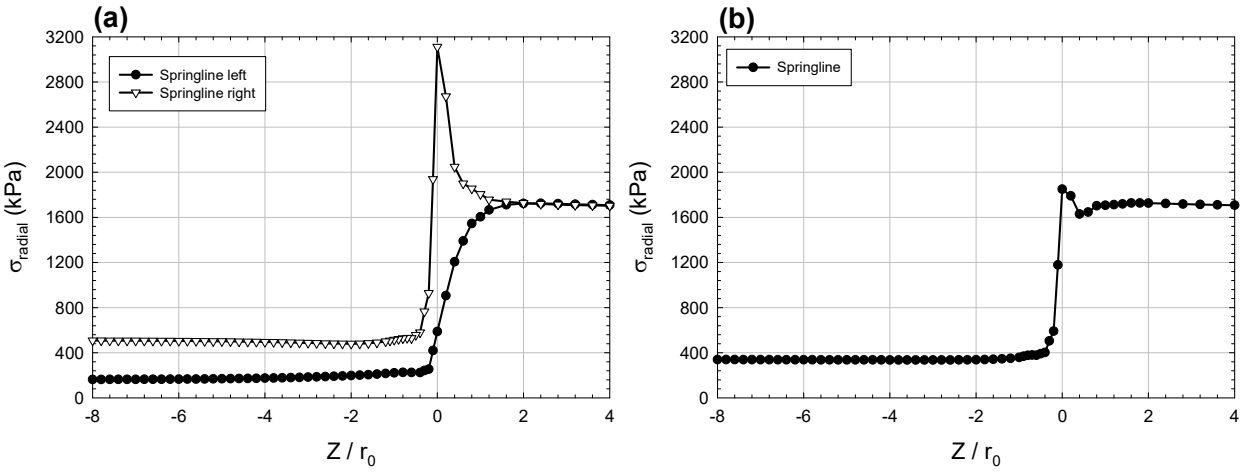

Figure 7.24 Radial stresses at points around the tunnel perimeter with normalized distance from the tunnel face for supported tunnel in elastic ground. (a) *3D*; (b) *3D no shear*.

The asymmetry in the radial stresses results in a load to the liner that is asymmetric as well, as one can see in Figure 7.25, which is a plot of the thrust force and bending moments far-behind the face, for the *3D* and *3D, no shear* scenarios. Consistent with previous findings and discussion, the thrust force and bending moments in the liner are symmetric for the *3D, no shear* scenario, but they are not for the *3D* scenario. Since the observed asymmetry is caused by induced in-plane displacements near the face due to the presence of the $\tau_{xz,ff}$, the internal forces in the liner are asymmetric also for full-slip conditions, i.e. when the contact between the ground and liner is frictionless (not shown in the figures).

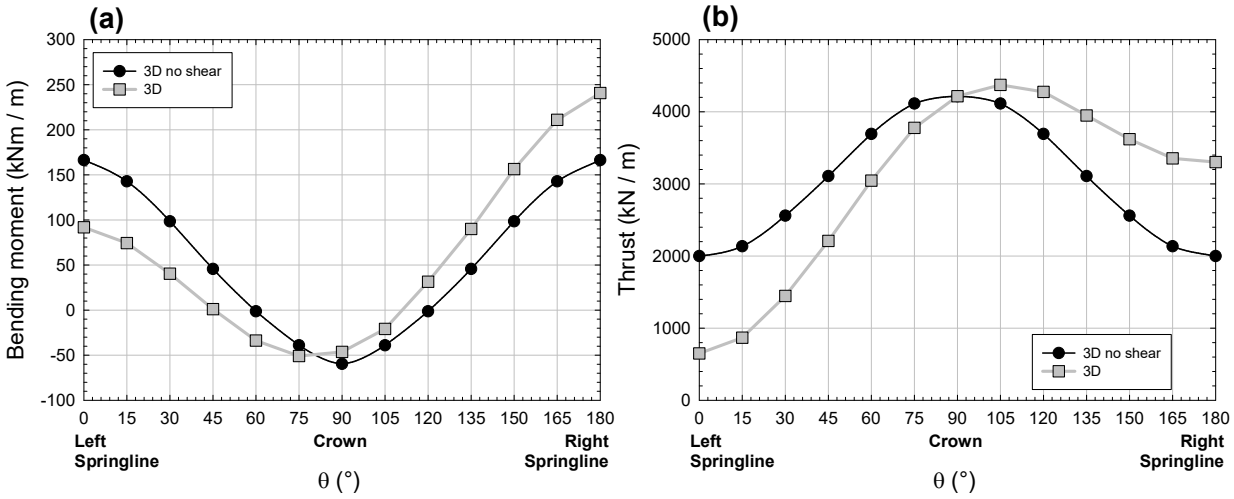

Figure 7.25 Internal forces along the tunnel perimeter for *3D* and *3D no shear* far-behind the face (at a distance $10r_0$ behind the face). Bending moments (a) and Thrust force (b).

7.4.3 Tunnel in elastoplastic ground

The results presented so far were obtained considering elastic ground; thus, stress-strains were not affected by the stress history. This is not the case for elastoplastic ground. To investigate the 3D face effects on elastoplastic ground, the model now includes the Mohr-Coulomb failure criterion with a non-associated flow rule. The ground properties are E=1GPa, ν=0.2, γ=27kN/m^3, c=100kPa, φ=45° and dilatancy angle of 0°. The construction sequence is considered with an excavation round length of $0.2r_0$ and no unsupported length. Unsupported and supported tunnels are assessed.

Figure 7.26 shows the plastic zone developed around the tunnel far behind the face, for the *3D* and *3D, no shear* scenarios, for supported and unsupported tunnels. The plastic zone in this paper is defined as the region that undergoes equivalent plastic strains larger than 10^{-3}. As expected, the installation of the support reduces substantially the size of the plastic zone and may even prevent the development of plastic deformations. The plastic zone for the *3D no shear* scenarios is symmetric because $\tau_{xz,ff}$ is zero; thus, deformations around the tunnel are symmetric. In contrast, the plastic zone for the *3D* scenarios is asymmetric; it is larger on the right-hand side than on the left-hand side because of $\tau_{xz,ff}$, which affects the stress paths near the tunnel, as shown in Figure 7.17. It is interesting to note that, overall, the size of the ground yielding around the tunnel is larger for the *3D* scenarios than for the *3D, no shear* scenarios. This is expected given that the far-field shear stress increases the deviatoric stresses, as one can see in Figure 7.17.

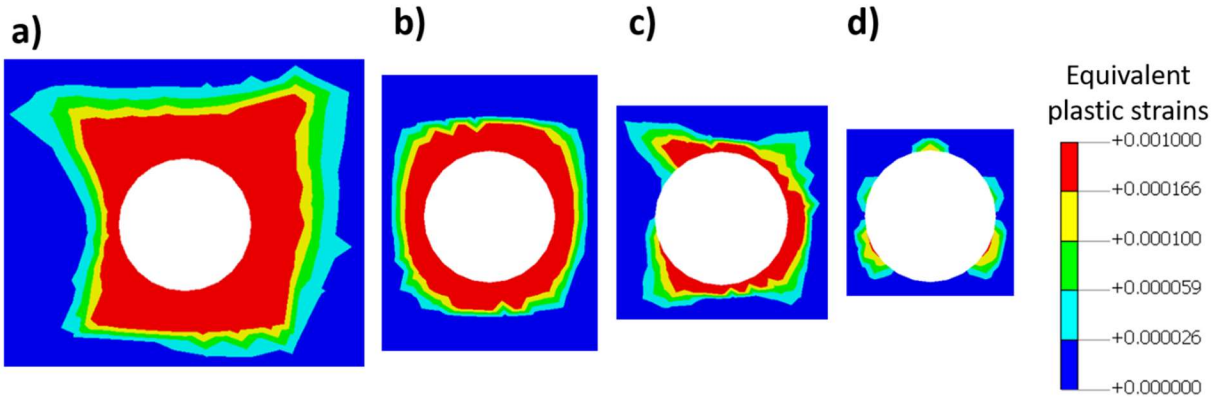

Figure 7.26 Plastic zone around the tunnel far behind the face for tunnels in elastoplastic ground; (a) unsupported, *3D*; (b) unsupported, *3D no shear*; (c) supported, *3D*; (d) supported, *3D no shear*.

Figure 7.27 shows the horizontal convergence at the two points on the springline with the normalized distance Z/r_0 for the *3D* and *3D, no shear* scenarios, and for the supported and unsupported tunnels on elastic and on elastoplastic ground. The displacements on elastoplastic ground have a saw-tooth shape, which is the numerical response to the step-by-step excavation of the tunnel in elastoplastic ground (Möller, 2006; Vitali et al., 2017; Vlachopoulos & Diederichs, 2009). Figure 7.27 shows the average displacements of the saw-tooth shape. As expected, the displacements on elastoplastic ground are larger than on elastic ground, but the differences observed for the unsupported tunnels are much larger than for the supported tunnels. This is because the support reduces substantially the plastic deformations around the tunnel, as shown in Figure 7.26. Tunnel convergence for the *3D* scenario is larger than for *3D no shear* scenario on elastoplastic ground, but it is the same on elastic ground. This is expected because the plastic zone is larger for *3D* than for *3D no shear* scenario; thus, plastic deformations are larger. The convergence is the same on elastic ground, as discussed before.

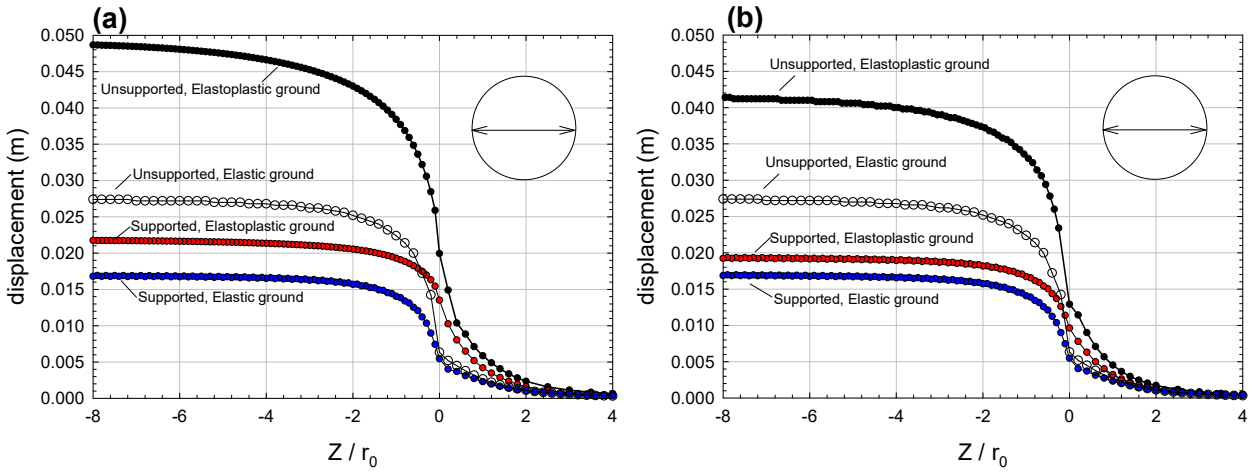

Figure 7.27 Radial displacement at the right springline with normalized distance from the face, for unsupported and supported tunnel in elastic and elastoplastic. (a) 3D; (b) 3D no shear.

Figure 7.28 shows the displacements with the normalized distance Z/r_0 at points at the tunnel perimeter for the unsupported and for supported tunnels for the 3D scenario. Because of the asymmetric plastic zone developed around the tunnel, the ground movements far-behind the face are asymmetric. Note that the radial displacements at the left and right of the tunnel, at the springline, are not the same far behind the face. Horizontal displacements near the face are observed at the crown and at the invert. These movements are associated with a horizontal rigid

body motion due to the presence of the far-field shear stress, similar to what was found for the cases analyzed in elastic ground.

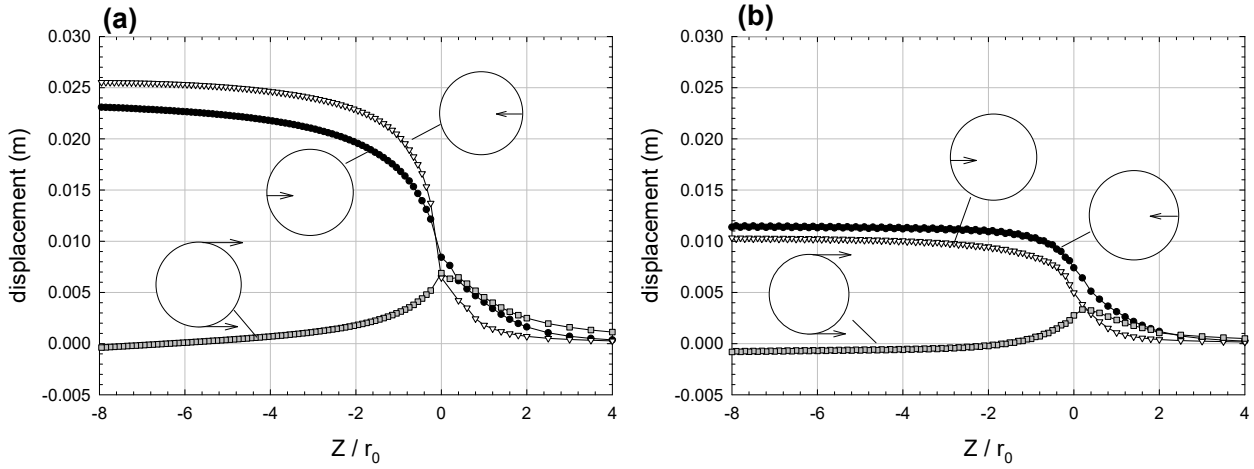

Figure 7.28 Displacements at points around the tunnel perimeter with normalized distance from the face, for the 3D scenario in elastoplastic ground. (a) *unsupported*; (b) *supported*.

The radial displacements (u_{radial}) far-behind the face along the tunnel perimeter for supported and unsupported tunnel, for the *3D* and *3D no shear* scenarios, are shown in Figure 7.29; results from a 2D simulation of the unsupported tunnel are included for comparison. The 2D simulation assumes plane strain conditions and has the same horizontal and vertical far-field stresses ($\sigma_{xx,ff}$ and $\sigma_{yy,ff}$) as the two *3D* scenarios, but the influence of the axial and shear stresses ($\sigma_{zz,ff}$ and $\tau_{xz,ff}$) and face effects are neglected. Figure 7.29(a), for the unsupported tunnel, shows that the results from the *2D* and *3D no shear* have a similar shape, are symmetric, and that the displacements from the *3D, no shear* scenario are larger than from the 2D. This is reasonable given that the size of the plastic zone increases when the axial stress $\sigma_{zz,ff}$ and face effects are included (Vitali et al., 2018). The radial displacements are the largest for the *3D* scenario and are not symmetric, again because the plastic zone size is larger and not symmetric, as shown in Figure 7.26. Therefore, 2D models are likely to underpredict ground deformations because they neglect the axial stresses and face effects. Further, the far-field axial shear, $\tau_{xz,ff}$, strongly affects the ground response around the tunnel by inducing asymmetric deformations. For the supported tunnel, Figure 7.29(b), the differences in the radial displacements far-behind the face, between the *3D* and *3D no shear* scenarios, are smaller than those observed for the unsupported tunnel because the presence of the liner reduces the size of the plastic zone around the tunnel.

Figure 7.30 and 31 show the axial displacements (w) around the tunnel perimeter for the unsupported and supported tunnel, respectively, in elastoplastic ground with normalized distance from the face, Z/r_0, for the *3D* and *3D no shear* scenarios (the 2D model would not produce axial displacements). For the *3D, no shear* scenario, Figures 7.30(b) and 31(b), the axial displacements are maximum at the face and do not disappear behind the face, contrary to what was observed for the unsupported tunnel in elastic ground. This, of course, is because of the unrecoverable plastic deformations produced. For the *3D* scenario, the axial displacements are asymmetric close and far-behind the face. The axial displacements are generally larger for the *3D* scenario than for *3D no shear* scenario, which is consistent with the plastic zone being larger for *3D* than for *the 3D no shear* scenario. As expected, the magnitude of the axial displacements is reduced when the tunnel is supported, as one can see by comparing Figures 7.30(a) and 31(a).

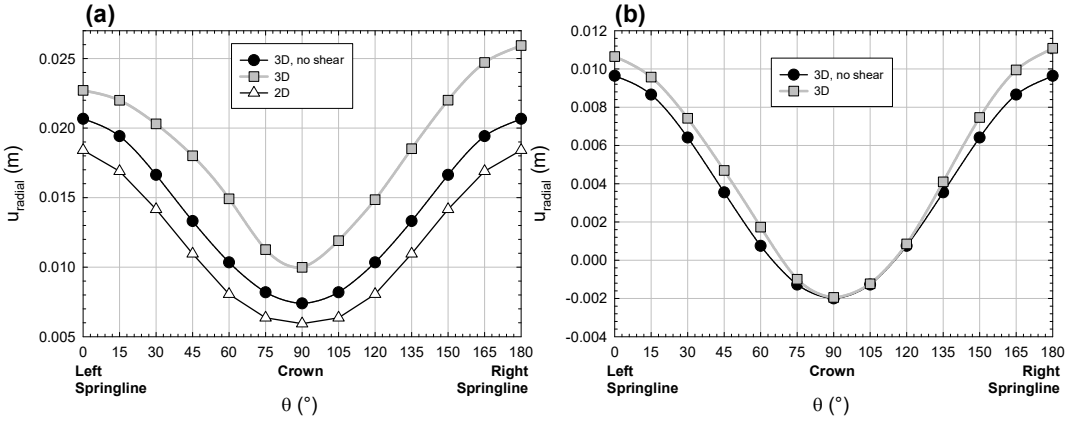

Figure 7.29 Radial displacements far-behind the face around the tunnel perimeter of a tunnel in elastoplastic ground. Positive values denote inward movement. (a) *unsupported*; (b) *supported*.

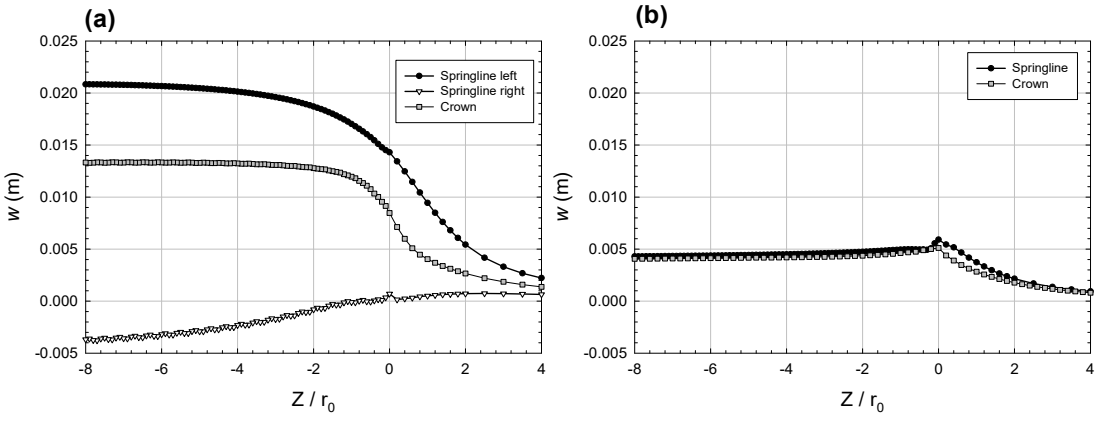

Figure 7.30 Axial displacements at points around the tunnel perimeter with normalized distance from the unsupported tunnel face in elastoplastic ground. (a) *3D* scenario (b) *3D no shear* scenario.

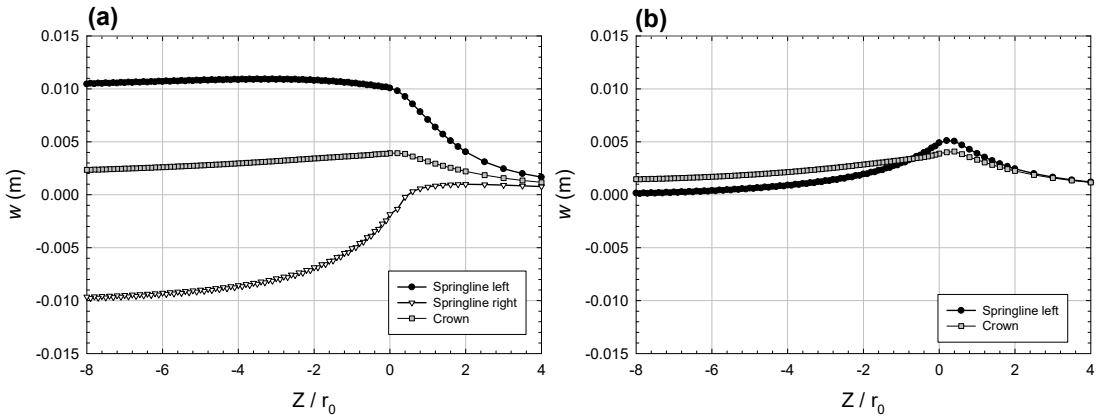

Figure 7.31 Axial displacements at points around the tunnel perimeter with normalized distance from the supported tunnel face in elastoplastic ground. (a) *3D* scenario (b) *3D no shear* scenario.

7.5 Conclusions

Far-field shear stresses are present whenever a tunnel is not aligned with one of the principal stress directions. The effects of the far-field shear stress, $\tau_{xz,ff}$, are often neglected by the customary assumption that the tunnel is aligned with one of the principal stresses. An analytical solution is presented to calculate the axial displacements and axial shear stresses far behind the face of shallow tunnels in elastic ground, due to the far-field shear stresses. The analytical solution considers the presence of the ground surface and gravity by using complex variable analysis and conformal mapping techniques. The solution provided can be combined with the analytical solution obtained by Verruijt and Booker (2000) to determine the full 3D displacement and stress fields far-behind the face of an unsupported shallow tunnel in elastic ground. This combination is possible because equilibrium and compatibility equations can be decoupled into two problems: in-plane and out-of-plane, for an infinite shallow tunnel in elastic ground. The analytical solution has been verified by comparing its predictions with results from 3D FEM models.

Near the face, the stress paths of points in the ground near the tunnel are complex due to longitudinal and transversal arching. The stress paths are obtained using 3D FEM models, which include step-by-step excavation. The results show that the far-field shear stress strongly affects the stress paths of points in the ground near the face, due to the constraint on displacements imposed by the face. The results show that, near the face, the far-field shear stresses produce radial displacements and a rigid body motion of the tunnel cross-section. This is an interesting observation that suggests that, near the face, the in-plane stresses and deformations due to the far-

field stresses normal to the axis of the tunnel are coupled with the out-of-plane shear stresses and axial deformations associated with the far-field shear stress. When a liner is installed close to the face, the coupling between shear stresses and in-plane deformations remains even far-behind the face. The finding has two important consequences: one, that the assumption commonly made, when using analytical solutions, that the response of a supported tunnel far behind the face can be obtained by decoupling the far-field in-plane and out-of-plane stresses may not be correct even in elastic ground; and two, the loss of symmetry of the solution for a supported tunnel. In other words, full 3D numerical simulations are required to properly capture the interplay that exists between ground and support when the tunnel is not aligned with the direction of the far-field principal geostatic stresses, i.e. when a far-field shear stress appears. If 3D face effects can be neglected, the decoupling between in-plane and out-of-plane stresses is valid, as shown by Vitali et al. (2018).

In elastoplastic ground, the asymmetry of stresses near the face causes the development of an asymmetric plastic zone around the tunnel. Hence, the displacements around the tunnel near the face and far-behind the face are asymmetric. Such asymmetric response has been observed for both supported and unsupported tunnels but, as expected, the presence of the liner decreases the magnitude of the deformations compared to those of the unsupported tunnel. Further, the presence of the far-field shear stress increases the overall size of the plastic zone with respect to that of a tunnel aligned with the far-field principal stress directions.

Numerical results of an unsupported tunnel misaligned with the far-field principal stresses in elastoplastic ground show that 2D models yield values of the radial displacements at the perimeter of the excavation that are too low compared to those from 3D models. They also do not capture the asymmetry of the response. The reason is because 2D models neglect face effects and the far-field axial stresses. The results improve in magnitude with a 3D numerical analysis but ignoring the far-field shear stress; however, the asymmetry of the response is not captured. In other words, full 3D analysis is needed to completely capture the effects of the tunnel misalignment with the geostatic stresses.

Nomenclature

Ψ = angle between tunnel axis and major horizontal principal stress;

Ω = complex variable, x+iy;

ζ = complex variable, $\xi+i\eta$;

α = tunnel radius in the ζ-plane;

σ_v = vertical stress;

σ_h = minor principal horizontal stress;

σ_H = major principal horizontal stress;

K_{Hv} = principal stress ratio (σ_H / σ_v);

K_{hv} = principal stress ratio (σ_h / σ_v);

r, θ = polar coordinates in the Ω-plane;

ρ, φ = polar coordinates in the ζ -plane;

x, y, z: coordinate system attached to the tunnel, with z-axis parallel to the tunnel axis;

$\sigma_{xx,ff}$ = far-field horizontal stress normal to the tunnel axis;

$\sigma_{yy,ff}$ = far-field vertical stress normal to the tunnel axis;

$\sigma_{zz,ff}$ = far-field axial stress parallel to the tunnel axis;

$\tau_{zx,ff}$ = far-field out-of-plane shear stress;

w = axial displacement;

u_{radial} = radial displacement;

$u_{tangential}$ = tangential displacement;

u_x = horizontal displacement;

G = shear modulus;

E = Young modulus;

v = Poisson ratio;

γ = unit weight;

φ = friction angle;

c = cohesion;

r_0 = tunnel radius;

r_i = internal tunnel radius;

h = tunnel depth, distance between ground surface and tunnel centerline;

d = model depth, distance between bottom boundary and tunnel centerline;

Z = axial distance from the tunnel face;

Acknowledgments

The research is being partially supported by the research funding agency of the Brazilian government CNPq (“Conselho Nacional de Desenvolvimento Cientifico”). The authors

acknowledge the support from CNPq and from Midas company, which kindly provided the license of Midas GTX NX software, used in the present work.

7.6 References

Almeida e Sousa, J., Negro, A., Matos Fernandes, M., & Cardoso, A. S. (2011). Three-Dimensional Nonlinear Analyses of a Metro Tunnel in São Paulo Porous Clay, Brazil. *Journal of Geotechnical and Geoenvironmental Engineering*, *137*(4), 376–384. https://doi.org/10.1061/(ASCE)GT.1943-5606.0000433

Armand, G., Noiret, A., Zghondi, J., & Seyedi, D. M. (2013). Short- and long-term behaviors of drifts in the Callovo-Oxfordian claystone at the Meuse/Haute-Marne Underground Research Laboratory. *Journal of Rock Mechanics and Geotechnical Engineering*, *5*(3), 221–230. https://doi.org/10.1016/j.jrmge.2013.05.005

Bobet, A. (2001). Analytical Solutions for Shallow Tunnels in Saturated Ground. *Journal of Engineering Mechanics,* 127(12): 1258-1266. https://doi.org/10.1061/(ASCE)0733-9399

Bobet, A. (2003). Effect of pore water pressure on tunnel support during static and seismic loading. *Tunnelling and Underground Space Technology*, *18*(4), 377–393. https://doi.org/10.1016/S0886-7798(03)00008-7

Bobet, A. (2011). Lined circular tunnels in elastic transversely anisotropic rock at depth. *Rock Mechanics and Rock Engineering*, *44*(2), 149–167. https://doi.org/10.1007/s00603-010-0118-1

Brady, B. H. G., and Bray, J. H. The boundary element method for determining stresses and displacements around long openings in a triaxial stress field. *International Journal of Rock Mechanics and Mining Sciences & Geomechanics Abstracts*. Vol. 15. No. 1. Pergamon, 1978.

Brady, B. H. G., & Brown, E. T. (2006). *Rock Mechanics for underground mining: Third edition*. *Rock Mechanics for underground mining: Third edition*. https://doi.org/10.1007/978-1-4020-2116-9

Brown, E. T., & Hoek, E. (1978). Trends in relationships between measured in-situ stresses and depth. *International Journal of Rock Mechanics and Mining Sciences*, *15*(4), 211–215. https://doi.org/10.1016/0148-9062(78)91227-5

Cantieni, L., & Anagnostou, G. (2009). The effect of the stress path on squeezing behavior in tunneling. *Rock Mechanics and Rock Engineering*, *42*(2), 289–318. https://doi.org/10.1007/s00603-008-0018-9

Chou, W. I., & Bobet, A. (2002). Predictions of ground deformations in shallow tunnels in clay. *Tunnelling and Underground Space Technology*, *17*(1), 3–19. https://doi.org/10.1016/S0886-7798(01)00068-2

Eberhardt, E. (2001). Numerical modelling of three-dimension stress rotation ahead of an advancing tunnel face. *International Journal of Rock Mechanics and Mining Sciences*, *38*(4), 499–518. https://doi.org/10.1016/S1365-1609(01)00017-X

Einstein, H., & Schwartz, C. (1979). Simplified analysis for tunnel supports. *ASCE J Geotech Eng Div*, *105*(4), 499–518.

Evans, K. F., Engelder, T., & Plumb, R. A. (1989). Appalachian Stress Study .1. a Detailed Description of Insitu Stress Variations in Devonian Shales of the Appalachian Plateau. *Journal of Geophysical Research-Solid Earth and Planets*, *94*, 7129–7154.

Gomes, R. a. M. P., & Celestino, T. B. (2009). Influence of physical and geometrical parameters on three-dimensional load transfer mechanism at tunnel face. *Canadian Geotechnical Journal*, *46*(7), 855–868. https://doi.org/10.1139/T09-016

Goodman, R. E. (1989). *Introduction to rock mechanics*. https://doi.org/10.1016/0148-9062(81)90521-0

Haimson, B. C., Lee, M. Y., & Song, I. (2003). Shallow hydraulic fracturing measurements in Korea support tectonic and seismic indicators of regional stress. *International Journal of Rock Mechanics and Mining Sciences*, *40*(7–8), 1243–1256. https://doi.org/10.1016/S1365-1609(03)00119-9

Hoek, E. (2008). *Practical Rock Engineering*. https://doi.org/10.2113/gseegeosci.14.1.55

Kirsch, G. (1898). Die theorie der elastizitat und die bedurfnisse der festigkeitslehre. *Veit. Ver. Deut. Ing.*, *42*, 497–807.

Ledesma, A., & Alonso, E. E. (2017). Protecting sensitive constructions from tunnelling: the case of World Heritage buildings in Barcelona. *Géotechnique*, (10), 1–12. https://doi.org/10.1680/jgeot.SiP17.P.155

Martin, C. D., & Kaiser, P. K. (1996). Mine-by Experiment Committee report, Phase 1: excavation response, summary and implications. *Atomic Energy of Canada Limited, Report AECL–11382. AECL Research, Chalk River, Ont.*

McGarr, a, & Gay, N. C. (1978). State of Stress in the Earth's Crust. *Ann. Rev. Earth Planet. Sci.*, *6*, 405–436.

Möller, S. (2006). *Tunnel induced settlements and structural forces in linings*. PhD Thesis, Institute of Geotechnical Engineering, Universitat of Stuttgart, Stuttgart.

Ng, C. W. W., Lee, G. T. K., Ng, C. W. W., & Lee, G. T. K. (2005). Three-dimensional ground settlements and stress- transfer mechanisms due to open-face tunnelling. *Canadian Geotechnical Journal*, *42*, 1015–1029. https://doi.org/10.1139/T05-025

Park, E. S., Choi, B. H., Bae, S. H., & Jeon, S. (2014). Horizontal stresses at shallow depths in Seoul (Korea) gneissic region. *Rock Engineering and Rock Mechanics: Structures in and on Rock Masses - Proceedings of EUROCK 2014, ISRM European Regional Symposium*, 399–404.

Park, K. H. (2005). Analytical solution for tunnelling-induced ground movement in clays. *Tunnelling and Underground Space Technology*, *20*(3), 249–261. https://doi.org/10.1016/j.tust.2004.08.009

Pinto, F., & Whittle, A. J. (2014). Ground Movements due to Shallow Tunnels in Soft Ground. I: Analytical Solutions. *Journal of Geotechnical and Geoenvironmental Engineering*, *140*(4), 04013040. https://doi.org/10.1061/(ASCE)GT.1943-5606.0000948

Pinto, F., Zymnis, D. M., & Whittle, A. J. (2014). Ground Movements due to Shallow Tunnels in Soft Ground. II: Analytical Interpretation and Prediction. *Journal of Geotechnical and Geoenvironmental Engineering*, *140*(4), 04013041. https://doi.org/10.1061/(ASCE)GT.1943-5606.0000947

Strack, O. E., & Verruijt, A. (2002). A complex variable solution for a deforming buoyant tunnel in a heavy elastic half-plane. *International Journal for Numerical and Analytical Methods in Geomechanics*, *26*(12), 1235–1252. https://doi.org/10.1002/nag.246

Verruijt, A. (1997). A complex variable solution for a deforming circular tunnel in an elastic half-plane. *International Journal for Numerical and Analytical Methods in Geomechanics*, *21*(2), 77–89. https://doi.org/10.1002/(SICI)1096-9853(199702)21:2<77::AID-NAG857>3.0.CO;2-M

Verruijt, A., & Booker, J. R. (2000). Complex variable analysis of Mindlin' s tunnel problem, in: Proceedings of Developments in Theoretical Geomechanics - The John Booker Memorial Symposium. Rotterdam; Jannuary, 2000.

Vitali, O. P. M., Celestino, T. B., & Bobet, A. (2018). Analytical solution for tunnels not aligned with geostatic principal stress directions. *Tunnelling and Underground Space Technology*, *82*(12), 394–405. https://doi.org/10.1016/j.tust.2018.08.046

Vitali, O. P. M., Celestino, T. B., & Bobet, A. (2019a). Buoyancy effect on shallow tunnels, *International Journal of Rock Mechanics and Mining Sciences*, *114*(2), 1–6. https://doi.org/10.1016/j.ijrmms.2018.12.012

Vitali, O. P. M., Celestino, T. B., & Bobet, A. (2019b). Shallow Tunnel Not Aligned with the Geostatic Principal Stress Directions. In Proceedings of *Geo-Congress2019, Geotechnical Special Publication (GSI)*. Philadelphia,PA.

Vitali, O. P. M., Celestino, T., & Bobet, A. (2017). 3D finite element modelling optimization for deep tunnels with material nonlinearity. *Underground Space*, *3*(2), 125–139. https://doi.org/10.1016/j.undsp.2017.11.002

Vlachopoulos, N., & Diederichs, M. S. (2009). Improved longitudinal displacement profiles for convergence confinement analysis of deep tunnels. *Rock Mechanics and Rock Engineering*, *42*(2), 131–146. https://doi.org/10.1007/s00603-009-0176-4

Wileveau, Y., Cornet, F. H., Desroches, J., & Blumling, P. (2007). Complete in situ stress determination in an argillite sedimentary formation. *Physics and Chemistry of the Earth*, *32*(8–14), 866–878. https://doi.org/10.1016/j.pce.2006.03.018

8. PROGRESSIVE FAILURE DUE TO TUNNEL MISALIGNMENT WITH GEOSTATIC PRINCIPAL STRESSES

VITALI, O. P. M.; CELESTINO, & BOBET, A. (2019). Progressive failure due to tunnel misalignment with geostatic principal stresses. In: Proceedings of *ISRM 14th International Congress on Rock Mechanics*: 2292-2299.

Abstract

When the axis of the tunnel is not parallel to one of the far-field (geostatic) principal stresses, far-field axial shear stresses are present, which distort the tunnel in the axial direction and affect the stress paths of the ground near the face of the tunnel. The goal of the paper is to investigate the effects of tunnel misalignment with the far-field principal stresses on the progressive failure of the ground around the tunnel. A well-documented experimental tunnel in a massive granite rock mass is used as reference. 3D FEM modelling is conducted to back calculate the tunnel response and to assess the effects of the tunnel misalignment. The misaligned tunnel shows failure at locations not predicted when the tunnel is aligned with the intermediate principal stress. The numerical results suggest that the misalignment may lead to asymmetric spalling of the tunnel walls.

8.1 Introduction

Rock masses may present remarked in-situ stress anisotropy because of its complex formation processes. It is highly unlikely that a tunnel is excavated totally or in part aligned with the far-field, or geostatic, principal stresses. It has been accepted that the worst-case scenario is when the tunnel is aligned with the far-field intermediate principal stress. In this case, the stress concentrations around the tunnel are maximized and stress-induced failure is more likely to occur. To minimize this effect, there have been recommendations to align the tunnel with the major principal stress (Goodman, 1989). However, for most civil applications, the tunnel direction is given, so the alignment between tunnel and principal stresses is improbable. Yet, little research has been conducted to investigate the effects of misalignment on tunnel behavior (Vitali et al., 2018; Vitali et al., 2019a; Vitali et al., 2019b). When the tunnel is not aligned with the principal stresses, far-field axial shear stresses are present that distort the tunnel cross-section in the axial direction (Vitali et al., 2018). As shown by Vitali et al. (2019b), the far-field axial shear stress

induces asymmetric displacements near the face; thus, the stress paths near the tunnel face are heavily affected by the far-field axial shear stress. As a consequence, if the tunnel has a stiff support installed near the face and/or the ground is elastoplastic, the ground displacements far behind the face could be asymmetric. For instance, Vitali et al. (2019b) showed that the plastic zone around the tunnel could be highly asymmetric because of the effects of the far-field axial shear stress near the tunnel face. Such asymmetry can only be captured by 3D FEM modeling of the misaligned tunnel, which is rarely conducted for tunnel design or even for research. So far, to the authors' best knowledge, no investigation has been conducted on the influence of tunnel misalignment on stress-induced progressive failure of the rock around the excavation. This paper seeks to provide insight on this topic. The paper uses a well-documented experimental tunnel at the URL in Canada, using 3D FEM model, to investigate the effects of the far-field axial shear stress on the progressive failure of the rock around the tunnel excavation.

A large investigation campaign was conducted at the Underground Research Laboratory (URL) in Canada (Martin & Kaiser, 1996). The goal of the research program was to investigate the behavior of the massive Lac du Bonnet granite at a large depth, and assess the suitability of the site for nuclear waste storage. Laboratory tests, in-situ tests and instrumented experimental tunnels were completed at the site (Martin & Kaiser, 1996). A progressive failure of one of the tunnels was extensively studied (Hajiabdolmajid, et al., 2003; Hajiabdolmajid, et al., 2002; Hajiabdolmajid & Kaiser, 2002; Martin, 1997; Renani & Martin, 2018). The tunnel was excavated aligned with the intermediate principal stress to maximize the concentration of stresses and, thus, induce a larger failure zone around the excavation. It was observed that failure at the tunnel wall started at stress levels that were substantially smaller than the unconfined compressive strength (UCS) of the intact rock. Detailed description of the tunnel is provided by Martin (1997) and by Martin & Kaiser (1996). The instrumentation of this experimental tunnel included seismic and acoustic sensors and triaxial strain gages to measure the stresses at points near the tunnel perimeter. The tunnel was circular, with 3.5m diameter, and unsupported. The excavation was conducted with rounds of 0.5 to 1m length. The in-situ stresses were, in MPa, σ_1=60±3, σ_2=45±4 and σ_3=11±2 (Martin, 1997, Hajiabdolmajid et al., 2003). Figure 8.1 shows the geometry of the tunnel with the failure zone, the principal stresses with respect to the tunnel and the location of the triaxial strain gages (SM5 and SM10) installed to monitor the rock response. A localized failure occurred at the location of the largest stress concentration. The failure zone had a V-notched shape, which is typical of brittle

rock masses (Kaiser et al., 2000; Martin et al., 1999). The depth of the failure zone near the crown extended up to 1.3 times the tunnel radius (i.e., 2.275m). Note that σ_3 was not aligned with the vertical direction; it was shifted approximately14° with respect to the vertical axis.

The progressive failure of Lac du Bonnet granite has been widely investigated in the laboratory (Martin & Chandler, 1994) and in the field (Martin, 1997). Based on damage controlled uniaxial compression tests, Martin & Chandler (1994) observed that progressive failure started when the deviatoric stress reached the crack damage stress (σ_{cd}). Afterwards, the cohesion degraded and the frictional strength increased as damage (i.e. cracks) accumulated in the rock until it reached the rock residual strength. Martin (1997) suggested that progressive failure around the tunnel was governed mostly by the loss of cohesion because of the low confinement stresses. To reproduce the observed mechanical behavior, Hajiabdolmajid et al. (2002) and Hajiabdolmajid et al. (2003) proposed a new constitutive model, denominated "Cohesion Weakening and Frictional Strengthening" (CWFS), where the cohesion and the friction angle are a function of plastic strains. Using this model, those authors were able to reproduce the progressive failure observed in the tunnel. Recently, Renani & Martin (2018) proposed an updated version of this constitutive model (non-linear CWFS model) that considers a non-linear evolution of the friction mobilization and cohesion loss during progressive failure. Using the non-linear CWFS model, the authors investigated the progressive failure of several tunnels in brittle rock and the stress-strain behavior of the damage-controlled uniaxial compression tests conducted by Martin & Chandler (1994). The authors showed that the non-linear CWFS model could reproduce the progressive failure observed.

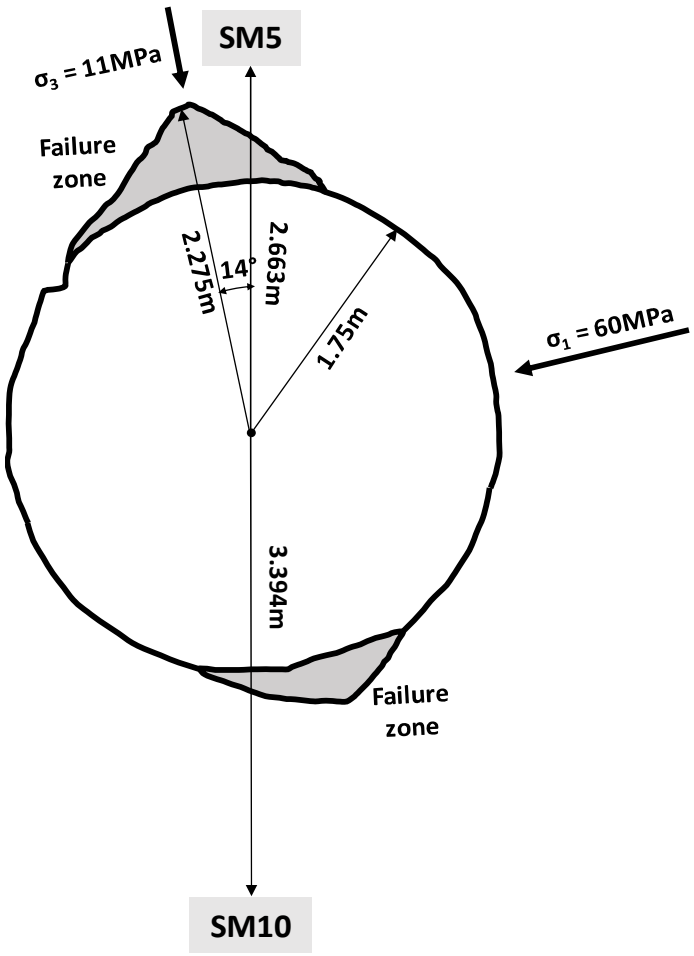

Figure 8.1 URL tunnel. Details of the failure zone, principal stresses and strain gages location (after Martin & Kaiser, 1996).

8.2 The Non-Linear CWFS model

The nonlinear CWFS model proposed by Renani & Martin (2018) is an updated version of the CWFS model first proposed by Hajiabdolmajid et al. (2002). The intent of the model is to capture the progressive failure of brittle rock masses by considering cohesion loss (c) and mobilization of the friction angle (ϕ) as a function of the equivalent plastic strain (ε_p), thus:

$$\tau_f = \sigma_N \tan\left(\phi(\varepsilon_p)\right) + c(\varepsilon_p) \tag{1}$$

Where:

$$\varepsilon_p = \int \sqrt{\frac{2}{3}\dot{\varepsilon}_{ij}\dot{\varepsilon}_{ij}}\, dt \tag{2}$$

Renani & Martin (2018) recommended the following cohesion degradation and frictional strength mobilization functions for in-situ rocks:

$$c(\varepsilon_p) = c_{residual} + (c_{initial} - c_{residual}) \left[2 - \frac{2}{1 + e^{-5\frac{\varepsilon_p}{\varepsilon_{p,residual}}}} \right] \quad (3)$$

$$\phi(\varepsilon_p) = \phi_{initial} + (\phi_{residual} - \phi_{initial}) \left[\frac{2}{1 + e^{-5\frac{\varepsilon_p}{\varepsilon_{p,residual}}}} - 1 \right] \quad (4)$$

Where: $c_{initial}$ and $\phi_{initial}$ are the initial strength properties; that is, the cohesion and the friction angle of the undamaged rock mass (ε_p=0); $c_{residual}$ and $\phi_{residual}$ are the residual strength properties and $\varepsilon_{p,\,residual}$ is the equivalent plastic strain required to reach the residual state.

The non-linear CWFS constitutive model is implemented in Midas GTS NX software, which is the FEM code used in this paper. The dependencies of cohesion with ε_p and friction angle (ϕ) with ε_p are used as input for the model, as well as the elastic properties of the rock (E, ν). Figure 8.2 shows the non-linear cohesion reduction with plastic strain (c vs. ε_p) and the non-linear frictional strength mobilization (ϕ vs. ε_p) adopted to represent the rock mass, in this investigation. The plots are based on expressions (3) and (4) provided by Renani & Martin (2018). As illustrated in Figure 8.2, for ε_p= 0 (i.e. no plastic deformations), the cohesion is equal to 50 MPa (initial cohesion) and the mobilized friction angle is zero ($\phi_{initial}$). As the plastic strain increases, the cohesion decreases while the mobilized friction angle increases. Both cohesion and friction angle reach the residual values when the equivalent plastic strain is 0.5% ($\varepsilon_{p,residual}$). The residual values are 10 MPa for the cohesion and 42° for the friction angle. The stress-strain curves for different confinement stresses are also presented in Figure 8.2. Because there is no mobilized frictional strength before yielding (i.e. ϕ=0° for ε_p=0), the onset of the progressive failure does not depend on the confinement stress. The model predicts a linear-elastic behavior until the deviatoric stress (σ_1-σ_3) reaches the initial strength of the rock mass (determined by $c_{initial}$). Afterwards, damage begins to accumulate in the rock mass and the behavior is governed by the interplay that exists between cohesion loss and friction mobilization, where the confinement stress plays an important role. The elastic properties adopted are: *E=60 GPa, v=0.25.* The rock properties are consistent

with those reported in the literature for the *Lac du Bonnet* granite (Renani & Martin, 2018, Martin & Chandler, 1994, Martin, 1997 and Hajiabdolmajid et al., 2002).

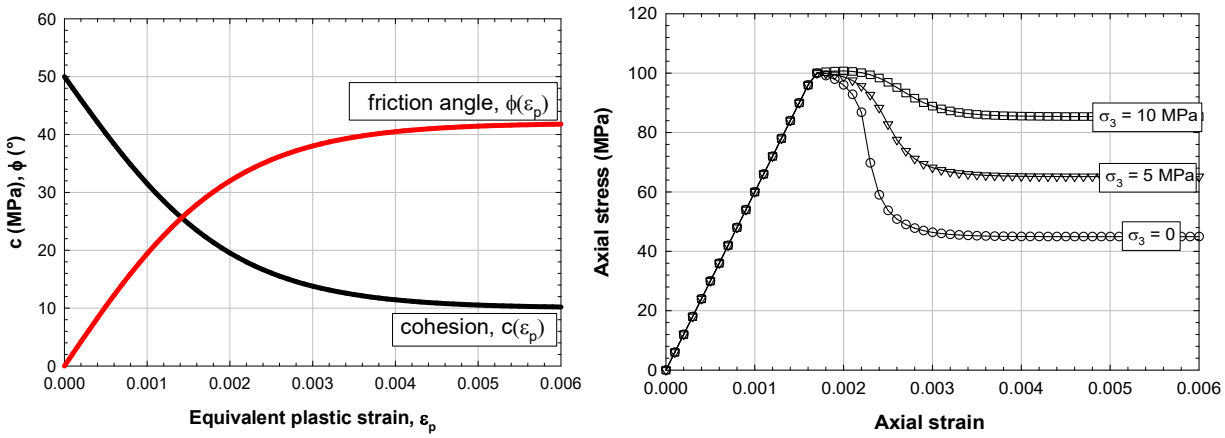

Figure 8.2 Cohesion loss and friction angle mobilization with equivalent plastic strain and stress-strain curves.

8.3 Model of URL tunnel

A 3D FEM model was built to investigate the tunnel. Figure 8.3 shows the discretization used for the simulation. The model was large enough such that boundary effects were avoided (Vitali et al, 2017). Given that the tunnel was aligned with the direction of σ_2, it was possible to take advantage of the existing symmetry, so that only one quarter of the problem was discretized. The mesh was built using 1st order elements with a very refined grid such that the size and the shape of the failure zone near the tunnel opening could be determined. The geostatic far-field stress was generated by applying a uniform pressure to the top, left and front boundaries of the mesh (Figure 8.3, left). The pressures were $\sigma_{horizontal}=\sigma_1=60\ MPa$, $\sigma_{vertical}=\sigma_3=11\ MPa$ and $\sigma_{longitudinal}=\sigma_2=45\ MPa$. The 3D excavation sequence (i.e. step by step procedure, Vitali et al., 2017) was simulated using an excavation round length of 0.5m. The model was run using the non-linear CWFS model with the properties shown in Figure 8.2.

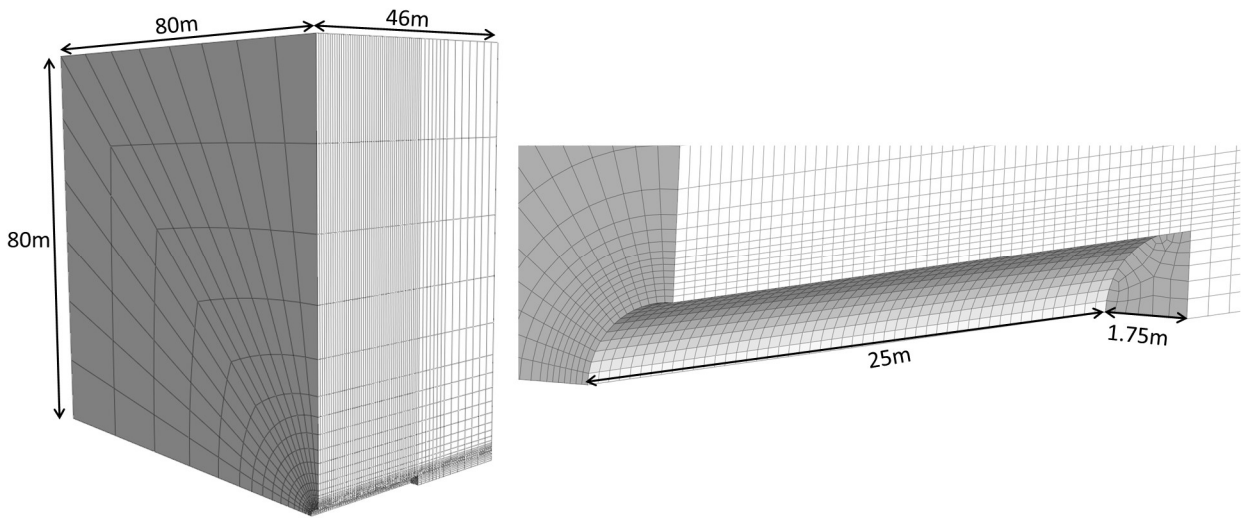

Figure 8.3 Finite element mesh. Model dimensions and mesh discretization near the opening.

Figure 8.4 shows the principal stresses (σ_1 and σ_3), at the location of the strain gages SM5 and SM10 (Figure 8.1), with the distance from the tunnel face (D_{face}) normalized with respect to the tunnel radius ($R_{tunnel}=1.75\ m$). The figure compares the major and the minor principal stresses obtained numerically with the stresses measured in-situ (Martin, 1997). The agreement between the numerical results and the field data is better for cell SM10 than for SM5. This is because the cell SM10 was located far from the failure zone such that the rock mass remained within its linear elastic regime, while cell SM5, which was close to the failure zone, was affected by the failure of the rock. Figure 8.5 shows the geometry of the failure zone measured in-situ and predicted by the model. The X-axis is aligned with σ_1 and the Y-axis, with σ_3. As one can see, the shape and depth of the failure zone predicted numerically are consistent with those observed in the field. Note that the failed rock mass detached from the tunnel wall and fell into the tunnel. Since the failure zone was close to SM5 (Figure 8.1), its readings were probably affected by the failure.

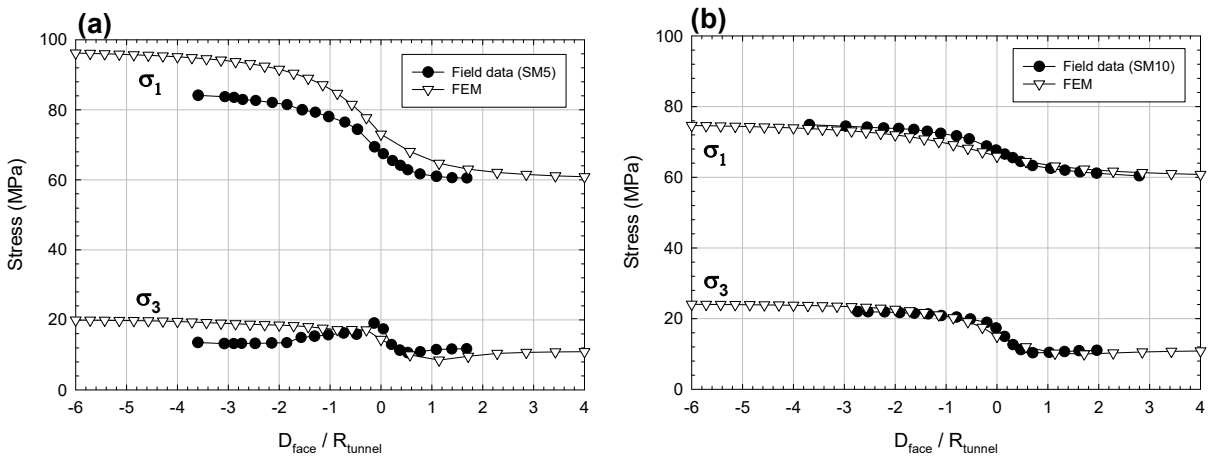

Figure 8.4 Principal stresses near the tunnel perimeter. (a) stresses at cell SM5, 2.663 m from the center of the tunnel and (b) stresses at cell SM7, 3.394 m from the center of the tunnel.

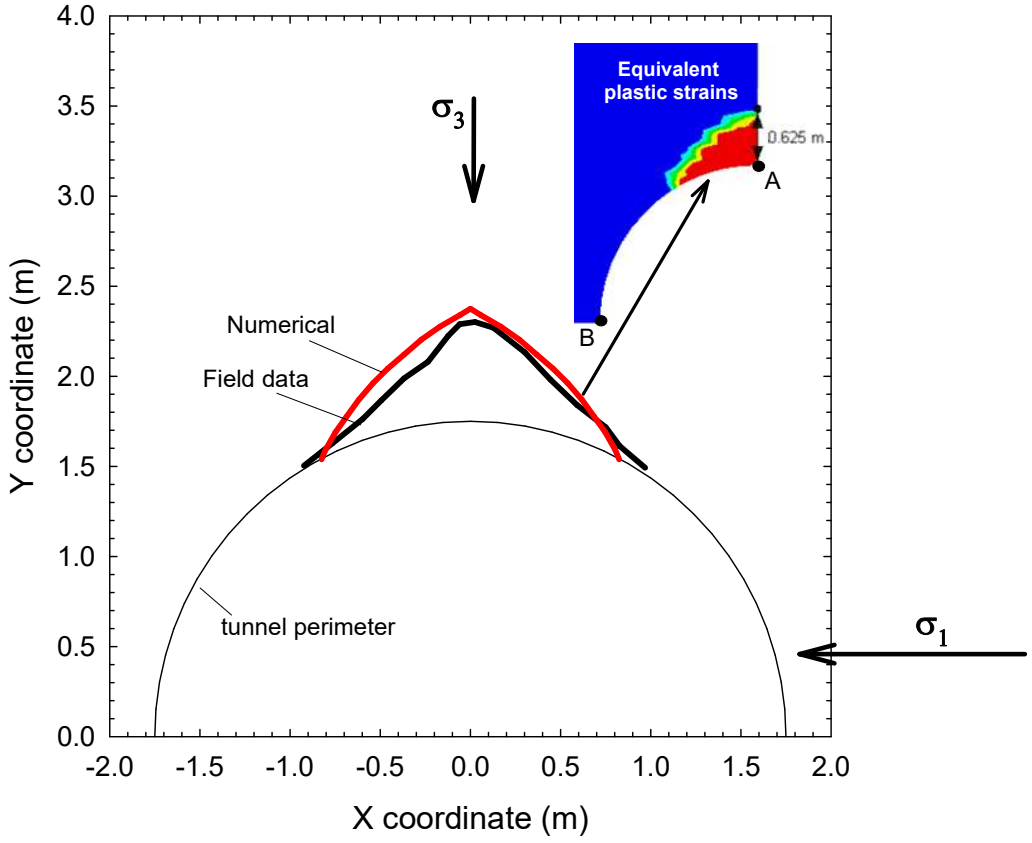

Figure 8.5 Geometry of the failure zone measured in the field and the plastic zone predicted by the numerical model.

8.4 Estimated Failure of URL tunnel if not aligned with far-field principal stresses

The comparison shown before between the numerical results and the field data from the experimental tunnel indicates that the numerical model adequately represents the actual tunnel behavior. To investigate the influence of potential tunnel misalignment with the far-field principal stresses, a new 3D FEM model was built. In the model, the axis of the tunnel was at 45° with σ_2 and σ_1, as indicated in Figure 8.6. The far-field stresses, defined with respect to the tunnel, were $\sigma_{xx,ff}=\sigma_{zz,ff}=52.5$ MPa, $\sigma_{yy,ff}=\sigma_3=11$ MPa and $\tau_{xz,ff}=7.5$ MPa, where z is parallel to the tunnel axis (Figure 8.6). The model consisted of a refined structured mesh at the center (i.e. the same discretization used before) connected to the boundaries with an unstructured mesh. The refined mesh is shown in Figure 8.6. The model was large enough to avoid boundary effects. The excavation sequence was also reproduced in the model, i.e. a step by step procedure (Vitali et al., 2017). The misalignment of the tunnel with the principal stresses produces far-field axial shear stresses ($\tau_{xz,ff}$) that distort the tunnel cross-section in the axial direction, as shown in Figure 8.7, and makes the stress paths near the tunnel face asymmetric.

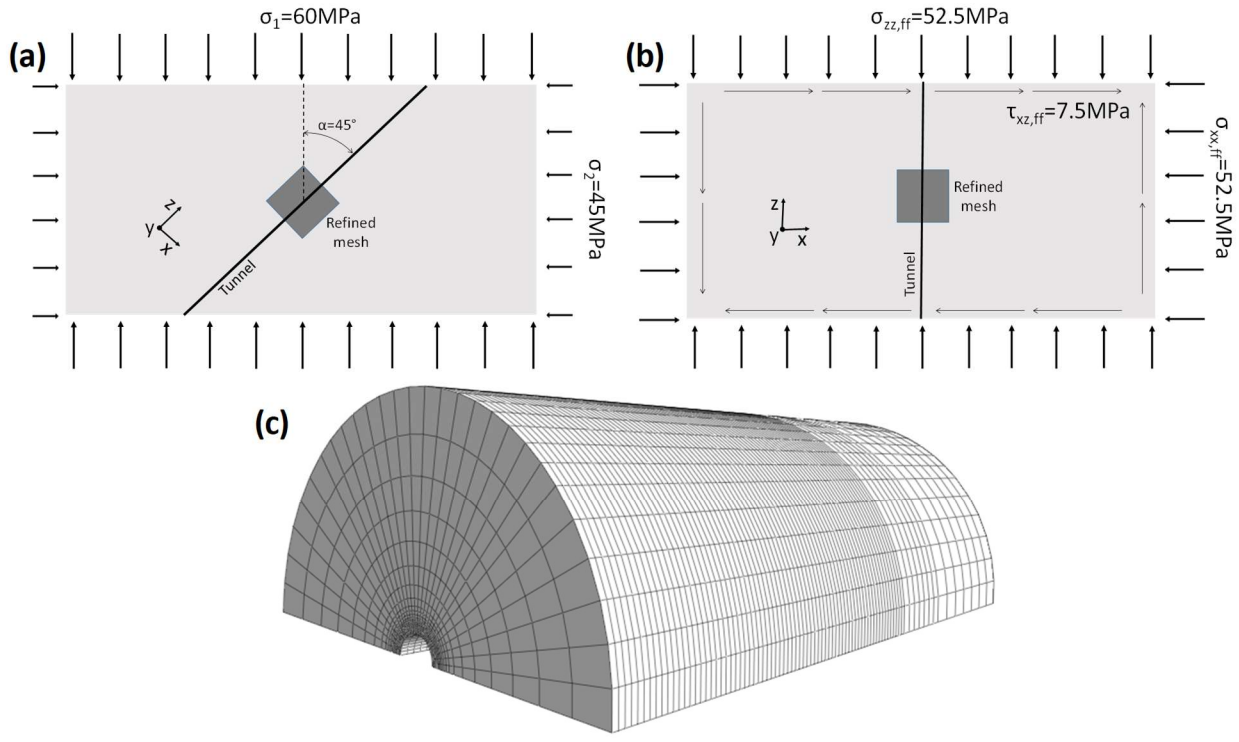

Figure 8.6 3D FEM model of the tunnel not aligned with the far-field principal stresses directions. (a) tunnel; (b) stresses with respect to the tunnel axis and; (c) refined mesh at the center of the model.

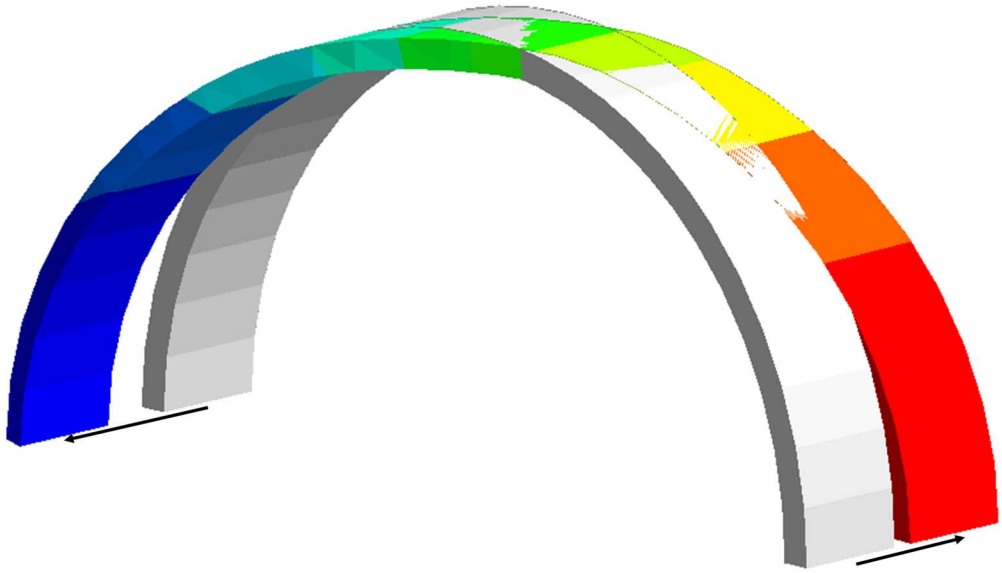

Figure 8.7 Deformed cross section in the axial direction, far-behind the tunnel face.

Figure 8.8 compares the failure zones obtained numerically for the tunnel aligned with σ_2 (α=90°, Figure 8.3) and for the misaligned tunnel (α=45°, Figure 8.6). As expected, the V-notched failure zone is larger for α=90° because the concentration of stresses around the tunnel is the largest when the tunnel is aligned with σ_2. However, the failure zone for the misaligned tunnel extends along one of the sides of the tunnel. This indicates that the far-field axial shear stress could produce spalling on one side of the tunnel, which would not occur when the tunnel is aligned with σ_2. Figure 8.9 shows the deviatoric stresses with distance from the face of the tunnel normalized with respect to the tunnel radius at the springline, for α=45° (points B1 and B2 in Figure 8.8). For α=90°, the stresses at points B1 and B2 are exactly the same because of the symmetry; however, for α=45°, the symmetry is lost and the stresses are different as a consequence of the far-field axial shear stress ($\tau_{xz,ff}$). Note that the deviatoric stress at point B2 increases as the point approaches the face of the tunnel and, near the face, the deviatoric stress abruptly increases causing yielding. In contrast, at point B1, the deviatoric stress decreases as the point moves to the face of the tunnel. Similar to B2, the deviatoric stress increases abruptly at the face, but it remains small and no yield is induced. All this suggests a possible asymmetric spalling at the tunnel walls when a far-field shear stress is present.

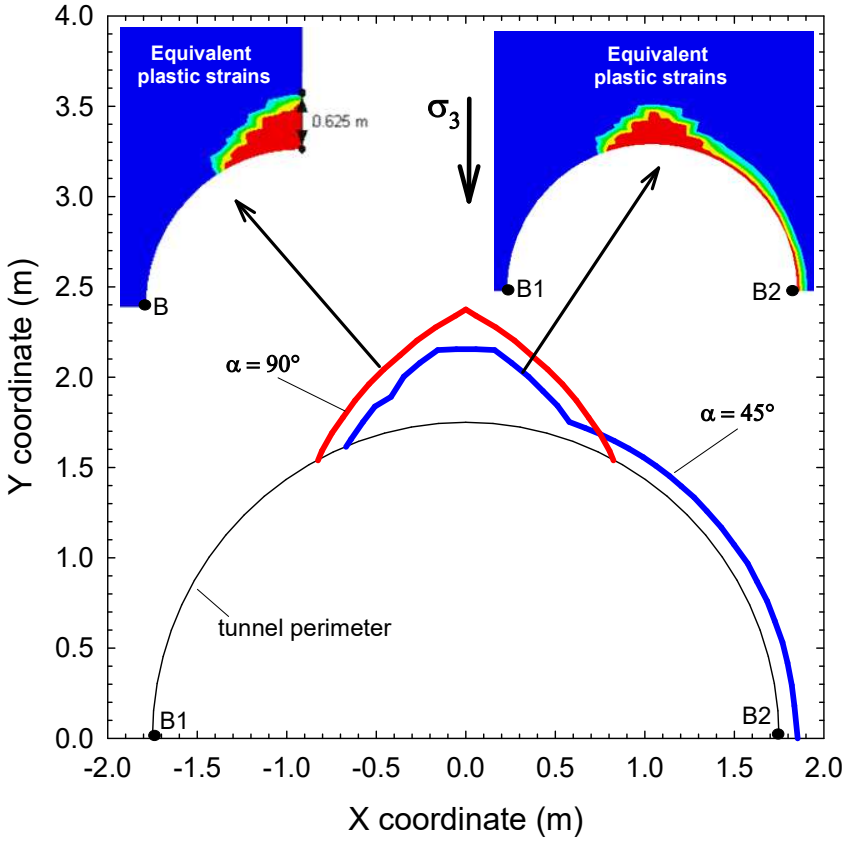

Figure 8.8 Geometry of the failure zone for α=45° and α=90°.

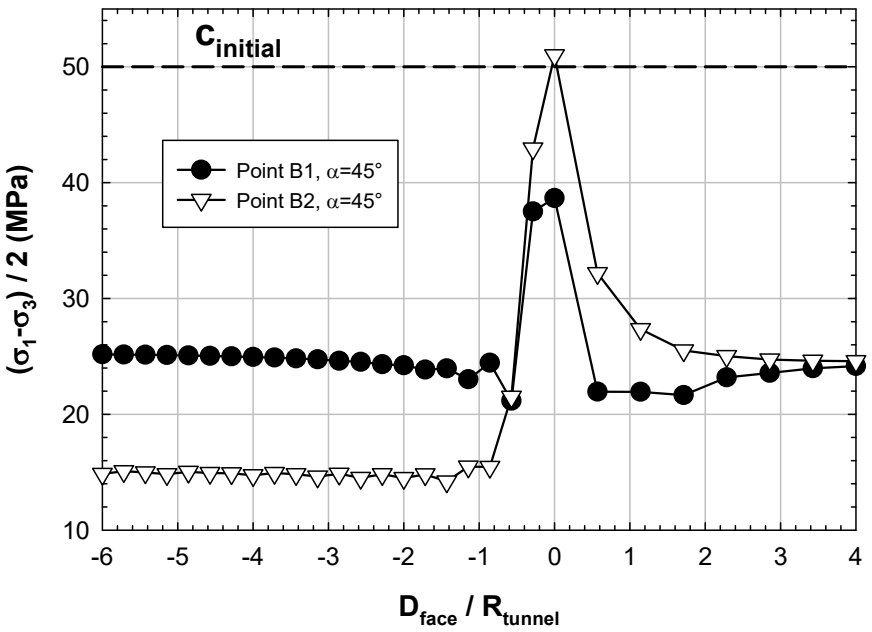

Figure 8.9 Deviatoric stresses normalized with distance to the face, for α=45°.

8.5 Conclusion

The progressive failure of a tunnel not aligned with the principal stresses is investigated in this paper. The well-documented URL experimental tunnel is used for that purpose. The tunnel was excavated aligned with the intermediate principal stress in a massive granite rock mass, with remarked stress anisotropy. As a consequence of the large stress concentrations around the tunnel induced by the excavation, a failure zone with a V-notched shape was formed. A 3D FEM model was used to investigate the tunnel's response. The mechanical behavior of the rock mass was simulated using an advanced constitutive model that included progressive failure of brittle rock masses. The numerical model predicted accurately the size and the shape of the failure zone observed in the field and stresses at points near the face of the tunnel. The same tunnel geometry and rock properties were used to investigate what would occur if the tunnel was not aligned with the intermediate principal stresses. The presence of a far-field axial shear stress induced distortions in the axial direction of the tunnel and made the stress paths at points in the rock near the tunnel face asymmetric. The model predicted a smaller V-notched failure zone for the misaligned tunnel than of the aligned tunnel but, because of the presence of the far-field axial shear stress, plastic strains developed along the wall of the tunnel at locations other than those predicted in the aligned tunnel. The numerical results indicated that the presence of a far-field axial shear stress could induce asymmetric spalling on the tunnel walls. This failure would not be predicted if the tunnel was assumed to be aligned with the intermediate principal stress. Thus, the numerical results suggest that the tunnel aligned with the intermediate principal stress may not be the worst-case scenario.

Acknowledgments

The research is being partially supported by the research funding agency of the Brazilian government CNPq ("Conselho Nacional de Desenvolvimento Cientifico"). The authors acknowledge the support from CNPq and from Midas company, which kindly provided the license of Midas GTX NX software, used in the present work.

8.6 References

Goodman, R.E., 1989. *Introduction to Rock Mechanics*. 2nd ed., John Wiley and Sons, New York.

Hajiabdolmajid, V. H., Kaiser, P. K., Martin, C. D. (2003). Mobilised strength components in brittle failure of rock. *Géotechnique*, 53, No 3, 327-336. https://doi.org/10.1680/geot.2003.53.3.327

Hajiabdolmajid, V., & Kaiser, P. (2002). Brittleness of rock and stability assessment in hard rock tunneling. *Tunnelling and Underground Space Technology*, 18 (1), 35-48. https://doi.org/10.1016/S0886-7798(02)00100-1

Hajiabdolmajid, V., Kaiser, P. K., & Martin, C. D. (2002). Modelling brittle failure of rock. *International Journal of Rock Mechanics and Mining Sciences*, 39 (6), 731–741. https://doi.org/10.1016/S1365-1609(02)00051-5

Kaiser, P. K., Diederichs, M. S., Martin, C. D., Sharp, J., & Steiner, W. (2000). Underground works in hard rock tunnelling and mining. *Proceedings of GeoEng 2000*, Melbourne.

Martin, C. D. (1997). Seventeenth Canadian Geotechnical Colloquium: The effect of cohesion loss and stress path on brittle rock strength. *Canadian Geotechnical Journal*, 34(5): 698-725 https://doi.org/10.1139/t97-030

Martin, C. D., & Chandler, N. A. (1994). The progressive fracture of Lac du Bonnet granite. *International Journal of Rock Mechanics and Mining Sciences*. 31(6): 643-659 https://doi.org/10.1016/0148-9062(94)90005-1

Martin, C. D., Kaiser, P. K., & McCreath, D. R. (1999). Hoek-Brown parameters for predicting the depth of brittle failure around tunnels. *Canadian Geotechnical Journal*. 36(1): 136-151, https://doi.org/10.1139/t98-072

Martin, C. D; Kaiser, P. K (1996). Mine-by Experiment Committee report, Phase 1: excavation response, summary and implications. Atomic Energy of Canada Limited, Report AECL–11382. AECL Research, Chalk River, Ont.

Renani R., H., & Martin, C. D. (2018). Cohesion degradation and friction mobilization in brittle failure of rocks. *International Journal of Rock Mechanics and Mining Sciences*, 106, 1–13. https://doi.org/10.1016/j.ijrmms.2018.04.003

Vitali, O. P. M., Celestino, T. B., & Bobet, A. (2018). Analytical solution for tunnels not aligned with geostatic principal stress directions. *Tunnelling and Underground Space Technology*, 82, 394–405. https://doi.org/10.1016/j.tust.2018.08.046

Vitali, O. P. M., Celestino, T.B., & Bobet, A. (2017). 3D finite element modelling optimization for deep tunnels with material nonlinearity. *Underground Space*, 3(2), 125–139. https://doi.org/10.1016/j.undsp.2017.11.002

Vitali, O. P. M., Celestino, T.B., & Bobet, A. (2019a). Shallow Tunnel not aligned to the geostatic principal stress directions. *GEO-CONGRESS 2019, Geotechnical Special Publication (GSP 313)*, 214-222, Philadelphia, PA, United States.

Vitali, O. P. M., Celestino, T. B., & Bobet, A. (2019b). Shallow tunnels misaligned with geostatic principal stress directions: analytical solution and 3D face effects. *Tunnelling and Underground Space Technology*, 89, 268-283. https://doi.org/10.1016/j.tust.2019.04.006

9. ANALYTICAL SOLUTION FOR A DEEP CIRCULAR TUNNEL IN ANISOTROPIC GROUND AND ANISOTROPIC GEOSTATIC STRESSES

VITALI, O. P. M.; CELESTINO, & BOBET, A. (2019). Analytical solution for a deep circular tunnel in anisotropic ground and anisotropic geostatic stresses. Manuscript under review for publication in a peer-reviewed journal.

Abstract

Rock masses that have a well-defined structure may also present a remarked in-situ stress anisotropy; thus, the misalignment of a tunnel with the geostatic principal stresses and/or with the principal axes of material anisotropy is very likely. Analytical solutions for tunnels in transversely anisotropic rock available in the literature assume alignment of the tunnel with the geostatic principal stresses and with one of the principal directions of the material anisotropy (i.e. 2D plane strain condition). Such assumption is quite restrictive. In this paper, a new analytical formulation for circular deep tunnels in full anisotropic rock is presented. It provides the full stress and displacement fields around a tunnel misaligned with the geostatic principal stresses or with the directions of material anisotropy. The analytical solution has been verified by comparing its predictions with results from 3D FEM modelling, for a number of scenarios with increasing complexity. A parametric analysis has been conducted to investigate the interplay that exists between the orientation of the axis of the tunnel and the directions of the principal geostatic stresses and/or the directions of material anisotropy.

9.1 Introduction

Rock masses that have a complex origin may also present a remarked stress and material anisotropy. The literature is rich in measurements of in-situ stresses (Brown and Hoek 1978; Evans et al. 1989; Gysel 1975; Haimson et al. 2003; Martin and Kaiser 1996; McGarr and Gay 1978; Park et al. 2014; Perras et al. 2015; Souček et al. 2017; Wileveau et al. 2007; Zhang et al.. 2017; Zhao et al. 2015) and anisotropic rock properties (Amadei et al. 1987; Batugin and Nirenburg 1972; Exadaktylos 2001; Park and Min 2015b; Worotnicki 1993) that show that anisotropy is expected in rock. When a tunnel is excavated in a rock mass, misalignment of the tunnel axis with the geostatic principal stresses and/or with the principal directions of material anisotropy is very likely.

However, in tunnel design and even in research, the effects of tunnel misalignment are often neglected. Research shows (Vitali et al. 2018, 2019a and 2019b) that far-field axial shear stresses are present as a result of the misalignment, which in turn distort the tunnel cross section in the axial direction (i.e. the axial shear stresses produce anti-symmetric axial displacements around the tunnel). If the rock mass is isotropic and elastic, and the tunnel is unsupported, far behind the face of the tunnel, the in-plane deformations are decoupled from the out-of-plane deformations (Vitali et al. 2018 and 2019a). However, if the rock mass is anisotropic and elastic or elastoplastic and the tunnel is misaligned with the principal directions of material anisotropy, the in-plane and out-of-plane deformations are coupled. This is so because the compliance matrix (D) is fully populated. Schubert et al. (2005) and Schubert et al. (1995) reported axial displacements in opposite directions at the tunnel walls (i.e. anti-symmetric axial displacements) in anisotropic rock masses (phyllites and shear zones), which were confirmed later using numerical models (Goricki et al., 2005; Schubert and Mendez, 2017).

Rock anisotropy tends to be more pronounced when a well-defined structure is present, such as bedding, stratification, layering, foliation, joints or flows. This is the case for metamorphic rocks such as schists, slates, quartzites, mudstones and phyllites. Marked material anisotropy is also found in sedimentary rock masses such as shales, sandstones and claystones because of the direction of material deposition and the presence of bedding planes. A particular rock structure of interest is that of transverse anisotropy, which can be taken as a good approximation for a number of rocks, including metamorphic and sedimentary. The presence of such structure may induce significant differences in strength and stiffness of the rock mass along a direction parallel to the structure, i.e. parallel to bedding, and along a direction perpendicular, i.e. perpendicular to the bedding plane. Worotnicki (1993) compiled results of the stiffness ratio E_1/E_3 (E_1 is parallel to the structure and E_3, perpendicular) that showed that granites, sandstones, gneisses and amphibolites had small to moderate anisotropy (i.e. 70% of the tested rocks had $E_1/E_3 < 1.3$, 80% $E_1/E_3 < 1.5$ and only 3% had $E_1/E_3 > 2$); mudstones, slates, phyllites and schists showed high anisotropy (50% had $E_1/E_3>2$ and 30% had $E_1/E_3<1.5$; also note that the maximum measured stiffness ratio was 6); limestones, marbles and dolomites (carbonatic rocks) showed low to moderate anisotropy (60% had $E_1/E_3 < 1.3$, 80% had $E_1/E_3 < 1.5$, with the largest $E_1/E_3 = 1.7$). Park and Min (2015a) found a stiffness ratio E_1/E_3 of 1.4 for Asan Gneiss; 1.75 for Boryeong shale and 3.8 for Yeoncheon schist, which is consistent with the compiled data previously presented. Tonon and Amadei (2002)

conducted a 2D FEM parametric analysis to assess the influence of the stiffness anisotropy on tunnel behavior. The authors observed that, even for a highly anisotropic ground ($E_1/E_3 = 3.25$), the stress field around an unsupported tunnel was not significantly affected by the stiffness ratio, but the displacement field was. A similar conclusion was obtained by Fortsakis et al. (2012), who, after conducting a series of 2D FEM analyses, concluded that the assumption of an equivalent isotropic ground might lead to an underestimation of the ground deformations.

The rock mass anisotropy may also affect the geostatic stress field (Amadei 1996; Amadei and Pan 1992; Amadei et al. 1987; Tonon and Amadei 2003). According to Amadei and Pan (1992), for a pure gravity-induced stress field, the vertical stress is a principal stress and is given by the overburden weight, the major horizontal stress is aligned with the structure, which is the stiffer direction, and the minor horizontal stress is perpendicular. In addition, tectonic activity increases the horizontal stresses and affects stress anisotropy. Hoek and Brown (1978) compiled a large number of stress ratios ($\sigma_v/\sigma_{h,ave}$), with depth, for a variety of rock masses around the world. At depths shallower than 300m, the horizontal stress was often larger than the vertical stress, with stress ratios of 1 to 5. Haimson et al. (2003), measured the horizontal stresses at shallow depths (from 7.2m to 244.2m depth) in gneissic and granitic rock masses in a seismic area near Seoul, South Korea. The minor horizontal stress was, in most locations, larger than the vertical stress. Also, the major horizontal stress (σ_H) was often significantly larger than the minor horizontal stress (σ_h); the ratio σ_H/σ_h ranged from 1.2 to 2.3. These observations were supported by Park et al. (2014). Large anisotropic horizontal stresses are also reported by Wileveau et al. (2007), who obtained ratios of σ_H/σ_h ranging from 1.3 to 2 in limestone, and by Perras et al. (2015), who reported ratios σ_H/σ_h ranging from 1 to 3.2.

Most analytical solutions for tunnels in anisotropic rock have been developed with the assumption of elastic behavior and plane strain conditions (Bobet 2011, 2016a, 2016b; Bobet and Yu 2016; Pachoud and Schleiss 2016; Manh et al. 2014; Zhang and Sun, 2011). The assumption of elasticity often limits the range of applications of the closed-form solutions to those cases where the medium is stiff or the ground deformations are small. Indeed, Choi and Bobet (2002), Pinto et al (2014) and Park (2005) reported good predictions for ground deformations around shallow tunnels using analytical solutions and Ledesma and Alonso (2017) obtained reasonable ground deformations for tunnels excavated near sensitive historic structures, using analytical solutions. The assumption of plane strain (i.e. 2D) implicitly assumes tunnel alignment with both the

geostatic principal stresses and the directions of material anisotropy. Despite their obvious limitations, analytical solutions are widely used in tunnel design because they allow a fast and robust assessment of the tunnel performance and can be used as reference to sophisticated numerical models.

In this paper, a new analytical solution for an unsupported deep circular tunnel in a full anisotropic elastic rock is presented. The solution provides the 3D stress and displacement fields around the opening. Its predictions are verified using a 3D FEM model.

9.2 Analytical solution

It is assumed that the tunnel is deep, has a circular cross section, is unsupported and the surrounding rock is fully anisotropic. Throughout the paper, the coordinate system XYZ (see Figure 9.1) is used, where the tunnel is aligned with the Z-axis, the Y-axis is vertical and the X-axis, horizontal. Figure 9.1a shows the problem: a tunnel in an anisotropic rock with an arbitrary geostatic stress field. The far-field stresses are represented in the XYZ coordinate system; that is, $\sigma_{xx,ff}$ is the horizontal far-field stress, $\sigma_{yy,ff}$ is the vertical far-field stress, $\sigma_{zz,ff}$ is the axial far-field stress, and $\tau_{xy,ff}$, $\tau_{xz,ff}$, $\tau_{yz,ff}$ are the far-field shear stresses. The problem is decomposed into two: Problem 1, Figure 9.1b, with the geostatic stresses but with no tunnel; and Problem 2, Figure 9.1c, with the tunnel and with stresses applied to the perimeter of the tunnel that are equal to those of the free field but with opposite sign. As one can see, the addition of Problems 1 and 2, in Figures 1b and 1c, results in the problem shown in Figure 9.1a. The solution of Problem 1 is straightforward: the stresses in the rock mass are equal to those of the free field, while the displacements are taken as zero, to represent the initial conditions, i.e. before the tunnel is excavated. The stresses at the perimeter of the tunnel in Problem 1 are given by equations (1) to (3). The angle θ is the polar coordinate, as shown in Figure 9.2. These stresses, with the sign changed, are applied to the perimeter of the tunnel in Problem 2.

$$\sigma_{rr}^{ff} = \frac{1}{2}\left(\sigma_{xx}^{ff} + \sigma_{yy}^{ff}\right) + \frac{1}{2}\left(\sigma_{xx}^{ff} - \sigma_{yy}^{ff}\right)\cos 2\theta + \tau_{xy}^{ff}\sin 2\theta \tag{1}$$

$$\tau_{r\theta}^{ff} = -\frac{1}{2}\left(\sigma_{xx}^{ff} - \sigma_{yy}^{ff}\right)\sin 2\theta + \tau_{xy}^{ff}\cos 2\theta \tag{2}$$

$$\tau_{rz}^{ff} = \tau_{xz}^{ff}\cos\theta + \tau_{yz}^{ff}\sin\theta \tag{3}$$

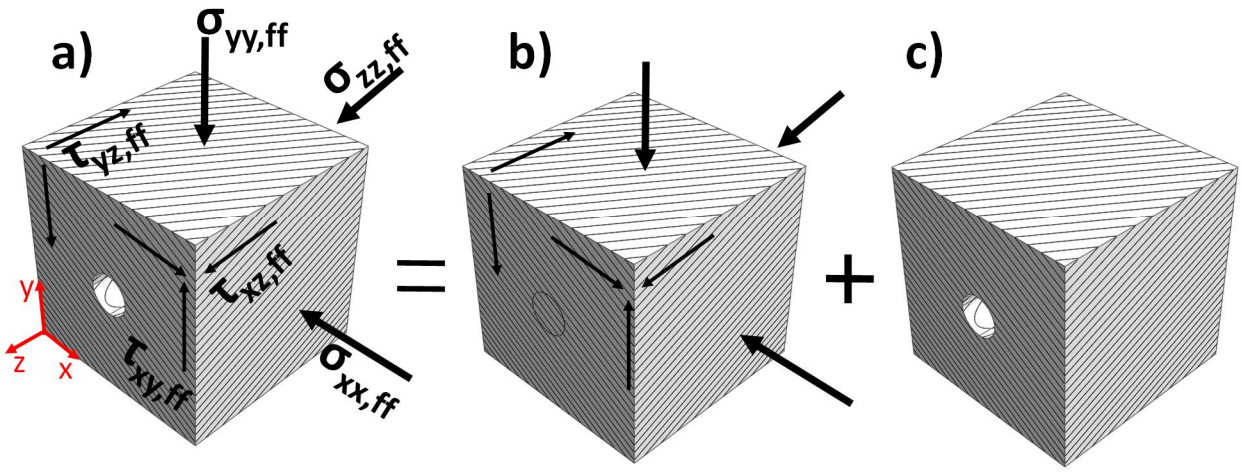

Figure 9.1 Division of a complex problem into two simpler problems. a) Anisotropic rock mass and geostatic stresses; b) Anisotropic rock mass without tunnel and with geostatic stresses; and c) Anisotropic rock mass with tunnel.

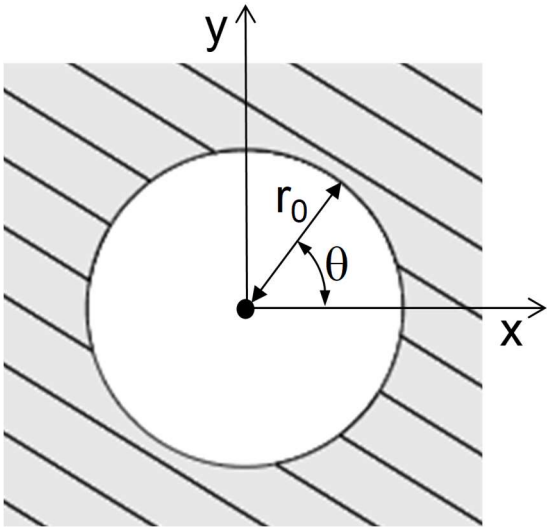

Figure 9.2 Tunnel opening and polar coordinates; r_0 is the tunnel radius.

Problem 2 describes a long tunnel along the Z axis. That is, variables cannot change along the Z axis, i.e. $\partial/\partial z = 0$; thus, the equilibrium equation ($\nabla \cdot \sigma + \vec{b} = 0$), in the absence of body forces, reduces to equations (4) to (6) and the compatibility of strains to equation (7).

$$\frac{\partial \sigma_{xx}}{\partial x} + \frac{\partial \tau_{yx}}{\partial y} = 0 \tag{4}$$

$$\frac{\partial \tau_{xy}}{\partial x} + \frac{\partial \sigma_{yy}}{\partial y} = 0 \tag{5}$$

$$\frac{\partial \tau_{xz}}{\partial x}+\frac{\partial \tau_{yz}}{\partial y}=0 \tag{6}$$

$$\frac{\partial^2 \gamma_{xy}}{\partial x \partial y}-\frac{\partial^2 \varepsilon_{xx}}{\partial y^2}-\frac{\partial^2 \varepsilon_{yy}}{\partial x^2}=0 \tag{7}$$

The stress-strain relationship for a full anisotropic elastic rock is given by equation (8).

$$\begin{Bmatrix} \varepsilon_{xx} \\ \varepsilon_{yy} \\ \varepsilon_{zz} \\ \gamma_{yz} \\ \gamma_{xz} \\ \gamma_{xy} \end{Bmatrix} = \begin{bmatrix} S_{11} & S_{12} & S_{13} & S_{14} & S_{15} & S_{16} \\ S_{12} & S_{22} & S_{23} & S_{24} & S_{25} & S_{26} \\ S_{13} & S_{23} & S_{33} & S_{34} & S_{35} & S_{36} \\ S_{14} & S_{24} & S_{34} & S_{44} & S_{45} & S_{46} \\ S_{15} & S_{25} & S_{35} & S_{45} & S_{55} & S_{56} \\ S_{16} & S_{26} & S_{36} & S_{46} & S_{56} & S_{66} \end{bmatrix} \begin{Bmatrix} \sigma_{xx} \\ \sigma_{yy} \\ \sigma_{zz} \\ \tau_{yz} \\ \tau_{xz} \\ \tau_{xy} \end{Bmatrix} \tag{8}$$

Where the matrix S_{ij} is the compliance matrix. Because of the infinite tunnel, $\partial/\partial z=0$, the axial deformations (ε_{zz}) are zero; thus, the axial stress (σ_{zz}) can be expressed as:

$$\sigma_{zz}=-\frac{1}{S_{33}}\left(S_{13}\sigma_{xx}+S_{23}\sigma_{yy}+S_{34}\tau_{yz}+S_{35}\tau_{xz}+S_{36}\tau_{xy}\right) \tag{9}$$

The compliance matrix can be written as:

$$\begin{Bmatrix} \varepsilon_{xx} \\ \varepsilon_{yy} \\ \varepsilon_{zz} \\ \gamma_{yz} \\ \gamma_{xz} \\ \gamma_{xy} \end{Bmatrix} = \begin{bmatrix} \beta_{11} & \beta_{12} & 0 & \beta_{14} & \beta_{15} & \beta_{16} \\ \beta_{12} & \beta_{22} & 0 & \beta_{24} & \beta_{25} & \beta_{26} \\ 0 & 0 & 0 & 0 & 0 & 0 \\ \beta_{14} & \beta_{24} & 0 & \beta_{44} & \beta_{45} & \beta_{46} \\ \beta_{15} & \beta_{25} & 0 & \beta_{45} & \beta_{55} & \beta_{56} \\ \beta_{16} & \beta_{26} & 0 & \beta_{46} & \beta_{56} & \beta_{66} \end{bmatrix} \begin{Bmatrix} \sigma_{xx} \\ \sigma_{yy} \\ \sigma_{zz} \\ \tau_{yz} \\ \tau_{xz} \\ \tau_{xy} \end{Bmatrix} \tag{10}$$

Where:

$$\beta_{ij}=S_{ij}-\frac{S_{i3}S_{3j}}{S_{33}} \tag{11}$$

The equations of equilibrium are satisfied by defining two stress functions F and H such that:

$$\sigma_{xx}=\frac{\partial^2 F}{\partial y^2};\ \sigma_{yy}=\frac{\partial^2 F}{\partial x^2};\ \tau_{xy}=-\frac{\partial^2 F}{\partial x \partial y};\ \tau_{xz}=\frac{\partial H}{\partial y};\ \tau_{yz}=-\frac{\partial H}{\partial x} \tag{12}$$

Defining the complex variable z as: $z = X + \mu Y$, where μ is a complex number, and imposing the compatibility equation (7) and that $\partial\gamma_{yz}/\partial x = \partial\gamma_{xz}/\partial y$, equations (13) and (14) are obtained.

$$\begin{aligned}&\left(\beta_{11}\mu^4 - 2\beta_{16}\mu^3 + (2\beta_{12}+\beta_{66})\mu^2 - 2\beta_{26}\mu + \beta_{22}\right)\frac{\partial^4 F}{\partial z^4}\\&+\left(\beta_{15}\mu^3 - (\beta_{14}+\beta_{56})\mu^2 + (\beta_{25}+\beta_{46})\mu - \beta_{24}\right)\frac{\partial^3 H}{\partial z^3} = 0\end{aligned} \tag{13}$$

$$\left(\beta_{15}\mu^3 - (\beta_{14}+\beta_{56})\mu^2 + (\beta_{25}+\beta_{46})\mu - \beta_{24}\right)\frac{\partial^3 F}{\partial z^3} + \left(\beta_{55}\mu^2 - 2\beta_{45}\mu + \beta_{44}\right)\frac{\partial^2 H}{\partial z^2} = 0 \tag{14}$$

The two equations can be used to obtain the functions F and H by e.g. substitution. This results in equation (15). The equation is satisfied when μ are the roots of the canonic equation (16). There are six roots, but three are the conjugates.

$$\begin{bmatrix}\mu^6\left(\beta_{11}\beta_{55} - \beta_{15}^{\,2}\right) + \mu^5\left(-2\beta_{11}\beta_{45} - 2\beta_{16}\beta_{55} + 2\beta_{15}(\beta_{14}+\beta_{56})\right) +\\ \mu^4\left(\beta_{11}\beta_{44} + 4\beta_{16}\beta_{45} + (2\beta_{12}+\beta_{66})\beta_{55} - (\beta_{14}+\beta_{56})^2 - 2\beta_{15}(\beta_{25}+\beta_{46})\right) +\\ \mu^3\left(-2\beta_{16}\beta_{44} - 2\beta_{45}(2\beta_{12}+\beta_{66}) - 2\beta_{26}\beta_{55} + 2\beta_{15}\beta_{24} + 2(\beta_{14}+\beta_{56})(\beta_{25}+\beta_{46})\right) +\\ \mu^2\left(\beta_{44}(2\beta_{12}+\beta_{66}) + 4\beta_{26}\beta_{45} + \beta_{22}\beta_{55} - 2\beta_{24}(\beta_{14}+\beta_{56}) - (\beta_{25}+\beta_{46})^2\right) +\\ \mu\left(-2\beta_{26}\beta_{44} - 2\beta_{22}\beta_{45} + 2\beta_{24}(\beta_{25}+\beta_{46})\right) + \left(\beta_{22}\beta_{44} - \beta_{24}^{\,2}\right)\end{bmatrix}\frac{\partial^4 F}{\partial z^4} = 0 \tag{15}$$

$$\begin{aligned}&\mu^6\left(\beta_{11}\beta_{55} - \beta_{15}^{\,2}\right) + \mu^5\left(-2\beta_{11}\beta_{45} - 2\beta_{16}\beta_{55} + 2\beta_{15}(\beta_{14}+\beta_{56})\right) +\\ &\mu^4\left(\beta_{11}\beta_{44} + 4\beta_{16}\beta_{45} + (2\beta_{12}+\beta_{66})\beta_{55} - (\beta_{14}+\beta_{56})^2 - 2\beta_{15}(\beta_{25}+\beta_{46})\right) +\\ &\mu^3\left(-2\beta_{16}\beta_{44} - 2\beta_{45}(2\beta_{12}+\beta_{66}) - 2\beta_{26}\beta_{55} + 2\beta_{15}\beta_{24} + 2(\beta_{14}+\beta_{56})(\beta_{25}+\beta_{46})\right) +\\ &\mu^2\left(\beta_{44}(2\beta_{12}+\beta_{66}) + 4\beta_{26}\beta_{45} + \beta_{22}\beta_{55} - 2\beta_{24}(\beta_{14}+\beta_{56}) - (\beta_{25}+\beta_{46})^2\right) +\\ &\mu\left(-2\beta_{26}\beta_{44} - 2\beta_{22}\beta_{45} + 2\beta_{24}(\beta_{25}+\beta_{46})\right) + \left(\beta_{22}\beta_{44} - \beta_{24}^{\,2}\right) = 0\end{aligned} \tag{16}$$

The solution of the system of equations 13 and 14 is singular when the tunnel is aligned with one of the principal directions of material anisotropy. The solution is given in Appendix 1.

Defining, following Lekhnitskii (1936), $\phi_1(z_1) = F'_1(z_1)$, $\phi_2(z_2) = F'_2(z_2)$ and $\phi_3(z_3) = \frac{1}{\lambda_3}H(z_3)$, the expressions for stresses and displacements are:

$$\sigma_{xx} = 2\,\mathrm{Re}\left[\mu_1^{\,2}\phi'_1(z_1) + \mu_2^{\,2}\phi'_2(z_2) + \mu_3^{\,2}\lambda_3\phi'_3(z_3)\right] \tag{17}$$

$$\sigma_{yy} = 2\,\mathrm{Re}\left[\phi'_1(z_1) + \phi'_2(z_2) + \lambda_3\phi'_3(z_3)\right] \tag{18}$$

$$\tau_{xy} = -2\,\mathrm{Re}\left[\mu_1\phi'_1(z_1) + \mu_2\phi'_2(z_2) + \mu_3\lambda_3\phi'_3(z_3)\right] \tag{19}$$

$$\tau_{yz} = -2\,\mathrm{Re}\left[\lambda_1\phi'_1(z_1) + \lambda_2\phi'_2(z_2) + \phi'_3(z_3)\right] \tag{20}$$

$$\tau_{xz} = 2\mathrm{Re}\left[\mu_1\lambda_1\phi'_1(z_1) + \mu_2\lambda_2\phi'_2(z_2) + \mu_3\phi'_3(z_3)\right] \tag{21}$$

$$u_x = 2\,\mathrm{Re}\left(\sum_{k=1}^{2}\left(\beta_{11}\mu_k^2 + \beta_{12} - \beta_{16}\mu_k + \lambda_k\left(\beta_{15}\mu_k - \beta_{14}\right)\right)\phi_k + \left[\lambda_3\left(\beta_{11}\mu_3^2 + \beta_{12} - \beta_{16}\mu_3\right) + \beta_{15}\mu_3 - \beta_{14}\right]\phi_3\right) \tag{22}$$

$$u_y = 2\,\mathrm{Re}\left(\sum_{k=1}^{2}\left(\beta_{12}\mu_k + \frac{\beta_{22}}{\mu_k} - \beta_{26} + \lambda_k\left(\beta_{25} - \frac{\beta_{24}}{\mu_k}\right)\right)\phi_k + \left[\lambda_3\left(\beta_{12}\mu_3 + \frac{\beta_{22}}{\mu_3} - \beta_{26}\right) + \left(\beta_{25} - \frac{\beta_{24}}{\mu_3}\right)\right]\phi_3\right) \tag{23}$$

$$u_z = 2\,\mathrm{Re}\left(\sum_{k=1}^{2}\left(\beta_{14}\mu_k + \frac{\beta_{24}}{\mu_k} - \beta_{46} + \lambda_k\left(\beta_{45} - \frac{\beta_{44}}{\mu_k}\right)\right)\phi_k + \left[\lambda_3\left(\beta_{14}\mu_3 + \frac{\beta_{24}}{\mu_3} - \beta_{46}\right) + \left(\beta_{45} - \frac{\beta_{44}}{\mu_3}\right)\right]\phi_3\right) \tag{24}$$

Where $z_k = X + \mu_k Y$, and μ_k are the roots of equation (16), and

$$\lambda_1 = -\frac{\left(\beta_{15}\mu_1^3 - (\beta_{14} + \beta_{56})\mu_1^2 + (\beta_{25} + \beta_{46})\mu_1 - \beta_{24}\right)}{\left(\beta_{55}\mu_1^2 - 2\beta_{45}\mu_1 + \beta_{44}\right)} \tag{25}$$

$$\lambda_2 = -\frac{\left(\beta_{15}\mu_2^3 - (\beta_{14} + \beta_{56})\mu_2^2 + (\beta_{25} + \beta_{46})\mu_2 - \beta_{24}\right)}{\left(\beta_{55}\mu_2^2 - 2\beta_{45}\mu_2 + \beta_{44}\right)} \tag{26}$$

$$\lambda_3 = -\frac{\left(\beta_{15}\mu_3^3 - (\beta_{14} + \beta_{56})\mu_3^2 + (\beta_{25} + \beta_{46})\mu_3 - \beta_{24}\right)}{\left(\beta_{11}\mu_3^4 - 2\beta_{16}\mu_3^3 + (2\beta_{12} + \beta_{66})\mu_3^2 - 2\beta_{26}\mu_3 + \beta_{22}\right)} \tag{27}$$

The functions φ_k are defined as Laurent series. That is,

$$\phi_k = \sum_{m=1}^{\infty} A_{km}\zeta_k^{-m}\text{ , where k =1, 2, 3} \tag{28}$$

Where:

$$z_k = \frac{r_0}{2}\left[(1 - i\mu_k)\zeta_k + (1 + i\mu_k)\frac{1}{\zeta_k}\right] \tag{29}$$

The complex coefficients A_{km} can be determined by imposing the boundary conditions at $r=r_o$, i.e. at the perimeter of the opening. That is,

$$2\,\mathrm{Re}\left[\phi_1(z_1) + \phi_2(z_2) + \lambda_3\phi_3(z_3)\right] = \int\left(-\sigma_{rr}\sin\theta - \tau_{r\theta}\cos\theta\right)r_0 d\theta \tag{30}$$

$$2\,\mathrm{Re}\left[\mu_1\phi_1(z_1) + \mu_2\phi_2(z_2) + \mu_3\lambda_3\phi_3(z_3)\right] = \int\left(\sigma_{rr}\cos\theta - \tau_{r\theta}\sin\theta\right)r_0 d\theta \tag{31}$$

$$2\,\mathrm{Re}\left[\lambda_1\phi_1(z_1) + \lambda_2\phi_2(z_2) + \phi_3(z_3)\right] = \int\tau_{rz}r_0 d\theta \tag{32}$$

This results in the following system of linear equations:

$$\begin{cases} A_{11}+A_{21}+\lambda_{31}A_{31}-\lambda_{32}A_{32}=-\dfrac{1}{2}\sigma_{yy}^{ff}r_0 \\ A_{12}+A_{22}+\lambda_{31}A_{32}+\lambda_{32}A_{31}=\dfrac{1}{2}\tau_{xy}^{ff}r_0 \\ \mu_{11}A_{11}-\mu_{12}A_{12}+\mu_{21}A_{21}-\mu_{22}A_{22}+\left(\mu_{31}\lambda_{31}-\mu_{32}\lambda_{32}\right)A_{31}-\left(\mu_{32}\lambda_{31}+\mu_{31}\lambda_{32}\right)A_{32}=\dfrac{1}{2}\tau_{xy}^{ff}r_0 \\ \mu_{11}A_{12}+\mu_{12}A_{11}+\mu_{21}A_{22}+\mu_{22}A_{21}+\left(\mu_{31}\lambda_{31}-\mu_{32}\lambda_{32}\right)A_{32}+\left(\mu_{32}\lambda_{31}+\mu_{31}\lambda_{32}\right)A_{31}=-\dfrac{1}{2}\sigma_{xx}^{ff}r_0 \\ \lambda_{11}A_{11}-\lambda_{12}A_{12}+\lambda_{21}A_{21}-\lambda_{22}A_{22}+A_{31}=\dfrac{1}{2}\tau_{yz}^{ff}r_0 \\ \lambda_{11}A_{12}+\lambda_{12}A_{11}+\lambda_{21}A_{22}+\lambda_{22}A_{21}+A_{32}=-\dfrac{1}{2}\tau_{xz}^{ff}r_0 \end{cases} \tag{33}$$

Where:

$$\begin{aligned} &\mu_k=\mu_{k1}+i\mu_{k2} \\ &A_k=A_{k1}+iA_{k2}\text{ , k= 1, 2, 3.} \\ &\lambda_k=\lambda_{k1}+i\lambda_{k2} \end{aligned} \tag{34}$$

A case of particular interest is that of a rock mass with orthotropic elasticity, (Amadei et al. 1987; Worotnicki 1993). The compliance matrix in (8) can be defined with nine elastic properties, and takes the form shown in (35).

$$\varepsilon=D\sigma\rightarrow\begin{Bmatrix}\varepsilon_{xx}\\ \varepsilon_{yy}\\ \varepsilon_{zz}\\ \gamma_{yz}\\ \gamma_{xz}\\ \gamma_{xy}\end{Bmatrix}=\begin{bmatrix} \dfrac{1}{E_x} & -\dfrac{\nu_{yx}}{E_y} & -\dfrac{\nu_{zx}}{E_z} & 0 & 0 & 0 \\ -\dfrac{\nu_{yx}}{E_y} & \dfrac{1}{E_y} & -\dfrac{\nu_{zy}}{E_z} & 0 & 0 & 0 \\ -\dfrac{\nu_{zx}}{E_z} & -\dfrac{\nu_{zy}}{E_z} & \dfrac{1}{E_z} & 0 & 0 & 0 \\ 0 & 0 & 0 & \dfrac{1}{G_{yz}} & 0 & 0 \\ 0 & 0 & 0 & 0 & \dfrac{1}{G_{zx}} & 0 \\ 0 & 0 & 0 & 0 & 0 & \dfrac{1}{G_{yx}} \end{bmatrix}\begin{Bmatrix}\sigma_{xx}\\ \sigma_{yy}\\ \sigma_{zz}\\ \tau_{yz}\\ \tau_{xz}\\ \tau_{xy}\end{Bmatrix} \tag{35}$$

Equation (35) is written such that the axes xyz are the principal directions of material anisotropy, and thus the tunnel is aligned with one of the principal directions, i.e. the z direction. When this is not the case, the compliance matrix (D) is rotated following the procedure shown in

(36), using Voigt's notation, such as the axis Z ends up being the axis of the tunnel. Note that the rotated compliance matrix may be fully populated.

$$\varepsilon = D\sigma \rightarrow R_{\varepsilon}\varepsilon = D\left(R_{\sigma}\sigma\right) \rightarrow \varepsilon = \left(R_{\sigma}{}^{T} D R_{\sigma}\right)\sigma \rightarrow \varepsilon = D'\sigma \quad (36)$$

Note that: $R_{\varepsilon}{}^{-1} = R_{\sigma}{}^{T}$. The rotation matrices and details about the rotation convention are provided in Appendix 2.

The analytical solution for a tunnel in an orthotropic elastic material not aligned with the principal directions of material anisotropy is verified using a 3D FEM model. The FEM model is built using 2nd order hexahedral elements and the mesh is refined enough such that the numerical results are accurate (Vitali et al. 2017). The numerical model consists of two phases: the 1st one generates the geostatic stress field; the 2nd, represents the tunnel excavation (through deactivation of the elements inside the tunnel perimeter). The numerical results are extracted from the nodes at the tunnel perimeter. The material properties adopted are: E_x*=2GPa;* E_y*= 1GPa;* E_z*= 3GPa;* ν_{xy}*=0.2;* ν_{xz}*=0.3;* ν_{yz}*=0.4;* G_{xy}*=0.7GPa;* G_{xz}*=0.8GPa;* G_{yz}*=0.5GPa*. The principal directions of material anisotropy are rotated with respected to the tunnel axis using the ZXZ-rotation convention. It is assumed that the Euler angles are α=30°; β=45° and γ=20°. The far-field stresses are: $\sigma_{yy,ff}$ *= 20MPa,* $\sigma_{xx,ff}$*=10MPa and* $\sigma_{zz,ff}$*=5MPa* (compression is taken as positive). Note that it is assumed that the tunnel is aligned with the principal stresses, but misaligned with the principal directions of material anisotropy. Figure 9.3 compares the stresses and displacements along the tunnel perimeter obtained with the analytical solution with those with the 3D FEM model. The stresses and the displacements are normalized with respect to the far-field vertical stress (σ_v) and to the tunnel radius (r_0), respectively. The good match between analytical and numerical results shows that the analytical solution is essentially correct. It is interesting to note that even though the tunnel is aligned with the geostatic principal stress directions, there are axial displacements and axial shear stresses. This is due to the coupling of normal strains with shear stresses and also of the shear strains with normal stresses, because of the rotated compliance matrix D. Note also that stresses and displacements show no symmetry, as it would be when the tunnel was aligned with one of the principal directions of material anisotropy.

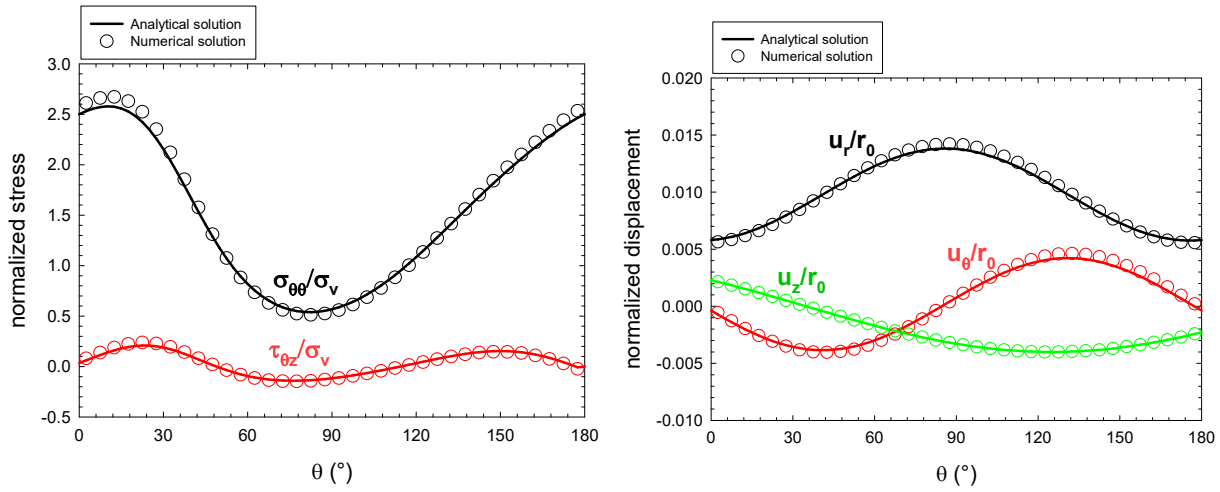

Figure 9.3 Analytical and numerical stresses normalized with respect to the vertical stress and displacements normalized with respect to the tunnel radius around the tunnel perimeter for orthotropic elastic rock mass.

9.3 Discussion

Rock masses may present structure determined by e.g. schistosity, foliation, stratification, bedding, etc., that may induce anisotropy. Despite the complexity that this introduces, the rock mass behavior can be well approximated with the assumption of transverse anisotropy (Amadei et al. 1987; Batugin and Nirenburg 1972; Worotnicki 1993). This requires six elastic properties that can be determined from conventional laboratory tests or from theoretical approximations (Exadaktylos 2001). The compliance matrix in (35) is still valid, but with $E_x=E_z$, $\nu_{yz}=\nu_{yx}$ and $G_{yz}=G_{yx}$.

The orientation of the predominant structure is conventionally defined with two angles: the dip (α_1) and the strike angle (α_2); see Figure 9.4. Note that it is assumed that the "Z" axis, i.e. the axis of the tunnel, is aligned with the North. In other words, the strike angle is given with respect to the axis of the tunnel. Note that when $\alpha_1=0°$, the structure is horizontal and the tunnel is aligned with one of the principal directions of material anisotropy. The rotation matrix, needed to express the compliance matrix in the XYZ coordinate system, is obtained through rotation, which is expressed in terms of the angles α_1 and α_2 and is given in Appendix 3. Appendix 4 provides a Matlab code to find stresses and displacements at the tunnel perimeter (i.e. $r=r_0$) using the analytical solution for transversely anisotropic rock mass.

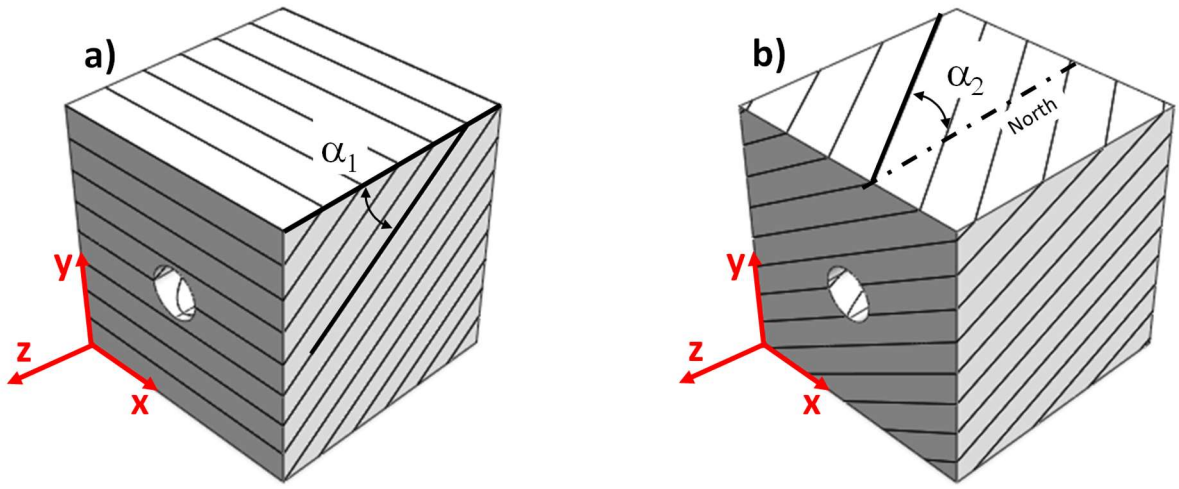

Figure 9.4 Orientation of structural planes. (a) strike perpendicular to tunnel axis; (b) strike at an angle with the tunnel axis. The North is assumed parallel to the Z-axis.

The effects of tunnel misalignment with the rock mass principal directions of material anisotropy has been left largely unexplored. Yet, there is field evidence of anti-symmetric axial displacements in tunnels in foliated rock (Schubert et al. 2005; Schubert and Budil 1995), thought to be caused by the anisotropic properties of the rock mass. Also, it has been known that the far-field axial shear stresses induce axial distortions in the tunnel cross-section (Vitali et al. 2018, 2019a and 2019b). To understand better the implications of tunnel misalignment on ground response, a parametric analysis has been conducted. The analyses are geared to explore the effects of tunnel orientation with the principal directions of the geostatic stresses (Figure 9.5), and with the principal directions of material anisotropy (Figure 9.6). The following information is used in all cases: σ_v= 5MPa, σ_h= 5MPa and σ_H= 10MPa and: $E_z = E_x$ = 3GPa (Young modulus parallel to the isotropic planes); E_y = 1GPa (Young modulus perpendicular to the isotropic planes); $G_{xy} = G_{yz}$ = 0.5GPa (shear modulus perpendicular to the isotropic planes); G_{xz} =0.8 GPa (shear modulus parallel to the isotropic planes); $\nu_{yz} = \nu_{xy}$ = 0.2 and; ν_{xz}= 0.4. The geostatic stress field adopted corresponds to a point at 200m depth with stress anisotropy in the range found in rock masses (Brown and Hoek 1978; Evans et al. 1989; Gysel 1975; Haimson et al. 2003; Martin and Kaiser 1996; McGarr and Gay 1978; Park et al. 2014; Perras et al. 2015; Souček et al. 2017; Wileveau et al. 2007; Zhang et al. 2017; Zhao et al. 2015). The material properties adopted are credible for highly anisotropic rock masses, such as slates, schists and phyllites. Note that the ratio E_x/E_y = 3 is on the upper limit of the range presented by Worotnicki (1993).

Figure 9.5 illustrates the plan view of the tunnel orientation with the principal stress directions and the principal directions of material anisotropy. The tunnel is assumed horizontal and at an angle Ψ with the major horizontal stress (σ_H). The far-field stresses, expressed in the coordinated system XYZ (attached to the tunnel), as a function of the angle Ψ, are given in equations (37) to (40). As the tunnel rotates (i.e. as Ψ increases from 0° to 90°), the far-field horizontal stress, $\sigma_{xx,ff}$, increases and is maximum at Ψ=90°, while the vertical stress ($\sigma_{yy,ff}$) remains constant. The far-field axial shear stress ($\tau_{xz,ff}$) is zero for Ψ=0° and Ψ=90° and is maximum for Ψ=45°.

$$\sigma_{xx,ff} = \sin^2(\psi)\sigma_H + \cos^2(\psi)\sigma_h ; \quad (37)$$

$$\sigma_{yy,ff} = \sigma_v ; \quad (38)$$

$$\sigma_{zz,ff} = \cos^2(\psi)\sigma_H + \sin^2(\psi)\sigma_h ; \quad (39)$$

$$\tau_{xz,ff} = \frac{\sigma_H - \sigma_h}{2}\sin(2\psi) ; \quad (40)$$

Figure 9.6 describes three different rock structure scenarios: horizontal structure, $\alpha_1 = 0^o$ (e.g. horizontal bedding, Figure 9.6a), vertical structure, $\alpha_1 = 90^o$ (e.g. vertical bedding, Figure 9.6b), and inclined structure, $\alpha_1 = 45^o$ (Figure 9.6c). The scenarios are investigated considering the major horizontal principal stress, σ_H, parallel to the strike (α_2) (Figure 9.5a), and the major horizontal principal stress perpendicular to the strike (Figure 9.5b). For a horizontal structure, α_1=0°, the tunnel and the geostatic principal horizontal stresses (σ_H and σ_h) are aligned with the rock structure for any Ψ. Those scenarios are chosen because they encompass a variety of cases common in practice.

When Ψ=45°, the two cases, namely σ_H parallel to α_2 (Figure 9.5a) and σ_H perpendicular to α_2 (Figure 9.5b) have the same far-field horizontal stress ($\sigma_{xx,ff}$= 7.5Mpa), the same vertical stress ($\sigma_v = \sigma_{yy,ff}$= 5Mpa), the same strike (α_2=45°) and dip angles, the same far-field axial shear stress ($\tau_{xz,ff}$), but different direction ($\tau_{xz,ff}$=±2.5MPa). Thus, the two cases are used to show the influence of the far-field axial shear stress ($\tau_{xz,ff}$) on the tunnel behavior.

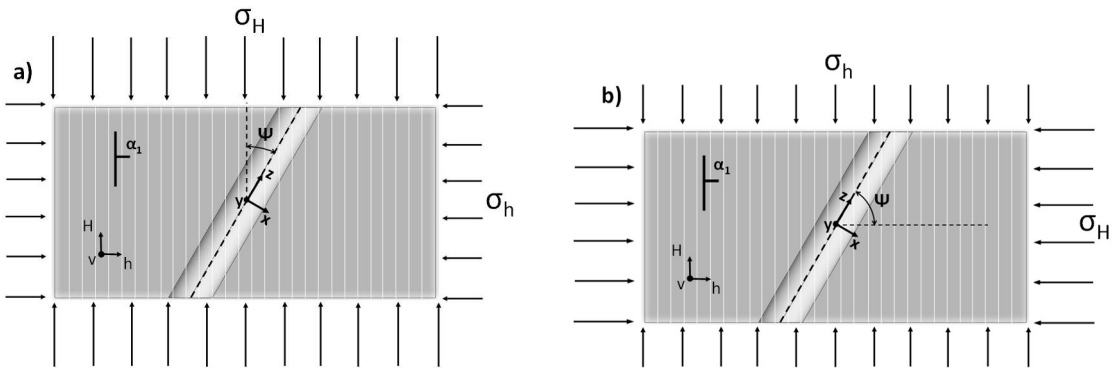

Figure 9.5 Plan view of a tunnel misaligned with the principal horizontal stresses in a transversely anisotropic rock mass. (a) Major horizontal stress (σ_H) parallel to the strike (α_2); (b) Minor horizontal stress (σ_H) parallel to the strike (α_2).

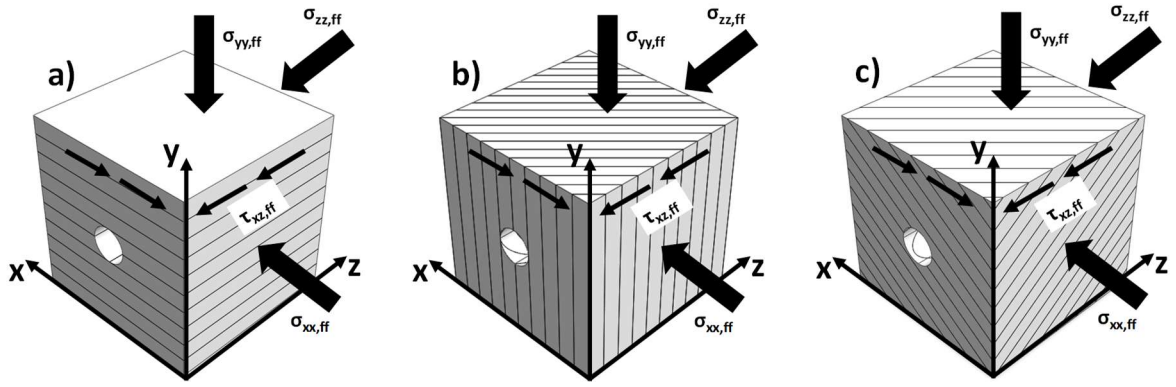

Figure 9.6 Tunnel at angle Ψ=45° with the major horizontal stress, with dip angles, α_1: (a) 0°; (b) 90°; and (c) 45°.

9.3.1 Horizontal bedding (α_1 = 0°)

Figures 9.7 and 8 show the normalized stresses and displacements at the tunnel perimeter (i.e. at $r=r_0$) for a tunnel in a horizontally stratified rock mass (i.e. α_1=0°, Figure 9.6a) with Ψ=45°. In this case, the tunnel is aligned with one of the principal directions of material anisotropy for any angle Ψ; thus, the problem is decoupled (i.e. the in-plane and out-of-plane responses are independent of each other). Figure 9.7 compares the analytical and the numerical results for α_1=0° and Ψ=45° in terms of the normalized tangential stresses, $\sigma_{\theta\theta}/\sigma_v$, normalized tangential axial shear stresses, $\tau_{z\theta}/\sigma_v$, and normalized radial, u_r/r_0, tangential, u_θ/r_0, and axial, u_z/r_0, displacements at the tunnel perimeter ($r=r_0$). The excellent match between analytical and numerical results shows that the analytical solution is correct. The tangential stresses ($\sigma_{\theta\theta}$) are symmetric with respect to the vertical and horizontal axes; $\sigma_{\theta\theta}$ is maximum at the crown and at the invert and minimum at the

springline. The tangential axial shear stresses ($\tau_{\theta z}$) are anti-symmetric with respect to the vertical axis; they are zero at the springline and maximum at the crown and invert. Radial and tangential displacements (u_r and u_θ) are symmetric; u_r is almost constant along the tunnel perimeter, the maximum is at the crown and at the invert and the minimum at the springline. The u_θ is small around the tunnel, negligible when compared to u_r. The axial displacements (u_z) are anti-symmetric; they are zero at the crown and invert and maximum at the springline. Thus, the tunnel is distorted in the axial direction about the vertical axis.

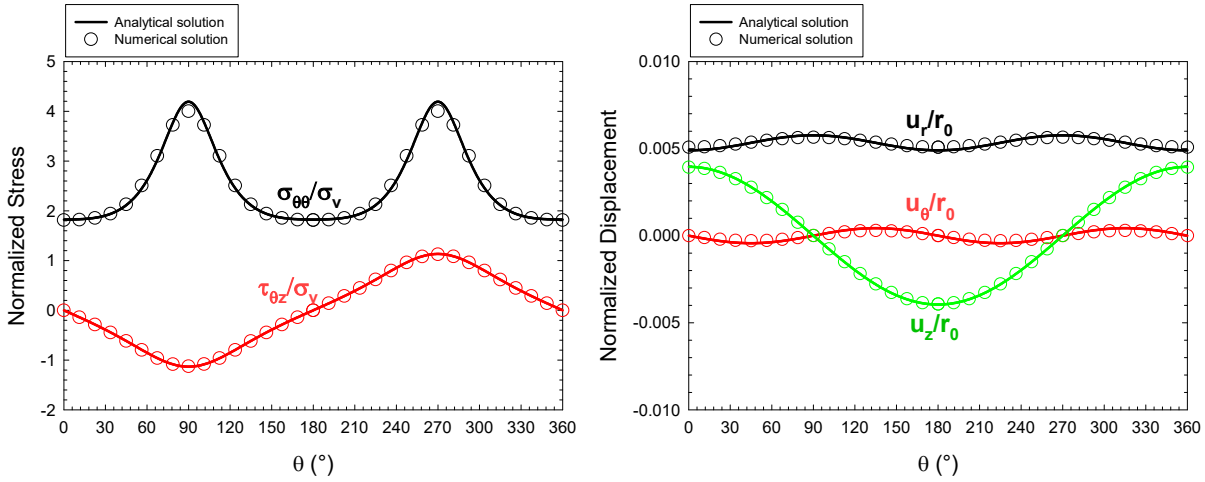

Figure 9.7 Normalized stresses and displacements around the tunnel perimeter for horizontally stratified rock mass and Ψ=45°.

Figure 9.8 shows, as a function of the tunnel angle Ψ, the tunnel convergence normalized with the tunnel radius, i.e. the difference in radial displacements divided by the radius, on the horizontal and vertical axes, as well as the normalized axial displacements at the springline. The horizontal convergence is minimum for Ψ=0°, i.e. when the tunnel is aligned with σ_H and it increases as the tunnel rotates, reaching a maximum at Ψ=90°, when the tunnel is aligned with σ_h. In contrast, the vertical convergence is maximum at Ψ=0° and it decreases as the tunnel rotates, with a minimum at Ψ=90°. The axial displacements are zero at Ψ=90° and Ψ=0°, when the tunnel is aligned with the principal horizontal stresses, and is maximum at Ψ=45°, when the far-field axial shear is maximum. These are expected results. What is interesting is to note how the orientation of the tunnel with the far-field stresses affects the results. If it is assumed that the tunnel is aligned with the major principal horizontal stresses, the vertical convergence is overpredicted, the horizontal underpredicted and the axial displacements are also underpredicted.

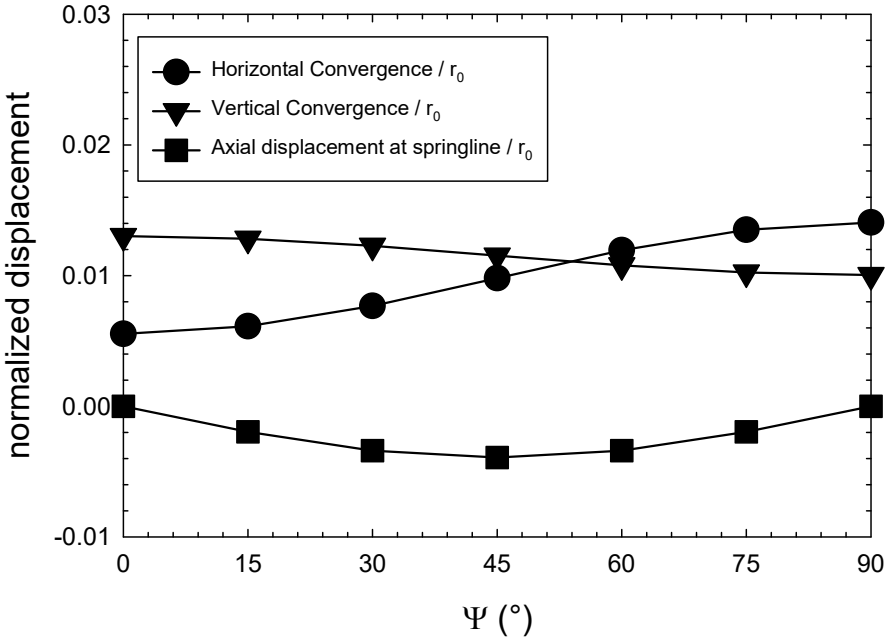

Figure 9.8 Tunnel convergence and axial displacements with Ψ for horizontally stratified rock mass.

9.3.2 Vertical bedding ($\alpha_1 = 90°$)

Three cases are investigated when α_1=90°, namely σ_H parallel to α_2(Figure 9.5a); σ_H perpendicular to α_2 (figure 9.5b) and a "no shear" case (i.e. $\tau_{xz,ff}$ =0). The "no shear" case includes the same far-field stresses, but the far-field axial shear stress is zero; this case is included to illustrate the errors produced when misalignment of the tunnel with the far-field geostatic stresses is not considered (i.e. $\tau_{xz,ff}$ =0). Figures 9.9 to 11 show the normalized displacements and stresses around the tunnel perimeter for the three cases, when Ψ=45°. Displacements and stresses at the tunnel perimeter are determined with the analytical formulation and with a 3D FEM modelling; the results show an excellent agreement.

The results are consistent with the symmetry of the problem; that is, $\sigma_{\theta\theta}$, u_r and u_θ are symmetric with respect to the vertical and horizontal axes through the center of the tunnel, while $\tau_{\theta z}$ and u_z are anti-symmetric with respect to the vertical axis and symmetric with respect to the horizontal axis. The evolution of $\sigma_{\theta\theta}$, u_r and u_θ with the polar coordinate, θ, follows the same trend in all three cases: $\sigma_{\theta\theta}$ is maximum at the crown and invert (i.e. θ= 90° and 270°) and minimum at the springline (i.e. θ= 0° and 180°), while u_r is maximum at the springline and minimum at the crown and invert. The magnitude of $\sigma_{\theta\theta}$ is almost not affected by the presence of the far-field axial

shear stress, but the radial and tangential displacements are affected. In contrast, the evolution of $\tau_{\theta z}$ and u_z is very different in each case. This is expected because of the presence of $\tau_{xz,ff}$. In all three cases, $\tau_{\theta z}$ is zero at the springline and maximum at the crown and at the invert, while u_z is zero at the crown and at the invert and maximum at the springline. Again, this is expected because of the symmetry of the problem. Observe that the presence of the far-field axial shear stress substantially increases the tangential axial shear stresses ($\tau_{\theta z}$) around the tunnel perimeter.

The presence of the far-field axial shear, $\tau_{xz,ff}$, and the misalignment of the tunnel with the principal directions of material anisotropy both produce axial distortions of the tunnel cross section about its vertical axis. What is interesting is that when σ_H is perpendicular to α_2, the axial distortion produced by $\tau_{xz,ff}$ and by the material anisotropy have the same direction, while when σ_H is parallel to α_2, the axial distortions have opposite directions. This explains why the axial and radial displacements are the largest when σ_H is perpendicular to α_2 and the smallest when σ_H is parallel to α_2. The axial and radial displacements when $\tau_{xz,ff}$ is not considered lie between the displacements when $\tau_{xz,ff}$ is considered. Thus, $\tau_{xz,ff}$ may increase or decrease the ground deformation around the tunnel, depending on the orientation of the geostatic principal stress directions with respect to the principal directions of material anisotropy. Note that in the previous case (i.e. horizontal bedding, α_1=0°), $\tau_{xz,ff}$ had no influence on the radial displacements, neither the rock structure induced axial deformations or tangential axial shear stresses around the tunnel perimeter. Thus, the cases where the tunnel is misaligned with the principal directions of material anisotropy substantially increase the complexity of the problem, and so ignoring any tunnel misalignment may lead to inaccurate ground deformations.

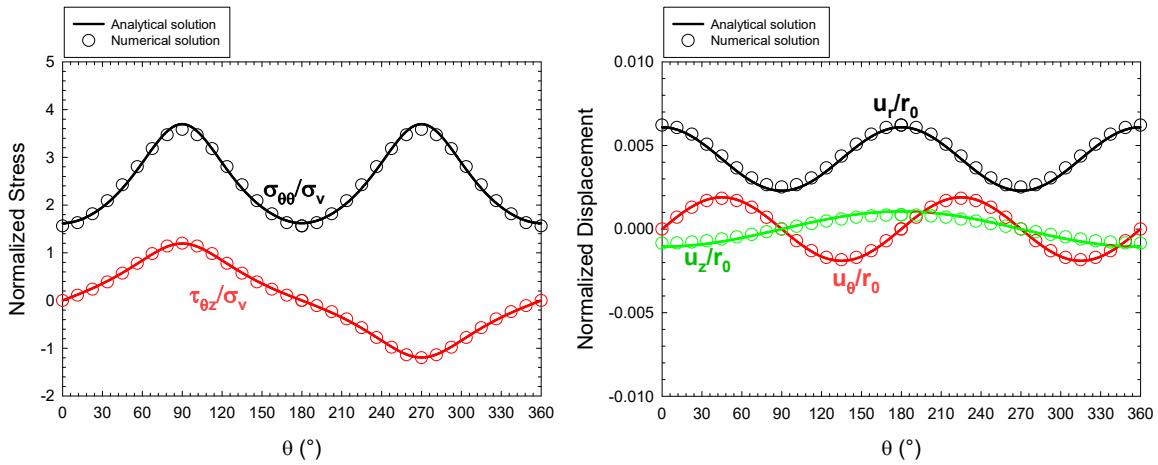

Figure 9.9 Normalized stresses and displacements around the tunnel perimeter for rock mass with vertical structure (α_1=90°), for Ψ=45° and σ_H parallel to α_2.

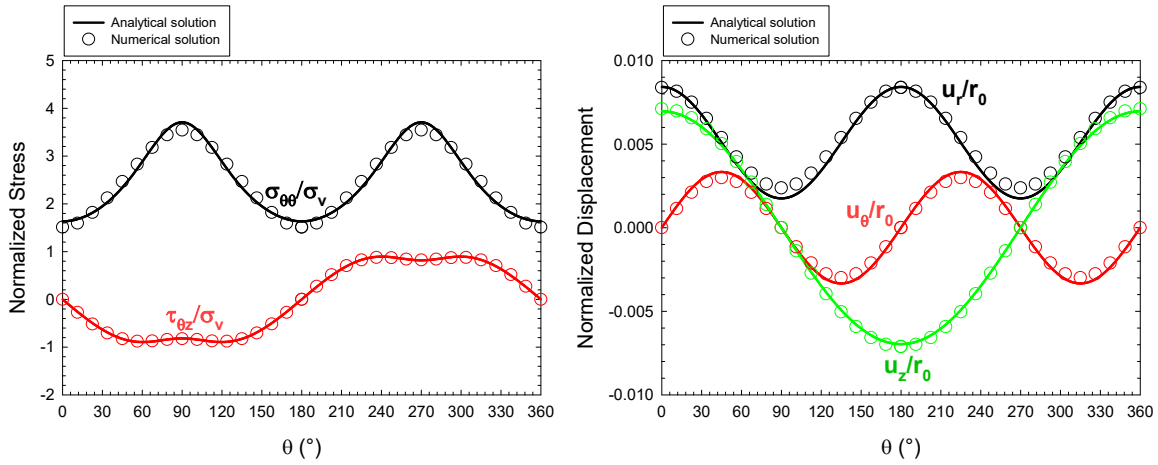

Figure 9.10 Normalized stresses and displacements around the tunnel perimeter for rock mass with vertical structure (α_1=90°), for Ψ=45° and σ_H perpendicular to α_2.

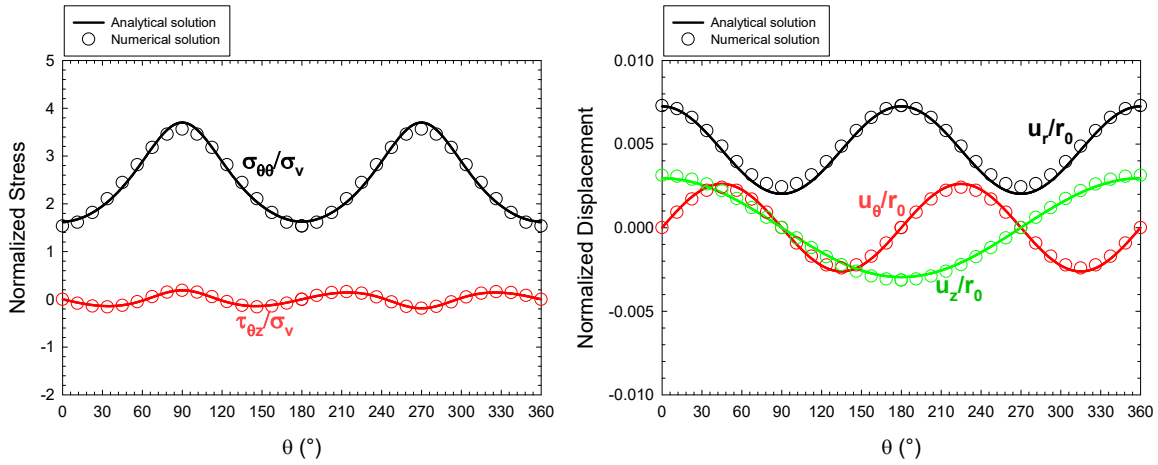

Figure 9.11 Normalized stresses and displacements around the tunnel perimeter for rock mass with vertical structure (α_1=90°), for Ψ=45° and "no shear" (i.e. $\tau_{xz,ff}$=0).

Figure 9.12 plots, for the case of σ_H parallel to α_2 (Figure 9.5a) and for different tunnel orientations, Ψ, the normalized tunnel convergence along the vertical and horizontal axes through the center of the tunnel, as well as the normalized axial displacements at the springline. The figure includes results for the "no axial shear" case. As one can see, the vertical convergence has a weak dependence on tunnel orientation, while the results of horizontal convergence and axial displacements depend on the misalignment of the tunnel with respect to the major horizontal stress. It is interesting to observe that neglecting the far-field axial shear in the calculations results in overestimating vertical convergence and axial displacements; for the latter, the direction of the axial displacements is opposite to what it should be. It is also interesting to note that the horizontal

convergence is not the largest when Ψ=90°, i.e. when the tunnel is aligned with σ_h and thus $\sigma_{xx,ff}$ is maximum. The reason for this is that, in this case, σ_H is parallel to the bedding, which is the stiffer direction; thus, as the tunnel rotates, the increase of the horizontal stress, which would increase the horizontal displacements, is compensated by the increase of the horizontal stiffness. The axial displacements without $\tau_{xz,ff}$ are larger than with $\tau_{xz,ff}$, which is counterintuitive. The reason again is because of the orientation of the tunnel with the soft/stiff directions of the rock mass; indeed, the axial distortion produced by $\tau_{xz,ff}$ and by the misalignment of the tunnel with the directions of material anisotropy compensate each other. This "compensation" reduces the axial and radial displacements around the tunnel with the angle Ψ.

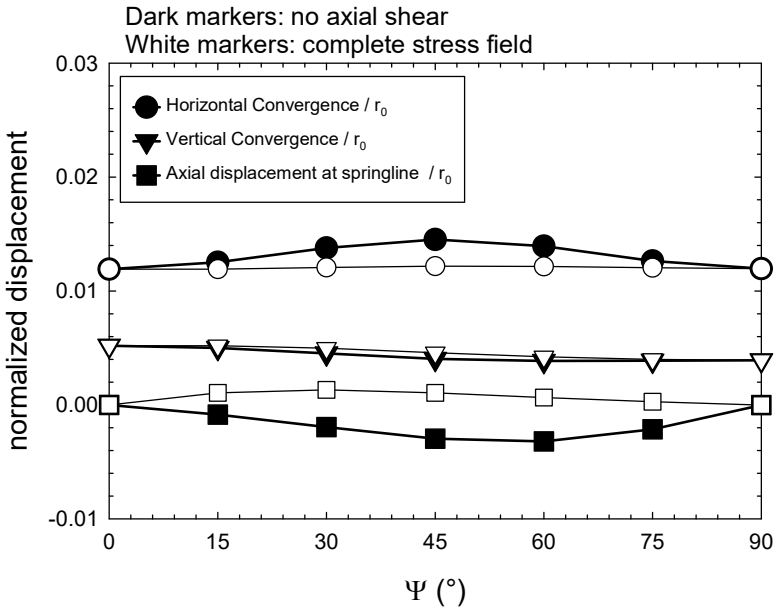

Figure 9.12 Tunnel convergence and axial displacements when σ_H is parallel to α_2 (Figure 9.5a), with alignment Ψ, for α_1=90°.

The case with σ_H perpendicular to α_2 (Figure 9.5b) is shown in Figure 9.13. The trends for convergence and axial displacements are similar, with and without $\tau_{xz,ff}$. In all the cases, the horizontal convergence increases and the vertical convergence decreases as the tunnel rotates from Ψ=0° to 90°. The horizontal convergence is larger than the vertical, for any Ψ. While the difference between horizontal and vertical convergence is small for Ψ=0°, it is quite large for Ψ=90° (the horizontal convergence is 16.1 times larger than the vertical). This substantial increase is due to the fact that the major horizontal stress is perpendicular to the bedding planes, which is the softer orientation of the rock mass; thus, as the tunnel rotates, the horizontal stress increases and the

horizontal stiffness decreases. Different than what was found for the case with σ_H parallel to α_2 in Figure 9.12, is that the horizontal convergence is larger when the far-field stresses include the far-field shear than when it does not. Also, the axial displacements with $\tau_{xz,ff}$ are larger than without $\tau_{xz,ff}$. This is because, in this case, distortions due to $\tau_{xz,ff}$ and due to the orientation of the material anisotropy are both in the same direction; thus axial and radial displacements are larger.

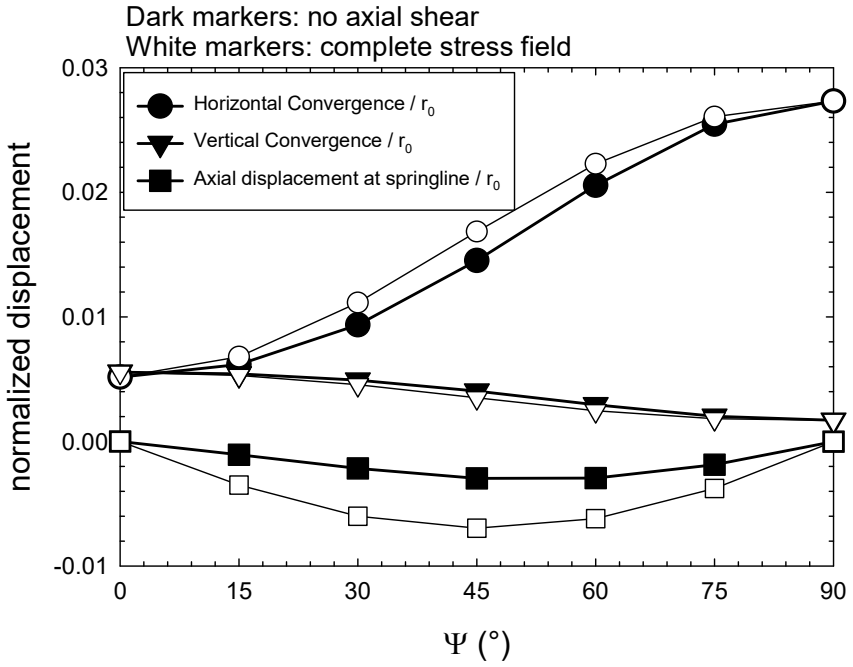

Figure 9.13 Tunnel convergence and axial displacements when σ_H is perpendicular to α_2 (Figure 9.5b), with alignment Ψ, for α_1=90°.

9.3.3 Inclined bedding (α_1 = 45°)

The same three cases (i.e. σ_H parallel to α_2, σ_H perpendicular to α_2 and "no shear"), discussed in the previous section, are also investigated, but for inclined bedding, α_1=45°. Figures 9.14 to 16 show the normalized displacements and stresses around the tunnel perimeter, for α_1 = 45°, Ψ=45°, σ_H parallel to α_2 (figure 9.14), σ_H perpendicular to α_2 (figure 9.15), and "no shear", $\tau_{xz,ff}$ =0, (figure 9.16). Displacements and stresses at the tunnel perimeter were determined with the analytical formulation and with the 3D FEM modelling. As one can see, the results match, which further supports the notion that the analytical solution is correct. The results in all three cases lose the symmetry that was present in the previous scenarios, i.e. when the axis of the tunnel is aligned with one of the principal directions of the material anisotropy (i.e. horizontal bedding, α_1=0°). Because the rock structure is inclined with respect to the tunnel, the axis of distortion (i.e.

anti-symmetry axis of axial displacements) and the location of the maximum and minimum convergence change with the angle Ψ and with the orientation of the principal horizontal stresses with respect to the rock structure (Figure 9.5). It is interesting to note that, similar to the case with vertical bedding (α_1=90°), the larger ground displacements occur when σ_H is perpendicular to the strike direction and are smaller when σ_H is parallel to the strike direction. The ground displacements obtained with no far-field axial shear stress (i.e. no axial shear) lie in between. It is also interesting to note that the far-field axial shear stress has little influence on $\sigma_{\theta\theta}$ (i.e. the tangential stresses around the tunnel perimeter are similar in all cases), but has a large influence on the tangential axial shear stress. The tangential axial shear stresses ($\tau_{\theta z}$) are substantially larger when $\tau_{xz,ff}$ is present. The far-field axial shear stress has a minor influence on the location of the maximum and minimum radial displacements; as one can see in figures 9.14 to 16, the maximum convergence is similar in all cases; it is observed at: θ= 153° for "no shear"; θ= 151° for σ_H parallel to α_2 and; θ=154.5° for σ_H perpendicular to α_2. In contrast, the axial displacements are zero at: θ=36° for "no shear"; θ=120.5° for σ_H parallel to α_2 and; θ=72.5° for σ_H parallel to α_2; these results show that $\tau_{xz,ff}$ heavily affects the position of the axis of distortion (the axis of anti-symmetry). Note that, in all cases, the location of the minimum convergence makes a 90° angle with the maximum convergence and the location of the maximum axial displacement also makes a 90° angle with the axis of distortion.

Figure 9.17 shows the deformed meshes in the axial direction for α_1=45° and Ψ=45°, for the three cases assessed, namely "no shear", σ_H parallel to α_2 (figure 9.5a) and, σ_H perpendicular to α_2 (figure 9.5b). For the "no shear" case ($\tau_{xz,ff}$=0), the axis of distortion is located in the 1st and 3rd quadrants, at θ=36°. When σ_H is parallel to α_2, the axis of distortion is shifted to the 2nd and 4th quadrants (figure 9.17b), located at θ=-60°. It is because, similar to α_1=90°, the distortion caused by $\tau_{xz,ff}$ and by the material anisotropy have opposite directions, so that the resultant axial distortion is shifted by 84.5° when $\tau_{xz,ff}$ is included. When σ_H is perpendicular to α_2, the axis of distortion is in the 1st and 3rd quadrants, at θ=72.5°. In this case, also similar to α_1=90°, the distortions produced by $\tau_{xz,ff}$ and by the material anisotropy have the same direction, since $\tau_{xz,ff}$ distorts the tunnel cross-section about the vertical axis, the resultant axis of distortion is shifted by 36.5° towards the vertical when $\tau_{xz,ff}$ is included, remaining in the same quadrant as the "no shear" case.

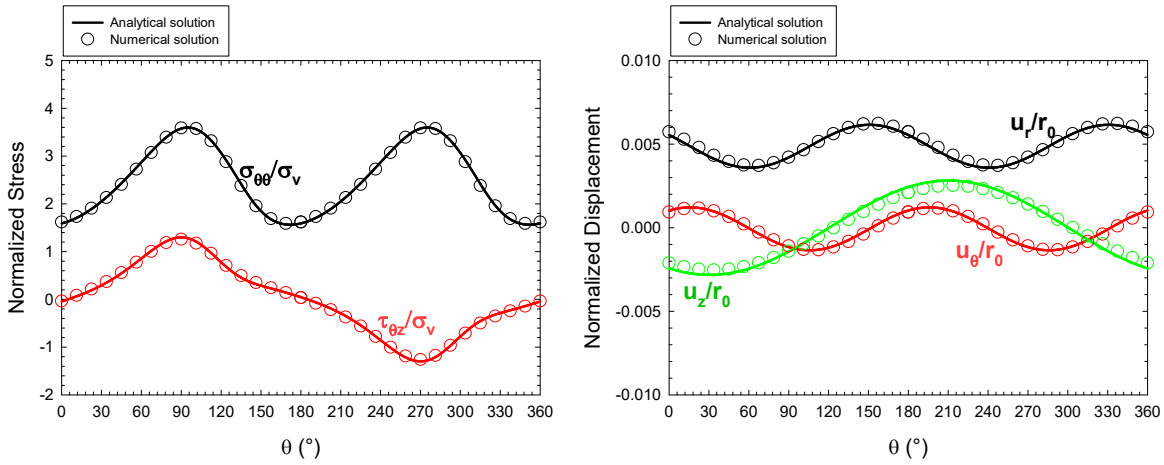

Figure 9.14 Normalized stresses and displacements around the tunnel perimeter for rock mass with α_1=45°, Ψ=45° and σ_H parallel to α_2.

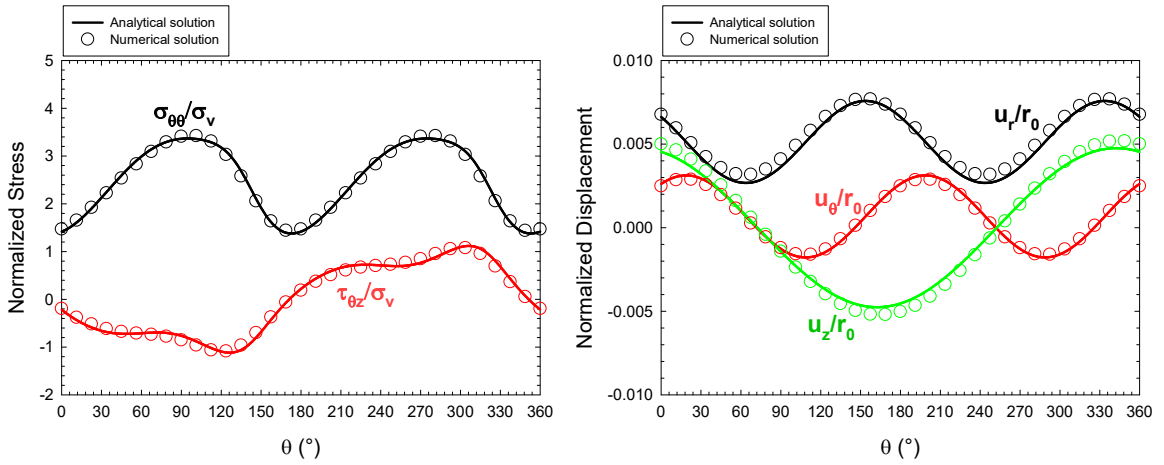

Figure 9.15 Normalized stresses and displacements around the tunnel perimeter for rock mass with α_1=45°, Ψ=45° and σ_H perpendicular to α_2.

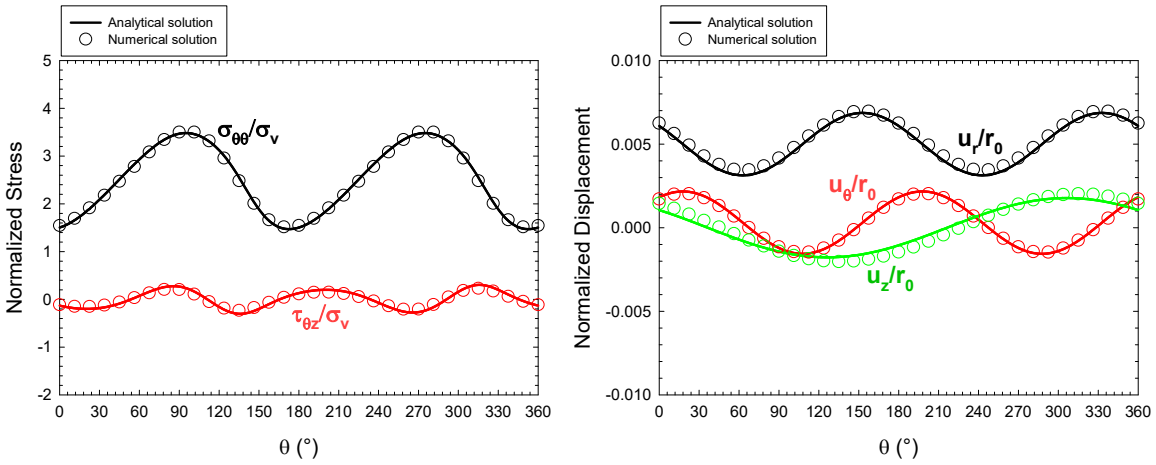

Figure 9.16 Normalized stresses and displacements around the tunnel perimeter for rock mass with α_1=45° for Ψ=45° and "no shear" ($\tau_{xz,ff}$=0).

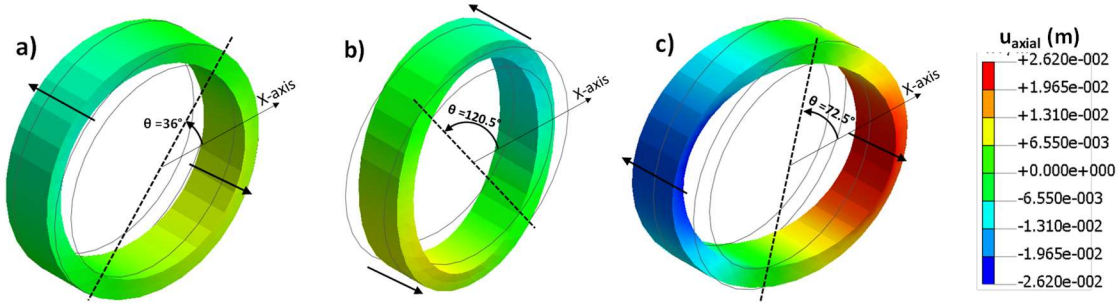

Figure 9.17 Deformed meshes in the axial direction for α_1=45° and Ψ=45° a) "no shear"; b) σ_H parallel to α_2 and; c) σ_H perpendicular to α_2.

Figure 9.18 shows the maximum and minimum convergence and the maximum axial displacement at the tunnel perimeter, with Ψ, when σ_H is parallel to α_2. The results with no axial shear ($\tau_{xz,ff}$ =0) are presented to assess the influence of $\tau_{xz,ff}$ on the tunnel behavior. The figure also shows the location (i.e. polar coordinate) of the axis where the maximum convergence occurs, and the location of the axis of distortion. The maximum convergence with no $\tau_{xz,ff}$ is larger than when considering the shear. This is similar to what was observed in the case of vertical bedding, α_1=90°; however, the minimum convergence with no $\tau_{xz,ff}$ is slightly smaller than when including the shear. Similar to vertical bedding case (α_1=90°), the maximum convergence occurs when Ψ=45° instead of at 90°, when the far-field horizontal stress, $\sigma_{xx,ff}$, is maximum. This is the result of the opposite effects of the axial distortions caused by $\tau_{xz,ff}$ and of the rock structure, so the ground deformations around the tunnel are reduced. The axial displacements are zero for Ψ=0° because, at this orientation, the tunnel is aligned with the strike direction of the rock structure. As the tunnel rotates,

axial displacements are induced because of the tunnel misalignment with the horizontal principal stresses and with the principal directions of material anisotropy. The maximum axial displacements have no symmetry with the angle Ψ; they are larger when the far-field axial shear stress, $\tau_{xz,ff}$, is considered. When Ψ=90°, the tunnel is aligned with the minor horizontal stress and is perpendicular to the strike direction of the bedding; thus, the axial displacements are caused by the inclined bedding dipping towards the tunnel.

It is interesting to note that the location (i.e. polar coordinate θ) of the maximum convergence and of the axis of distortion changes significantly as the tunnel rotates. For Ψ=0°, the tunnel is aligned with major horizontal stress, σ_H, and with the strike direction of the bedding; thus, no axial displacement is induced, the maximum convergence occurs at θ=135°, and the minimum convergence, at 45°. As the tunnel rotates, the maximum convergence changes its position from θ=135°, when Ψ=90°, to 180° (i.e. horizontal axis), when Ψ=0°. As one can see, $\tau_{xz,ff}$ has little influence on the position of the axis of maximum convergence. However, the position of the axis of distortion is heavily affected by $\tau_{xz,ff}$. The axis of distortion is located between 90° and 180° when the far-field axial shear, $\tau_{xz,ff}$, is included (i.e. complete stress field) and between 0° and 90° when it is not included (i.e. no axial shear). This indicates that the presence of the far-field axial shear stress shifts the axis of distortion, as shown in figure 9.17. This is the result of the opposite effects on axial distortions of tunnel misalignment with the rock structure and of the far-field axial shear, $\tau_{xz,ff}$. When Ψ=90°, the tunnel is aligned with the minor horizontal stress, σ_h, (i.e. $\tau_{xz,ff}$=0) and is perpendicular to the strike, so the bedding is dipping towards the tunnel; thus, the maximum convergence and the axis of distortion are both located in the horizontal axis (i.e. θ=0° or 180°).

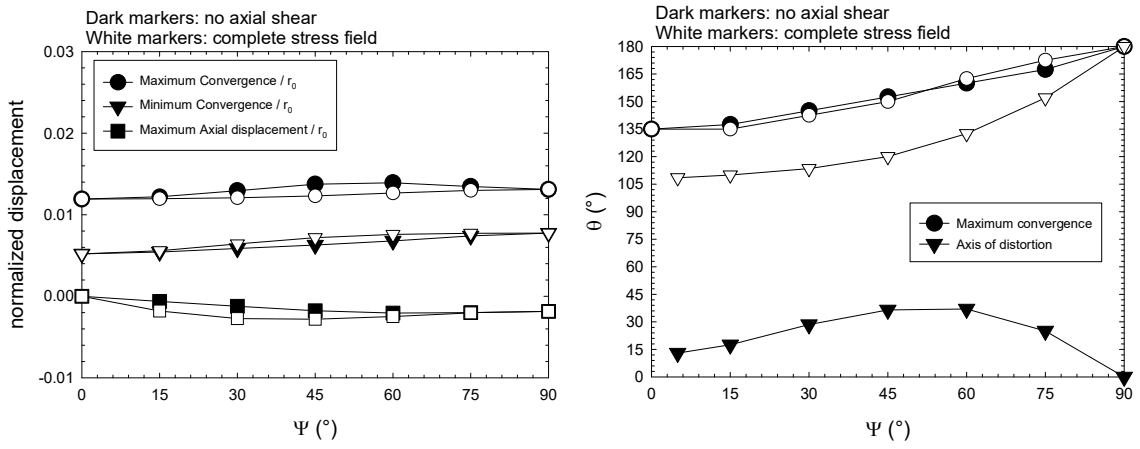

Figure 9.18 Transverse and axial displacements of the tunnel when σ_H is parallel to α_2 (Figure 9.5a), with Ψ, for α_1=45°.

Figure 9.19 shows the maximum and minimum convergence, the maximum axial displacement at the tunnel perimeter, the position of the maximum convergence, and the position of the axis of distortion, with Ψ, when σ_H is perpendicular to α_2. The similarities with the results from α_1=90° and σ_H perpendicular to α_2 are noteworthy: the maximum convergence increases with Ψ, i.e. the smallest convergence is for Ψ=0° and largest for Ψ=90°; the maximum horizontal convergence and the maximum axial displacements are larger when the far-field axial shear stress is included than when it is not. However, the maximum convergence when the rock structure is vertical (α_1=90°) is larger than when the it is inclined (α_1=45°). Note that, for Ψ>45°, the tunnel convergence is substantially larger when the major horizontal stress is perpendicular to the strike direction than when it is parallel. It is because the direction parallel to the strike is stiffer than the direction perpendicular. In this case, the axial distortion of the tunnel cross-section caused by the far-field axial shear stress, $\tau_{xz,ff}$, and by the material anisotropy have the same direction; thus, the axial displacements are amplified when $\tau_{xz,ff}$ is considered. Observe that the axial displacement when $\tau_{xz,ff}$ is considered is consistently larger than the axial displacements when $\tau_{xz,ff}$ is neglected.

Figure 9.19 shows that the position of the maximum convergence is almost not affected by $\tau_{xz,ff}$, while the position of the axis of distortion is heavily affected. For Ψ=0°, the tunnel is aligned with σ_H and is perpendicular to α_2; because in this case $\sigma_{xx,ff}$ and $\sigma_{yy,ff}$ are equal, the axis of maximum convergence is vertical (θ=90°) given that the vertical direction is softer than the horizontal direction. As the tunnel rotates, the position of maximum convergence changes from θ=90°, when Ψ=0°, to θ=162.5°, when Ψ=90°. The axis of distortion, irrespective of whether $\tau_{xz,ff}$ is included or not, is in the first quadrant. The axis of distortion is horizontal (θ= 0° or 180°) when Ψ=0°. Note that there is no axis of distortion when Ψ=90° because, for this orientation, the tunnel is aligned with the minor horizontal stress and with the strike direction of the rock structure, so no axial displacements are induced. Note that the presence of $\tau_{xz,ff}$ shifts the axis of distortion towards the vertical (i.e. θ=90°), but the axis remains in the same quadrant. This occurs because $\tau_{xz,ff}$ distorts the tunnel cross-section about the vertical axis; thus, the resultant axis of distortion is in between the vertical and the axis of distortion when the far-field axial shear stress, $\tau_{xz,ff}$, is not present (i.e. no axial shear case).

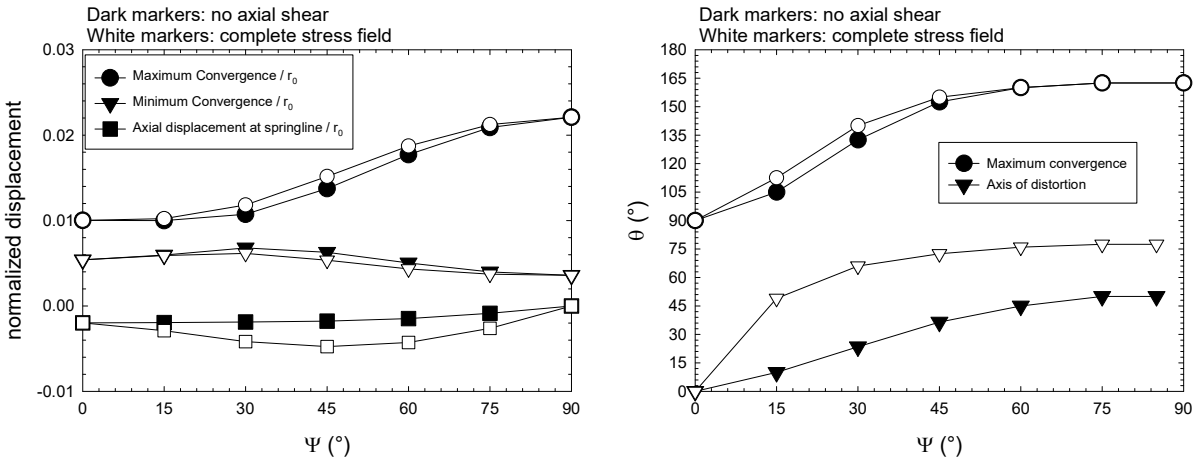

Figure 9.19 Transverse and axial displacements of the tunnel when σ_H is perpendicular to α_2 (Figure 9.5b), with Ψ, for α_1=45°.

In summary, the studied cases show that the ground deformations around the tunnel in anisotropic rock masses are heavily affected by: (1) the orientation of the tunnel with respect to the rock structure; (2) the orientation of the tunnel with respect to the geostatic principal stresses; and (3) the orientation of principal direction of the geostatic principal stresses with respect to the principal directions of material anisotropy. For horizontal bedding (i.e. α_1=0°), the tunnel is aligned with the principal direction of material anisotropy for any angle Ψ; thus, in-plane and out-plane deformations are decoupled such that the rock structure does not produce axial deformations around the tunnel, nor the far-field axial shear stress affects the in-plane deformations. This is not the case for vertical bedding (i.e. α_1=90°) and for inclined bedding (i.e. α_1=45°), where the tunnel is misaligned with the geostatic principal stresses and with the principal directions of material anisotropy; thus, anti-symmetric axial displacements are induced around the tunnel and the radial displacements are affected by the far-field axial shear stresses. For vertical bedding (i.e. α_1=90°), the axis of distortion is vertical because the rock structure and the far-field axial shear stress distort the tunnel cross-section about the same axis (i.e. the vertical). It is observed that when the major horizontal stress is parallel to the strike direction, the axial distortions produced by the far-field axial shear is opposite to that caused by the rock structure; thus, axial and radial displacements around the tunnel are reduced when the far-field axial shear stress is considered. However, when the major horizontal stress is perpendicular to the strike direction, the axial distortions of the tunnel cross-section due to the tunnel misalignment with respect to the rock structure and to the geostatic

horizontal principal stresses have the same direction, so the axial and radial displacements around the tunnel are amplified when the far-field axial shear stress is present.

When the rock structure dips towards the tunnel, the axial distortions of the tunnel cross-section and the location of the maximum radial displacements are heavily dependent on the angle Ψ (Figure 9.5). This is because the distortion caused by the rock structure is no longer about the vertical axis and depends on the strike direction, while the axial distortion caused by the far-field axial shear stress is about the vertical axis for any Ψ. Similar to the case with vertical bedding, for the inclined bedding, the ground deformations are reduced when the major horizontal stress is parallel to the strike direction and are amplified when the major horizontal stress is perpendicular to the strike.

It is interesting to note that, among all cases studied, the largest and the smallest maximum tunnel convergence occurs when the bedding is vertical (α_1=90°), and when the major horizontal stress is perpendicular to the strike direction (Figure 9.5b). The largest maximum convergence occurs for Ψ=90° (i.e. tunnel aligned with the minor horizontal stress) and the smallest, for Ψ=0° (i.e. when the tunnel is aligned with the major horizontal stress). In this case, the softest material direction of the rock mass is perpendicular to the bedding and the stiffest material direction is parallel. When the bedding is vertical and major horizontal stress is perpendicular to the strike direction, the largest stress is acting along the softest material direction, maximizing the displacements.

9.4 Conclusions

A new analytical solution for unsupported deep tunnels in full anisotropic rock mass is presented. The analytical solution explicitly considers the coupling of in-plane and out-of-plane deformations by taking into the formulation the fully populated compliance matrix of an anisotropic rock mass. Thus, it provides the full stress and displacement fields far-behind the face of an unsupported, circular and deep tunnel misaligned with the geostatic principal stress directions and with the principal directions of material anisotropy. The analytical solution is verified using 3D FEM modeling on a variety of scenarios with increasing complexity. An excellent match between the analytical and numerical results is obtained, which shows that the analytical solution is essentially correct. The analytical solution has potential applications to practice because it

expands previous solutions where the tunnel was aligned with one of the principal geostatic stress directions and with one of the principal directions of material anisotropy.

The interplay between the tunnel misalignment with the rock structure of a transversely anisotropic rock mass and with the geostatic principal stress directions is assessed. The results show that the tunnel misalignment produces axial displacements around the tunnel perimeter (i.e. axial distortion of the tunnel cross-section). The results also show that, for the cases investigated, the axial and radial displacements around the tunnel are larger when the major horizontal principal stress is perpendicular to the strike and smaller when the major horizontal stress is parallel to the strike, when the tunnel is not aligned with the principal horizontal stresses. When the major horizontal stress is parallel to the strike, the axial distortions due to the misalignment with the far-field stresses and with principal directions of material anisotropy have opposite effects; thus, deformations are reduced. However, when the major horizontal stress is perpendicular to the strike, the axial distortions, due to tunnel misalignment with the far-field stresses and with the material anisotropy have complementary effects; so the rock mass deformation around the tunnel is amplified. The analyses highlight the importance of the coupling between in-plane and out-of-plane stresses and deformations of tunnels in anisotropic rock masses and provides insights into the complex interplay that exists between the direction of the tunnel and the far-field stress directions and the directions of material anisotropy.

Nomenclature

Ψ = angle between tunnel axis and major horizontal principal stress;

z = complex variable, x+iμy;

σ_v = vertical stress;

σ_h = minor principal horizontal stress;

σ_H = major principal horizontal stress;

r, θ = polar coordinates in the xy-plane;

X, Y, Z: coordinate system attached to the tunnel, with Z-axis parallel to the tunnel axis;

$\sigma_{xx,ff}$ = far-field horizontal stress normal to the tunnel axis;

$\sigma_{yy,ff}$ = far-field vertical stress normal to the tunnel axis;

$\sigma_{zz,ff}$ = far-field axial stress parallel to the tunnel axis;

$\tau_{zx,ff}$, $\tau_{yx,ff}$ = far-field out-of-plane shear stresses;

$\tau_{xy,ff}$ = far-field out-of-plane shear stresses;

$\sigma_{\theta\theta}$ = tangential stress;

$\tau_{\theta z}$ = tangential axial shear stress;

u_θ = tangential displacement;

u_r = radial displacement;

u_z = axial displacement;

G = shear modulus;

E = Young modulus;

v = Poisson ratio;

r_0 = tunnel radius;

Acknowledgments

The research is being partially supported by the research funding agency of the Brazilian government CNPq ("Conselho Nacional de Desenvolvimento Cientifico"). The authors acknowledge the support from CNPq and from Midas company, which kindly provided the license of Midas GTX NX software, used in the present work.

9.5 References

Amadei B, Savage WZ, Swolfs HS. Gravitational stresses in anisotropic rock masses. *Int. J. Rock Mech. Min. Sci.* 1987, 24(1): 5–14.

Amadei B, Pan E. Gravitational stresses in anisotropic rock masses with inclined strata. *Int. J. Rock Mech. Min. Sci.* 1992, 29(3):225–236.

Amadei B. Importance of anisotropy when estimating and measuring in situ stresses in rock. *Int. J. Rock Mech. Min. Sci. Geomech.* 1996, 33(3):293–325.

Batugin SA, Nirenburg RK. Approximate relation between the elastic constants of anisotropic rocks and the anisotropy parameters. *Sov. Min. Sci.* 1972, 8(1):5-9.

Bobet A. Deep tunnel in transversely anisotropic rock: complementary solutions. *Rock Mech. Rock Eng.* 2016, 49(12): 3817–3822.

Bobet A. Lined circular tunnels in elastic transversely anisotropic rock at depth," *Rock Mech. Rock Eng.*, vol. 44, no. 2, pp. 149–167, 2011.

Bobet A, Yu H. Full stress and displacement fields for steel-lined deep pressure tunnels in transversely anisotropic rock. *Tunn. Undergr. Sp. Technol.* 2016, 56:125–135.

Bobet A. Deep tunnel in transversely anisotropic rock with groundwater flow. *Rock Mech. Rock Eng.* 2016, 49(12):4817–4832.

Brown ET, Hoek E. Trends in relationships between measured in-situ stresses and depth. *Int. J. Rock Mech. Min. Sci.* 1978, 15(4): 211–215.

Chou WI, Bobet A. Predictions of ground deformations in shallow tunnels in clay. *Tunn. Undergr. Sp. Technol.* 2002, 17(1):3–19.

Evans KF, Engelder T, Plumb RA. Appalachian Stress study .1. a detailed description of in-situ stress variations in devonian shales of the appalachian plateau. *J. Geophys. Res. Earth Planets*. 1989, 94: 7129–7154.

Exadaktylos GE. On the constraints and relations of elastic constants of transversely isotropic geomaterials. *Int. J. Rock Mech. Min. Sci.* 2001, 38(7):941-956.

Fortsakis P, Nikas K, Marinos KV, Marinos P. Anisotropic behaviour of stratified rock masses in tunnelling. *Eng. Geol.* 2012, 141–142: 74–83.

Goricki A, Button AE, Schubert W, Pötsch M, Leitner R. The influence of discontinuity orientation on the behaviour of tunnels. *Felsbau*. 2005, 23(5):12–18.

Gysel M. In-Situ stress measurements of the primary stress state in the Sonnenberg tunnel in Lucerne, Switzerland. *Tectonophysics*. 1975, 29: 301–314.

Haimson BC, Lee MY, Song I. Shallow hydraulic fracturing measurements in Korea support tectonic and seismic indicators of regional stress. *Int. J. Rock Mech. Min. Sci*. 2003, 40(7-8): 1243–1256.

Ledesma A, Alonso EE. Protecting sensitive constructions from tunnelling: the case of World Heritage buildings in Barcelona. *Géotechnique*. 2017, 10:1–12.

Lekhnitskii SG, *Theory of elasticity of an anisotropic elastic body*. Holden-Day Inc., San Francisco, 1963.

Manh HT, Sulem J, Subrin D. A Closed-form solution for tunnels with arbitrary cross section excavated in elastic anisotropic ground. *Rock Mech. Rock Eng.* 2014, 48(1):277-288.

Martin CD, Kaiser PK. Mine-by Experiment Committee report, Phase 1: excavation response, summary and implications. Atomic Energy of Canada Limited, Report AECL–11382. AECL Research, Chalk River, Ont, 1996.

McGarr A, Gay NC. State of Stress in the Earth's Crust. *Ann. Rev. Earth Planet. Sci.* 1978, 6: 405–436.

Pachoud AJ, Schleiss AJ. Stresses and displacements in steel-lined pressure tunnels and shafts in anisotropic rock under quasi-static internal water pressure. *Rock Mech. Rock Eng.* 2016, 49(4):1263-1287.

Park B, Min KB. Bonded-particle discrete element modeling of mechanical behavior of transversely isotropic rock. *Int. J. Rock Mech. Min. Sci.* 2015, 76: 243-255.

Park ES, Choi BH, Bae SH, Jeon S. Horizontal stresses at shallow depths in Seoul (Korea) gneissic region. In: Rock Eng. Rock Mech. Struct. Rock Masses - Proceedings of EUROCK 2014, ISRM European Regional Symposium: 399–404, 2014.

Park KH. Analytical solution for tunnelling-induced ground movement in clays. *Tunn. Undergr. Sp. Technol.* 2005, 20(3):249–261.

Perras MA, Wannenmacher H, Diederichs MS. Underground excavation behaviour of the Queenston formation: tunnel back analysis for application to shaft damage dimension prediction. *Rock Mech. Rock Eng.* 2015, 48(4):1647-1671.

Pinto F, Whittle AJ. Ground movements due to shallow tunnels in soft ground. I: analytical solutions. *J. Geotech. Geoenvironmental Eng.* 2014, 140(4):04013040.

Schubert W, Budil A. The importance of longitudinal deformation in tunnel excavation. In: Proceedings of 8th ISRM Congress on Rock Mechanics, 1995:1411–1414.

Schubert P, Klopčič J, Štimulak A, Ajdič I, Logar J. Analysis of characteristic deformation patterns at the Trojane tunnel in Slovenia. *Felsbau*, 2005, 23(5):25-30.

Schubert W, Mendez JMD. Influence of foliation orientation on tunnel behavior. *Procedia Engineering*. 2017, 191:880-885.

Souček K *et al.* Geotechnical characterization of Bukov underground research facility. *Procedia Engineering*. 2017, 191:711-718.

Tonon F, Amadei B. Effect of elastic anisotropy on tunnel wall displacements behind a tunnel face. *Rock Mech. Rock Eng.* 2002, 35(3):141-160.

Tonon F, Amadei B. Stresses in anisotropic rock masses: An engineering perspective building on geological knowledge. *Int. J. Rock Mech. Min. Sci.* 2003, 40(7–8):1099–1120.

Vitali OPM, Celestino TB, Bobet A. 3D finite element modelling optimization for deep tunnels with material nonlinearity. *Undergr. Sp.* 2017, 3(2):125–139.

Vitali OPM, Celestino TB, Bobet A. Analytical solution for tunnels not aligned with geostatic principal stress directions. *Tunn. Undergr. Sp. Technol.* 2018, 82: 394–405.

Vitali OPM, Celestino TB, Bobet A. Shallow tunnels misaligned with geostatic principal stress directions: analytical solution and 3D face effects. *Tunn. Undergr. Sp. Technol.* 2019, 89: 268-283a.

Vitali OPM, Celestino TB, Bobet A. Shallow tunnel not aligned with the geostatic principal stress directions. In: Proceedings of Geo-Congress2019, Geotechnical Special Publication. 2019b, GSP 313:214-222.

Wileveau Y, Cornet FH, Desroches J, Blumling P. Complete in situ stress determination in an argillite sedimentary formation. *Phys. Chem. Earth*. 2007, 32(8–14):866–878.

Worotnicki G. *13 – CSIRO Triaxial Stress Measurement Cell*. In: Rock testing and site characterization: principles, practice and projects. 1993, 329-394.

Zhao XG *et al.* In-situ stress measurements and regional stress field assessment in the Xinjiang candidate area for China's HLW disposal. *Eng. Geol.* 2015, 197:42-56.

Zhang C, Chen Q, Qin X, Hong B, Meng W, Zhang Q. In-situ stress and fracture characterization of a candidate repository for spent nuclear fuel in Gansu, northwestern China. *Eng. Geol.* 2017, 231:218-229.

Zhang Z, Sun Y. Analytical solution for a deep tunnel with arbitrary cross section in a transversely isotropic rock mass. *Int. J. Rock Mech. Min. Sci.* 2011, 48(8):1359-1363.

9.6 Appendix 1

When the tunnel axis is aligned with one of the principal directions of material anisotropy of an orthotropic or transversely anisotropic elastic rock mass, the compliance matrix has the form shown in (A.1), and introduces a singularity to the general solution presented in the paper.

$$\begin{Bmatrix} \varepsilon_{xx} \\ \varepsilon_{yy} \\ \varepsilon_{zz} \\ \gamma_{yz} \\ \gamma_{xz} \\ \gamma_{xy} \end{Bmatrix} = \begin{bmatrix} S_{11} & S_{12} & S_{13} & 0 & 0 & 0 \\ S_{12} & S_{22} & S_{23} & 0 & 0 & 0 \\ S_{13} & S_{23} & S_{33} & 0 & 0 & 0 \\ 0 & 0 & 0 & S_{44} & 0 & 0 \\ 0 & 0 & 0 & 0 & S_{55} & 0 \\ 0 & 0 & 0 & 0 & 0 & S_{66} \end{bmatrix} \begin{Bmatrix} \sigma_{xx} \\ \sigma_{yy} \\ \sigma_{zz} \\ \sigma_{yz} \\ \sigma_{xz} \\ \sigma_{xy} \end{Bmatrix} \tag{A.1}$$

The system of equations (13) and (14) is no longer coupled and is given by equations (A.2) and (A.3).

$$\left(\mu^4\beta_{11} + (2\beta_{12} + \beta_{66})\mu^2 + \beta_{22}\right)\frac{\partial^4 F}{\partial z^4} = 0 \tag{A.2}$$

$$\left(\mu^2\beta_{55} + \beta_{44}\right)\frac{\partial^2 H}{\partial z^2} = 0 \tag{A.3}$$

The roots can be obtained directly from (A.4) and (A.5).

$$\mu^2 = \frac{-(2\beta_{12} + \beta_{66}) \pm 2\sqrt{(\beta_{12} + \beta_{66})^2 - \beta_{11}\beta_{22}}}{2\beta_{11}} \tag{A.4}$$

$$\mu^2\beta_{55} + \beta_{44} = 0 \rightarrow \mu_3 = i\sqrt{\frac{\beta_{44}}{\beta_{55}}} \tag{A.5}$$

Also, λ_k=0, where k=1, 2, 3.

9.7 Appendix 2 – Rotation of the compliance matrix using Euler angles

The rotation of the compliance matrix (D) can be conducted using the Euler's angles. The convention adopted follows the zxz or x-convention, where the first rotation, α, is about the z-axis, which is the axis of the tunnel; the second rotation is β, about the axis x', which is the rotated x axis; and the third rotation, γ, is about the z''-axis, which is the rotated z axis. See figure 9.20. The rotation matrices, using Voigt's notation, are:

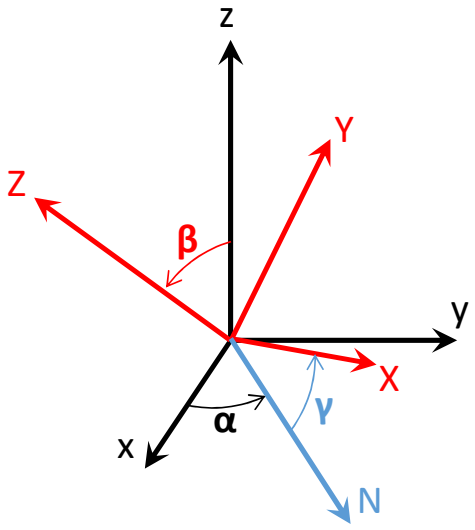

Figure 9.20 zxz-convention for the Euler angles.

$$R_1 = \begin{bmatrix} \cos^2\alpha & \sin^2\alpha & 0 & 0 & 0 & -\frac{1}{2}\sin(2\alpha) \\ \sin^2\alpha & \cos^2\alpha & 0 & 0 & 0 & \frac{1}{2}\sin(2\alpha) \\ 0 & 0 & 1 & 0 & 0 & 0 \\ 0 & 0 & 0 & \cos\alpha & \sin\alpha & 0 \\ 0 & 0 & 0 & -\sin\alpha & \cos\alpha & 0 \\ \sin(2\alpha) & -\sin(2\alpha) & 0 & 0 & 0 & \cos 2\alpha \end{bmatrix} \quad \text{(A.6)}$$

$$R_2 = \begin{bmatrix} 1 & 0 & 0 & 0 & 0 & 0 \\ 0 & \cos^2\beta & \sin^2\beta & -\frac{1}{2}\sin(2\beta) & 0 & 0 \\ 0 & \sin^2\beta & \cos^2\beta & \frac{1}{2}\sin(2\beta) & 0 & 0 \\ 0 & \sin(2\beta) & -\sin(2\beta) & \cos 2\beta & 0 & 0 \\ 0 & 0 & 0 & 0 & \cos\beta & \sin\beta \\ 0 & 0 & 0 & 0 & -\sin\beta & \cos\beta \end{bmatrix} \quad \text{(A.7)}$$

$$R_3 = \begin{bmatrix} \cos^2\gamma & \sin^2\gamma & 0 & 0 & 0 & -\frac{1}{2}\sin(2\gamma) \\ \sin^2\gamma & \cos^2\gamma & 0 & 0 & 0 & \frac{1}{2}\sin(2\gamma) \\ 0 & 0 & 1 & 0 & 0 & 0 \\ 0 & 0 & 0 & \cos\gamma & \sin\gamma & 0 \\ 0 & 0 & 0 & -\sin\gamma & \cos\gamma & 0 \\ \sin(2\gamma) & -\sin(2\gamma) & 0 & 0 & 0 & \cos 2\gamma \end{bmatrix} \quad \text{(A.8)}$$

The rotated compliance matrix is obtained by:

$$D' = R_1 R_2 R_3 D R^T_3 R^T_2 R^T_1 \rightarrow \varepsilon = D'\sigma \quad \text{(A.9)}$$

9.8 Appendix 3 – Rotation of compliance matrix using dip and strike angles

The orientation of discontinuities in rock masses are commonly described using the dip angle, α_1, and the strike, α_2, as illustrated in Figure 9.4. Note that it is assumed that the North is aligned with the axis of the tunnel, i.e. with the z-axis. Assuming that the x-axis is horizontal, the y-axis, vertical, and the z-axis is aligned with the tunnel, the rotation matrix, using Voigt's notation, is:

$$R=\begin{bmatrix} t_x t_x & t_y t_y & t_z t_z & 2t_y t_z & 2t_x t_z & 2t_x t_y \\ n_x n_x & n_y n_y & n_z n_z & 2n_y n_z & 2n_x n_z & 2n_x n_y \\ s_x s_x & s_y s_y & s_z s_z & 2s_y s_z & 2s_x s_z & 2s_x s_y \\ n_x s_x & n_y s_y & n_z s_z & n_y s_z + n_z s_y & n_x s_z + n_z s_x & n_x s_y + n_y s_x \\ t_x s_x & t_y s_y & t_z s_z & t_y s_z + t_z s_y & t_x s_z + t_z s_x & t_x s_y + t_y s_x \\ t_x n_x & t_y n_y & t_z n_z & t_y n_z + t_z n_y & t_x n_z + t_z n_x & t_x n_y + t_y n_x \end{bmatrix} \tag{A.10}$$

$$D' = \left(R^T D R\right) \sigma \rightarrow \varepsilon = D' \sigma \tag{A.11}$$

Where $n = (n_x, n_y, n_z)$ is the normal vector to the rock mass structure and $s = (s_x, s_y, s_z)$ and $t = (t_x, t_y, t_z)$ are the vectors parallel to the plane of the structure. They are defined, in terms of dip and strike angles, as:

$$n = \begin{Bmatrix} -\sin\alpha_1 \sin\alpha_2 \\ \cos\alpha_1 \\ \sin\alpha_1 \cos\alpha_2 \end{Bmatrix}; \qquad s = \begin{Bmatrix} -\cos\alpha_1 \sin\alpha_2 \\ -\sin\alpha_1 \\ \cos\alpha_1 \cos\alpha_2 \end{Bmatrix}; \qquad t = \begin{Bmatrix} \cos\alpha_2 \\ 0 \\ \sin\alpha_2 \end{Bmatrix} \tag{A.12}$$

9.9 Appendix 4 – Matlab code for a tunnel in transversely anisotropic rock

The Matlab code that can be used to solve the proposed analytical solution is included. This code was written using version R2016b. The code provides the stresses and displacements at the tunnel perimeter for an unsupported tunnel in a transversely anisotropic rock mass. The Matlab code reads the input data from an excel spreadsheet (Figure 9.21) and generates another excel spreadsheet with the results. The input data are: 1) Transversely anisotropic material properties; 2) Dip and strike direction angles; 3) The far-field stresses; 4) the tunnel radius and 5) the number of divisions along the tunnel perimeter where results are obtained.

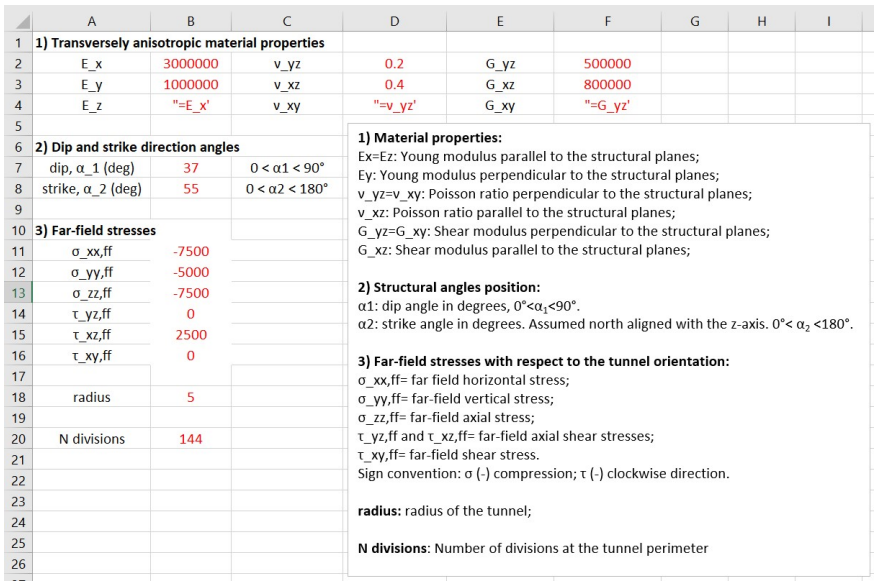

	A	B	C	D	E	F
1	**1) Transversely anisotropic material properties**					
2	E_x	3000000	v_yz	0.2	G_yz	500000
3	E_y	1000000	v_xz	0.4	G_xz	800000
4	E_z	"=E_x'	v_xy	"=v_yz'	G_xy	"=G_yz'
5						
6	**2) Dip and strike direction angles**					
7	dip, α_1 (deg)	37	0 < α1 < 90°			
8	strike, α_2 (deg)	55	0 < α2 < 180°			
9						
10	**3) Far-field stresses**					
11	σ_xx,ff	-7500				
12	σ_yy,ff	-5000				
13	σ_zz,ff	-7500				
14	τ_yz,ff	0				
15	τ_xz,ff	2500				
16	τ_xy,ff	0				
17						
18	radius	5				
19						
20	N divisions	144				

1) Material properties:
Ex=Ez: Young modulus parallel to the structural planes;
Ey: Young modulus perpendicular to the structural planes;
v_yz=v_xy: Poisson ratio perpendicular to the structural planes;
v_xz: Poisson ratio parallel to the structural planes;
G_yz=G_xy: Shear modulus perpendicular to the structural planes;
G_xz: Shear modulus parallel to the structural planes;

2) Structural angles position:
α1: dip angle in degrees, 0°<α_1<90°.
α2: strike angle in degrees. Assumed north aligned with the z-axis. 0°< α_2 <180°.

3) Far-field stresses with respect to the tunnel orientation:
σ_xx,ff= far field horizontal stress;
σ_yy,ff= far-field vertical stress;
σ_zz,ff= far-field axial stress;
τ_yz,ff and τ_xz,ff= far-field axial shear stresses;
τ_xy,ff= far-field shear stress.
Sign convention: σ (-) compression; τ (-) clockwise direction.

radius: radius of the tunnel;

N divisions: Number of divisions at the tunnel perimeter

Figure 9.21 Excel sheet format for the input data for the Matlab code. The excel file should be named *INPUT.xlsx*.

```
function [] = TunnelAniso

%****************************************
% READING INPUT DATA

filename = 'INPUT.xlsx';
xlRange = 'B2:B3';
E = xlsread(filename,xlRange);
filename = 'INPUT.xlsx';
xlRange = 'D2:D3';
v = xlsread(filename,xlRange);
filename = 'INPUT.xlsx';
xlRange = 'F2:F3';
G = xlsread(filename,xlRange);
filename = 'INPUT.xlsx';
xlRange = 'B7:B8';
Alpha = xlsread(filename,xlRange);
% to avoid singularity
if Alpha(2)==90
    Alpha(2)=89.9;
end
filename = 'INPUT.xlsx';
xlRange = 'B11:B16';
Sff = xlsread(filename,xlRange);
Sxff=Sff(1);
Syff=Sff(2);
Szff=Sff(3);
Txyff=Sff(6);
Tyzff=Sff(4);
Txzff=Sff(5);
filename = 'INPUT.xlsx';
```

```
xlRange = 'B18:B18';
r = xlsread(filename,xlRange);
filename = 'INPUT.xlsx';
xlRange = 'B20:B20';
N = xlsread(filename,xlRange);
n_= 360/N;
N=N+1;

%*********************************************************
% ASSEMBLING COMPLIANCE MATRIX

Alpha = (pi()/180)*Alpha; % angles in rad
s_a1 = sin(Alpha(1));
s_a2 = sin(Alpha(2));
c_a1 = cos(Alpha(1));
c_a2 = cos(Alpha(2));

% Unit vector (equation A.12)
n = [-s_a1*s_a2, c_a1, s_a1*c_a2];
s = [-c_a1*s_a2, -s_a1,c_a1*c_a2];
t = [c_a2, 0, s_a2];

% Rotation matrix (equation A.10)
R_S=[t(1)^2,     t(2)^2,    t(3)^2,    2*t(2)*t(3),          2*t(1)*t(3),
2*t(1)*t(2);
     n(1)^2,     n(2)^2,    n(3)^2,    2*n(2)*n(3),          2*n(1)*n(3),
2*n(1)*n(2);
     s(1)^2,     s(2)^2,    s(3)^2,    2*s(2)*s(3),          2*s(1)*s(3),
2*s(1)*s(2);
     n(1)*s(1), n(2)*s(2), n(3)*s(3), n(2)*s(3)+n(3)*s(2),
n(1)*s(3)+n(3)*s(1), n(1)*s(2)+n(2)*s(1);
     t(1)*s(1), t(2)*s(2), t(3)*s(3), t(2)*s(3)+t(3)*s(2),
t(1)*s(3)+t(3)*s(1), t(1)*s(2)+t(2)*s(1);
     t(1)*n(1), t(2)*n(2), t(3)*n(3), t(2)*n(3)+t(3)*n(2),
t(1)*n(3)+t(3)*n(1), t(1)*n(2)+t(2)*n(1)];

%Compliance matrix for transversely anisotropic elastic rock mass (equation
35)
D = [   1/E(1),  -v(1)/E(2) ,   -v(2)/E(1),  0,      0,          0;
      -v(1)/E(2),   1/E(2),     -v(1)/E(1),  0,      0,          0;
      -v(2)/E(1), -v(1)/E(1),     1/E(1),    0,      0,          0;
           0,          0,           0,    1/G(1),   0,          0;
           0,          0,           0,      0,     1/G(2),      0;
           0,          0,           0,      0,      0,        1/G(1)];

%Rotated compliance matrix (equation A.11)
D_rot = R_S'*D*R_S;

%Beta matrix (equation 11)
B = zeros(6);
for i=1:6
    for j=1:6
        B(i,j)=D_rot(i,j)-(D_rot(i,3)*D_rot(3,j))/D_rot(3,3);
    end
end
```

```
% ------------------------------------------------------------------
% Check if the case is singular
if s_a2==1 || s_a1==0 || s_a1==1 && s_a2==0

% roots for the in-plane stresses (equation A.2)
a=zeros(5,1);
a(1)=B(1,1);
a(2)=0;
a(3)=(2*B(1,2)+B(6,6));
a(4)=0;
a(5)=B(2,2);

L=roots(a);
mi=[0,0,0];
mi(1)=L(1);
mi(2)=L(3);

% roots for out-of-plane stresses (equation A.3)
a=zeros(3,1);
a(1)=B(5,5);
a(2)=0;
a(3)=B(4,4);
L=roots(a);
mi(3)=L(1);

%lambda vector
l=[0,0,0];

% Coefficients A (equations 33 and 34)
F=zeros(4);
F = [1,0,1,0;
    0,1,0,1;
    real(mi(1)),-imag(mi(1)),real(mi(2)),-imag(mi(2));
    imag(mi(1)),real(mi(1)),imag(mi(2)),real(mi(2))];
L = zeros(1,4);
L = (r/2)*[-Syff, Txyff, Txyff, -Sxff];
A=inv(F)*L';

A1= complex(A(1),A(2));
A2= complex(A(3),A(4));
A3= complex(0.5*r*Tyzff,-0.5*r*Txzff);

% if it is not singular
else

% Coefficients of the 6th order polynomium (equation 16)
a=zeros(7,1);
a(1)=B(1,1)*B(5,5)-B(1,5)^2;
a(2)=-2*B(1,1)*B(4,5)-2*B(1,6)*B(5,5)+2*(B(1,4)+B(5,6))*B(1,5);
a(3)=B(1,1)*B(4,4)+4*B(1,6)*B(4,5)+(2*B(1,2)+B(6,6))*B(5,5)-(B(1,4)+B(5,6))^2
-2*(B(2,5)+B(4,6))*B(1,5);
a(4)=-2*B(1,6)*B(4,4)-2*(2*B(1,2)+B(6,6))*B(4,5)-
2*B(2,6)*B(5,5)+B(1,5)*B(2,4)+2*(B(1,4)+B(5,6))*(B(2,5)+B(4,6))+B(2,4)*B(1,5)
;
```

```
a(5)=(2*B(1,2)+B(6,6))*B(4,4)+4*B(2,6)*B(4,5)+B(2,2)*B(5,5)-
2*(B(1,4)+B(5,6))*B(2,4)-(B(2,5)+B(4,6))^2;
a(6)=-2*B(2,6)*B(4,4)-2*B(2,2)*B(4,5)+2*(B(2,5)+B(4,6))*B(2,4);
a(7)=B(2,2)*B(4,4) - B(2,4)^2;

L=roots(a);

mi=[0,0,0];
mi(1)=L(1);
mi(2)=L(3);
mi(3)=L(5);

% lambda vector (equations 25 to 27)
l=[0,0,0];
l(1)= -( B(1,5)*mi(1)^3 - (B(1,4)+B(5,6))*mi(1)^2 + (B(2,5)+B(4,6))*mi(1) -
B(2,4)) / (B(5,5)*mi(1)^2 - 2*B(4,5)*mi(1) + B(4,4));
l(2)= -( B(1,5)*mi(2)^3 - (B(1,4)+B(5,6))*mi(2)^2 + (B(2,5)+B(4,6))*mi(2) -
B(2,4)) / (B(5,5)*mi(2)^2 - 2*B(4,5)*mi(2) + B(4,4));
l(3)= -( B(1,5)*mi(3)^3 - (B(1,4)+B(5,6))*mi(3)^2 + (B(2,5)+B(4,6))*mi(3) -
B(2,4)) / ...
        (B(1,1)*mi(3)^4 - 2*B(1,6)*mi(3)^3 + (2*B(1,2) + B(6,6))*mi(3)^2 -
2*B(2,6)*mi(3) + B(2,2));

% Coefficients A (equation 33 to 34)
F=zeros(6);
F = [   1       ,      0       ,    1       ,     0         ,
real(l(3))                                        , -imag(l(3)) ;
        0       ,      1       ,    0       ,     1         ,
imag(l(3))                                        ,  real(l(3)) ;
    real(mi(1)) , -imag(mi(1)) ,real(mi(2)) ,-imag(mi(2))    ,
real(mi(3))*real(l(3)) -  imag(mi(3))*imag(l(3)), -imag(mi(3))*real(l(3)) -
real(mi(3))*imag(l(3)) ;
    imag(mi(1)) , real(mi(1))  ,imag(mi(2)) ,real(mi(2))     ,
imag(mi(3))*real(l(3)) + real(mi(3))*imag(l(3))   ,  real(mi(3))*real(l(3)) -
imag(mi(3))*imag(l(3))  ;
    real(l(1))  , -imag(l(1))  ,real(l(2))  ,-imag(l(2))     ,
1                                       ,
0                                  ;
    imag(l(1))  , real(l(1))   ,imag(l(2))  ,real(l(2))      ,
0                                       ,
1                                  ];

L = (r/2)*[-Syff, Txyff, Txyff, -Sxff, Tyzff, -Txzff];

A=inv(F)*L';

A1= complex(A(1),A(2));
A2= complex(A(3),A(4));
A3= complex(A(5),A(6));

end

%*****************************************************************
% Calculation of stresses and displacements at the tunnel perimeter
```

```
% Polar coordinate tetha (t) at the tunnel perimeter
t=zeros(N,1);
for i=1:N
    t(i)=(i-1)*n_*(pi()/180);
end

%auxiliars
aux1=zeros(N,1);
for i=1:N
   aux1(i)=complex(cos(t(i)),sin(t(i)));
end
aux2=zeros(N,1);
for i=1:N
   aux2(i)=complex(sin(t(i)),cos(t(i)));
end

%Stress Function PHI at the tunnel perimeter, r=r0 (from equations 28 and 29)
PHI1=zeros(N,1);
PHI2=zeros(N,1);
PHI3=zeros(N,1);
for i=1:N
   PHI1(i)=A1*aux1(i);
   PHI2(i)=A2*aux1(i);
   PHI3(i)=A3*aux1(i);
end

%Derivative of the Stress Function PHI at the tunnel perimeter, r=r0 (from
equations 28 and 29)
diffPHI1=zeros(N,1);
diffPHI2=zeros(N,1);
diffPHI3=zeros(N,1);
for i=1:N
   diffPHI1(i)=A1*(1/r)*aux2(i)*(1/(sin(t(i)) - mi(1)*cos(t(i))));
   diffPHI2(i)=A2*(1/r)*aux2(i)*(1/(sin(t(i)) - mi(2)*cos(t(i))));
   diffPHI3(i)=A3*(1/r)*aux2(i)*(1/(sin(t(i)) - mi(3)*cos(t(i))));
end

%Stresses at the tunnel perimeter (figure 1c), eq. 17 to 21.
Sx=zeros(N,1);
Sz=zeros(N,1);
Sy=zeros(N,1);
Txy=zeros(N,1);
Tyz=zeros(N,1);
Tzx=zeros(N,1);
for i=1:N
Sx(i)=2*real((mi(1)^2)*diffPHI1(i) + (mi(2)^2)*diffPHI2(i) +
(mi(3)^2)*l(3)*diffPHI3(i));
Sy(i)=2*real(diffPHI1(i) + diffPHI2(i) + l(3)*diffPHI3(i));
Txy(i)=-2*real(mi(1)*diffPHI1(i) + mi(2)*diffPHI2(i) +
mi(3)*l(3)*diffPHI3(i));
Tyz(i)=-2*real(l(1)*diffPHI1(i) + l(2)*diffPHI2(i) + diffPHI3(i));
Tzx(i)=2*real(mi(1)*l(1)*diffPHI1(i) + mi(2)*l(2)*diffPHI2(i) +
mi(3)*diffPHI3(i));
end

%Axial normal stress (equation 9)
```

```
for i=1:N
    Sz(i)= -(1/D_rot(3,3))*(D_rot(1,3)*Sx(i) + D_rot(2,3)*Sy(i) +
D_rot(3,4)*Tyz(i) + D_rot(3,5)*Tzx(i) + D_rot(3,6)*Txy(i));
end

%Stresses at the tunnel perimeter (figure 1b)
Stff=zeros(N,1);
Srff=zeros(N,1);
Trtff=zeros(N,1);
Trzff=zeros(N,1);
Ttzff=zeros(N,1);
for i=1:N
    Srff(i)=0.5*(Sxff+Syff)-0.5*(Syff-Sxff)*cos(2*t(i)) + Txyff*sin(2*t(i));
    Stff(i)=0.5*(Sxff+Syff)+0.5*(Syff-Sxff)*cos(2*t(i)) - Txyff*sin(2*t(i));
    Trtff(i) = 0.5*(Syff-Sxff)*sin(2*t(i)) + Txyff*cos(2*t(i));
    Trzff(i) = Txzff*cos(t(i)) + Tyzff*sin(t(i));
    Ttzff(i) = -Txzff*sin(t(i)) + Tyzff*cos(t(i));
end

%Stresses at the tunnel perimeter (figure 1a)
St=zeros(N,1);
Sr=zeros(N,1);
Ttz=zeros(N,1);
Trz=zeros(N,1);
Trt=zeros(N,1);
for i=1:N
    Sr(i)= Srff(i) + 0.5*(Sx(i)+Sy(i))-0.5*(Sy(i)-
Sx(i))*cos(2*t(i))+Txy(i)*sin(2*t(i));
    St(i)= Stff(i) + 0.5*(Sx(i)+Sy(i))+0.5*(Sy(i)-Sx(i))*cos(2*t(i)) -
Txy(i)*sin(2*t(i));
    Trt(i)= Trtff(i)+ 0.5*(Sy(i)-Sx(i))*sin(2*t(i)) + Txy(i)*cos(2*t(i));
    Trz(i) = Trzff(i)+ Tzx(i)*cos(t(i)) + Tyz(i)*sin(t(i));
    Ttz(i) = Ttzff(i)+ -Tzx(i)*sin(t(i)) + Tyz(i)*cos(t(i));
end
Sxx = Sxff + Sx;
Syy = Syff + Sy;
Szz = Szff + Sz;
Txy = Txyff + Txy;
Txz = Txzff + Tzx;
Tyz = Tyzff + Tyz;

% Displacements at the tunnel perimeter (equation 22 to 24).
Ux=zeros(N,1);
Uy=zeros(N,1);
Uz=zeros(N,1);
Ur=zeros(N,1);
Ut=zeros(N,1);
for i=1:N
    Ux(N+1-i)= real(2*PHI1(i)*((B(1,1)*(mi(1)^2) + B(1,2) - B(1,6)*mi(1) +
l(1)*(B(1,5)*mi(1) - B(1,4))))+...
                2*PHI2(i)*((B(1,1)*(mi(2)^2) + B(1,2) - B(1,6)*mi(2) +
l(2)*(B(1,5)*mi(2) - B(1,4))))+...
                2*PHI3(i)*(l(3)*(B(1,1)*(mi(3)^2) + B(1,2) - B(1,6)*mi(3)) +
B(1,5)*mi(3) - B(1,4)));
    Uy(N+1-i)= real(2*PHI1(i)*(B(1,2)*mi(1) + (B(2,2)/mi(1)) - B(2,6) +
l(1)*(B(2,5) - (B(2,4)/mi(1))))+...
```

```
                2*PHI2(i)*(B(1,2)*mi(2) + (B(2,2)/mi(2)) - B(2,6) +
l(2)*(B(2,5) - (B(2,4)/mi(2))))+...
                2*PHI3(i)*(l(3)*(B(1,2)*mi(3) + (B(2,2)/mi(3)) - B(2,6)) +
B(2,5) - (B(2,4)/mi(3))));
    Uz(N+1-i)= real(2*PHI1(i)*(B(1,4)*mi(1) + (B(2,4)/mi(1)) - B(4,6) +
l(1)*(B(4,5) - (B(4,4)/mi(1))))+...
                2*PHI2(i)*(B(1,4)*mi(2) + (B(2,4)/mi(2)) - B(4,6) +
l(2)*(B(4,5) - (B(4,4)/mi(2))))+...
                2*PHI3(i)*(l(3)*(B(1,4)*mi(3) + (B(2,4)/mi(3)) - B(4,6)) +
B(4,5) - (B(4,4)/mi(3))));
end

for i=1:N
    Ur(i) = -(cos(t(i))*Ux(i) + sin(t(i))*Uy(i));
    Ut(i) = -sin(t(i))*Ux(i) + cos(t(i))*Uy(i);
end

%Export results to an excel spreadsheet.
for i=1:N
   t(i) = t(i)*(180/pi());
end

filename = 'Results_Aniso.xlsx';
T = table(t,Sr, St, Trt, Trz, Ttz, Ur, Ut, Uz, Ux, Uy, Sxx, Syy, Txy, Txz,
Tyz, Szz);
writetable(T,filename);



end
```

10. 3D FACE EFFECTS OF TUNNELS MISALIGNED WITH THE PRINCIPAL DIRECTIONS OF MATERIAL AND STRESS ANISOTROPY

VITALI, O. P. M.; CELESTINO, & BOBET, A. (2019). 3D face effects of tunnels misaligned with the principal directions of material and stress anisotropy. Manuscript under review for publication in a peer-reviewed journal.

Abstract

Rock masses may present remarked stress anisotropy or fabric structure, such as foliation and bedding; thus, it is likely that a tunnel is misaligned with the geostatic principal stress directions, with the principal material directions, or with both. Anti-symmetric axial displacements and axial shear stresses are induced as a consequence of the tunnel misalignment. However, the effects of the misalignment near the face are still unknown. In this paper, the 3D face effects on tunnels misaligned with the geostatic principal stress directions and/or with the material principal directions are investigated. 3D FEM modeling is conducted for unsupported and supported tunnels. A transversely anisotropic elastic model is selected to represent the structured rock mass. The results show that misaligned tunnels undergo asymmetric deformations near the face. The radial deformations far-behind the face are symmetric for unsupported tunnels, but they are asymmetric for supported tunnels. The reason for this is that asymmetric deformations near the face affect ground-support interaction. As a consequence, the internal forces in the tunnel support are also asymmetric; further, the support forces may be larger than those of a tunnel aligned with the geostatic principal stress.

10.1 Introduction

Tunnel construction is a three-dimensional problem, and so the importance of the stress redistribution that occurs near the face of the tunnel cannot be overstated. Near the face, axial displacements and axial shear stresses are induced, which cause the rotation of the principal stress directions in the ground around the tunnel (Eberhardt, 2001). If the tunnel is supported, the radial stresses at the tunnel perimeter reduce to zero on the unsupported span behind the face and increase to a constant value far-behind the face (Cantieni and Anagnostou, 2009; Almeida e Sousa *et al.*, 2011). Thus, the importance of considering 3D face effects to properly predict ground and support

deformations due to tunneling is widely recognized in the literature; for instance, it is well-established in the literature that 3D models predict ground deformations more accurately than 2D models, when compared with field measurements (Galli et al., 2004; Möller, 2006; Yeo *et al.*, 2009; Almeida e Sousa *et al.*, 2011; Svoboda and Masin, 2011; Janin *et al.*, 2015, Vermeer et al, 2002). This is so because 2D tunnel analysis fails to reproduce the stress paths, near the face, that the ground undergoes during construction (Cantieni and Anagnostou, 2009). Thanks to recent advances in hardware and software, 3D numerical analyses of tunnels are nowadays feasible in practice.

Most research on 3D face effects on tunnels has been conducted assuming that the tunnel is aligned with one of the geostatic principal stress directions. However, rock masses may present remarked stress anisotropy (Gysel, 1975; Brown and Hoek, 1978; McGarr and Gay, 1978; Evans et al., 1989; Martin and Kaiser, 1996; Haimson et al., 2003; Wileveau *et al.*, 2007; Zhao *et al.*, 2013, 2015; Park *et al.*, 2014; Perras et al., 2015; Zhang *et al.*, 2017; Souček *et al.*, 2017), due to e.g. tectonic movements (Haimson et al., 2003; Park *et al.*, 2014). An extensively data survey of the geostatic stress fields in rock masses was conducted by McGarr and Gay (1978) over 77 sites around the world, and the average, plus or minus one standard deviation, of the principal stress ratios found was: $\sigma_1/\sigma_2=1.45 \pm 0.40$; $\sigma_1/\sigma_3=2.42 \pm 1.14$; and $\sigma_2/\sigma_3=1.66 \pm 0.5$. The data showed that the geostatic stress field was quite anisotropic and variable; thus, the most probable scenario, for any tunnel, is that of being misaligned with the geostatic principal stress directions. As a consequence, far-field axial shear stresses are present along the direction of the tunnel and produce anti-symmetric axial displacements around the tunnel; that is, the tunnel cross-section is distorted in the axial direction (Vitali et al., 2018; Vitali et al., 2019a; Vitali et al., 2019b, Vitali et al., 2019c, Vitali et al., 2019d). Interestingly, the presence of the far-field axial shear stress is often neglected in tunnel design, and yet the importance of the tunnel alignment with the principal stress directions is well-recognized in the technical literature. For instance, Goodman, (1989) recommends aligning the axis of the tunnel or cavern with the geostatic major principal stress such that stress concentrations around the tunnel are minimized. When this is not the case, as shown by Vitali et al., (2019b), far-field axial shear stresses appear that cause asymmetric deformations near the face and that strongly affect the ground-support interaction and the plastic deformations around the tunnel. One of the consequences of the asymmetric deformations near the face is that the internal forces in the liner and the plastic zone around the tunnel are asymmetric (Vitali et al., 2019b).

Vitali et al., (2019c) studied numerically the effects of tunnel misalignment with the geostatic principal stress directions of an experimental tunnel at the URL in Canada (Martin, 1997) in a massive granite rock mass. The authors observed that asymmetric spalling at the tunnel walls could occur if the tunnel was not aligned with the principal geostatic stress directions.

Also, investigation of 3D face effects on tunnels often assumes that the ground is isotropic. However, the ground, e.g. rock masses, may have a remarkable fabric structure such as foliation, schistosity, stratification, bedding, joint sets, etc.; thus, an anisotropic behavior of the ground is expected. Worotnicki (1993) observed that, for structured rock masses such as mudstones, slates, phyllites and schists, the stiffness anisotropy was very high. For instance, the author indicated that more than 50% of the laboratory data on these rocks showed that the material stiffness parallel to the structural planes was, as average, two times larger than perpendicular to the structural planes, and could be as high as six times. In the field, tunnel instrumentation data on NATM tunnels in highly anisotropic ground contains evidence of asymmetric deformations and opposite axial displacements in opposite directions at each springline (Schubert and Budil, 1995; Goricki *et al.*, 2005; Schubert *et al.*, 2005; Schubert and Moritz, 2011; Klopčič and Logar, 2014; Lenz *et al.*, 2017). This behavior is often associated with anisotropic properties (e.g. foliation and schistosity) or with heterogeneities of the rock mass. For instance, Schubert *et al.*, (2005) associated the asymmetric radial displacements at the springline with the presence of synclines and anticlines, observed in the geological mapping of the tunnel face, and the anti-symmetric axial displacements, also at the springlines, with the axial component of strains due to buckling and sliding of inclined schistosity near the tunnel walls.

In this paper, the 3D face effects of tunnels misaligned with the rock mass structural planes and/or with the geostatic principal stress directions are investigated. 3D FEM modeling of unsupported and supported tunnels are conducted. The rock mass is represented by transversely anisotropic elastic model. This is consistent with the technical literature, where, a transversely anisotropic model is often used to approximate the behavior of structured rock masses (see e.g. Batugin and Nirenburg (1972) and Exadaktylos (2001) who found that a transversely anisotropic elastic model was able to predict the rock mass behavior observed in the laboratory). The interplay between the tunnel misalignment with principal stresses and with the rock mass structure is assessed. Further, the ground deformations and the internal forces in the liner of a misaligned

tunnel are compared with those of a tunnel aligned with the minor horizontal stress, which is often assumed as the worst scenario for tunnel design.

10.2 Numerical model

3D FEM models were built to investigate the 3D face effects of tunnels not aligned with the principal directions of material and/or stress anisotropy. The finite element mesh was refined and was made large enough to ensure accuracy of the results (Vitali et al., 2017). 2nd order hexahedron elements were adopted. The FEM mesh consisted of a structured refined grid at the center of the model (Figure 10.1) connected with the boundaries by an unstructured mesh. Figure 10.2 illustrates the mesh of the excavated tunnel with the liner, reference positions and tunnel coordinate system. The reference positions are: (1) far-ahead the face; that is, where the geostatic stress field is found; (2) at the face; and (3) far-behind the face, where the 3D face effects no longer affect the stresses and displacements around the tunnel. The coordinate system XYZ in Figure 10.2 was chosen such that the tunnel was aligned with the Z-axis, which was taken as positive in the direction of excavation, the Y-axis was vertical and the X-axis, horizontal. The tunnel cross section was circular and had a 5m radius. The length of the hexahedron elements along the tunnel was 1m (i.e. $0.2r_0$). The axial mesh refinement was sufficient to ensure accurate results (Vitali et al., 2017). The FEM models included several phases to represent the tunnel excavation sequence. The first phase generated the geostatic stress field. The next phases simulated the tunnel excavation process by sequentially deactivating the elements inside the excavation rounds and activating the elements representing the support, if present. An excavation and support round of 1m (i.e. $0.2r_0$) was adopted. The tunnel support was simulated with shell elements. It was assumed that the tunnel was installed immediately after the excavation, so the unsupported span was zero. No relative slip between the liner and the tunnel was allowed (i.e. no-slip condition). Figure 10.2 illustrates the mesh near the face of a supported tunnel

The rock mass was represented by a transversely anisotropic elastic model. The orientation of the rock mass structure was determined by the dip angle (α_1) and by the strike direction (α_2). It was assumed that the tunnel was aligned with the North in the horizontal direction, so the dip was the vertical angle between the tunnel and the structural planes and the strike was the horizontal angle between the tunnel axis and the structural planes. When α_1=0°, the structural planes are horizontal. The rock mass properties adopted for all cases discussed in this paper were: Young

modulus perpendicular to the structural planes (E_1) equal to 1GPa; Young modulus parallel to the structural planes (E_2=E_3), 3GPa; in-plane Poisson ratio (ν_{23}), 0.333; out-of-plane Poisson ratio (ν_{13}= ν_{12}), 0.25; in-plane Shear modulus (G_{23}), 1.125GPa; and out-of-plane Shear modulus (G_{23}= G_{13}), 0.667GPa. The selected properties are typical of highly anisotropic rock masses such as phyllites, slates schists and quartzites (Worotnicki, 1993). The support of the tunnel was approximated using a linear-elastic model with Young modulus (E) equal to 25GPa and Poisson ratio (ν) equal to 0.2, which are typical properties of reinforced concrete. The thickness of the liner was 0.5m (i.e. $0.1r_0$), which is typical for a 5m tunnel radius.

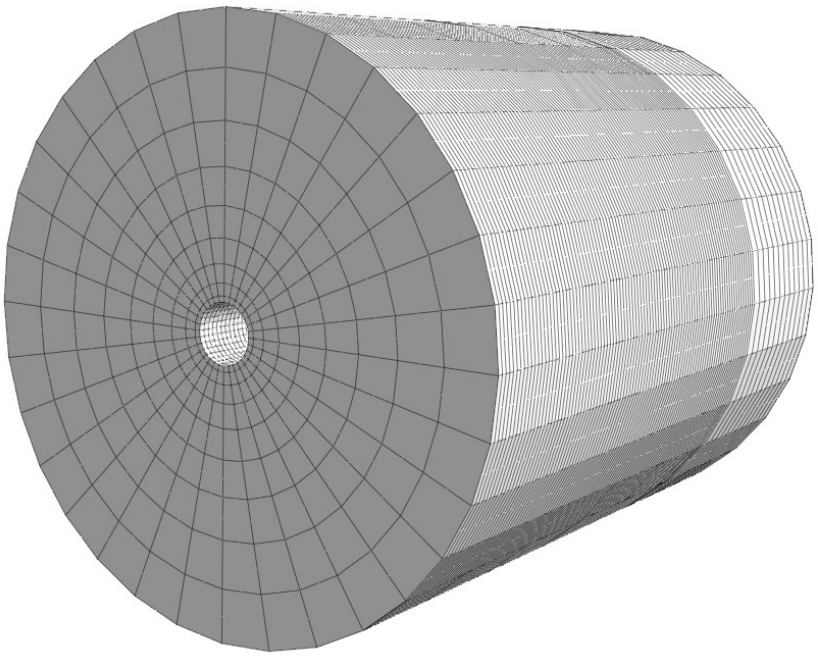

Figure 10.1 Refined mesh at the center of the model, far-from the boundaries.

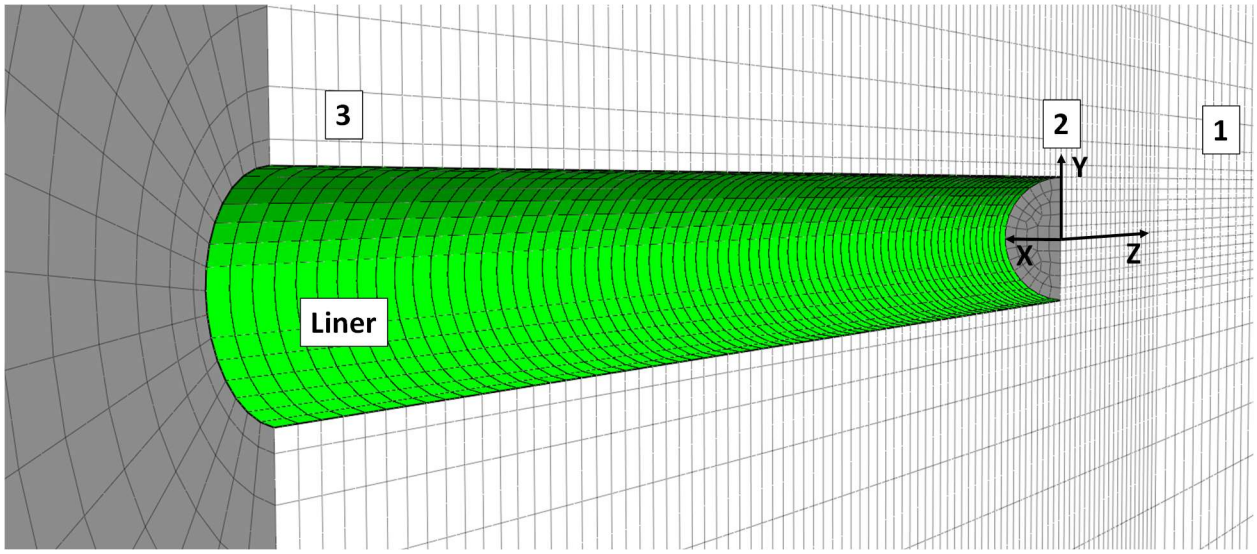

Figure 10.2 FEM mesh near the face. Reference positions and coordinate system. (1) far-ahead of the face; (2) at the tunnel face; and (3) far-behind the face. The Z-axis is the tunnel axis; the X-axis is the horizontal axis, and the Y-axis is the vertical axis.

10.3 3D face effects due to the rock mass structure

Tunnels misaligned with the rock mass structure are investigated in this section. An isotropic stress field was adopted to isolate the effects of the rock structure from those of the far-field stress. The far-field principal stresses were 5MPa that corresponded to an overburden of about 200m. To investigate displacements and stresses near the face, the following cases were investigated: rock structure with dip angles (α_1) 0°, 45°, 90° and 135° and strike direction (α_2) of 0° and 45°. Figure 10.3 illustrates the cases with α_2=0° that represent tunnels perpendicular to the strike direction and are used to investigate the effects of the dip on tunnel behavior; those cases are discussed first. Figure 10.3a shows a tunnel aligned with the structural planes when the dip angle is 0° (i.e. horizontal stratification); Figure 10.3b shows the rock mass structural planes dipping behind the face with α_1=45°; Figure 10.3d, dipping ahead of the face with α_1=135°; and Figure 10.3c when the dip angle is 90° (i.e. vertical stratification). The case with strike direction 45° (α_2=45°) is more complex, as the tunnel is not aligned with any of the principal directions of material anisotropy, and is discussed later.

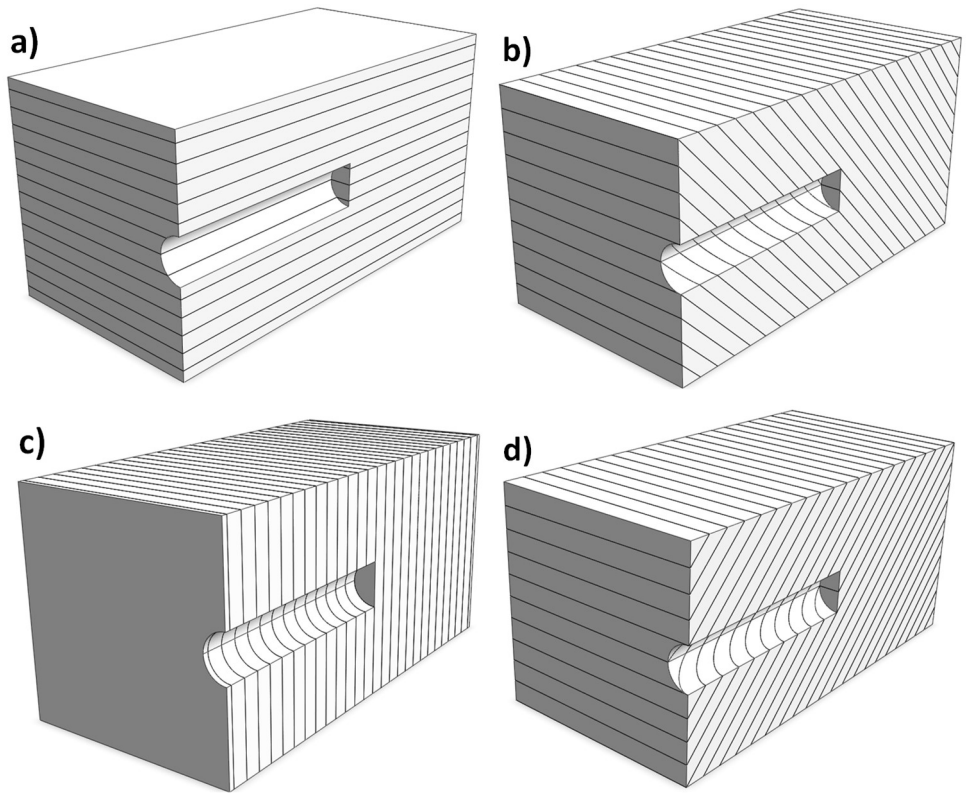

Figure 10.3 Rock mass structure with respect to the tunnel, for strike direction (α_2) 0°. Dip angles (α_1) of (a) 0°; (b) 45°; (c) 90°; (d) 135°.

Figure 10.4 is a plot of the normalized horizontal and vertical tunnel convergence, with respect to the tunnel radius (r_0), and the distance from the face (Z), normalized with respect to the tunnel radius, for dip angles 0°, 45°, 90° and 135°. The strike angle is 0° in all the cases (cases shown in Figure 10.3). As one can see, tunnel convergence starts to increase approximately at $4r_0$ ahead of the face and reaches a constant at approximately $4r_0$ behind the face of the tunnel. Both vertical and horizontal convergences are the largest for α_1=0° and the smallest for α_1=90°. The results for α_1=45° and for α_1=135° are exactly the same because of symmetry. Also, the vertical convergence is larger than the horizontal, except for α_1=90°, where they are the same. For α_1=0°, the tunnel is aligned with the rock mass structure; thus, the rock mass stiffness in the vertical direction is the smallest (i.e. along the direction perpendicular to the rock mass structural planes), while in the horizontal direction it is the largest (i.e. parallel to the rock mass structural planes). When α_1=90°, the tunnel is perpendicular to the structural planes, as shown in Figure 10.3c, and thus, on the tunnel cross section, the rock is isotropic and has the largest stiffness.

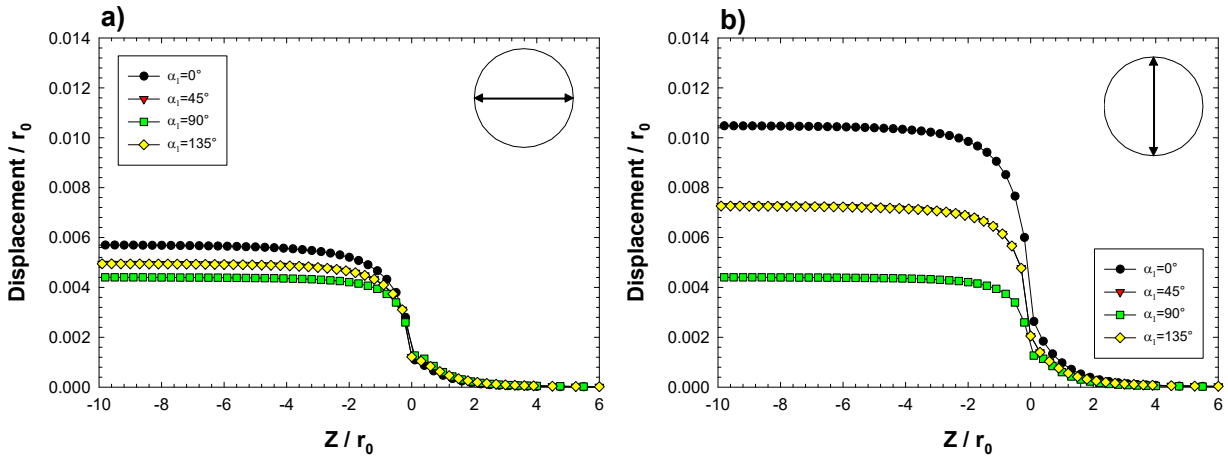

Figure 10.4 Normalized tunnel convergence with respect to the tunnel radius with the normalized distance from the face with respect to the tunnel radius for strike angle (α_2) 0°. (a) horizontal convergence; (b) vertical convergence.

Figure 10.5 shows the normalized radial displacements at the tunnel perimeter with respect to the tunnel radius, as well as the deformed cross section of the tunnel at the face and far-behind the face, for dip angles (α_1) 0°, 45°, 90° and 135°. As already mentioned, the radial displacements are the largest for α_1=0° and the smallest for α_1=90°. Far-behind the face, the radial displacements are symmetric in all cases; at the face, they are asymmetric for α_1=45° and 135° and symmetric for α_1=0° and 90°. The deformed cross section far-behind the face has an ellipsoidal shape for α_1=0°, 45° and 135° and a circular shape for α_1=90°. The radial displacements for α_1=45° and 135° are the same far-behind the face, but they are different at the face. Interestingly, at the face, there is a vertical translation of the tunnel cross-section when α_1=45° and 135°, which is downwards for α_1=45° and upwards for α_1=135°. These vertical translations are not present far-behind the face of the tunnel. When the tunnel is aligned with the principal material directions (i.e. α_1=0° and 90°), no vertical translation of the tunnel cross-section occurs.

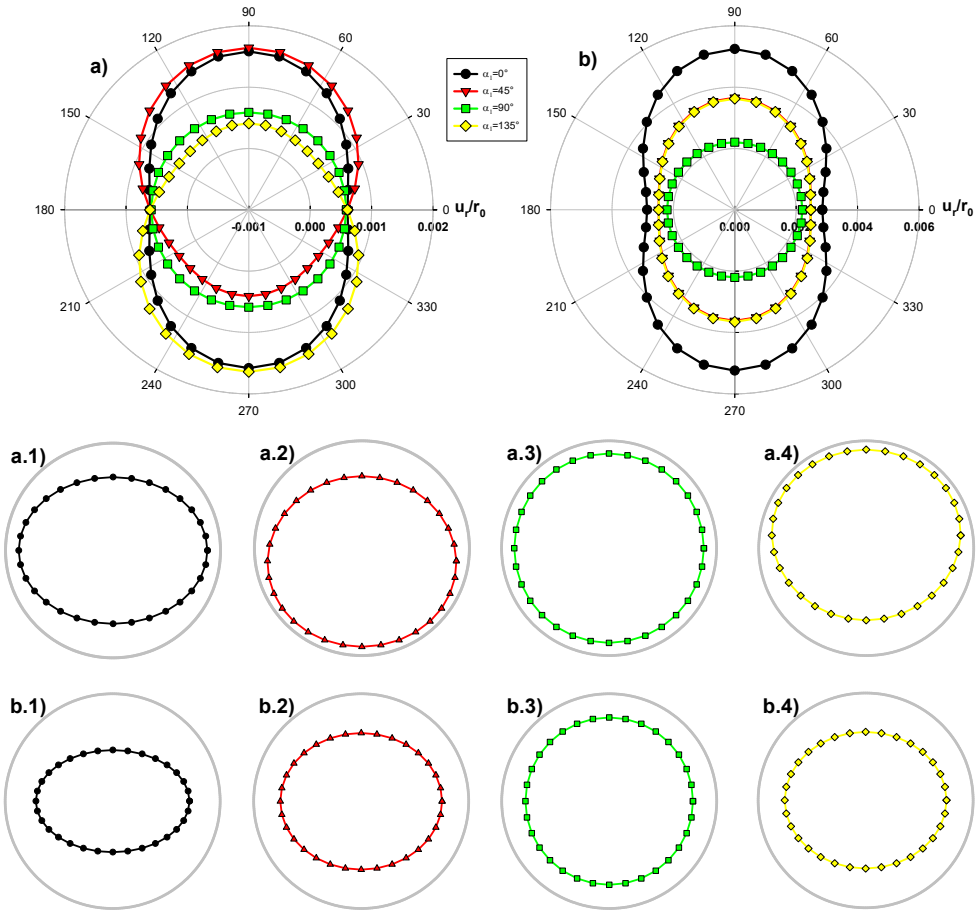

Figure 10.5 Normalized radial displacements at the tunnel perimeter, with respect to the tunnel radius, and deformed tunnel cross-section, for strike angle (α_2) 0°. (a) at the face; (b) far-behind the face. Deformations are magnified by a factor of 200 at the face and by 100 far-behind the face.

Figure 10.6 presents the normalized radial displacements at the crown and at the invert of the tunnel and the vertical translation (normalized by the tunnel radius), with the distance from the tunnel face (also normalized with respect to the tunnel radius), for α_1=45°. As one can see in Figure 10.6a, the radial displacements at the crown and at the invert are different near the face of the tunnel, but they are the same far-behind the face. Also, the vertical translation of the cross section starts near face and is maximum at the face (i.e. Z=0). Figure 10.6b shows "corrected" radial displacements (the vertical translation is subtracted), with the distance from the face. Interestingly, the corrected radial displacements are the same near the face (the differences are within numerical

error), which indicates that the vertical translation is, in reality, a rigid body vertical motion of the tunnel.

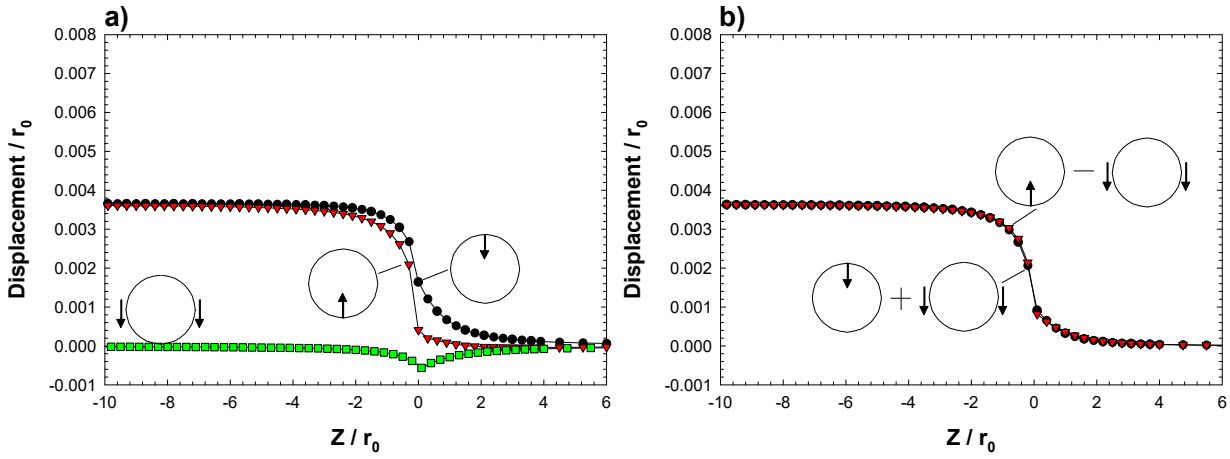

Figure 10.6 Normalized radial displacements and vertical translation of the tunnel cross section with respect to the tunnel radius, with the normalized distance from the face with respect to the tunnel radius for α_1=45° and α_2=0°. (a) radial displacements and vertical translation; (b) corrected radial displacements.

Figure 10.7 shows the normalized stress paths with respect to the vertical stress at points near the tunnel perimeter, for the dip angles (α_1) 0°, 45° and 90°. The stresses are computed at the springline, at the crown and at the invert, at a distance of $0.1r_0$ from the tunnel perimeter to avoid the mathematical singularity that occurs due to the sharp corner at the intersection of the tunnel face and the tunnel perimeter. The stress paths follow the same trend at all points. Far ahead of the face of the tunnel, i.e. at location (1) in Figure 10.2, the stresses are those of the geostatic stress field. Ahead of the face, as the distance from the face decreases, the shear stresses increase substantially; behind the face, the shear stresses continue to increase with distance from the face until reaching a constant value (location (3) in Figure 10.2). The mean stresses increase near the face (at location (2) in Figure 10.2) and decrease behind the face. For the three dip angles, the stress paths at the springlines are symmetric. For α_1=0° (Figure 10.7a), the stress paths at the invert and at the crown are the same, as expected, but different at the springlines. For α_1=45° (Figure 10.7b), the stress paths are all different, and are associated with the downwards rigid body displacement of the tunnel cross section near the face, as shown in Figures 10.5 and 10.6. The downwards rigid body displacement compresses the ground underneath the tunnel and relieves the ground above. Because of the similarities between α_1=45° and α_1=135°, the stresses at the crown

for α_1=45° are exactly the same as the stresses at the invert for α_1=135° and vice-versa. For α_1=90° (Figure 10.7c), the stress paths are exactly the same at points around the tunnel perimeter, due to symmetry.

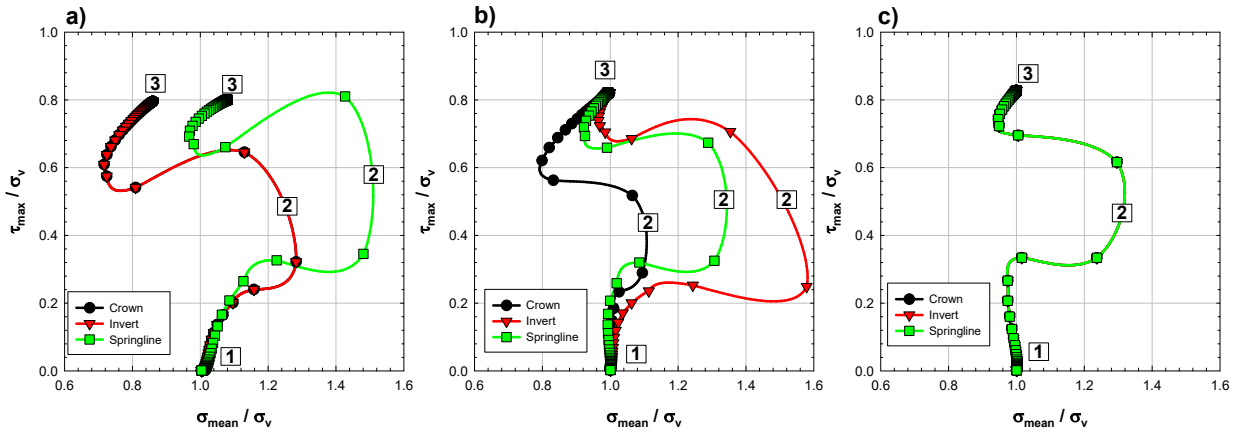

Figure 10.7 Normalized stress paths with respect to the vertical stress, for strike angle (α_2) 0°. (a) dip angle (α_1) 0°; (b) dip angle (α_1) 45°; (c) dip angle (α_1) 90°.

Figure 10.8 shows the axial displacements with respect to the tunnel radius with the distance from the tunnel face, both normalized with respect to the tunnel radius, for dip angles (α_1) 0°, 45°, 90°. At the springlines, for all cases, axial displacements are mobilized near the face and are maximum at the face. The axial displacements reduce to zero far behind the face. For α_1=0° and 90°, at the crown and invert (Figures 10.8a and 10.8c), no axial displacements are induced far-behind the face because the tunnel is aligned with the rock mass structure; however, axial displacements are induced near the face. For α_1=45° (Figure 10.8b), axial displacements at the crown and at the invert are produced far-behind the face and have the same magnitude, but opposite directions. Because of the symmetry, the axial displacements at the crown for α_1=45° are exactly the same as at the invert for α_1=135° and vice-versa.

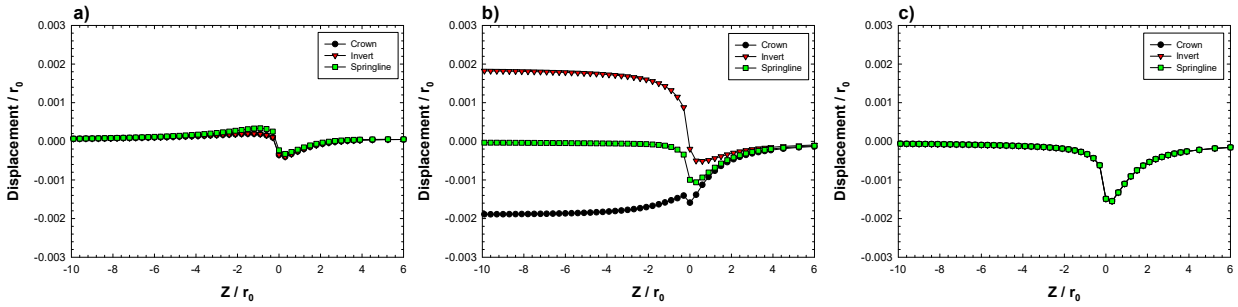

Figure 10.8 Normalized axial displacements with respect to the tunnel radius with the normalized distance from the face with respect to the tunnel radius, for strike angle (α_2) 0°. (a) dip angle (α_1) 0°; (b) dip angle (α_1) 45°; (c) dip angle (α_1) 90°.

The normalized axial displacements along the tunnel perimeter, for the case with α_1=45° are plotted in Figure 10.9. At the face (i.e. Z=0), the axial displacements are asymmetric. They are the largest at the crown and the smallest at the invert. Far-behind the face, the axial displacements are anti-symmetric. The horizontal axis is the axis of anti-symmetry, so the axial displacements are maximum at the crown and at the invert and zero at the springline. The axial displacements at the face can be understood within the context of the rigid body displacement of the tunnel cross section explained earlier. The face of the tunnel constrains the axial displacements induced around the tunnel perimeter. As consequence, asymmetric radial deformations are induced near the face (note that for α_1=0° and 90°, Figure 10.8, no anti-symmetric axial displacements are induced far-behind the face and the ground deformations near the face are symmetric, as shown in Figure 10.5).

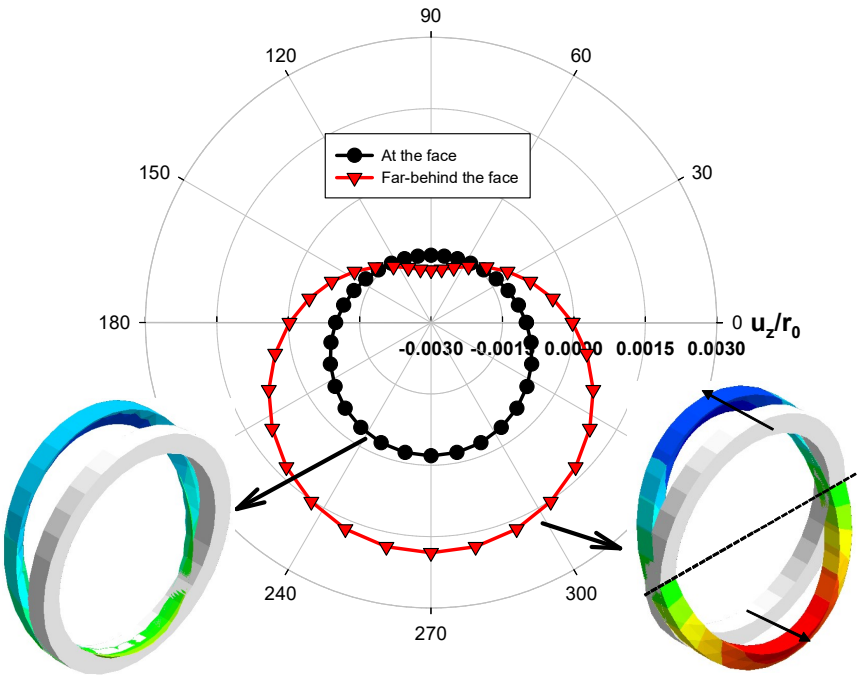

Figure 10.9 Normalized axial displacements with respect to the tunnel radius at the tunnel perimeter for α_1=45° and α_2=0°. The colors of the axially deformed tunnel cross-sections are associated with the magnitude of the axial displacements and are kept to help the visualization of the deformed shape.

The preceding discussion focused on the influence of the dip angle on the tunnel response, while the strike of the rock structure remained aligned with the horizontal axis of the tunnel (i.e. α_2=0°). In the following, the effect of the tunnel misalignment with the strike is investigated. To that end, the following cases were considered: strike direction, α_2=45°, with dip angles 0°, 45° and 90°. Figure 10.10a shows the tunnel misaligned with the vertical structural planes (i.e. α_1=90°) and Figure 10.10b shows the tunnel misaligned with the inclined structural planes (i.e. α_1=45°); for dip angle (α_1) 0°, the rock mass structure is horizontal and is shown in Figure 10.3a. Note that, for α_1=0°, the strike angle has no influence in the results because the horizontal tunnel is always aligned with the rock structure. The same isotropic geostatic stress field, as before, was adopted.

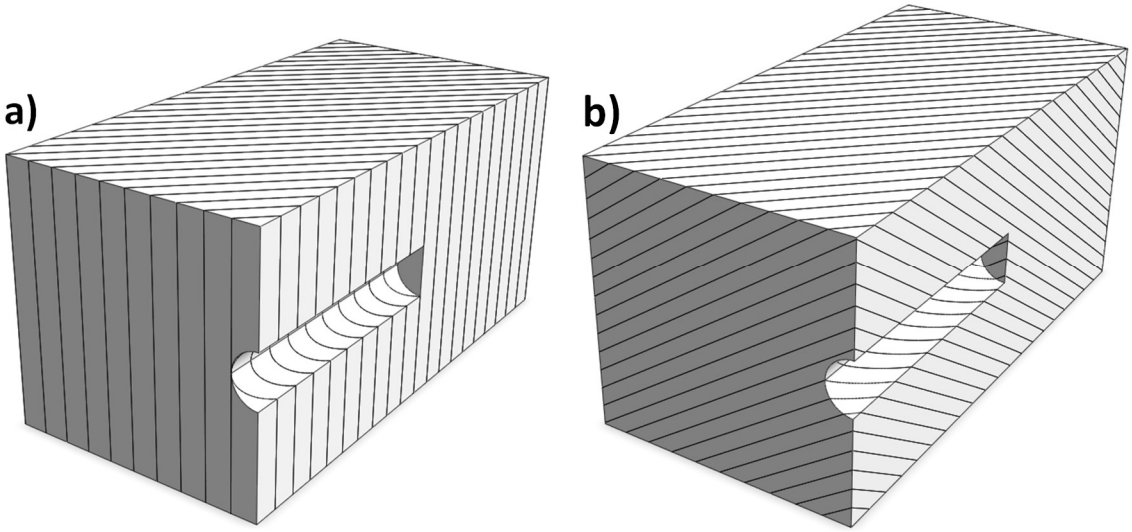

Figure 10.10 Rock mass structure with strike direction (α_2) 45°. Dip angles (α_1): (a) 90°; (b) 45°.

Figure 10.11 shows the normalized horizontal and vertical tunnel convergence, with respect to the tunnel radius, with the distance from the face, also normalized with respect to the tunnel radius, for dip angles (α_1) 0°, 45° and 90° and strike angle (α_2) 45°. As one can see, and similar to the previous cases with α_2= 0°, tunnel convergence starts to increase approximately at $4r_0$ ahead of the face and reaches a constant at approximately $4r_0$ behind the face of the tunnel. For α_1=0°, the horizontal convergence is smaller than the vertical. The opposite occurs for α_1=90° and for α_1=45°. A comparison between the results for α_2=45° and for α_2=0° (Figure 10.4) indicates that the horizontal convergences increase as the strike angle rotates (α_2) from 0° to 45°. In contrast, the vertical convergences are slightly affected with the strike rotation. When the strike angle (α_2) is 0°, the rock mass stiffness in the horizontal direction is always the largest irrespective of the dip angle (α_1). As the strike angle rotates, the stiffness in the horizontal direction decreases; thus, the horizontal convergence increases. Thus, the numerical results show that the strike direction affects the most the horizontal displacements, while the dip angle, the vertical.

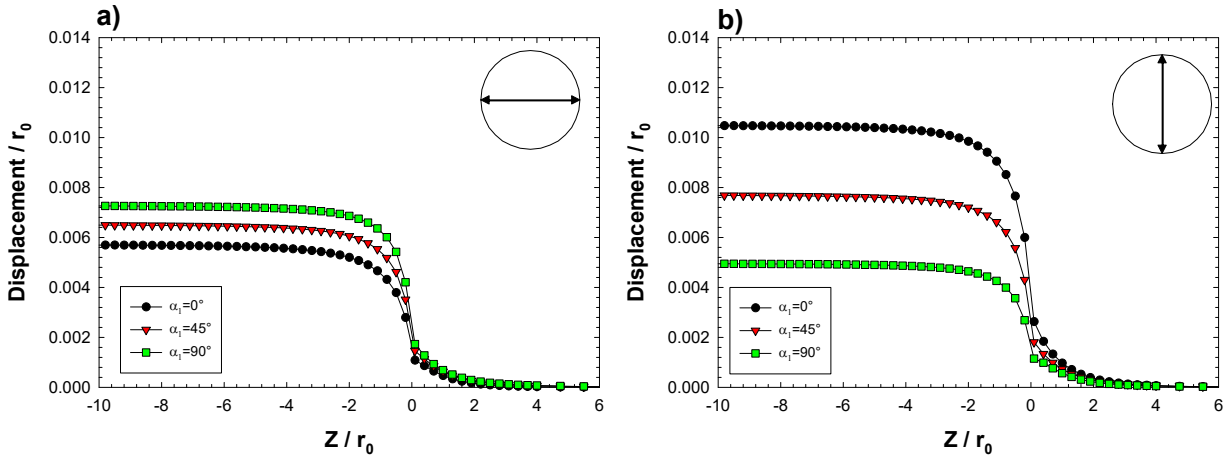

Figure 10.11 Normalized tunnel convergence with respect to the tunnel radius with the normalized distance from the face with respect to the tunnel radius, for strike angle (α_2) 45°. (a) horizontal convergence; (b) vertical convergence.

The normalized radial displacements at the tunnel perimeter and the deformed tunnel cross section, for dip angles (α_1) of 0°, 45° and 90° and strike (α_2) 45°, are shown in Figure 10.12. For α_1=0°, the deformed cross section has a symmetric ellipsoidal shape, with maximum convergence in the vertical direction and minimum in the horizontal. This is expected since the tunnel is aligned with the structure of the rock. For α_1=45°, the ground deformations are asymmetric at the face and are ellipsoidal far-behind the face, with a maximum radial displacement at θ=125° and a minimum at θ=35°; at the face, there is a translation of the tunnel cross section in the diagonal direction downwards and towards the right springline (Figure 10.12.a.2). For α_1=90°, the radial displacements at the face are asymmetric and are symmetric far-behind the face. At face, there is a translation of the tunnel cross section in the horizontal direction towards the right springline (Figure 10.12.a.3). Far behind the face, the deformed cross section has a symmetric ellipsoidal shape, with maximum convergence in the horizontal direction and minimum in the vertical. It is interesting to compare the results from α_2=45° with those from α_2=0°. For the case with a dip angle (α_1) of 90°, the misalignment with the strike direction increases the magnitude of the radial displacements at the tunnel perimeter and produces asymmetric deformations at the tunnel face (i.e. a horizontal translation towards the right springline); for the case with a dip angle (α_1) of 45°, the tunnel misalignment with α_2 affected the direction of the translation at the face (vertical and downwards for α_1=45° and α_2=0°, Figure 10.5.a.2, and downwards, towards the right, for α_1=45° and α_2=45°, Figure 10.12.a.2) and the location where the maximum and minimum convergence

occurred far-behind the face. As shown in Figure 10.12.b.2, for α_1=45° and α_2=45°, the deformed cross-section far-behind the face is distorted. The maximum radial displacement occurs at θ=125° and the minimum, at θ=35°. For α_1=45° and α_2=0°, (Figure 10.5.b.2) the deformed cross-section far-behind the face is symmetric with respect to the horizontal and vertical axis. Thus, the maximum radial deformation is along the vertical direction (θ=90°) and the minimum along the horizontal direction (θ=0°).

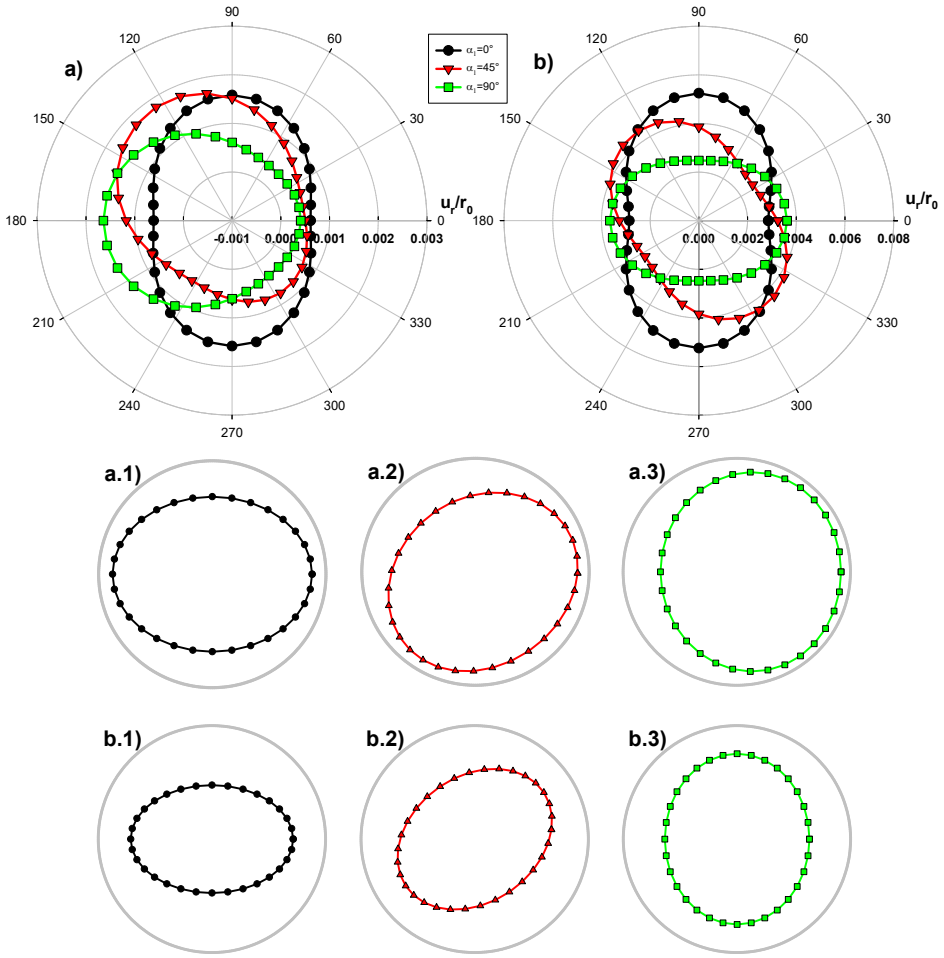

Figure 10.12 Normalized radial displacemets at the tunnel perimeter ,with respect to the tunnel radius, and deformed tunnel cross-section for strike angle (α_2) 45°. (a) at the face; (b) far-behind the face. Deformations are magnified by a factor of 200 at the face and by 100 far-behind the face.

Figure 10.13 shows the radial displacements and the translation motion of the tunnel (this is justified in the next few sentences) at θ=125°, where the radial displacements are maximum, with distance from the face. The displacements and the distance from the face are normalized with

respect to the tunnel radius. Near the face, the radial displacements are asymmetric and a translation of the tunnel cross-section occurs. Far-behind the face, the radial displacements at θ=125° and θ=305° are the same and there is no rigid body displacement. Figure 10.13b shows the radial displacements at θ=125° and θ=305° without the rigid body displacement component (i.e. corrected radial displacements, where deformations are subtracted from the translation of the tunnel cross-section). As one can see, the corrected radial displacements with the distance from the face are the same, with differences of the order of the numerical approximation. This is consistent with the case α_1=45° and α_2=0° discussed before. These results indicate that the asymmetry near the face due to the tunnel misalignment with the rock structure is due to a rigid body displacement of the tunnel cross-section.

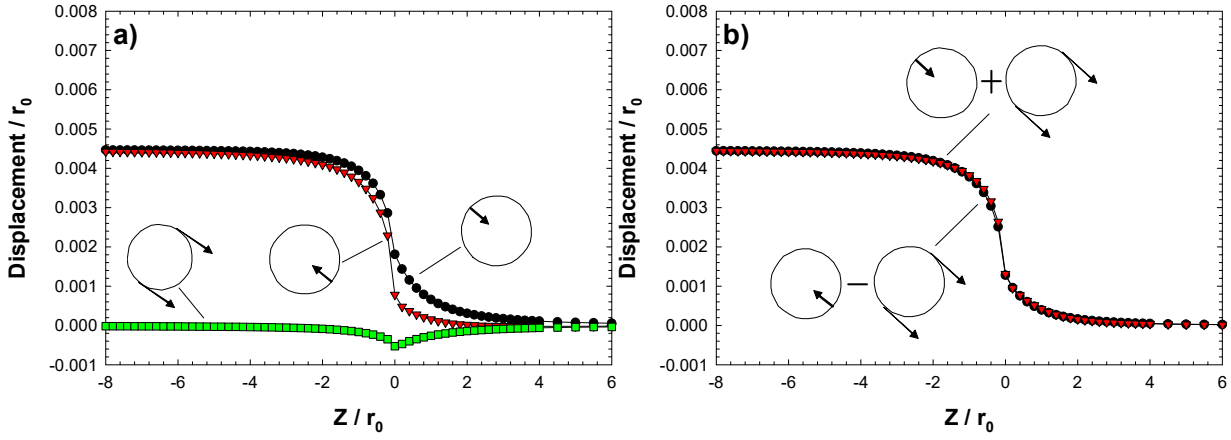

Figure 10.13 Normalized radial displacements and translation displacement of the tunnel cross section with respect to the tunnel radius, with the normalized distance from the face with respect to the tunnel radius for α_1=45° and α_2=45°. (a) radial displacements and rigid body displacements and (b) corrected radial displacements.

The normalized stress paths with respect to the vertical stress at different points near the tunnel perimeter for strike angle 45° and dip angles 0°, 45° and 90° are presented in Figure 10.14. The stresses are taken at $0.1r_0$ from the tunnel perimeter to avoid the mathematical singularities caused by the corner at the face of tunnel. The stresses for α_1=0° are the same of those presented in Figure 10.7a. Similar to the stress paths for strike angle 0° (Figure 10.7), the four locations present a loading stress path with an abrupt increase of the stresses near the face. For α_1=45° and α_2=45° (figure 10.14a), the stress paths near the face are asymmetric at the springlines and at the crown and invert. As shown in Figures 10.12 and 10.13, for α_1=45° and α_2=45°, a rigid body

motion occurs downwards and towards the right. Near the face, the stresses at the invert and at the right springline are larger than at the crown and at the left springline, respectively. This is caused because the rigid body displacement near the face unloads the crown and the left springline and loads the invert and the right springline. For α_1=90° and α_2=45° (Figure 10.14b), the stress paths at the crown and at the invert are the same; however, the stress paths are different at the springlines. The reason for this is because the radial displacements are symmetric at the crown and invert and asymmetric at the springlines. As shown in Figure 10.12, for α_1=90° and α_2=45°, a horizontal rigid body displacement towards the right springline occurs at the face. Thus, the stresses are larger at the right springline than at the left because the rigid body displacement compresses the ground in the right springline and unloads the ground at the left springline.

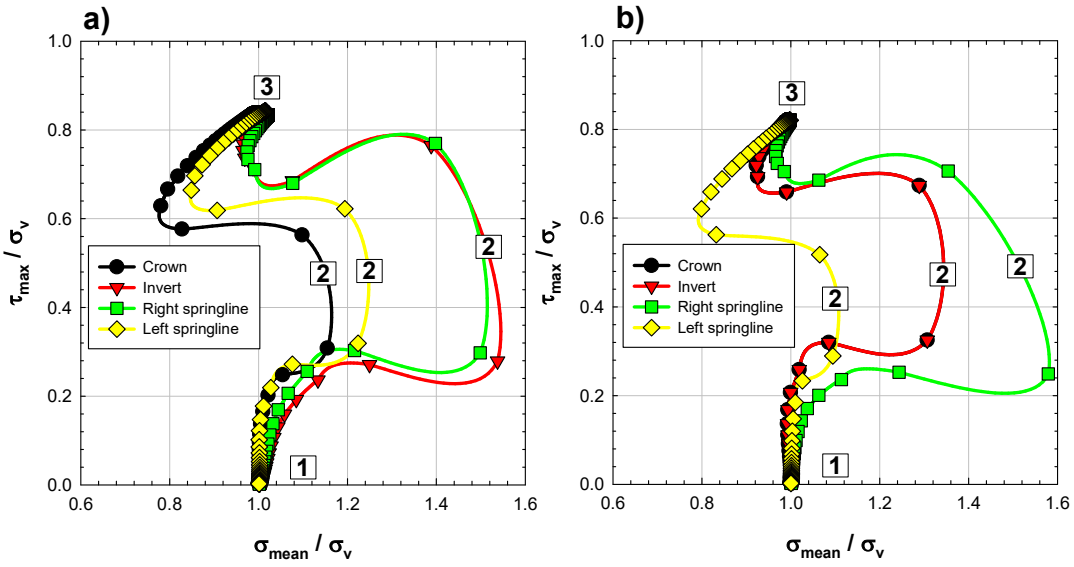

Figure 10.14 Normalized stress paths with respect to the vertical stress, for strike angle (α_2) 45°. (a) Dip angle (α_1) 45°; (b) Dip angle (α_1) 90°.

Figure 10.15 shows the normalized axial displacements at the tunnel perimeter with respect to the tunnel radius, for α_2=45° and α_1=45°. At the face, the axial displacements are asymmetric and, far behind the face, are anti-symmetric, with the axis of anti-symmetry at θ=35°. Comparing the axial displacements for α_1=45° and α_2=45° with those for α_1=45° and α_2=0° (Figure 10.9), one can see that the strike angle changes the position of the axis of anti-symmetry, but not the magnitude of the axial displacements (i.e. the maximum axial displacement for α_2=0°is 4% larger than the maximum axial displacement for α_2=45°, which is considered negligible). Near the face,

the asymmetric axial deformations are constrained, which induce asymmetric radial displacements, as shown in Figures 10.12 and 10.13. Note that the radial displacements are symmetric far-behind the face (Figure 10.12.b.2.), where there is no constraint to the anti-symmetric axial displacements.

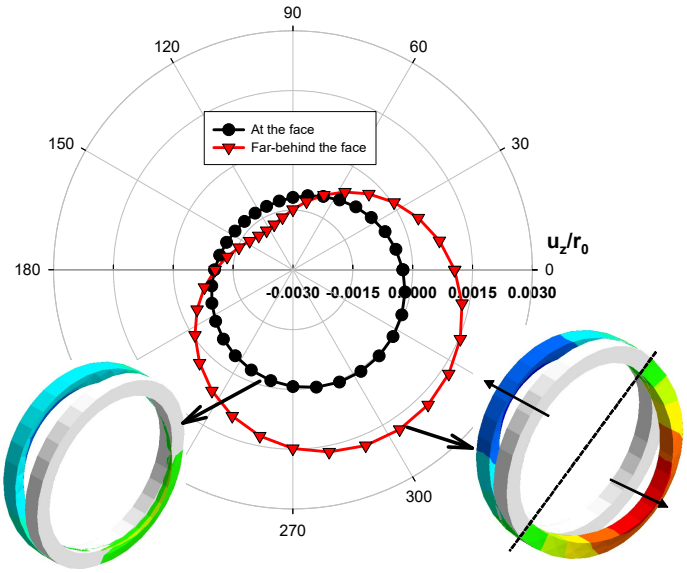

Figure 10.15 Normalized axial displacements at the tunnel perimeter with respect to the tunnel radius for α_1=45° and α_2=45°. The colors of the axially deformed tunnel cross-sections are associated with the magnitude of the axial displacements and are kept to help the visualization of the deformed shape.

10.4 3D face effects due to stress anisotropy

In addition to the anisotropic behavior already discussed, rock masses may present stress anisotropy (Gysel, 1975; Brown and Hoek, 1978; McGarr and Gay, 1978; Evans et al., 1989; Martin and Kaiser, 1996; Haimson et al., 2003; Wileveau *et al.*, 2007; Zhao *et al.*, 2013, 2015; Park *et al.*, 2014; Perras et al., 2015; Zhang *et al.*, 2017; Souček *et al.*, 2017). When the tunnel is not aligned with one of the geostatic principal stress directions, far-field axial shear stresses appear. In this section, the 3D face effects of unsupported tunnels misaligned with the rock mass structure and with the geostatic principal stress directions are investigated. A structured rock mass with dip angle (α_1) 45° and strike direction (α_2) 45° (Figure 10.10b) is selected. An anisotropic geostatic stress field is adopted assuming that the vertical axis is one of the principal stress directions. A vertical stress (σ_v) of 5MPa as the intermediate principal stress, a minor principal horizontal stress (σ_h) of 5MPa, and a major principal horizontal stress (σ_H) of 10MPa, are adopted. The somewhat large horizontal stress anisotropy ratio of 2 is often reported in the literature (Gysel, 1975; Evans

et al., 1989; Haimson et al., 2003; Park *et al.*, 2014; Souček *et al.*, 2017). Figure 10.16 shows the plan view of the misaligned tunnel with the horizontal principal stresses. Figure 10.16a shows the major principal horizontal stress perpendicular to the strike of the rock structure and Figure 10.16b, parallel to the strike. Three scenarios are investigated, as listed in Table 10.1 (the coordinate system is that attached to the tunnel, as shown in Figure 10.2). In scenario one, the largest horizontal stress is perpendicular to the strike of the rock structure; in scenario two, the far-field axial shear stress is neglected; and in scenario three, the smallest horizontal stress is parallel to the strike. The three scenarios have the same far-field horizontal stress ($\sigma_{xx,ff}$), the same vertical stress (σ_v) and the same tunnel orientation with respect to the rock structure (α_1=α_2=45°). The only difference among scenarios is the far-field axial shear stress, as shown in Table 10.1.

Table 10.1 Far-field geostatic stresses in the tunnel coordinate system for the three scenarios studied.

Scenario	$\sigma_{xx,ff}/\sigma_v$	$\tau_{xz,ff}/\sigma_v$
1) σ_H perpendicular to α_2	1.5	0.5
2) no far-field axial shear	1.5	0
3) σ_H parallel to α_2	1.5	-0.5

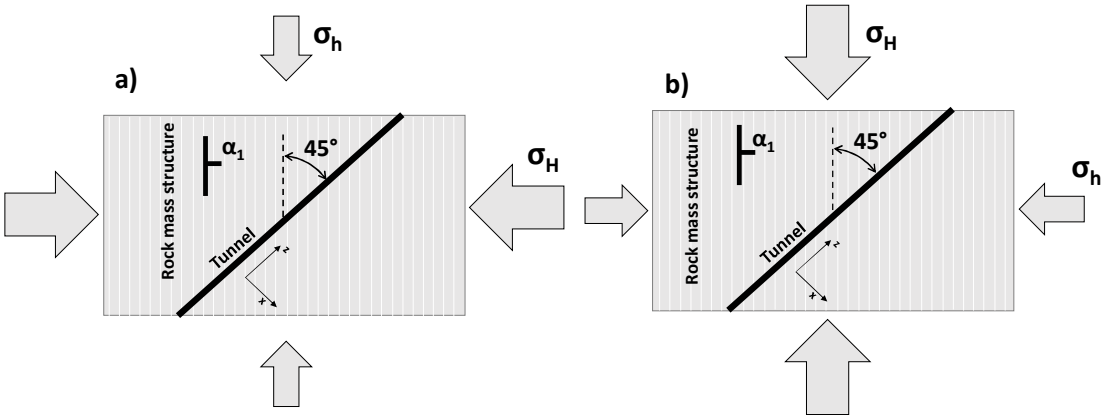

Figure 10.16 Tunnel orientation with respect to the rock mass structure and geostatic stresses. (a) major principal (largest horizontal) stress (σ_H) perpendicular to the strike direction (α_2); and (b) minor principal (smallest horizontal) stress parallel to the strike direction (α_2).

Figure 10.17 shows the normalized axial displacements at the tunnel perimeter with respect to the tunnel radius, for the three scenarios. Axial displacements are asymmetric at the face and anti-symmetric far-behind the face. The axial displacements are larger when σ_H is perpendicular

to α_2 (scenario one) and smaller when σ_H is parallel to α_2 (scenario two). Note how the position of the axis of anti-symmetry changes with the far-field axial shear stress. The axis is in the 1st quadrant when σ_H is perpendicular to α_2 (scenario one) and for the "no far-field axial shear stress" scenario (scenario two), while it is in the second quadrant when σ_H is parallel to α_2 (scenario three). This is the result of the combination of the anti-symmetric axial displacements, due to the tunnel misalignment with the rock mass structural planes, and the anti-symmetric axial displacements due to the far-field axial shear stress. For scenario one (σ_H perpendicular to α_2), the anti-symmetric axial displacements produced by the rock mass structure and by the far-field axial shear stress have the same direction; thus, the axial displacements are increased. For scenario three (σ_H parallel to α_2), the anti-symmetric axial displacements due to the rock mass structure and due to the far-field axial shear stress have opposite direction; thus, the axial displacements are reduced.

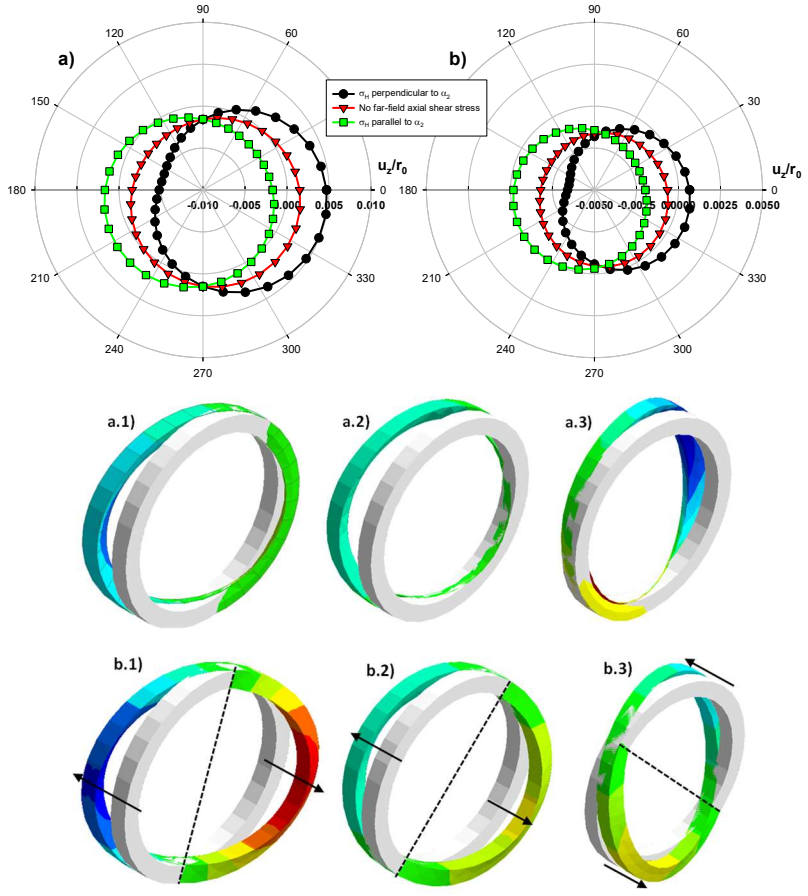

Figure 10.17 Normalized axial displacements at the tunnel perimeter with respect to the tunnel radius for dip angle (α_1) 45° and strike angle (α_2) 45°. (a) at the face; (b) far-behind the face; (1) σ_H perpendicular to α_2; (2) no far-field axial shear stress; (3) σ_H parallel to α_2. The colors of the axially deformed tunnel cross-sections are associated with the magnitude of the axial displacements and are kept to help the visualization of the deformed shape.

Figure 10.18 shows the normalized radial displacements at the tunnel perimeter and the deformed cross section of the tunnel for the anisotropic geostatic stress fields (i.e. the three scenarios shown in Table 10.1) and for an isotropic geostatic stress field (Figure 10.12, $\alpha_1=\alpha_2=45°$). The ground deformations at the face are asymmetric, but symmetric (i.e. ellipsoidal shape with symmetries along the major and minor axes of the ellipse) far-behind the face. For scenario one (σ_H perpendicular to α_2), large inward radial displacements occur, at the face, on the left side of the tunnel. This can be associated with a translation of the cross section downwards and towards the right (see later for further discussion). For scenario two, where no far-field axial shear stresses are considered, the asymmetric deformations at the face are less remarkable than for the other two scenarios; a downwards and towards the right translation of the cross section occurs. For scenario three (σ_H parallel to α_2), the opposite is observed; that is, there are large inward radial displacements on the right side of the tunnel. Thus, a translation of the tunnel cross-section downwards and towards the left occurs. Far behind the face, the deformed cross section of the three scenarios has an ellipsoidal shape with the maximum radial displacement at $\theta=157.5°$ and the minimum at $\theta=67.5°$. Interestingly, the far-field axial shear stress did not affect the location of maximum and minimum radial displacements far-behind the face, but heavily affected the radial deformations at the tunnel face. Among the three scenarios, the radial displacements are the largest for scenario one (σ_H perpendicular to α_2) and the smallest for scenario three (σ_H parallel to α_2). This observation is associated with the anti-symmetric axial displacements produced by the rock structure and by the far-field axial shear stress. As shown in Figure 10.17, the axial displacements for scenario one are the largest because the anti-symmetric axial displacements caused by the rock structure and by the far-field axial shear stress have the same sign, i.e. they add to each other. Because the rock mass is transversely anisotropic and the tunnel is not aligned with the rock structure, in-plane and out-of-plane deformations are coupled (Vitali et al. 2019d). Thus, the larger the axial displacements, the larger the radial displacements. For the isotropic geostatic stress case with the same orientation with respect to the rock structure of the three scenarios (i.e. $\alpha_1=\alpha_2=45°$), the radial displacements were smaller than the ones with the adopted anisotropic geostatic stress state. The maximum radial displacement occurred at $\theta=125°$ and the minimum at $\theta=35°$. Thus, the far-field stress anisotropy affected the shape of the deformed tunnel cross-section near and far-behind the face, as shown in Figure 10.18.

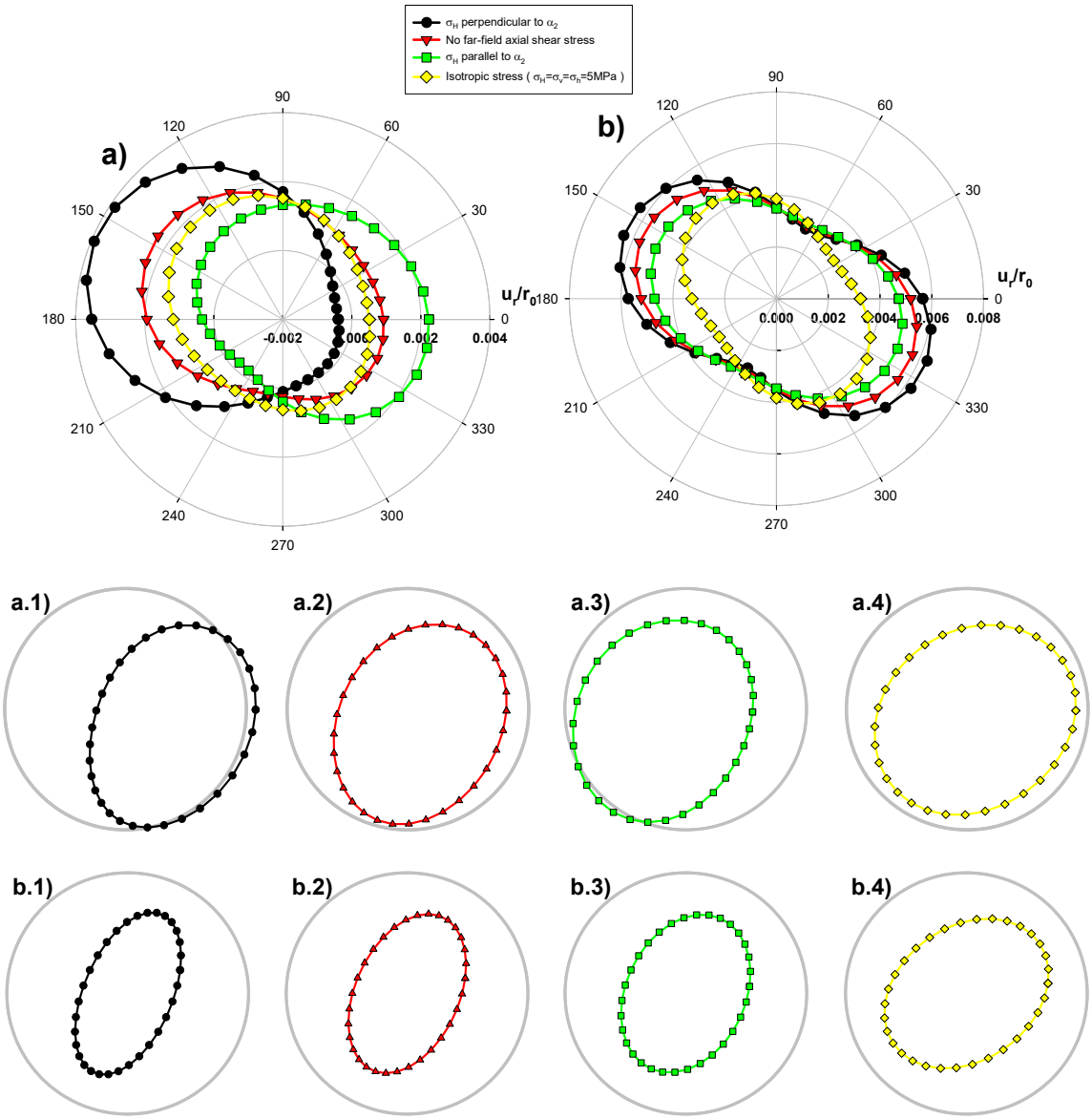

Figure 10.18 Normalized radial displacements at the tunnel perimeter and deformed tunnel cross-section for α1=45° and α2=45°. (a) at the face; (b) far-behind the face. Deformations are magnified by a factor of 200 at the face and by 100 far-behind the face.

Figure 10.19 shows the normalized maximum and minimum convergence of the tunnel with the normalized distance from the face, for the three scenarios (Table 10.1). As already mentioned, the maximum convergence occurs at θ=157.5° and the minimum at 67.5°. In all scenarios, the tunnel deformations start to increase at a distance of $4r_0$ ahead the face and reach steady state at $4r_0$ behind the face in all scenarios; note that this observation is similar to what was

found in preceding analyses involving only the rock anisotropy. At the face (Z=0), the radial displacements abruptly increase. The maximum convergence is larger when σ_H is perpendicular to α_2 and smaller when σ_H is parallel to α_2. The minimum convergence, Figure 10.19(b) is similar for the three scenarios. Figure 10.20 shows the normalized radial displacements at θ=157.5° and at θ=337.5°, the locations of maximum deformation, and the translation of the tunnel cross section with the normalized distance from the face for scenarios one (σ_H is perpendicular to α_2) and two (no far-field axial shear stress). Scenarios one and two presented a cross-section translation downwards and towards the right, at the face (figure 10.18.a.1 and 10.18.a.2). The radial displacements at θ=157.5° and at θ=337.5° are different near the face but are the same far-behind the face. A translation of the cross section is observed near the face; the magnitude of the translation is larger for scenario one (σ_H perpendicular to α_2) than for scenario two (no far-field axial shear). This is expected because the translation is associated with the axial displacements near the face. Since the axial displacements are larger for scenario one, the magnitude of the translation is expected to be larger as well. Figure 10.20 also presents the radial displacements without the cross section translation (i.e. the corrected radial displacements). For scenario one (σ_H is perpendicular to α_2), the corrected radial displacements are asymmetric near the face (i.e. different radial displacements at θ=157.5° and at θ=337.5°). For scenario two (no far-field axial shear stress), the corrected radial displacements are symmetric with the distance from the face (i.e. radial displacements at θ=157.5° and at θ=337.5° are the same). Vitali et al. (2019b) observed that the asymmetries near the face on an unsupported tunnel misaligned with the geostatic principal stresses in an isotropic elastic ground could be decomposed into a rigid body displacement of the tunnel cross-section and anti-symmetric radial displacements at the tunnel perimeter. For scenario one, the asymmetric deformations near the face are more complex because of the anisotropic properties of the rock mass. The asymmetric radial displacements near the face caused by the rock structure seem to be caused by a rigid body displacement of the tunnel cross-section, while the asymmetric deformations due to the far-field axial shear stress in the presence of anisotropic rock, is more complex. Figure 10.21 shows the normalized radial displacements at θ=67.5° and θ=247.5°, the location of the minimum radial displacements, and the cross section translation for scenario three (σ_H parallel to α_2) and the corrected radial displacements. For this scenario, the tunnel cross-section translation is downwards and towards the left. As one can see in figure 10.20, the corrected

radial displacements are asymmetric near the face, which is similar to scenario one and consistent with Vitali et al. (2019b).

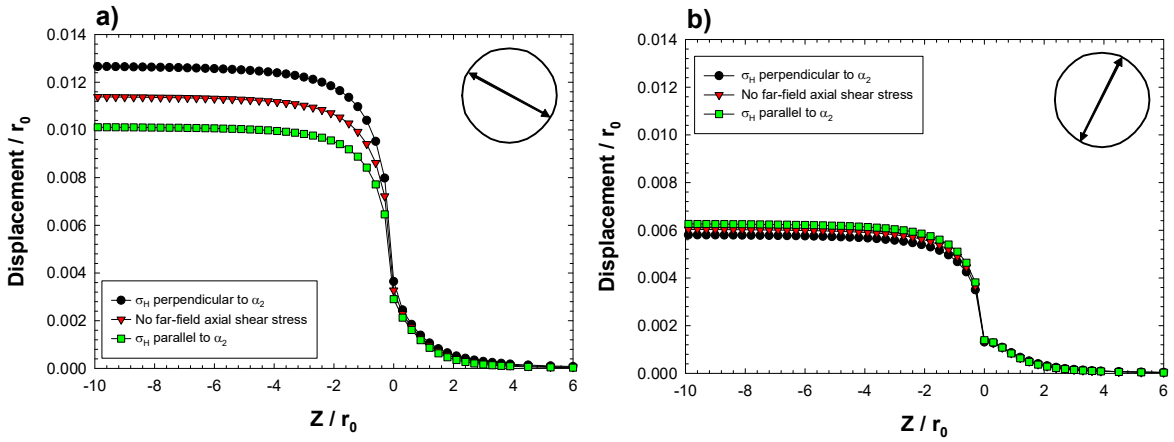

Figure 10.19 Normalized convergence with respect to the tunnel radius with normalized distance from the tunnel face; (a) maximum convergence at θ=157.5°; and (b) minimum convergence at 67.5°.

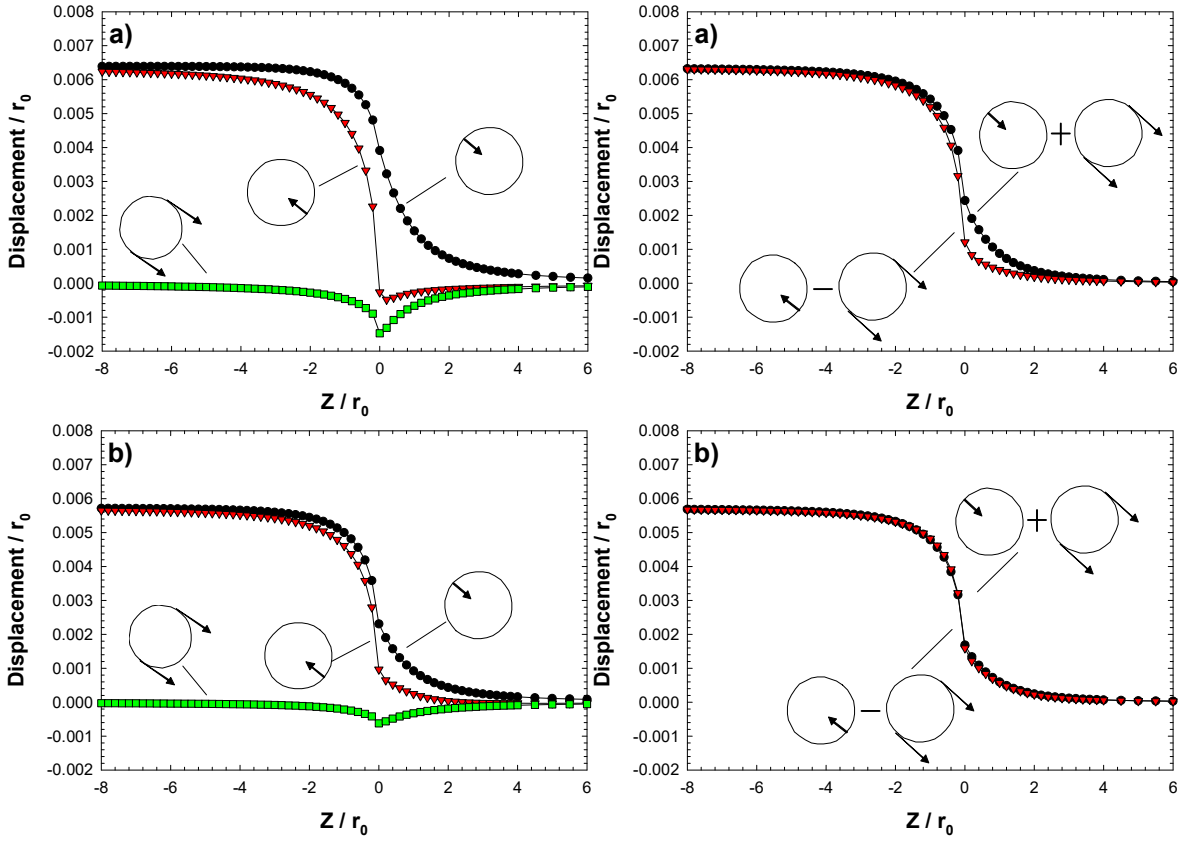

Figure 10.20 Normalized radial displacements and cross section translation with respect to the tunnel radius, with the normalized distance from the face with respect to the tunnel radius, at θ=157.5° and at θ=337.5°. (a) σ_H perpendicular to α_2; (b) "no far-field axial shear stress".

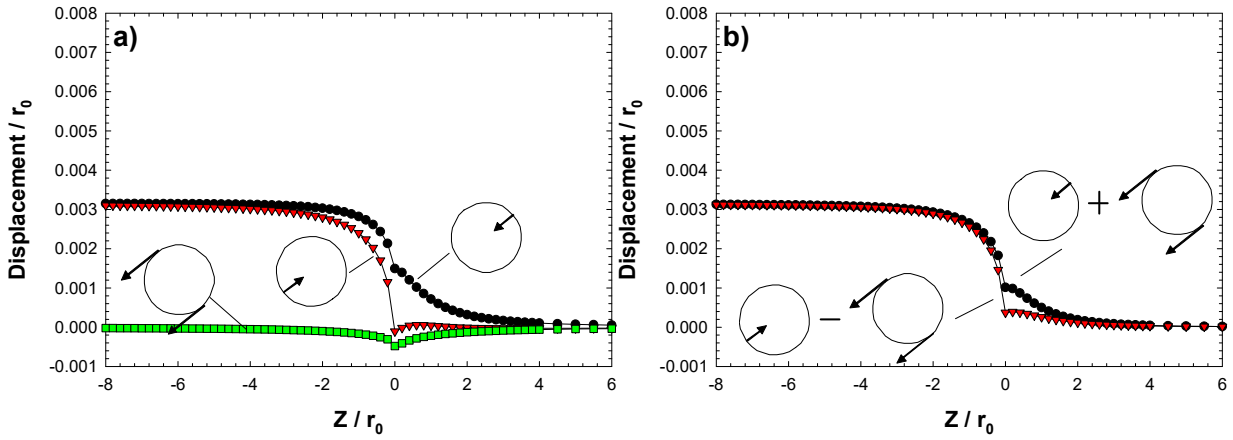

Figure 10.21 Normalized radial displacements and cross section translation with respect to the tunnel radius, with the normalized distance from the face with respect to the tunnel radius for σ_H parallel to α_2 and for θ=67.5° and θ=247.5°. (a) normalized radial diplacements and cross section translation; and (b) corrected radial displacements.

The normalized stress paths at points near the tunnel, with respect to the vertical stress, for the three scenarios (Table 10.1) are shown in Figure 10.22. The stresses are taken $0.1r_0$ from the tunnel perimeter to avoid singularities at the corners. The stress paths at the crown and at the invert (bottom of figure 10.22) are different for the three scenarios. Near the face, at location (2) in Figure 10.2, the stresses at the invert are larger than at the crown for all scenarios. The reason for this is the downward translation of the tunnel cross-section that occurs in all the three scenarios, as shown in figures 10.18, 10.20 and 10.21. Thus, the ground underneath the tunnel is compressed near the face, while the ground above is unloaded. The stress paths at the crown and at the invert are similar to those shown in Figures 10.14a, for $\alpha_1=\alpha_2=45°$ and isotropic geostatic stress field. The top plots of Figure 10.22 represent the stress paths at the springline; Figure 10.22a, for scenario one (σ_H perpendicular to α_2), Figure 10.22b for scenario two and Figure 10.22c for scenario 3. Figure 10.22a shows that at the right springline, ahead of the face, both maximum shear and mean effective stresses increase as the distance from the face decreases; that is, the ground is taking load as it approaches the tunnel face; near the face, at location (2) in Figure 10.2, the stresses abruptly increase; behind the face, the stresses decrease as the distance from the face increases until the stress state is constant far-behind the face; so, the ground unloads behind the face. At the left springline, the opposite behavior is observed: there is unloading ahead of the face and loading behind the face. For scenario 2 ("no far-field axial shear stress"), Figure 10.22b, the right and left

springlines show loading ahead of the face and unloading behind the face; however, the stress paths are asymmetric. Near the face, the stresses on the right are larger than on the left. For scenarios one and two, the cross section translation near the face is towards the right (Figures 10.18 and 10.20); thus, the right springline is loaded, while the left is unloaded. For scenario three (σ_H parallel to α_2), Figure 10.22c, there is unloading ahead of the face and loading behind the face at the right springline. At the left springline, the opposite happens (i.e. loading ahead of the face and unloading behind the face). For scenario three, the tunnel cross section translation is towards the left (Figures 10.18 and 10.21); thus, the left springline is compressed near the face while the right springline is unloaded. It is interesting to note that the maximum shear stresses are larger when the far-field axial shear stress is included. Note that the unloading ahead of the face only happens when the far-field axial shear stress is present. It is related to the more pronounced asymmetric deformations near the face that happen when the far-field axial shear stress is present, as discussed in figures 10.18, 10.20 and 10.21. When the far-field axial shear stress was present (scenarios one and three, Figures 10.18.a.1 and 10.18.a.3), at the face, outward radial displacements occurred at one side of the tunnel and large inward displacements occurred at the opposite side. When the far-field axial shear stress was neglected (scenario two, Figure 10.18.a.2), no outwards radial displacement occurred, and the inward displacements were smaller. Thus, the asymmetric deformations at the face induced opposite stress paths at the opposite sides of the tunnel, as shown in the top plots a) and c) of Figure 10.22. The stress paths at points around the tunnel perimeter for the isotropic geostatic stress case were considerably less asymmetric than the scenarios with anisotropic geostatic stress. In the isotropic geostatic stress field, all points around the tunnel perimeter had a loading stress path, with an abrupt increase of stresses near the face, until a constant value was reached far-behind the face. This is similar to the stress paths at the crown and invert in scenarios one, two and three, but different to the stress paths at the springlines. It shows that the complexity of the stress paths near the face increases substantially if the geostatic stress field is anisotropic, especially if the tunnel is not aligned with one of the principal stress directions.

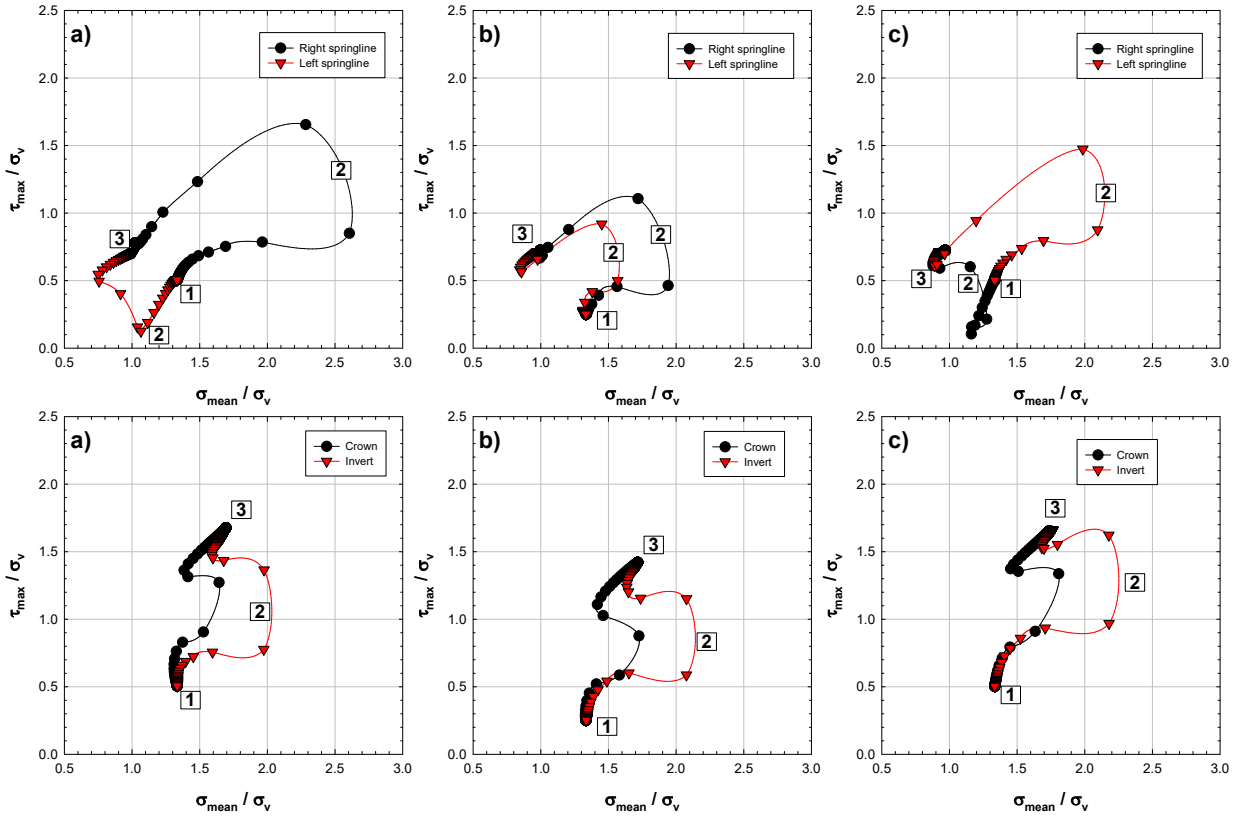

Figure 10.22 Normalized stress paths with respect to the vertical stress. (a) σ_H perpendicular to α_2; (b) "no far-field axial shear stress"; (c) σ_H parallel to α_2.

10.5 Effects on ground-structure interaction

The asymmetric deformations near the face that occur when the tunnel is misaligned with the rock structure or with the geostatic principal stresses do affect the interaction between the tunnel liner and the ground. To investigate the effects of the tunnel misalignment on supported tunnels, 3D FEM modeling considering a liner installed immediately after the round excavation was conducted (Figure 10.2) for the three scenarios investigated in the previous section (Table 10.1). The length of the excavation round was $0.2r_0$. The liner was represented by shell elements with thickness $0.1r_0$ and linear-elastic behavior. The elastic properties for the liner were Young modulus (E) 25GPa and Poisson ratio (ν) 0.2, which are typical of elastic properties of reinforced concrete. No slip was allowed between the liner and the ground. The dip and strike angles (i.e. α_1=45° and α_2=45°, see Figure 10.10b) and the rock mass properties of previous sections were adopted.

Figure 10.23 shows the normalized radial displacements at θ=157.5° and at θ=337.5°, the locations where the radial displacements are maximum with respect to the tunnel radius, with the normalized distance from the face with respect to the tunnel radius, for the three scenarios. As expected, the radial displacements are substantially smaller than those for the unsupported tunnel (Figure 10.19). The radial displacements near the face and far-behind the face are asymmetric. For σ_H perpendicular to α_2, the radial displacements far-behind the face at θ=157.5° are larger than at θ=337.5°. In contrast, when σ_H is parallel to α_2, the radial displacements at θ=337.5° are larger. This has important implications for the liner, as one can see in Figure 10.24, which is a plot of the radial stresses normalized with respect to the far-field vertical stress, for the three scenarios (Table 10.1). In the figure, the stresses are taken at $0.1r_0$ from the tunnel perimeter. For scenario one, when σ_H is perpendicular to α_2 (Figure 10.24a), the radial stresses at the right springline increase at the face and abruptly decrease behind the face; then, they increase with the distance from the face until constant far-behind the face. At the left springline, the radial stresses decrease ahead of the face as the distance from the face decreases; behind the face, the radial stresses slightly increase with the distance from the face until constant far-behind the face. Note that the radial stresses at the left springline are smaller than at the right. This is consistent with the asymmetric radial displacements discussed in Figure 10.23a, where one can see that right springline is compressed while the left is unloaded. For scenario two, no far-field axial shear stress", Figure 10.24b, the radial stresses at the right and left springline are similar ahead of the face, but they are different behind the face; the radial stresses are larger at the right springline than at the left. For scenario three, when σ_H is parallel to α_2 (Figure 10.24c), the radial stresses are similar to those when σ_H is perpendicular to α_2 but inverted; that is, the radial stresses are larger at the left springline than at the right. This is consistent with the asymmetric radial displacements (Figure 10.23c). Note that the radial stresses at the springlines for scenarios one and three are asymmetric ahead of the face, but they are symmetric for scenario two. This is related with the pronounced asymmetric stresses (discussed in Figure 10.22) and deformations (discussed in Figures 10.18, 10.20 and 10.21) observed near the face when the far-field axial shear stress is present. The radial stresses at the crown are similar in all three scenarios; they decrease ahead of the face and increase behind the face until constant. Note that the radial stresses far behind the face at the crown are larger than at the springline. This is the result of the far-field horizontal stress ($\sigma_{xx,ff}$) being larger than the vertical

stress (i.e. $\sigma_{xx,ff}=1.5\sigma_v$, table 10.1); thus, the stress concentrations are maximum at the crown and at the invert.

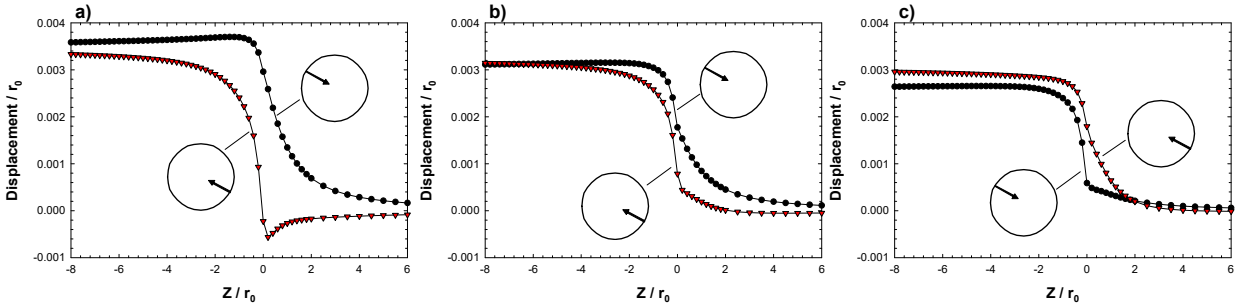

Figure 10.23 Normalized radial displacements at θ=157.5° and at θ=337.5° with respect to the tunnel radius, with the normalized distance from the face with respect to the tunnel radius, for supported tunnel. (a) σ_H perpendicular to α_2, (b) no far-field axial shear stress, (c) σ_H parallel to α_2.

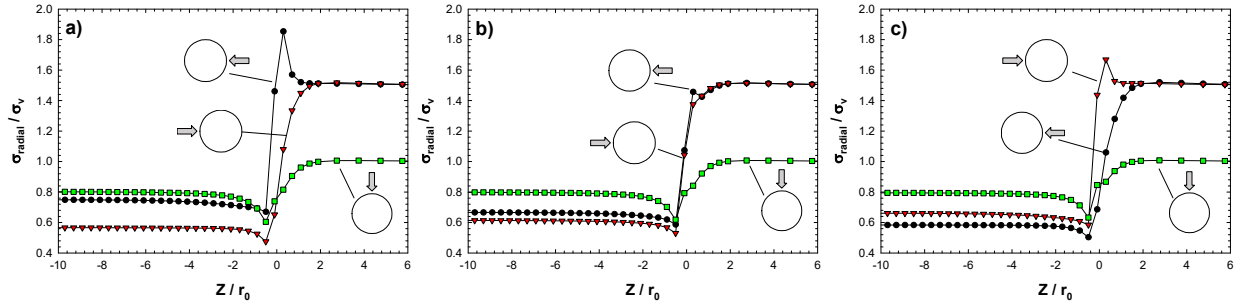

Figure 10.24 Normalized radial stresses with respect to the tunnel radius, with the normalized distance from the face with respect to the tunnel radius. (a) σ_H perpendicular to α_2, (b) no far-field axial shear stress, (c) σ_H parallel to α_2.

The forces in the liner far-behind the face, normalized with respect to the vertical stress and the tunnel radius, are shown in Figure 10.25. As one can see, for all scenarios, the internal forces are asymmetric because of the asymmetric radial stresses far-behind the face (Figure 10.24). The internal forces are larger for scenario one, when σ_H is perpendicular to α_2 and smaller for scenario three, when σ_H is parallel to α_2. This is expected, because the ground deformations are larger when σ_H is perpendicular to α_2, as shown in Figures 10.18, 10.19 and 10.23. The thrust forces are maximum near the crown, and the bending moments are the largest at the right springline when σ_H is perpendicular to α_2 and for the "no far-field axial shear stress" scenario, and at the left springline when σ_H is parallel to α_2. The figure shows that, when σ_H is perpendicular to α_2 and for

the “no far-field axial shear stress” scenario, both bending moments and thrust forces are larger at the right springline than at the left. In contrast, when σ_H is parallel to α_2, the internal forces are larger at the left springline than at the right. This is consistent with the asymmetric radial stresses far-behind the face, as shown in Figure 10.24. The radial stresses at the right springline are larger than at the left when σ_H is perpendicular to α_2 and for the “no far-field axial shear stress”, while the opposite is observed when σ_H is parallel to α_2.

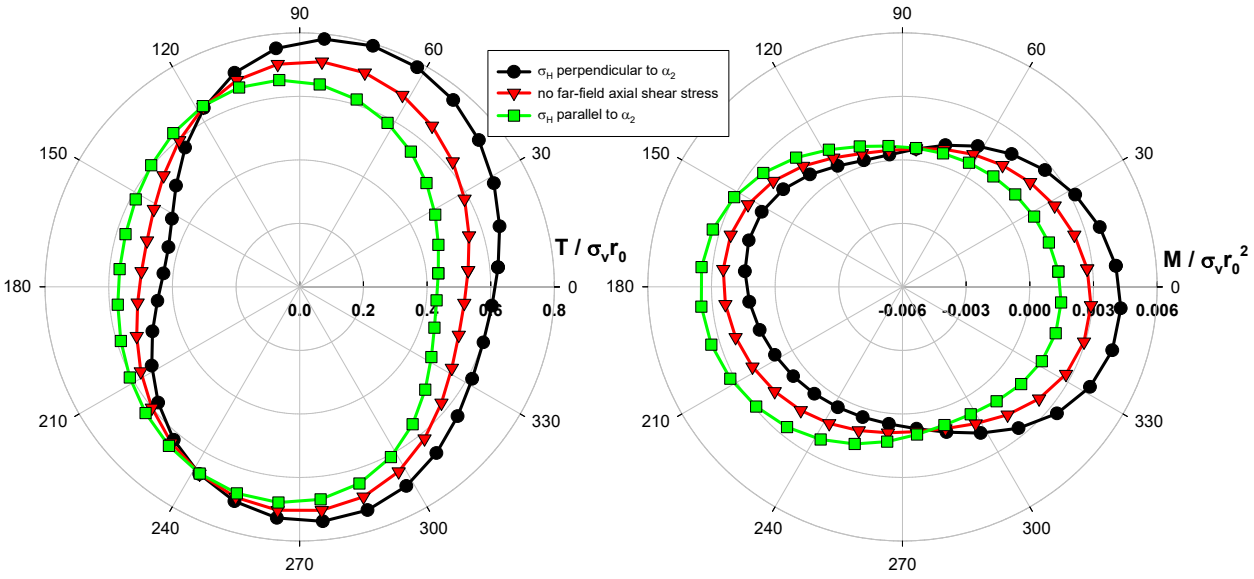

Figure 10.25 Normalized internal forces, thrust (T) and bending moments (M), with respect to the vertical stress and tunnel radius.

10.6 Conclusions

Rock masses may present both remarked stress anisotropy and anisotropic mechanical properties. Despite the well-recognized importance of tunnel alignment with the geostatic principal stress directions, few research has been conducted so far to investigate the effects of tunnel misalignment with the principal stresses. 3D face effects on tunnels misaligned with the geostatic principal stress directions and/or with the rock mass structure were investigated in this paper. 3D FEM simulations were performed using a transversely anisotropic elastic model to represent the rock mass and an isotropic elastic model for the tunnel liner.

The 3D face effects on tunnels misaligned with the rock mass structure were assessed under the assumption of an isotropic stress state and unsupported excavation. The tunnel misalignment with the rock mass structure induces anti-symmetric axial displacements far-behind the face. The

reason for this is that, when the tunnel is misaligned with the principal axes of material anisotropy, the in-plane and the out-of-plane stresses and deformations around the tunnel are coupled (Vitali et al., 2019d). Thus, anti-symmetric axial displacements are induced even when no far-field axial shear stress is present. Near the face, asymmetric radial displacements occurred, while they were symmetric far-behind the face. The reason for the loss of symmetry at the face was because the anti-symmetric axial displacements were constrained by the presence of the face of the tunnel, which caused asymmetric radial deformations near the face, so the symmetry of displacements around the tunnel was lost. It was observed that a translation of the tunnel cross section occurred near the face, which was maximum at the face. When the translation was subtracted from the radial displacements at the tunnel perimeter, the corrected radial displacements were symmetric; in other words, the asymmetry near the face was due to a rigid body displacement of the tunnel cross section. As a consequence, the stresses near the face of the tunnel were also asymmetric. One side of the tunnel was subjected to larger stresses than the other, because one side was compressed by the tunnel rigid body displacement, while the other was unloaded. When the tunnel was aligned with one of the principal axes of material anisotropy, no anti-symmetric axial displacements were induced and no asymmetric deformations occurred at the face. This is because when the tunnel aligns with the rock structure, in-plane and out-of-plane stresses and deformations are decoupled (similar to an isotropic ground); thus, no anti-symmetric axial displacements were induced and, as a consequence, no asymmetric radial displacements occurred near the face.

The response of tunnels misaligned with both geostatic principal stress directions and with the rock mass structure were assessed through the case of a tunnel inclined 45° with the major horizontal principal stress in a structured rock mas with dip angle of 45° and strike of 45° (i.e. assuming tunnel aligned with the North direction). Three scenarios were selected: major horizontal stress perpendicular to the strike; major horizontal stress parallel to the strike and a case where the far-field axial stress was not included, i.e. the “no far-field axial shear stress” scenario. The three scenarios had the same vertical and horizontal far-field stresses and the same orientation of the tunnel with respect to the rock structure. The appearance of the far-field axial shear stress produced anti-symmetric axial displacements far-behind the face and asymmetric radial displacements near the face of the tunnel. When the major horizontal stress was perpendicular to the strike, the anti-symmetric axial displacements produced by the rock structure and by the far-field axial shear stress had the same direction, so the axial displacements were increased. The opposite was observed

when the major horizontal stress was parallel to the strike direction, so the axial displacements were reduced. The radial displacements were larger when the major horizontal stress was perpendicular to the rock structure and smaller when the major horizontal stress was parallel. The radial displacements were asymmetric near the face and with ellipsoidal deformed shape far-behind the face in all three scenarios. The asymmetric deformations near the face were more pronounced when the far-field axial shear stress was present. It was observed that a translation of the tunnel cross-section occurred near the face. It is interesting to note that, when the translation motion was subtracted from the radial displacements, the corrected radial displacements were asymmetric near the face when the far-field axial shear stress was present, but they were symmetric when the far-field axial shear stress was not present. Thus, the numerical results indicated that the asymmetric deformations near the face caused by the rock structure were due to a rigid body displacement of the tunnel cross section. For a misaligned tunnel with the geostatic principal stresses in an isotropic elastic ground, Vitali et al. (2019b) showed that the asymmetric radial displacements at the face due to the far-field axial shear stress could be decomposed into a rigid body displacement of the tunnel cross-section and anti-symmetric radial displacements. The scenarios investigated in this paper were more complex because of the rock mass anisotropy. In all three scenarios, the stresses near the face were asymmetric as a consequence of the asymmetric deformations.

For unsupported tunnels in transversely anisotropic elastic ground, the radial displacements far-behind the face are always symmetric, while asymmetric deformations only happen at or near the face. If the tunnel is supported, the asymmetric deformations affect the interaction between the liner and the ground. As a result, the radial displacements and the radial stresses at the tunnel perimeter far-behind the face are asymmetric, and thus, the internal forces in the liner, i.e. thrust and bending moment, are also asymmetric. The ground deformations and the liner internal forces are the largest when the major horizontal stress is perpendicular to the strike direction of the rock mass structure and are the smallest when parallel to the strike.

Acknowledgments

The research was partially supported by the research funding agency of the Brazilian government CNPq (“Conselho Nacional de Desenvolvimento Cientifico”). The authors

acknowledge the support from CNPq and from Midas company, which kindly provided the license of Midas GTX NX software, used in the present work.

10.7 References

Almeida e Sousa J., Negro A., Matos Fernandes M., Cardoso, A.S., 2011. Three-Dimensional Nonlinear Analyses of a Metro Tunnel in São Paulo Porous Clay, Brazil, Journal of Geotechnical and Geoenvironmental Engineering, 137(4), pp. 376–384.

Batugin SA, Nirenburg RK. 1972. Approximate relation between the elastic constants of anisotropic rocks and the anisotropy parameters. Sov. Min. Sci. 8(1):5-9.

Brown ET, Hoek E., 1978. Trends in relationships between measured in-situ stresses and depth. Int. J. Rock Mech. Min. Sci. 15(4): 211–215.

Button E., Leitner R., Poetsch M., Schubert W., 2006. Spatial relationships between discontinuity orientation and system behavior in underground excavations. In: Proceedings of ARMA 41st U.S. Symposium on Rock Mechanics. ARMA/USRMS 06-957.

Cantieni, L., Anagnostou, G., 2009. The effect of the stress path on squeezing behavior in tunneling. Rock Mechanics and Rock Engineering, 42(2), 289–318.

Eberhardt, E., 2001. Numerical modelling of three-dimension stress rotation ahead of an advancing tunnel face. International Journal of Rock Mechanics and Mining Sciences, 38(4), 499–518.

Evans K.F., Engelder T., Plumb R.A., 1989. Appalachian Stress study .1. a detailed description of in-situ stress variations in devonian shales of the appalachian plateau. J. Geophys. Res. Earth Planets. 94: 7129–7154.

Exadaktylos G.E., 2001. On the constraints and relations of elastic constants of transversely isotropic geomaterials. Int. J. Rock Mech. Min. Sci. 38(7):941-956.

Galli, G., Grimaldi, A., Leonardi, A., 2004. Three-dimensional modelling of tunnel excavation and lining. Computers and Geotechnics. 31(3), pp. 171–183.

Goodman, R. E., 1989. Introduction to rock mechanics. doi: 10.1016/0148-9062(81)90521-0.

Goricki A, Button A.E., Schubert W., Pötsch M., Leitner R., 2005. The influence of discontinuity orientation on the behaviour of tunnels. Felsbau. 23(5):12–18.

Gysel M., 1975. In-Situ stress measurements of the primary stress state in the Sonnenberg tunnel in Lucerne, Switzerland. Tectonophysics. 29: 301–314.

Haimson B.C., Lee M.Y., Song I., 2003. Shallow hydraulic fracturing measurements in Korea support tectonic and seismic indicators of regional stress. Int. J. Rock Mech. Min. Sci. 40(7-8): 1243–1256.

Janin J.P., Dias D., Emeriault F., Kastner R., Le Bissonnais H., Guilloux A., 2015. Numerical back-analysis of the southern Toulon tunnel measurements: A comparison of 3D and 2D approaches. Engineering Geology, 195: 42–52.

Klopčič, J., Logar, J., 2014. Effect of relative orientation of anisotropy planes to tunnel axis on the magnitude of tunnelling displacements. International Journal of Rock Mechanics and Mining Sciences. 71: 235-248.

Lenz, G., Kluckner A., Holzer R., Stadlmann T., Schachinger, T., Gobiet G., 2017. Prediction of fault zones based on geological and geotechnical observations during tunnel construction. Geomechanics and Tunneling, 10(4): 366–379.

Martin, C. D., 1997. Seventeenth Canadian Geotechnical Colloquium: The effect of cohesion loss and stress path on brittle rock strength. Canadian Geotechnical Journal, 34(5): 698-725.

Martin C.D., Kaiser P.K., 1996. Mine-by Experiment Committee report, Phase 1: excavation response, summary and implications. Atomic Energy of Canada Limited, Report AECL–11382. AECL Research, Chalk River, Ont.

McGarr A, Gay N.C., 1978. State of Stress in the Earth's Crust. Ann. Rev. Earth Planet. Sci. 6: 405–436.

Moller, S., 2006. Tunnel induced settlements and structural forces in linings PhD thesis. Stuttgart: Institute of Geotechnical Engineering, Universitat of Stuttgart.

Park E.S., Choi B.H., Bae S.H., Jeon S., 2014. Horizontal stresses at shallow depths in Seoul (Korea) gneissic region. In: Rock Eng. Rock Mech. Struct. Rock Masses - Proceedings of EUROCK 2014, ISRM European Regional Symposium: 399–404.

Perras M.A., Wannenmacher H., Diederichs M.S., 2015. Underground excavation behaviour of the Queenston formation: tunnel back analysis for application to shaft damage dimension prediction. Rock Mech. Rock Eng. 48(4):1647-1671.

Schubert P, Klopčič J, Štimulak A, Ajdič I, Logar J., 2005. Analysis of characteristic deformation patterns at the Trojane tunnel in Slovenia. *Felsbau*, 23(5):25-30.

Schubert W, Budil A., 1995. The importance of longitudinal deformation in tunnel excavation. In: Proceedings of 8th ISRM Congress on Rock Mechanics:1411–1414.

Schubert, W., Moritz, B., 2011. State of the art in evaluation and interpretation of displacement monitoring data in tunnels. Geomechanics and Tunneling, 4(5): 371–380.

Souček K., et al., 2017. Geotechnical characterization of Bukov underground research facility. Procedia Engineering. 191:711-718.

Svoboda, T., Masin, D., 2011. Comparison of displacement field predicted by 2D and 3D finite element modelling of shallow NATM tunnels in clays. Geotechnik, 34(2): 115−126.

Vermeer P.A., Bonnier, P.G., Moller, S.C., 2002. On a smart use of 3D-FEM in tunneling. IN: Numerical models in geomechanics; NUMOG VIII: 361-366.

Vitali O.P.M., Celestino T.B., Bobet A., 2017. 3D finite element modelling optimization for deep tunnels with material nonlinearity. Undergr. Sp.3(2):125–139.

Vitali O.P.M., Celestino T.B., Bobet A., 2018. Analytical solution for tunnels not aligned with geostatic principal stress directions. Tunn. Undergr. Sp. Technol. 82: 394–405.

Vitali O.P.M., Celestino T.B., Bobet A., 2019a. Shallow tunnel not aligned with the geostatic principal stress directions. In: Proceedings of Geo-Congress2019, GSP 313:214-222.

Vitali O.P.M., Celestino T.B., Bobet A., 2019b. Shallow tunnels misaligned with geostatic principal stress directions: analytical solution and 3D face effects. Tunn. Undergr. Sp. Technol. 89: 268-283.

Vitali O.P.M., Celestino T.B., Bobet A., 2019c. Progressive failure due to tunnel misalignment with geostatic principal stresses. In: Proceedings of ISRM 14th International Congress on Rock Mechanics: 2292-2299.

Vitali, O. P. M., Celestino, T. B., Bobet, A., 2019d. Analytical solution for a deep circular tunnel in anisotropic ground and anisotropic geostatic stresses. Manuscript under review for publication in a peer-reviewed journal.

Wileveau Y, Cornet F.H., Desroches J., Blumling P., 2007. Complete in situ stress determination in an argillite sedimentary formation. Phys. Chem. Earth. 32(8–14):866–878.

Worotnicki G., 2013. 13 – CSIRO Triaxial Stress Measurement Cell. In: Rock testing and site characterization: principles, practice and projects: 329-394.

Yeo, C. H., Lee, F. H., Tan, S. C., Hasegawa, O., Suzuki, H., Shinji, M., 2009. Three dimensional numerical modelling of a NATM tunnel. Japanese Committee for Rock Mechanics. 5(1), 33–38.

Zhang C., Chen Q., Qin X., Hong B., Meng W., Zhang Q., 2017. In-situ stress and fracture characterization of a candidate repository for spent nuclear fuel in Gansu, northwestern China. Eng. Geol. 231:218-229.

Zhao, X. G. et al., 2013. In-situ stress measurements and regional stress field assessment of the Beishan area, China. Eng. Geol. 163:26-40.

Zhao X.G. et al., 2015. In-situ stress measurements and regional stress field assessment in the Xinjiang candidate area for China's HLW disposal. Eng. Geol. 197:42-56.

11. TUNNEL MISALIGNMENT WITH GEOSTATIC PRINCIPAL STRESS DIRECTIONS IN ANISOTROPIC ROCK MASSES

VITALI, O. P. M.; CELESTINO, & BOBET, A. (2019). Tunnel misalignment with geostatic principal stress directions in anisotropic rock masses. Soils and Rocks, São Paulo, 43(1): 123-138, January-March, 2020. DOI: 10.28927/SR.431123

Abstract

Rock masses may present remarked stress anisotropy, and so it is likely that a tunnel is misaligned with the geostatic principal stress directions. As a consequence, anti-symmetric axial displacements and axial shear stresses are induced around the tunnel due to the presence of far-field axial shear stresses. Limited research has been conducted on the effects of the far-field axial shear stress on tunnel behavior. This paper investigates the effects of tunnel misalignment with the geostatic principal stresses in anisotropic rock masses. 3D FEM modeling of a tunnel misaligned 45° with the principal horizontal stresses is conducted. An anisotropic geostatic stress field is considered, with the major horizontal stress two times larger than the vertical stress and the minor horizontal stress equal to the vertical stress. The anisotropic behavior of the rock mass is represented by a transversely anisotropic elastic model, with properties typical of anisotropic rock masses. Tunnels in horizontally and vertically-structured rock masses are assessed. Unsupported and supported tunnels are investigated. The results show that asymmetric deformations and asymmetric stresses are induced near the face of the tunnel as a result of the tunnel misalignment with the geostatic principal stresses and with the rock mass structure. These asymmetric deformations near the face affect the ground-support interaction such that the internal forces in the liner are also asymmetric.

11.1 Introduction

The literature shows that rock masses are likely to present remarked geostatic stress anisotropy and anisotropic mechanical properties. This is a consequence of the rock complex formation processes. According to Brady & Brown (2006), the main factors affecting rock mass properties and geostatic stresses are: topography (elevations and valleys); residual stresses (due to cooling, for instance); tectonic movements; fracturing and jointing; and inclusions. Thus, geostatic

stresses and mechanical properties are expected to be complex as well. In-situ stress measurements in rock masses show large horizontal stresses and significant horizontal stress anisotropy (Gysel, 1975; Brown and Hoek, 1978; McGarr and Gay, 1978; Evans, Engelder and Plumb, 1989; Martin, 1997; Haimson, Lee and Song, 2003; Wileveau *et al.*, 2007; Zhao *et al.*, 2013, 2015; Park *et al.*, 2014; Perras, Wannenmacher and Diederichs, 2015; Souček *et al.*, 2017). For instance, (Martin, 1997) reported a highly anisotropic stress field in a massive granitic rock mass in Canada. The average stresses were: σ_1/σ_2=1.2±0.1 and σ_1/σ_3=3.9±0.5. Gysel (1975) presented the geostatic stress field measured in two sections along the Sonnerberg tunnel (Lucerne, Switzerland), in sandstone. The stress ratios were σ_1/σ_3=2.33, σ_1/σ_2=2.10 on one of the sections and σ_1/σ_3=4.29, and σ_1/σ_2=1.70 on the other. Haimson et al. (2003) and Park et al. (2014) evaluated the geostatic stress field of the granitic and gneissic rock masses in South Korea, near Seoul, in an active seismic area. The measured horizontal stresses showed large stress anisotropy and were consistently larger than the vertical stress. An extensive compilation of 77 geostatic stresses was conducted by McGarr and Gay (1978), where the interval, with 95% confidence, for each principal stress ratio was: σ_1/σ_2=1.45±0.80 and σ_1/σ_3=2.42±2.28. These data show that the expected stress anisotropy in rock is indeed high and quite variable.

The importance of tunnel alignment with the geostatic principal stress directions is recognized in the literature. Goodman (1989) recommends aligning the tunnel or cavern with the major principal stress to minimize stress concentrations around the opening. Convergence measurements of tunnels constructed in the Underground Research Laboratory (URL) in France showed the importance of the tunnel orientation with respect to the geostatic principal stress directions. These tunnels were excavated in an anisotropic Claystone rock mass at 490m depth, with average principal stress ratios σ_h/σ_v=1 and σ_H/σ_v =1.3 (Wileveau et al., 2007). Because of the sedimentation process, the rock had an oriented structure (horizontal bedding), and thus anisotropic mechanical properties, with E_1/E_3 varying from 1.2 to 2 (Armand et al., 2013). Experimental tunnels were excavated parallel and perpendicular to σ_H. A supported circular tunnel of radius 2.6m, aligned with σ_H, showed horizontal convergence of 37 to 58mm and vertical convergence of 24 to 30mm. A similar tunnel aligned with σ_h showed horizontal convergence of 19mm to 34mm and vertical convergence of 112mm to 158mm (Armand et al., 2013).

Tunnel design is commonly conducted assuming that the tunnel is aligned with one of the geostatic principal stress directions and yet, as previously discussed, the assumption is unrealistic.

When the tunnel is misaligned with the geostatic principal stress directions, far-field axial shear stresses are present. These axial shear stresses induce anti-symmetric axial displacements and axial shear stresses far-behind the tunnel face (Vitali et al., 2018; Vitali et al.,2019a; Vitali et al., 2019b; Vitali at al., 2019c). On shallow tunnels in isotropic ground, Vitali et al. (2019b) observed that the far-field axial shear stress induced asymmetric deformations and stresses near the face and that ground-support interaction and yielding around the tunnel, if any, were affected by the asymmetric deformations near the face. Vitali et al. (2019c) investigated the effects of tunnel misalignment on the progressive failure around the well-documented experimental tunnel at the URL in Canada (Martin, 1997). They found that no plastic deformations at the tunnel walls occurred when the tunnel was aligned with the minor principal stress, but asymmetric spalling would occur if the tunnel was not aligned with the geostatic principal stresses.

Asymmetric deformations of the tunnel walls have been observed on tunnels in structured rock masses, such as phyllites and slates. For instance, asymmetric radial displacements at the tunnel wall, horizontal displacements at the crown and axial displacements at the springline are often measured on the shotcrete support of NATM tunnels in anisotropic rock masses (Schubert and Budil, 1995; Goricki *et al.*, 2005; Schubert *et al.*, 2005; Schubert and Moritz, 2011; Klopčič and Logar, 2014; Lenz *et al.*, 2017). Those asymmetric deformations are commonly associated with the anisotropic properties of the rock mass and with localized heterogeneities. Button *et al.*, (2006) observed that the asymmetric deformation patterns observed in the field could be partially reproduced numerically in tunnels not aligned with the rock mass structure. Tonon and Amadei, (2002), Tonon and Amadei (2003) and Fortsakis *et al.*, (2012) highlighted the importance of considering the anisotropic properties of the rock mass in numerical models to obtain more accurate ground deformation predictions (they assumed, however, that the tunnel was aligned with the geostatic principal stresses). In this paper, the influence of the tunnel misalignment with the geostatic principal stresses in anisotropic rock masses is assessed, for unsupported and supported tunnels, through 3D FEM modeling. Horizontally- and vertically-structured rock masses are considered. A transversely anisotropic elastic model is adopted to represent the rock mass.

11.2 3D FEM model

3D FEM modeling was conducted to investigate tunnels misaligned with the geostatic principal stresses in anisotropic rock masses. A tunnel misaligned 45° with the major principal

horizontal stress, in a transversely anisotropic rock mass, is assumed. The rock mass is assumed elastic with the following properties: Young modulus perpendicular to the structural planes (E_1), 1GPa; Young modulus parallel to the structural planes (E_2=E_3), 3GPa; in-plane Poisson ratio (ν_{23}), 0.333; out-of-plane Poisson ratio (ν_{13}= ν_{12}), 0.25; in-plane Shear modulus (G_{23}), 1.125GPa; and out-of-plane Shear modulus (G_{23}= G_{13}), 0.667GPa. These properties are typical of highly anisotropic rock masses, such as phyllites and slates. According to Worotnicki (1993), more than 50% of highly structured rock masses present a E_1/E_2 ratio larger than 2. For the simulations, horizontal and vertical structural planes are considered (i.e. dip angles 0° and 90°, respectively). The geostatic principal stresses are: vertical stress (σ_v), 5MPa (the vertical stress is assumed as a principal stress), minor horizontal stress (σ_h), 5MPa and major horizontal stress (σ_H), 10MPa. This is not an unusual anisotropic stress field, according to e.g. Gysel, 1975; Evans et al., 1989; Haimson et al., 2003; Wileveau *et al.*, 2007; Park *et al.*, 2014; Souček *et al.*, 2017. Two directions for the major horizontal stress are evaluated: σ_H perpendicular to the strike and σ_H parallel to the strike of the rock structure (i.e. perpendicular or parallel to the e.g. rock bedding; note that the direction of the horizontal stresses for a tunnel parallel to the rock structure does not change the results due to the symmetry of the problem).

Figure 11.1 shows the FEM mesh built for the investigation. The tunnel is circular with radius (r_0) 5m. 2nd order hexahedron elements are used. The mesh refinement and the size of the model (Figure 11.1a) are selected to ensure the accuracy of the results, following the recommendations provided by Vitali et al. (2017). Figure 11.1b illustrates the plan view of the mesh with the boundary conditions, where Ψ=45° is the angle that the tunnel makes with the principal horizontal stresses. The geostatic stress field is generated by applying a load pressure at the boundaries with the same magnitude as the geostatic principal stresses. Given the anisotropic rock masses investigated (i.e. horizontally- and vertically-structured rock masses) and that the vertical axis is a principal stress direction, it is possible to take advantage of the symmetry of the problem and use only half the discretization. The mesh consists of a refined structured grid at the center of the model, where the results are extracted, linked to the boundaries by an unstructured grid, as shown in Figures 11.1c and 11.1d.

Supported and unsupported tunnels are considered. The 3D FEM simulation follows the excavation sequence of the tunnel by deactivating the elements inside the excavation round and activating the elements that represent the tunnel support, if present. The simulations are run in two

steps: the first step generates the geostatic stress field, and the second, the excavation and support, if present. The liner is represented by shell elements with thickness 0.5m ($0.1r_0$). No slip between ground and liner is allowed. Figure 11.2 illustrates the mesh near the face of a supported tunnel. The liner, if included, is installed immediately after the excavation; that is, the unsupported span is zero. In Figure 11.2, position 1 indicates a location far-ahead of the face of the tunnel and represents the region not affected by the tunnel excavation; position 2 is at the face of the tunnel; and position 3, far-behind the face of the tunnel, where stresses and displacements are independent of the distance from the face of the tunnel.

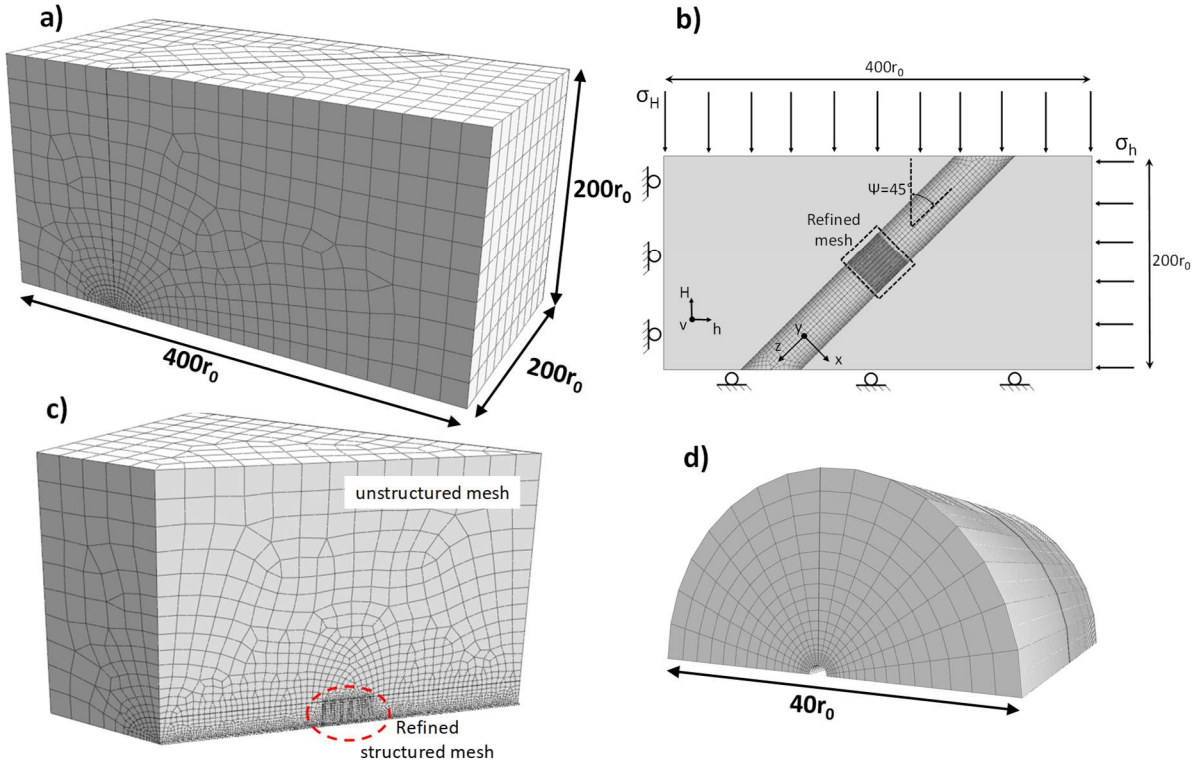

Figure 11.1 FEM mesh. (a) Model dimensions; (b) plan view and boundary conditions; (c) vertical cross section along the tunnel and; (d) refined mesh at the center of the model.

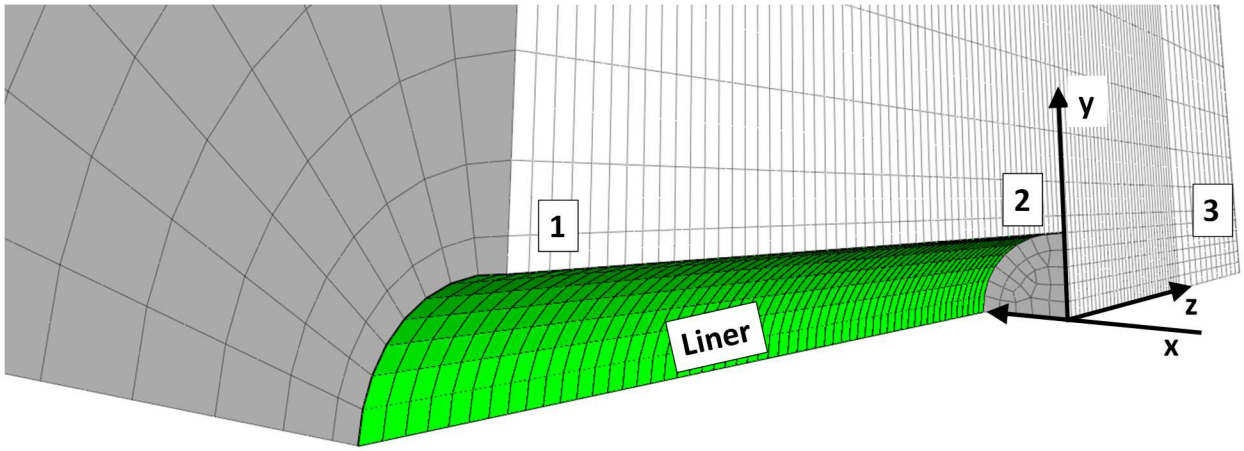

Figure 11.2 Mesh near the face of the supported tunnel, with the coordinate system XYZ attached to the tunnel. Position (1) represents a point far ahead of the face; (2), at the face (i.e. Z=0); and (3), far-behind the face.

11.3 Tunnel in horizontally structured rock mass

Horizontal stratification is not uncommon in sedimentary and even metamorphic rock masses. The effects of such structure on tunnels misaligned with the geostatic principal stresses are analyzed through a number of simulations where the tunnel is horizontal and, thus, aligned with the rock mass structure. Two cases are studied: (1) far-field stresses $\sigma_{xx,ff}=\sigma_{zz,ff}=7.5$MPa, $\sigma_{yy,ff}=5$MPa, $\tau_{xz,ff}=2.5$MPa (tunnel oriented at $\Psi=45^{o}$ with the far-field principal stresses) and (2) same far-field stresses, but no far-field shear, i.e. $\sigma_{xx,ff}=\sigma_{zz,ff}=7.5$MPa, $\sigma_{yy,ff}=5$MPa, $\tau_{xz,ff}=0$, to investigate the influence of the far-field axial shear.

Figure 11.3 shows the horizontal and vertical tunnel convergence, normalized with the tunnel radius, with the distance from the face, normalized also with the tunnel radius, for the two cases. Displacements start to increase at $4r_0$ ahead of the face, abruptly increase at the face and increase further behind the face until they are constant at about $4r_0$ behind the face. Tunnel deformations are identical in both cases, which indicates that the far-field axial shear stress has no influence on the results. It is interesting to note that the vertical and the horizontal tunnel deformations are similar, despite the fact that the far-field horizontal stress is larger than the vertical. The reason for this is that the stiffness of the ground parallel to the rock mass structure is the largest and the stiffness perpendicular to the structure is the smallest. So, in the simulations, the (larger) horizontal stress is parallel to the stiffest rock mass direction and the (smaller) vertical stress is parallel to the softest rock mass direction, and so the two effects compensate each other.

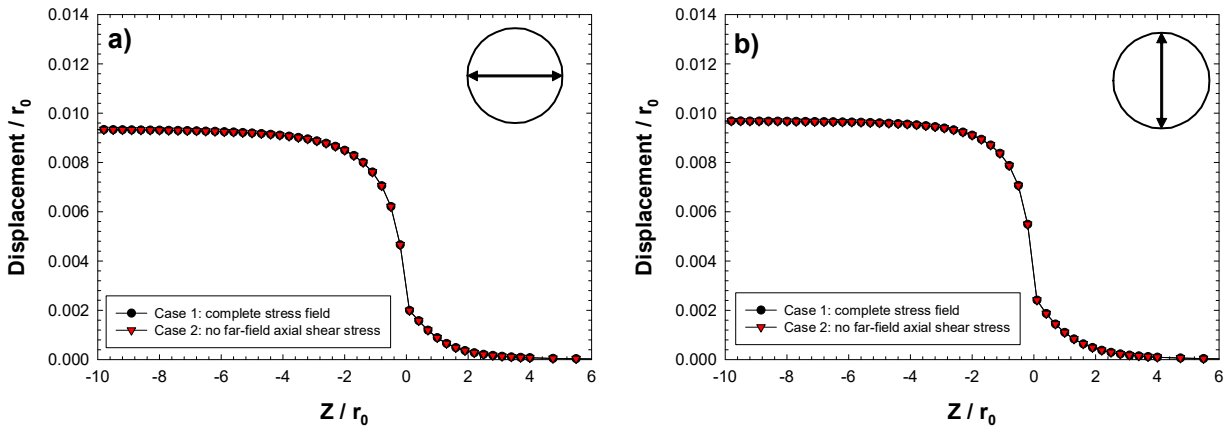

Figure 11.3 Normalized tunnel convergence with respect to the tunnel radius with the normalized distance from the face with respect to the tunnel radius for unsupported tunnel. (a) horizontal convergence, (b) vertical convergence.

Figure 11.4 shows the normalized radial displacements and the deformed cross-section at the face and far behind the face. For case (2), with no far-field axial shear stress, the deformations are symmetric at the face and far-behind the face. For case (1), with the complete stress field, the deformations at the tunnel perimeter are symmetric far-behind the face, but asymmetric at the face, where the tunnel cross section translates towards the right. Far-behind the face, the deformed cross section in both cases is exactly the same, which shows that the far-field axial shear stress does not affect the radial displacements far-behind the face. This is because, when the tunnel axis is aligned with one of the principal material directions, in-plane and out-of-plane deformations are decoupled (Vitali et al., 2019d).

The normalized radial displacements at the springline, on the right and left, and the tunnel cross section translation are presented in Figure 11.5. For case (1), complete stress field, the radial displacements are asymmetric from a distance of $4r_0$ ahead of the face to about $6r_0$ behind the face. A translation of the tunnel cross section occurs near the face, which is maximum at the face (i.e. at Z=0). For case (2), the radial displacements at the springline do not change with the distance from the face; that is, no translation of the tunnel cross section occurs. Thus, the presence of the far-field axial shear stress induces asymmetric deformations near the face. Figure 11.6 shows the normalized "corrected" radial displacements with the normalized distance from the face, for case (1). The corrected radial displacement is the radial displacement without the translation of the tunnel cross section, as indicated in Figure 11.6. The corrected radial displacements are

asymmetric near the face, which is consistent with Vitali et al. (2019b). The authors observed that the far-field axial shear stress caused asymmetric radial deformation near the face of a shallow tunnel in isotropic ground. Those asymmetric radial displacements could be decomposed into a rigid body displacement of the tunnel cross section and anti-symmetric radial displacements.

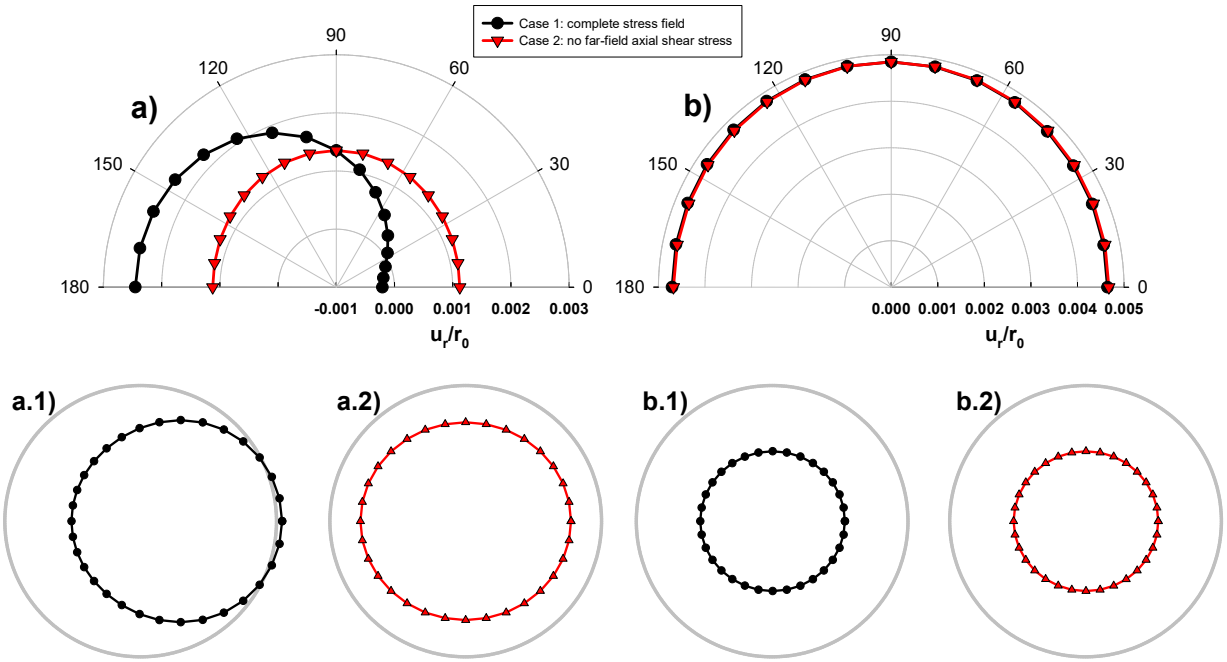

Figure 11.4 Normalized radial displacemets at the tunnel perimeter with respect to the tunnel radius and deformed tunnel cross-section, for unsupported tunnel. (a) at the face; (b) far-behind the face. Deformations are magnified 200 times at the face and 100 times far-behind the face.

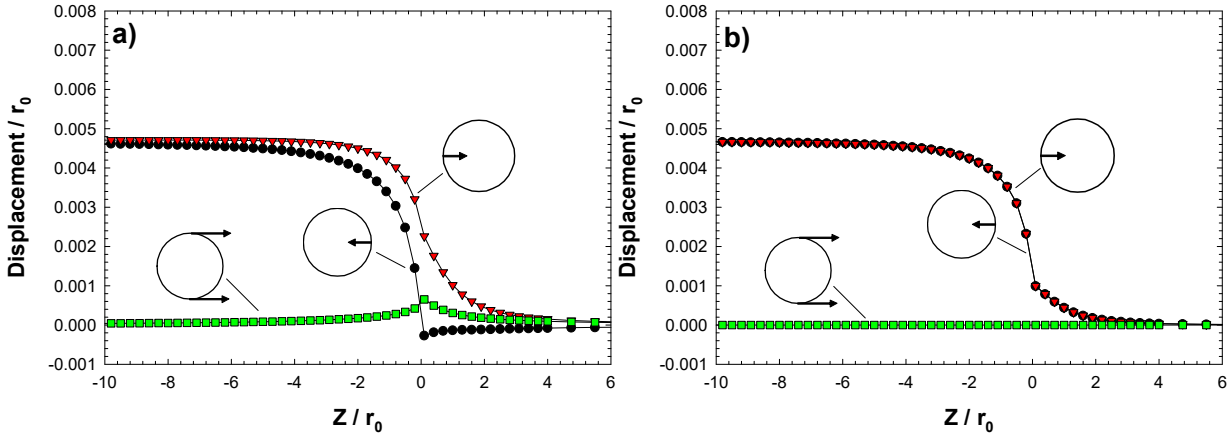

Figure 11.5 Normalized displacements with respect to the tunnel radius, with normalized distance from the face with respect to the tunnel radius. (a) Case 1, complete stress field; (b) Case 2, no far-field axial shear.

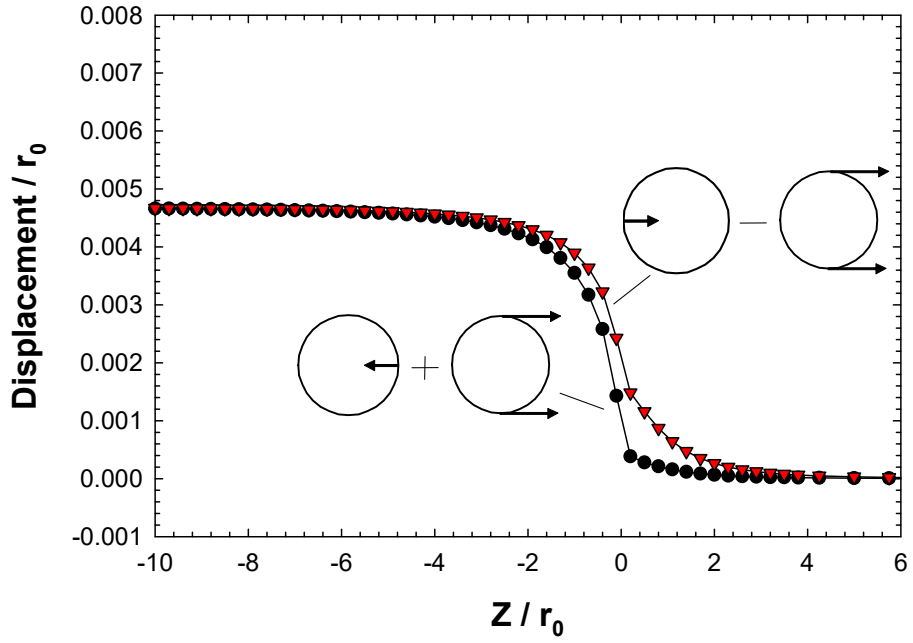

Figure 11.6 Normalized displacements with respect to the tunnel radius with the normalized distance from the face with respect to the tunnel radius. Case 1, complete stress field.

The stress paths, normalized with respect to the vertical stress, at points near the tunnel perimeter (i.e. at right and left springline and at the crown) are shown in Figure 11.7 (see Figure 11.2 for location of points 1, 2, 3). The stresses were computed at a distance of $0.1r_0$ from the tunnel perimeter, to minimize the disturbance due to the corner between face and tunnel. For Case 1 (complete stress field), on the right-hand side of the springline, the rock stresses increase towards the face of the tunnel, i.e. both mean stress and maximum shear stress increase; close to the face, the stresses abruptly increase, while they steadily decrease behind the face until they reach a constant value. On the left-hand side, the opposite is observed; that is, unloading ahead of the face and loading behind the face. Note that far behind the face of the tunnel, the two stress paths yield the same results. The asymmetry of the stress paths is consistent with the asymmetric deformations near the face discussed previously. Indeed, there is a horizontal translation of the tunnel cross section towards the right near the face, as shown in Figure 11.4, that results in compression of the rock at the right springline, while the rock at the left springline is unloaded. For Case 2, no far-field axial shear stress, the two stress paths are exactly the same. There is loading ahead of the face and unloading behind the face. Note that unloading ahead of the face was observed only when the far-field axial shear stress was present. Figure 11.8 presents the normalized stress paths at the

crown for case 1 (complete stress field) and case 2 (no far-field axial shear). The stresses at the crown and at the invert are the same because of the symmetry of the problem. The stress paths for the two cases follow a loading path ahead and behind the tunnel face, with an increase of the mean effective stress near the face. The shear stresses are larger for case 1 than for case 2 because of the presence of the far-field axial shear stress.

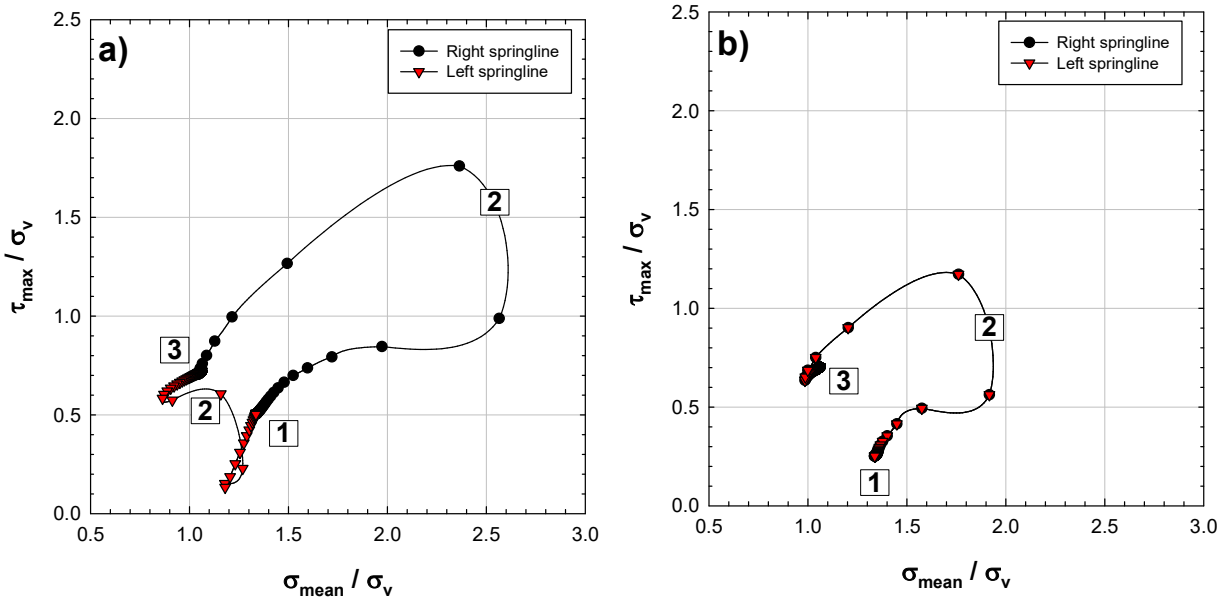

Figure 11.7 Normalized stress paths with respect to the vertical stress. (a) Case 1, complete stress field ; (b) Case 2, no far-field axial shear. Numbers 1, 2, 3 denote location (see Figure 11.2).

Figure 11.9 shows the normalized axial displacements at the tunnel perimeter, for Case 1 (complete stress field; for Case 2, no axial displacements were induced far-behind the face). As one can see in the Figure, anti-symmetric axial displacements are induced far-behind the face. The axial displacements are maximum at the springline and zero at the crown; those are produced by the far-field axial shear stress. At the face, the axial displacements are asymmetric due to the constraints produced by the tunnel face (Figure 11.4). For Case 2, where the far-field axial shear stress is neglected, no anti-symmetric axial displacements are induced and so, no asymmetric radial deformations occur near the face.

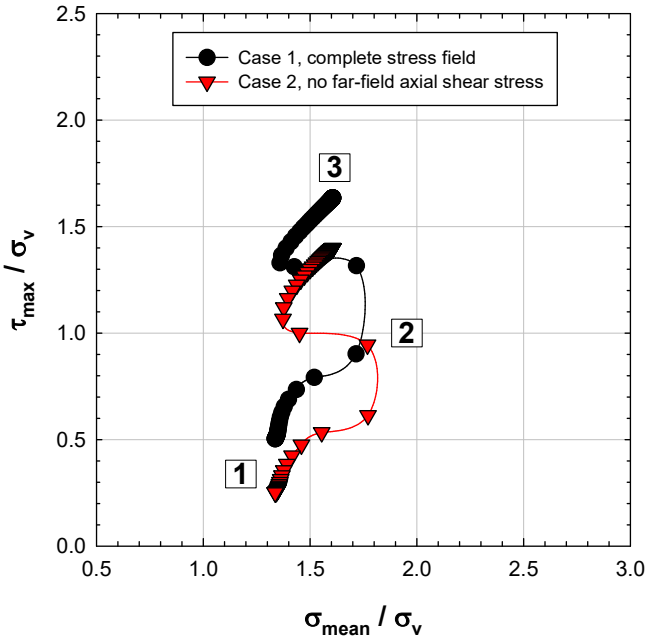

Figure 11.8 Stress paths at the crown.

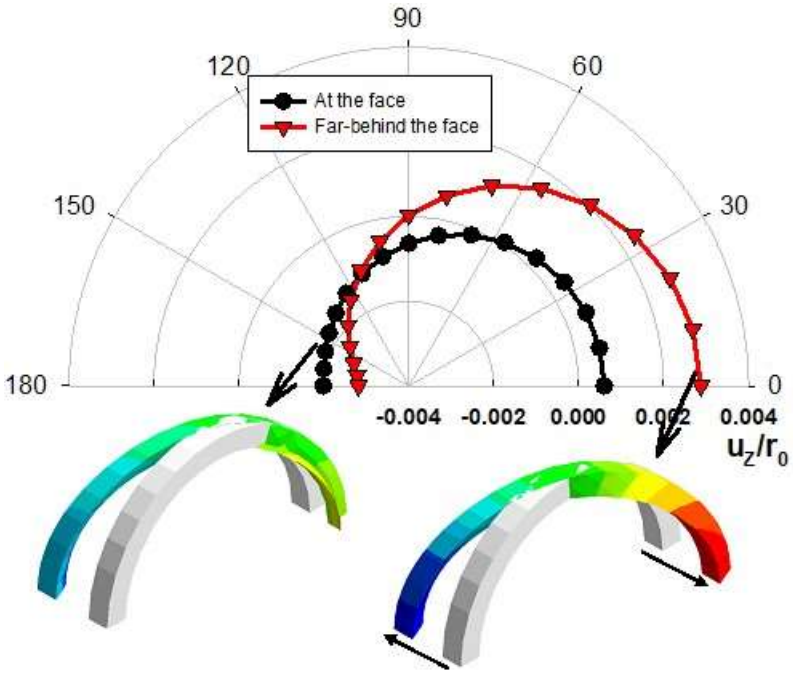

Figure 11.9 Normalized axial displacements with respect to the tunnel radius along the tunnel perimeter for Case 1, complete stress field. Unsupported tunnel. The colors of the deformed tunnel cross-section are associated with the magnitude of the axial displacements and are shown to help with the visualization.

If a liner is installed near the face, the asymmetric radial deformations may affect the stresses in the support. To investigate the influence of the far-field axial shear stress on supported tunnels in a horizontally structured rock masses, the two cases previously discussed are analyzed again, but with a liner placed close to the face (Figure 11.2). Figure 11.10 shows the normalized radial displacements with the normalized distance from the face. For Case 1, complete stress field, the radial displacements at the springline are asymmetric near the face and far behind the face. For Case 2, no far-field axial shear, the radial displacements at the springline are always symmetric. Consistent with the findings from the unsupported tunnel, the asymmetric deformations are caused by the anti-symmetric axial displacements induced by the far-field axial shear stress.

Figure 11.11 shows the normalized radial stresses at the tunnel perimeter, with respect to the vertical stress, with the normalized distance from the face. For Case 1, complete stress field, on the right-hand side of the springline, the radial stresses increase at the face and abruptly decrease behind the face; then, they slightly increase with the distance from the face until they are constant. On the left-hand side of the springline, the radial stresses decrease ahead of the face as the distance from the face decreases and then, behind the face, they increase with distance until they are constant. The radial stresses on the right are larger than on the left springline, which is consistent with the asymmetric deformations near the face. Note that there is a translation of the tunnel cross section towards the right (Figure 11.4.a.1), which compresses the right springline and unloads the left. For Case 2, the radial stresses are the same (i.e. both abruptly decrease at the face and slightly increase behind the face until they are constant far-behind the face). It is interesting to note that the radial stresses at the crown are similar in both cases. At the crown, the radial stresses decrease ahead of the face and increase behind the face until they reach a constant value. Note that, behind the face, the radial stresses at the crown are larger than at the springline. Figure 11.12 shows the internal forces in the liner, normalized with respect to the vertical stress and the tunnel radius. The internal forces (i.e. thrust forces and bending moments) are symmetric for Case 2 (no far-field axial shear) and asymmetric for Case 1 (complete stress field), where they are larger on the right than on the left. This observation is consistent with the asymmetric radial displacements that occur at the tunnel perimeter. Note also that Case 1 produces the largest internal forces.

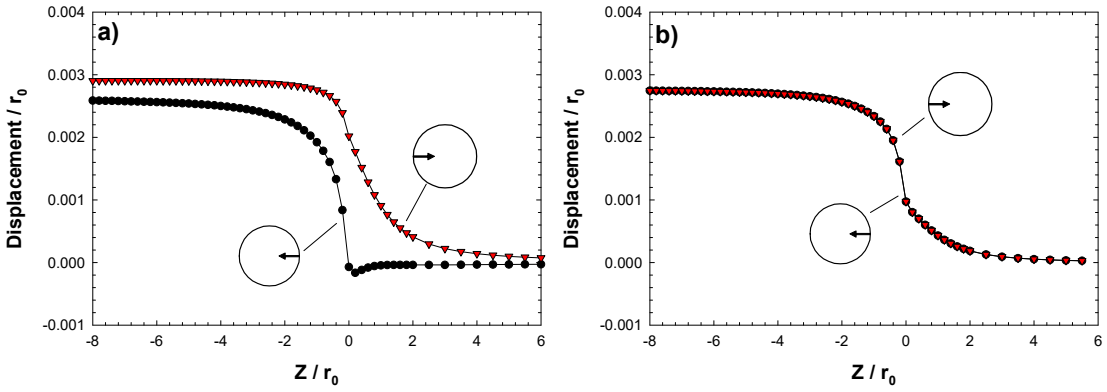

Figure 11.10 Normalized radial displacements with respect to the tunnel radius with the normalized distance from the face with respect to the tunnel radius, for supported tunnel. (a) Case 1, complete stress field and, (b) Case 2, no far-field axial shear.

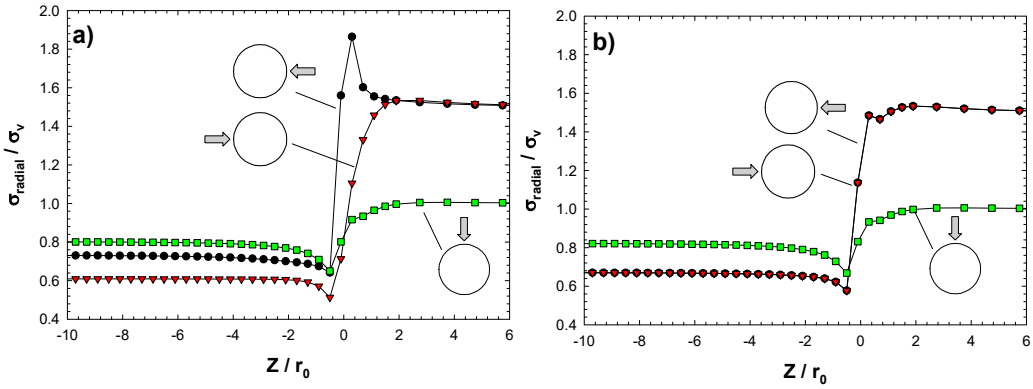

Figure 11.11 Normalized radial stresses with respect to the far-field vertical stress with the normalized distance from the face with respect to the tunnel radius, for supported tunnel. (a) Case 1, complete stress field; (b) Case 2, no far-field axial sher stress.

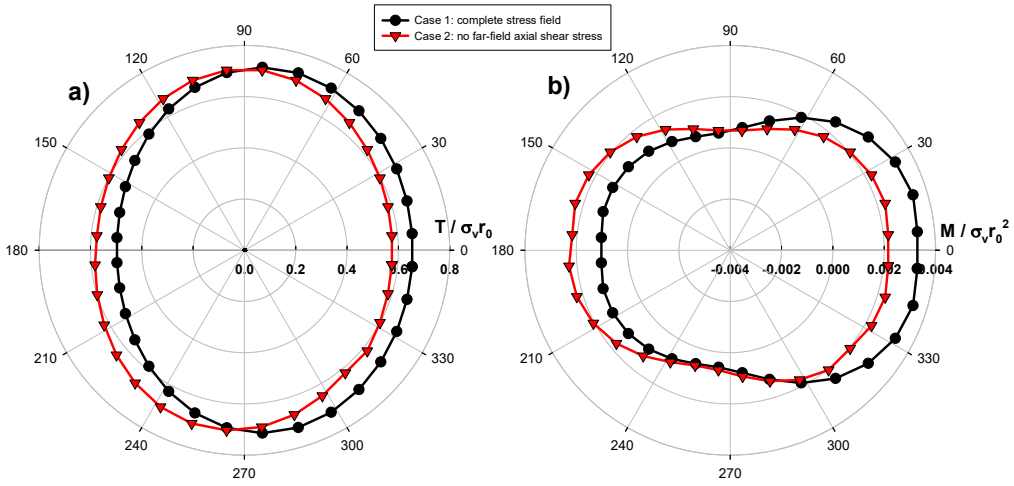

Figure 11.12 Normalized internal forces with respect to the vertical stress and tunnel radius. (a) Thrust (b) Bending moment.

11.4 Tunnel in vertically-structured rock mass

In this case, the tunnel is inclined 45° with the strike of the rock structure and with the geostatic principal horizontal stresses, as shown in Figure 11.13. The figure also shows the boundary conditions of the FEM model, which are analogous to those in Figure 11.2. Three cases are investigated: (1) major horizontal stress (σ_H) perpendicular to the strike; (2) no far-field axial shear stress; and (3) major horizontal stress (σ_H) perpendicular to the strike. The far-field horizontal and axial stress are the same in all three scenarios (i.e. $\sigma_{xx,ff}$=$\sigma_{zz,ff}$=7.5MPa). When σ_H is perpendicular to the strike (case 1), the far-field axial shear stress ($\tau_{xz,ff}$) is 2.5MPa, and when parallel to the strike (case 3), $\tau_{xz,ff}$= -2.5MPa. Case 2 assumes $\tau_{xz,ff}$=0.

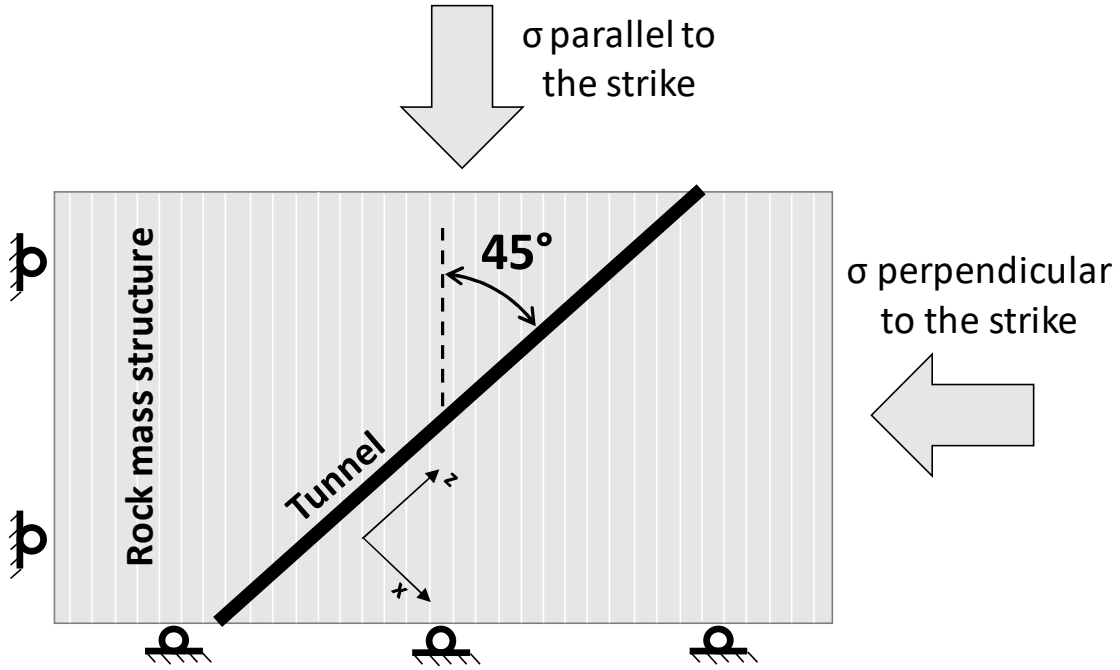

Figure 11.13 Plan view of the tunnel misaligned with the vertically structured rock mass and boundary conditions.

The axial displacements at the tunnel perimeter, normalized with respect to the tunnel radius, are presented in Figure 11.14, for an unsupported tunnel. In all cases, axial displacements are induced far behind the face. The axial displacements are asymmetric at the face and anti-symmetric far-behind the face. The axis of anti-symmetry far-behind the face is the vertical axis in all three cases, so the maximum axial displacements are at the springline and there are no axial displacements at the crown or invert. This is because of the presence of the far-field axial shear

stress and because of the tunnel misalignment with the rock mass structure. It is interesting to note that the axial displacements for Case 2, no far-field shear, are larger than for Case 3, σ_H parallel to the strike, but smaller than for Case 1, σ_H perpendicular to the strike. The reason for this is that, when σ_H is perpendicular to the strike, the axial distortions produced by the far-field axial shear stress and by the rock mass anisotropy complement each other, while when σ_H is parallel to the strike, they have opposite effects.

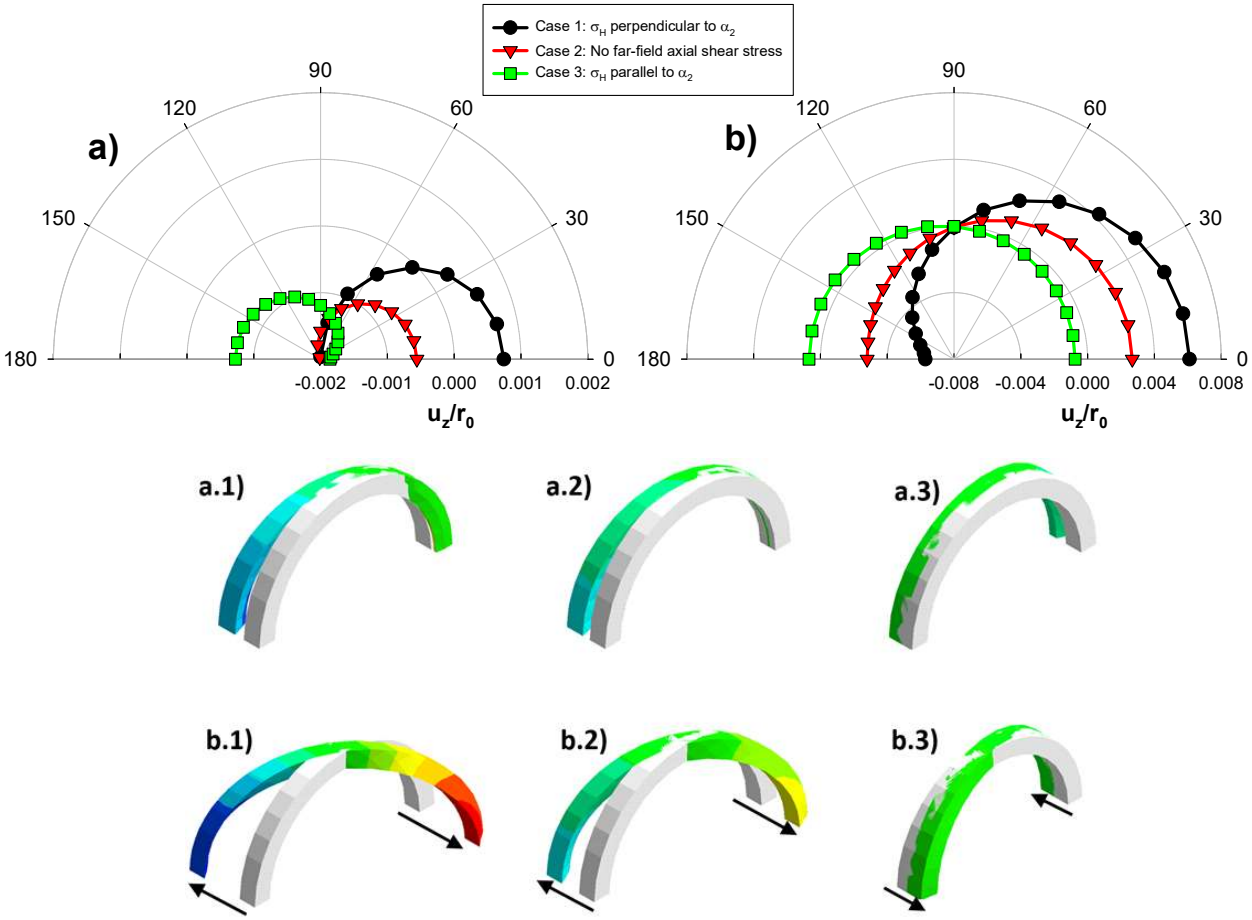

Figure 11.14 Normalized axial displacements of the tunnel: (a) at the face; (b) far-behind the face. The colors of the axially deformed tunnel cross-sections are associated with the magnitude of the axial displacements and are used for visualization purposes.

Figure 11.15 shows the normalized horizontal and vertical tunnel displacements with the normalized distance from the face of the tunnel. The displacements of Case 1 with horizontally structured rock mass are plotted for comparison. The vertical displacements are similar in all three cases with vertically structured rock mass and are smaller than those with horizontally structured rock mass. The reason for this is because the rock stiffness in the vertical direction is the largest

for vertically structured rock mass and the smallest for horizontally structured rock mass. For vertically structured rock mass, the horizontal displacements are larger for Case 1 (σ_H perpendicular to the strike) and smaller for Case 3 (σ_H parallel to the strike). This is due to the compliance matrix of the transversely anisotropic elastic model, which is fully populated when the tunnel is misaligned with one of the principal axes of material anisotropy. Thus, in-plane and out-of-plane stresses and deformations are coupled. As a consequence, radial displacements are affected by the far-field axial shear stresses. Note that when the tunnel is aligned with one of the principal axes of the material anisotropy, in-plane and out-of-plane deformations are decoupled. As a consequence, the far-field axial shear stress has no influence to the radial displacements far-behind the face (see e.g. Figures 11.4 and 11.5 for horizontally-structured rock mass). The horizontal convergence for Case 1 with horizontally structured rock mass is smaller than with vertically structured rock mass, because the rock mass stiffness is the largest in the horizontal direction than when the rock mass structure is horizontal.

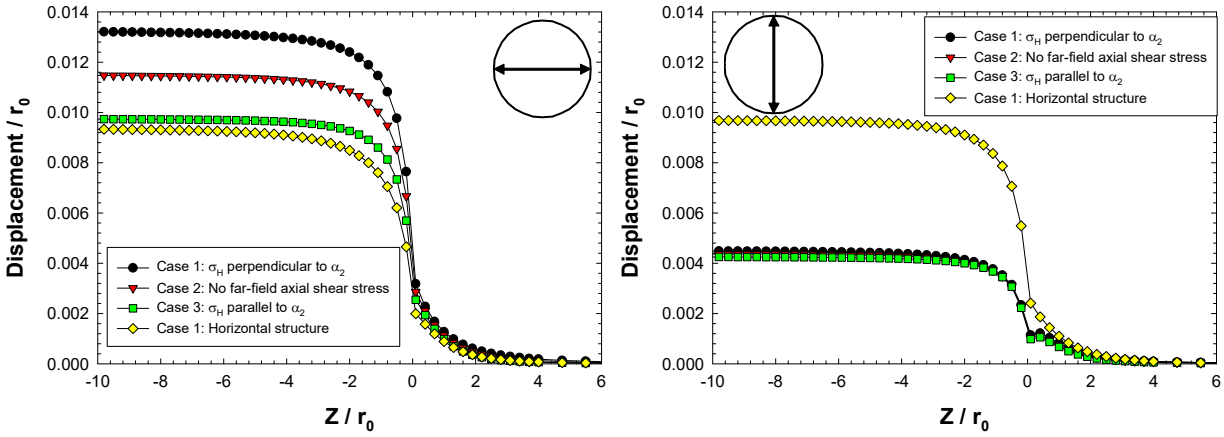

Figure 11.15 Normalized horizontal and vertical tunnel convergence, with respect to the tunnel radius, with the normalized distance from the face, with respect to the tunnel radius. Unsupported tunnel.

Figure 11.16 shows the normalized radial displacements and the deformed tunnel cross-section of the cases with vertically structured rock mass and of Case 1, with horizontally structured rock mass, which is included for comparison. At the face of the tunnel, the radial displacements are always asymmetric, but they are symmetric far-behind the face. As explained before, the asymmetric deformations near the face occur because the anti-symmetric axial displacements are constrained by the face of the tunnel. Note that the asymmetric deformations at the face and the

symmetric deformations far-behind the face are larger when σ_H is perpendicular to the strike (case 1) and smaller when σ_H is parallel to the strike (case 3). At the face, a horizontal translation of the tunnel cross section occurs for all cases. The translation is towards the right for Case 1 (σ_H perpendicular to the strike, Figure 11.16.a.1), Case 2 (no far-field axial shear stress, Figure 11.16.a.2) and for Case 1 with horizontally structured rock mass (Figure 11.16.a.4), but it is towards the left for Case 3 (σ_H parallel to the strike). As one can see in Figure 11.16, the deformed tunnel cross-section has a pronounced ellipsoidal shape far-behind the face when the rock structure is vertical (Cases 1 to 3). This is the result of a larger far-field horizontal stress than vertical, and the fact that the larger horizontal stress is applied in the direction of the smaller stiffness of the rock. The opposite happens in the horizontally structured rock mass, as discussed in the previous section.

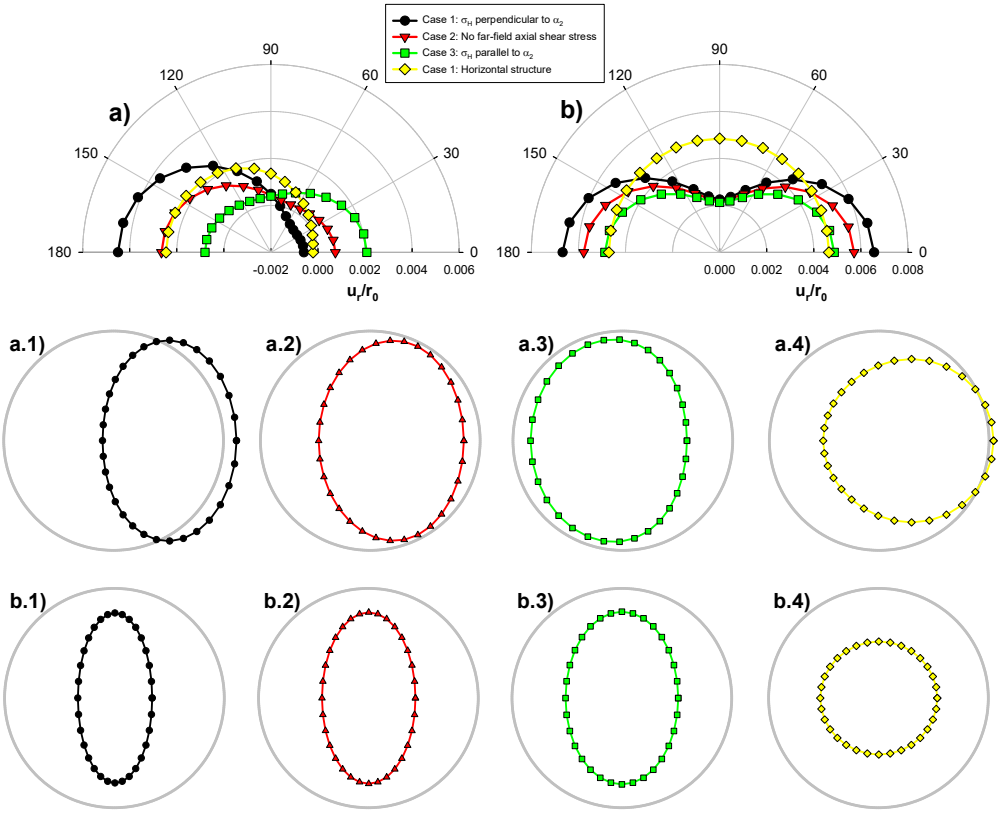

Figure 11.16 Normalized radial displacements at the tunnel perimeter with respect to the tunnel radius and deformed tunnel cross-section, for unsupported tunnel. (a) at the face; (b) far-behind the face. Deformations are magnified 200 times at the face and 100 times far-behind the face.

Figure 11.17 shows the normalized radial displacements at the springline and the horizontal translation of the tunnel cross section with the normalized distance from the face of the tunnel. The radial displacements on the left and right at the springline are different near the face but are the same far-behind the face. The horizontal translation of the tunnel cross section occurs near the face in all three scenarios; it is maximum at the face and reduces to zero far behind the face. Figure 11.17 also shows the "corrected" radial displacements, which are the radial displacements without the translation, as indicated in the graphs. For Case 2, no far-field axial shear stress, the corrected radial displacements are the same (within numerical approximation) on both sides of the springline. For Cases 1 and 3, where the far-field axial shear stress is not zero, the corrected radial displacements near the face are asymmetric. Thus, the horizontal translation observed in Case 2, no far-field axial shear, is in reality a horizontal rigid body displacement of the tunnel cross section, while in Cases 1 and 3, where the far-field axial shear stress is present, the deformations are more complex. The combination of rock anisotropy and far-field axial shear produces a response of the rock around the tunnel quite different (and more complex) than when the rock is isotropic. Indeed, in isotropic elastic ground, Vitali et al. (2019b) observed that the asymmetric radial deformations near the face due to a far-field axial shear stress could be decomposed into a rigid body displacement of the tunnel cross-section and anti-symmetric radial displacements, which is not always the case in anisotropic rock.

Figure 11.18 shows the stress paths at the springline, normalized with respect to the vertical stress. The labels (1, 2 and 3) shown in Figure 11.18 refer to positions far-ahead of the face (1), at the face (2), and far-behind the face (3), as indicated in Figure 11.2. The stresses are extracted at a distance of $0.1r_0$ from the tunnel perimeter, to avoid the mathematical singularity at the corner formed between the tunnel face and the excavation. As a consequence of the asymmetric deformations near the face, the stress paths are asymmetric near the face as well. For Case 1, σ_H perpendicular to the strike, the rock on the right-hand side of the springline takes load ahead of the face, the stresses increase near the face, and then they decrease behind the face. On the left, the stresses decrease ahead of the face and increase behind the face. Note that the stresses on the right and left springlines far-behind the face are the same. The stress paths are consistent with a horizontal translation of the tunnel cross section towards the right, which compresses the rock at the springline, to the right, and unloads to the left. The opposite is observed for Case 3, σ_H parallel to the strike. On the right, there is unloading ahead of the face and loading behind the face; on the

left springline, there is loading ahead of the face and unloading behind. Note that the tunnel translation in Case 3 is towards the left. For Case 2, no far-field axial shear stress, both sides of the springline follow the same stress path. The stresses near the face are larger at the right springline, which is consistent with the observed horizontal translation towards the right. It is interesting to note that the unloading stress path ahead of the face is only observed when the far-field axial shear stress is present. Figure 11.19 shows the normalized stress paths at the crown with respect to the vertical stress, for the three cases with vertically structured rock mass, and for Case 1, with horizontally structured rock mass, which is included for comparison. As one can see, all the stresses increase near the face. The shear stresses are smaller for Case 2, no far-field axial shear stress, than for the other cases. Far-behind the face, the stress state for Case 1, σ_H perpendicular to the strike, and Case 3, σ_H parallel to the strike, are the same and slightly different than for Case 1, with horizontally structured rock mass. This finding suggests that the orientation of the rock structure with respect to the tunnel strongly affects the ground deformations around the tunnel, particularly near the face of the tunnel, but has limited influence on the stresses around the tunnel far-behind the face.

The asymmetric deformations found near the face may affect the liner, if the tunnel is supported. This is investigated by running three new cases, all analogous to the previous cases discussed, but with a liner placed close to the face (Figure 11.2). The results are presented in Figures 11.20 and 11.21. Figure 11.20 shows the normalized radial stresses with the normalized distance from the tunnel face. As a consequence of the asymmetric deformations near the face, the radial stresses at the tunnel perimeter are asymmetric near and far-behind the face. The largest stress asymmetries occur for Case 1, when σ_H is perpendicular to the strike, and the smallest for Case 2, no far-field axial shear stress. The radial stresses are larger at the right springline when σ_H is perpendicular to the strike and when there is no far-field axial shear stress, but are larger at the left when σ_H is parallel to the strike. This is consistent with the direction of the tunnel cross section translation observed. The radial stresses at the crown are similar for the three cases and are larger than the stresses at the springline, given that the horizontal stress is larger than the vertical (i.e. stress concentrations are larger at the crown). Figure 11.21 shows the internal forces of the liner normalized with respect to the vertical stress and the tunnel radius. The internal forces are always asymmetric. The thrust is larger at the crown and at the invert and is smaller at the springline, while the bending moments are larger at the springline. The internal forces are larger for Case 1,

when σ_H is perpendicular to the strike and are smaller for Case 3, when σ_H is parallel to the strike. This is expected because the radial deformations are larger for Case 1 and smaller for Case 3, as shown in Figures 11.15, 11.16 and 11.17. It is interesting to note that the internal forces for the cases with far-field axial shear stress (Cases 1 and 3) are more asymmetric than the case with no far-field axial shear stress (Case 2).

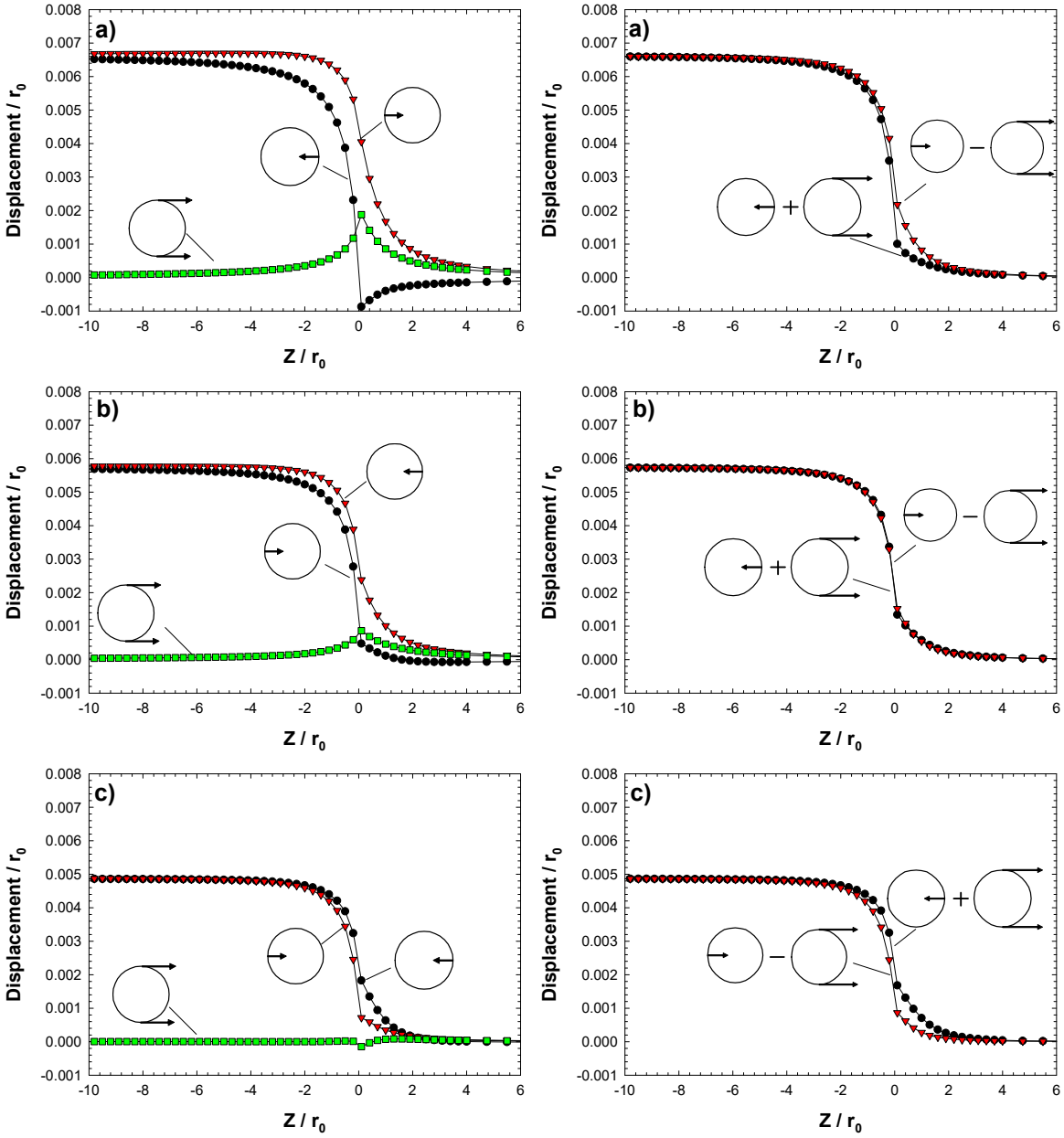

Figure 11.17 Normalized radial and horizontal translation of the tunnel cross section with respect to the tunnel radius with the normalized distance from the face with respect to the tunnel radius, for unsupported tunnel. (a) Case 1, σ_H perpendicular to the strike; (b) Case 2, no far-field axial shear stress and; (c) Case 3 σ_H parallel to the strike.

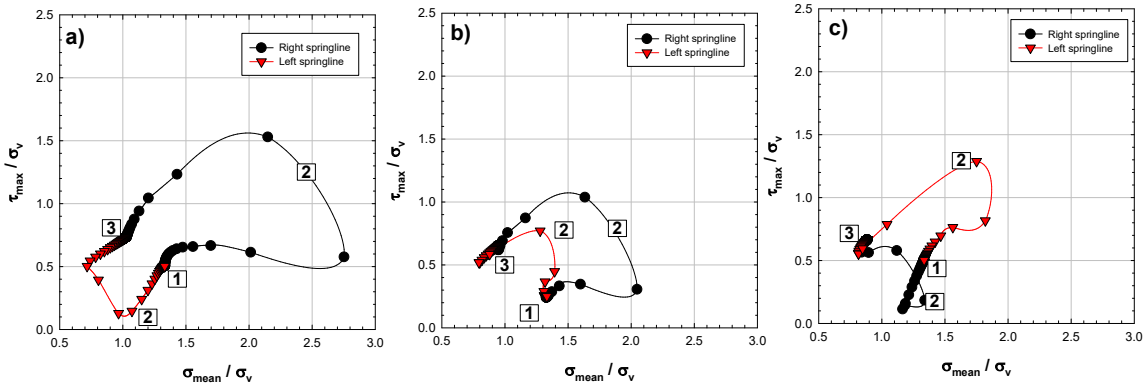

Figure 11.18 Normalized stress paths with respect to the vertical stress for unsupported tunnel. (a) Case 1: σ_H perpendicular to the strike; (b) Case 2, no far-field axial shear stress; and (c) Case 3, σ_H parallel to the strike.

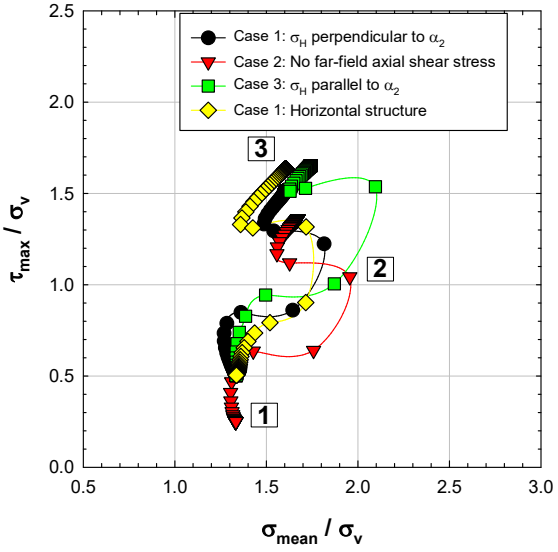

Figure 11.19 Stress paths at the crown.

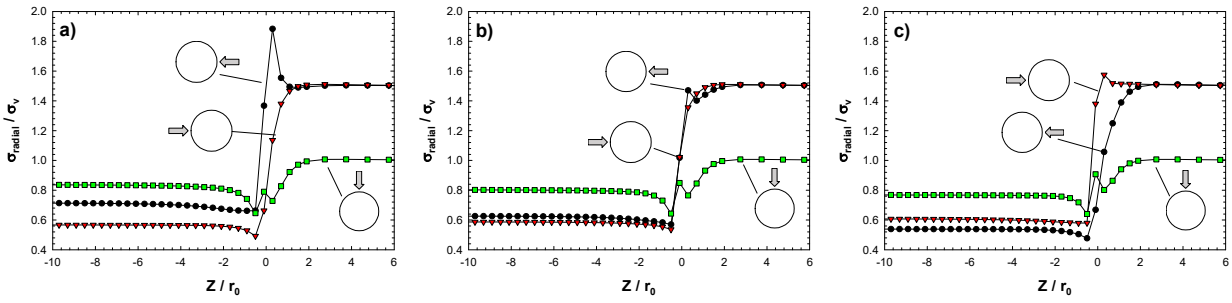

Figure 11.20 Normalized radial stresses with respect to the vertical stress with the normalized distance from the face with respect to the tunnel radius, for supported tunnel. (a) Case 1, σ_H perpendicular to the strike; (b) Case 2, no far-field axial shear stress; and (c) Case 3, σ_H parallel to the strike.

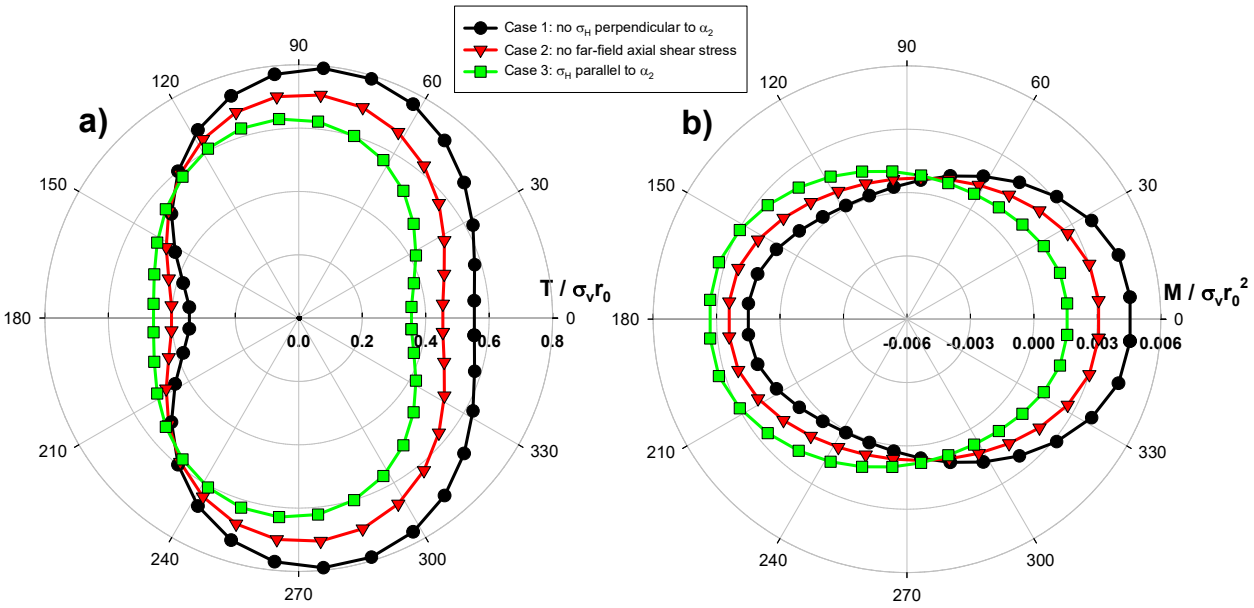

Figure 11.21 Normalized internal forces with the vertical stress and tunnel radius. (a) Thrust; (b) Bending moment.

11.5 Conclusions

The effects of the tunnel misalignment with the geostatic principal stress directions in anisotropic rock masses are investigated in this paper. Far-field axial shear stresses are present when the tunnel is not aligned with the geostatic principal stress directions. Anti-symmetric axial displacements and axial shear stresses are induced around the tunnel due to the tunnel misalignment with the geostatic principal stress directions and with the principal material directions. Near the face, axial displacements are constrained by the face of the tunnel; as a consequence, asymmetric radial deformations occur near the face. 3D FEM simulations of a tunnel at 45° with the horizontal principal stresses have been performed, with an anisotropic geostatic stress field. Two scenarios have been investigated: a horizontal tunnel in rock mass with horizontal structure, and in a rock mass with a vertical structure. In both scenarios, the rock response is approximated through a transversely anisotropic elastic model. Both unsupported and supported tunnels are considered.

For the scenario with the horizontally-structured rock mass, the tunnel is always aligned with the rock mass structure. Asymmetric radial deformations near the face of the tunnel occur when a far-field axial shear stress is present. Far-behind the face, for the unsupported tunnel, the radial displacements are symmetric, which indicates that the far-field axial shear stress does not

affect the radial displacements far-behind the face. The reason is that, when the tunnel is aligned with one of the principal material directions, in-plane and out-of-plane deformations are decoupled. For supported tunnels, the asymmetric deformations near the face affect the liner response. Far behind the face, asymmetric radial displacements and stresses are present, so the internal forces in the liner are asymmetric.

For the scenario where the rock mass structure is vertical and the tunnel axis makes an angle of 45° with the strike or the rock structure, axial displacements and axial shear stresses are induced around the tunnel. Three scenarios are being investigated: major horizontal stress parallel to the strike direction, major horizontal stress perpendicular to the tunnel direction and no far-field axial shear stress. Far-behind the face, the induced axial displacements are always anti-symmetric with respect to the vertical axis. The largest axial displacements occur when σ_H is perpendicular to the strike and the smallest when σ_H is parallel to the strike. This is because, when σ_H is perpendicular to the strike, the axial distortion of the tunnel cross section produced by the far-field axial shear stress and by the rock mass structure complement each other. The opposite happens when σ_H is parallel to the strike. Near the face, asymmetric deformations are induced. The asymmetric radial deformations near the face are larger when σ_H is perpendicular to the strike and smaller when σ_H is parallel. The same is true far-behind the face of the tunnel. In other words, the far-field axial shear stress affects the radial displacements far-behind the face when the tunnel is misaligned with the principal directions of material anisotropy. For supported tunnels, the radial stresses at the tunnel perimeter are asymmetric near the face and far-behind the face. Thus, the internal forces in the tunnel liner are asymmetric. The largest internal forces occur when σ_H is perpendicular to the strike and the smallest when σ_H is parallel to the strike.

The ground deformations far-behind the tunnel face are heavily affected by the orientation of the rock mass structure with the tunnel. For the horizontally structured rock mass, the deformed tunnel cross section far-behind the face has a slightly ellipsoidal shape (i.e. the radial displacements at the springline are similar to those at the crown and invert). In contrast, for vertically-structured rock mass, the deformed tunnel cross section has a pronounced ellipsoidal shape, where the radial displacements at the springline are substantially larger than at the crown and invert. For this specific case, the far-field horizontal stress is larger than the vertical. Thus, for horizontally-structured rock mass, the largest stresses are aligned with the stiffest material direction (i.e. parallel to the rock structure) and the smallest stresses are aligned with the softest

material direction (i.e. perpendicular to the strike). The opposite occurs for vertically-structured rock mass. The rock stresses near the tunnel perimeter for horizontally- and vertically-structured rock mass are similar far-behind the face, which seems to suggest that rock anisotropy has a modest influence on the stresses far behind the face of the tunnel.

The results presented in this paper provide insight into the complex behavior of tunnels in anisotropic rock masses, and highlight the importance of considering the tunnel misalignment with the geostatic principal stress directions and with the rock mass structural planes. Also, the results show the importance of the orientation of the geostatic principal stress directions with respect to the principal directions of material anisotropy.

Acknowledgments

The research is being partially supported by the research funding agency of the Brazilian government CNPq ("Conselho Nacional de Desenvolvimento Cientifico"). The authors acknowledge the support from CNPq and from Midas company, which kindly provided the license of Midas GTX NX software, used in the present work.

11.6 References

Armand, G., Noiret, A., Zghondi, J., & Seyedi, D. M., 2013. Short- and long-term behaviors of drifts in the Callovo-Oxfordian claystone at the Meuse/Haute-Marne Underground Research Laboratory. Journal of Rock Mechanics and Geotechnical Engineering, *5*(3), 221–230.

Brady, B. H. G. and Brown, E. T., 2006. Rock Mechanics for underground mining: Third edition: doi: 10.1007/978-1-4020-2116-9.

Brown ET, Hoek E., 1978. Trends in relationships between measured in-situ stresses and depth. Int. J. Rock Mech. Min. Sci. 15(4): 211–215.

Button E., Leitner R., Poetsch M., Schubert W., 2006. Spatial relationships between discontinuity orientation and system behavior in underground excavations. In: Proceedings of ARMA 41st U.S. Symposium on Rock Mechanics. ARMA/USRMS 06-957.

Evans K.F., Engelder T., Plumb R.A., 1989. Appalachian Stress study .1. a detailed description of in-situ stress variations in devonian shales of the appalachian plateau. J. Geophys. Res. Earth Planets. 94: 7129–7154.

Fortsakis P, Nikas K, Marinos KV, Marinos P., 2012. Anisotropic behaviour of stratified rock masses in tunnelling. Eng. Geol. 141–142: 74–83.

Goricki A, Button A.E., Schubert W., Pötsch M., Leitner R., 2005. The influence of discontinuity orientation on the behaviour of tunnels. Felsbau. 23(5):12–18.

Gysel M., 1975. In-Situ stress measurements of the primary stress state in the Sonnenberg tunnel in Lucerne, Switzerland. Tectonophysics. 29: 301–314.

Haimson B.C., Lee M.Y., Song I., 2003. Shallow hydraulic fracturing measurements in Korea support tectonic and seismic indicators of regional stress. Int. J. Rock Mech. Min. Sci. 40(7-8): 1243–1256.

Hoek, E., 2007. Practical Rock Engineering, 2007 ed.

Klopčič, J., Logar, J., 2014. Effect of relative orientation of anisotropy planes to tunnel axis on the magnitude of tunnelling displacements. International Journal of Rock Mechanics and Mining Sciences. 71: 235-248.

Lenz, G., Kluckner A., Holzer R., Stadlmann T., Schachinger, T., Gobiet G., 2017. Prediction of fault zones based on geological and geotechnical observations during tunnel construction. Geomechanics and Tunneling, 10(4): 366–379.

Martin, C. D., 1997. Seventeenth Canadian Geotechnical Colloquium: The effect of cohesion loss and stress path on brittle rock strength. Canadian Geotechnical Journal, 34(5): 698-725.

McGarr A, Gay N.C., 1978. State of Stress in the Earth's Crust. Ann. Rev. Earth Planet. Sci. 6: 405–436.

Park E.S., Choi B.H., Bae S.H., Jeon S., 2014. Horizontal stresses at shallow depths in Seoul (Korea) gneissic region. In: Rock Eng. Rock Mech. Struct. Rock Masses - Proceedings of EUROCK 2014, ISRM European Regional Symposium: 399–404.

Perras M.A., Wannenmacher H., Diederichs M.S., 2015. Underground excavation behaviour of the Queenston formation: tunnel back analysis for application to shaft damage dimension prediction. Rock Mech. Rock Eng. 48(4):1647-1671.

Schubert W, Budil A., 1995. The importance of longitudinal deformation in tunnel excavation. In: Proceedings of 8th ISRM Congress on Rock Mechanics:1411–1414.

Schubert P, Klopčič J, Štimulak A, Ajdič I, Logar J., 2005. Analysis of characteristic deformation patterns at the Trojane tunnel in Slovenia. Felsbau, 23(5):25-30.

Schubert, W., Moritz, B., 2011. State of the art in evaluation and interpretation of displacement monitoring data in tunnels. Geomechanics and Tunneling, 4(5): 371–380.

Souček K., et al., 2017. Geotechnical characterization of Bukov underground research facility. Procedia Engineering. 191:711-718.

Tonon F., Amadei B., 2002. Effect of elastic anisotropy on tunnel wall displacements behind a tunnel face. Rock Mech. Rock Eng. 35(3):141-160.

Tonon F., Amadei B., 2003. Stresses in anisotropic rock masses: An engineering perspective building on geological knowledge. Int. J. Rock Mech. Min. Sci. 40(7–8):1099–1120.

Vitali O.P.M., Celestino T.B., Bobet A., 2017. 3D finite element modelling optimization for deep tunnels with material nonlinearity. Undergr. Sp.3(2):125–139.

Vitali O.P.M., Celestino T.B., Bobet A., 2018. Analytical solution for tunnels not aligned with geostatic principal stress directions. Tunn. Undergr. Sp. Technol. 82: 394–405.

Vitali O.P.M., Celestino T.B., Bobet A., 2019a. Shallow tunnel not aligned with the geostatic principal stress directions. In: Proceedings of Geo-Congress2019, GSP 313:214-222.

Vitali O.P.M., Celestino T.B., Bobet A., 2019b. Shallow tunnels misaligned with geostatic principal stress directions: analytical solution and 3D face effects. Tunn. Undergr. Sp. Technol. 89: 268-283.

Vitali O.P.M., Celestino T.B., Bobet A., 2019c. Progressive failure due to tunnel misalignment with geostatic principal stresses. In: Proceedings of ISRM 14th International Congress on Rock Mechanics: 2292-2299.

Vitali, O. P. M., Celestino, T. B., Bobet, A., 2019d. Analytical solution for a deep circular tunnel in anisotropic ground and anisotropic geostatic stresses. Manuscript under review for publication in a peer-reviewed journal.

Wileveau Y, Cornet F.H., Desroches J., Blumling P., 2007. Complete in situ stress determination in an argillite sedimentary formation. Phys. Chem. Earth. 32(8–14):866–878.

Worotnicki G., 2013. 13 – CSIRO Triaxial Stress Measurement Cell. In: Rock testing and site characterization: principles, practice and projects: 329-394.

Zhao, X. G. et al., 2013. In-situ stress measurements and regional stress field assessment of the Beishan area, China. Eng. Geol. 163:26-40.

Zhao X.G. et al., 2015. In-situ stress measurements and regional stress field assessment in the Xinjiang candidate area for China's HLW disposal. Eng. Geol. 197:42-56.

12. DEFORMATION PATTERNS AND 3D FACE EFFECTS OF TUNNELS MISALIGNED WITH GEOSTATIC PRINCIPAL STRESSES IN ISOTROPIC AND ANISOTROPIC ROCK MASSES

VITALI, O. P. M.; CELESTINO, & BOBET, A. (2020). Deformation patterns and 3D face effects of tunnels misaligned with the geostatic principal stresses in isotropic and anisotropic rock masses. 54th US Rock Mechanics /Geomechanics Symposium (ARMA 2020).

Abstract

Rock masses may present remarked stress anisotropy, and so the geostatic horizontal stresses may be highly anisotropic and larger than the overburden stress. Therefore, the alignment of a tunnel with one of the geostatic principal stress directions is improbable; thus, far-field axial shear stresses are likely to be present in the direction of the tunnel. In addition, rock masses may have important material anisotropy due to the presence of structure, e.g. bedding, foliation and stratification; so, a tunnel is also likely to be misaligned with the principal material directions of the rock mass. Those misalignments are often neglected in tunnel design and yet, their effects are not well explored in the literature. In this paper, the deformation patterns and the 3D face effects on tunnels misaligned with the principal directions of stress and material anisotropy are explored.

12.1 Introduction

Rock masses may present remarked stress and material anisotropy and, yet, tunnel design often neglects the tunnel orientation with the principal directions of stress and material anisotropy. However, the importance of the tunnel orientation with respect to the geostatic principal stress directions is well recognized. Experimental tunnels had been constructed in an Underground Research Laboratory (URL) in France, where the URL was placed at 490m depth in an anisotropic Claystone rock mass. Tunnels were excavated parallel and perpendicular to the major horizontal stress (σ_H). A supported circular tunnel of radius 2.6m aligned with σ_H showed a horizontal convergence of 37 to 58mm and a vertical convergence of 24 to 30mm. A similar tunnel aligned with the minor horizontal stress (σ_h) showed horizontal convergence of 19mm to 34mm and vertical convergence of 112mm to 158mm (Armand et al., 2013). These field data illustrate the importance of the tunnel orientation with respect to the geostatic principal stresses. Indeed, it has

been long known that a tunnel should be aligned with the geostatic major principal stress to minimize stress concentrations around the opening (Goodman, 1989).

When the tunnel is not aligned with the geostatic principal stresses, the far-field stresses can be decomposed into stresses in the plane of the tunnel cross-section and perpendicular to the cross-section, i.e. axial normal and shear stresses. The far-field axial shear stresses cause anti-symmetric axial displacements and shear stresses along the axis of the tunnel. Near the face, the axial displacements are partially constrained by the face, which causes asymmetric radial displacements and stresses near the face (Vitali et al. 2018, 2019a, 2019b, 2019c). If the tunnel is unsupported and in an elastic rock, Vitali et al. 2019b showed that the asymmetric radial displacements at the face can be divided into a rigid body displacement of the tunnel cross section and anti-symmetric radial displacements. The asymmetric deformations near the face disappear far-behind the face, where the radial displacements are symmetric, and the anti-symmetric axial displacements are not constrained. However, if the tunnel is supported and/or the rock mass is elastoplastic, the radial displacements far-behind the face may be asymmetric. The asymmetric stresses near the face may produce an asymmetric plastic zone around the tunnel if the rock mass is elastoplastic. Further, the pressure in the liner may be asymmetric; thus, asymmetric internal forces might occur in the tunnel support (Vitali et al. 2019b and 2019c).

If the rock mass has anisotropic properties, the tunnel misalignment with the principal directions of material anisotropy also induces anti-symmetric axial displacements and axial shear stresses along the tunnel. The reason for this is that the tunnel response is fully coupled in the transverse and longitudinal directions (i.e. the compliance matrix of the system is fully populated, Vitali et al. 2020a). Vitali et al. 2020a showed that the asymmetric radial displacement near the face of an unsupported tunnel misaligned with the principal material directions in a transversely anisotropic elastic rock mass under isotropic stress state is due to a rigid body displacement of the tunnel cross section. However, when the geostatic stress field is anisotropic and the tunnel also is misaligned with the principal stress directions, the asymmetric deformations near the face are rather complex. Thus, misaligned tunnels in anisotropic rock masses are substantially more difficult to analyze than misaligned tunnels in isotropic rock masses, where axial displacements and in-plane stresses are decoupled (Vitali et. 2020a, 2020b and 2020c). Asymmetric radial deformations and anti-symmetric axial displacements around tunnels in anisotropic rock masses are commonly observed (Schubert and Budil 1995, Schubert et al. 2005), but, so far, the sources

of these deformations are not clearly identified. It is possible that those deformations were associated with the misalignment of the tunnel axis with the principal directions of stress and/or material anisotropy.

In this paper, the deformation patterns and the 3D face effects of misaligned tunnels in isotropic and anisotropic rock masses are presented. The analyses were done using 3D FEM modeling. The models were built following the recommendations provided by Vitali et al. (2017), to ensure accurate numerical results. The tunnels were unsupported and circular, with radius (r0) of 5m. The isotropic rock mass was represented by an elastic model with E = 2GPa (Young modulus) and ν = 0.33 (Poisson ratio). The anisotropic rock mass was characterized by a transversely anisotropic elastic model with: $E_1 = E_3 = 3.33$GPa (Young modulus parallel to the isotropic planes); $E_2 = 0.67$GPa (Young modulus perpendicular to the isotropic planes); $G_{12}=G_{23}=0.51$GPa (shear modulus perpendicular to the isotropic planes); $G_{13}=1.25$GPa (shear modulus parallel to the isotropic planes); $\nu_{23} =\nu_{12} = 0.25$ and; $\nu_{13}= 0.33$. Where "1" and "3" are directions parallel to the rock structure and "2", perpendicular. Those properties are representative of a highly anisotropic rock mass, such as slate, schist or phyllite. Note that the ratio E1/E2 = 5 is on the upper limit of the range reported by Worotnicki (1993). The orientation of the rock structural planes is given by the dip angle (α_1) and by the strike direction. A dip angle (α_1) of 45° was chosen for this study. A major horizontal stress (σ_H) of 10MPa, minor horizontal stress (σ_h) of 5MPa and vertical stress of 5MPa were adopted. The vertical stress corresponded to an overburden of about 200m. The selected geostatic stress anisotropy was within the range found in the literature (Mcgarr and Gay 1978; Willeaveau et al. 2007; Brown and Hoek, 1978; Haimson et al. 2003). Note that $E = (E_1+E_2)/2 = 2$GPa. Thus, the isotropic rock mass had the average stiffness of the anisotropic rock mass.

Different orientations of the tunnel with respect to the principal stress directions were assessed for two scenarios, as shown in Figures 12.1 and 12.2. Scenario 1 (Figure 12.1) considered the major horizontal stress aligned with the rock structure. In scenario 2 (Figure 12.2), the minor horizontal stress was aligned with the rock mass structure. The tunnel was horizontal and made an angle Ψ with the major horizontal stress (σ_H), as indicated in Figures 12.1 and 12.2. The far-field stresses, in the coordinate system attached to the tunnel (illustrated in Figures 12.1 and 12.2), are:

$$\sigma_{xx,ff} = \sin^2(\psi)\sigma_H + \cos^2(\psi)\sigma_h ; \quad (1)$$

$$\sigma_{yy,ff} = \sigma_v ; \quad (2)$$

$$\sigma_{zz,ff} = \cos^2(\psi)\sigma_H + \sin^2(\psi)\sigma_h ; \quad (3)$$

$$\tau_{xz,ff} = \frac{\sigma_H - \sigma_h}{2}\sin(2\psi) ; \quad (4)$$

Where the axis z is parallel to the direction of the tunnel and the axis, x, perpendicular; note that the axis y remains unchanged and is vertical.

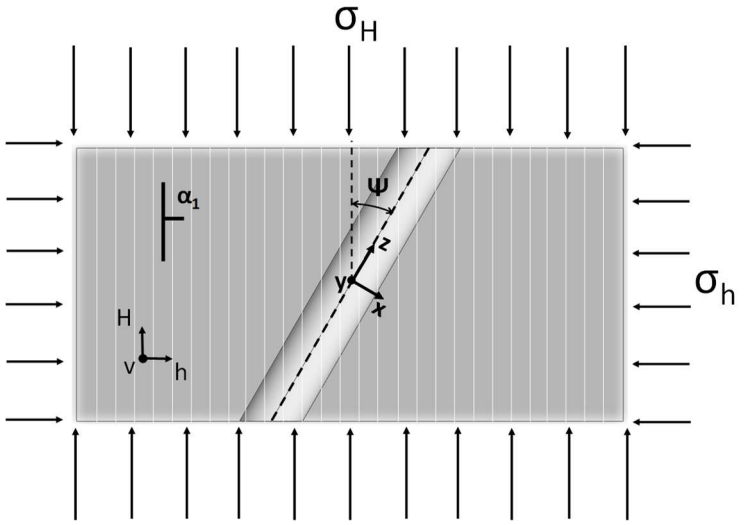

Figure 12.1 Plan view of the case with major horizontal stress parallel to the rock structure, scenario 1.

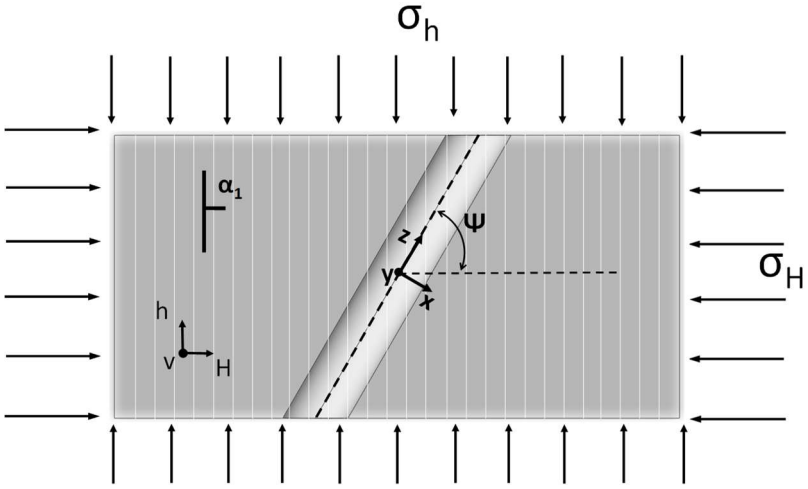

Figure 12.2 Plan view of the case with minor horizontal stress parallel to the rock structure, scenario 2.

When Ψ=0°, the tunnel is aligned with the major horizontal stress (σ_H); thus, the far-field horizontal stress ($\sigma_{xx,ff}$) is minimum (i.e. $\sigma_{xx,ff} = \sigma_h$) and no far field axial shear stress ($\tau_{xz,ff}$) is present. As the tunnel rotates, the far-field horizontal stress ($\sigma_{xx,ff}$) increases and the far-field axial

shear stress ($\tau_{xz,ff}$) appears. The far-field axial shear stress is maximum when Ψ=45°. For this angle: the far-field axial shear stress ($\tau_{xz,ff}$) was -2.5MPa for scenario 1 and 2.5MPa for scenario 2 (i.e. the same magnitude but opposite direction), and the far-field horizontal stress was 7.5MPa for scenarios 1 and 2. When Ψ=90°, the tunnel is aligned with the minor horizontal stress (σ_h); thus, the horizontal stress ($\sigma_{xx,ff}$) is maximum (i.e. $\sigma_{xx,ff} = \sigma_H$), and no far-field shear is present. A case with no far-field axial shear stress (i.e. no shear, $\tau_{xz,ff}$=0) is included to assess its influence. That is $\sigma_{xx,ff}$, $\sigma_{yy,ff}$, $\sigma_{zz,ff}$ are the same as before, but $\tau_{xz,ff}$ is neglected. The far-field axial shear stress does not affect the radial displacements far-behind the face if the tunnel is unsupported and the rock mass is isotropic and elastic (Vitali et al. 2018, 2019a, 2019b); however, the radial deformations are affected by the far-field axial shear stress if the rock mass has anisotropic properties (Vitali et al. 2020a, 2020b and 2020c).

12.2 Deformations Far-Behind the Face

The maximum radial displacements ($u_{r,max}$) far-behind the face at the tunnel perimeter, with the angle Ψ, for scenario 1 (Figure 12.1) are plotted in Figure 12.3. This figure also illustrates the deformed tunnel cross sections for Ψ=0°, 45° and 90°. The displacements were normalized with respect to the tunnel radius (r_0).

For the isotropic rock mass, as Ψ increased from 0° to 90°, the maximum radial displacement increased, because of the increase on the far-field horizontal stress. In contrast, for anisotropic rock mass, the maximum radial displacements decreased with Ψ. This occurred because the stiffness of the rock mass parallel to the structural planes was substantially larger than the stiffness perpendicular to those planes. For Ψ=0° in scenario 1, the tunnel aligns with the rock structure and with σ_H; thus, the horizontal rock mass stiffness is the smallest and the far-field horizontal stress is the smallest as well ($\sigma_{xx,ff} = \sigma_h$). As the tunnel rotates, the far-field horizontal stress ($\sigma_{xx,ff}$) increases, but the horizontal stiffness of the rock mass also increases, compensating the larger horizontal stresses ($\sigma_{xx,ff}$). Interestingly, the maximum radial displacements for the tunnel in anisotropic rock with no shear were larger than with the full stress field; thus, showing that the presence of the far-field axial shear stress reduced the radial displacements. For isotropic rock, the deformed cross section was symmetric with the horizontal and vertical axes being the axes of symmetry; the maximum radial displacement was always at the springline (except for Ψ=0°, where the radial displacements were uniform along the tunnel perimeter). For anisotropic rock, the

location of the maximum radial displacement changed as the tunnel rotated; thus, the deformed cross sections were not symmetric with respect to the vertical and horizontal axes (except for Ψ=90°). The maximum radial displacements were larger for the anisotropic rock when Ψ was between 0° and 45° and for the isotropic rock when Ψ ranged from 45° to 90°.

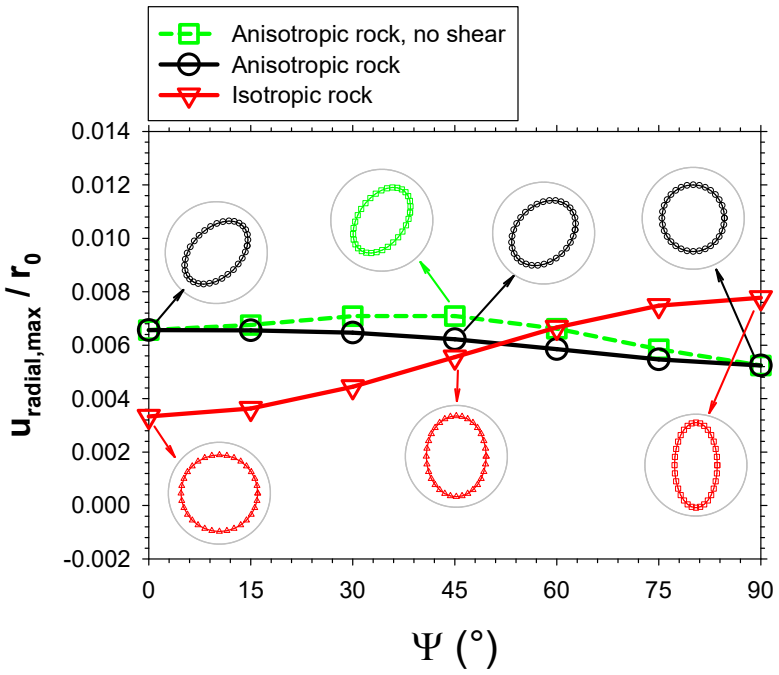

Figure 12.3 Maximum radial displacement ($u_{r,max}$) at the tunnel perimeter normalized with respect to the tunnel radius (r_0) with angle Ψ, for scenario 1. The displacements of the deformed cross-sections are amplified 75 times.

The normalized maximum axial displacements ($u_{axial,max}/r_0$), with Ψ, and the axially deformed cross sections for Ψ = 45° and 90° are presented in Figure 12.4. For isotropic rock, the axial displacements were zero for Ψ equal 0° and 90° since, at these angles, the tunnel was aligned with one of the principal stress directions. The axial displacements were maximum at Ψ=45°, the direction at which the far-field axial shear stresses are the largest. The axial displacements were anti-symmetric with respect to the vertical axis, as illustrated by the deformed cross sections in the figure. Note that the left springline displaced forward while the right springline, backward. For anisotropic rock, the axial displacements were zero for Ψ=0° because the tunnel was aligned with the major horizontal stress and with the rock mass structure. As the tunnel rotated, the maximum axial displacements increased until Ψ=45° and were almost constant from Ψ=45° to 90°. For Ψ=90°, even though no far-field axial shear stress was present, the tunnel was not aligned with the

rock structure and, thus, anti-symmetric axial displacements were induced along the tunnel. Because of the material anisotropy, the axis of anti-symmetry changed as the tunnel rotated. It is interesting to note that the axial displacements for anisotropic rock with no axial shear were slightly larger than when the far-field axial shear stress was included. For anisotropic rock with no shear, the magnitude of the maximum axial displacements at the tunnel perimeter with the angle Ψ (Figure 12.1) were similar to those when the far-field axial shear stress was included. At Ψ=45°, the axis of anti-symmetry is located at 33° from the horizontal and the right springline displaces forward while the left, backward. It is interesting to note that this is in the opposite direction of the axial distortion caused by the far-field axial shear stress in isotropic rock, as one can see in the axially deformed cross-sections presented in Figure 12.4. Thus, the rock anisotropy and the far-field axial shear stress produced anti-symmetric axial displacements in the opposite directions. As a consequence, the axis of anti-symmetry was shifted to near horizontal and the ground deformations were reduced.

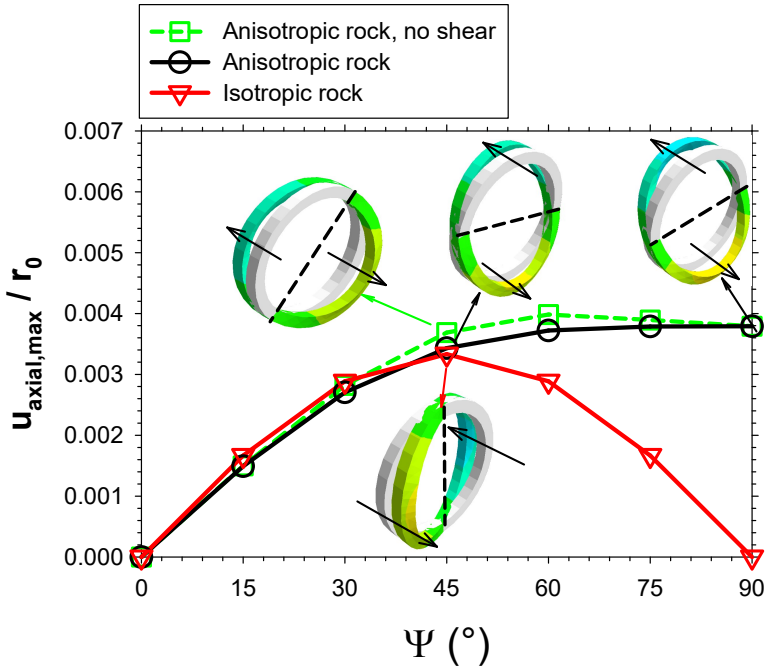

Figure 12.4 Maximum axial displacement ($u_{axial,max}$) at the tunnel perimeter normalized with respect to the tunnel radius (r_0) with angle Ψ, for scenario 1. The axially-deformed cross sections were taken from the FEM software used in this work (Midas GTS NX). The colors are included to enhance visualization.

The normalized maximum radial displacements at the tunnel perimeter with the angle Ψ, for scenario 2 (Figure 12.2), are presented in Figure 12.5, as well as the deformed tunnel cross section for Ψ=0°, 45° and 90°. Note that the plots of $u_{r,max}$ for scenarios 1 and 2 are the same for the isotropic rock. For the anisotropic rock, the maximum radial displacement ($u_{r,max}$) increased with Ψ, which was the opposite than in scenario 1, where the $u_{r,max}$ decreased with Ψ. When Ψ was between 45° to 90° in scenario 2 (Figure 12.5), the maximum radial displacement was substantially larger for the tunnel in anisotropic rock than for the tunnel in isotropic rock, and larger than for the tunnel in anisotropic rock in scenario 1 (Figure 12.3). The reason for this is because, in scenario 2, the minor horizontal stress was aligned with the stiffest rock mass direction. When Ψ was 0°, the far-field horizontal stress was minimum ($\sigma_{xx,ff} = \sigma_h$) and rock stiffness on the horizontal plane was maximum; thus, as the tunnel rotated, the horizontal stress increased while the horizontal stiffness of the rock mass decreased, amplifying the ground deformations. It is interesting to note that the radial displacements for anisotropic rock with no far-field axial shear stress were smaller than with the full stress field. It is the opposite in scenario 1. Thus, in scenario 2, the far-field axial shear stress contributed to increase the radial displacements far-behind the face. As with scenario 1, the location where the maximum radial displacement occurred changed with Ψ. For Ψ=45°, scenarios 1 and 2 only differed from each other by the direction of the far-field axial shear; however, the maximum radial displacement for scenario 2 was 33% larger than for scenario 1 (this observation is revisited later when discussing axial displacements).

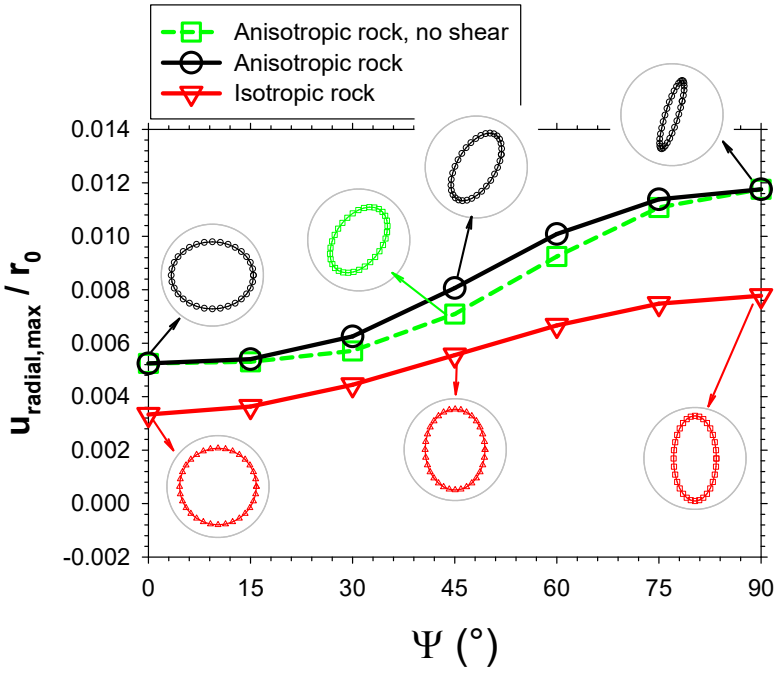

Figure 12.5 Maximum radial displacement ($u_{r,max}$) at the tunnel perimeter normalized with respect to the tunnel radius (r_0) with angle Ψ, for scenario 2. The displacements of the deformed cross-sections are amplified 75 times.

Figure 12.6 shows the normalized maximum axial displacements at the tunnel perimeter, with Ψ, for scenario 2. For isotropic rock, the maximum axial displacements for scenarios 1 and 2 had the same magnitude, the axis of anti-symmetry had the same orientation (i.e. vertical), but the direction of the axial distortion was the opposite from each other because the far-field axial shear stresses had opposite directions. Note that the left springline for the isotropic rock mass case displaced backward in scenario 2 and forward in scenario 1. For anisotropic rock with the full far-field stresses, the maximum axial displacements were substantially larger than for isotropic rock and for the case of anisotropic rock with no far-field axial shear stress. This is different from scenario 1, where the axial displacements in anisotropic rock with no shear were slightly larger than in anisotropic rock with full far-field stress. As one can see in the axially deformed tunnel cross-sections presented in Figure 12.6, when Ψ=45°, the anti-symmetric axial displacements for the tunnel in isotropic rock (with shear) and in anisotropic rock with no far-field axial shear had the same direction, i.e. forward on the right springline and backward on the left springline; thus, the axial displacements due to the rock anisotropy and due to the far-field axial shear stress have the same direction and thus they add to each other, producing larger deformations around the tunnel

(compare results with anisotropic rock between scenario 1, Figure 12.4, and scenario 2, Figure 12.6). The axis of anti-symmetry changed substantially with Ψ; note that for Ψ=0°, the axis of anti-symmetry was horizontal while for Ψ=45°, it was quasi- vertical. For Ψ=45°, when scenarios 1 and 2 only differ by the direction of the far-field axial shear, the axial deformations from scenarios 1 and 2 were substantially different (i.e. the axis of anti-symmetry was in a different position and the maximum axial displacement for scenario 2 was approximately two times larger than for scenario 1; compare Figure 12.6 with Figure 12.4).

These numerical results suggest that the axial displacements produced by the far-field axial shear stresses and by the rock mass material anisotropy may compensate or supplement each other. For scenario 1, the anti-symmetric axial displacements induced by the far-field stress and by the rock anisotropy had opposite sign; thus, axial and radial displacements at the tunnel perimeter of the tunnel were smaller than those in anisotropic rock with no far-field axial shear stress. For scenario 2, the anti-symmetric axial displacements due to the far-field stresses and due to the rock anisotropy had the same sign; thus, axial and radial displacements were amplified with respect to the tunnel in anisotropic rock with no far-field axial shear stress.

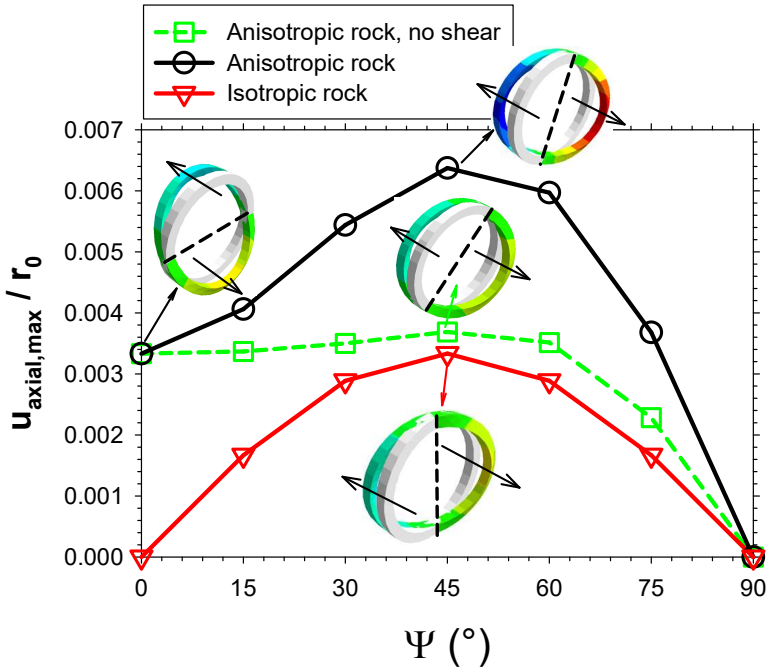

Figure 12.6 Maximum axial displacement ($u_{axial,max}$) at the tunnel perimeter normalized with respect to the tunnel radius (r_0) with angle Ψ, for scenario 2. The axially deformed cross sections were taken from the FEM software used in this work (Midas GTS NX). The colors are included to enhance visualisation.

12.3 Deformations Near the Face

Near the face, any far-field anti-symmetric axial displacements are partially constrained by the face of the tunnel; consequently, asymmetric radial displacements occur near the face (Vitali et al. 2019b, 2019c, 2020b and 2020c). Those asymmetric deformations near the face are explored in this section for scenarios 1 and 2 when Ψ=45°. Scenarios 1 and 2 only differ by the direction of the far-field axial shear stress when Ψ=45° (Figures 12.1 and 12.2); that is, the far-field horizontal, vertical and axial stresses are the same on both scenarios ($\sigma_{xx,ff}$= $\sigma_{zz,ff}$= 7.5 MPa and $\sigma_{yy,ff}$= 5 MPa) and the far-field axial shear stress has the same magnitude but opposite directions ($\tau_{xz,ff}$= -2.5 MPa in scenario 1 and $\tau_{xz,ff}$ = 2.5 MPa in scenario 2). The case of the tunnel in anisotropic rock neglecting the far-field axial shear stress ($\tau_{xz,ff}$= 0) was included to investigate the influence of the far-field axial shear stress. The tunnel orientation with respect to the rock mass structural planes when Ψ=45° is illustrated in Figure 12.7.

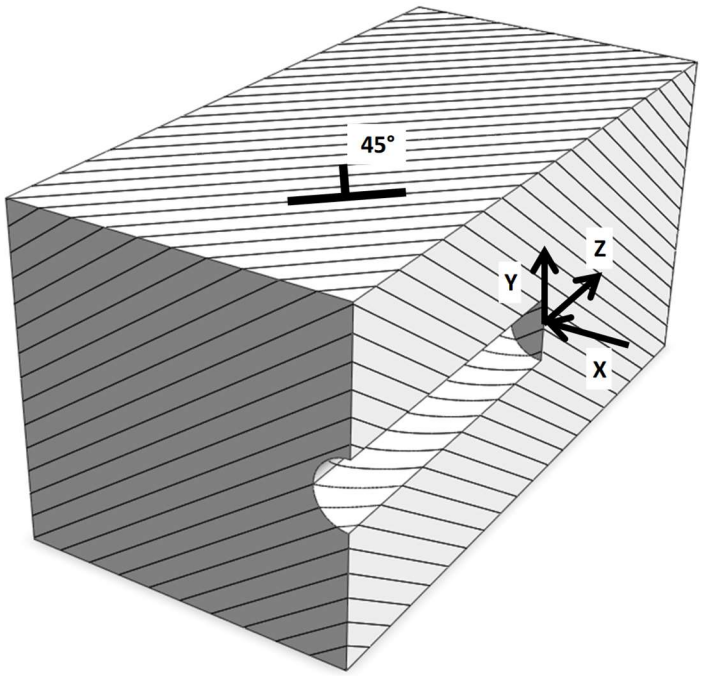

Figure 12.7 Tunnel orientation with respect to the rock mass structure for Ψ=45°. The lines in the figure represent the direction of the rock mass structure, with a dip angle of 45°.

Normalized radial displacements (u_r/r_0) with normalized distance from the face (Z/r_0), deformed cross section at the face (Z=0) and far-behind the face ($Z=6r_0$) are presented in Figures 12.8 and 12.9. Those plots show the radial displacements with the distance from the face at the

locations of maximum and minimum radial displacements for tunnels in isotropic and in anisotropic rock masses in scenarios 1 (Figure 12.8) and 2 (Figure 12.9). As one can see in the plots, the tunnel face affected the radial displacements from a distance of $4r_0$ ahead of the face to $4r_0$ behind the face, for the tunnels in isotropic and anisotropic rock mass. Beyond the distance of $4r_0$, the radial displacements were symmetric, and so this distance defines the extent of the influence of the face.

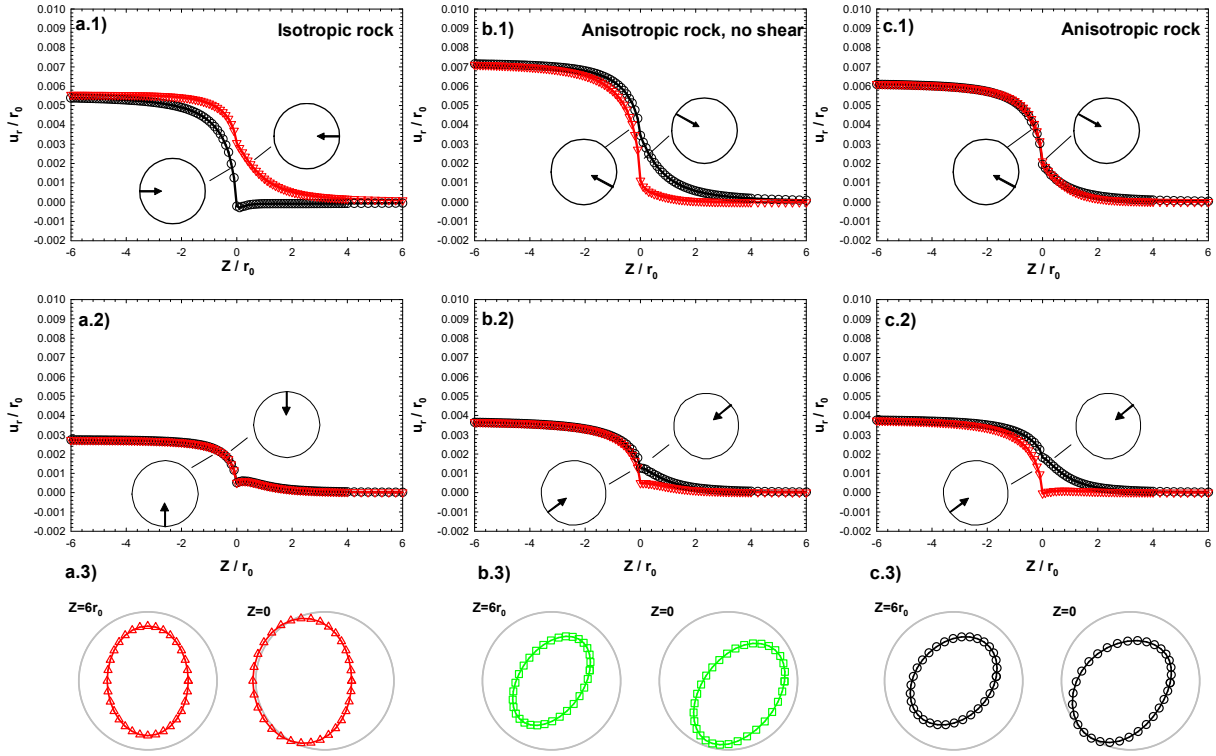

Figure 12.8 Radial displacements near the face for scenario 1 and Ψ=45°. (a) isotropic rock; (b) anisotropic rock with no far-field axial shear stress; and (c) anisotropic rock with complete stress field. (1) maximum radial displacements with distance from the face, both normalized with respect to the tunnel radius; (2) normalized minimum radial displacements with normalized distance from the face; (3) deformed tunnel cross section far-behind the face (i.e. at $6r_0$ behind the face, $Z=6r_0$), and at the face ($Z=0$). The deformed cross sections are amplified 75 times far-behind the face and 200 times at the face.

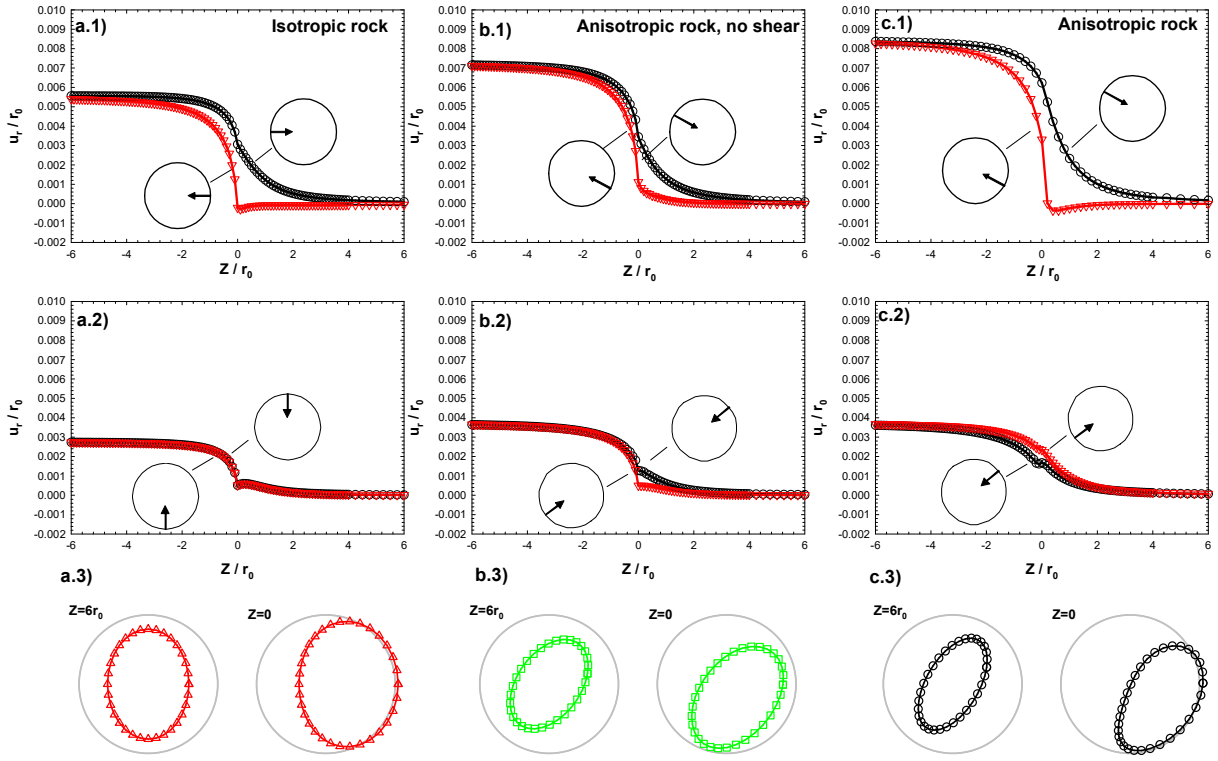

Figure 12.9 Radial displacements near the face for scenario 2 and Ψ=45°. (a) isotropic rock; (b) anisotropic rock with no far-field axial shear stress; and (c) anisotropic rock with complete stress field. (1) maximum radial displacements with distance from the face, both normalized with respect to the tunnel radius; (2) normalized minimum radial displacements with normalized distance from the face; (3) deformed tunnel cross section far-behind the face (i.e. $6r_0$ behind the face, $Z=6r_0$), and at the face ($Z=0$). The deformed cross sections are amplified 75 times far-behind the face and 200 times at the face.

Figure 12.8(a) shows the radial displacements for the isotropic rock mass in scenario 1 when Ψ=45°. The maximum radial displacements occurred at the springlines and the minimum radial displacements at the crown and invert. Far-behind the face, the deformed cross section was symmetric; however, near the face, the radial displacements were asymmetric. The tunnel cross-section translated horizontally towards the left springline at the face, as shown in figure 12.8(a3). Note that pronounced asymmetric deformations occurred at the springlines, while the radial displacements at the crown and at the invert were symmetric (note that the vertical is the axis of anti-symmetry of the axial displacements; thus, the maximum axial displacements occur at the springlines). Figure 12.8b shows the radial displacements for the tunnel in anisotropic rock mass with no far-field axial shear stress. Far-behind the face, as shown in Figure 12.8(b3), the radial

displacements at the tunnel perimeter were symmetric about an inclined axis and asymmetric near the face. At the face, the tunnel cross-section translated downwards and towards the right springline. The maximum radial displacements were highly asymmetric near the face while the minimum radial displacements were slightly asymmetric. The radial displacements near the face for the tunnel in anisotropic rock with full stress field are shown in figure 12.8(c). Similar to the other cases, the radial displacements were asymmetric near the face and symmetric far-behind the face. The tunnel cross-section translated downwards and towards the left springline near the face. Note that, different from the other cases (i.e. isotropic rock and anisotropic rock with no shear), the maximum radial displacements were almost symmetric near the face, while the minimum radial displacements were highly asymmetric. The radial displacements were smaller for the tunnel in anisotropic rock with full stress field than in anisotropic rock with no far-field axial shear stress. The asymmetric radial displacements produced by the far-field axial shear stress (i.e. translation towards the left springline) and those produced by the rock anisotropy (i.e. translation downwards and towards the right springline) compensate each other in scenario 1.

Figure 12.9(a) shows the radial displacements near the face for the tunnel in isotropic rock in scenario 2 with Ψ=45°. Far-behind the face, the radial displacements were the same as in scenario 1. Near the face, the tunnel cross-section translated towards the right springline (opposite direction than in scenario 1). This occurred because the direction of the anti-symmetric axial displacements is related to the direction of tunnel translation near the face. Since the case "anisotropic rock, no shear" neglects the far-field axial shear stress, Figure 12.9(b) is exactly the same as Figure 12.8(b) because the only difference between scenarios 1 and 2, when Ψ =45°, is the direction of the far-field axial shear stress. Figure 12.9(c) shows the radial displacements near the face for the tunnel in anisotropic rock with full stress field. The maximum radial displacements were highly asymmetric near the face, while the minimum radial displacements were slightly asymmetric. The radial displacements were larger for the tunnel in anisotropic rock with full stress field than in anisotropic rock with no far-field axial shear stress. At the face, as shown in figure 12.9(c3), the tunnel cross-section translated downwards and towards the right springline. The asymmetric deformations near the face produced by the far-field axial shear stress and by the rock anisotropy supplemented each other, producing more pronounced asymmetric deformations near the face and larger ground deformations.

12.4 Conclusion

The deformation patterns and the 3D face effects on misaligned tunnels in isotropic and anisotropic rock masses were investigated in this paper. 3D FEM modelling was conducted to analyze different orientations of the tunnel axis with respect to the major horizontal stress in isotropic and anisotropic rock masses. For comparison purposes, the stiffness of the isotropic rock mass was the average stiffness of the anisotropic rock mass.

In isotropic elastic rock, the far-field axial shear stresses did not affect the radial deformations far-behind the face of an unsupported tunnel (Vitali et al. 2018, 2019a, 2019b). The radial displacements were larger when the tunnel was aligned with the minor horizontal stress (Ψ=90°) and smaller when the tunnel was aligned with the major horizontal stress (Ψ=0°). The axial displacements were the largest when Ψ=45°, because, for this orientation, the far-field axial shear stress was maximum. The axis of anti-symmetry was vertical; thus, the maximum axial displacements occurred at the springline. Near the face, the far-field axial shear stress produced asymmetric radial displacements; these extended from four tunnel radii ahead of the face to four tunnel radii behind the face. At the face, the tunnel cross-section translated horizontally towards the springline; thus, the radial displacements at the springlines were asymmetric but they were symmetric at the crown and invert. The asymmetric radial displacements were related to the anti-symmetric axial displacements; that is, the largest asymmetry on the radial displacements occurred at the springlines (horizontal direction), which was where the axial displacements were maximum; and no asymmetric radial displacements occurred where the axis of anti-symmetry was located (at the crown and invert, in the vertical direction). Far-behind the face, where the axial displacements were not constrained, the radial displacements were symmetric and the axial displacements, anti-symmetric.

Tunnels in transversely anisotropic elastic ground misaligned with the geostatic principal stress directions and with the axes of material anisotropy are substantially more complex than tunnels not aligned with the geostatic principal stresses in isotropic elastic ground. When the tunnel is misaligned with the principal directions of material anisotropy, the axial shear stresses are coupled with the in-plane deformations (i.e. the compliance matrix is fully populated, Vitali et al. 2020a); thus, the far-field axial shear stresses affect the radial deformations far-behind the face. Misaligned tunnels in anisotropic rock were explored for two scenarios: major horizontal stress aligned with the rock structure (scenario 1); and minor horizontal stress aligned with the rock

structure (scenario 2). For scenario 1, the radial displacements were larger when the tunnel was aligned with the major horizontal stress (Ψ=0°) and were smaller when the tunnel was aligned with the minor horizontal stress (Ψ=90°). This may not be expected considering the recommendation of aligning the tunnel with the major principal stress (Goodman, 1989). The reason for this behavior is that, given that the largest rock mass stiffness was parallel to the rock structure, when the major horizontal stress was aligned with the rock structure (i.e. scenario 1), the larger deformations that should occur with the larger stresses were reduced due to the larger stiffness of the rock mass. On the other hand, for scenario 2, the radial displacements were substantially larger when the tunnel was aligned with the minor horizontal stress (Ψ=90°) than when the tunnel was aligned with the major horizontal stress (Ψ=0°). This is expected because, for scenario 2 where the minor horizontal stress is aligned with the rock structure, the larger stresses were applied along the direction of smaller stiffness, thus producing larger deformations. To investigate the influence of the far-field axial shear stress, the misaligned tunnels in anisotropic rock were analyzed neglecting the far-field axial shear stress. The presence of the far-field axial shear stress reduced the radial and the axial displacements in scenario 1 and increased them in scenario 2. In scenario 1, the far-field axial shear stress and the rock anisotropy produced anti-symmetric axial displacements in opposite directions, compensating each other; thus, the ground deformations around the tunnel were reduced. In scenario 2, the anti-symmetric axial displacements produced by the rock anisotropy and by the far-field axial shear stress were in the same direction; thus, those axial displacements supplemented each other, increasing the ground deformations.

The deformations near the face were investigated for scenarios 1 and 2 when Ψ=45°. When the tunnel made 45° with the major horizontal stress towards the minor horizontal stress, the tunnels in scenarios 1 and 2 had the same orientation with respect to the rock structure, had the same far-field horizontal, vertical and axial stresses, and the same far-field axial shear stress but with opposite direction; thus, the only difference between scenarios 1 and 2, when Ψ=45°, is the direction of the far-field axial shear stress. In addition, a tunnel in anisotropic rock mass with no far-field axial shear stress was analyzed to assess the influence of the far-field axial shear stress. Near the face, highly asymmetric radial displacements were observed. The ground deformations for scenario 2 were substantially larger than for scenario 1. In scenario 1 (major horizontal stress aligned with the rock structure), the asymmetric radial displacements near the face produced by

the far-field axial shear stress and by the rock anisotropy compensated each other, while those asymmetric deformations supplemented each other in scenario 2.

The large differences observed between scenarios 1 and 2 highlight the importance of the orientation of the geostatic principal stresses with respect to the rock mass structural planes. Further, for the selected rock mass properties, geostatic stresses and the scenarios explored, the ground deformations were generally larger and more asymmetric near the face for misaligned tunnels in anisotropic rock than in isotropic rock. The results presented in this paper highlight the importance of considering the anisotropic properties of the rock mass as well as the full geostatic stress field; thus, 3D FEM modeling is needed for the design of misaligned tunnels and caverns in anisotropic rock masses.

Acknowledgments

The research is being partially supported by the research funding agency of Brazilian government CNPq ("Conselho Nacional de Desenvolvimento Cientifico"). The authors acknowledge the support from CNPq and also Midas company, which kindly provided the license of Midas GTX NX software, used in the present work.

12.5 References

Armand, G., Noiret, A., Zghondi, J., & Seyedi, D. M. (2013). Short- and long-term behaviors of drifts in the Callovo-Oxfordian claystone at the Meuse/Haute-Marne Underground Research Laboratory. Journal of Rock Mechanics and Geotechnical Engineering, 5(3), 221–230. https://doi.org/10.1016/j.jrmge.2013.05.005

Brown, E. T., & Hoek, E. (1978). Trends in relationships between measured in-situ stresses and depth. International Journal of Rock Mechanics and Mining Sciences, 15(4), 211–215. https://doi.org/10.1016/0148-9062(78)91227-5

Goodman, R. E. (1989). Introduction to rock mechanics. https://doi.org/10.1016/0148-9062(81)90521-0

Haimson, B. C.; Lee, M. Y.; Song, I. (2003). Shallow hydraulic fracturing measurements in Korea support tectonic and seismic indicators of regional stress. International Journal of Rock Mechanics and Mining Sciences, 40(7–8), 1243–1256. https://doi.org/10.1016/S1365-1609(03)00119-9

McGarr, a, & Gay, N. C. (1978). State of Stress in the Earth's Crust. Ann. Rev. Earth Planet. Sci., 6, 405–436.

Schubert W, Budil A., 1995. The importance of longitudinal deformation in tunnel excavation. In: Proceedings of 8th ISRM Congress on Rock Mechanics:1411–1414.

Schubert P, Klopčič J, Štimulak A, Ajdič I, Logar J., 2005. Analysis of characteristic deformation patterns at the Trojane tunnel in Slovenia. Felsbau, 23(5):25-30.

Vitali, O. P. M.; Celestino; Bobet, A. (2017). 3D finite element modelling optimization for deep tunnels with material nonlinearity. Underground Space, 3(2), 125–139. https://doi.org/10.1016/j.undsp.2017.11.002

Vitali, O. P. M.; Celestino; Bobet, A. (2018). Analytical solution for tunnels not aligned with geostatic principal stress directions. Tunnelling and Underground Space Technology, 82: 394–405. https://doi.org/10.1016/j.tust.2018.08.046

Vitali, O. P. M.; Celestino; Bobet, A. (2019a). Shallow tunnel not aligned with the geostatic principal stress directions. In: Proceedings of Geo-Congress2019, GSP 313:214-222. https://ascelibrary.org/doi/10.1061/9780784482155.023

Vitali, O. P. M.; Celestino; Bobet, A. (2019b). Shallow tunnels misaligned with geostatic principal stress directions: analytical solution and 3D face effects. Tunnelling and Underground Space Technology. 89: 268-283. https://doi.org/10.1016/j.tust.2019.04.006

Vitali, O. P. M.; Celestino; Bobet, A. (2019c). Progressive failure due to tunnel misalignment with geostatic principal stresses. In: Proceedings of ISRM 14th International Congress on Rock Mechanics: 2292-2299.

Vitali, O. P. M.; Celestino; Bobet, A. (2020a). Analytical solution for a deep circular tunnel in anisotropic ground and anisotropic geostatic stresses. Manuscript under review for publication in a peer-reviewed journal.

Vitali, O. P. M.; Celestino; Bobet, A. (2020b). 3D face effects of tunnels misaligned with the principal directions of material and stress anisotropy. Manuscript under review for publication in a peer-reviewed journal.

Vitali, O. P. M.; Celestino; Bobet, A. (2020c). Tunnel misalignment with geostatic principal stress directions in anisotropic rock masses. Manuscript under review for publication in a peer-reviewed journal.

Wileveau, Y., Cornet, F. H., Desroches, J., & Blumling, P. (2007). Complete in situ stress determination in an argillite sedimentary formation. Physics and Chemistry of the Earth, 32(8–14), 866–878. https://doi.org/10.1016/j.pce.2006.03.018

Worotnicki G. 13 – CSIRO Triaxial Stress Measurement Cell. In: Rock testing and site characterization: principles, practice and projects. 1993, 329-394.

13. CONCLUSIONS

The main findings of the doctoral research are presented here. Note that each chapter has its own detailed conclusion; thus, the focus of this chapter is on the overall outcomes of the research.

13.1 Numerical modeling of tunnels

The research work involved an exhaustive numerical modeling campaign using the Finite Element Method (FEM). The numerical models were three-dimensional and non-linear in most cases. 3D numerical modelling of tunnels demands great computational effort, and this is probably the main reason why 3D modelling is hard to implement in engineering practice, despite recent advances on hardware and software. However, there is a tendency towards 3D FEM modeling in Engineering Practice. The 3D modelling of tunnels requires a refined mesh near the tunnel and several phases to simulate the construction sequence. Soils and rocks are better represented by elastoplastic models, which may require several iteration steps to reach convergence. Thus, 3D modelling of tunnels may be very time consuming even using modern computers and well-developed FEM software. For instance, Do et al., (2014) reported that a 3D tunnel model with 1,100,000 nodes required 2 weeks to run in a 2.67GHz core i7 RAM 24G computer.

In the research conducted, an extensive 3D numerical modeling campaign was conducted to optimize 3D FEM models for tunnels considering different levels of material nonlinearity (i.e. size of the plastic zone near the tunnel). Optimization here means determination of the smallest model size with the coarsest mesh to achieve the desired accuracy. Since the research required running many 3D models, some of them with high material nonlinearity, it was important to do preliminary work to reduce the processing time and guarantee accurate results. A paper was written with the results obtained and was published in a peer-reviewed journal (Vitali et al. 2017). For 3D nonlinear FEM analyses, it was observed that a coarser mesh with 2^{nd} order elements (i.e. quadratic interpolation) provided more accurate results than a finer mesh with 1^{st} order elements (i.e. linear interpolation) with the same number of nodes. Thus, 2^{nd} order elements are recommended. The size of the FEM model is heavily dependent on the size of the plastic zone developed around the

tunnel. The larger the plastic zone, the larger the model must be. Thus, recommendations for model dimensions based on linear-elasticity may lead to large errors in highly nonlinear analyses.

Tunnels can be divided into deep and shallow according to their proximity to the ground surface. Deep tunnels can be modeled by placing the boundaries far from the opening and assuming that the influence of the self-weight increasing with depth (i.e. gravity loading) can be neglected, i.e. the stress field is not a function of depth (Bobet, 2003). Shallow tunnels, on the other hand, are more complex, given that the presence of the ground surface needs to be accounted for and gravity loading must be considered. Also, the bottom boundary of a shallow tunnel, when numerically modeled, strongly affects the vertical displacement field because of the unloading produced by removal of the weight of the material inside the opening (such unloading is reflected as a singularity when the problem is solved with the Theory of Elasticity). The tunnel excavation removes weight from the ground, and so an upward unbalanced force appears, causing upward vertical movements to the ground. It is denominated in the literature as "*buoyancy*". The magnitude of those upward displacements depends on the distance from the tunnel to the bottom boundary of the model – the deeper the model, the larger are the upward displacements. Obviously, this is physically unrealistic, yet mathematically correct. This problem was analyzed using 2D and 3D FEM numerical models and the analytical solution developed by Verruijt & Booker (2000). It was found that the importance of the location of the bottom boundary decreased when the ground stiffness increased with depth (which is expected even for uniform geomaterials due to the increase of confinement). A paper was written on this issue and was published in a peer-reviewed journal (Vitali et al. 2019a)

The New Austrian Tunneling Method (NATM, Rabcewics, 1964) has been successfully used worldwide. Most of the tunnels in Sao Paulo, Brazil, have been excavated following the NATM principles. One of these tunnels, the Paraiso tunnel, is a well-documented case by Parreira et al. (1991). This tunnel was excavated in residual porous soil, which is a soil typical of Tropical regions, and had large surface settlements. Ground deformation control is of utmost importance on tunneling in urban environments to avoid damage to nearby buildings and facilities. To investigate strategies to minimize ground deformations, the Paraiso tunnel was analyzed using a 3D FEM nonlinear analysis. An excellent match between numerical and field data was obtained. With the model thus verified, different construction sequences were simulated numerically using 3D nonlinear FEM analysis; more specifically, the impact of different construction and support

strategies on the surface settlements was assessed. A paper was written with the results and was submitted for publication in a peer-reviewed journal (Vitali at al. 2020a). It was observed that the construction sequence had strong influence on the ground deformations induced by tunneling. The numerical results showed that: (1) reducing the unsupported span and increasing the stiffness of the tunnel liner effectively reduced the induced ground deformations; (2) the benches were highly efficient to reduce the ground deformations ahead of the face and to increase the face stability; (3) the early closure of the tunnel liner reduced the ground deformations behind the face and; (4) a umbrella system made of continuous reinforced jet grouting columns along the tunnel perimeter reduced significantly the ground deformations around the tunnel; however, the drilling and grouting operations could cause large ground deformations, that could be even larger than those from the tunnel excavation itself, as reported by Farrell et al. 2006. Note that 2D tunnel analyses are not able to capture the influence of important construction aspects such as the stiffness of the liner, the presence of the benches and the early or late closure of the tunnel liner. Thus, 3D FEM modeling should be conducted for more reliable tunnel analysis.

13.2 Tunnels misaligned with the geostatic principal stress directions in isotropic ground

When the axis of the tunnel is not aligned with one of the directions of the far-field principal stresses, anti-symmetric axial displacements around the tunnel are produced. The complete far-field stress is decomposed into stresses acting on the cross section of the tunnel and axial stresses; the latter include both axial and shear stresses. Four papers addressing the issue of tunnels not aligned with the principal geostatic stresses were written (Vitali et al. 2018, 2019b, 2019c, 2019d). With the assumption of elasticity, a complete solution was obtained by the addition of the effects of the stress-decomposition. That is, for a deep circular tunnel, the Kirsch or Einstein-Schwartz solutions (Kirsch, 1898; Einstein and Schwartz, 1979) can be used to obtain the ground and liner, if present, stresses and displacements due to the stresses acting on the cross section of the tunnel; for an unsupported shallow tunnel, the solution is given by Verruijt & Booker (2000). New analytical solutions were found to calculate the axial shear stress and the axial displacement fields around a circular tunnel for supported and unsupported deep tunnels and for unsupported shallow tunnels, with the assumption that all materials remain within their elastic regime. The solutions were verified by comparing results with 3D FEM simulations. Excellent agreement between numerical and analytical results were obtained (Vitali et al. 2018 and 2019b).

Far-behind the face, the anti-symmetric axial displacements associated with the far-field shear did not affect the radial displacements on unsupported tunnels in isotropic elastic ground. But near the face, the anti-symmetric axial displacements were partially constrained by the tunnel face; consequently, the radial displacements near the face were asymmetric. It was observed that the asymmetric radial displacements near the face could be decomposed into a rigid body displacement of the tunnel cross-section and into anti-symmetric radial displacements along the tunnel perimeter. As a consequence of the asymmetric radial deformations near the face, the stresses near the face were also asymmetric. Those asymmetries near the face could affect the ground deformations far-behind the face in an elastoplastic ground or if a liner was installed near the face. In elastoplastic ground, the plastic zone around the tunnel could be asymmetric as a result of the asymmetric stresses near the face. If the tunnel is supported, the asymmetric radial displacements near the face produce an asymmetric loading on the tunnel liner; thus, the liner internal forces are asymmetric. Those results show that the far-field axial shear stress and the 3D face effects strongly affect the ground deformations around the tunnel. 2D tunnel analysis neglects the far-field axial shear stresses and the 3D face effects; thus, the asymmetric deformations are missed and the ground deformations may be underpredicted. Therefore, for the design of tunnels in rock masses with high geostatic stress anisotropy, 3D FEM analysis is recommended.

A well-documented experimental tunnel in the Underground Research Laboratory (URL) in Canada (Martin, 1997) was chosen to investigate the effects of tunnel misalignment with the geostatic principal stresses. A paper was written with these results (Vitali et al. 2019d). This URL was located in a massive granite rock mass with highly anisotropic stresses. The experimental tunnel was excavated aligned with the intermediate principal stress. An advanced constitutive model, suitable to reproduce the progressive failure of massive rock masses, was adopted, i.e. the Cohesion Weakening and Frictional Strengthening model (Renani and Martin, 2018). The 3D FEM model accurately reproduced the size and shape of the V-notched failed zone at the tunnel crown and the radial and tangential stresses near the tunnel. The good agreement between numerical results and field data validated the numerical model. To investigate the effects of the tunnel misalignment, a numerical model of the tunnel making an angle of 45° with the intermediate principal stress with the major horizontal stress was built. The same FEM mesh, boundary conditions, rock mass properties and geostatic stress field used were adopted. Anti-symmetric axial displacements were induced around the tunnel, and asymmetric radial displacements occurred near

the face. The failed zone around the misaligned tunnel was asymmetric, with the plastic zone extending to one side of the springline. The result suggests that asymmetric spalling at the tunnel walls, which is commonly observed in tunnels in massive rock masses, may be caused by the misalignment of the tunnel with the principal stress directions.

13.3 Tunnels misaligned with the geostatic principal stress directions in anisotropic ground

Rock masses may present remarked fabric structure; thus, pronounced anisotropic properties are expected. Further, alignment of the tunnel with one of the principal directions of rock mass anisotropy is unlikely. Tunnels in anisotropic ground misaligned with the geostatic principal stress directions and with the axes of material anisotropy are substantially more complex than tunnels not aligned with the principal stresses in isotropic ground. When the tunnel is misaligned with both principal directions of material and stress anisotropy, the axial shear stresses are coupled with the in-plane deformations of the tunnel (i.e. the compliance matrix is fully populated); thus, the far-field axial shear stresses affect the radial deformations far-behind the face. Four papers were written on misaligned tunnels in anisotropic rock masses (Vitali et al. 2020b, 2020c, 2020d and 2020e). An analytical solution was developed for unsupported tunnels in a general far-field stress state in a full anisotropic elastic ground. The analytical results were compared with the numerical results from a 3D FEM analysis for several complex scenarios. Numerical and analytical solutions matched. A Matlab code to solve the analytical solution for transversely anisotropic elastic rock mass was written and was provided in Vitali et al. 2020b.

The misalignment of the tunnel with the principal material directions, even for isotropic geostatic stresses, produced anti-symmetric axial displacements around the tunnel perimeter. Near the face, asymmetric radial displacements occurred because of the anti-symmetric axial displacements being constrained by the tunnel face. Since anti-symmetric axial displacements are produced by both misalignments (i.e. with the geostatic principal stresses and with the axes of material anisotropy), the orientation of the principal geostatic stresses with respect to the axes of material anisotropy plays an important role. If the tunnel is not aligned with the geostatic principal stresses and with the principal directions of material anisotropy, the far-field axial shear stresses, depending on the orientation of the tunnel, may increase or decrease the anti-symmetric axial displacements induced, in turn, by the rock anisotropy. Asymmetric deformations around tunnels

in anisotropic rock masses are commonly observed (Schubert and Budil 1995, Schubert et al. 2005), but, so far, the sources of the asymmetric deformations have not been clearly identified. It is possible that those asymmetric deformations were associated with the tunnel misalignment with the principal directions of stresses and material anisotropy.

13.4 Future developments

A natural continuation of this research is to investigate 3D face effects and develop new analytical solutions for misaligned tunnels in isotropic and anisotropic rock masses considering water seepage, seismic loading and the support with ground anchors. It would be very interesting to look into tunnels not aligned with the geostatic principal stresses and with the axes of material anisotropy considering sophisticated constitutive models for anisotropic rock masses and anisotropic flow with consolidation effects (excess pore pressure generation and its dissipation with time). High quality field and laboratory data are available for the experimental tunnels of the Underground Research Laboratory in France (ANDRA). Tunnels were built with different orientations with respect to the principal stress directions. The field data showed that the influence of the tunnel orientation with respect to the principal stress directions was remarkable. The data available for the ANDRA's tunnels could be used to investigate misaligned tunnels with water seepage and pore pressure dissipation with time.

13.5 References

Do, N. A., Dias, D., Oreste, P., & Djeran-Maigre, I. (2014). Three-dimensional numerical simulation of a mechanized twin tunnels in soft ground. Tunnelling and Underground Space Technology, 42, 40–51. https://doi.org/10.1016/j.tust.2014.02.001

Bobet, A. (2003). Effect of pore water pressure on tunnel support during static and seismic loading. Tunnelling and Underground Space Technology, 18(4), 377–393. https://doi.org/10.1016/S0886-7798(03)00008-7

Einstein, H., & Schwartz, C. (1979). Simplified analysis for tunnel supports. ASCE J Geotech Eng Div, 105(GT4), 499–518.

Farrell R, Mair R, Sciottic A, Pigorinic A, 2014. Building response to tunneling. Soils and Foundation; 54(3):269–279.

Kirsch, G. (1898). Die theorie der elastizitat und die bedurfnisse der festigkeitslehre. Veit. Ver. Deut. Ing., 42, 497–807.

Martin, C. D. (1997). Seventeenth Canadian Geotechnical Colloquium: The effect of cohesion loss and stress path on brittle rock strength. *Canadian Geotechnical Journal*, 34(5): 698-725 https://doi.org/10.1139/t97-030

Parreira, A. B. (1991). *Analysis of shallow tunnels in soil. The NATM Paraíso Tunnel at Paulista Avenue in São Paulo City*. Ph.D. dissertation, Catholic Univ. of Rio de Janeiro, Rio de Janeiro, Brazil (in Portuguese).

Rabcewicz L.V. (1964/1965) The new Austrian tunnelling method. Water Power, Part 1: November 1964, 571-515, Part 2: January 1965, 19-24.

Renani R., H., & Martin, C. D. (2018). Cohesion degradation and friction mobilization in brittle failure of rocks. International Journal of Rock Mechanics and Mining Sciences, 106, 1–13. https://doi.org/10.1016/j.ijrmms.2018.04.003

Schubert W, Budil A., 1995. The importance of longitudinal deformation in tunnel excavation. In: Proceedings of 8th ISRM Congress on Rock Mechanics:1411–1414.

Schubert P, Klopčič J, Štimulak A, Ajdič I, Logar J., 2005. Analysis of characteristic deformation patterns at the Trojane tunnel in Slovenia. Felsbau, 23(5):25-30.

Verruijt, A., & Booker, J. R. (2000). Complex variable analysis of Mindlin' s tunnel problem, in: Proceedings of Developments in Theoretical Geomechanics - The John Booker Memorial Symposium. Rotterdam; Jannuary, 2000.

Vitali, O. P. M.; Celestino; Bobet, A. (2017). 3D finite element modelling optimization for deep tunnels with material nonlinearity. Underground Space, 3(2), 125–139. https://doi.org/10.1016/j.undsp.2017.11.002

Vitali, O. P. M.; Celestino; Bobet, A. (2019a). Buoyancy effect on shallow tunnels. International Journal of Rock Mechanics and Mining Sciences. 114(2), 1–6. https://doi.org/10.1016/j.ijrmms.2018.12.012

Vitali, O. P. M.; Celestino; Bobet, A. (2020a). Construction strategies for a NATM tunnel in Sao Paulo, Brazil, in residual soil. Manuscript under review for publication in a peer-reviewed journal.

Vitali, O. P. M.; Celestino; Bobet, A. (2018). Analytical solution for tunnels not aligned with geostatic principal stress directions. Tunnelling and Underground Space Technology, 82: 394–405. https://doi.org/10.1016/j.tust.2018.08.046

Vitali, O. P. M.; Celestino; Bobet, A. (2019b). Shallow tunnels misaligned with geostatic principal stress directions: analytical solution and 3D face effects. Tunnelling and Underground Space Technology.89: 268-283. https://doi.org/10.1016/j.tust.2019.04.006

Vitali, O. P. M.; Celestino; Bobet, A. (2019c). Shallow tunnel not aligned with the geostatic principal stress directions. In: Proceedings of Geo-Congress2019, GSP 313:214-222. https://ascelibrary.org/doi/10.1061/9780784482155.023

Vitali, O. P. M.; Celestino; Bobet, A. (2019d). Progressive failure due to tunnel misalignment with geostatic principal stresses. In: Proceedings of ISRM 14th International Congress on Rock Mechanics: 2292-2299.

Vitali, O. P. M.; Celestino; Bobet, A. (2020b). Analytical solution for a deep circular tunnel in anisotropic ground and anisotropic geostatic stresses. Manuscript under review for publication in a peer-reviewed journal.

Vitali, O. P. M.; Celestino; Bobet, A. (2020c). 3D face effects of tunnels misaligned with the principal directions of material and stress anisotropy. Manuscript under review for publication in a peer-reviewed journal.

Vitali, O. P. M.; Celestino; Bobet, A. (2020d). Tunnel misalignment with geostatic principal stress directions in anisotropic rock masses. Manuscript under review for publication in a peer-reviewed journal.

Vitali, O. P. M.; Celestino; Bobet, A. (2020e). Deformation patterns and 3D face effects of tunnels misaligned with the geostatic principal stresses in isotropic and anisotropic rock masses. 54th US Rock Mechanics /Geomechanics Symposium (ARMA 2020).